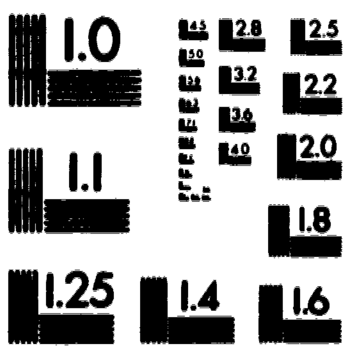
1.0
2.8
2.5
3.2
2.2
3.6
4.0
2.0
1.1
1.8
1.25
1.4
1.6

UNIVERSITY OF ALBERTA

A MAGNETOTELLURIC STUDY IN THE REGION OF THE INTERSECTION OF THE MESSEJANA FAULT AND THE FERREIRA-FICALHO OVERTHRUST IN PORTUGAL

BY

©

ANTONIO CORREIA

A thesis submitted to the Faculty of Graduate Studies and Research in partial fulfillment of the requirements for the degree of DOCTOR OF PHILOSOPHY

IN

GEOPHYSICS

DEPARTMENT OF PHYSICS

EDMONTON, ALBERTA

SPRING 1994

ISBN 0-612-11181-4

UNIVERSITY OF ALBERTA

RELEASE FORM

NAME OF THE AUTHOR: Antonio Correia

TITLE OF THE THESIS: A magnetotelluric study in the region of the intersection of the Messejana fault and the Ferreira-Ficalho overthrust in Portugal.

DEGREE: Doctor of Philosophy

YEAR THIS DEGREE GRANTED: 1994

Antonio Correia

DEPARTMENT OF PHYSICS

UNIVERSITY OF EVORA

7000 EVORA, PORTUGAL

DATED: JANUARY 12, 1994.

UNIVERSITY OF ALBERTA

FACULTY OF GRADUATE STUDIES AND RESEARCH

The undersigned certify that they have read, and recommend to the Faculty of Graduate Studies and Research for acceptance, a thesis entitled A MAGNETOTELLURIC STUDY IN THE REGION OF THE INTERSECTION OF THE MESSEJANA FAULT AND THE FERREIRA-FICALHO OVERTHRUST IN PORTUGAL submitted by ANTONIO CORREIA in partial fulfillment of the requirements for the degree of DOCTOR OF PHILOSOPHY in GEOPHYSICS.

F.W. Jones

E.R. Kanasewich

J.-C. Mareschal

S.S. Sheinin

D.R. Schmitt

R.D. Morton

DATE: January 7, 1994

DEDICATION

To my father, who was always unfailing in his support for my work, but who, unfortunately, was unable to see the completion of this project.

ABSTRACT

A magnetotellric (MT) survey was performed in southern Portugal in the region of the intersection of the Messejana fault and the Ferreira-Ficalho overthrust where a geothermal anomaly with heat flow density values higher than 200 mW/m² has been reported to exist. During the field work 34 MT sites were occupied. The data from the 34 sites were processed using tensorial techniques to give the crustal electrical resistivity distribution. The results of the MT survey are compared with other geophysical surveys that were previously performed in southern Portugal (seismic, gravimetric, aeromagnetic and geothermal) and interpretation of the available data indicates that the geothermal anomaly is shallow and is probably a result of fluid flow along zones that coincide with the Messejana and Vidigueira faults and the Ferreira-Ficalho overthrust. Furthermore, one-dimensional geothermal modelling shows that the values of the surface heat flow density reported for the area of the geothermal anomaly should not be used to extrapolate temperature to middle and/or lower crustal levels.

A one-dimensional (1D) inversion technique is applied to the data obtained at the 34 MT sites and the resulting 1D models are used to construct two-dimensional (2D) electrical models along certain profiles and a three-dimensional (3D) electrical model of the study area. The results of the 2D and 3D modelling show good agreement with the field data and

clearly indicate that the use of MT profiling to interpret MT data should be used carefully if 3D geological structures are suspected to exist in the study area. The results of the electromagnetic modelling also indicate that the use of 1D inversion models and the Berdichevsky invariant provided good approximations for the purpose of constructing and interpreting the 2D and 3D electrical models of the study area from the field data.

The MT survey shows that the Ossa-Morena and South-Portuguese zones have quite different electrical characteristics and two low electrical resistivity regions with different origins were delineated within the study area. The low electrical resistivity zone in the north appears to be the result of fluid flow while the zone in the south appears to be related to the existence of carbon in the geological formations.

An attempt to model the electromagnetic static shift effect and quantify it did not give good results. The results demonstrate that distinguishing between static shift effects due to small local inhomogeneities and variations in the apparent electrical resistivity curves due to true but small scale structures is not a simple matter. New modelling algorithms must be developed in order to quantify the static shift effect so that corrections for it can be made with confidence.

ACKNOWLEDGMENTS

This work is the result of an interactive collaboration between the author and many people and institutions.

First of all I would like to thank Dr. F.W. Jones for his support, help and friendship.

I also would like to thank Dr. R. Hutton, G. Dawes, P. Jones and K. MacDonald for their help during the first stages of the work in Portugal and in Edinburgh, and M. Ertman and A. Kalvey for their friendship and help in computing matters.

I thank Dr. J.-M. Maillol and D. Cossu for all the good moments we spent together and I also express my gratitude to the group of friends that I had the pleasure to meet in Edmonton; their friendship made my stay in Canada a very good experience. I thank them all for what they have done for me and my family.

I also would like to thank the following institutions for their financial support during several stages of this work: The University of Évora, The University of Alberta, Empresa de Desenvolvimento Mineiro, Junta Nacional de Investigaçăo Cientifica and Fundaçăo Calouste Gulbenkian.

To my wife and son I thank for their unconditional support and for being there when I needed them.

Finally, I would like to remember Dr. R. Lambert whose help is recognized; unfortunately, he was not able to see the end of this work.

TABLE OF CONTENTS

LIST OF TABLES

LIST OF FIGURES

CHAPTER I

INTRODUCTION

1.1. Objectives of the study

Geothermal work carried out in Portugal since 1980 indicates that heat flow density (HFD) values higher than 160 mW/m^2 are found in the south-central region (Haenel and Staroste, 1988) in an area centered at about 38°10'N and 8°0'W (see Figure 1.1).

Regions with high HFD values generally show geothermal manifestations at the surface that result from geological and/or geophysical processes taking place in the Earth's crust. That is not the case in southern Portugal. In all other geophysical surveys performed in the region so far, there has been no indication of the cause of the geothermal anomaly, known as the Alentejo Geothermal Anomaly (AGA).

It is well established that temperature affects most of the physical parameters of rocks, and, in particular, the electrical conductivity or, its inverse, the electrical resistivity.

The fact that the bulk electrical conductivities of rocks increase with temperature suggests that electrical methods should be well suited to determine or infer the electrical structures of high HFD regions where high electrical conductivity anomalies (or low electrical resistivity anomalies) are expected to coincide with the high HFD anomalies. Electrical methods have been routinely used to investigate geothermal exploration targets with a reasonable degree of success (Martinez-Garcia, 1990).

With this in mind, a geoelectrical survey using the magnetotelluric (MT) method was performed over the AGA with the objectives of delineating its geoelectrical structure and understanding its geological and geophysical characteristics within the regional geological framework. This should provide some insight into the origin and evolution of the anomaly. At the same time, the survey constituted a feasability study in the sense that the region is geologically complex and the quality of data possible to obtain during the field work was not known. This latter aspect was particularly important because future MT work has been proposed for other areas in southern Portugal, which is a well known mining region. Furthermore, two-dimensional (2D) and three-dimensional (3D) geoelectrical models can be constructed from the MT survey data and these can be used to interpret the deep geological structure of the region and the AGA. This is the first such work for southern Portugal using MT methods.

One problem of considerable current interest in MT work is that of static shift. Although the spacings between the MT stations in this study is too large to allow any objective analysis of the static shift effect in the region of the AGA, a modelling procedure in three dimensions has

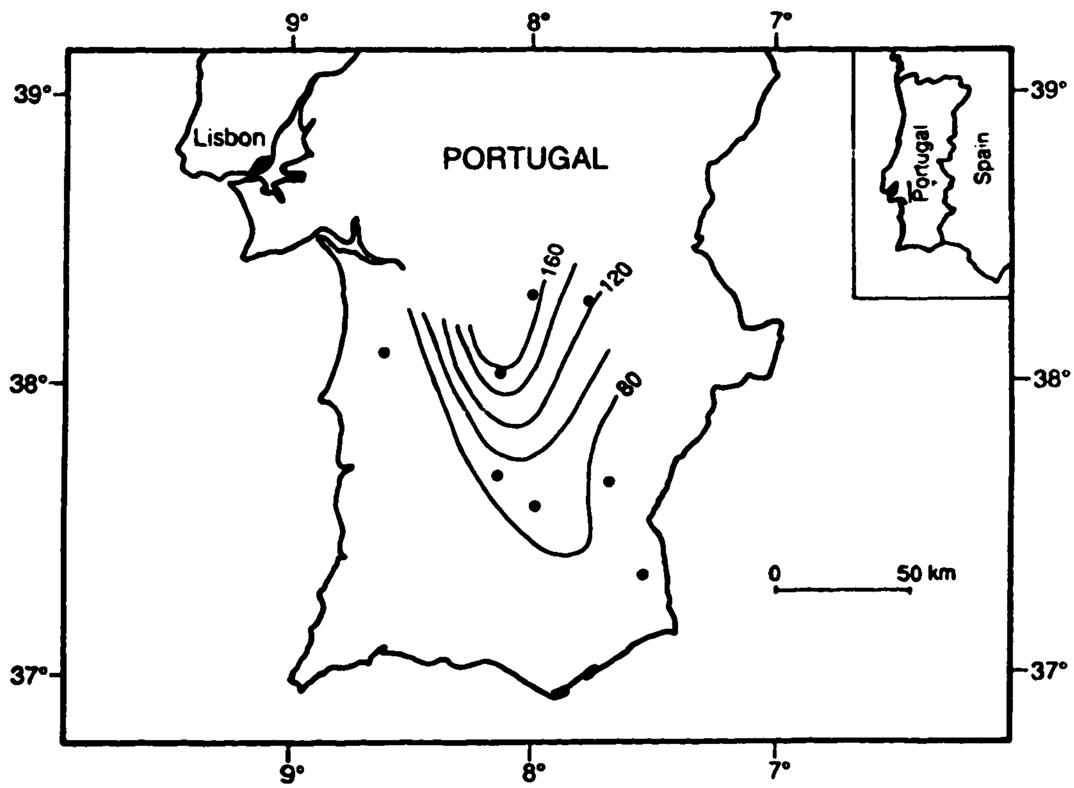

Fig. 1.1: Heat flow density for southern Portugal. Contours in mW/m² (redrawn from Haenel and Staroste, 1988).

been used to investigate the effect and the results are discussed in terms of the south-central Portugal MT survey.

1.2. Electrical properties of rocks

In MT prospecting the physical parameter of interest is the electrical resistivity (from now on called resistivity) or the electrical conductivity (from now on called conductivity) of the geological formations. The geophysical importance of the resistivity results from its relationship with other physical, compositional, and structural parameters. These, in turn, depend on other factors such as temperature, pressure, composition, oxygen fugacity, phase, porosity, permeability, fluid content, amount of melt, and others (Keller and Frischknecht, 1966; Shankland and Waff, 1974; Shankland, 1975; Duba, 1976; Parkhomenko, 1982).

The aim of the MT method, and in fact all other geoelectrical methods, is to determine the resistivity distribution in the Earth's subsurface. A wide range of possible phenomena occur that may enter into the interpretation of crustal and upper mantle resistivities. These include: aqueous solutions that exist in fractures, fissures, and pores in rocks; hydrated minerals, such as clay and serpentine; graphite; sulphur (Connerney et al., 1980; Shankland and Ander, 1983; Lee et al., 1983; Gough, 1986; Haak and Hutton, 1986); and partial melt (Schwarz et al., 1985). The interpretation in terms of one or more of the above phenomena in any situation and justification for the particular choice is difficult and, in some cases, leads to controversy (Jödicke, 1990).

Resistivity can also be determined in the laboratory using rock samples. However, such measured resistivity values may be 2 or 3 orders of magnitude larger than the values obtained in field surveys. The reason for these differences is that the laboratory conditions differ from "in situ" conditions, i. e., the rock samples may be partially or totally dehydrated and the sample temperatures may differ considerably from the "in situ" temperatures. In addition, the differences between the representative sample sizes leads to differences in the estimated resistivities (Shankland and Ander, 1983). Despite this, laboratory studies have shown that the single most important parameter affecting resistivity (or conductivity) is temperature. Its effect is, nevertheless, markedly different at low temperatures (a few hundred degrees Celsius) from its effect at high temperatures (higher than 800 degrees Celsius). At low temperatures, such as those found in the upper crust, electrical properties of rocks are essentially determined by the properties of the aqueous solutions that fill the fractures, fissures, or pores. In this case, solid conduction is negligible and liquid ionic conduction is the main conduction mechanism. On the other hand, at temperatures above 800 degrees Celsius, which are characteristic of the lower crust and upper mantle, solid conduction increases significantly and probably dominates liquid ionic conduction. Liquid ionic conduction is absent or very low because of the low porosity imposed by lithostatic pressure there. The main conduction mechanism in the lower crust and upper mantle is solid ionic or electronic conduction.

At high temperatures, experimental data have shown that in ionic crystals the relationship between resistivity (or conductivity) and temperature takes the form (Keller and Frischknecht, 1966; Parkinson, 1983):

$$\sigma = \frac{1}{\rho} = \sigma_e \exp\left(\frac{E_e}{kT}\right) + \sigma_i \exp\left(\frac{E_i}{kT}\right)$$

where σ and ρ are the conductivity and resistivity, respectively; σ_e and σ_i are limiting conductivities approached at very high temperatures for extrinsic (due to crystal defects and impurities) and intrinsic (due to thermal motion) conductivities, respectively; E_e and E_i are characteristic energies (known as activation energies) for extrinsic and intrinsic conductivity, respectively; k is Boltzmann's constant; and T is the absolute temperature. This relationship holds as a characteristic property of rocks at high temperatures and varies little from sample to sample. At low temperatures the relationship is highly variable for different samples of the same rock type. Electrical properties of rocks are comprehensively discussed by Collett and Katsube (1973), Olhoeft (1980), Parkhomenko (1982), and Keller (1987), and others.

1.3. General geology of the study area

According to Ribeiro et al.(1979), Julivert et al. (1980), and Munhá (1981), the core of the Iberian Peninsula is an Hercynian cratonic block, bordered to the northeast and southeast by segments of the Alpine belt (Pyrenean and Betic orogens) and to the northwest, west, and southwest by the Atlantic Ocean. The Hercynian belt outcrops largely in the western part of Iberia, forming what is known as the Hesperian or Iberian Massif; to the east it plunges gently under a Meso-Cenozoic platform cover. The Iberian Massif is crossed by Hercynian structures trending NW-SE and to the north describes an arc known as the Ibero-Armorican arc.

The Iberian Massif exhibits a longitudinal zonation, as in many other European Hercynian massifs, and is divided, from north to south, into five geotectonic units: Cantabrian, West-Asturian-Leonese, Central Iberian, Ossa-Morena, and South-Portuguese zones. These zones are generally separated by deep first order tectonic features.

The Iberian Hercynian belt also shows a fan-like pattern with steep structures in the core and outward vergences in the margins. In its southwest branch (the region of the MT study) the contact between the internal and external zones (corresponding to the Ossa-Morena and South-Portuguese zones) corresponds to a major overthrust known as

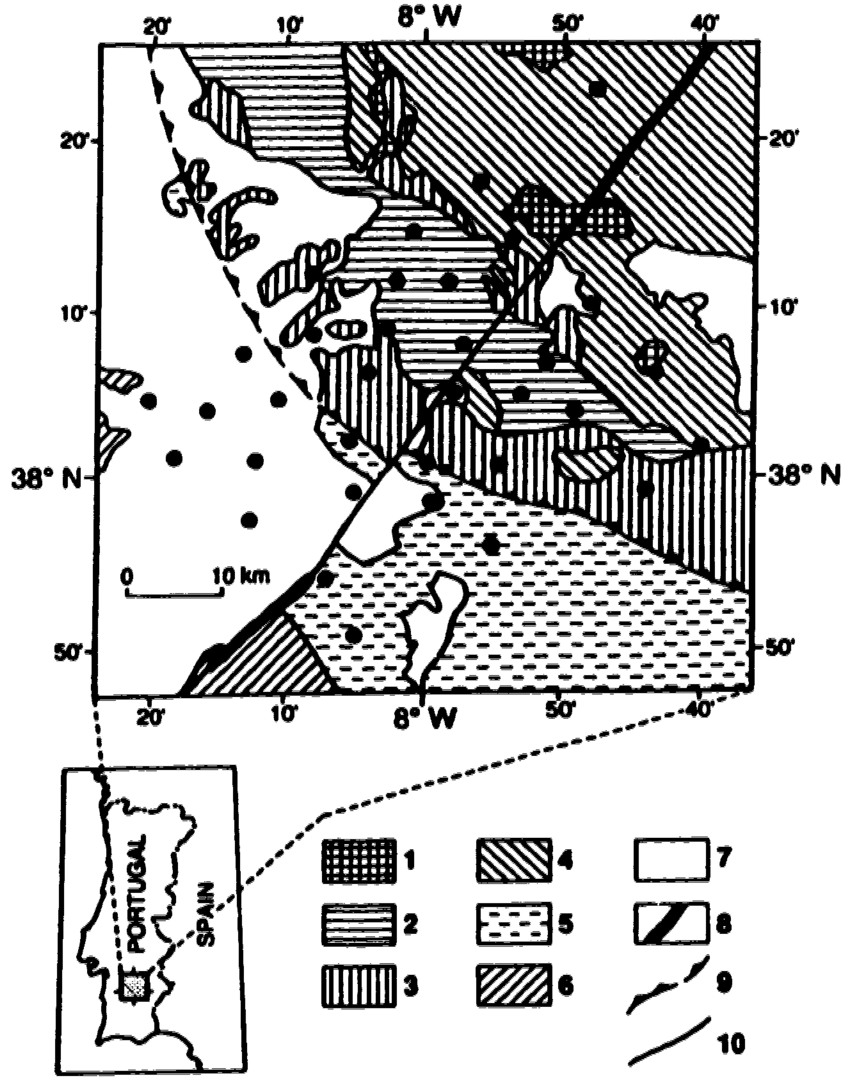

Fig. 1.2: Geological sketch of the study area. The dots represent the MT sites. 1-granite; 2-porphyry; 3-gabbro-diorite complex; 4-undifferentiated Precambrian rocks; 5-undifferentiated Devonian rocks; 6-undifferentiated Carboniferous rocks; 7-Cenozoic terranes; 8-doleritic dyke associated with the Messejana fault; 9-Ferreira-Ficalho overthrust; 10-Messejana fault. (redrawn from the Geological Map of Portugal, Geological Survey of Portugal, 1968).

the Ferreira do Alentejo-Ficalho overthrust (from now on called the Ferreira-Ficalho overthrust), which trends approximatelly NW-SE (see Figure 1.2).

The Ossa-Morena zone is characterized by Precambrian and Lower Paleozoic rocks showing intense deformation, and widespread plutonism and magmatism. As the Ferreira-Ficalho overthrust is approached from the NE, basic and ultra-basic rocks are more common than granitic rocks. On the other hand, the Upper Paleozoic is more fully developed in the South-Portuguese zone where there is little plutonism and the metamorphism is low grade; there are also some volcanic and sedimentary deposits that were deformed during the Hercynian orogeny.

The study area is also crossed by another major tectonic feature known as the Messejana fault. This left lateral strike-slip fault cuts and offsets, up to 4 km, Hercynian structures, and trends approximately NE-SW. The Messejana fault begins in the Atlantic Ocean, traverses the whole of southern Portugal, and disappears in Spain beneath Tertiary formations. Its origin seems to be related to the opening of the Atlantic Ocean in Early to Middle Triassic times (Schermerhorn et al., 1978). A doleritic dyke system was emplaced along the Messejana fault by a multiple intrusive process during Early and Middle Jurassic and possibly starting in late Triassic.

Figure 1.2 is a simplified geological map of the area where the magnetotelluric survey was performed. Also shown are the locations of the Messejana fault and the Ferreira-Ficalho overthrust, as well as the locations of the MT sites. The area covered by the magnetotelluric survey is approximatelly 2,500 km² and has little topographic variation.

More detailed geological information about the study area and surrounding regions can be found in Lemos de Sousa and Oliveira (1983), Oliveira (1984), and Julivert and Martinez (1987).

1.4. Previous geophysical work in the region of the study area

A few seismic refraction surveys have been performed in southern Portugal, including the study area (Mueller et al., 1973; Sousa Moreira et al., 1977; Hirn et al., 1981; Caetano, 1983; Banda, 1988; Mendes-Victor et al., 1988; Mueller and Ansorge, 1989). In these surveys, linear and fan-like profiles were used. The data and the results are difficult to interpret, and show that the crust in southern Portugal is complex. They indicate that the Moho has irregular topography and varies between 28 and 34 km deep, and the seismic P wave velocity (v) for the upper mantle is about 8.1 km/s. Furthermore, they indicate that a low velocity layer exists in the crust with P wave velocity values varying between 5.3 and 5.6 km/s, and lies between approximately 10 to 20 km depth. This layer separates the upper crust (v=6.5 km/s) from the lower crust (v=7.5 km/s).

There is also some evidence that the Messejana fault coincides with a deepening of the Moho of about 2 to 4 km towards the SE. Regionally, however, the Moho becomes shallower towards the SW (about 27 km deep). In general, the seismic refraction work performed so far does not provide a clear picture of the regional characteristics of the crust in southern Portugal. The main conclusion is that interpretation of the seismic results is difficult because of the geological complexity of the region.

Gravimetric maps of Portugal in the scale 1:1,000,000 (free-air, Bouguer, and isostatic) were published by the Portuguese Geodetic Survey in 1958. At that time the density of gravimetric stations and profiles was low and those maps are now being up-dated with new data from different sources (Torres and Lisboa, 1988). However, the general features observed in the old maps are present in the up-dated ones. Figure 1.3 is the Bouguer anomaly map based on the 1958 published results. In southern Portugal the gravimetric field shows a decrease in complexity from NE to SW. This is generally interpreted as a decrease of the regional crustal thickness (Cadavid, 1977), which is in agreement with results from the seismic refraction surveys. It is interesting to note that the Ferreira-Ficalho overthrust separates the region into two quite different gravimetric domains. To the NE, several short wavelength gravimetric anomalies can be identified, which correspond to the mafic

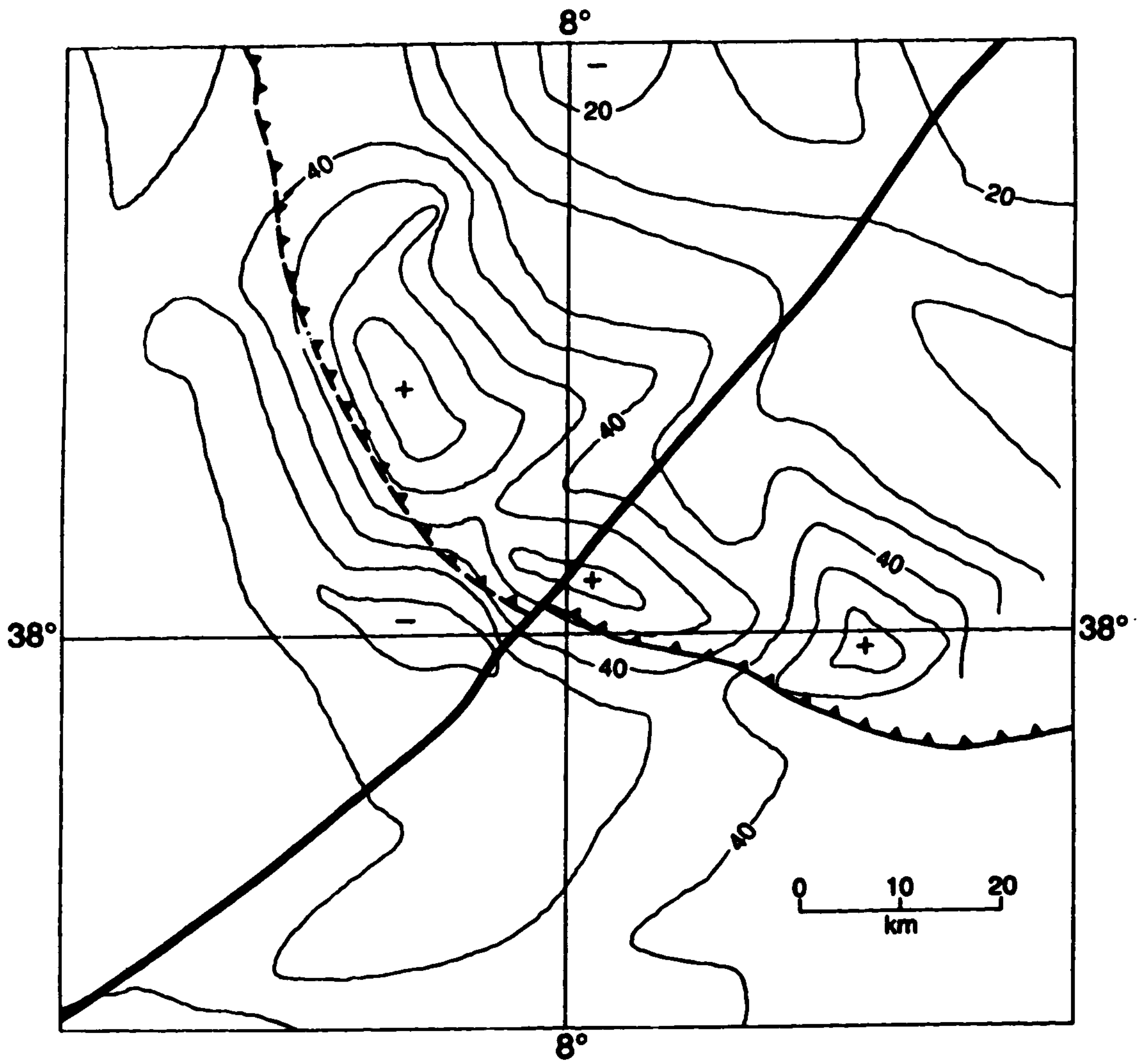

Fig. 1.3: Complete Bouguer anomaly map for the region of the MT study. The contour interval is 5 mgal. (redrawn from the Complete Bouguer Anomaly Map of Portugal, 1958).

intrusions that can be seen in Figure 1.2, while to the SW gravity values change gradually and short wavelength anomalies are absent. On the other hand, the presence of the Messejana fault is not apparent in the gravimetric data. This is probably a result of the low density coverage of the early gravimetric surveys; in fact, more dense gravimetric data obtained by mining companies and Portuguese state agencies show the fault and associated doleritic intrusion as well as the 4 km sinistral displacement referred to previously (Torres and Lisboa, 1988; Bengala and Nolasco, pers. commun., 1990).

In 1991 an up-dated aeromagnetic map of Portugal in the scale 1:1,000,000 was published by the Geological Survey of Portugal (Miranda and Mendes-Victor, 1991). The mean flight altitude was 3000 m with line spacing of 10 km and the tie-lines spacing was 40 km. As in the Bouguer anomaly map, the aeromagnetic map (Figure 1.4) shows a good correlation between the longitudinal zonation of the Iberian Hercynian structures and the magnetic signature (Miranda et al., 1988). This is particularly evident in the region of the MT study, where the Ferreira-Ficalho overthrust divides the region into two different magnetic domains which correspond to the Ossa-Morena and South-Portuguese zones. In magnetic terms, the Ossa-Morena zone is characterized by short wavelength (less than 10 km) and medium amplitude (of the order of 100 nT) directly polarized magnetic anomalies. Referring to Figure 1.2, it is seen that these anomalies

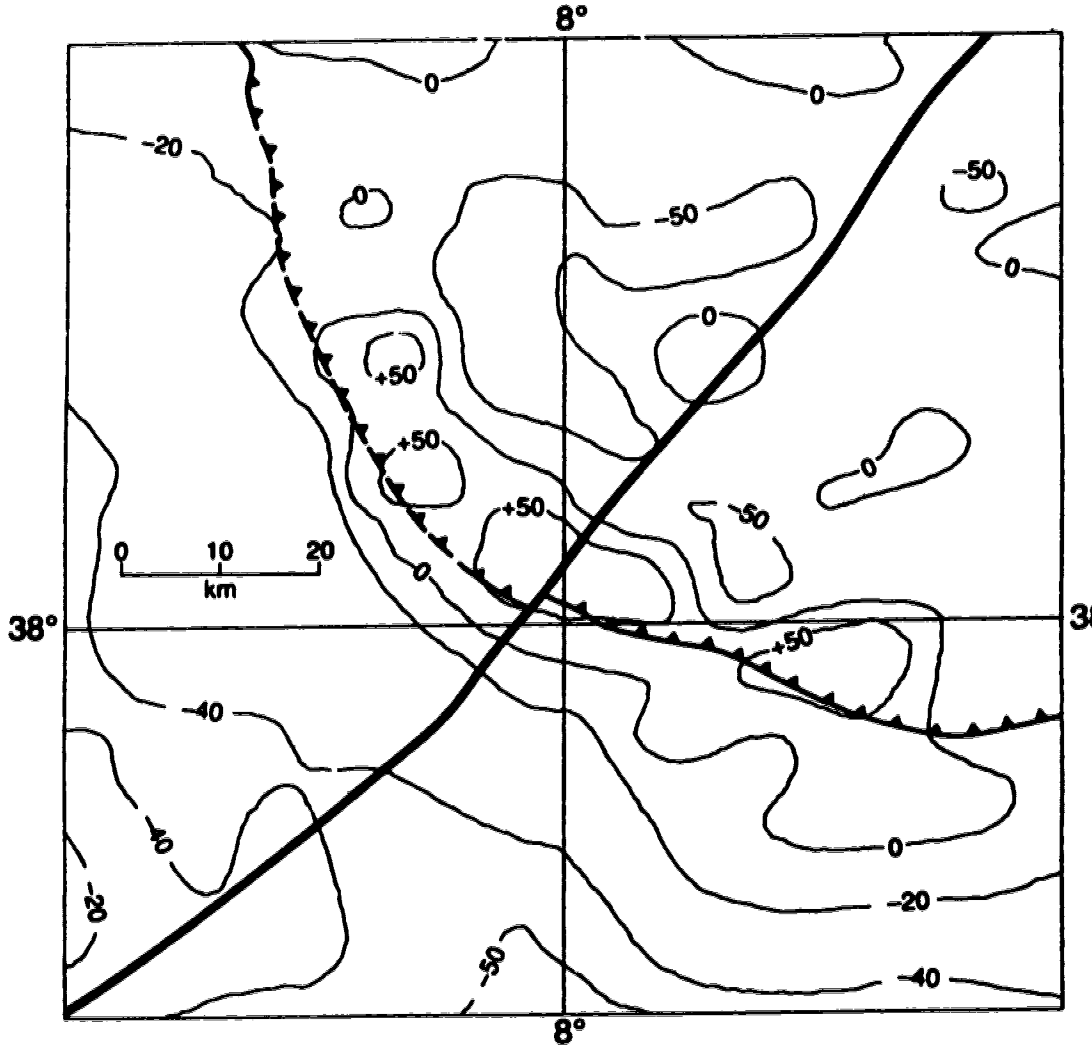

Fig. 1.4: Total field aeromagnetic anomaly map for the region of the MT study. Contours in nT (redrawn from Total Field Aeromagnetic Map of Portugal, 1991).

correlate well with the gabbro-dioritic complex. By contrast, the South-Portuguese zone is characterized by small amplitude (less than 10 nT) negative anomalies with wavelengths of the order of tens of kilometers. An interesting feature of this up-dated aeromagnetic map is that the Messejana fault, and the associated doleritic intrusions, do not appear to have magnetic signatures, which is contrary to what was expected.

One of the first attempts to compile geothermal data collected in Portugal up to 1987 was published in the "Atlas of the Geothermal Resources in the European Community, Austria and Switzerland" as a heat flow density map for southern Portugal (Haenel and Staroste, 1988). The main feature of that map is a geothermal anomaly with HFD values as high as 160 mW/m^2. Subsequent work by Duque (1991) and Duque and Mendes-Victor (1991, 1993) confirmed the general trends indicated in the map and the geothermal anomaly reported in the atlas. They suggested, based on additional corrections applied to the geothermal data set and several more HFD determinations, that the HFD values for the central region of the AGA are as high as 200 mW/m^2. The heat flow density values were calculated by measuring the temperatures at several depths in mining wells that were thought to have reached thermal equilibrium, and multiplying the geothermal gradients obtained in that way by the thermal conductivities measured on rock samples from cores obtained from the same wells. A more detailed description of the geothermal data set can be found in Correia et al. (1982), Duque (1984), Mendes-Victor et al. (1986), and Correia et al. (1993). To constrain the HFD values calculated for the AGA, chemical analyses were performed on rock samples collected in some of the geological formations that outcrop in the AGA region to estimate regional heat production rates (Correia, 1991; and Correia et al., 1993). Recently, C. Almeida (pers. commun., 1991) provided results from some new geothermal data obtained in southern Portugal in an area that includes the area of the MT study. His results indicate lower HFD values than those previously reported with values that range between 60 and 90 mW/m^2.

It sould be noted that the AGA has not been detected by any other geophysical method than the geothermal method. Therefore, it was hoped that, because of the relationship between temperature and electrical conductivity (or resistivity), the magnetotelluric survey over the geothermal anomaly could shed some light on the thermal state of the Alentejo Geothermal Anomaly.

In summary, two aspects of previous geophysical surveys performed in southern Portugal should be emphasized. First, there is an apparent distinction (in geological and geophysical terms) between the Ossa-Morena and South-Portuguese zones: the former is more complex than the latter and the line of separation is the Ferreira-Ficalho overthrust. Second, the Messejana fault, which appears to be an important tectonic feature of southern Portugal, is not clearly evident in the gravimetric and aeromagnetic maps, as should be expected geologically.

CHAPTER II

GENERAL MAGNETOTELLURIC THEORY

2.1. Brief historical account

It seems to have been Airy (1868) who made the first systematic study of the relationship between the magnetic and telluric fields on the Earth. However, Tikhonov (1950), in the Soviet Union, first realised the potential of using the Earth's natural electromagnetic fields in Geophysics, and Cagniard (1953) in France was the first to devise a method for obtaining the conductivity distribution inside the Earth. This was the beginning of the magnetotelluric method for geophysical prospecting.

Cagniard's method consists of measuring the amplitudes and phases of the orthogonal horizontal magnetic and electric (also called telluric) field vectors at a sounding site on the surface of the Earth. In this method there are two implicit assumptions: first, that the inducing electromagnetic field is a plane wave, and second, the Earth consists of plane horizontal homogeneous layers. Neither assumption is true in practise and the first one gave rise to considerable controversy. Wait (1954) questioned the validity of the first assumption because ionospheric sources (one of the main sources of the magnetotelluric field) are finite and do not generate normally incident plane waves at the Earth's surface. The problem associated with finite sources was further developed by Wait (1962) and Price (1962), who elaborated a general magnetotelluric theory which included them. Subsequently, Madden and Nelson (1964) and Srivastava (1965) were able to show, through the use of computer models, that for the real Earth the plane wave source field assumption is valid for periods up to 1000 seconds.

It soon became apparent that experimental results were not consistent with Cagniard's first assumption in areas with lateral conductivity contrasts. This problem was addressed by Neves (1957) who first recognized the tensorial nature of the relationship between the magnetic and telluric fields and that it would reduce to the Cagniard case in one-dimensional situations.

During the four decades since Tikhonov and Cagniard published their papers, the magnetotelluric method has substantially developed in all aspects: theoretical, data acquisition and analysis. The books edited by Vozoff (1986) and Nabighian (1988) illustrate the evolution of the method since the beginning of the fifties.

2.2. The source fields

A detailed account of the origin and characteristics of the natural electromagnetic fields relevant to the MT method can be found, for instance, in Rokityansky (1982), Kaufman and Keller (1981), and Vozoff (1988).

Magnetotelluric (MT) and audiofrequency magnetotelluric (AMT) methods use the natural time-varying electric and magnetic fields observed at the Earth's surface to determine the resistivity distribution in its subsurface. For exploration purposes the range of frequencies of interest lies between 10^{-4} and 10^{4} Hz and, in general, the MT method uses signals that are in the frequency range 10^{-4} to 10 Hz while the AMT method uses signals in the frequency range 10 to 10^{4} Hz. Such a distinction will not be made between MT and AMT in this work, and when referring to MT methods or fields, the whole range 10^{-4} to 10^{4} Hz is implied. Both MT and AMT will be referred to in general as the MT method.

Detailed descriptions of the sources and morphologies of the natural electromagnetic fields is found in Keller and Frischknecht (1966), Matsushita and Campbell (1967), and Jacobs (1970). These fields interact with the electrically conducting Earth, and it is the nature of this interaction that is observed in the MT method.

By definition, the magnetotelluric field is the time-varying portion of the Earth's magnetic field, together with the currents it induces inside the Earth (Keller and Frischknecht, 1966). The magnetic and electric signals that are detected at the Earth's surface originate from these fields, and have periods from less than 1 millisecond to several years. The average amplitude spectrum of the electromagnetic oscillations has a minimum at about 1 Hz, and this minimum divides the spectrum into two portions that correspond to two different types of phenomena. For frequencies above 1 Hz the magnetotelluric field is generally produced by electrical discharges (lightning) that occur in the atmosphere; for frequencies below 1 Hz the magnetotelluric field is generated by complex interactions between the stationary part of the Earth's magnetic field and the solar wind.

Worldwide thunderstorm activity is the main source of MT signals above 1 Hz. There are three principal storm centers, and these are located in equatorial South America (Brazil), central Africa, and the southwest Pacific (Malaysia). Each of these centers has on average 100 storm days per year (Kaufman and Keller, 1981). Since these storm centers are distributed around the globe, on average there is a storm occuring at any given time (Patra and Mallick, 1980). For the whole globe, the frequency of lightning flashes is estimated to be between 100 and 1000 per second (Vozoff, 1991). At a particular site, the MT signals, also known by the terms atmospherics or sferics, depend on the strength, frequency of occurence of lightning flashes, and on the distance from the point of lightning discharge. This implies that the MT signals are largest in tropical regions, on summer afternoons.

Some large sferics propagate around the world in a waveguide mode between the Earth's surface and the ionosphere. Since the height of the ionosphere changes during the day (about 60 km in daytime and 90 km at night), the waveguide dimension changes with time. Furthermore, as the electromagnetic wave travels, some of the frequencies will be attenuated while some will be enhanced. The enhanced ones, that result from resonance effects in the Earth-ionosphere cavity, are called Schumann resonances and have a fundamental mode near 8 Hz and higher modes near 14, 20, and 26 Hz.

Man-made electromagnetic noise also constitutes a (usually undesirable) source of frequencies above 1 Hz. The most important originate from power lines and are generally avoided by choosing the MT sites far away from them and by the use of notch filters incorporated in the equipment.

The MT fields at frequencies below 1 Hz, generally known as micropulsations, are generated by complex physical interactions that take place in the magnetosphere, though these interactions are not yet well understood. Micropulsations arise from electromagnetic energy that is generated by large current loops in the ionosphere and which is transmitted to the Earth's surface through the atmosphere. These current loops are considered to have their origin in hydromagnetic or Alfven waves that result from the interaction between the solar wind and the Earth's main geomagnetic field.

Micropulsation amplitudes range from a fraction of a nanotesla to a few hundred nanoteslas, which indicates that their generation probably involves two or more different physical processes. Following Jacobs et al. (1964), Keller and Frischknecht (1966), Kaufman and Keller (1981), and Rokityansky (1982), micropulsations can be divided into regular pulsations called Pc (pulsation continuous), irregular pulsations called Pi (pulsation irregular), and "pearl" pulsations (Pp). Micropulsations have periods that vary between 0.2 and 1000 seconds.

The nature of the micropulsations observed at a particular time at a particular site depends on the time of the day, the state of the local ionosphere, the level of geomagnetic activity (essentially controlled by solar activity), the time in the solar cycle, and seasonal effects. On records of the variations of magnetic and electric field components, regular pulsations are the most prominent and irregular pulsations generally appear as damped trains of waves that follow each other in an irregular sequence. "Pearl" pulsations, which occur at sunrise and sunset, are amplitude modulated with periods of 20 to 30 seconds.

2.3. Basic electromagnetic theory relevant to MT methods

When performing a MT survey the main objective is to determine the resistivity (or the conductivity) distribution inside the Earth from measurements of time-varying magnetic and electric fields at its surface. Maxwell's equations describing the behaviour of the electromagnetic fields are therefore used to study those fields and the way they interact with subsurface structures.

Experimental work done by Faraday and Ampère led to the following equations that generally carry their names, i.e., Faraday's law,

$$\nabla \times \bar{E} = -\frac{\partial \bar{B}}{\partial t} \tag{2.1}$$

and Ampère's law,

$$\nabla \times \bar{H} = \frac{\partial \bar{D}}{\partial t} + \bar{J}, \tag{2.2}$$

where $\bar{E}$, $\bar{B}$, $\bar{H}$, $\bar{D}$, and $\bar{J}$ are respectively, the electric field intensity (in volt per meter), the magnetic induction (in weber per square meter or Tesla), the magnetic field intensity (in ampere per meter), the dielectric displacement (in coulomb per square meter), and the electric current density (in ampere per square meter).

Equations (2.1) and (2.2), together with the relations

$$\nabla \cdot \bar{B} = 0 \tag{2.3}$$

and

$$\nabla \cdot \bar{D} = \rho_e, \tag{2.4}$$

where ρ_e is the electric charge density (in coulomb per cubic meter), constitute what are known as Maxwell's equations. If the Earth can be considered as a homogeneous medium with resistivities less than 10^4 ohm.m, free electric charges dissipate in less than 10^{-6} seconds (Stratton, 1941). Furthermore, for geophysical purposes and for frequencies lower than 10^5 Hz, $\nabla \cdot \vec{D} = 0$, though this is more the exception than the rule in the real Earth.

Faraday's and Ampère's laws are uncoupled differential equations. Nevertheless, they are coupled through the following equations:

$$\vec{D} = \tilde{\varepsilon}(\omega, \vec{E}, \vec{r}, t, T, p, \ldots) \cdot \vec{E}, \tag{2.5}$$

$$\vec{B} = \tilde{\mu}(\omega, \vec{B}, \vec{r}, t, T, p, \ldots) \cdot \vec{H}, \tag{2.6}$$

and

$$\vec{J} = \tilde{\sigma}(\omega, \vec{E}, \vec{r}, t, T, p, \ldots) \cdot \vec{E} \tag{2.7}$$

in which $\tilde{\varepsilon}$, $\tilde{\mu}$, and $\tilde{\sigma}$ are the dielectric permittivity, magnetic permeability, and electric conductivity tensors, respectively. These tensors depend on angular frequency (ω), electric field ($\vec{E}$) or magnetic induction ($\vec{B}$), position ($\vec{r}$), time (t), temperature (T), and pressure (p). In general these tensors are complex quantities. However, when applying equations (2.5), (2.6), and (2.7) to solve problems related to the Earth, some simplifying assumptions are made. It is generally assumed that the media of interest are linear, isotropic and homogeneous, and that the electrical properties are independent of time, temperature, and pressure. Furthermore, the magnetic permeability is assumed to be that of free space, i.e., $\mu = \mu_0 = 4\pi \cdot 10^{-7}$ H/m. With these assumptions the constitutive relations (2.5 to 2.7) reduce to (Ward and Hohmann, 1987):

$$\bar{D} = \varepsilon\bar{E} \tag{2.8}$$

$$\bar{B} = \mu\bar{H} \tag{2.9}$$

$$\bar{J} = \sigma\bar{E} \tag{2.10}$$

where the dielectric permittivity, ε, and the electrical conductivity, σ, are still complex functions of the angular frequency, and the magnetic permeability is real.

In complicated situations where interpretation is not straightforward and modelling must be extensively used, the above assumptions do not always apply (Ward and Hohmann, 1987). That is the case, for instance, when anisotropy and inhomogeneities are included in electromagnetic boundary-value problems to help interpret the data. Furthermore, in deep crustal studies, temperature and pressure effects should be considered, as well as the variability of electrical conductivity as a result of change in moisture content, such as can occur in soils.

Applying the curl operator to Faraday's and Ampère's equations, and using the constitutive equations and the vector identity $\nabla \times \nabla \times \bar{a} = \nabla\nabla \cdot \bar{a} - \nabla^2 \bar{a}$ the following equations are obtained:

$$\nabla^2 \vec{E} = \mu\varepsilon \frac{\partial^2 \vec{E}}{\partial t^2} + \mu\sigma \frac{\partial \vec{E}}{\partial t} \tag{2.11}$$

and

$$\nabla^2 \vec{H} = \mu\varepsilon \frac{\partial^2 \vec{H}}{\partial t^2} + \mu\sigma \frac{\partial \vec{H}}{\partial t} \tag{2.12}$$

which are wave equations for $\vec{E}$ and $\vec{H}$.

Equations (2.11) and (2.12) can be further simplified when applied to Earth problems. If they are Fourier transformed the following equations are obtained:

$$\nabla^2 \vec{E} = \left(i\mu\sigma\omega - \mu\varepsilon\omega^2\right)\vec{E} \tag{2.13}$$

and

$$\nabla^2 \vec{H} = \left(i\mu\sigma\omega - \mu\varepsilon\omega^2\right)\vec{H} \tag{2.14}$$

where the wave number, k, is given by

$$k^2 = \left(i\mu\sigma\omega - \mu\varepsilon\omega^2\right). \tag{2.15}$$

However, for Earth materials at frequencies lower than 10^5 Hz, $\mu\varepsilon\omega^2 << \mu\sigma\omega$ (Keller and Frischknecht, 1966), which means that displacement currents are negligible when compared with conduction currents. In this case, equation (2.15) reduces to $k^2 = i\mu\sigma\omega$ and equations (2.13) and (2.14) become

$$\nabla^2 \bar{E} = i\mu\sigma\omega\bar{E} \qquad (2.16)$$

and

$$\nabla^2 \bar{H} = i\mu\sigma\omega\bar{H} \qquad (2.17)$$

which are diffusion equations for $\bar{E}$ and $\bar{H}$ in the frequency domain. Since in equations (2.11) and (2.12) the terms associated with displacement currents are the second order time derivatives of the $\bar{E}$ and $\bar{H}$ fields, when displacement currents are ignored and a time dependence of the form $e^{i\omega t}$ is assumed, these equations reduce to:

$$\nabla^2 \bar{E} = \mu\sigma\frac{\partial \bar{E}}{\partial t} \qquad (2.18)$$

and

$$\nabla^2 \bar{H} = \mu\sigma\frac{\partial \bar{H}}{\partial t}. \qquad (2.19)$$

To simplify the analysis of the above diffusion equations it is usual to choose a cartesian coordinate system such that only one component of the electric field is non-zero. In electromagnetic induction studies in the Earth, the X direction is considered positive toward the north, the Y direction positive toward the east, and the Z direction positive downward. If only E_x is non-zero, for instance, equation (2.18) reduces to

$$\frac{\partial^2 E_x}{\partial z^2} = \mu\sigma\frac{\partial E_x}{\partial t} \qquad (2.20)$$

and has solutions of the type

$$E_x = Ce^{i\omega t}e^{kz} \tag{2.21}$$

Where C is an arbitrary constant. However, from equation (2.15), k has two values, i.e.,

$$k = \pm\sqrt{i\mu\sigma\omega} \tag{2.22}$$

and therefore the general solution of equation (2.20) is:

$$E_x = Ae^{i\omega t}e^{-kz} + Be^{i\omega t}e^{kz} \tag{2.23}$$

where A and B are two arbitrary constants. In the case of a homogeneous half-space, E_x must be zero as z approaches infinity, B must be zero, and so

$$E_x = Ae^{i\omega t}e^{-kz} \tag{2.24}$$

with $k = \sqrt{i\mu\sigma\omega} \equiv \alpha + i\beta$ and $\alpha = \beta = \sqrt{\mu\sigma\omega/2}$. A similar procedure can be used to produce the solution for the $\vec{H}$ field.

Equation (2.24) can be written explicitly as

$$E_x = Ae^{i\omega t}e^{-\alpha z}e^{-i\beta z} \tag{2.25}$$

where A represents the amplitude of the electromagnetic wave, $e^{i\omega t}$ indicates that it varies sinusoidally with time, $e^{-\alpha z}$ indicates attenuation with depth, and $e^{-i\beta z}$ indicates that it varies sinusoidally with depth. The factor $e^{-\alpha z}$ leads to the definition of skin-depth as a measure of the depth of penetration of an electromagnetic wave, δ, which is the depth at which its amplitude is reduced to 1/e of its surface value, i.e.,

$$\delta = \sqrt{\frac{2}{\mu\sigma\omega}}. \tag{2.26}$$

From this equation it is apparent that the skin-depth (depth of penetration) depends on the characteristics of the medium traversed (through σ), as well as the frequency (through $\omega = f/2\pi$). Qualitatively, this means that long period (low frequency) electromagnetic waves penetrate deeper than short period (high frequency) ones, and the higher the resistivity of the medium traversed the greater the depth of penetration.

Geoelectromagnetic problems are generally boundary-value problems and, therefore, the appropriate boundary conditions must be applied whenever interfaces exist between different media. At a boundary the normal components of $\bar{H}$ and the tangential components of $\bar{E}$ are continuous across it; the tangential component of $\bar{H}$ is continuous if there are no surface currents at the boundary; the normal component of $\bar{D}$ is discontinuous, due to charge accumulation at the boundary; and the normal components of the current density and the static potential of $\bar{E}$ and $\bar{H}$ are all continuous. More details about boundary conditions generally used in electromagnetic problems can be found in Stratton (1941) and Ward and Hohmann (1987).

In electromagnetic methods, particularly magnetotelluric methods, the concept of impedance is of foremost importance. This is because it allows the resistivity distribution as a function of frequency at a measuring site to be determined. By definition (Keller and Frischknecht, 1966), the impedance, Z, is the ratio between two mutual orthogonal components of the electric and magnetic fields, i.e.,

$$Z = \frac{E_x}{H_y} = -\frac{E_y}{H_x} \tag{2.27}$$

where Z has the unit of resistance (ohm). On the other hand, it can be shown (for instance, Keller and Frischknecht, 1966) that at the surface of a homogeneous and isotropic Earth the equation

$$Z = \sqrt{i\mu\rho\omega} = \sqrt{\frac{i\mu\omega}{\sigma}} \tag{2.28}$$

holds. Combining equations (2.27) and (2.28), the following formula for the resistivity is obtained

$$\rho = \frac{-i}{\mu\omega}\left(\frac{E_x}{H_y}\right)^2 = \frac{i}{\mu\omega}\left(\frac{E_y}{H_x}\right)^2 \qquad (2.29)$$

from which resistivities as a function of frequency can be calculated, given the electric and magnetic components of the fields measured at the Earth's surface. In formula (2.29), the presence of $\underline{i}$ indicates that a phase difference of 45° exists between the electric and magnetic fields. In terms of the amplitude of ρ, formula (2.29) can be written as

$$\rho = \frac{1}{\mu\omega}\left|\frac{E_x}{H_y}\right|^2. \qquad (2.30)$$

It should be noted that two distinct kinds of electromagnetic signals, those below 1 Hz and those above 1 Hz, and which have different origins, propagate through the atmosphere until they penetrate the Earth's subsurface. Below 1 Hz (ionospheric origin) the waves travel vertically, while above 1 Hz (sferics) they travel almost horizontally in a wave-guided mode. After penetrating the Earth's surface both travel vertically, which means that the latter are refracted at a large angle. This is a result of the large contrast between the electrical properties of the Earth's atmosphere and the Earth itself, and means that both waves, as far as calculations below the Earth's surface are considered, can be seen as normally incident electromagnetic waves (Stratton, 1941).

2.4. One-, two-, and three-dimensional formulations

The simplest Earth model consists of a homogeneous conducting half-space with a plane surface with air above it. This model was already introduced in the previous section to illustrate the concepts of skin-depth (equation (2.26)) and resistivity (equation (2.30)). Strictly speaking, these two formulas are only valid for a homogeneous medium. It will be shown that their physical meaning and form change when inhomogeneous media are to be considered.

Although the Earth is far from one-dimensional, its representation by a series of n horizontal, homogeneous layers is useful and applicable for certain geological environments, such as sedimentary basins. In such cases, where resistivity is only a function of depth, it is possible to demonstrate (e.g., in Keller and Frischknecht, 1966) that the general expression of the impedance at the Earth's surface is given by

$$Z = \frac{-i\mu\omega}{k_1}\coth\left[k_1h_1 + \coth^{-1}\left\{\frac{k_1}{k_2}\coth\left(k_2h_2 + \cdots \coth^{-1}\left\{\frac{k_{n-2}}{k_{n-1}}\coth\left(k_{n-1}h_{n-1} + \coth^{-1}\frac{k_{n-1}}{k_n}\right)\right\}\cdots\right)\right\}\right] \tag{2.31}$$

where h_i represents the thickness of layer i, where i=1 for the uppermost layer. In this representation, the resistivity obtained by measuring the mutually orthogonal components of the electric and magnetic fields at the Earth's surface is an "apparent resistivity" defined by

$$\rho_a = \frac{1}{\mu\omega}\left|\frac{E_x}{H_y}\right|^2 = \frac{1}{\mu\omega}\left|\frac{E_y}{H_x}\right|^2 . \tag{2.32}$$

Despite the fact that equations (2.30) and (2.32) are identical in form, they represent different quantities. In the first, ρ represents the real resistivity of the homogeneous half-space, while, in the latter, ρ_a is (in some way) a weighted average of the true resistivities of the n layers. One of the objectives of an interpreter is to determine the values of those resistivities from measurements of the electric and magnetic fields performed at the surface of the top layer.

It was seen that for an homogeneous Earth, a constant phase difference of 45° exists between the electric and magnetic fields, with E_x leading H_y. However, this is no longer true for the n-layer case. In fact, by definition, the phase is given by the argument of the impedance ($Z=|Z|e^{i\phi}$) obtained at the Earth's surface. But, from equation (2.31), it is apparent that it changes with the number of layers and their thicknesses, and the frequency. This indicates that phase can also be used to determine the resistivity distribution as a function of frequency and, after application of some inversion procedure, as a function of depth. As a rule, the phase tends to 45° at high frequencies. As frequency decreases the phase increases with a decrease in resistivity, and decreases when resistivity increases.

During the first work to use MT methods in geophysical prospecting, researchers began to realize that interpretation employing one-dimensional models was often impossible or misleading due to geologic complexity. Therefore, a more advanced formulation or model was necessary in order to interpret data obtained in geological situations that are more complex than one-dimensional. The new approximation considers the real Earth to be two-dimensional. In this case, the resistivity varies with depth and in one of the horizontal directions, say Y, generally perpendicular to the structural strike. In this situation, the component of the electric field induced in the X direction (E_x) will be, in part, due to the inducing magnetic component in the Y direction (H_y) and, in part, due to the currents, induced by the magnetic component in the X direction (H_x) that were deflected by the geological structure and so contribute to the total electric field in the X direction. In mathematical terms, this situation can be described by the equation

$$E_x = Z_{xx} H_x + Z_{xy} H_y \tag{2.33}$$

where Z_{xx} and Z_{xy} represent the contributions from H_x and H_y to E_x. Similar reasoning is valid for the component of the electric field in the Y direction (E_y) and so

$$E_y = Z_{yx} H_x + Z_{yy} H_y. \tag{2.34}$$

The two equations (2.33) and (2.34) are frequency dependent and are generally written in a more compact form (Cantwell, 1960),

$$\begin{bmatrix} E_x \\ E_y \end{bmatrix} = \begin{bmatrix} Z_{xx} & Z_{xy} \\ Z_{yx} & Z_{yy} \end{bmatrix} \cdot \begin{bmatrix} H_x \\ H_y \end{bmatrix}, \tag{2.35}$$

which represents a tensor relationship between the electric and magnetic field components as measured at the Earth's surface. The Z_{ij} are the tensor elements of the so-called impedance tensor. In a one-dimensional Earth (homogeneous half-space or layered) equations (2.33) and (2.34) will simplify. In fact, since there is no deflection of the induced currents by vertical structures, only magnetic field components perpendicular to a certain direction will induce an electric field in that direction, and the equations reduce to $E_x = Z_{xy}H_y$ and $E_y = Z_{yx}H_x$, as they should; furthermore, $Z_{xx} = Z_{yy} = 0$, and $Z_{xy} = -Z_{yx} \neq 0$ by symmetry reasons. Also, for a purely two-dimensional situation, when the strike direction of the 2-D structure is parallel to the X or Y directions of the measuring reference frame, $Z_{xx} = Z_{yy} = 0$ and $Z_{xy} \neq Z_{yx} \neq 0$. These results can be thought of as a consequence of the symmetry of the problem and will be formally explained later. In general, however, for two-dimensional situations in which the measuring reference frame is not aligned with the structure, $Z_{xx} = -Z_{yy} \neq 0$ as well as $Z_{xy} \neq Z_{yx} \neq 0$.

The impedance tensor appearing in equation (2.35) has three invariants (Rokityansky, 1982):

$$
\begin{aligned}
I_1 &= Z_{xx}Z_{yy} - Z_{xy}Z_{yx} \\
I_2 &= Z_{xx} + Z_{yy} \\
I_3 &= Z_{xy} - Z_{yx}
\end{aligned}
$$

Since for two-dimensional structures $Z_{xx} = -Z_{yy} \neq 0$, then for such structures the invariant I_2 equals zero. Therefore, if the impedance tensor obtained at a certain site shows a trace equal to zero (i.e., $I_2 = 0$), it can be concluded that the Earth structure is two-dimensional. Furthermore, there is a particular reference frame in which both impedance tensor diagonal elements equal zero. If, for instance, the angle θ (measured in a clockwise direction), between the X direction (linked to the measuring reference frame X,Y,Z) and the strike direction of the geological structure (linked to the reference frame X',Y',Z') is known, it is possible to calculate the rotated impedances Z'_{ij}, (where theoretically both diagonal elements are zero) by performing the following matrix operation (Swift, 1967)

$$\begin{bmatrix} Z'_{xx} \\ Z'_{xy} \\ Z'_{yx} \\ Z'_{yy} \end{bmatrix} = \begin{bmatrix} C^2 & CS & CS & S^2 \\ -CS & C^2 & -S^2 & CS \\ -CS & -S^2 & C^2 & CS \\ S^2 & -CS & -CS & C^2 \end{bmatrix} \cdot \begin{bmatrix} Z_{xx} \\ Z_{xy} \\ Z_{yx} \\ Z_{yy} \end{bmatrix} \qquad (2.36)$$

where C and S stand for $\cos\theta$ and $\sin\theta$, respectively.

In the previous example $Z'_{xx} = Z'_{yy} = 0$. However, the angle θ is not usually known at the beginning and, in this case, a criterium must be found to rotate the impedance tensor by an angle θ_0 that makes Z'_{xx} and Z'_{yy} equal to zero. This criterium was suggested by Swift (1967) and is described by Vozoff (1972). The main idea is to maximize the value of $|Z'_{xy}(\theta)|^2 + |Z'_{yx}(\theta)|^2$ for a particular angle θ_0. This can be achieved by differentiating $Z'_{xy}(\theta)$ and $Z'_{yx}(\theta)$ given by equation (2.36) and finding the value of θ_0, measured clockwise, for which the maximization is accomplished. The angle θ_0 is given by

$$\theta_0 = \frac{1}{4}\tan^{-1}\frac{(Z_{xx}-Z_{yy})(Z_{xy}+Z_{yx})^* + (Z_{xx}-Z_{yy})^*(Z_{xy}+Z_{yx})}{|Z_{xx}-Z_{yy}|^2 - |Z_{xy}+Z_{yx}|^2} \qquad (2.37)$$

where the star means complex conjugate. However, this equation has four solutions at 90° intervals, which means two possible strike directions perpendicular to one another. To choose between them it is necessary to have some other independent information such as the relationship between the magnitudes of the measured horizontal and vertical components of the magnetic field, or some geological constraint.

Although the tensor description above is straightforward, complications arise when data are used to calculate the elements of the impedance tensor and the data are contaminated by noise. This means that even in two-dimensional situations the diagonal elements of the impedance tensor are not necessarily zero in a reference frame where one of the axes is parallel to the strike.

The mathematical formulation for two-dimensional structures can be more formally carried out by using the fact that an arbitrary electromagnetic field in a homogeneous, source-free region can be expressed as the sum of a transverse magnetic (TM) field and a transverse electric (TE) field (Morse and Feshbach, 1964). The usefulness of this theorem resides in the fact that in 2D cases Maxwell's equations decouple into TE and TM modes if the horizontal directions of the reference frame are chosen in such a way that one is parallel to and the other perpendicular to the strike of the structure. Furthermore, this results is an advantage in the enforcement of boundary conditions when using numerical techniques. An electromagnetic wave is said to be E-polarized (TE mode) if the electric field is along the strike and to be H-polarized (TM mode) if the magnetic field intensity is along the strike. The major simplification of this approach results from the fact that primary E-polarized waves generate secondary waves that are E-polarized, while primary H-polarized waves generate secondary waves that are H-polarized (Orange, 1989). Therefore, any electromagnetic signal can be decomposed into E-polarized and H-polarized waves. In mathematical terms the above decomposition can be made as follows. Neglecting displacement currents, equations (2.1)and (2.2) are giving in the frequency domain by (Ward and Hohmann, 1987):

$$\nabla \times \bar{E} = -i\mu\omega\bar{H} \qquad (2.38)$$

and

$$\nabla \times \bar{H} = \sigma\bar{E}. \qquad (2.39)$$

Considering a reference frame which has the X direction parallel to the structure's strike, the above equations, in component form, reduce to (e.g., Jones and Price, 1970):

$$\frac{\partial H_z}{\partial y} - \frac{\partial H_y}{\partial z} = \sigma E_x \tag{2.40}$$

$$\frac{\partial H_x}{\partial z} = \sigma E_y \tag{2.41}$$

$$\frac{\partial H_x}{\partial y} = -\sigma E_z \tag{2.42}$$

$$\frac{\partial E_z}{\partial y} - \frac{\partial E_y}{\partial z} = -i\mu\omega H_x \tag{2.43}$$

$$\frac{\partial E_x}{\partial z} = -i\mu\omega H_y \tag{2.44}$$

$$\frac{\partial E_x}{\partial y} = i\mu\omega H_z . \tag{2.45}$$

Equations (2.40), (2.44), and (2.45) involve only E_x, H_y, and H_z and correspond to the E-polarization mode (electric field parallel to the X direction). Equations (2.41), (2.42), and (2.43) involve only H_x, E_y, and E_z and correspond to the H-polarization mode (magnetic field parallel to the X direction). Eliminating H_y and H_z from the first set of three equations gives

$$\frac{\partial^2 E_x}{\partial y^2}+\frac{\partial^2 E_x}{\partial z^2}=i\mu\omega\sigma E_x. \qquad (2.46)$$

Eliminating E_y and E_z from the second set of three equations gives

$$\frac{\partial^2 H_x}{\partial y^2}+\frac{\partial^2 H_x}{\partial z^2}=i\mu\omega\sigma H_x. \qquad (2.47)$$

Analytical solutions for these equations are only known for a few simple structures (Rankin, 1962; d'Erceville and Kunetz, 1962; Weaver, 1963; Hobbs, 1975), and in most 2-D cases numerical methods have to be used to calculate the response functions. There are essentially four numerical techniques in use: the finite difference method (Patrick and Bostick, 1969; Jones and Price, 1970; Jones and Pascoe, 1971, 1972; Williamson et al., 1974; Brewitt-Taylor and Weaver, 1976; Weaver and Brewitt-Taylor, 1978), the finite element method (Coggon, 1971; Silvester and Harlam, 1972; Reddy and Rankin, 1973; Wannamaker et al., 1986), the transmission line analogy (Madden and Thompson, 1965; Swift, 1967,1971; Ku et al., 1973), and the integral equation method (Hohmann, 1971; Patra and Mallick, 1980).

As previously stated, in an ideal 2D structure, the impedance tensor can be rotated by an angle that makes $Z_{xx}=Z_{yy}=0$, $Z_{xy}=E_x/H_y$ and $Z_{yx}=E_y/H_x$. However, these values are rotated values into the strike direction and so they correspond to the TE and TM modes, respectively. It is then possible to write $Z_{xy} \equiv Z_{TE} \equiv E_x/H_y$ and $Z_{yx} \equiv ZT_{TM} \equiv -E_y/H_x$, and finally, using the definitions of apparent resistivity ρ_a and phase ϕ

$$\rho_{xy} = \frac{1}{\mu\omega}\left|Z_{xy}\right|^2 \equiv \frac{1}{\mu\omega}\left|Z_{TE}\right|^2 \equiv \frac{1}{\mu\omega}\left|\frac{E_x}{H_y}\right|^2 \tag{2.48}$$

$$\rho_{yx} = \frac{1}{\mu\omega}\left|Z_{yx}\right|^2 \equiv \frac{1}{\mu\omega}\left|Z_{TM}\right|^2 \equiv \frac{1}{\mu\omega}\left|\frac{E_y}{H_x}\right|^2 \tag{2.49}$$

and

$$\phi_{xy} = \tan^{-1}\left[\frac{\mathrm{Im}(Z_{xy})}{\mathrm{Re}(Z_{xy})}\right] \equiv \tan^{-1}\left[\frac{\mathrm{Im}(Z_{TE})}{\mathrm{Re}(Z_{TE})}\right] \tag{2.50}$$

$$\phi_{yx} = \tan^{-1}\left[\frac{\mathrm{Im}(Z_{yx})}{\mathrm{Re}(Z_{yx})}\right] \equiv \tan^{-1}\left[\frac{\mathrm{Im}(Z_{TM})}{\mathrm{Re}(Z_{TM})}\right] \tag{2.51}$$

where ρ_{xy} and ρ_{yx} represent resistivity values as functions of frequency calculated parallel and perpendicular to the strike of a twc-dimensional structure or model, respectively, and ϕ_{xy} and ϕ_{yx} are the calculated phases as functions of frequency parallel and perpendicular to the strike, respectively. It is now apparent that for each site in a 2D structure there are two calculated apparent resistivities and phases. This can introduce difficulties at the interpretation stage. Nevertheless, the results are more consistent with reality than are one-dimensional interpretation techniques.

Despite the fact that many geological situations can be studied and interpreted using the two-dimensional formulation just described, in the majority of the cases, the geological structures to be interpreted are three-dimensional in character. This means that the resistivity varies in the three spatial directions and only a few analytical or semi-analytical solutions are known for special cases (Bailey, 1977; Fischer et al., 1978). So, as in the 2D case, numerical solutions are used to simulate the responses of 3D models or structures. Hohmann (1987) reviews the situation up to 1988. Several techniques are now in use to simulate three-dimensional structures, such as the finite-difference technique (Jones and Pascoe, 1972; Lines and Jones, 1973a,b; Jones and Vozoff, 1978; Pridmore et al., 1981), the integral equation approach (Raiche, 1974; Weidelt, 1975; Ting and Hohmann, 1981; Das and Verma, 1982; Wannamaker et al., 1984a), thin sheet approximations (Dawson and Weaver, 1979; Ranganayaki and Madden, 1980; Park et al., 1983; Park, 1985), and hybrid techniques (Lee et al., 1981). Also some analogue 3-D studies have been performed (Rankin et al., 1965; Dosso, 1966, 1973; Dosso et al., 1980; Nienaber et al., 1981).

2.5. Impedance tensor estimation

In section 2.4 the concept of the impedance tensor was introduced as well as a method to calculate the apparent resistivities and phases from it. However, to calculate these functions and others that will be described later, it is necessary to process the field data (the measured electric and magnetic fields, probably contaminated by some kind of noise) to obtain the four elements of the impedance tensor for several frequencies. The processing techniques used in MT prospecting have been treated in a great number of publications (e.g., Swift, 1967; Sims et al., 1971; Vozoff, 1972; Hermance, 1973; Rokityansky, 1982; Vozoff, 1991).

The main objective of MT processing is to transform the generally noisy electromagnetic field data (a set of electric and magnetic time series) into a set of frequency-dependent impedance tensor elements, from which Earth response functions can be calculated. Basically, the MT data processing is a two step operation: first, spectral analysis of the recorded time series is performed, followed by an estimation of the impedance tensor elements. This means that equation (2.35) must be solved for Z_{ij} values, where the quantities E_x, E_y, H_x, and H_y represent the measured signals in the frequency domain.

The least-squares method is the most common approach to process magnetotelluric data. With two independent measurements of the electric components (E_x and E_y) and the magnetic components (H_x and H_y) it would be possible to calculate Z_{xx} and Z_{xy} of equation (2.33). In fact, after substitution, a set of two equations with two unknowns would be obtained. The same procedure could be applied to equation (2.34) to calculate Z_{yx} and Z_{yy}. However, the electric and magnetic field records always contain noise and it is therefore desirable to have more than two independent records so that averaging techniques can be used to reduce noise effects and to estimate the errors in the results. The least-squares estimate of Z_{xx} and Z_{xy} can be calculated by minimizing the function (Sims et al., 1971)

$$F_1 = \sum_{i=1}^{N}\left(E_{xi} - Z_{xx}H_{xi} - Z_{xy}H_{yi}\right)\left(E_{xi} - Z_{xx}H_{xi} - Z_{xy}H_{yi}\right)^* \tag{2.52}$$

where i represents the number of N independent measurements of E_x, H_x, and H_y at a given frequency, and the star means complex conjugate. Taking derivatives of the real and imaginary parts of equation (2.52) with respect to Z_{xx} and Z_{xy}, and setting them equal to zero one obtains

$$\sum_{i=1}^{N} E_{xi}H_{xi}^* = Z_{xx}\sum_{i=1}^{N} H_{xi}H_{xi}^* + Z_{xy}\sum_{i=1}^{N} H_{yi}H_{xi}^* \tag{2.53}$$

and

$$\sum_{i=1}^{N} E_{xi}H_{yi}^* = Z_{xx}\sum_{i=1}^{N} H_{xi}H_{yi}^* + Z_{xy}\sum_{i=1}^{N} H_{yi}H_{yi}^* \tag{2.54}$$

where the expressions involving the summation signs are auto-power and cross-power density spectra of the field components. Equations (2.53) and (2.54) may then be solved to obtain estimates of Z_{xx} and Z_{xy}. Equation (2.53) can be thought of as being obtained by multiplying equation (2.33) by H_{xi}^* and summing over the N measurements and equation (2.54) by multiplying equation (2.33) by H_{yi}^* and summing over the N measurements. If the electric field components (E_{xi} and E_{yi}) are used instead of the magnetic field components (H_{xi} and H_{yi}), the following equations are obtained:

$$\sum_{i=1}^{N} E_{xi}E_{xi}^* = Z_{xx}\sum_{i=1}^{N} H_{xi}E_{xi}^* + Z_{xy}\sum_{i=1}^{N} H_{yi}E_{xi}^* \qquad (2.55)$$

and

$$\sum_{i=1}^{N} E_{xi}E_{yi} = Z_{xx}\sum_{i=1}^{N} H_{xi}E_{yi}^* + Z_{xy}\sum_{i=1}^{N} H_{yi}E_{yi}^*. \qquad (2.56)$$

Equations (2.53), (2.54), (2.55), and (2.56) can now be used to calculate Z_{xx} and Z_{xy}, and since there are six distinct pairs there are six different estimates of Z_{xx} and Z_{xy}. For instance, for Z_{xy} the six estimates, represented by $\overline{Z}_{xy}$, are (Sims et al., 1971):

$$\overline{Z}_{xy} = \frac{<H_xE_x^*><E_xE_y^*> - <H_xE_y^*><E_xE_x^*>}{<H_xE_x^*><H_yE_y^*> - <H_xE_y^*><H_yE_x^*>}, \qquad (2.57)$$

$$\bar{Z}_{xy} = \frac{<H_x E_x^*><E_x H_x^*> - <H_x H_x^*><E_x E_x^*>}{<H_x E_x^*><H_y H_x^*> - <H_x H_x^*><H_y E_x^*>}, \tag{2.58}$$

$$\bar{Z}_{xy} = \frac{<H_x E_x^*><E_x H_y^*> - <H_x H_y^*><E_x E_x^*>}{<H_x E_x^*><H_y H_y^*> - <H_x H_y^*><H_y E_x^*>}, \tag{2.59}$$

$$\bar{Z}_{xy} = \frac{<H_x E_y^*><E_x H_x^*> - <H_x H_x^*><E_x E_y^*>}{<H_x E_y^*><H_y H_x^*> - <H_x H_x^*><H_y E_y^*>}, \tag{2.60}$$

$$\bar{Z}_{xy} = \frac{<H_x E_y^*><E_x H_y^*> - <H_x H_y^*><E_x E_y^*>}{<H_x E_y^*><H_y H_y^*> - <H_x H_y^*><H_y E_y^*>}, \tag{2.61}$$

and

$$\bar{Z}_{xy} = \frac{<H_x H_x^*><E_x H_y^*> - <H_x H_y^*><E_x H_x^*>}{<H_x H_x^*><H_y H_y^*> - <H_x H_y^*><H_y H_x^*>}, \tag{2.62}$$

where the auto-power and the cross-power density spectra are represented by products of the type $<A_i B_j^*>$.

Strictly speaking, the summations in equations (2.53), (2.54), (2.55), and (2.56) are only valid for a particular frequency. However, since the impedances are assumed to be slowly varying functions of frequency, the summation terms may be regarded as averages over a finite bandwidth. From the six estimates (equations (2.57)-(2.62)), equation (2.59) and equation (2.60) are unstable; the other four are stable and correctly predict the impedance value for one-dimensional cases if the incident fields are not highly polarized (Sims et al., 1971). These comments also apply to all other estimates of the impedance tensor elements Z_{xx}, Z_{yx}, and Z_{yy}, which are calculated in a similar manner to the one just described and also have two unstable and four stable estimates.

Noise is an ever present feature of magnetotelluric measurements and, therefore, it is important to know its influence in the impedance estimates. According to Sims et al. (1971), of the four stable estimates referred above, two are biased down by random noise in the magnetic components and are not biased by random noise in the electric components (e.g., equations (2.61) and (2.62)) and the other two are biased up by random noise in the electric components and are not biased by random noise in the magnetic components (i.e., equations (2.57) and (2.58)). In MT work, equation (2.62) is the most commonly used. A more detailed description about the effect of noise in MT processing can be found in Sims et al. (1971) and Rotikyansky (1982).

After estimating the values of the impedance tensor elements it is possible to calculate the electric field components E_x and E_y using the right hand side of equations (2.33) and (2.34). Conventionally, these calculated values are called predicted values and are represented by E_{xp} and E_{yp}. A comparison between the predicted electric field components and the observed electric field components gives a measure of the quality of the estimated impedance elements. The similarity between the predicted and the observed values can be calculated by the predicted coherency, defined by (Swift, 1967)

$$coh(E_i, E_{ip}) = \frac{< E_i E_{ip}^* >}{\left[< E_i E_i^* > < E_{ip} E_{ip}^* > \right]^2}. \tag{2.63}$$

The coherency function varies between 0 and 1, the latter indicating that the measured and the predicted signals are perfectly correlated.

The coherency function is useful to identify good and poor data. Nevertheless, it does not provide a means to correct poor data. The remote reference method (Goubau et al., 1978; Gamble et al., 1979 a, b; Clarke et al., 1983) provides, however, a way of acquiring and processing MT data that appears to be effective in compensating for noise. Because of the strong effect that geological inhomogeneities have on the electric field, in this method one assumes that the measured magnetic field components are less contaminated by noise than the electric field components. In practical terms, the magnetic field components are recorded simultaneously at two different sites, assuming that between each site the signals are highly correlated while the noise is uncorrelated. If H_{xr} and H_{yr} represent the magnetic components measured at the remote reference site, the impedance tensor elements can be estimated by multiplying equations (2.33) and (2.34) by H^*_{xr} and H^*_{yr} and averaging as previously described. This operation gives:

$$<E_x H^*_{xr}> = Z_{xx} <H_x H^*_{xr}> + Z_{xy} <H_y H^*_{xr}>,$$

$$<E_x H^*_{yr}> = Z_{xx} <H_x H^*_{yr}> + Z_{xy} <H_y H^*_{yr}>,$$

$$<E_y H^*_{xr}> = Z_{yx} <H_x H^*_{xr}> + Z_{yy} <H_y H^*_{xr}>,$$

and

$$<E_y H^*_{yr}> = Z_{yx} <H_x H^*_{yr}> + Z_{yy} <H_y H^*_{yr}>.$$

If the noise in the remote reference site is uncorrelated with the noise in the MT site (and since the above equations do not contain auto-power density spectra) the calculated impedance tensor elements will be unbiased by noise.

2.6. Dimensionality indicators

The Earth's subsurface is generally complex and interpreting MT data based only on resistivity and phase curves, would be difficult in the majority of situations. Therefore, it is useful to have surplus information to constrain the data to be interpreted in geological terms. These constraints are given by parameters calculated from the impedance tensor, such as the strike direction, the skew, the ellipticity, and the tipper.

The strike direction has already been discribed in section 2.4, where two-dimensional structures are discussed. This parameter can, however, be misleading because, even in 3D cases, where, in principle, a strike direction should not be defined, equation (2.37) yields a strike direction (Jones and Vozoff, 1978). On the other hand, in some 2D cases the strike direction is difficult to define due to noisy data. In this situation, the diagonal elements of the impedance tensor are far from being zero, as they should be in an ideal two-dimensional structure. Nevertheless, a plot of the strike direction as a function of frequency is generally a good indicator of how the strike direction varies with depth and can help to interpret MT data. Different ways of calculating and plotting strike direction indicators can be used and Vozoff (1991) gives some examples.

Another important dimensionality parameter is the impedance skew, S, generally known by the term "skew". It is defined as (Swift, 1967; Vozoff, 1972)

$$S = \frac{\left|Z_{xx} + Z_{yy}\right|}{\left|Z_{xy} - Z_{yx}\right|}. \qquad (2.64)$$

Since it is the ratio of two of the three invariants defined in section 2.4 (i.e., I_2 and I_3), it is rotationally invariant. For one- and two-dimensional, noise-free data, the skew should be zero. However, this is often not the case because there is always noise present in MT data. For three-dimensional structures, the skew is high but so far it is not clear what value should be taken as the upper limit for the onset of a 3D behaviour. Reddy et al. (1977), Ting and Hohmann (1981), and Park et al. (1983) suggest values of 0.4, 0.12, and 0.5 (or higher) respectively, as indicating 3D structures.

Another parameter used to identify 3D geological structures is the impedance ellipticity $\beta(\theta)$, known as "ellipticity" (Word et al., 1971), defined as

$$\beta(\theta) = \frac{|Z_{xx}(\theta) - Z_{yy}(\theta)|}{|Z_{xy}(\theta) + Z_{yx}(\theta)|} \qquad (2.65)$$

where θ represents a rotation angle of coordinates. For noise-free data, ellipticity is zero for 1D cases as well as for 2D cases where the X or Y directions are parallel to the strike direction. While the skew does not vary with a rotation of coordinates, ellipticity does.

As previously indicated, there is an ambiguity when trying to determine the strike direction of a 2D geological structure by means of equation (2.37). The tipper, defined by Vozoff (1972), can, however, help to solve the ambiguity. In fact, the relationship between the measured vertical component of the magnetic field, (H_z), and the measured horizontal components (H_x and H_y) can be expressed by (Everett and Hyndman, 1967; Madden and Swift, 1969)

$$H_z = T_x H_x + T_y H_y. \tag{2.66}$$

The quantities T_i are complex and can be visualized as operating on the horizontal magnetic field and tipping part of it into the vertical direction. By definition, the tipper is given by (Vozoff, 1972)

$$T = \sqrt{T_x^2 + T_y^2} \tag{2.67}$$

where T_x and T_y are given by:

$$T_x = \frac{<H_z H_x^*><H_y H_y^*> - <H_z H_y^*><H_y H_x^*>}{<H_x H_x^*><H_y H_y^*> - <H_x H_y^*><H_y H_x^*>}$$

and

$$T_y = \frac{<H_z H_y^*><H_x H_x^*> - <H_z H_x^*><H_x H_y^*>}{<H_y H_y^*><H_x H_x> - <H_y H_x^*><H_x H_y^*>}.$$

The products of the type $<H_i H_j^*>$ represent auto-power and cross-power density spectra. For a one-dimensional situation, the tipper is zero. For a two-dimensional situation T_x will be zero for the H-polarization case (i.e., the strike is parallel to the X direction). Therefore, in a general 2D case, the strike direction will be the one that makes T_x decrease to zero. The tipper can also be used to determine which side of a contact between two media is the more conductive one (Vozoff, 1991; Orange, 1989). A more comprehensive description of the dimensionality parameters available to MT work can be found in Beamish (1986).

CHAPTER III

FIELD WORK AND INITIAL RESULTS

3.1. Field equipment - the SPAM system

When using the magnetotelluric method to determine the Earth's conductivity distribution with depth, one must bear in mind the range of amplitudes of the signals that will be measured and the spectrum of frequencies over which the measurements will be made. Since the amplitude of the magnetic field is of the order of milligammas and the electric field is of the order of μV/m, it is necessary for the equipment used to detect and measure those signals to be a high gain and low noise amplifier-filter device. At the same time, it is useful to know the quality of the measurements and to have the possibility of appraising the site results in the field, and so it is desirable for the equipment to allow digitization of the analog signals measured by the magnetic and electric detectors.

For the field work of this study the SPAM (Short Period Automatic Magnetotelluric) Mk IIb system developed at the University of Edinburgh was used, in conjunction with electric and magnetic detectors. It allows real-time, in-field data acquisition and processing, and is capable of detecting and recording signals in the frequency range of 128 Hz to 0.031 Hz. To make best use of the available dynamic range, and for economic reasons, that wide spectrum

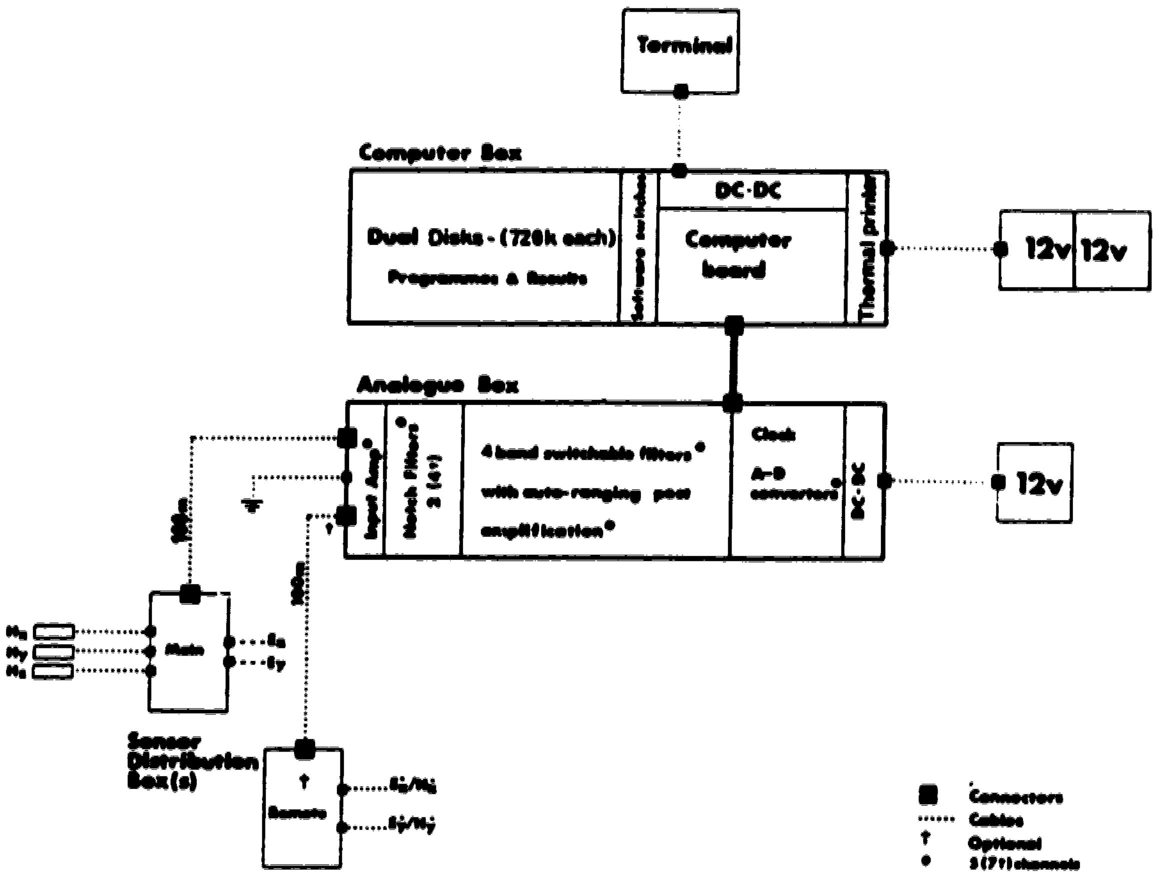

Fig. 3.1: Block diagram of the SPAM Mk IIb (from Dawes, 1990).

is divided into four overlapping bands (0, 1, 2, 3). Band 0 analyses frequencies between 128 and 16 Hz, band 1 frequencies between 16 and 2 Hz, band 2 frequencies between 2 and 0.25 Hz, and band 3 frequencies between 0.25 and 0.031 Hz.

The SPAM Mk IIb system is divided into three sub-systems: the sensor distribution box, the analog box, and the computer box (Dawes, 1990, SPAM Mk IIb User's Manual). Figure 3.1 shows a block diagram of the SPAM Mk IIb. The sensor box brings together up to 5 signals from the magnetic and electric sensors. These are three orthogonal magnetic signals (H_x, H_y, and H_z) and two orthogonal telluric or electric signals (E_x and E_y). Differential pre-amplifiers (to amplify the telluric signals) are included in the sensor box together with a power source to supply the magnetic sensors. The sensor box is connected to the analog box via a cable about 80 metres long in order to reduce interference to the magnetic and electric sensors. This cable transmits the signals and power to and from the sensors.

The analog box provides up to seven identical channels of signal processing and conversion, interfacing with the computer sub-system. It includes: pre-amplification and wide band filtering, to improve the signal to noise ratio and dynamic range; notch filtering, to remove artificial mains frequencies and odd harmonics; four band switchable filters, to split the broad band range into smaller bands; auto-ranging post amplification, to achieve optimal dynamic range of the widely varying natural signal levels; a clock generator and a control unit, to control the timing of the whole sub-system; individual sample and hold, and an analog to digital converter, to provide digitized data for the computer unit; and DC-DC converters, to allow efficient operation from a single 12 V battery.

The computer box performs data analysis and stores the results on floppy disks. Serial interfaces support a dual 3.5" floppy disk unit, a small portable LCD terminal, and an external data dump facility. Parallel interfaces drive a high speed thermal printer/plotter and provide all communications with the analog box. One of the floppy disks holds the programs for in-field analysis while the other stores the time series and analyzed data. The computer, the disk units, and the printer are powered via DC-DC converters from two 12 V batteries connected in series.

The magnetic sensors used during the field work were induction coils consisting of several thousand turns of fine copper wire wound on a core of high magnetic permeability material, and a low-noise pre-amplifier and components, all enclosed in a waterproof casing. The electric field measurements were performed using non-polarizing copper-copper sulphate electrodes. More detailed information about the SPAM Mk IIb can be found in the user's manual (Dawes, 1990).

3.2. Field procedures

When choosing a place for a magnetotelluric site one must always remember that cultural noise should be avoided. It can come from many sources, such as high voltage power lines that produce strong magnetic fields with frequencies of 50 or 60 Hz (depending on the country) and all odd harmonics. Other sources of cultural noise include electrified train lines, electrified fences, underground electric lines and pipes, farm machinery, local low power lines with poor transformers and poor earthing, radio transmitters and repeater stations, large metallic objects, passing vehicles, and so on. Noise can also result from physical movement or oscillations of the sensors. The site terrain should cover an approximate area of, at least, 50 m by 50 m, to accommodate the telluric lines, and should be as flat as possible. It should be away from rivers, lakes or interior seas because of the distorting effects they have on the induced electromagnetic fields. The site should not present great changes in the local geology and topography, and should provide a good contact between the ground and the non-polarizing electrodes. All these conditions are seldom met, but some compromise can always be achieved between the characteristics of the site and the quality of the signals measured and recorded.

After choosing the magnetotelluric site, the next step is to install the magnetic and electric sensors and set up the SPAM system. Considering that the site's centre is approximately marked by the sensor box, four cables of about 50 m are laid out in the north, south, east, and west directions. At the end of each of the cables a non-polarizing electrode is inserted into the ground and stabilized. To improve the electrical contact between the ground and the electrodes, it is common practice to wet a small volume of the ground where the electrodes are inserted. Each of the four electrodes is connected to its own cable, the other end of which is connected to the appropiate terminal on the sensor box. The north and south electrodes measure a potential difference that is used to determine the electric field in the N-S direction (with north considered positive) while the east and west electrodes measure a potential difference that is used to determine the electric field in the E-W direction (with east considered positive). The contact resistence between each pair of electrodes has to be checked. Generally values above 10 $k\Omega$ do not give reliable results and, in this case, an effort must be made to improve the electric contact between the ground and the electrodes. The spontaneous potential is also measured as a means to determine if the electrodes have reached electrical equilibrium with the soil and if the DC component of the telluric currents is sufficiently low. Figure 3.2 illustrates the typical field set-up of a MT site.

The magnetic sensors (coils) are the next devices to be installed. Two of them must be placed horizontally in small

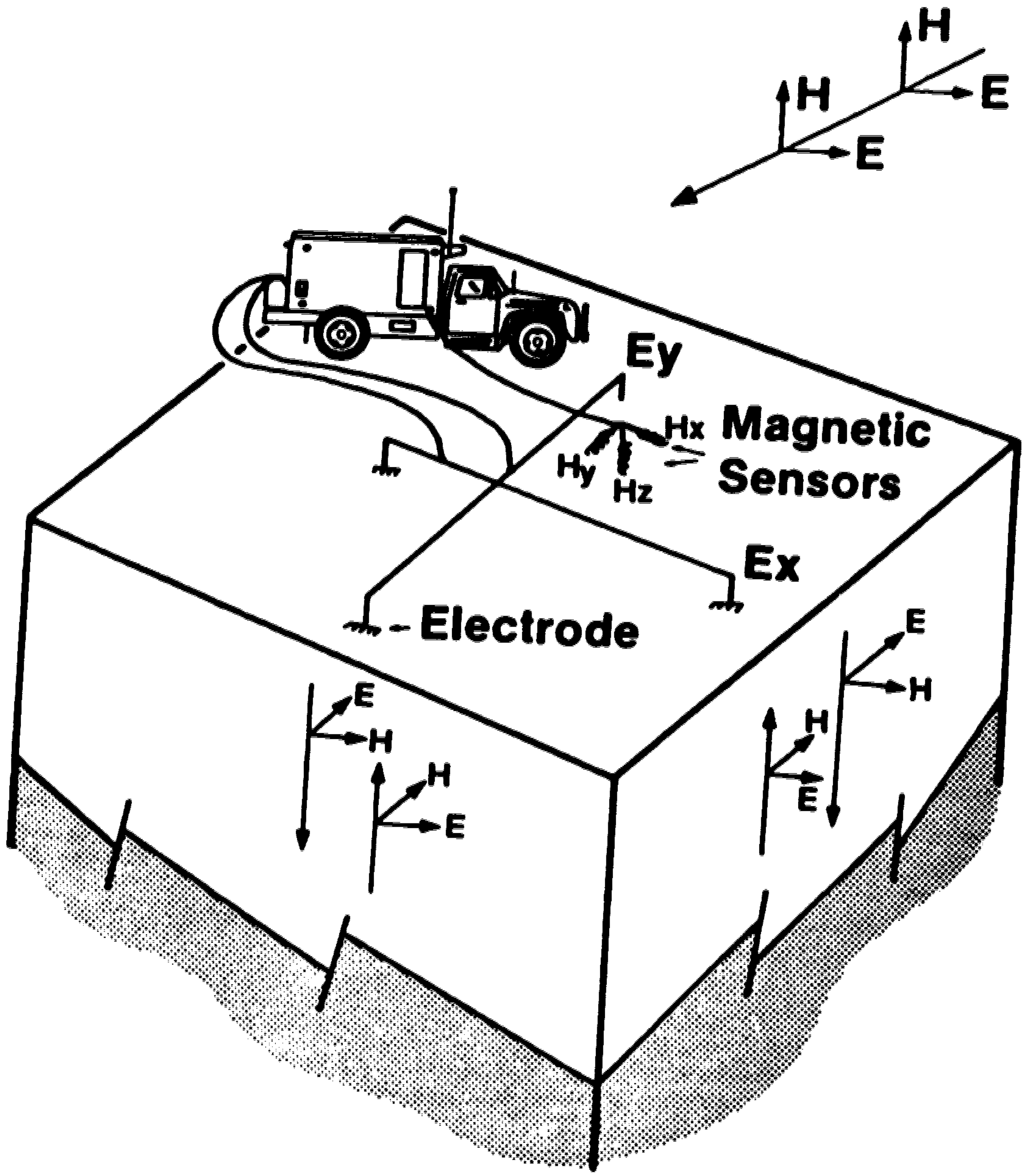

Fig. 3.2: Illustration of a typical magnetotelluric station set-up (modified from Sternberg et al.,1984).

trenches dug in the N-S and E-W directions and separated by about 5 m. The third coil must be placed vertically in a hole away from the other two. All the three coils must be leveled and covered with soil to avoid vibrations produced by wind. The same coils are always used in the same directions. As in the telluric lines, the coils are connected to the appropriate terminals in the sensor box by cables with no loops, which should also be covered with soil to avoid vibrations. In this study it was not possible to measure the vertical component of the magnetic field because of a breakdown of one of the coils. This was unfortunate and precluded some analysis that could have been done if that component had been measured.

After these initial operations, the sensor box is connected to the SPAM system through a multiconductor cable of about 80 m length. The whole system is then earthed and the tests and calibration begins. The initial tests are time consuming but, in order to be sure about the quality of the data, it is always a good policy to make them before initiating any measurements. The SPAM's user manual thoroughly describes all the tests to be performed. However, there are three tests that should be mentioned. The first is to determine the optimum gain so that there is no overload and saturation of the magnetic and telluric channels; the second consists of verifying the level of cultural noise that may be present in or near the MT site by using the notch filters for each channel (this procedure is particularly important for band 0); and the third consists of visually verifying with an oscilloscope the correlations between H_x and E_y, and between H_y and E_x (this gives indications about possible misconnected cables among the sensor box and the electric and magnetic sensors). After all tests are performed, measurements of the natural fields can begin.

The magnetotelluric field work in Portugal began in May, 1990 and lasted for four months. Besides the MT measurements, it also included field reconnaissance, equipment preparation, and contact with owners to seek authorization to occupy sites on private land. In total 34 magnetotelluric sites were occupied in two months of work. On average, each site was occupied for 12 to 14 hours with the exception of sites 1 and 28, where, because of equipment failure, the times of occupation were about 2 days each.

From the geology, it is apparent that the study region is three-dimensional (see Figure 2.2). Therefore, from the beginning of the work it was decided to cover the area with a two-dimensional array of magnetotelluric stations instead of the more common profiling technique.

3.3. In-field processing and field results

The SPAM system is capable of in-field processing. This is accomplished through a computer program with flowchart shown in Figure 3.3. In each band and channel the components of the magnetotelluric signals are analyzed by the program

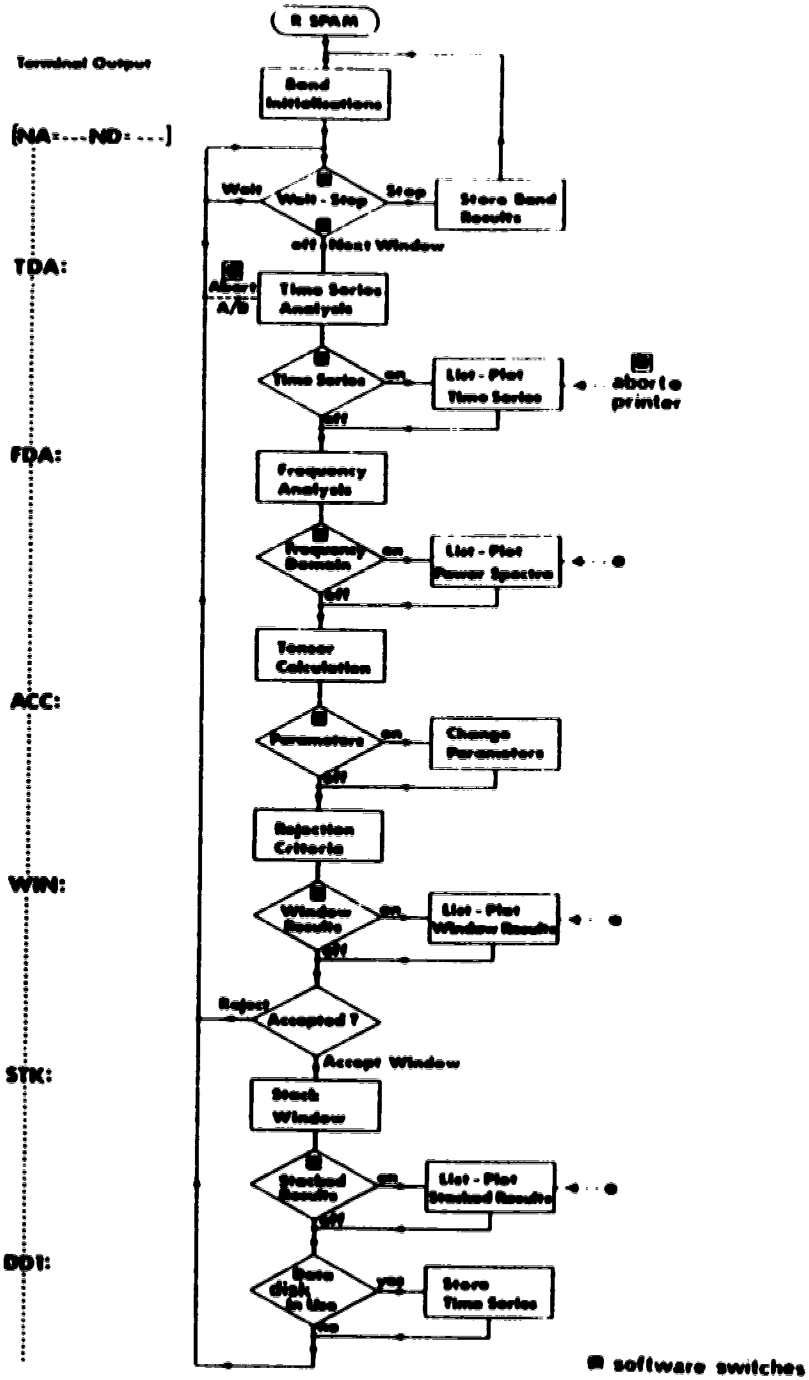

Fig. 3.3: Flowchart of the computer program for in-field processing (from Dawes, 1990).

in terms of several windows, generally 100 for band 0, 1, and 2. A window consists of 256 samples and if it satisfies preset criteria it is stored for further analysis. In this study the following criteria were used to accept windows in band 0, 1, and 2: the intensity level of the magnetic signals should be higher than 0.3 *mγ* for, at least, 5 frequencies in the window being analysed, and the coherency should be higher than 0.9. For band 3, however, because of the times involved in recording each window (about four minutes), all of them were accepted as good windows and statistically treated later in more detailed processing than the in-field processing. In a few cases, the above criteria for the first three bands had to be changed to allow the recording of windows with coherencies lower than 0.9. In any case, windows having coherencies lower than 0.8 were always rejected. Each window analysed by the SPAM system can be visually checked by plotting the time series for all channels in use, their power spectra, and their response functions. Averages for each window can also be seen. In Figure 3.3 an example of a printout of the in-field processing is shown.

In Appendix I, a map with the numbers and the relative positions of the MT sites is shown, as well as the data and results from the preliminary processing for the 34 MT sites. The actual locations of the MT sites are shown in Figure 1.2. For each site, the resistivities and phases in the N-S and E-W directions (ρ_{xy}, ρ_{yx}; ϕ_{xy}, ϕ_{yx}) are also given in

STACKED RESULTS........................ Page 0.0 Site 5 Band 2 Run 1 Win 100

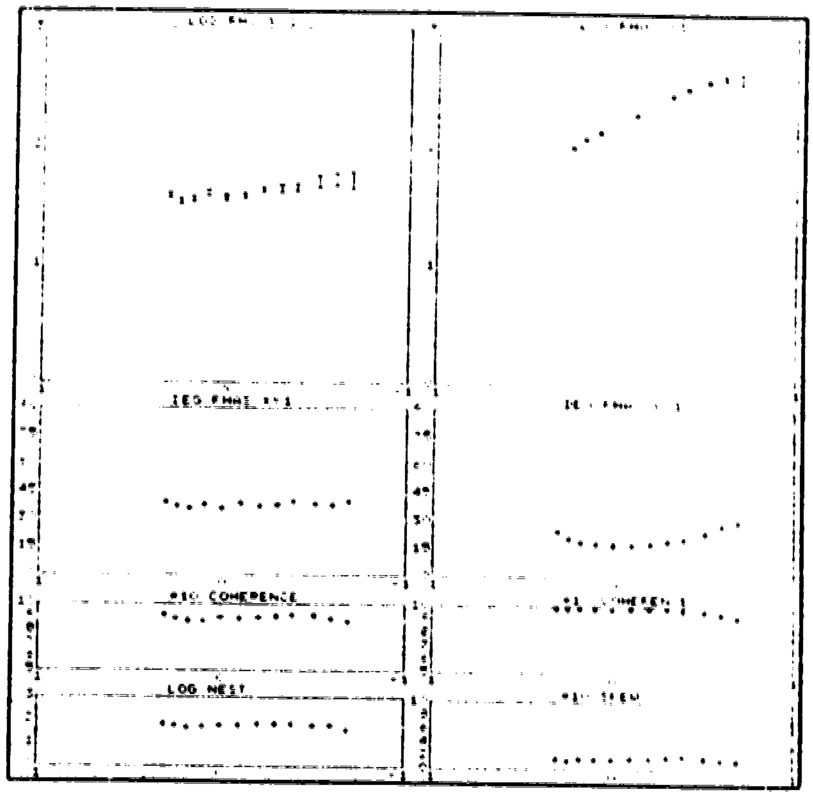

MT1

	FREQ	SKEW	RHOXY	PHXY	COHXY	RHOYX	PHYX	COHYX	NXY	ERHXY	NYX	ERHYX
1	2.000	0.15	30.82	-140.6	0.92	89.48	25.1	0.99	69	2.00	69	1.50
2	1.734	0.14	34.16	-142.5	0.89	104.04	21.0	0.99	64	2.24	64	2.60
3	1.404	0.15	36.11	-143.5	0.87	121.20	19.1	0.99	51	2.23	51	2.95
4	1.234	0.15	40.16	-141.0	0.88	140.96	18.4	0.99	55	2.18	55	3.07
5	1.000	0.15	36.78	-144.0	0.90	169.19	18.0	0.99	60	2.34	60	3.52
6	0.781	0.17	38.66	-141.3	0.89	202.10	17.6	0.99	65	2.79	65	5.17
7	0.625	0.17	43.21	-142.4	0.91	234.10	18.5	0.99	69	3.00	69	4.05
8	0.500	0.18	44.39	-141.0	0.91	293.18	19.7	0.98	69	4.12	69	8.02
9	0.406	0.20	45.33	-139.7	0.93	337.03	21.2	0.98	73	4.23	73	12.53
10	0.312	0.18	51.01	-140.9	0.92	385.05	24.3	0.97	60	6.50	60	15.10
11	0.250	0.16	53.15	-142.0	0.90	417.17	28.2	0.95	62	7.93	62	22.03
12	0.203	0.14	52.15	-140.1	0.88	400.22	30.4	0.92	41	9.79	41	44.25

Fig. 3.4: Example of printout of in-field processing for site 5. The graphs of the stacked results for the first run of band 2 are shown. The twelve frequencies for the band are shown, as well as the estimates of the skew, the apparent electrical resistivities in the XY (RHOXY) and YX (RHOYX) directions, the phases in the XY (PHXY) and YX (PHYX) directions, the coherences of the estimates in the XY (COHXY) and YX (COHYX) directions, and the number of apparent electrical resistivity estimates in the XY (NXY) and YX (NYX) directions and the associated errors (ERHXY) and (ERHYX).

Appendix I, as well as the resistivities and phases for the E-polarization (Major) and H-polarization (Minor) cases. Also shown are plots of the coherency for each frequency, the number of estimates, the skew, the angle of rotation θ for the four bands, and the determinant invariant resistivity (ρ_{inv}) and phase (ϕ_{inv}), which are defined by

$$\rho_{inv} = \frac{1}{\mu\omega}\left|Z_{det}\right|^2$$

and

$$\phi_{inv} = \tan^{-1}\frac{\left[\operatorname{Im} Z_{det}\right]}{\left[\operatorname{Re} Z_{det}\right]},$$

where Z_{det} is the determinant invariant impedance defined by the following formula (Berdichevsky and Dimitriev, 1976a):

$$Z_{det} = \left(Z_{xx}Z_{yy} - Z_{xy}Z_{yx}\right)^{1/2}. \tag{3.1}$$

3.4. The long period magnetotelluric study

At the same time that the magnetotelluric measurements were being made with the SPAM system, an associated electromagnetic survey was being carried out by another team, with the objective of obtaining magnetotelluric data for lower frequencies than those analysed and recorded by the SPAM system. The main intent was to collect data that would allow calculation of earth response functions for periods up to 5,000 seconds. To distinguish this long period magnetotelluric survey from the magnetotelluric survey performed with the SPAM system, from now on, the former will be called LMT. The author also participated in the LMT survey, essentially at a logistic level and, despite the fact that he did not operate the field equipment or process the data, it was agreed among the three participating universities (University of Alberta, Canada; University of Edinburgh, Scotland; and University of Evora, Portugal) that the processed results would be included in this dissertation.

The LMT data were processed by an undergraduate student of the Department of Geology and Geophysics of the University of Edinburgh, and the results were presented as an undergraduate fourth year memoir (MacDonald, 1991). The LMT work took place in the same region as the magnetotelluric survey and all LMT stations were located at previously occupied MT sites. Twelve LMT stations were installed but the collected data were good enough to be analysed for only five of them. This failure of the LMT survey was due to several reasons, mainly the age of the equipment and the high temperatures at the time of the survey.

Briefly, the LMT equipment at each site was composed of a geologger and a fluxgate control unit, a control box, a fluxgate magnetometer, and a set of three non-polarizing copper-copper sulphate electrodes. Each system was powered by a 12 V battery and a solar panel. The geologger and fluxgate control unit controlled the fluxgate magnetometer and recorded the three magnetic components on audio cassettes. Another unit, known as the tellurics box, was used to amplify the electric signals detected by the non-polarizing electrodes and to send them to the geologger, where they were also stored on audio cassettes. Each LMT site was occupied for several days and was visited every second day to retrieve the recorded cassettes and replace them, and to check the state of the equipment. Its layout was performed using the same precautions as described in section 3.3 for the magnetotelluric survey.

As previously mentioned, due to a breakdown of one of the coils of the SPAM equipment, it was not possible to measure the vertical magnetic field component. Although the LMT survey began almost a month after the beginning of the MT survey, it was hoped that it would be possible to calculate induction arrows (Parkinson, 1962; Gregori and Lanzerotti, 1980) for some of the MT sites from the long period data. Directions of the real induction arrows were indeed calculated for 5 of the 12 LMT stations and Table I gives a summary of their directions and magnitudes for short periods (about 500 seconds) and long periods (5,000 seconds). Figure 3.5 shows the real induction arrows for those two periods superimposed on a simplified tectonic map of the study area.

TABLE I

Real magnetic induction arrows calculated for 500 (short period) and 5,000 (long period) seconds. The directions, in degrees, are measured from north anti-clockwise (from MacDonald, 1991).

	Long period		Short period	
Site no.	Direction	Magnitude	Direction	Magnitude
1	110	0.4	270	0.2
14	135	0.6	310	0.15
15	120	0.75	135	0.4
28	140	0.5	270	0.3
31	140	0.4	0	0.2

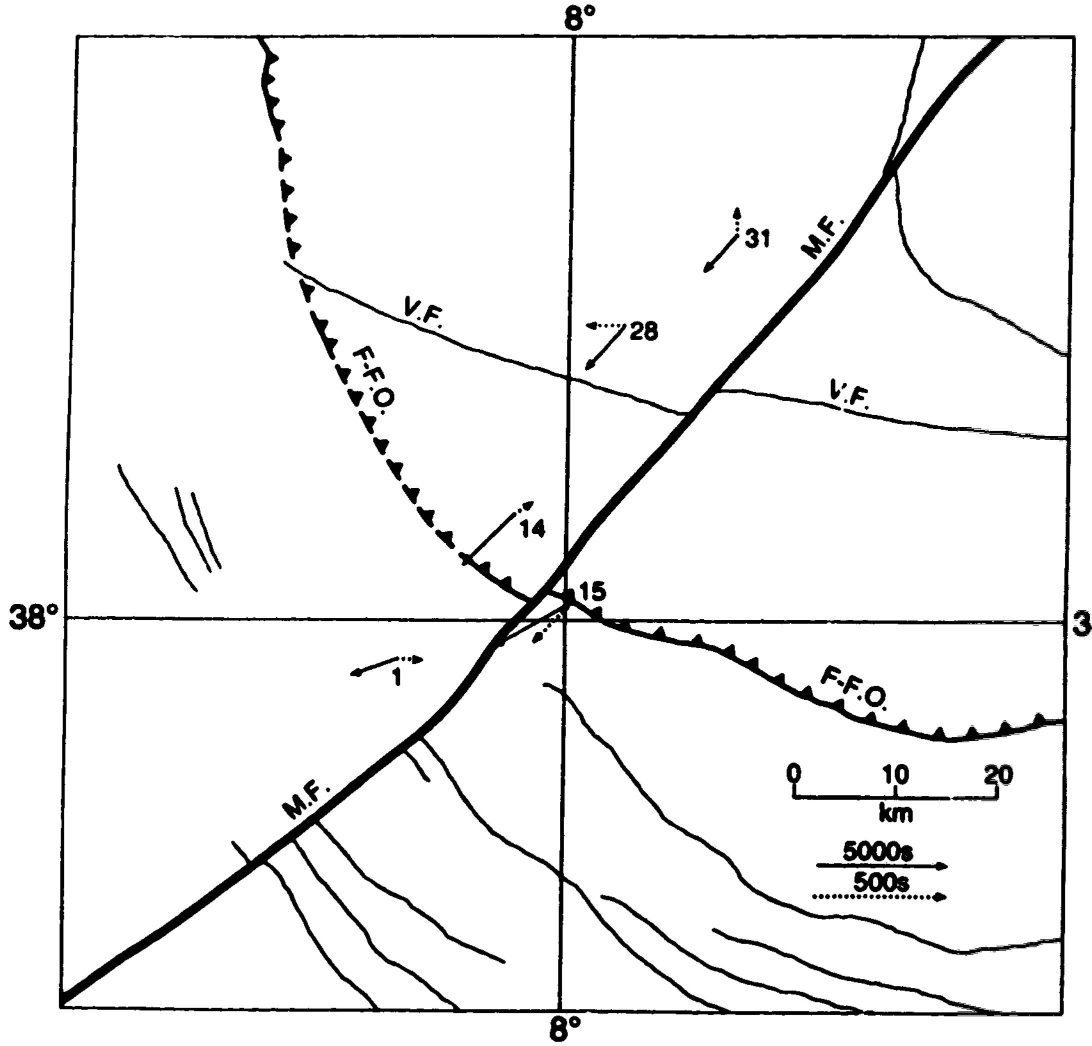

Fig. 3.5: Directions of the real induction arrows for 500 (dotted lines) and 5,000 seconds (solid lines) superimposed on a tectonic map of the study area. The Messejana fault and the Ferreira-Ficalho overthrust are identified. The Vidigueira fault is also shown (refer to discussion in Chapter VI).

From the LMT results reported by MacDonald (1991), the main conclusion is that the data collected in Portugal are too few for any sound geological interpretation based only in the LMT data. Nevertheless, the general trend of the induction arrows will be used and explored in the conclusions of this dissertation.

3.5. Some initial interpretations based on 1D EM models

This section is based on one paper published in a conference proceedings (Correia et al., 1991) and two papers that were accepted for publication in geophysical journals (Jones et al., 1992; Correia et al., 1993).

The study area (Figure 1.2) is geologically and tectonically complex and, apparently three-dimensional. Standard magnetotelluric methods to analyse three-dimensional structures are not yet available (Park and Livelybrooks, 1989; Vozoff, 1991). Therefore, an interpretation methodology had to be decided upon for the data collected in Portugal. At the time of the field work, it was thought that the most appropriate method would be to produce 2D and 3D numerical models for the study region and then attempt a geological interpretation. For this reason the MT sites were distributed over a grid configuration rather than a profile layout.

To produce 2D and 3D models it is necessary to have an initial model that will be refined and updated as the results of it are compared with the real data. With this in mind, and as a first approximation, a one-dimensional analysis of the data was performed. Therefore, despite the shortcomings of using a one-dimensional modelling approach (Park and Livelybrooks, 1989), a 1D model for each of the 34 magnetotelluric sites was produced. In Chapter IV more details will be given about the modelling procedures, difficulties and limitations.

The one-dimensional modelling used in this work is based on equation (3.1), which was reported to give fair to good initial results for 2D and 3D geological situations (Ranganayaki, 1984; Sule and Hutton, 1986; Ingham, 1988) and has been used by some authors, e.g., Kurtz (1982), Stanley et al. (1990), Beamish (1990), Kurtz et al. (1990), Dawes and Lagios (1991). In Appendix I, the resistivity and phase curves obtained using the determinant invariant of the impedance tensor are shown for each site.

The 1D models were produced using a hybrid Monte Carlo Hedgehog inversion scheme. In this method, a first guess of what the 1D stucture is, based on the shapes of the determinant invariant resistivity and phase curves, is used to generate several one-dimensional random models. The resistivity and phase curves for these models are then compared with resistivity and phase field curves. If the model and the field curves fit according to a preset criterion, the model is assumed to be a good one. If there is a misfit, the process continues until a fit is found. The models that are obtained with this method are given in terms of upper and lower bounds for the resistivities and depths to the boundaries between layers. In Appendix II, 1D models for each MT site are shown, as well as the fits between the model curves and the resistivity and phase field data.

Using the 1D models calculated as described above, resistivity contour maps were drawn for different depths. Figures 3.6 and 3.7 show two such maps for 500 and 10,000 m depth. The main characteristics of these two maps (and in fact all the maps that were drawn between those two depths) is the division of the region into several deep rooted high resistivity blocks separated by areas of low resistivity that coincide with the trends of the two major tectonic features that cross the area, i.e., the Messejana fault and the Ferreira-Ficalho overthrust. At shallow depths, north of the Ferreira-Ficalho overthrust, there are two regions of high electrical resistivity that extend to depths greater than 10,000 m, and a region of very low electrical resistivity north of them. In both electric resistivity highs, the electrical resistivity decreases with depth from about 3,000 and 2,500 ohm m at 500 m to about 1,500 and 2,000 ohm m at 10,000 m depth. These two regions are separated by a low resistivity zone that coincides with the Messejana fault. Southwest of the overthrust, electrical resistivities are lower than to the northeast and they decrease from 1,000 ohm m at 500 m depth to 500 ohm m at 2,000 m depth, and then increase to values of about 1,000 ohm m in some areas at 10,000 m depth. From Figures 3.6 and

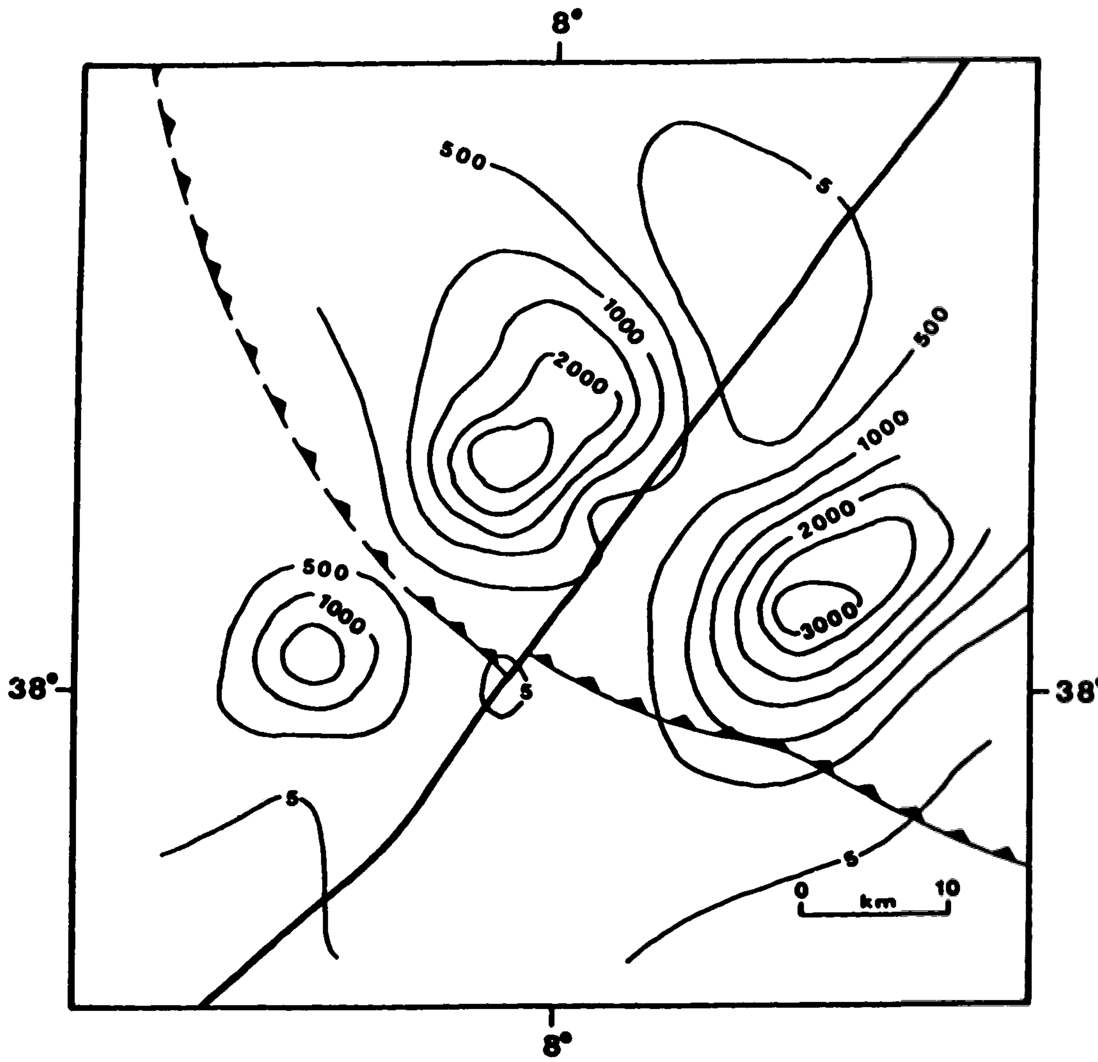

Fig. 3.6: Electrical resistivity at 500 m depth in ohm-m (thin lines). Also shown are the Messejana fault and the Ferreira-Ficalho overthrust (from Correia et al., 1993).

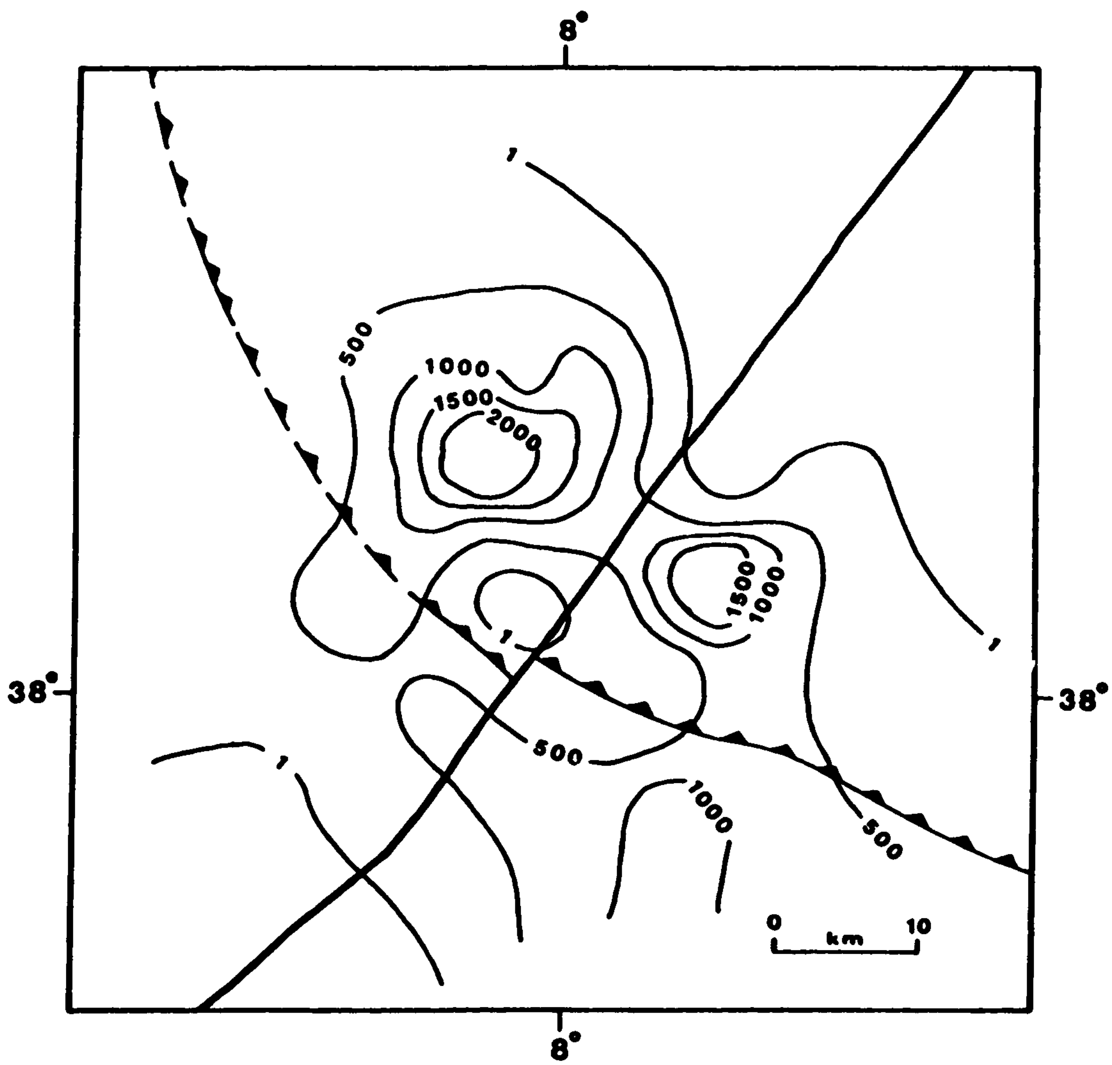

Fig. 3.7: The same as in Figure 3.6 but for 10,000 m depth (from Correia et al., 1993).

3.7 it is apparent that the geoelectrical structure of the study area becomes more complex as depth increases; this can be a real trend of the geological structure or may result from the fact that the resolution of the magnetotelluric method decreases with depth. On the other hand, the geoelectrical structure of the study area appears to be more complex southwest of the Ferreira-Ficalho overthrust than to the northeast. At this point it must be emphasized that the maps shown in Figures 3.6 and 3.7 are not geological or geophysical interpretations of the region of the MT study. Nevertheless, they are used as an initial input to produce 2D and 3D models.

An interesting result from this first 1D approximation is the fact that there is a general coincidence between low resistivity areas and faults or fault trends. It appears that the region where the MT study was performed may have been fractured into several high resistivity blocks by regional tectonic processes and the resulting faults and overthrust now constitute channels for fluid motion. This would explain the low resistivities measured in those areas. To some extent, this coincidence makes the author believe that the use of 1D models to produce 2D and 3D models is appropriate.

It should be mentioned that no static shift correction (Jones, 1992) was applied to the data collected in Portugal. Due to the geological complexity and the spacing among MT stations, it is impossible to determine if the observed shifts in some of the curves in Appendix I are the result of static shift or represent effects due to local geology.

3.6. Apparent electric resistivity and phase pseudosections

A visual inspection of the field data shown in Appendix I and the geological sketch of Figure 1.2 suggest that the study area has a two-dimensional (2D) or three-dimensional (3D) character depending on the scale of the area being considered. From geology, the central part of the region is certainly 3D. However, as can be inferred from Figure 1.2, if the MT sites along the edges of the study area are used to construct MT profiles, these apparently cross 2D geologic structures. Therefore, four MT profiles passing through those MT stations were considered and are shown in Figure 3.8.

Apparent electrical resistivity and phase data pseudosections associated with the four profiles were constructed for the study area. Pseudosections are plots of observed (or calculated from models) apparent electrical resistivities or phases determined from values at the stations of a certain profile, as a function of frequency, on a logarithmic scale as ordinate.

As discussed in Chapter II, two modes of electromagnetic excitation are possible in 2D structures (TE and TM modes) and therefore it is advisable to construct pseudosections in the directions corresponding to those two modes. This has the advantage that it allows the comparison

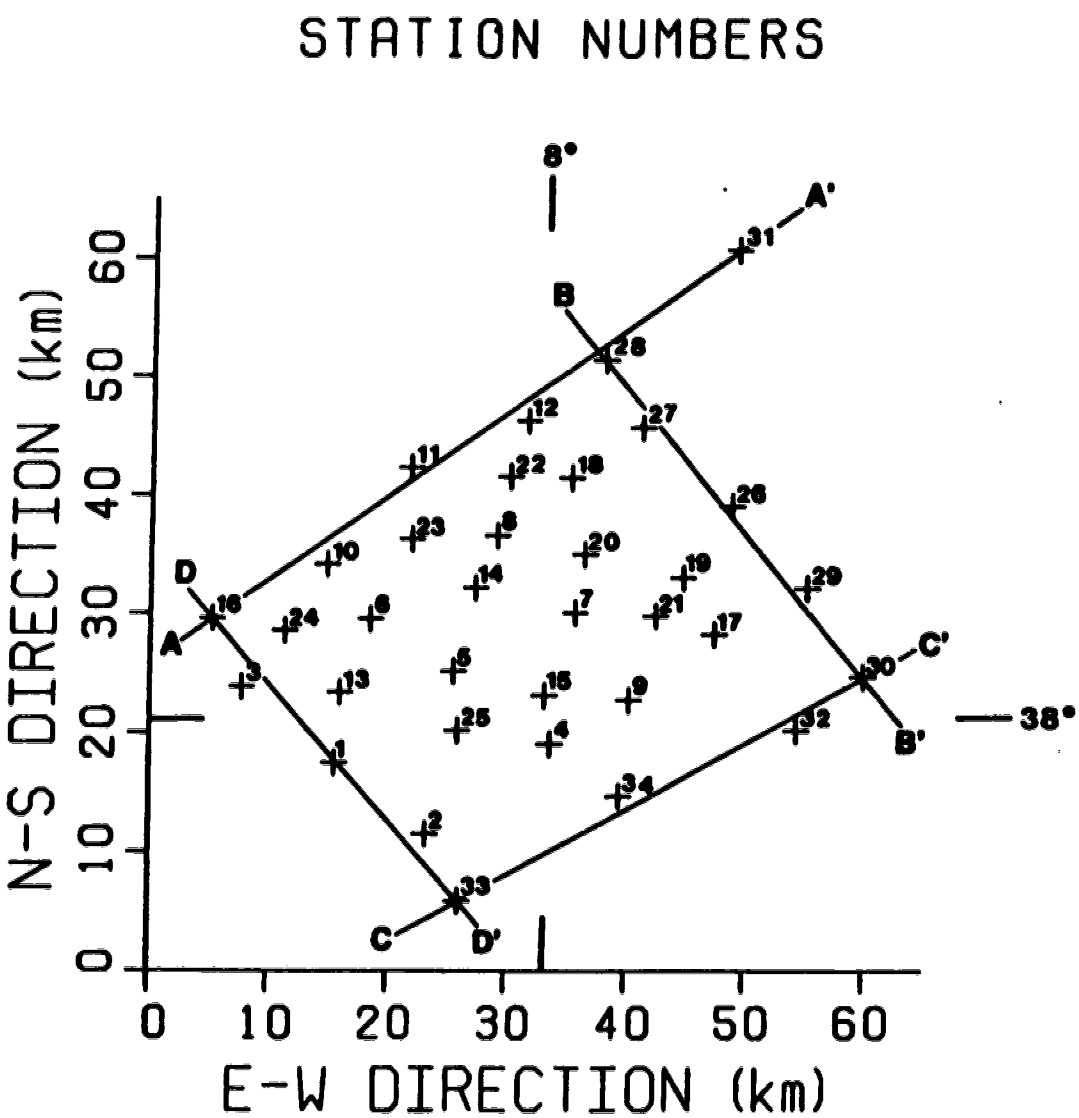

Fig. 3.8: Station numbers and MT profiles used to construct field data apparent electrical resistivity and phase pseudosections.

of field data pseudosections with response model pseudosections (to be discussed in Chapter IV). The two modes have different characteristics, an important one being that the TM mode is more sensitive to lateral variations of electrical resistivity than the TE mode (d'Erceville and Kunetz, 1962; Wannamaker et al., 1982; Dobrin and Savit, 1988). However, data pseudosections only allow a qualitative analysis of geoelectrical structures. A quantitative analysis is achieved by inversion or modelling, wherein apparent electrical resistivity and phase pseudosections, or even single site apparent electrical resistivity values and/or phases as functions of frequency, are transformed into resistivity-depth sections. This will be discussed in Chapter IV.

To construct the apparent electrical resistivity and phase pseudosections, the field data were rotated towards the strike direction using the procedure described in Chapter II: first, for each profile in Figure 3.8, the approximate strike direction was determined by measuring the angle between the general trend of the geological structures and the North-South direction, in a clockwise sense; second, the field data (i. e., the impedance tensors) for each MT station included in the profile were mathematically rotated by an amount equal to the measured angle; third, apparent electrical resistivity and phase pseudosections parallel (TE mode) and perpendicular (TM mode) to the geological strike were plotted. These plots can be seen in Figure 3.9. In each

2

PM-1 3½"x4" PHOTOGRAPHIC MICROCOPY TARGET
NBS 1010a ANSI/ISO #2 EQUIVALENT

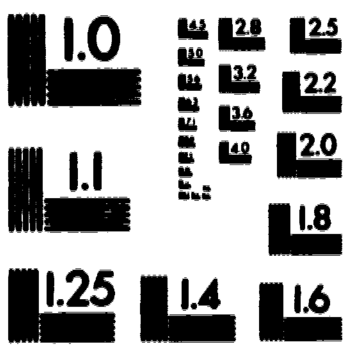

PRECISION℠ RESOLUTION TARGETS

page the rotated field apparent electrical resistivity and phase pseudosections are shown for the same profile and the same electromagnetic excitation mode.

Before attempting an interpretation of the field data pseudosections of Figure 3.9, the static shift effect that may affect magnetotelluric field data should be discussed (this effect will be considered in more detail in Chapter V). The aim of the magnetotelluric method is to determine the geoelectrical structure of the Earth's subsurface by simultaneously measuring the electric and magnetic field fluctuations at its surface. Small surficial or shallow conductivity inhomogeneities (of a few metres to tens of metres dimension) can influence the electric field measurements by deflecting the induced electric currents. As a result, the apparent electrical resistivity curves may be shifted up or down by an independent multiplication factor that depends on the conductivity of the heterogeneity (Berdichevsky and Dmitriev, 1976b; Sternberg et al., 1988; Jones, 1988). If apparent electrical resistivity curves affected by static shift are used to obtain resistivity-depth profiles by inversion or trial-and-error modelling, errors in both the calculated electrical resistivities and depths may occur. There is currently no general agreement on how to eliminate, compensate or reduce the static shift effect if it is present. Fortunately, static shift does not greatly affect phases (Jones, 1992), and therefore phase pseudosections can be used with some confidence to

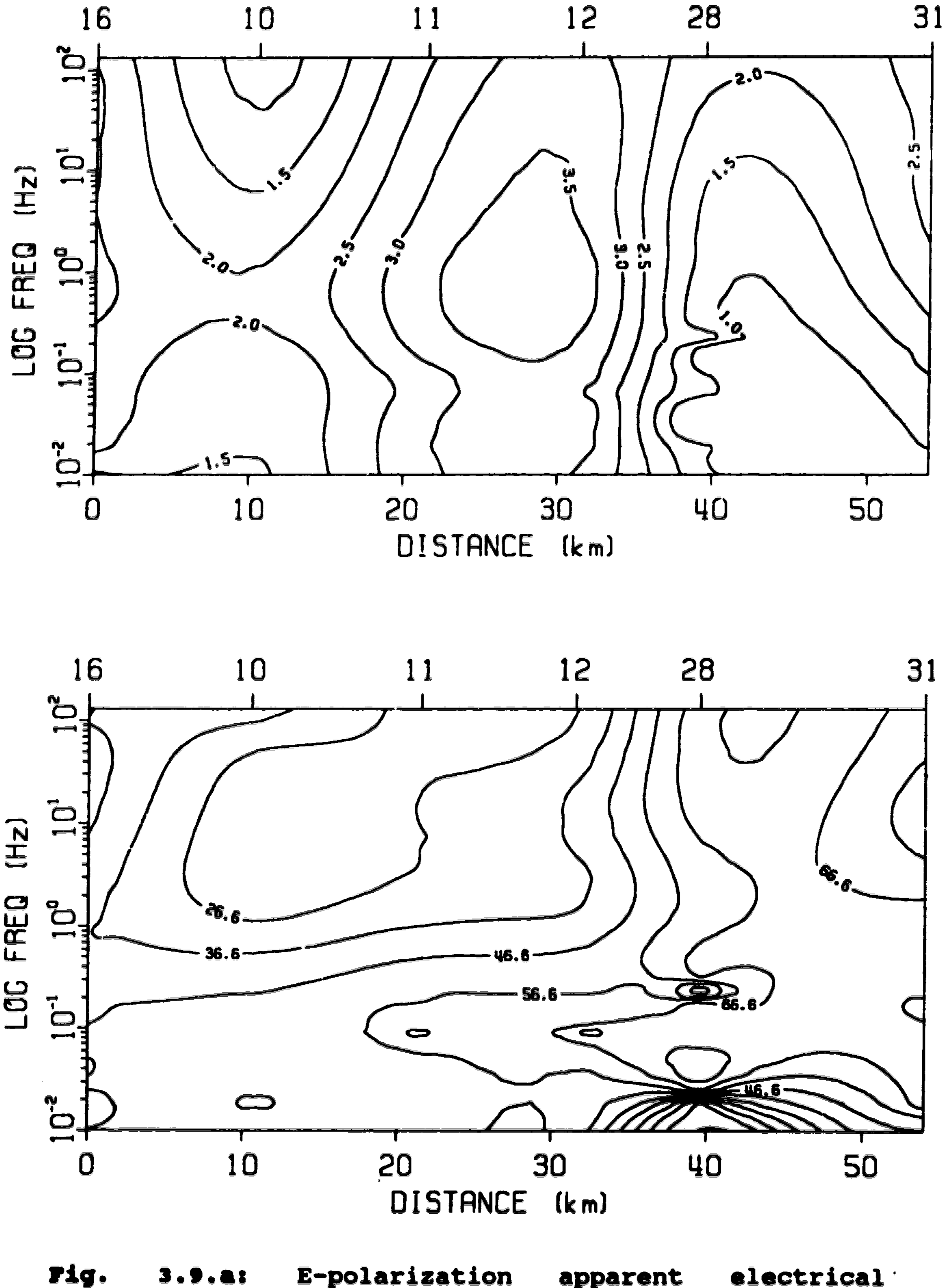

Fig. 3.9.a: E-polarization apparent electrical resistivity (top) and phase pseudosection (bottom) for profile AA' of Figure 3.8.

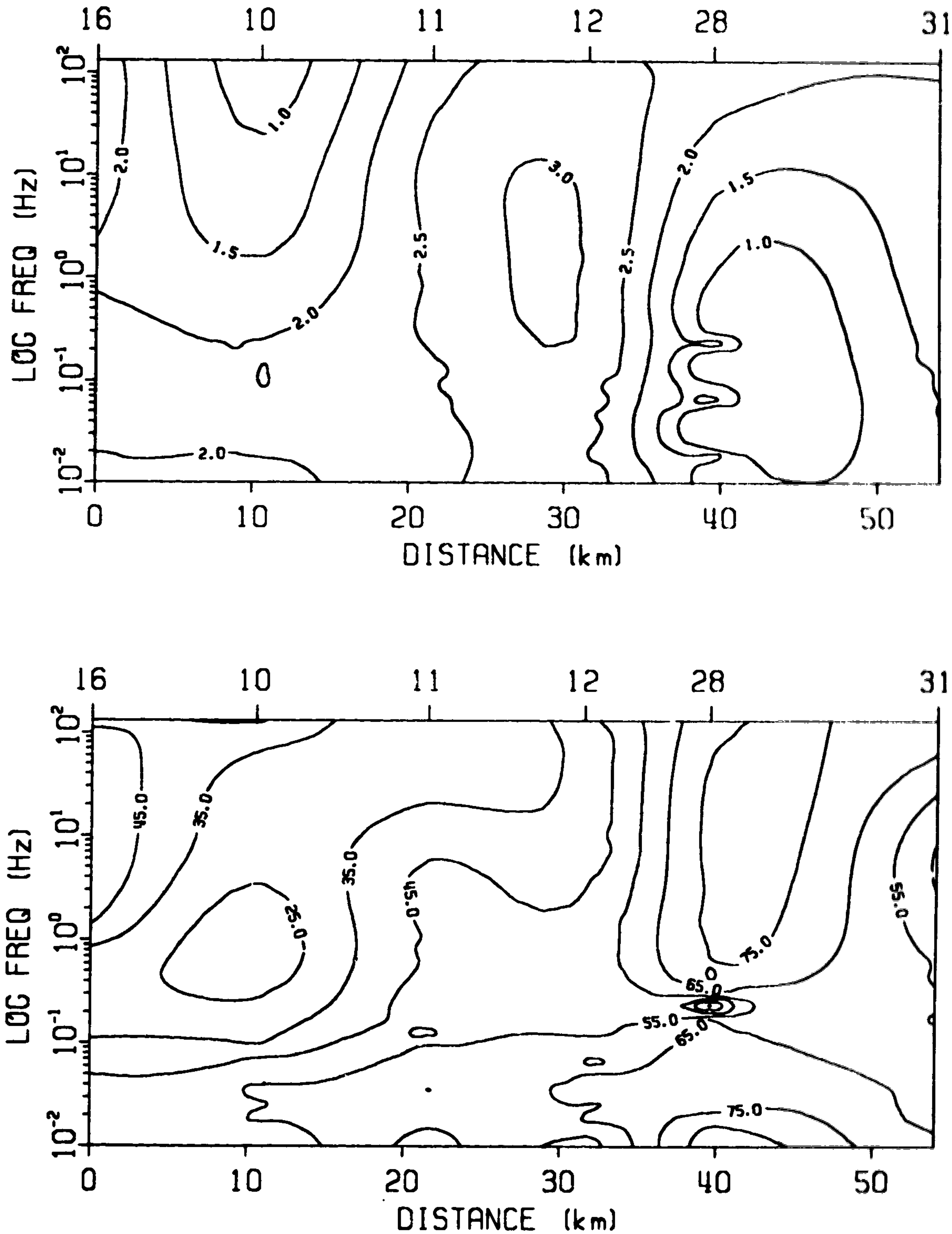

Fig. 3.9.b: The same as in Figure 3.9.a but for the H-polarization case.

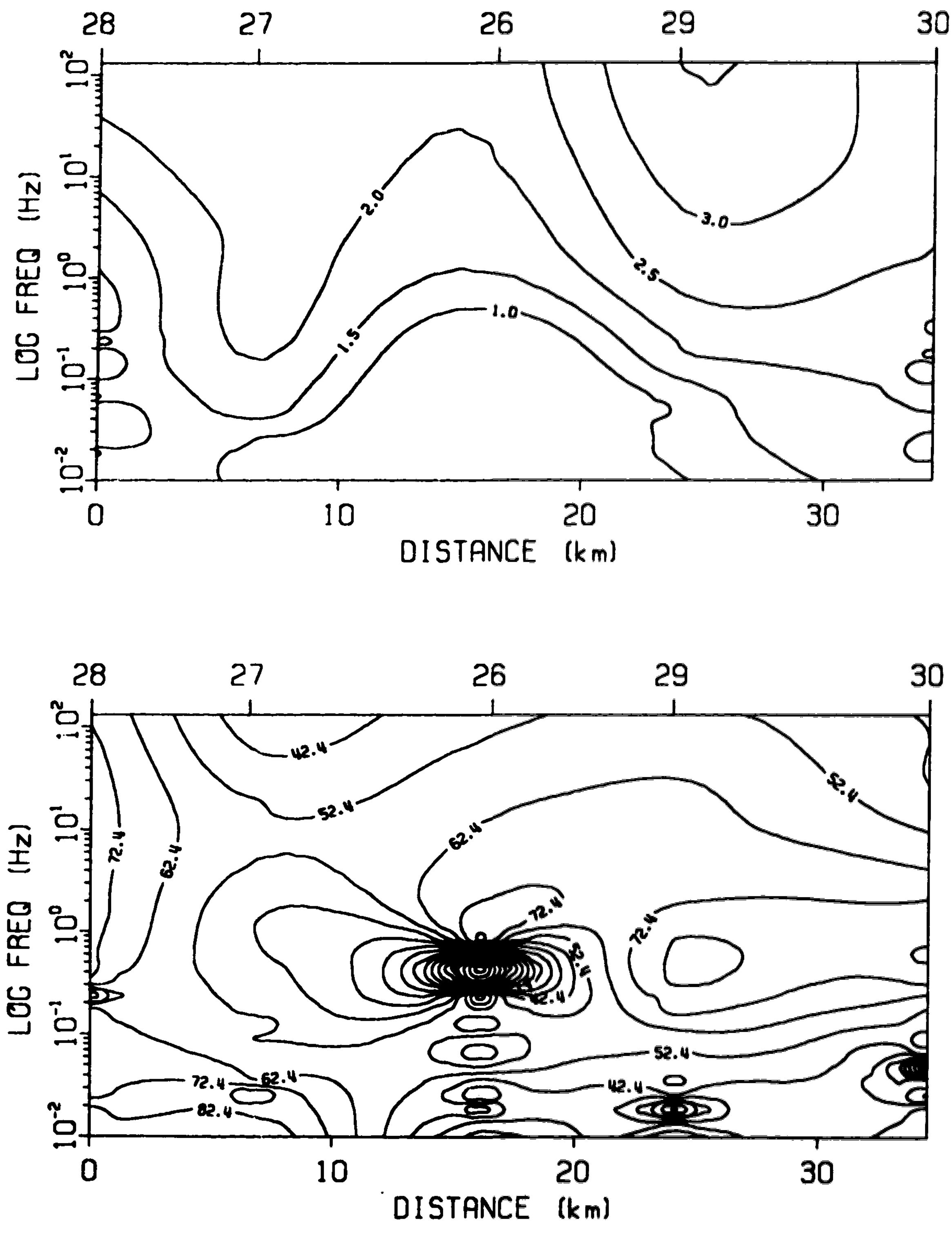

Fig. 3.9.c: E-polarization apparent electrical resistivity (top) and phase pseudosection (bottom) for profile BB' of Figure 3.8.

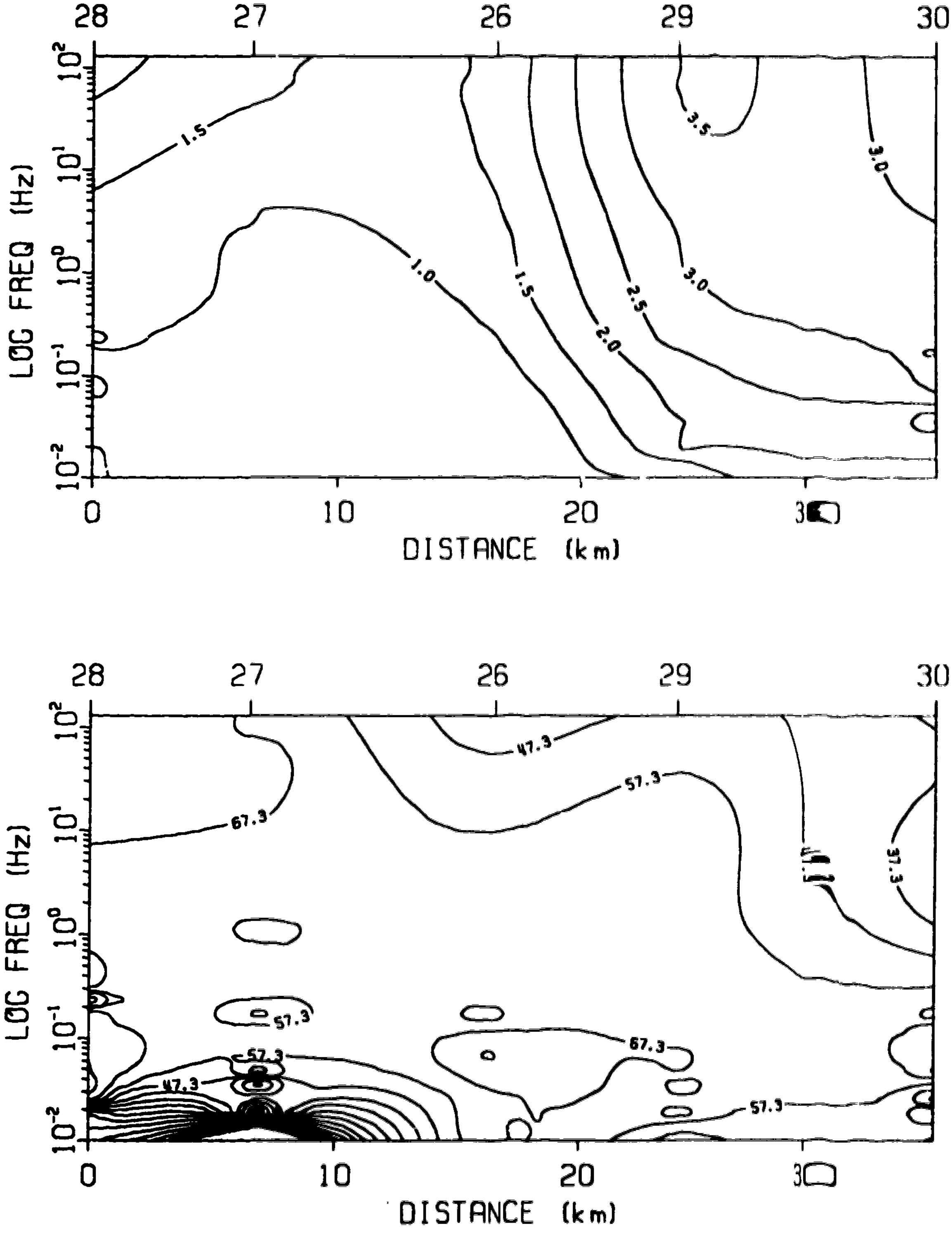

Fig. 3.9.d: The same as in Figure 3.9.c but for the H-polarization case.

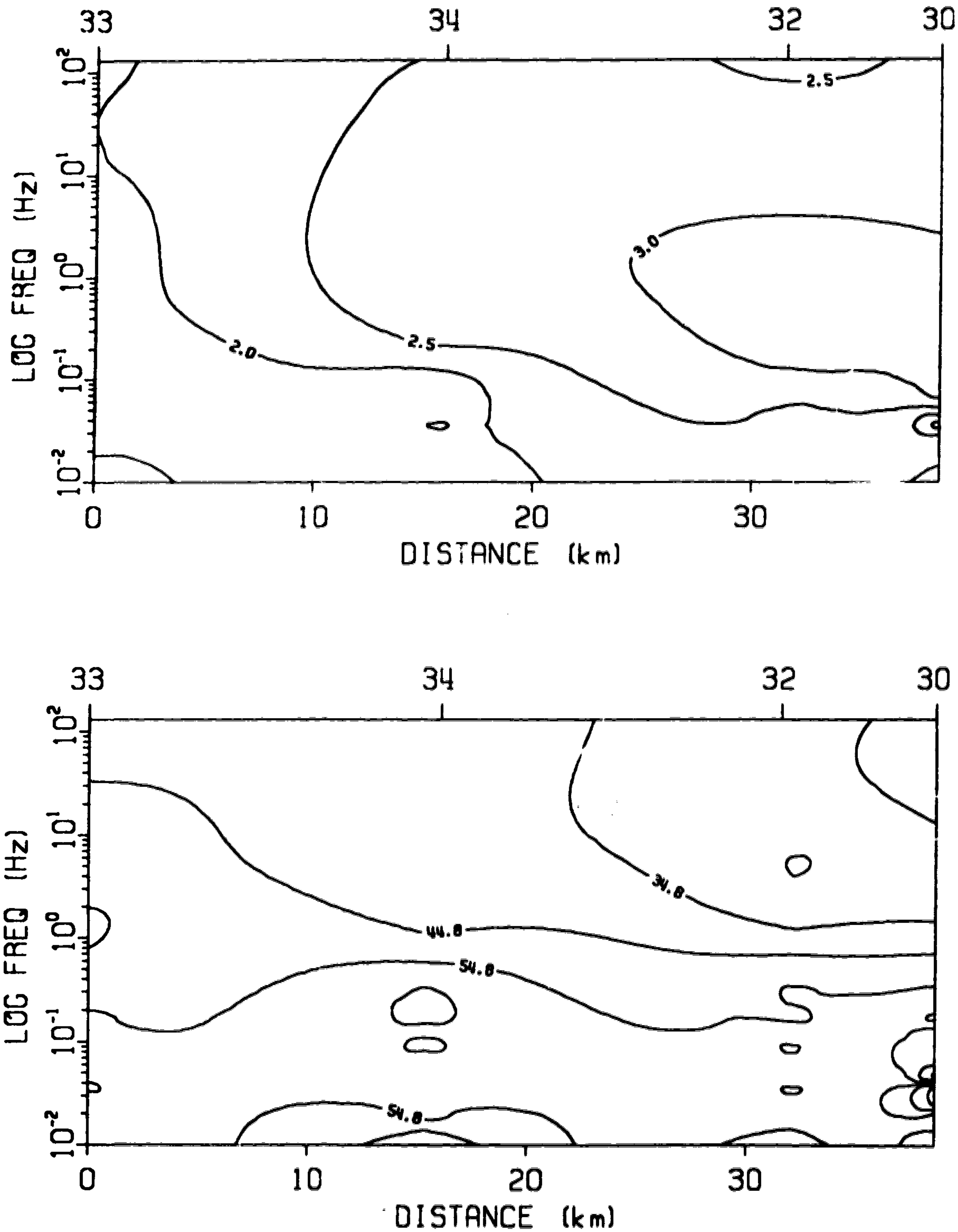

Fig. 3.9.e: E-polarization apparent electrical resistivity (top) and phase pseudosection (bottom) for profile CC' of Figure 3.8.

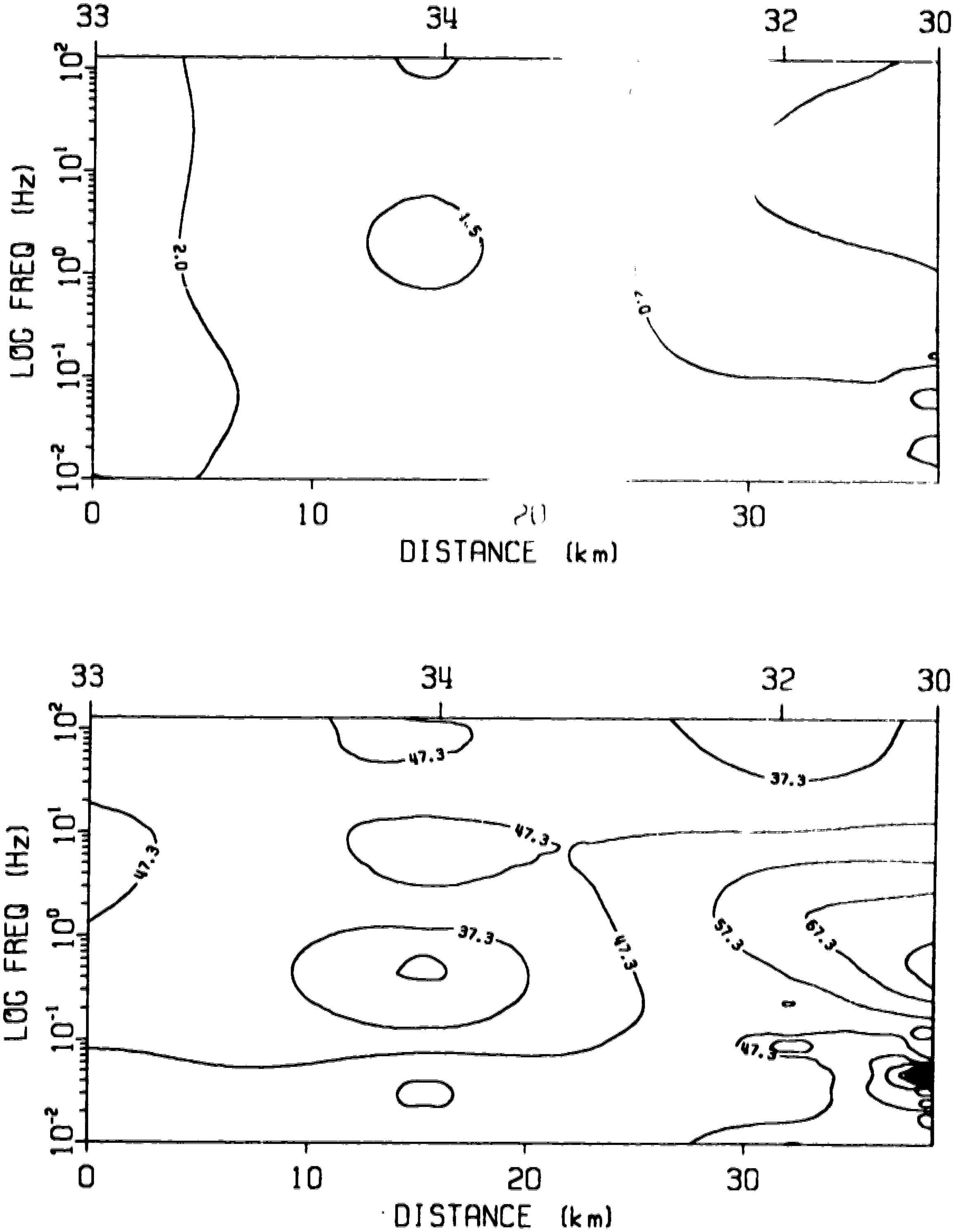

Fig. 3.9.f: The same as in Figure 3.8.e but for the H-polarization case.

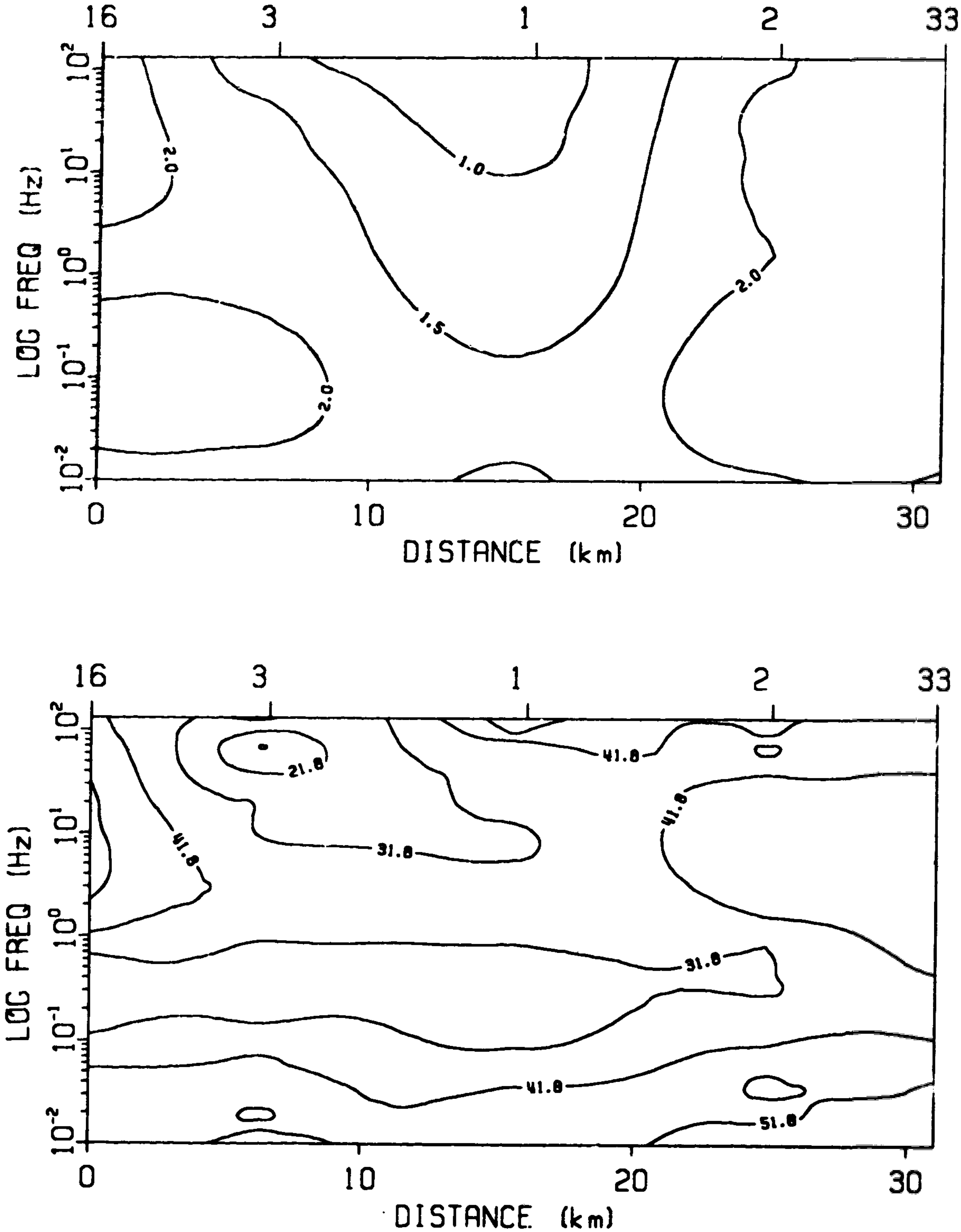

Fig. 3.9.g: E-polarization apparent electrical resistivity (top) and phase pseudosection (bottom) for profile DD' of Figure 3.8.

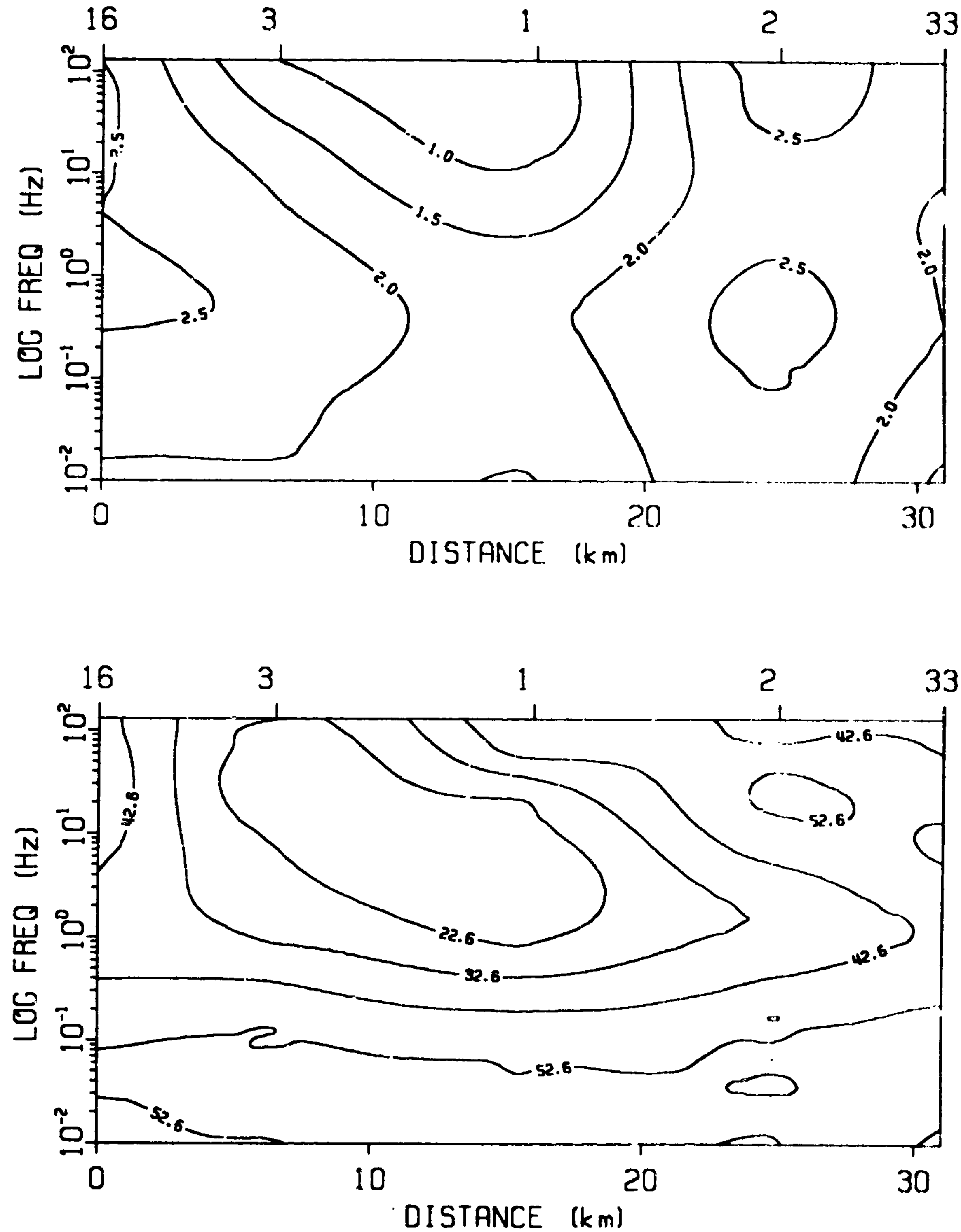

Fig. 3.9.h: The same as in Figure 3.9.g but for the H-polarization case.

qualitatively interpret MT profiles to provide information about the positions of conductive or resistive regions. Furthermore, because of the skin depth effect, high frequencies correspond to shallow depths while low frequencies correspond to greater depths. Therefore, if static shift problems are suspected in a MT survey, phase pseudosections will give more reliable information than the corresponding electrical resistivity pseudosections and, at the same time, will show the relative resistivity distribution in the surveyed area along a profile. A uniform half-space gives a phase value of 45° and phases greater than 45° indicate regions of higher electrical conductivity than the regions above, whereas phases smaller than 45° indicate regions of higher electrical resistivity than those above. With these ideas in mind, it is possible to undertake some general qualitative interpretations of the pseudosections shown in Figure 3.9. In the apparent electrical resistivity pseudosections the isolines are logarithms (base 10) of electrical resistivity and in the phase pseudosections the isolines are in degrees. Since phase pseudosections do not suffer from static shift problems, or at least are much less affected by them than apparent electrical resistivity pseudosections, they are relied on here to a greater extent than apparent electrical resistivity pseudosections to describe and qualitatively analyse the profiles.

For profile AA', with pseudosections are shown in Figures 3.9.a and 3.9.b, the phase values indicate two regions of different electrical conductivity with a contact lying between stations 12 and 28. This pattern is observed in both E- and H-polarization cases. In the apparent resistivity pseudosection the region near station 10 shows low resistivity, which may indicate that the results of this MT site are contaminated static shift. However, this is not confirmed in the field data (Appendix I). It is interesting to note that stations 28 and 31 indicate low electrical resistivities. They are located north of a fault (the Vidigueira fault) which actually trends approximately E-W and is not shown in the geological sketch of Figure 1.2. Also both of these stations are located on Precambrian to Silurian geologic formations and, therefore, the vertical contact between sites 12 and 28, inferred from both apparent electrical resistivity and phase pseudosections may correspond to the contact between those formations and the porphyry complex (see Figure 1.2). The Ferreira-Ficalho overthrust also affects the phase pseudosection of the H-polarization case which exhibit a relatively steep transition from a conductive to a resistive region between sites 10 and 11 (Figure 3.9.b).

The pseudosections for profile BB' are shown in Figures 3.9.c and 3.9.d. The phase pseudosections indicate that the region of the profile is of low resistivity since generally high phase values occur. Site 30 is, however, an exception.

Comparing the phase pseudosections with the apparent electrical resistivity pseudosections one is tempted to infer that sites 29 and 27 are contaminated by static shift effects. This is not confirmed by inspection of the field data in Appendix I, and the most probable conclusion is that the data reflect a real geological feature. In fact, both of these MT sites are located in a region where the surface geology is complex (see Figure 1.2). On the other hand, it is remarkable that the Messejana fault does not seem to have any geoelectrical expression along this profile. The reason may be that it crosses and offsets the same geologic formations.

In Figures 3.9.e and 3.9.f the pseudosections for profile CC' are shown. Both phase pseudosections show a general increase of phase as frequency decreases, which means that a decrease in electrical resistivity occurs as depth increases. An interesting feature of these pseudosections is that they are similar in character to the pseudosections of profile AA' (see Figures 3.9.a and Fig. 3.9.b). Considering the geologic map of Figure 1.2 and the station location map of Figure 3.8, it is seen that the region including stations 16, 10, 11 and 12 of profile AA' is similar to the region crossed by profile CC'. The similarities are reflected in both the E- and H-polarization cases and in both apparent electrical resistivity and phase pseudosections, especially in the H-polarization case. It appears that the Ferreira-Ficalho overthrust is well identified in geoelectrical terms in both profiles: between site 10 and 11 in profile AA' and between sites 34 and 32 in profile CC'. It also appears that for frequencies between 1 and 0.1 Hz there is a high electrical resistivity channel just southwest of the overthrust. The response in this frequency range places it between 3 and 10 km depth. So, as far as profiles AA' and CC' are concerned it is reasonable to assume that the geoelectrical structures are continuous along the Ferreira-Ficalho overthrust. However, the cause of the relatively higher electrical resistivity formation located between 3 and 10 km depth is uncertain.

The four pseudosections for profile DD' are shown in Figures 3.9.g and 3.9.h. The phase pseudosections indicate a fairly stratified distribution of electrical resistivity which generally decreases as frequency decreases (i.e., with depth). It is interesting to note again that the presence of the Messejana fault is not obvious. However, it is geographically located between stations 1 and 2 (closer to 2) and around the latter station there are intense phase fluctuations and the apparent electrical resistivity distribution is essentially vertical. This may be the electrical signature of the Messejana fault. Comparing profiles DD' and BB' it is apparent that they have little in common. The pseudosections of the former are smooth, while the corresponding pseudosections of the latter are more complicated with sharp variations in phase. These differences must, however, be linked to the fact that profile BB' crosses a region that is geologically more complex than that crossed by profile DD' (see geologic sketch of Figure 1.2).

From the above qualitative analysis it can be concluded that along the four profiles the electrical resistivity is generally low and varies between 30 and 1000 ohm-m, with a few zones of about 3000 ohm-m. Furthermore, the Messejana fault does not exhibit a particular electrical signature in the profiles considered, despite the fact that the electrical resistivity decreases near it. On the contrary, the Ferreira-Ficalho overthrust appears to be well identified in the profiles and there are indications that it separates two different geoelectric domains, which is expected from knowledge of the regional geology. These results show that different kinds of faults can have different electrical signatures and that the MT method is appropriate for locating them and possibly identifying the different types. This is an important result and should be further investigated because of its relevance to tectonic studies.

It should be remembered that the conclusions above were obtained from profiles with only 4 to 6 measurements sites, and it should be emphasized that so few sites are insufficient for a complicated region like the one of this MT study.

CHAPTER IV

INVERSION AND ELECTROMAGNETIC MODELLING RESULTS

4.1. Introduction

The main idea behind any geophysical modelling procedure is to derive an Earth model whose response reproduces the observed data. Earth models can be constructed using different properties depending on the geophysical survey carried out. In electromagnetic (EM) surveys, and in particular in MT work, electrical resistivity (or electrical conductivity) is the physical property used to construct EM models. If the response of such a model fits the real data, the next step is to interpret the model in terms of the geological structures.

Modelling can be performed using analogue as well as numerical techniques. Here only the latter will be described and applied.

After basic processing, the results of a MT survey are, for each MT site, a set of two apparent electrical resistivity versus frequency curves (in two mutually perpendicular directions) and two phase versus frequency curves in the same directions as the electrical apparent resistivities (see Chapters II and III). In the special case of a one-dimensional geological situation, the number of curves reduces to two, i.e., the two electrical apparent resistivity and the two phase curves reduce to one apparent resistivity curve and one phase curve. This is a consequence of the horizontal isotropy in one-dimensional problems, which means that electrical resistivity varies only with depth.

To associate the field results with the otherwise unknown geological structure, it is necessary to construct a model that approximates reality in the best way possible. Two main techniques may be used to construct models. The first is a trial-and-error method by which different plausible models are used to calculate response functions which are compared with real data; this is called direct or forward modelling. The second uses inversion methods which aim to obtain, through the use of theoretical relationships, model parameters from the actual data which produce responses that best fit those data. Many inversion methods are hybrid. This means that they calculate a set of model parameters that are used to calculate model responses in a forward manner, and these are then compared to the field data to test the accuracy of the model with subsequent adjustment and further comparison in an iterative manner. Good general descriptions of inversion methods as applied to EM induction problems can be found in Rokityansky (1982), Vozoff (1986, 1991), Hohmann (1988), and Whittall and Oldenburg (1992).

Since one-dimensional (1D), two-dimensional (2D), and three-dimensional (3D) geological structures are encountered in nature, one would expect inversion methods to be available for all cases. Several schemes for 1D inversion exist and are widely used in EM induction studies (Rokityansky, 1982; Vozoff, 1991; Wannamaker and Hohmann, 1991; Whittall and Oldenburg, 1992). However, this is not true for 2D and 3D inversion schemes. In fact, most of the 2D inversion schemes so far developed are essentially two-dimensional forward schemes that use 1D inversion results as input. Up to now, true 2D EM inversion schemes only seem to work well when applied to synthetic data. Since real data have noise and usually include 3D effects, models obtained from 2D inversion methods generally show spurious features (Wannamaker and Hohmann, 1991). The situation is even worse for 3D EM inversion, which is currently a subject of intense study (Vozoff, 1991).

4.2. 1D EM inversion and 1D EM modelling

One-dimensional inversion techniques are the most common in MT work and a thorough description of these techniques may be found in Whittall and Oldenburg (1992). In the present work, 2D and 3D modelling were performed, in which the models were constructed from 1D models obtained by applying a hybrid Monte-Carlo hedgehog inversion technique (Jones, 1977; Jones and Hutton, 1979; Dawes, 1980, Rokityansky, 1982) to the data from each MT site. This hybrid technique is an automatic trial-and-error inversion method.

Assume that the field data may be written as a vector

$$\bar{d} = (d_1, d_2, \ldots, d_M)$$

and the characteristics of the model sought are represented by a vector

$$\bar{x} = (x_1, x_2, \ldots, x_N)$$

with N degrees of freedom. Furthermore, for a certain model chosen, assume that

$$\psi = \sum_f \left(\log \rho_{a\ f}^{mes} - \log \rho_{a\ f}^{cal}\right)^2 + \sum_f \left(\phi_f^{mes} - \phi_f^{cal}\right)^2 \qquad (4.1)$$

measures the discrepancy between the calculated and the measured values of the response functions ρ_a and ϕ, where ρ_a represents the apparent electrical resistivity and ϕ the phase. In the equation, the sums are taken over all the frequencies (f) at which the measurements were performed, and the superscripts "mes" and "cal" indicate the measured and calculated quantities. The use of logarithms of the apparent resistivity has to do with arguments of log-normal resistivity distributions, as discussed by Bentley (1973).

An initial calculation begins with a starting model that may be constructed by visual inspection of the field curves or by curve matching if a set of master curves is available and the data are not too complicated, i.e., if no more than 3 or 4 layers are evident from the field apparent electrical resistivity and phase curves. A new model is then generated from the initial one according to $h'_i = h_i \cdot e^{r_i}$ and $\rho'_i = \rho_i \cdot 10^{r_{i+j}}$, where h_i and ρ_i are the initial thickness and resistivity of the ith layer, and r_i and r_{i+j} represent random numbers with zero mean and unit variance, which means that 68% of h'_i thicknesses generated lie between $h_i/2$ and $2h_i$, and 68% of ρ'_i resistivities generated lie between $\rho_i/10$ and $10\rho_i$. The response of the new model is then calculated and compared with the measured data. If the model response falls within a given confidence interval, the model is accepted; otherwise, it is rejected. In the former case, ψ is calculated from equation 4.1 by replacing ρ_a^{cal} by $\rho_a'^{cal}$, i.e., by replacing the apparent resistivity of the initial model by the new model's apparent resistivity at frequency *f*; and the same for ϕ^{cal} and ϕ'^{cal}. In case $\psi' < \psi$ the initial model parameters $\bar{x}$ are replaced by those of the latest model, i.e., $\bar{x}'$; otherwise, no replacement takes place. The procedure continues until the best fitting model is calculated through automatic computer routines.

In the case of the Portuguese data, for each site an initial model was chosen by inspection of the apparent resistivity versus frequency curve from the measured data and 100 random models were generated. From those models the best 10 were chosen and used to generate 100 more models from which the 10 best were again chosen. The process continued until the best fit between the data and the model calculated responses was found, according a predetermined least-squares criterium. The model parameters (electrical resistivitires and thicknesses of the layers) were then assumed to represent the 1D geological structure at that MT site. For most of the sites, the layer thicknesses and electrical resistivities of the model automatically chosen were bound by upper and lower limits, showing the non-unique character of the results. However, the differences between those bounds were generally small.

In Appendix II the results of the 1D Monte-Carlo hedgehog inversion are shown for the 34 sites occupied in the study area. Figure 4.1 shows the result of the inversion for site 1 as an example.

As mentioned in Chapter III, to perform the 1D inversions, the determinant invariant as described by Berdichevsky and Dimitriev (1976a) was used (equation (3.1)). In the iterative scheme to calculate the best fit model parameters, only the apparent electrical resistivity was used (see equation (4.1)) to compare field data with model results, and the number of layers was specified at the beginning of the inversion process.

4.3. Two-dimensional electromagnetic modelling

The fact that the four profiles considered for 2D modelling, and shown in Figure 3.8, are perpendicular to the Messejana fault and the Ferreira-Ficalho overthrust is not a coincidence. From the beginning of the field work, the

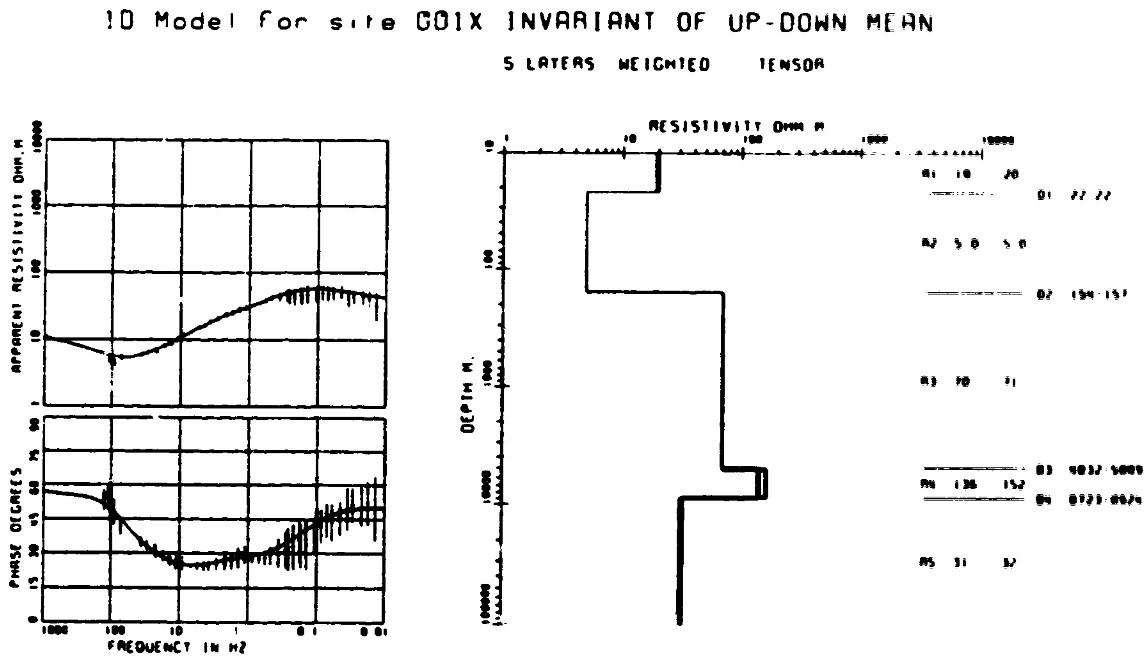

Fig. 4.1: Example of a 1D Monte-Carlo hedgehog inversion for site 1. The right part of the figure shows the model with R representing the layers electrical resistivities and D their depths. The left part of the figure shows the data apparent electrical resistivity and phase (crosses with error bars) and the apparent electrical resistivity and phase curves (solid lines) calculated from the model.

intent was to place some of the MT stations along profiles that would cross those two geological features perpendicularly. This arrangement would then provide data to allow 2D modelling to be attempted for those areas.

Two-dimensional, as well as three-dimensional model construction is a difficult task because of the uncertainties associated with the field data and the non-uniqueness of the model results. This means that acceptable models are never exhausted while looking for the best one. To construct 2D models along the profiles shown in Figure 3.8, the 1D inversion models of Appendix II were used. Along each profile, each station was represented by a sequence of layers with electrical resistivities and thicknesses given by the 1D models. Arbitrarily, vertical planes perpendicular to the profiles, and passing through the middle points between adjacent pairs of MT stations, were considered as the boundaries between their electrical resistivity distributions as functions of depth, as given by the 1D inversion models. As a requirement of the two-dimensional computer program that calculates the 2D model responses, the electrical resistivity distributions as functions of depth for the MT stations at the ends of each profile were extended to great distances, so that the model boundary values, which are held fixed during the calculation, do not influence the field perturbations related with conductivity variations along the profiles. Figures 4.2 to 4.5 show the four 2D models constructed using the MT stations along the

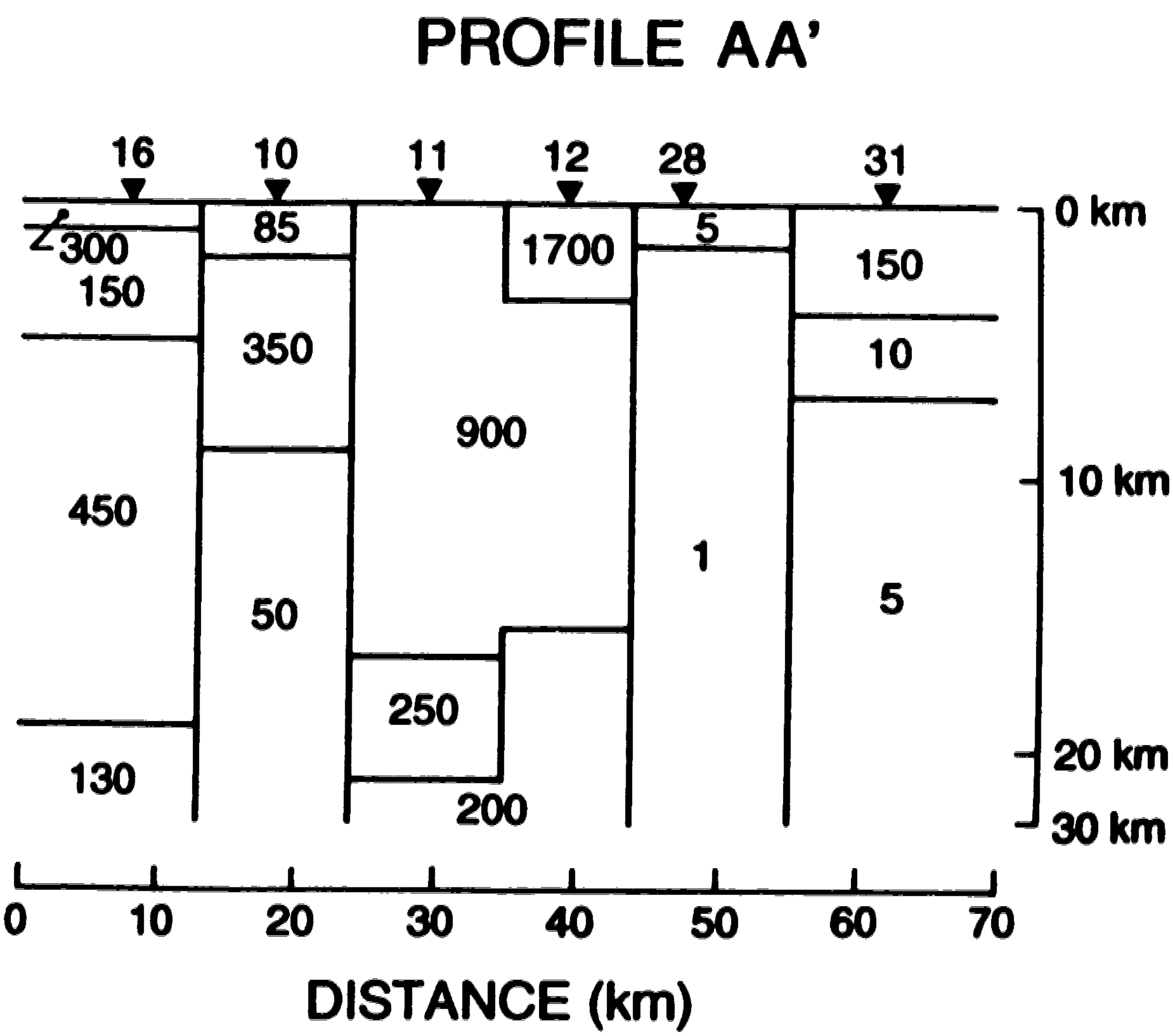

Fig. 4.2: Two-dimensional model for profile AA' of Figure 3.8.

PROFILE BB'

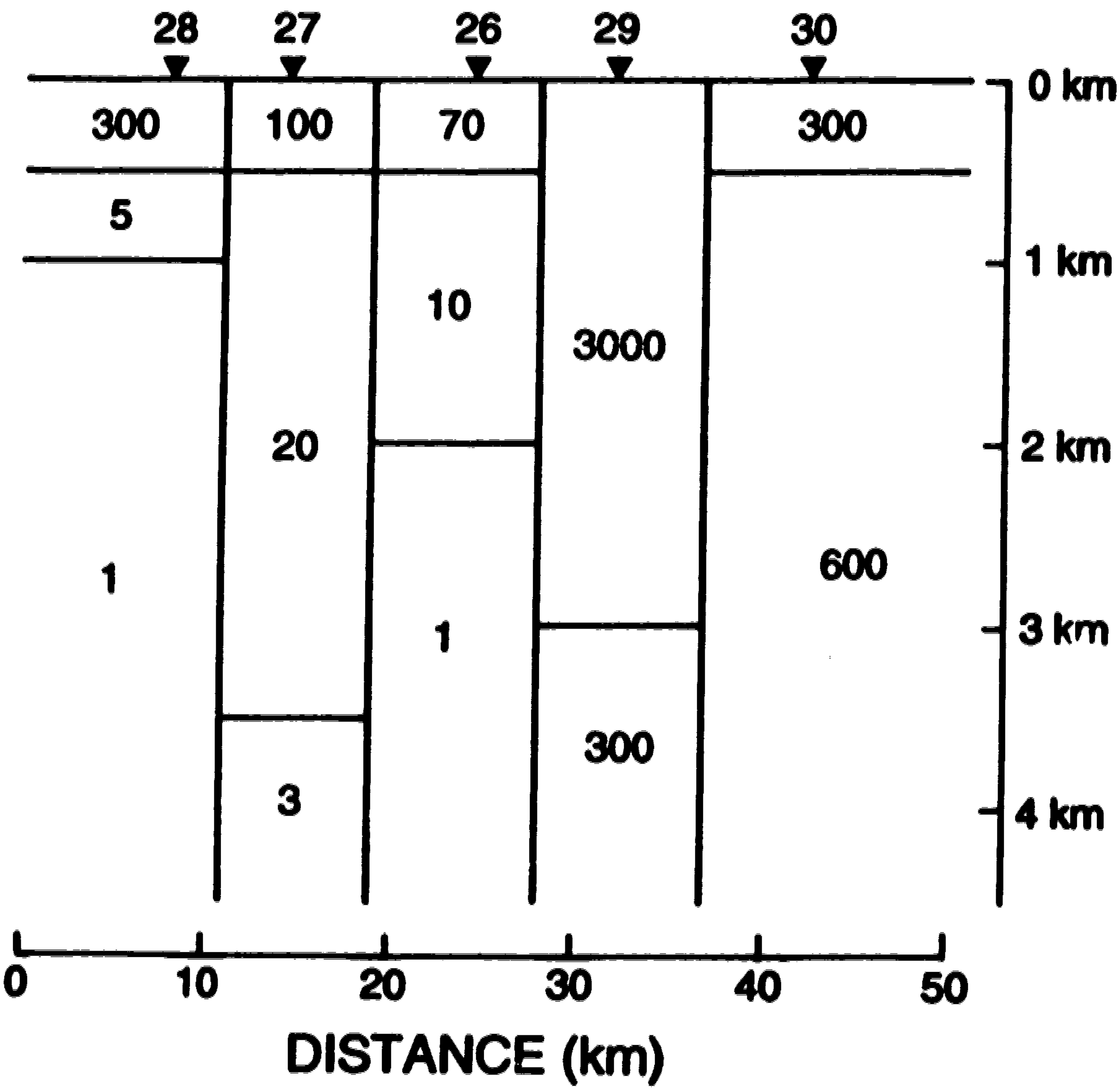

Fig. 4.3: Two-dimensional model for profile BB' of Figure 3.8. Note that the vertical scale of this figure differs from that of Figures 4.2, 4.4 and 4.5.

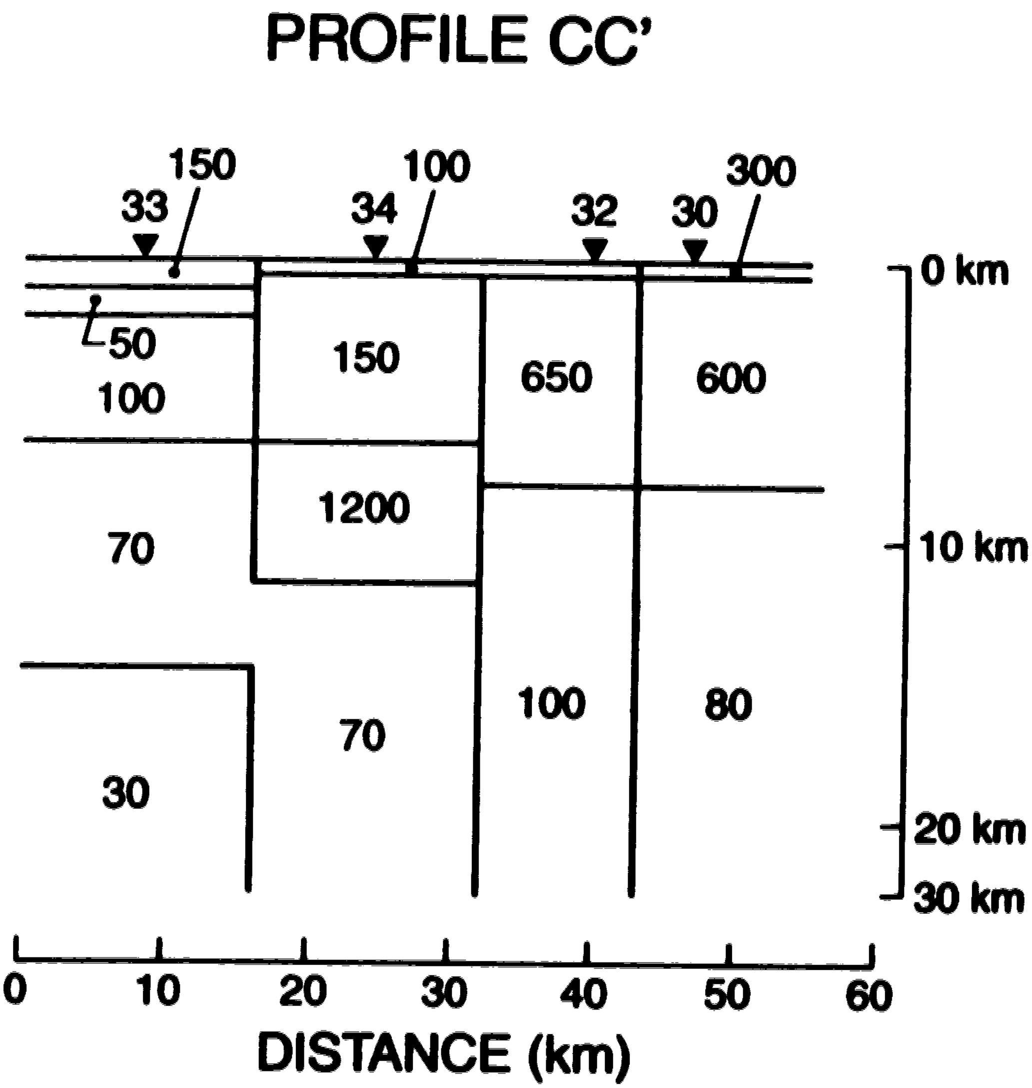

Fig. 4.4: Two-dimensional model for profile CC' of Figure 3.8.

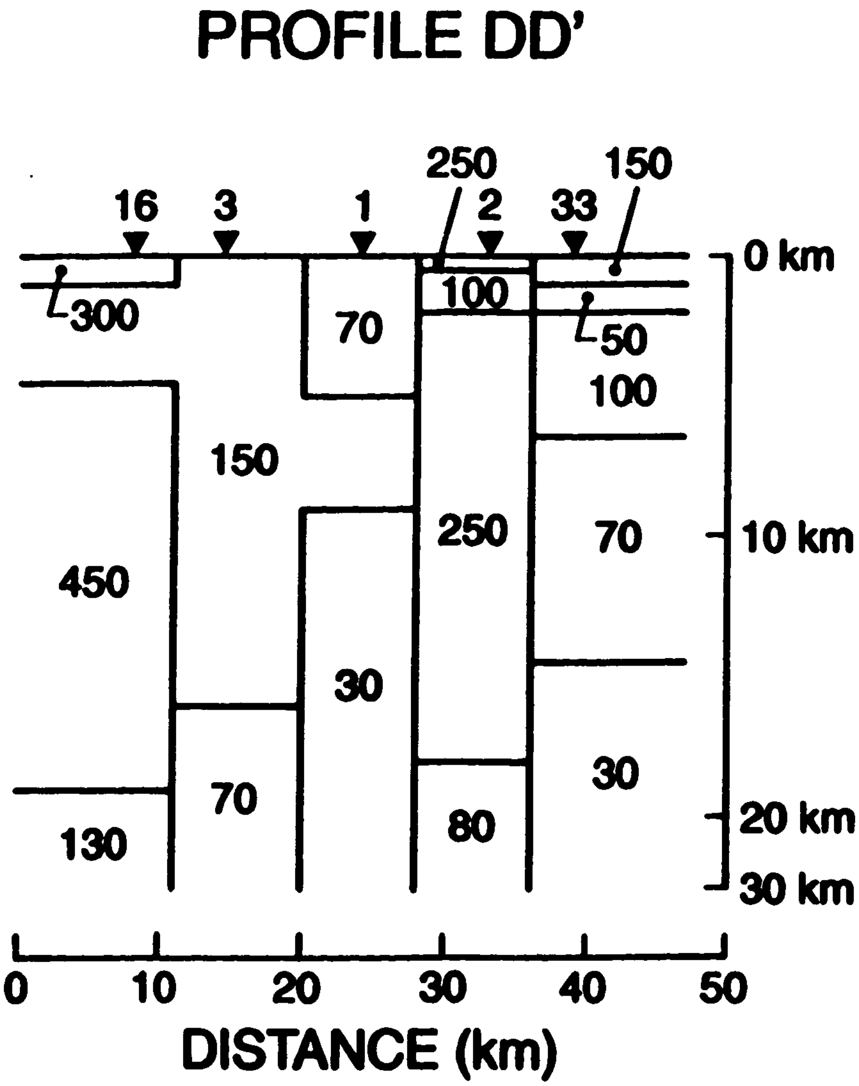

Fig. 4.5: Two-dimensional model for profile DD' of Figure 3.8.

edges of the study area (Figure 3.8). The number within each block gives the electrical resistivity of that block in ohm-m. To simplify the numerical models, these values are based on the 1D inversions, but are rounded off average values of close groups of electrical resistivities. Model calculations for different electrical resistivity distributions based on the 1D inversions were made, and it was found that the rounding and averaging processes did not appear to significantly influence the model results for each profile considered and, therefore, the simplest 2D models were adopted.

To calculate the electromagnetic responses of the 2D electrical resistivity profiles (or models) described above and shown in Figure 3.8, a finite-difference method developed by Jones and Price (1970) and programmed by Jones and Pascoe (1971) with modifications as indicated by Williamson et al. (1974) and discussed by Jones and Thomson (1974) (see also Brewitt-Taylor and Weaver (1976)) was used. The method involves the solution of equations (2.46) and (2.47) in finite-difference form over a mesh of grid points by the Gauss-Seidel iteration method (Smith, 1969). The mesh of grid points covers the area that is to be considered and the above equations, in finite-difference form, are solved iteratively at each point. In the calculation a mesh of 80 by 80 cells was used. To assess the convergence of the calculation, after each iteration a residual term was calculated. This residual was taken as the maximum value of the differences between the values of E_x E_y and E_z from the particular iteration being considered and those from the previous iteration for all points of the mesh. The iteration process continued until the residual was less than a specified value. In the present case that value was 0.00001 (in electric field units). A maximum of 2000 iterations was allowed but this number was never reached. An account of the finite-difference method and the boundary conditions used, as well as their application to 2D electromagnetic problems has been given in Jones and Price (1970, 1971), Jones and Pascoe (1971), Pascoe and Jones (1972) and Jones (1973).

Two ways of representing 2D structures are possible. One is to represent the electrical resistivity distribution as a function of depth and the other is to represent it as a pseudosection. The former is what geologists and geophysicists really look for while the latter is what they obtain from field data. Therefore, since forward modelling is a trial-and-error procedure, the results from the models should be presented in such a way that they may be compared with the real data. This means that the model results should be plotted as pseudosections.

Comparison between the model results and the real data should, in principle, allow descrimination between good and poor models and, in the latter cases, indicate how the results can be refined until the model results and field data fit within certain limits. In Figures 4.6-4.21, apparent electrical resistivity and phase pseudosections for

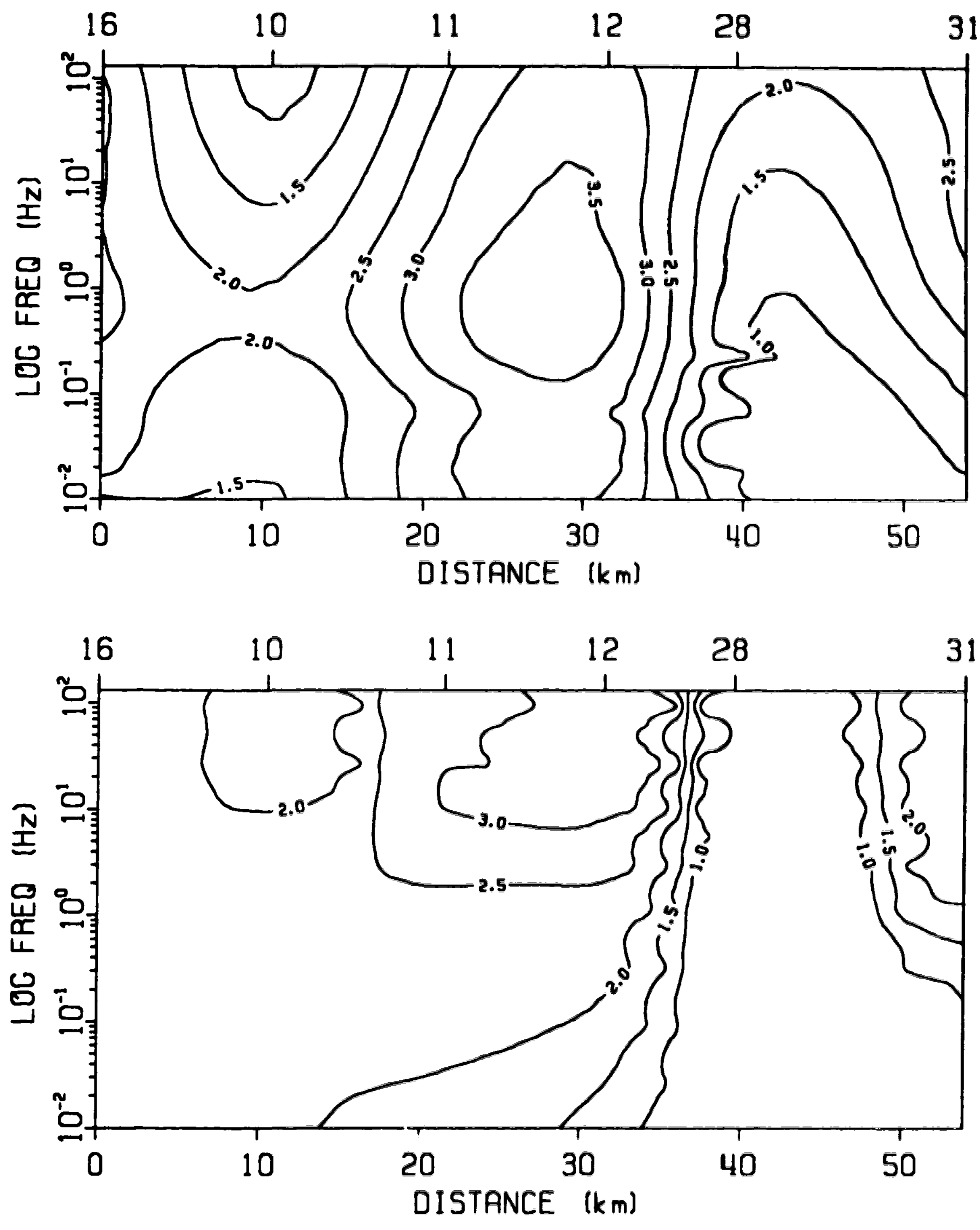

Fig. 4.6: TE mode - field data (top) and 2D model (bottom) electrical resistivity pseudosections for profile AA' of Figure 4.2.

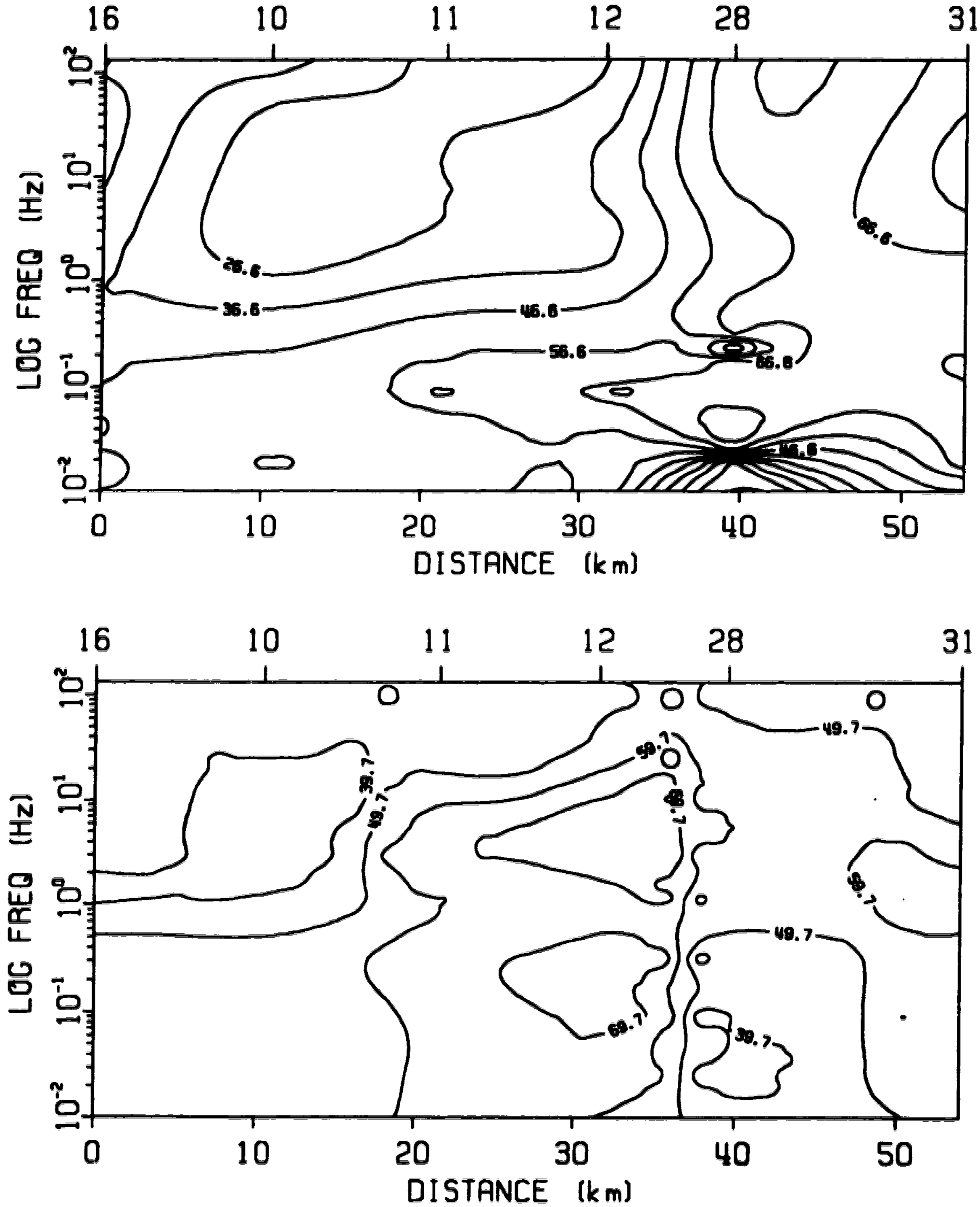

Fig. 4.7: TE mode - field data (top) and 2D model (bottom) phase pseudosections for profile AA' of Figure 4.2.

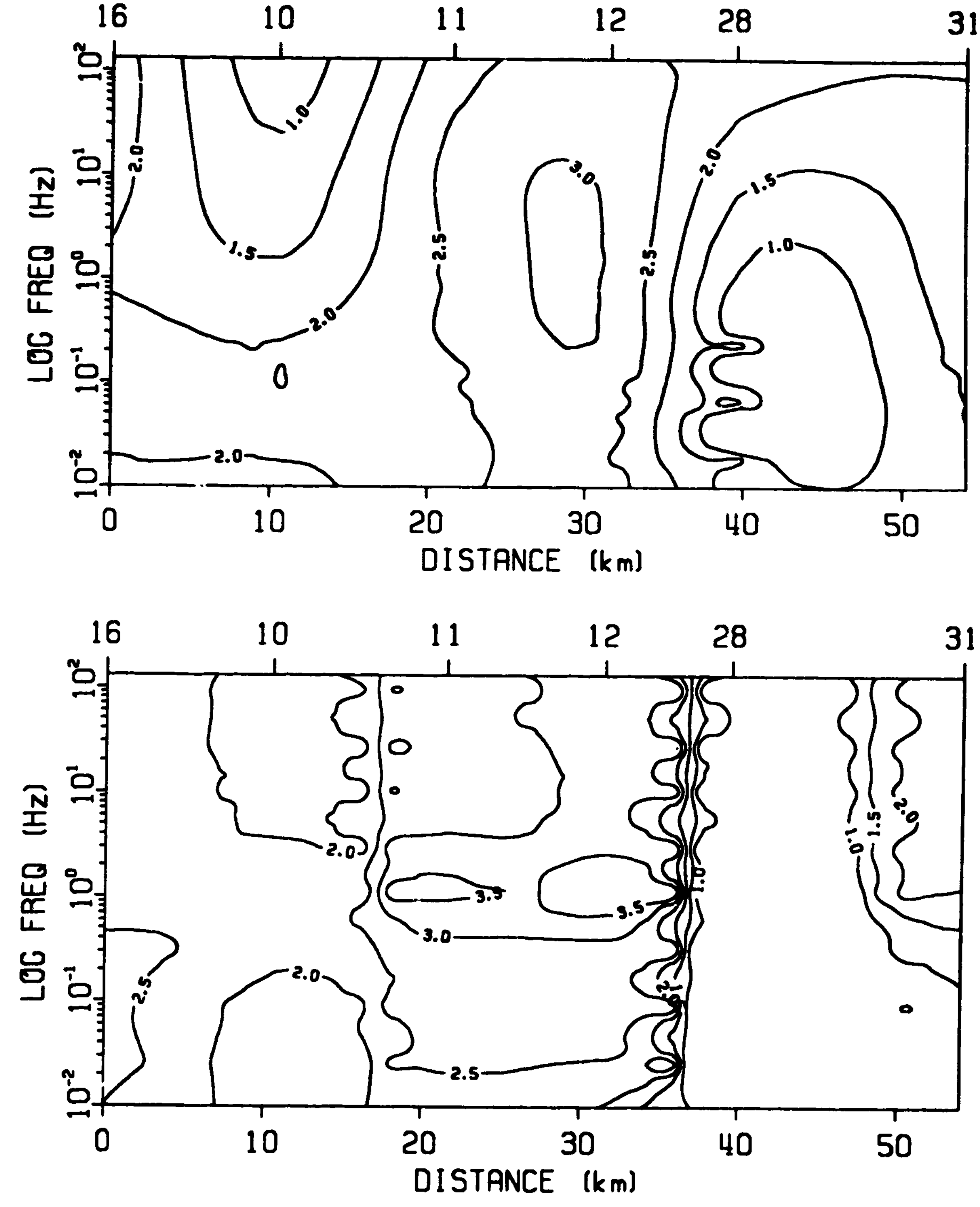

Fig. 4.8: TM mode - field data (top) and 2D model (bottom) electrical resistivity pseudosections for profile AA' of Figure 4.2.

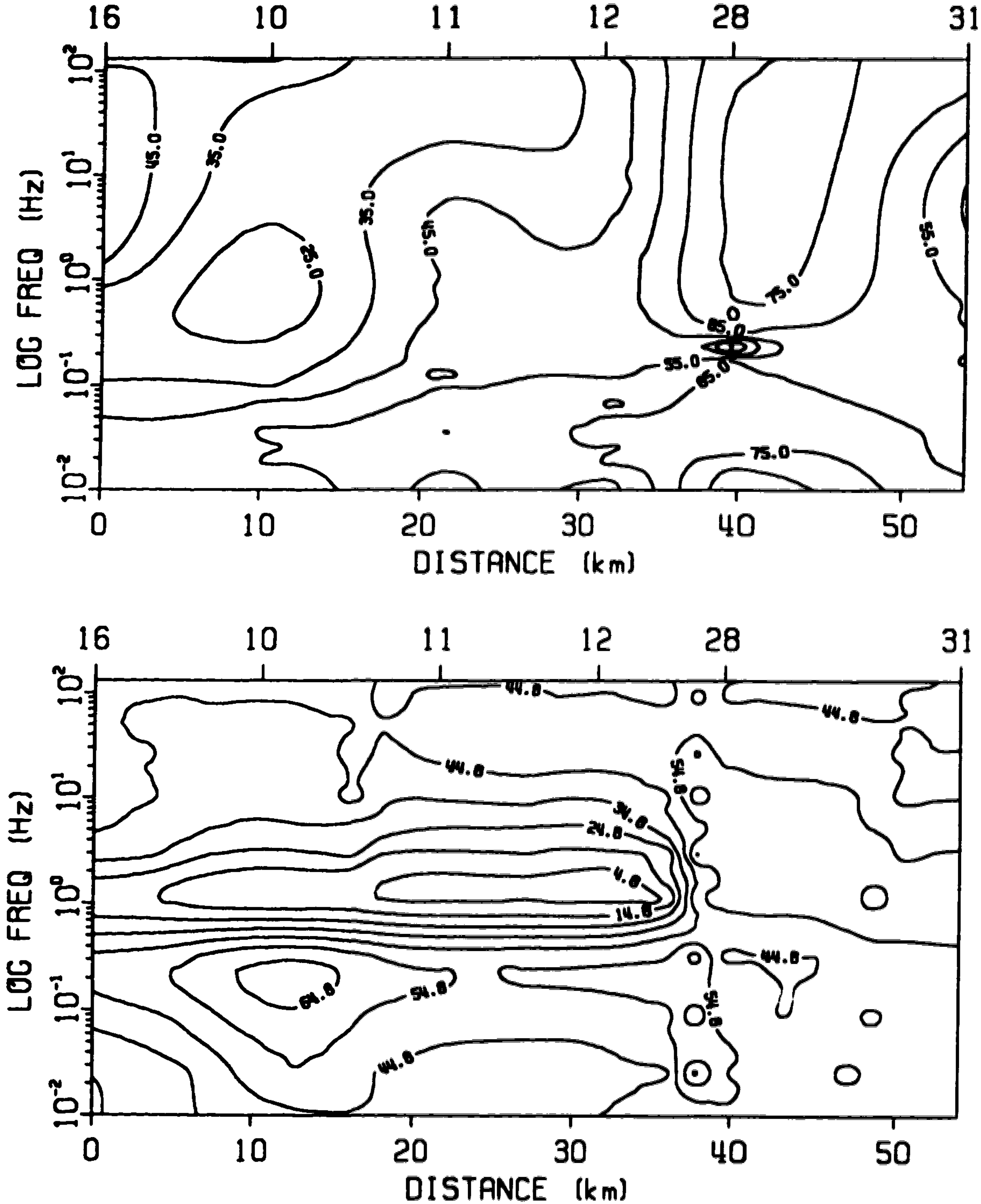

Fig. 4.9: TM mode - field data (top) and 2D model (bottom) phase pseudosections for profile AA' of Figure 4.2.

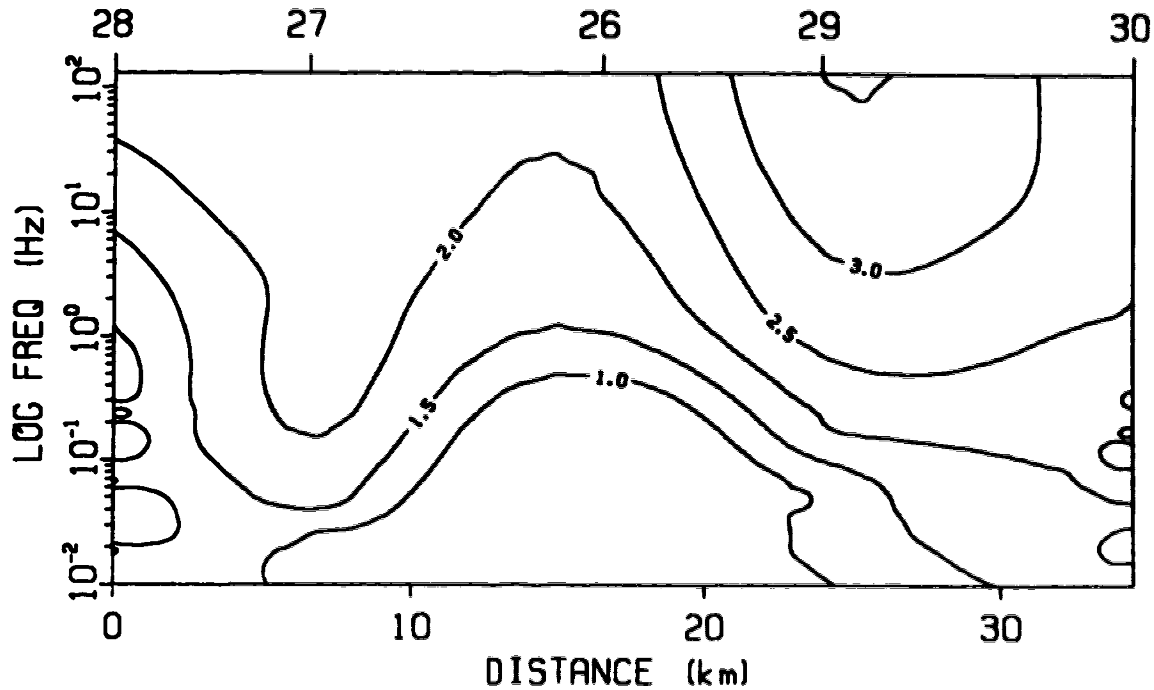

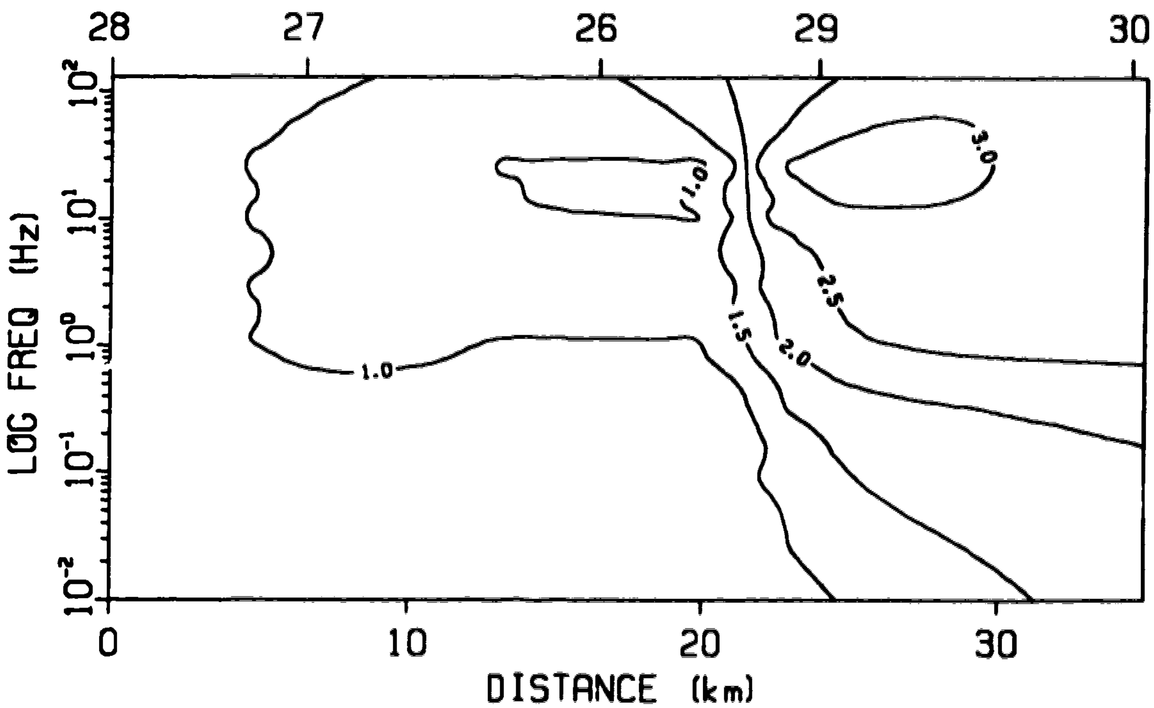

Fig. 4.10: TE mode - field data (top) and 2D model (bottom) electrical resistivity pseudosections for profile BB' of Figure 4.3.

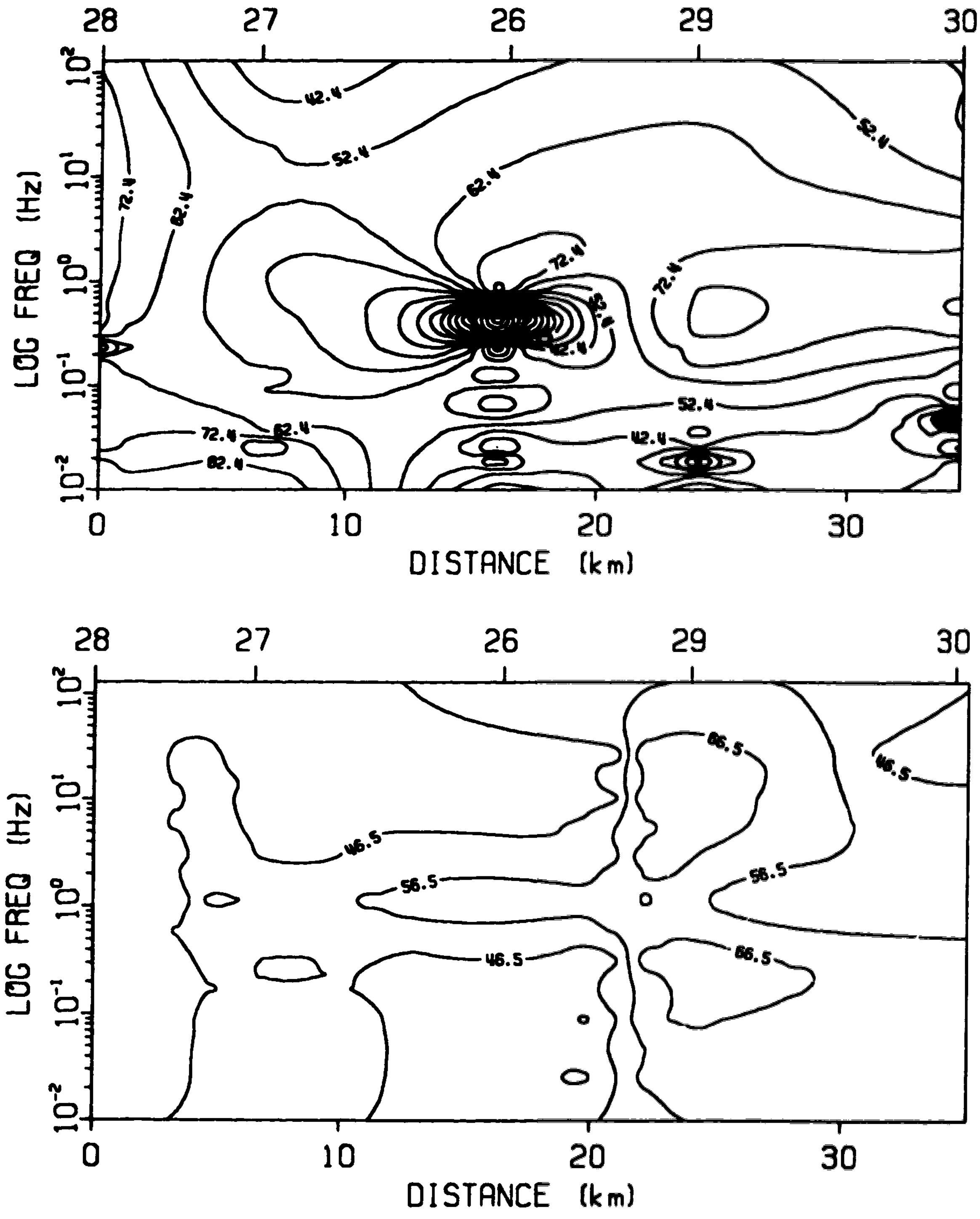

Fig. 4.11: TE mode - field data (top) and 2D model (bottom) phase pseudosections for profile BB' of Figure 4.3.

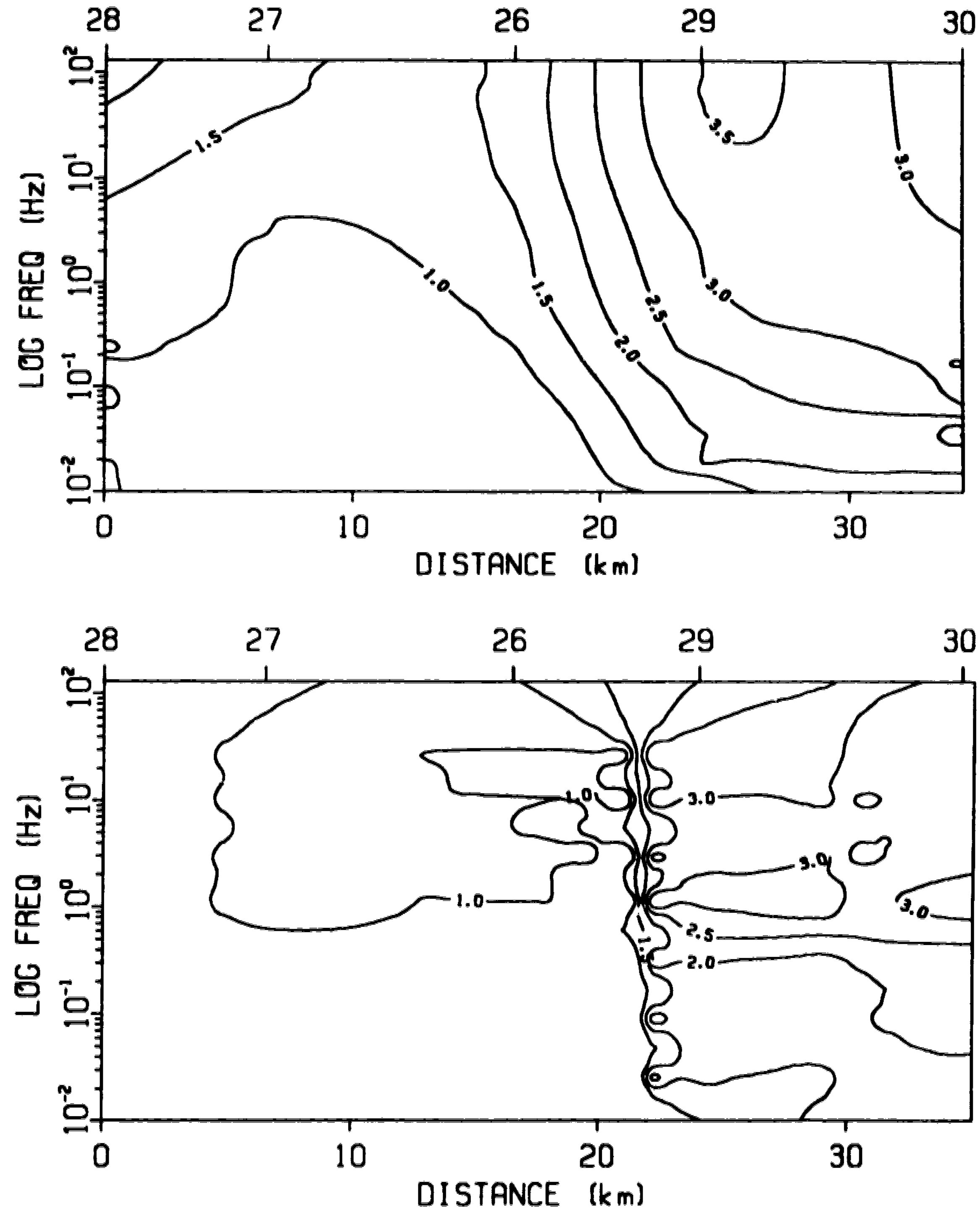

Fig. 4.12: TM mode - field data (top) and 2D model (bottom) electrical resistivity pseudosections for profile BB' of Figure 4.3.

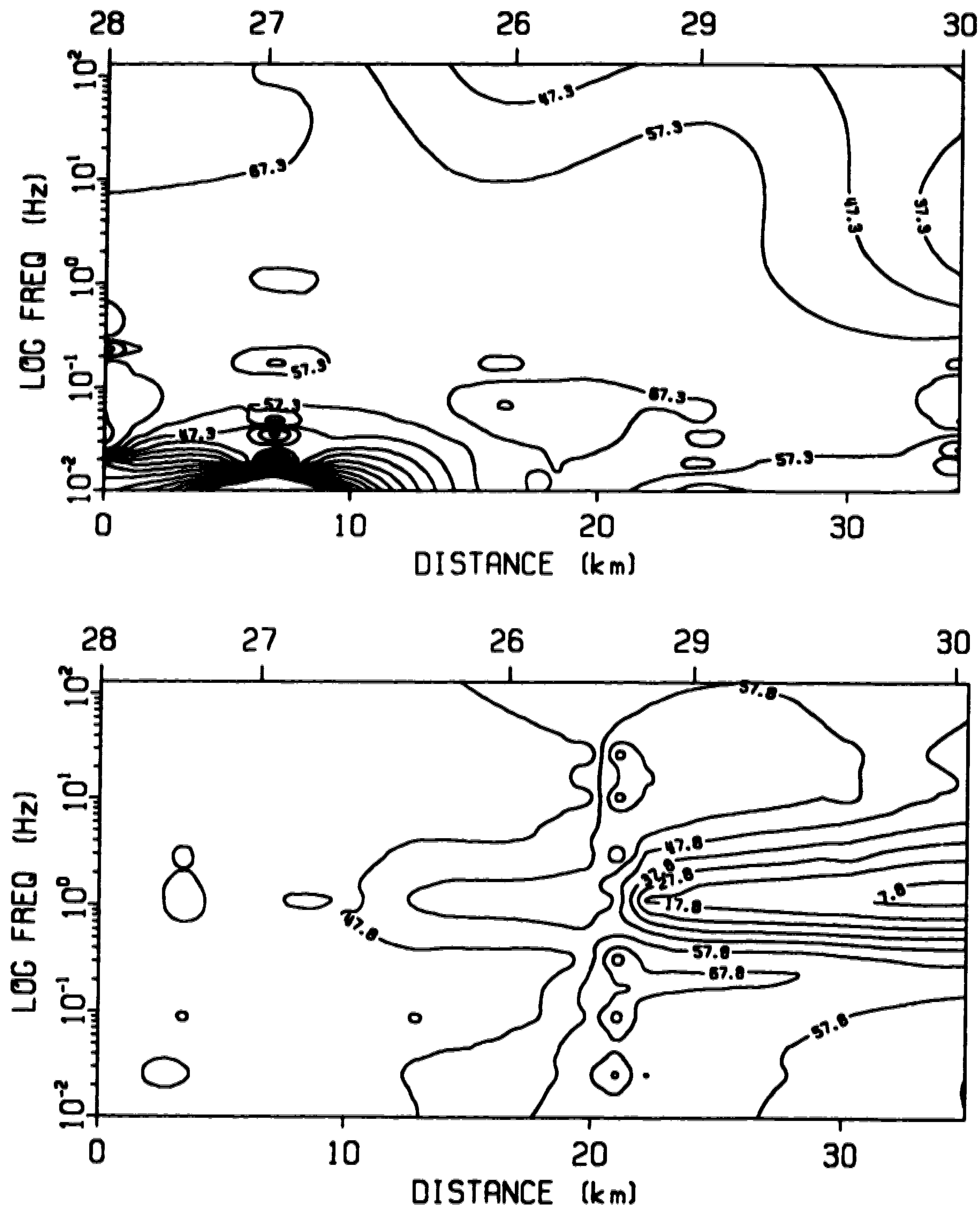

Fig. 4.13: TM mode - field data (top) and 2D model (bottom) phase pseudosections for profile BB' of Figure 4.3.

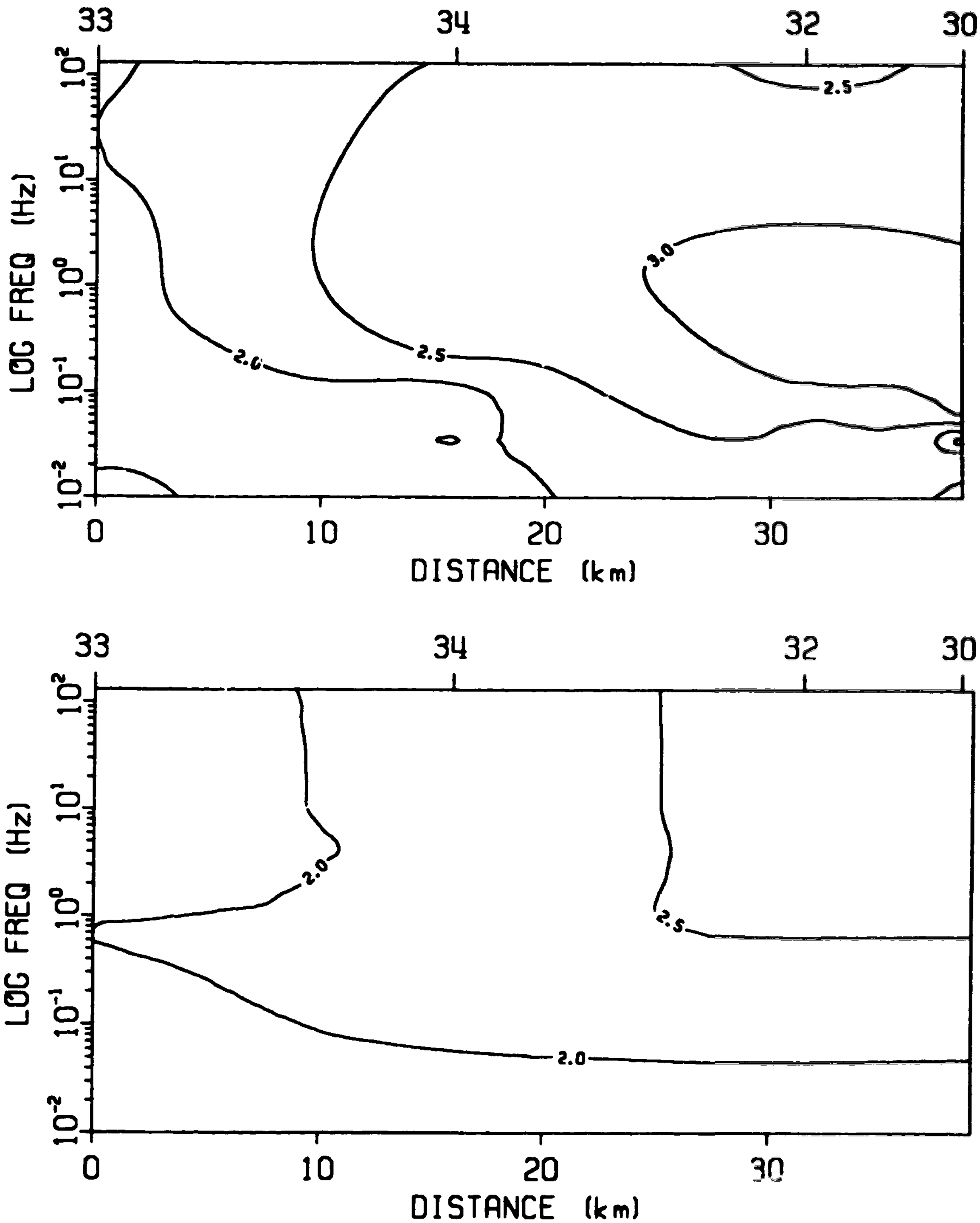

Fig. 4.14: TE mode - field data (top) and 2D model (bottom) electrical resistivity pseudosections for profile CC' of Figure 4.4.

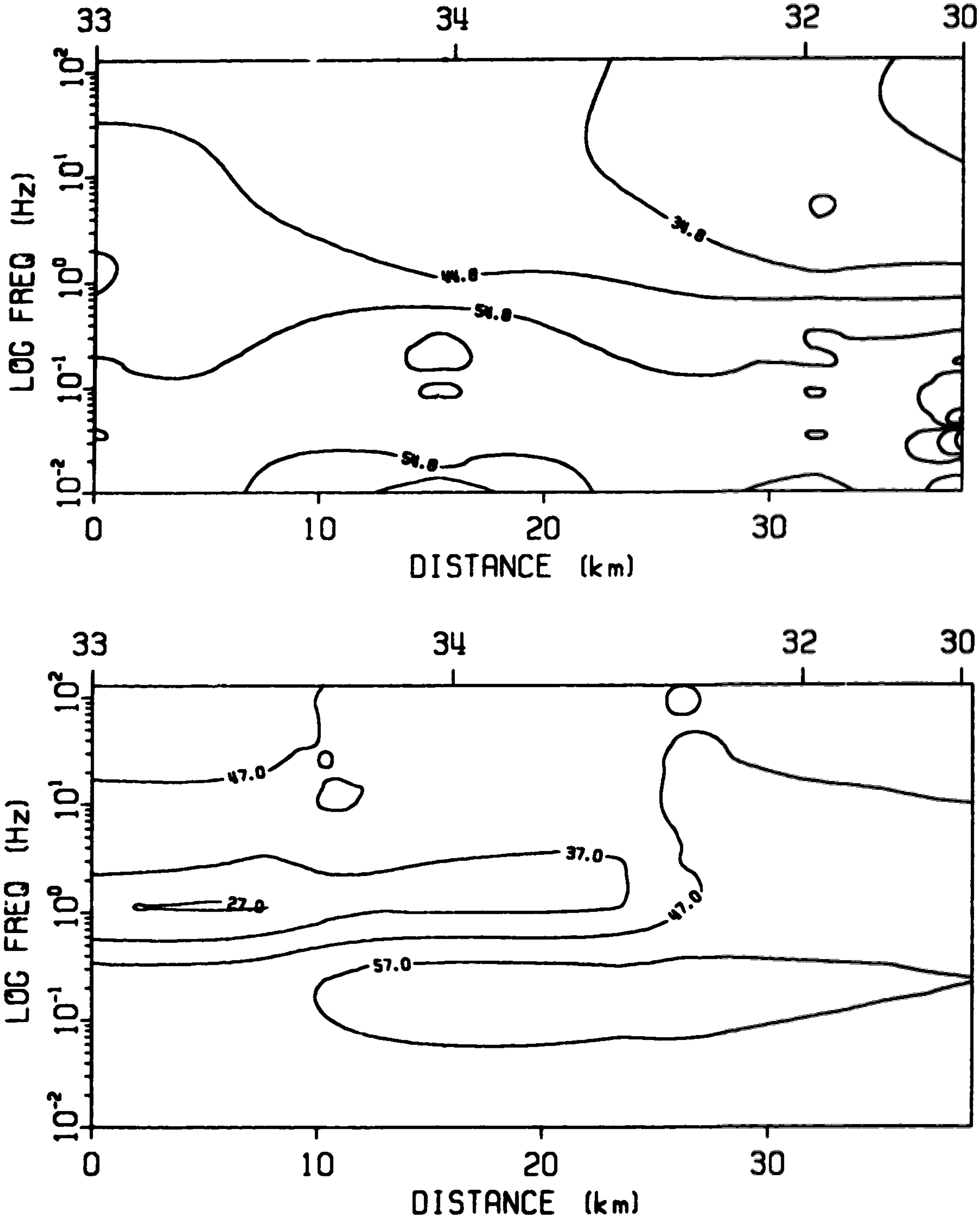

Fig. 4.15: TE mode - field data (top) and 2D model (bottom) phase pseudosections for profile CC' of Figure 4.4.

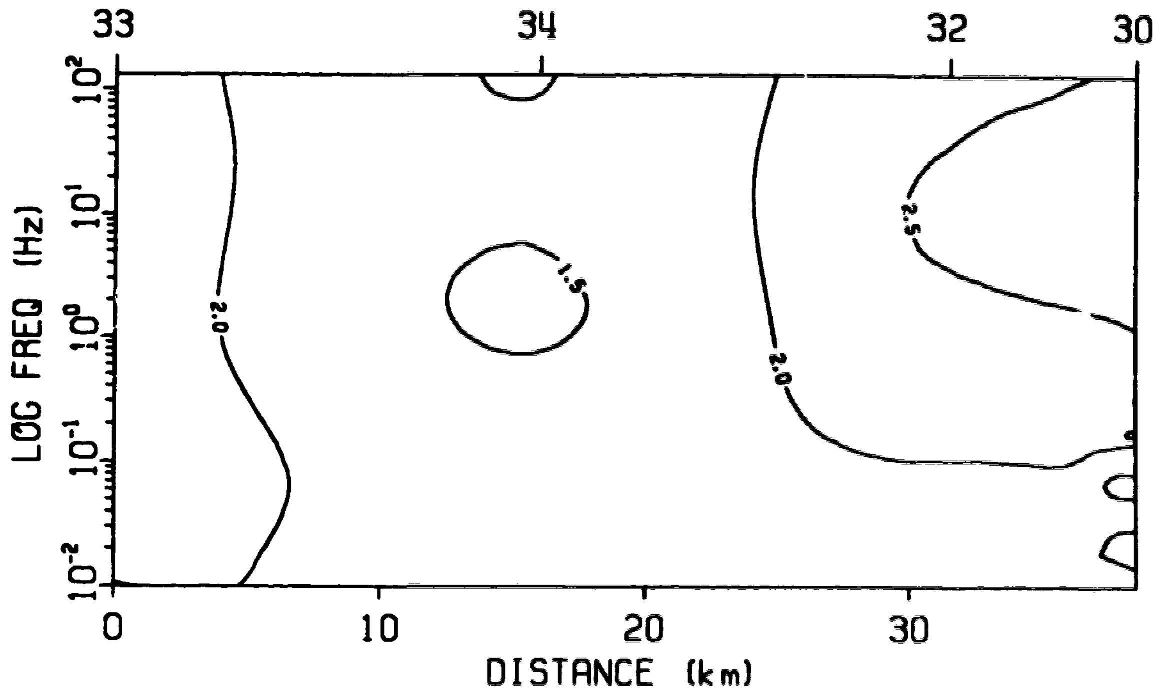

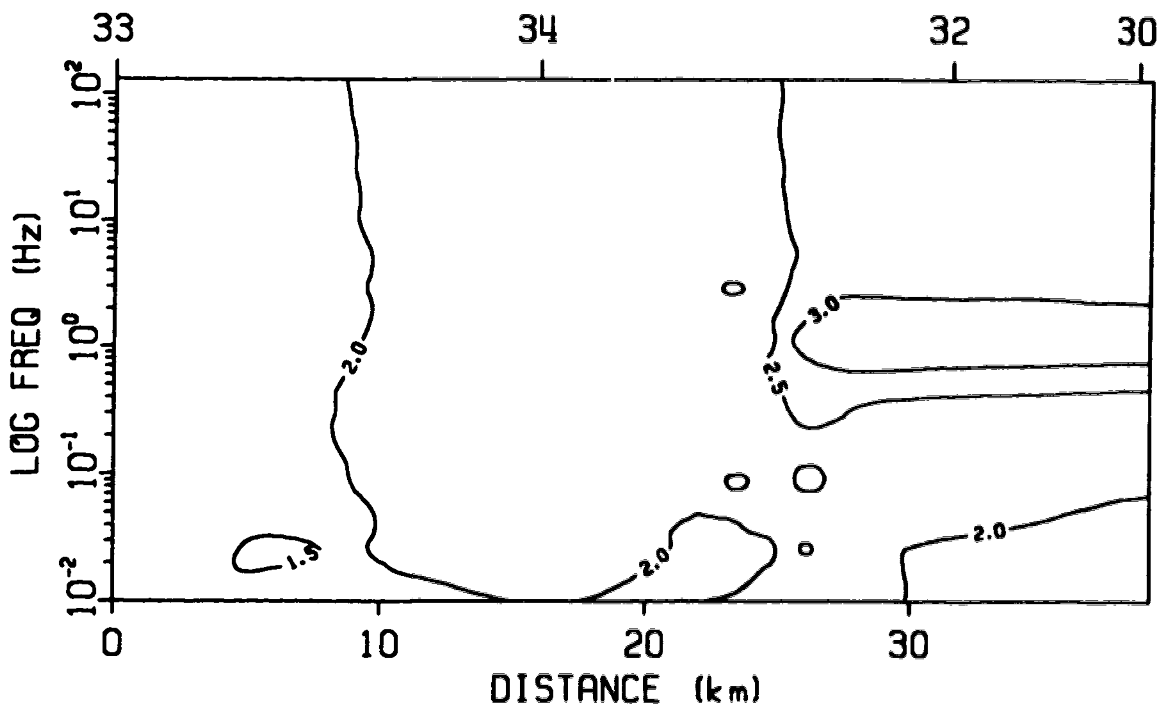

Fig. 4.16: TM mode - field data (top) and 2D model (bottom) electrical resistivity pseudosections for profile CC' of Figure 4.4.

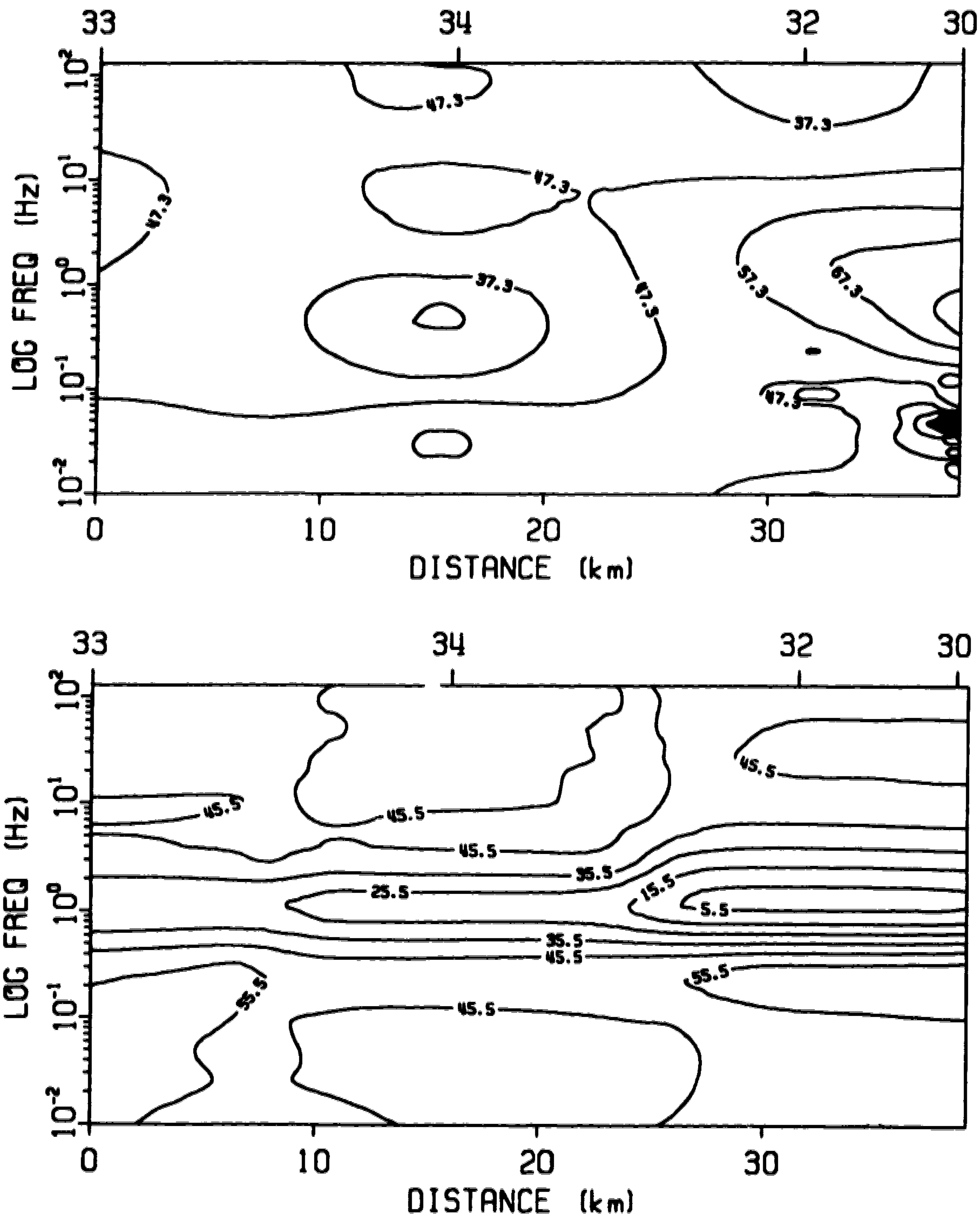

Fig. 4.17: TM mode - field data (top) and 2D model (bottom) phase pseudosections for profile CC' of Figure 4.4.

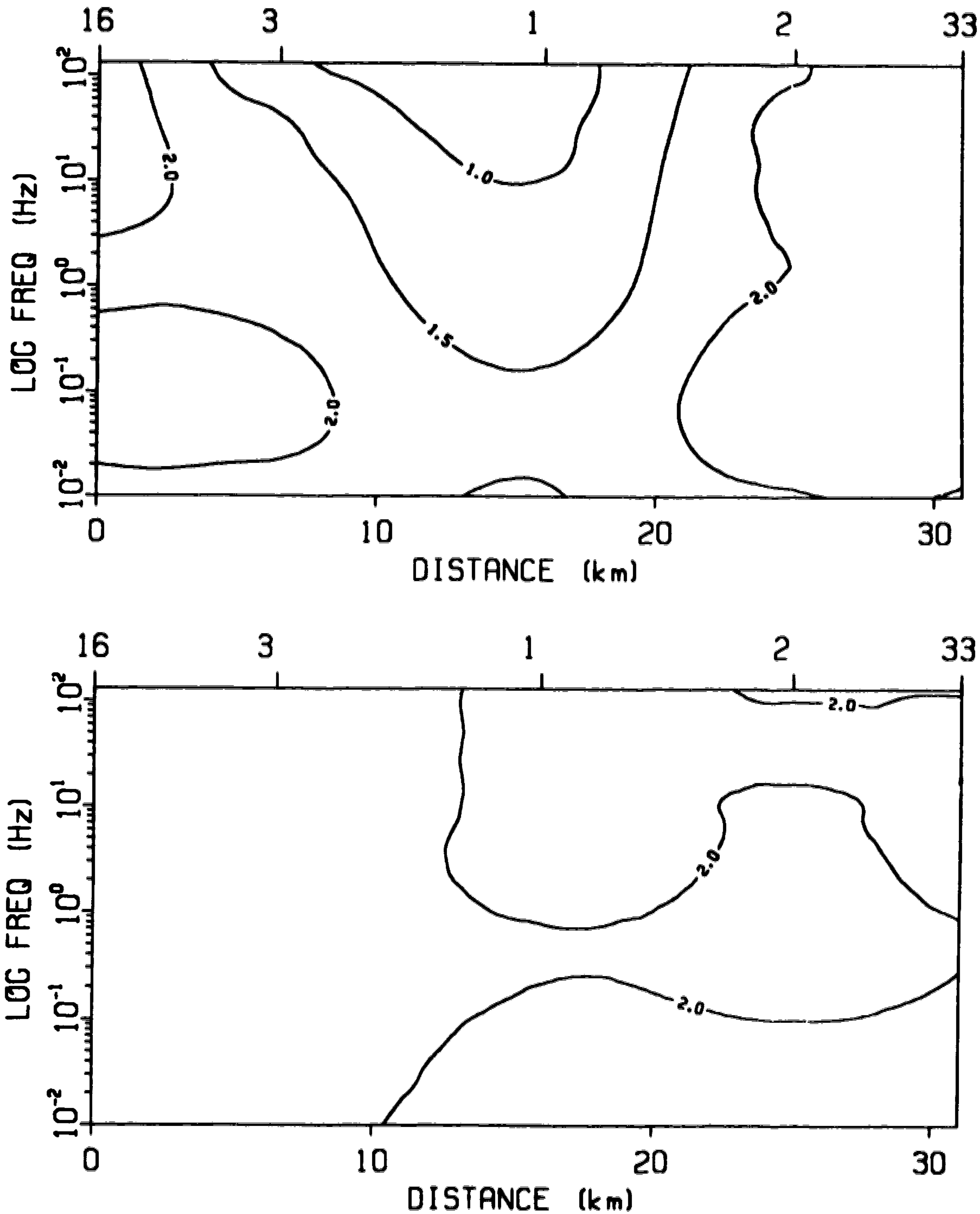

Fig. 4.18: TE mode - field data (top) and 2D model (bottom) electrical resistivity pseudosections for profile DD' of Figure 4.5.

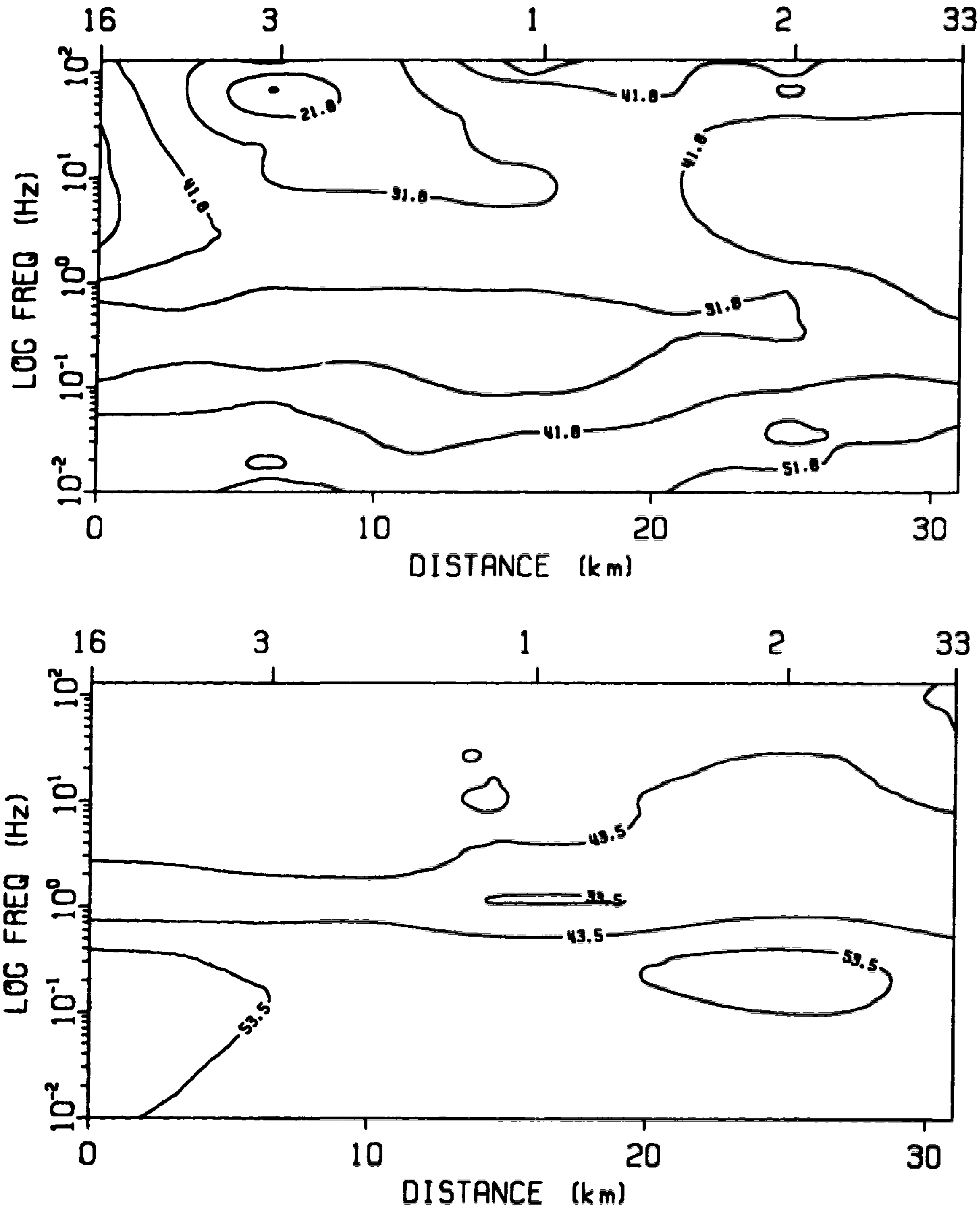

Fig. 4.19: TE mode - field data (top) and 2D model (bottom) phase pseudosections for profile DD' of Figure 4.5.

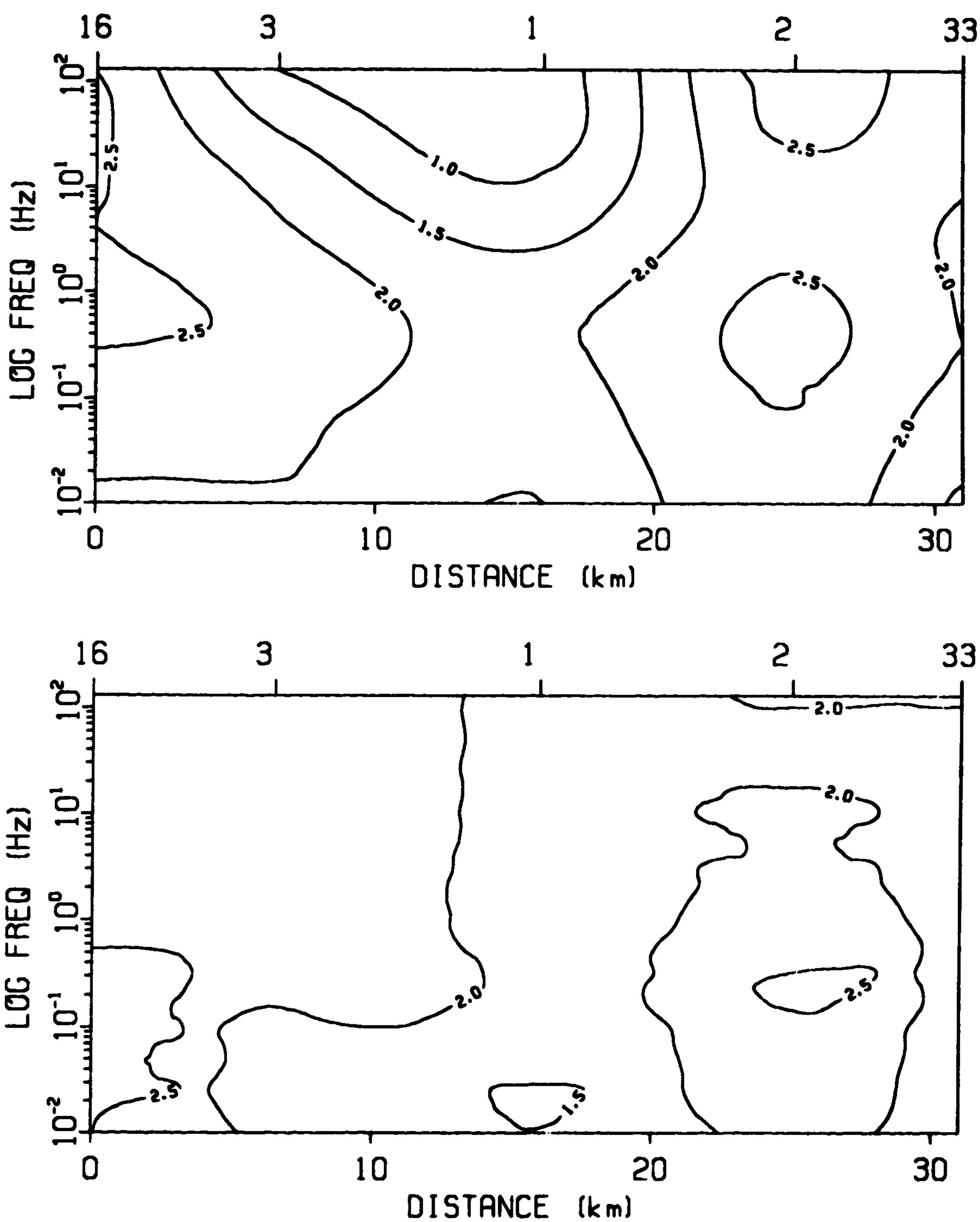

Fig. 4.20: TM mode - field data (top) and 2D model (bottom) electrical resistivity pseudosections for profile DD' of Figure 4.5.

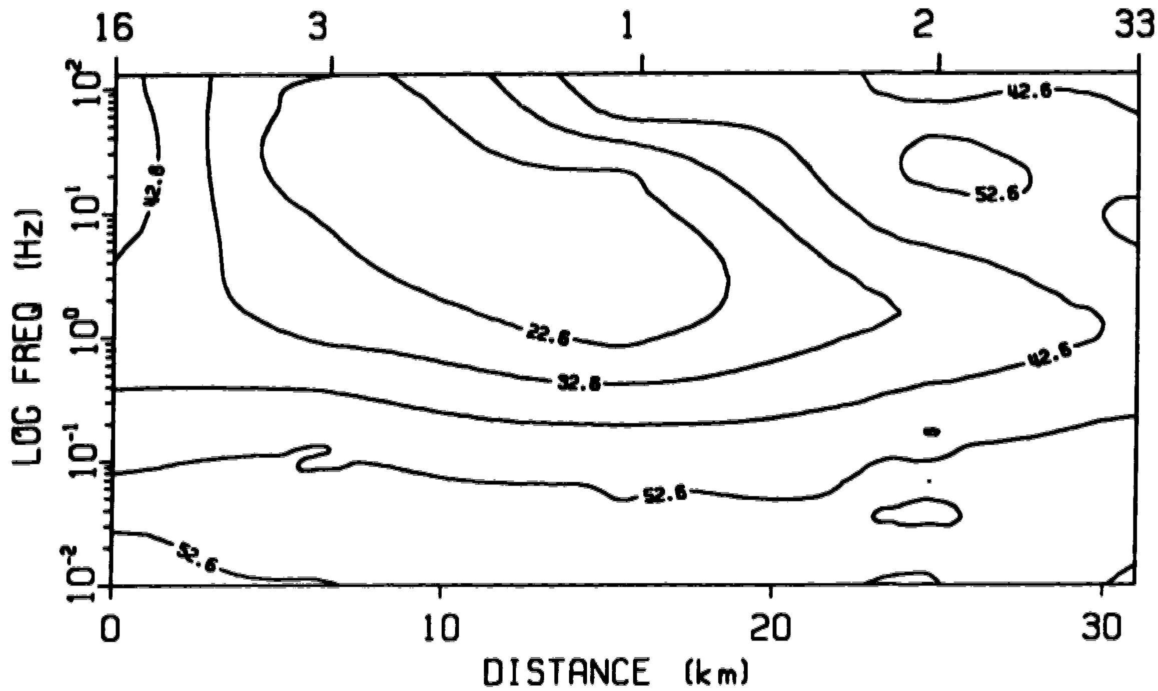

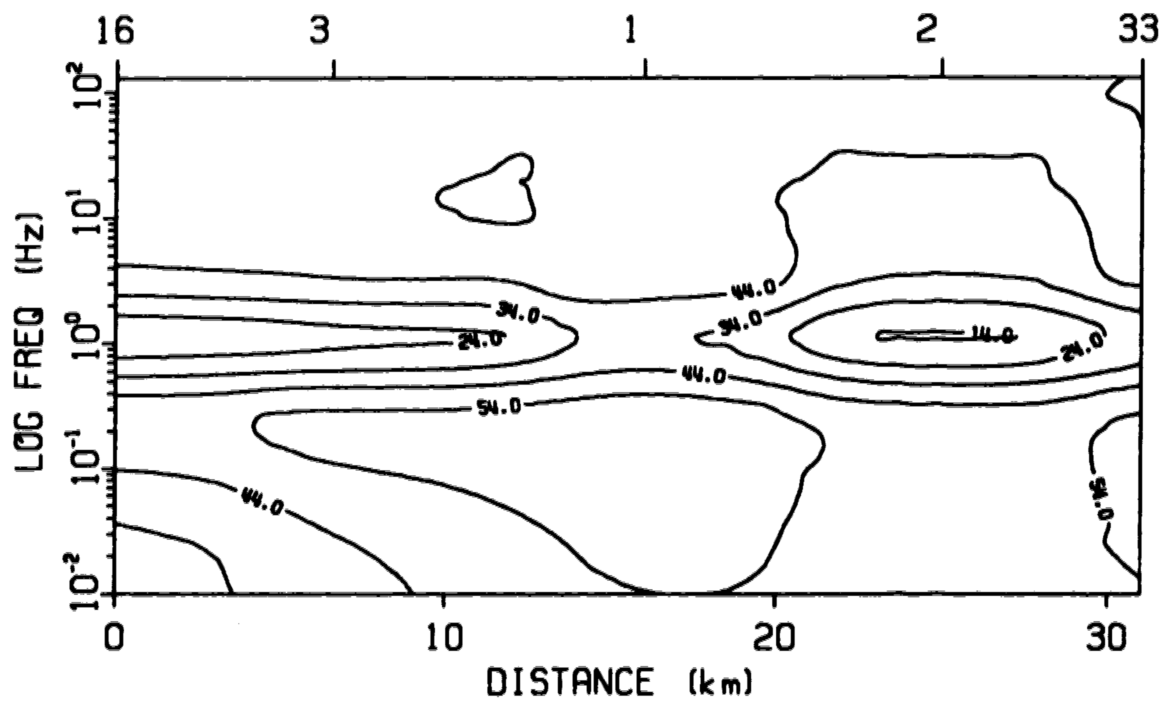

Fig. 4.21: TM mode - field data (top) and 2D model (bottom) phase pseudosections for profile DD' of Figure 4.5.

TE and TM modes are shown for each of the models constructed for each profile of Figure 3.8 (bottom parts of the figures). To compare with the field data, apparent electrical resistivity and phase pseudosections, constructed from the real data (Figure 3.9 of Chapter III), are also shown (top parts of the figures). In all figures the isolines of the apparent electrical resistivity pseudosections are the logarithms of the electrical resistivities (base 10) and in the phase pseudosections the isolines are in degrees. The discussion that follows is based on a paper that has been accepted for publication in the Proceedings Volume of the Third International Meeting of the Brazilian Geophysical Society (Correia and Jones, 1993).

A number of points can be noted when the comparison between the field data and the model responses is made. Generally, the field data are smoother than the model results. This is a consequence of the magnetotelluric method and the way nature behaves. In the real world there are usually no sharp electrical resistivity contrasts like those observed in Figures 4.2-4.5 and the transitions from one electrical resistivity to another are generally smoother than plan discontinuities. On the other hand, the MT method sounds a volume of rock and, therefore, any sharp electrical boundaries that exist will be integrated into a bulk apparent electrical resistivity, which is always smooth.

When considering 2D electrical resistivity models it is assumed that structures are infinite. This is clearly not the case in the study area and, among other things, the misfit between field data and model results can be an indication of the presence of 3D structures.

The results of the model for profile AA' (Figures 4.6-4.9) show that the main vertical discontinuities, as observed in the field data, are also observed in the model electrical resistivity pseudosections, in both the E- and H-polarization cases. This is also true for the model E-polarization phase pseudosection; however, in the H-polarization case some misfit exists between field data and model results.

The results of the model of profile BB' (Figures 4.10-4.13) show the same general behaviour as those for profile AA' and the main electrical discontinuities, as seen in the field data, are observed in the model apparent electrical resistivity pseudosections. However, both phase pseudosections show strong misfits between field data and model result pseudosections.

The situation for profile CC' (Figures 4.14-4.17) is similar to that for profile BB'. In this case, however, the greatest misfit is observed in the H-polarization phase pseudosections.

In the results for profile DD' (Figures 4.18-4.21), the main trends can be identified in both apparent electrical resistivity pseudosections as well as in the phase pseudosections. The field data and the model results for this profile are simpler than those for the other three profiles and this indicates that profile DD' crosses a region of less electrical complexity than the other profiles. The geological sketch of Figure 1.2 indicates that the MT stations located in the southwest part of the study area lie in a less geologically complicated region.

The set of models that is shown in Figures 4.2-4.5 corresponds to one of a number of different sets that were tested. The results obtained for the other electrical resistivity models were not substantially different from the results that are shown in Figures 4.6-4.21. This indicates that probably no purely 2D model will completely satisfy the observed data, and that 3D effects are superimposed on any 2D response. It is therefore not reasonable to try further to refine the 2D models. It is sufficient, and important, that the main effects of the electrical resistivity contrasts are observed in both the field data and model results, and that these effects reflect the presence of the two major tectonic features of the area, i.e., the Messejana fault and the Ferreira-Ficalho overthrust.

A further interesting observation from the field data and model result comparison is that a structure which was previously ignored appears in both the field data and model results of profile AA'. Between stations 12 and 28 there is an apparent vertical contact that coincides with the location of a fault that crosses the northern edge of the study are in an approximately east-west trend - the Vidigueira fault.

4.4. Three-dimensional electromagnetic modelling

As previously mentioned, the central region of the study area is three-dimensional (3D), and therefore an attempt was made to use a 3D model to quantify the local electrical resistivity structure.

The general 3D electromagnetic induction problem can be approached in the same way as the 2D case, and Maxwell's equations can be solved within a three-dimensional region by a finite-difference method. If displacement currents are neglected (Chapter II), and the electric and magnetic fields are assumed to vary sinosoidly with time, equations (2.1) and (2.2) may be written as:

$$\nabla \times \bar{E} = -i\mu\omega\bar{H} \tag{4.1}$$

and

$$\nabla \times \bar{H} = \sigma\bar{E} \, . \tag{4.2}$$

Taking the curl of equation (4.1) and using equation (4.2) and the vector identity $\nabla \times \nabla \times \bar{a} = \nabla\nabla \cdot \bar{a} - \nabla^2 \bar{a}$, the following equation is obtained:

$$\nabla^2 \bar{E} - \nabla\nabla \cdot \bar{E} = i\eta^2 \bar{E} \, , \tag{4.3}$$

where $\eta^2 = \mu\omega\sigma$. Equation (4.3) must then be solved for $\bar{E}$ in all regions. To do this, equation (4.3) can be written as a set of three scalar equations in Cartesian coordinates

$$\frac{\partial^2 E_x}{\partial y^2}+\frac{\partial^2 E_x}{\partial z^2}-\frac{\partial}{\partial x}\left[\frac{\partial E_y}{\partial y}+\frac{\partial E_z}{\partial z}\right]=i\eta^2 E_x$$

$$\frac{\partial^2 E_y}{\partial x^2}+\frac{\partial^2 E_y}{\partial z^2}-\frac{\partial}{\partial x}\left[\frac{\partial E_x}{\partial x}+\frac{\partial E_z}{\partial z}\right]=i\eta^2 E_y$$

$$\frac{\partial^2 E_z}{\partial x^2}+\frac{\partial^2 E_z}{\partial y^2}-\frac{\partial}{\partial z}\left[\frac{\partial E_x}{\partial x}+\frac{\partial E_y}{\partial y}\right]=i\eta^2 E_z\,.$$

These equations are written in finite-difference form and solved simultaneously for E_x, E_y and E_z at each point of a mesh which is superimposed over the region of interest by a Gauss-Seidel iteration technique. Since the main objective is to calculate the model response in terms of electrical resistivity and phase at the model surface corresponding to the surface of the Earth, the magnetic field must also be calculated. This can be done using the calculated electric field components by application of equation (4.1) solved for the magnetic field, i.e.,

$$\vec{H}=-\frac{1}{i\mu\omega}\nabla\times\vec{E}\,.$$

Details about the numerical technique can be found in Lines (1972), Lines and Jones (1973a, 1973b), Jones and Pascoe (1972) and Jones (1974).

The model of the study area was constructed using a three-dimensional mesh of $40 \times 40 \times 40 = 64,000$ cells. An initial model of $80 \times 80 \times 80 = 512,000$ was tried at the beginning, but it was not possible to run it in the Convex processing unit of the University of Alberta. This was unfortunate because the study area is geologically complex, and as a consequence of this limitation it was necessary to simplify the model with an accompanying decrease in resolution.

The constructed model was based on knowledge of the geology of the region of the MT survey and the results obtained after processing the field data (Appendixes II and III). One simplification that had to be introduced in the model was that the curvature of the Ferreira-Ficalho overthrust was not taken into account. Another simplification was that the deep low resistivity layers were assumed to extend to the Moho, 30 km deep. Furthermore, it was assumed that the study area could be modelled by considering the high electrical resistivity blocks, as obtained in the resistivity maps shown in Appendix III, to be embedded in a crust of electrical resistivity 100 ohm-m. The upper mantle was assumed to have an electrical resistivity of 50 ohm-m, which is consistent with values reported by Haak and Hutton (1986) and Jones (1992). Figure 4.22 shows the model with the four blocks. The details of the individual blocks are shown in Figure 4.23. The apparent electrical resistivities and phases were calculated using equations (2.48) - (2.51) and the results for site 8 are

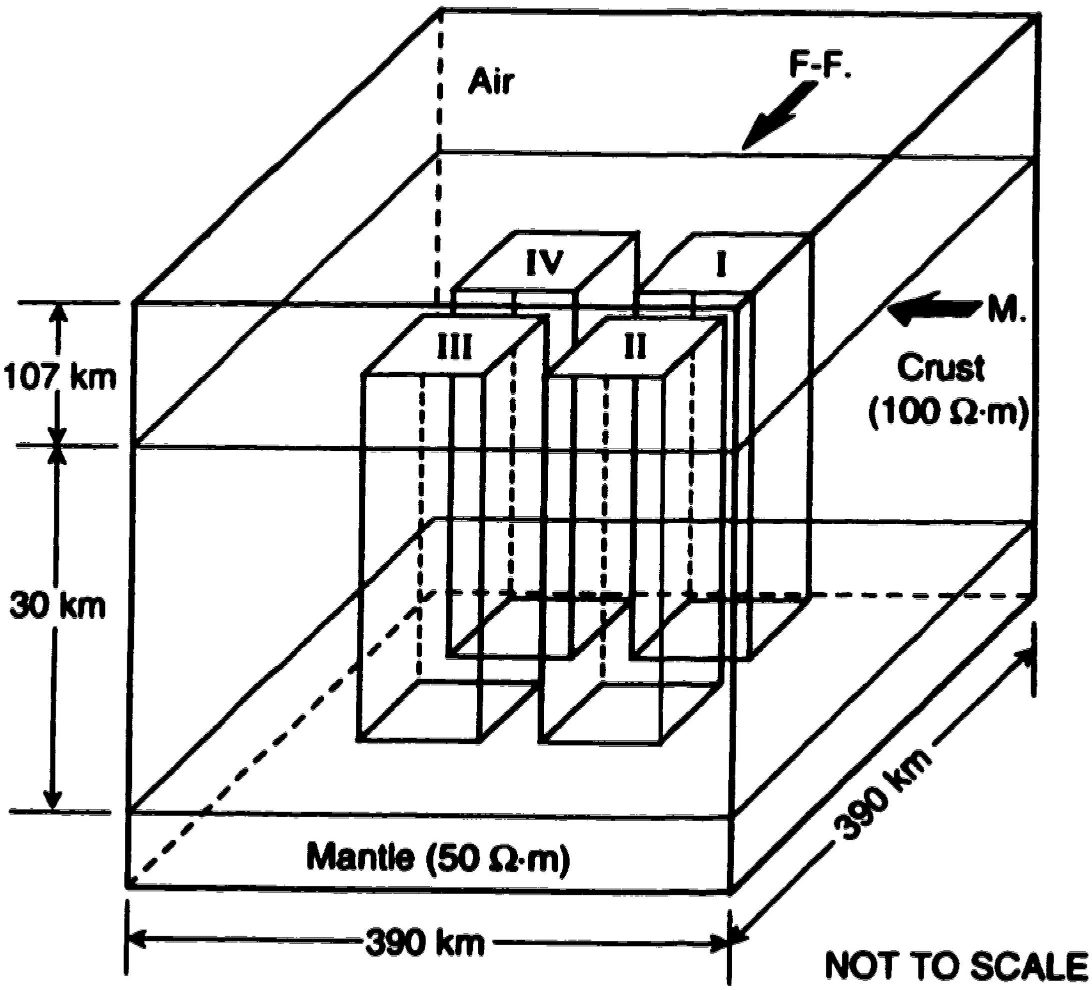

Fig. 4.22: Three-dimensional model of the study area. The numbers in arabic represent electrical resistivities in ohm-m. The four blocks in the middle of the model are identified with roman numbers and are detailed in Figure 4.23. F-F. indicates the position of the Ferreira-Ficalho overthrust and M. indicates the position of the Messejana fault.

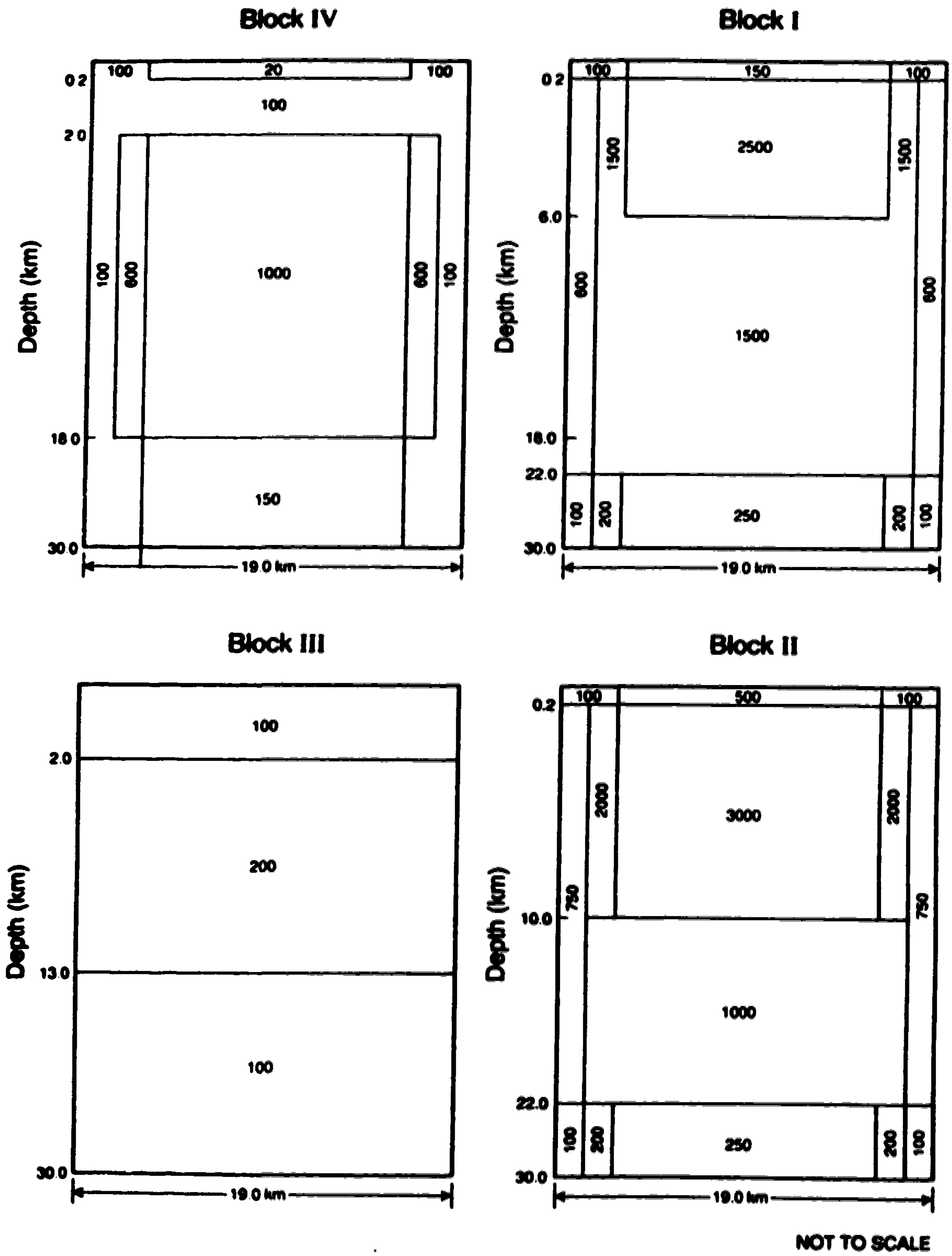

Fig. 4.23: Details of the four blocks (in cross-section) of the three-dimensional model shown in Figure 4.22. The numbers in arabic are electrical resistivities in ohm-m.

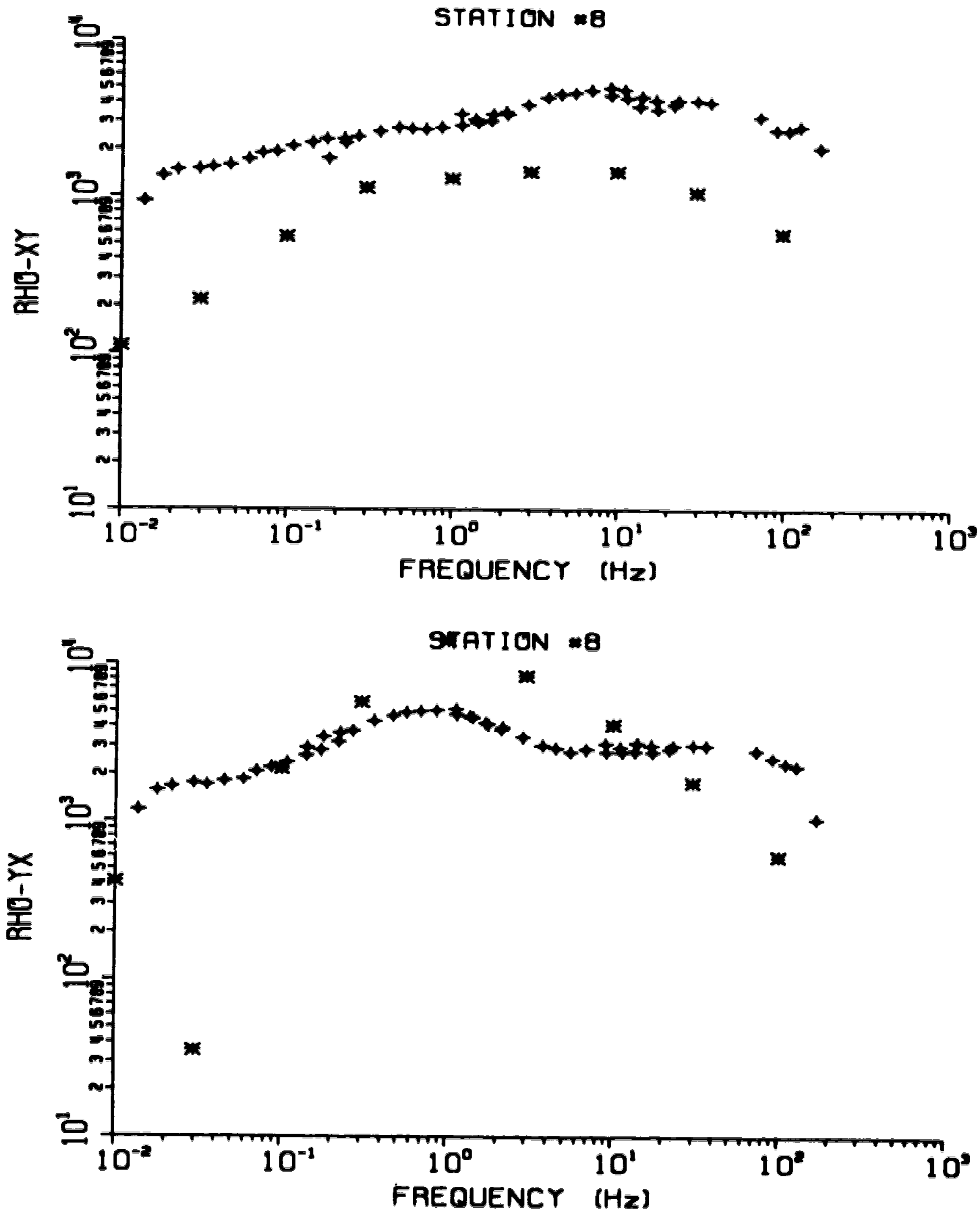

Fig. 4.24.a: Comparison between electrical resistivity for 3D model results (stars) and field data results (crosses) for site 8 (see text for explanation).

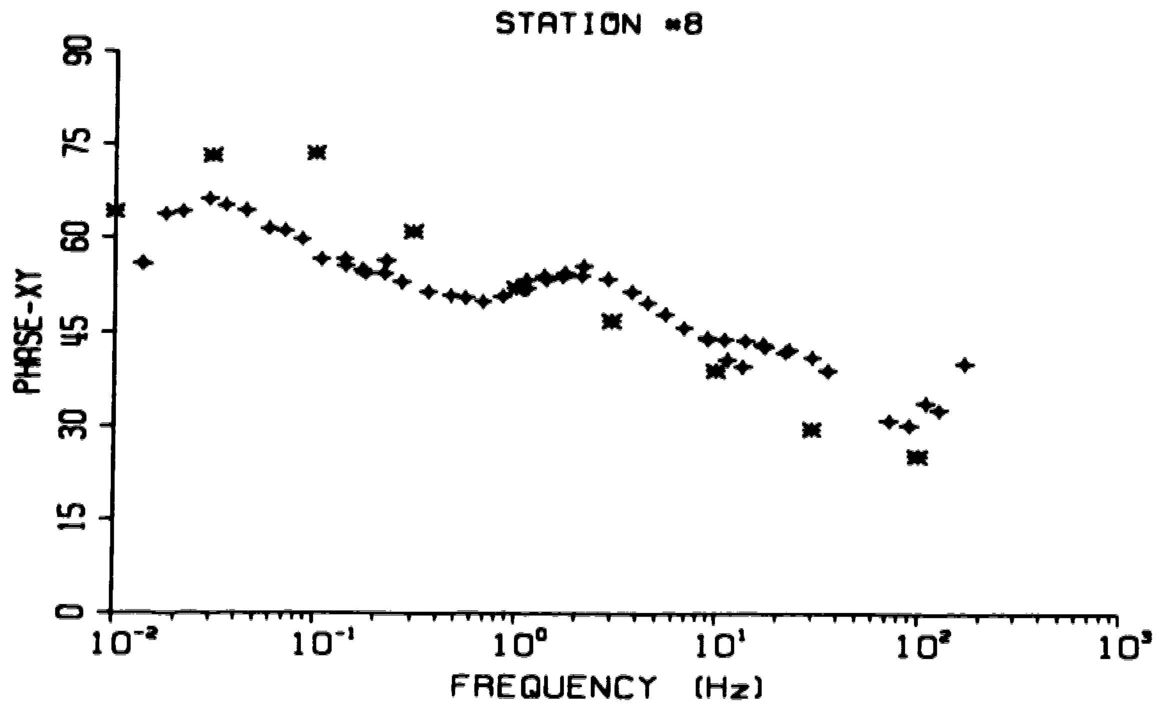

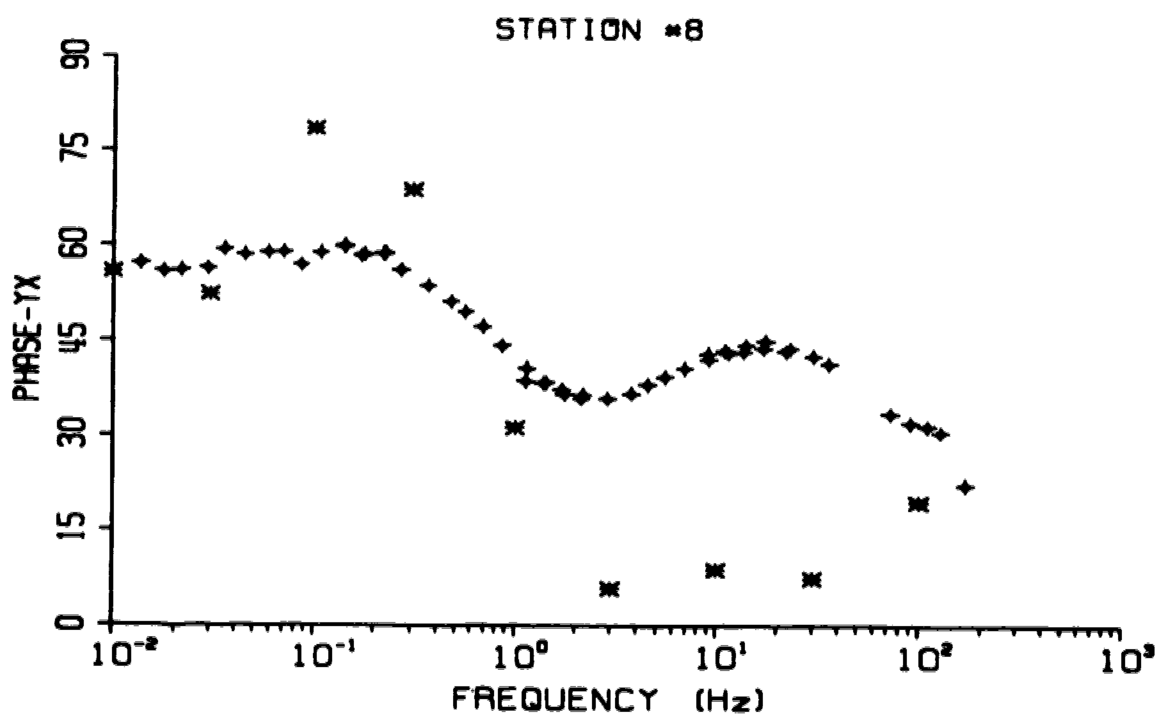

Fig. 4.24.b: Comparison between phase for 3D model results (stars) and field data results (crosses) for site 8 (see text for explanation).

shown in Figures 4.24.a-b. In these figures the stars represent the model results and the crosses represent the field data. Other sites used to compare the 3D model results with the field data are given in Appendix IV. Because of the limited model resolution, imposed by the $40 \times 40 \times 40$ mesh, only field results of MT sites that are located inside regions that correspond to the blocks shown in Figure 4.22 are compared with the 3D model results.

Nine frequencies were calculated for the 3D model (0.01, 0.03, 0.1, 0.3, 1, 3, 10, 30, 100 Hz), and these covered the frequency range of the MT survey. As in the 2D modelling (Section 4.2), for the 3D case a residual of 0.00001 was imposed to insure convergence of the calculated solution. The maximum number of iterations allowed for the calculation was 2000 but this number was never reached.

Comparison of the 3D model results and the field data (Figures 4.24.a-b and Appendix IV) shows that the coincidence between the two sets of results is remarkably good, considering the relative simplicity of the model, in all plots of electrical resistivity and phase in the XY "direction" (i.e., RHO XY and PHASE XY). However, the coincidence is generally not as good in the other direction, i.e., YX "direction" (RHO XY and PHASE YX). The lack of fit between the latter 3D model results and the field data in that direction is a consequence of the modelling program. The source of the natural magnetotelluric field is generally not strongly polarized in a particular direction. However, for calculation purposes, the 3D modelling program assumes that the source field is polarized in the X direction. The practical results of this assumption is that the magnitudes of the electric fields calculated at the surface of the model will generally be small in the Y direction and thus the electrical resistivity calculations (RHO YX and PHASE YX) will tend to be unstable. A possible solution to this difficulty would be to run the 3D model using different source polarization fields.

Sites 8, 12 and 22 are located in the region that corresponds to block I in the 3D model shown in Figure 4.22. This block is closest one to the center of the geothermal anomaly. Comparison between the field data and 3D model results confirms the general high electrical resistivity character of that area to approximately Moho depths.

A high resistivity character can also be inferred from the comparison between the field data and the 3D model results for sites 17, 19 and 21. These sites lie within block II of Figure 4.22.

Block III of Figure 4.22 corresponds to a low electrical resistivity area and its character can be identified in the electrical resistivity and phase curves of sites 4, 33 and 34. It is apparent from the comparison between field and model results that the electrical resistivities chosen for the 3D model are higher than appropiate for this area, which confirms that the area is an anomalously low electrical resistivity region.

Block IV of the 3D model corresponds to another high electrical resistivity region of the study area and this is seen in the electrical resistivity and phase curves for sites 6, 13 and 24. The comparison between field and model results indicate that the electrical resistivities at shallow depths (high frequencies) in the 3D model are higher than appropiate, particularly for sites 13 and 24.

The comparison between the field data and the 3D model results in the X direction (i.e., RHO XY and PHASE XY) are encouraging and indicate that it would be possible to refine the model to a point where a good fit may be obtained for most of the MT sites. A more quantitative analysis and interpretation for the study area might be achieved if 3D model with higher resolution could be used. This means that models with more than $40 \times 40 \times 40$ cells will be required, with the number of cells increasing with the increase in complexity of the structure to be represented. It must be emphasized, however, that even though the 3D model used here is just an approximation to the regional geology, the results from it support the interpretation that the region of the MT survey is characterized by the existence of high electrical resistivity blocks embedded in more conductive formations.

CHAPTER V

THE STATIC SHIFT EFFECT

5.1. Overview of the static shift effect

By definition, static shift effects are shifts of the apparent electrical resistivity versus frequency (or period) curves by the same multiplication factor at all frequencies between adjacent MT sites or between the two apparent electrical resistivity curves determined in two mutual perpendicular directions for the same site (Jones, 1988; Vozoff, 1991). The shifts are such that the shapes of the apparent electrical resistivity curves are maintained and the corresponding phase curves are unchanged.

Static shifts are related to distortions of the electric field caused by boundary charge buildup when relatively small and shallow or surficial geological inhomogeneities are present in the area where the MT survey is performed (Wannamaker et al., 1984b; Newman et al., 1986). Such inhomogeneities are ones with dimensions much less than the skin-depth at the highest frequency (lowest period) used in the survey. The charge buildup at the inhomogeneity boundary produces an enhancement or reduction of the total electric field and the apparent electrical resistivity curve is shifted towards higher resistivities when the electric and magnetic fields are measured over a resistive inhomogeneity, and shifted towards lower resistivities when measured over a conductive inhomogeneity. These qualitative results can easily be seen by considering equation (2.30) and the fact that magnetic field distortions due to small inhomogeneities are much smaller than the electric field distortions (Jiracek, 1990).

Formally the static shift effect can be described in the following way. When induced currents with density $\vec{J}$ flow through electrical inhomogeneities, surface electric charges with densities $\vec{J}\cdot\nabla(\varepsilon_o/\sigma)$ are created, where ε_o is the electrical permittivity and σ is the electrical conductivity. While the magnetic field ($\vec{H}=\nabla\times\vec{A}$) depends only on the current distribution through $\vec{A}$

$$\vec{A}(\vec{r})=\frac{1}{4\pi}\int_{vol}\frac{\vec{J}(\vec{r}\,')}{|\vec{r}-\vec{r}\,'|}\,dv'$$

the electric field $\vec{E}=\frac{\partial\vec{A}}{\partial t}-\nabla\phi$ depends on the charge distribution

$$\phi(\vec{r})=\frac{1}{4\pi}\int_{vol}\frac{\vec{J}\cdot\nabla(\varepsilon_o/\sigma)}{|\vec{r}-\vec{r}\,'|}\,dv'.$$

Thus the electric fields are more affected by electrical inhomogeneities than the magnetic fields.

Jones and Price (1970) first recognized that boundary charges may perturb electromagnetic fields, but Berdichevsky and Dmitriev (1976a, 1976b) were the first to describe the static shift effect in MT surveys and to propose a classification for the distorted electromagnetic fields into inductive and galvanic effects.

One of the main problems of the static shift effect is that the amount of shift cannot be measured or determined directly from a single MT site, and, to remove or compensate for it, another independent method is necessary to measure the ground electrical resistivity. Since magnetic fields are less distorted by inhomogeneities than electric fields, one method that is frequently used to calculate the amount of static shift is the transient electromagnetic method (TEM) which is a controlled-source magnetic field sounding method (Sternberg et al., 1988). This method determines the unperturbed (or less perturbed) apparent electrical resistivities in the upper sections of the area being surveyed which permits the MT apparent electrical resistivity curves to be shifted so that they are a smooth continuation of the electrical resistivity curves obtained by the TEM technique. Another curve shifting method often used consists in shifting the MT curves obtained in the same region in such a way that at long periods (low frequencies) all of them indicate the same electrical resistivity. This technique is based on the assumption that at depths of about

250-300 km the geoelectrical structure varies little in global terms (Rokityansky, 1982; Berdichevsky et al., 1989).

Electromagnetic Array Profiling (EMAP) (Bostick, 1986) is another method that is used which removes certain static shift effects. In this method it is assumed that 3D, 2D and E-polarization mode responses can be greatly reduced by using wavenumber domain low-pass filtering on MT data.

Other methodologies can also be employed, such as theoretical calculations by numerical modelling of static shift effects caused by surface or shallow inhomogeneities (Wannamaker et al., 1984a,b), statistical averaging (Berdichevsky et al., 1980; Kurtz et al., 1986), calculation of distortion tensors (Groom and Bailey, 1989; Bahr, 1988), calculation of invariants (Berdichevsky and Dmitiev, 1976a), or simply by incorporating in the interpretation the knowledge of the local geology or other available geophysical information.

For the Portuguese data, the use of the Berdichevsky invariant (Berdichevsky and Dmitriev, 1976a) provided compensation for the possible static shift effects present in some of the apparent electrical resistivty curves. However, because of the geological complexity of the study area and the spacing between MT stations, it is difficult to say whether the shifts observed in some of the curves are due to static shift effects or to the geological structures. In fact, the results of the 3D modelling described in Chapter IV indicate that static shift effects were not a major factor of inaccuracy and that the 1D inversions of the field data used to construct the 3D model of the study area were good first approximations.

5.2. Static shift modelling - field procedures approach

In the formula to calculate the apparent electrical resistivity for a given frequency (e.g. equation (2.30)) the electric and magnetic field intensities must be measured in orthogonal directions (see Figure 3.2). The magnetic field is directly measured using coils, but the electric field is calculated by dividing the potential difference between two electrodes by their separation distance. Often, in MT surveys, one or more of the four electrodes used to measured the potential differences in the two directions lie in geological inhomogeneities. It would therefore be useful to know how these inhomogeneities influence the calculated apparent electrical resistivity curves. In particular, it would be useful to quantify the amount of static shift in situations where the shape, size and electrical resistivity can be controlled in appropriate models. To perform this exercise the 3D modelling program as used in Chapter IV was applied to layered earth models with small inhomogeneities that are expected to produce static shift effects (Section 5.1).

The 3D modelling program calculates the electric field at every node of a mesh of $40\times40\times40$ cells. Since the purpose of the experiment is to reproduce field procedures, potential differences are calculated between nodes by using the general definition of electrical potential difference between points A and B (i.e. two electrodes), that is,

$$V_{AB} = \int_A^B \bar{E} \cdot d\bar{l}$$

where $\bar{E}$ is the electric field strength and $d\bar{l}$ is the elemental length along a certain path between A and B. In a mesh, and along direction X this intregal is approximately given by

$$V_{AB} = \sum_{i=1}^{N} E_{x_i} dx_i$$

where N is the number of mesh points used to calculate the potential difference, E_{x_i} is the electrical field component in the X direction at node i and dx_i is the distance between the node where E_{x_i} is calculated and the adjacent node. After calculating the potential difference between A and B, the average electric field at the center point in the X direction is given by

$$E_x = \frac{V_{AB}}{AB} = \frac{\sum_{i=1}^{N} E_{x_i} dx_i}{AB}.$$

In the uniform mesh that was used, the dx values were equal to 10 metres and N=4, so that the average electric field in the X direction was given by

$$E_x = \frac{1}{4}\sum_{i=1}^{4} E_{x_i}. \tag{5.1}$$

This means that using the potential difference approach between two points to calculate the electric field in a certain direction at the middle point is equivalent to averaging the electric field between those two points.

The main objective of the above method of calculation was twofold. First, it implies that potential differences, which are the quantities measured during the MT field work are used in the calculation, and second, it means that one of the electrodes (or both) of the measuring potential electrodes can be placed within the inhomogeneity to reproduce what may occur during field work.

The accuracy of the approximation represented by equation (5.1) was tested. As expected, the electric field values at each node of the mesh for the model without an inhomogeneity were equal to the values calculated using equation (5.1).

5.3. Results of the static shift modelling

To reproduce and study the static shift effect a three layered Earth with different inhomogeneities was used. The characteristics of the layered Earth were the following: the first layer was 2.338 km thick and had an electrical resistivity of 100 ohm-m and the second was 18 km thick and had an electrical resistivity of 1000 ohm-m. The half-space below these two layers had an electrical resistivity of 10 ohm-m. The electrical inhomogeneity was modelled by constructing square blocks in the centre of the model with resistivities that varied between 1 and 10 ohm-m. The sizes of the blocks were $120m \times 120m \times 80m$ and $60m \times 60m \times 8m$. Apparent electrical resistivities and phases were calculated for the model without the inhomogeneity and for those with the inhomogeneities for the same 9 frequencies used in Chapter IV. The results of the calculations for different distances from the centre of the inhomogeneity with dimensions $60m \times 60m \times 8m$ and with an electrical resistivity of 1 ohm-m are shown in Figures 5.1 to 5.4. In these figures the stars correspond to the model without inhomogeneity and the crosses to the model with inhomogeneity.

From the figures it is apparent that no static shift, as defined in Section 5.1, is observed and the inhomogeneity only makes the shape of the apparent electrical resistivity curve change at high frequencies. At low frequencies, the curves corresponding to the layered model with and without the inhomogeneity coincide. This same pattern is observed in the phase curves. Similar results were obtained for inhomogeneities with different sizes and electrical resistivities from that used to calculate the curves shown

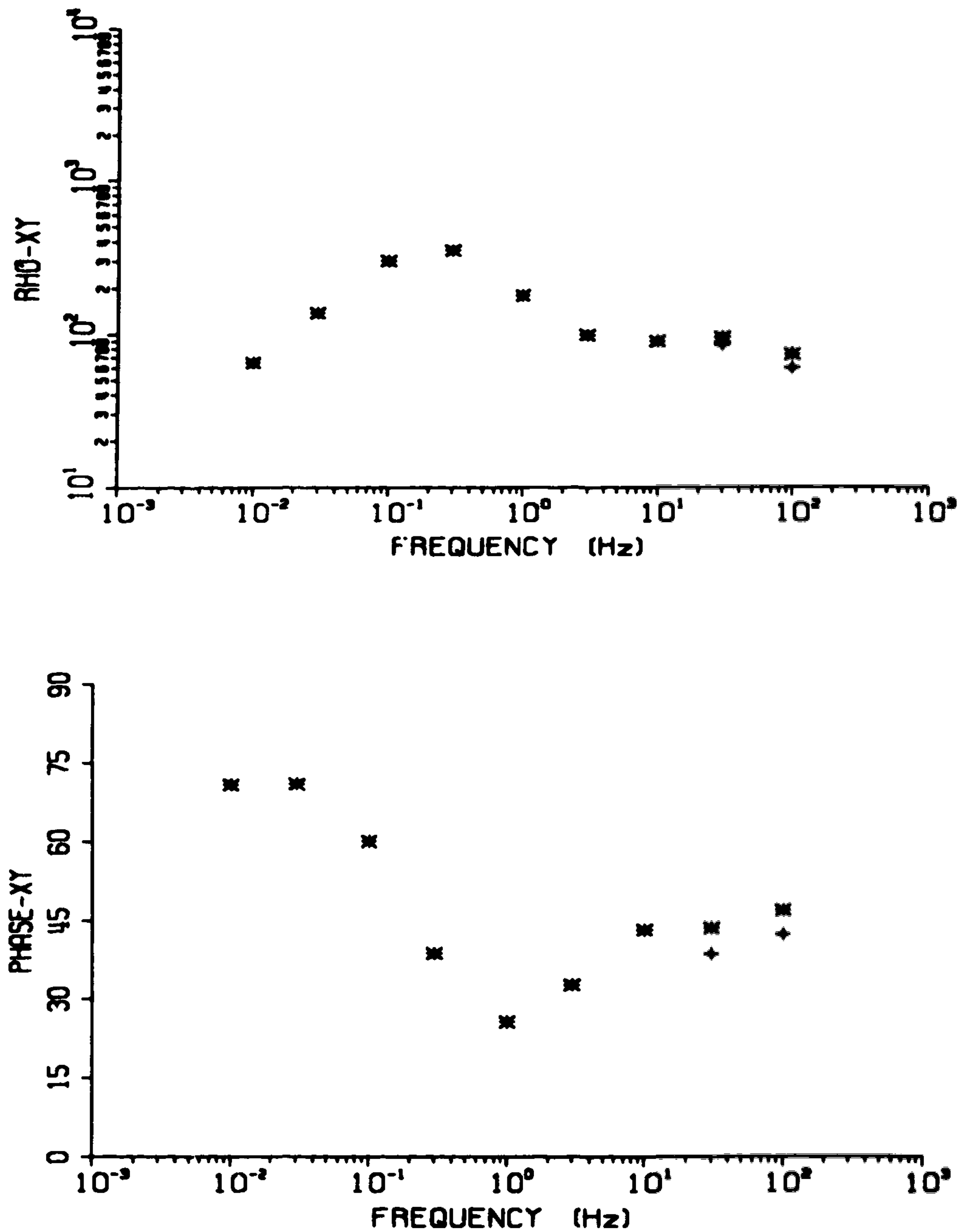

Fig. 5.1: Comparisons between the apparent electrical resistivities (top) and phases (bottom) for the case with no inhomogeneity (stars) and for the case with a 60m × 60m × 8m inhomogeneity (crosses), 100 m from its centre in the X direction (see text for explanation).

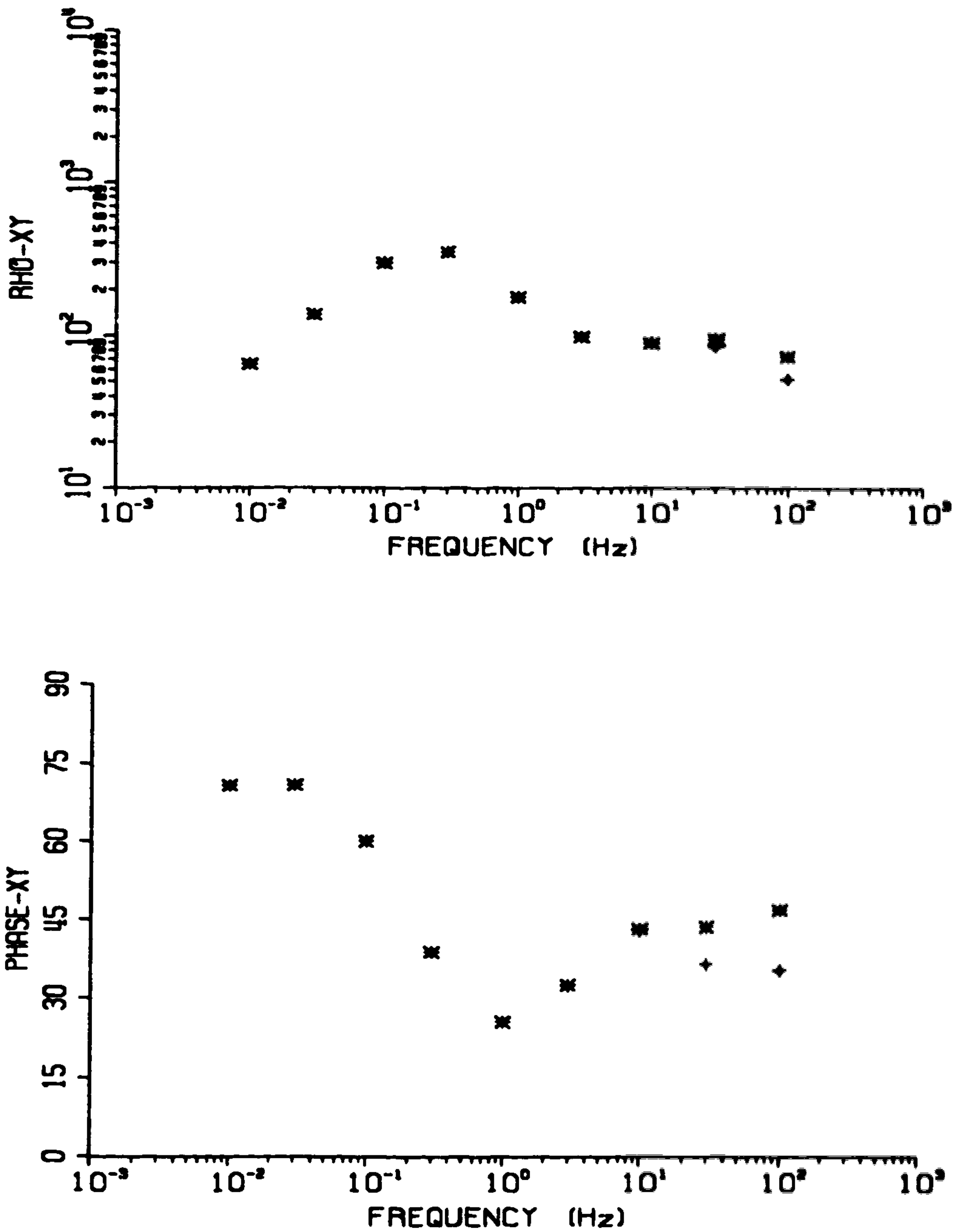

Fig. 5.2: The same as in Figure 5.1 for a distance of 70 m from the centre of the inhomogeneity in the X direction.

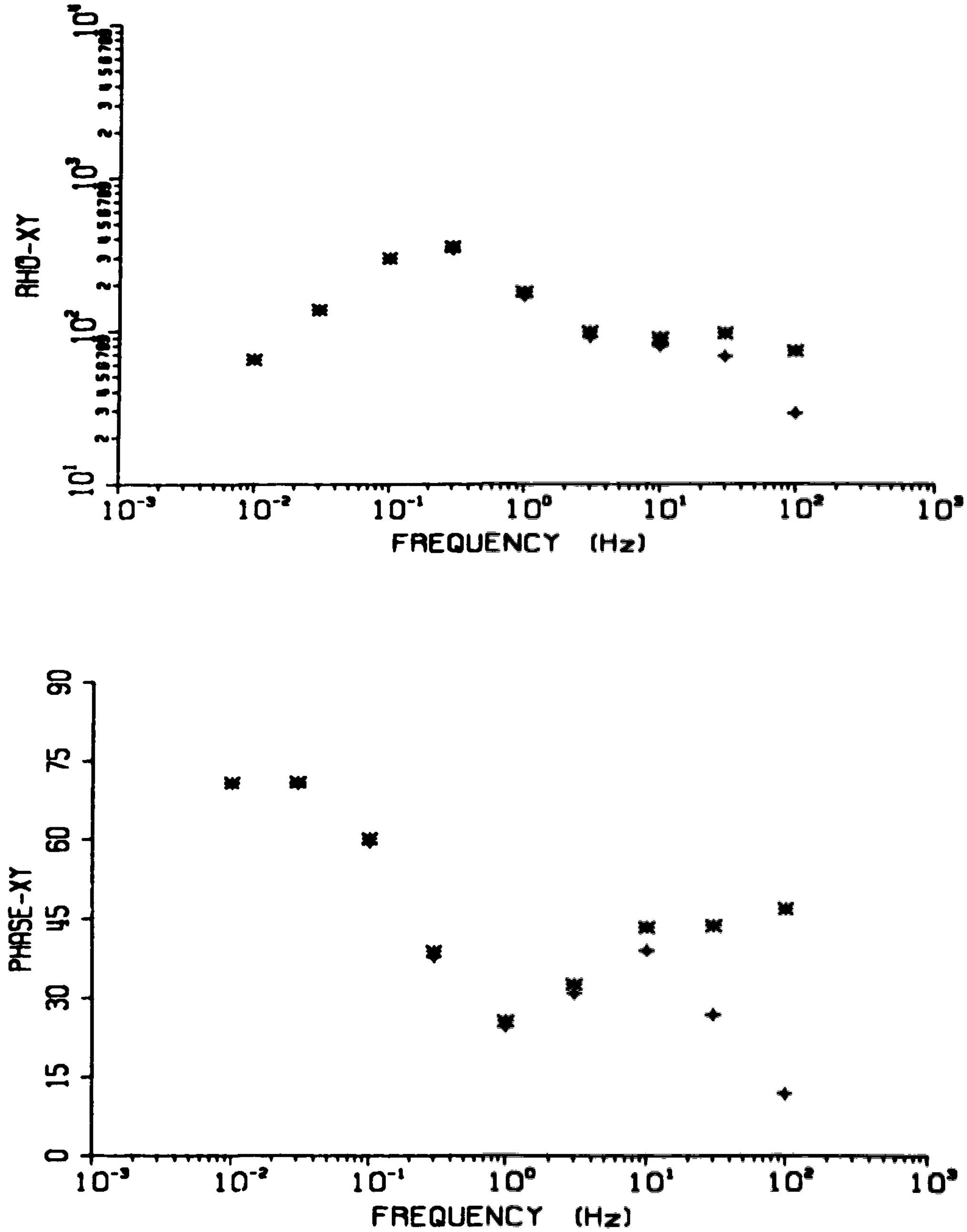

Fig. 5.3: The same as in Figure 5.1 but with one of the electrodes placed on top of the inhomogeneity. The centre of the measuring potential dipole is 30 m from the centre of the inhomogeneity in the X direction.

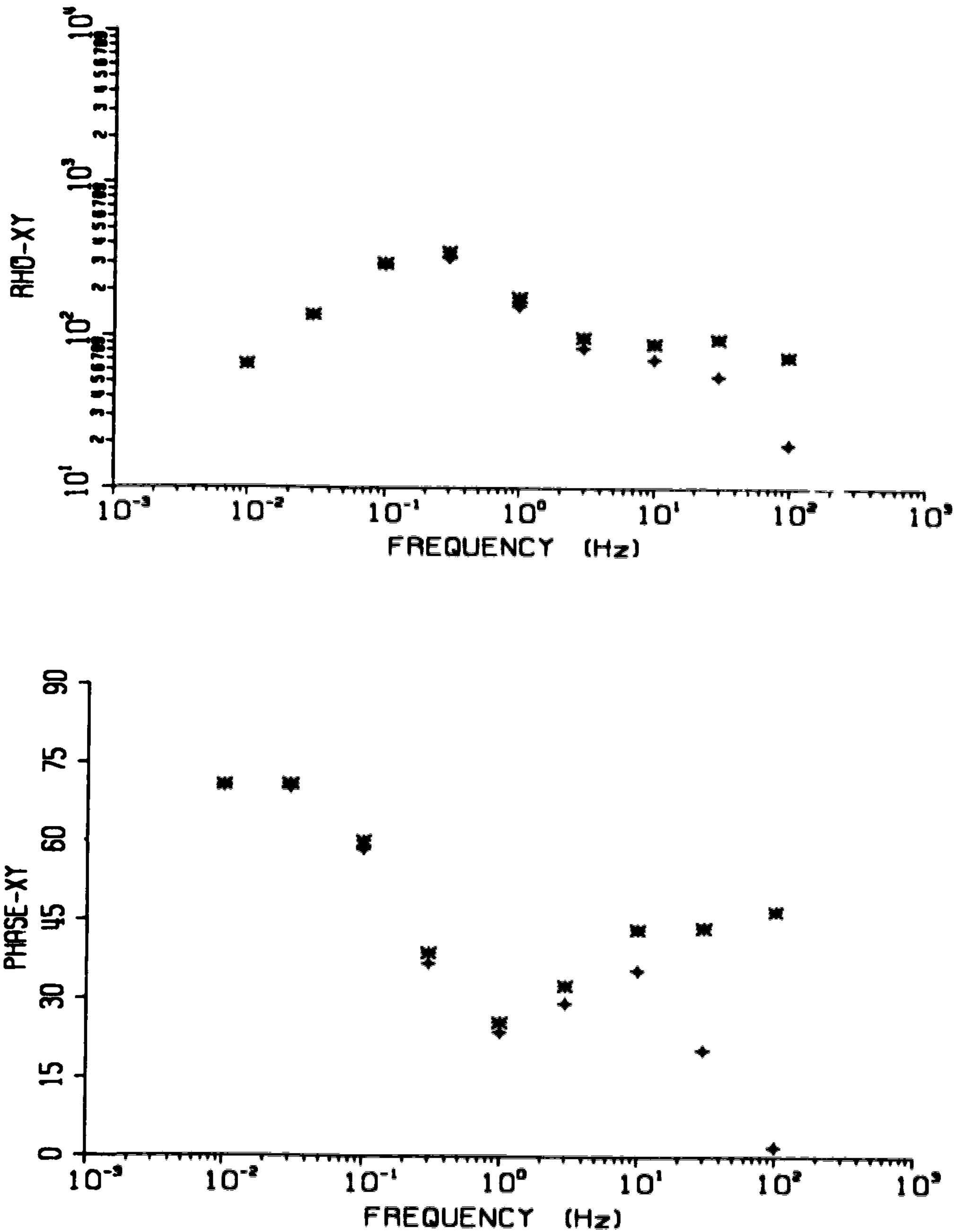

Fig. 5.4: The same as in Figure 5.1 but with both electrodes placed on top of the inhomogeneity. The centre of the measuring potential dipole (in the X direction) coincides with the centre of the inhomogeneity.

in Figures 5.1 to 5.4. Furthermore, calculations using different inhomogeneity electrical resistivities showed that the greater the contrast between the electrical resistivity of the inhomogeneity and the first layer of the model the greater the shift between the curves at higher frequencies. However, at lower frequencies the curves obtained from the two models were the same.

5.4. Conclusions

The main conclusion from the exercise described here is that the 3D modelling package used did not produce a static shift effect. The question that immediately arises is why not? The answer to this question is that boundaries between regions of different electrical resistivities in the 3D modelling program that was used here are represented by "transition zones" rather than abrupt discontinuities. It is assumed that the electrical resistivity varies smoothly between blocks of different electrical resistivity. This is, however, consistent with the way electrical resistivity varies in nature as mentioned in Chapter IV. Sharp linear electric resistivity contrasts rarely occur. On the other hand, to the author's knowledge, only one 3D modelling program has been used so far to successfully model static shifts. It is the program of Wannamaker et al. (1984a) which uses the integral equation approach (see Chapter II). Despite its capability to reproduce static shift effects, the integral equation approach method is limited to modelling simple 3D inhomogeneities in a layered (1D) half-space (Wannamaker and Hohmann, 1991). Much more work in modelling the static shift effect is needed in order to understand it in terms of the real world. In fact, it may be that because of the simple models that so far have been used to model static shift using the integral equation approach, the results are exaggerated in comparison with more accurate 3D models of real structures. As Jiracek (1990) says, no magical solutions to all problems of near surface electromagnetic distortions are available.

Despite the failure to model static shift effects and the impossibility of quantifying them in terms of the sizes and shapes of electrical resistivity inhomogeneities, the exercise led to a better understanding of the 3D modelling packages available and to the realization that there is no 3D modelling procedure yet that permits the incorporation of all the information required to construct accurate electrical models of the real world.

CHAPTER VI

DISCUSSION, INTERPRETATION AND CONCLUSIONS

6.1. Introduction

The main objective of the magnetotelluric work described up to now was to delineate a geothermal anomaly that is thought to exist in southern Portugal in geoelectrical terms. The use of the MT method is justified by the fact that temperature influences electrical resistivity (or its reciprocal, the electrical conductivity) and, therefore, geothermal anomalies should be detected as low electrical resistivity anomalies (high electrical conductivity anomalies). Implicit in this objective was the search for the origin of the geothermal anomaly which is suspected to be related to the complex geological features of the region where the MT study was performed.

The fact that the study area is crossed by two major tectonic features (the Messejana fault and the Ferreira-Ficalho overthrust) suggests that other questions may be addressed for the region, such as: how deep do the Messejana fault and the Ferreira-Ficalho overthrust penetrate into the crust and what are their geometries? Do these two tectonic features show any particular geoelectrical signature and are the high and low electrical resistivity areas identified during the survey a result of them? How can the high electrical resistivity regions be explained in an area that otherwise should have low electrical resistivity? And what is the relation between the geothermal anomaly and the geoelectrical pattern obtained for the area? Some of these questions will be discussed, suggested answers will be forwarded and interpretations will be explored.

Electrical resistivity of crustal rocks may vary from less than 0.1 to more than 100,000 ohm-m, depending on their compositions and states (Fig. 6.1). As in all geophysical methods, in geoelectromagnetic methods it is usual to define "normal" or average values that are generally used to compare with the results of a particular survey. For electromagnetic crustal surveys it useful to define what is considered a normal electrical resistivity crust. Based on compilations by Jones (1981), Shankland and Ander (1983), Haak and Hutton (1986), Hjelt (1988) and Schwarz (1990) it is assumed that the average electrical resistivity of the lower crust ranges from about 100 to about 1000 ohm-m. On the other hand, lower crustal electrical resistivities ranging from 10 to 500 ohm-m are considered as anomalously low (Haak and Hutton, 1986).

Because of the relationship between temperature and the composition and state of rocks, electromagnetic methods, and in particular MT methods, have provided information on the geochemical and petrological structure of the crust and have been frequently used to constrain crust mineralogy (Shankland and Ander, 1983; Gough, 1989; Hyndman and

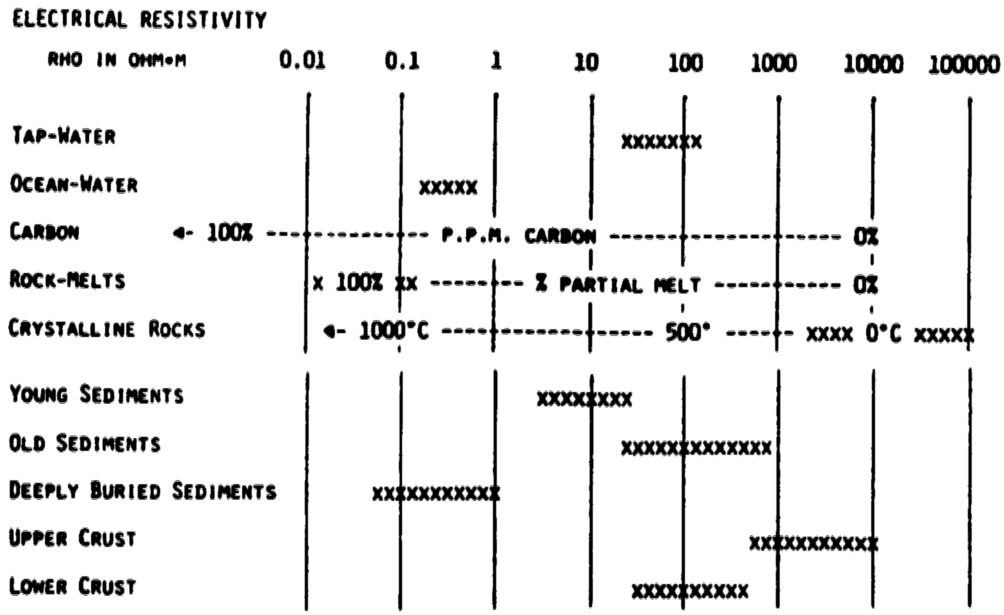

Fig. 6.1: Range of electrical resistivity of some natural and crustal formations (modified from Haak and Hutton (1986)).

Shearer, 1989; Jones, 1992).

6.2. Comparative analysis between the MT survey and other geophysical surveys

As referred to in Chapter I, several geophysical surveys have been carried out in southern Portugal. Figure 1.3 shows the Bouguer anomaly map for an area that includes the region of the present MT survey. Superimposed on that map are the Messejana fault and the Ferreira-Ficalho overthrust. The main feature of the map is the trend of positive anomalies that are located just north or northeast of the Ferreira-Ficalho overthrust. These positive anomalies correlate well with the two high electrical resistivity blocks that may be seen in Figure 3.6 and with the outcrops of the gabbro-diorite complex that are shown in the geologic sketch of Figure 1.2. It is interesting to note, however, that the positive Bouguer anomaly that is just north of the intersection between the Messejana fault and the Ferreira-Ficalho overthrust is not correlated with high electrical resistivity. If it is remembered that the electrical resistivity of a rock depends on its porosity and the salinity of fluids in the pores and/or the state of weathering, and the higher the porosity and the salinity of the fluids the lower the electrical resistivity, one can infer that the Messejana fault locally increases the porosity and permeability of the geological formations and contained saline water decreases their electrical resistivities. Water is also of lower density than the matrix material, and qualitatively, this would explain the smaller Bouguer anomaly observed in the faulted zones. South and southwest of the Ferreira-Ficalho overthrust the character of the Bouguer anomaly map is probably a result of the less complex geology and a more uniform density distribution than north and northeast of it.

It is also interesting to note that at all depths, at least northeast of the Ferreira-Ficalho overthrust, the two high electrical resistivity blocks are separated by a narrow stip zone of low electrical resistivity trending in the same direction as the Messejana fault (see Figures 3.6 and 3.7 and Appendix III). Since other geophysical and geological studies indicate that this fault affects the whole crust, it is suggested here that saline water decreases the electrical resistivity in the region of the fault and deep water flow takes place in the fault zone. The situation may be different southwest of the overthrust because the overthrust separates two distinct crustal blocks with different geological characteristics: the Ossa-Morena and the South-Portuguese zones (Ribeiro et al., 1979). In the latter, the estimated electrical resistivities are generally lower than those of the Ossa-Morena zone and so any contrast in electrical resistivity that exists between the higher porosity formations near the Messejana fault and the surrounding rock formations is not apparent.

Figure 1.4 shows the total field aeromagnetic anomaly map for the region of the MT survey with the Messejana fault and the Ferreira-Ficalho overthrust superimposed on it. Again, the main feature of the map is a correlation between a lineament of positive anomalies and the gabbro-diorite complex just north of the Ferreira-Ficalho overthrust. As in the Bouguer anomaly map, where a different gravimetric character between the Ossa-Morena and the South-Portuguese zones is apparent, different magnetic characters are also obvious for those two zones. In Chapter I it was mentioned that the Messejana fault, contrary to what was expected, does not show any particular magnetic signature. Using magnetization values measured by Schott et al. (1981) in rock samples from the dolerite dyke associated with the fault, Miranda et al. (1989) concluded that the dyke is less than 10 km deep, which is in contradiction with the results of Schermerhorn et al. (1978). This contradiction can, however, be resolved if it is assumed that the Messejana fault constitutes a conduit for water to flow to great depths. This would imply that the actual magnetization of the dolerite dyke has decreased to values of about 1 A/m (Schott et al., 1981) as a result of hydrothermal processes (Reynolds et al., 1990; Hildebrand et al., 1993).

A few seismic refraction surveys have also been performed in southern Portugal. The results of these indicate a deepening of the Moho by about 2-4 km toward the SE, but this cannot be seen in the results of the MT survey because of the Moho's depth and the range of frequencies used by the MT system to measure the natural electric and magnetic signals (128 to 0.031 Hz). However, the MT results do show that the porphyry complex has deeper roots NW of the Messejana fault than to the SE. On the other hand, the MT results do not show any electrical resistivity transition that may be correlated or associated with the low velocity zones between 10 and 20 km depth described by Mueller et al. (1973). Low velocity zones are generally related to "critical" temperature gradients and high porosities in rocks (Christensen, 1979) and, therefore, should appear as low electrical resistivity layers. However, the whole area of the MT study, and in particular the area southwest of the Ferreira-Ficalho overthrust, show values of electrical resistivity that are lower than the assumed normal values, as discussed in Section 6.1. An increase of electrical resistivity values is observed at some MT sites in the South-Portuguese zone at depths deeper than 20 km (see maps of Appendix III), and this may be an indication that the base of the low velocity zone is located there. This could be confirmed by performing a long period MT survey over the region.

The fact that a relationship exists between electrical resistivity and temperature (equation 1.1) was the main motivation for the MT survey over the Alentejo Geothermal Anomaly (AGA). The surprise came, however, when the heat flow density (HFD) map, as published in Haenel and Staroste (1988), was superimposed on the electrical resistivity maps. In Figure 6.2 that superposition can be seen for the

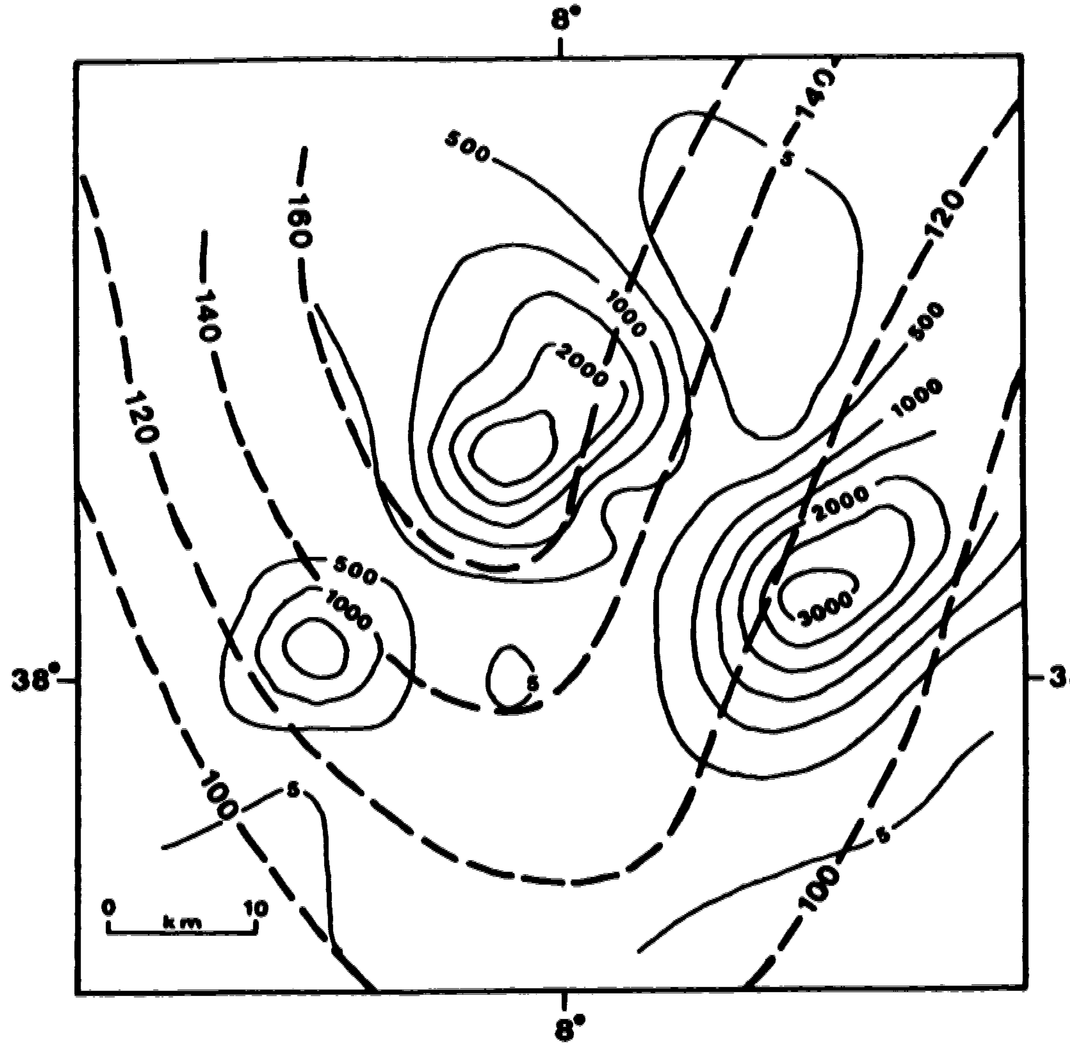

Fig. 6.2: Heat flow density map superimposed on the electrical resistivty map at 500 metres. The heat flow density isolines (dashed lines) are in mW/m² and the electrical resistivity isolines (solid lines) are in ohm-m.

electrical resistivity map at 500 m depth. It is observed that the region of highest HFD coincides with one of the high electrical resistivity blocks delineated by the MT survey. This result was not expected, and two working hypotheses were considered in order to interpret the lack of correlation between the MT results and the HFD data. The first assumed that the HFD values result from high heat production in the rock formations of the region, and the second assumed that hot water was flowing at relatively shallow depths (shallower than 500 m) in the region of the AGA. Of course, there is always the possibility that the HFD values have been overestimated. Concerning the first hypothesis, rock samples from the main geologic formations that outcrop in the area near the AGA were collected and uranium, thorium and potassium contents measured in order to estimate the heat productions per unit volume. The measurements were made by Dr. R. St. J. Lambert in the mass spectrometer laboratory of the University of Alberta. Since porphyı.. generally have high concentrations of radioactive elements, it was thought they would have high heat production values and thus could explain the high HFD values. Table II shows the calculated heat productions per unit volume that were obtained for the various rock types. These calculations were made using the heat production formula given by Rybach (1976). The results indicate fairly normal values with a maximum of 2.88 $\mu W/m^3$ for granitoid rocks. Assuming a heat conduction model for the crust, a

TABLE II

Heat production values (in $\mu W/m^3$) obtained in rock samples collected in the porphyry and gabbro-diorite complexes. The numbers in parentheses are the numbers of rock samples analysed (from Correia et al., 1993).

GABBRO-DIORITE COMPLEX			PORPHYRY COMPLEX
Gabbro (2)	Microdiorite (2)	Diorite (2)	Microgranite (5)
			2.87±0.25
0.27±0.02	0.83±0.14	1.60±0.14	2.70±0.24
			2.88±0.26
0.11±0.02	0.76±0.07	1.53±0.13	2.79±0.25
			2.58±0.23

surface HFD of 160 mW/m² and a heat production of 2.88 μW/m³ from the surface to a depth of 10 km, the reduced HFD (Roy et al., 1968) would be about 131 mW/m², if no other phenomena occur between 10 km depth and the Moho. This value is very high and the author is not aware of any region with such high reduced HFD.

6.3. One-dimensional thermal modelling

Recently Duque (1991) and Duque and Mendes-Victor (1991, 1993) reported new HFD results in the area of the AGA and stated that values in excess of 200 mW/m² exist there. To investigate the consequences of such HFD values, a one-dimensional conductive HFD model is used as a first approximation to estimate the temperature distribution in the crust where the highest HFD values occur. This approach is limited because of geological complexity of the region. However, since the last tectonothermal event occurred much more than 1,000,000 years ago and was probably related to the Hercynian orogeny (Berktold, 1983; Stegena and Meissner, 1985; Cermak and Lastovickova, 1987) it seems worthwhile to explore the one-dimensional (1D) model.

For an isotropic 1D Earth, for steady-state approach, the heat transfer equation is

$$\frac{d}{dz}\left(K\frac{dT}{dz}\right)+A(z)=0 \qquad (6.1)$$

where T is the temperature, z is the depth, A(z) is the heat production per unit volume and K is the thermal conductivity, which may vary with temperature. In this work, however, K will be considered to be constant.

The integration of equation (6.1) depends on the heat production distribution with depth, A(z). Generally only two heat production distributions are considered. The step model (Roy et al., 1968) and the exponential model (Lachenbruch, 1968). In the former, the heat production is assumed constant within the crust throughout a layer of thickness D (as defined below) and integration of equation (6.1) gives:

$$T(z) = T_o + \frac{Q}{K}z - \frac{A_o}{2K}z^2 \qquad (6.2)$$

where T_o is the surface temperature, Q is the HFD at the surface and A_o is the heat production per unit volume, also at the surface. In the latter, the heat production varies as

$$A(z) = A_o e^{-z/D} \qquad (6.3)$$

where D has the dimension of length and characterizes the vertical distribution of heat sources. In this case, integration of equation (6.1) gives

$$T = T_o + \frac{q}{K}z + \frac{A_o D^2}{K}\left(1 - e^{-z/D}\right) \qquad (6.4)$$

where $q = (Q - A_o D)$ is the reduced heat flow and is interpreted as the HFD that exists below those layers in which heat production occurs (Roy et al., 1968). The exponential model is usually considered the more realistic of the two (Lachenbruch and Bunker, 1971; Swanberg, 1972; Ormaasen and Raade, 1978), so it will be used to determine the temperature distribution with depth in the area of the AGA. The following parameters are chosen: since the highest HFD values are on or around the porphyry outcrop and laboratory analysis indicate heat production values of 2.88 $\mu W/m^3$ for that formation, the value of 3.0 $\mu W/m^3$ is assumed to represent the maximum heat production at the surface, A_o; T_o is assumed equal to 15 °C; D is assumed to be 10 km (Cermak and Lastovickova, 1987) and from Haenel and Staroste (1988) q ($q = (Q - A_o D)$) is taken equal to 130 mW/m^2; K is assumed to be 2.6 W/mK (Chapman and Furlong, 1992; Cermak and Lastovickova, 1987). Figure 6.3 shows the calculated geotherm for a surface HFD of 160 mW/m^2. To compare with this geotherm, geotherms characterized by the same parameters as above but for surface HFD values of 200 mW/m^2 (Duque and Mendes-Victor, 1993) and 90 mW/m^2 (Carlos Almeida, 1991, person. commun.) are also shown.

The geotherms of Figure 6.3 show that at a depth of 30 km, which in the study area corresponds to the average depth of the Moho (Mueller et al. 1973; Caetano, 1983; Hirn et al., 1981), the temperatures reach values of 1625 °C, for

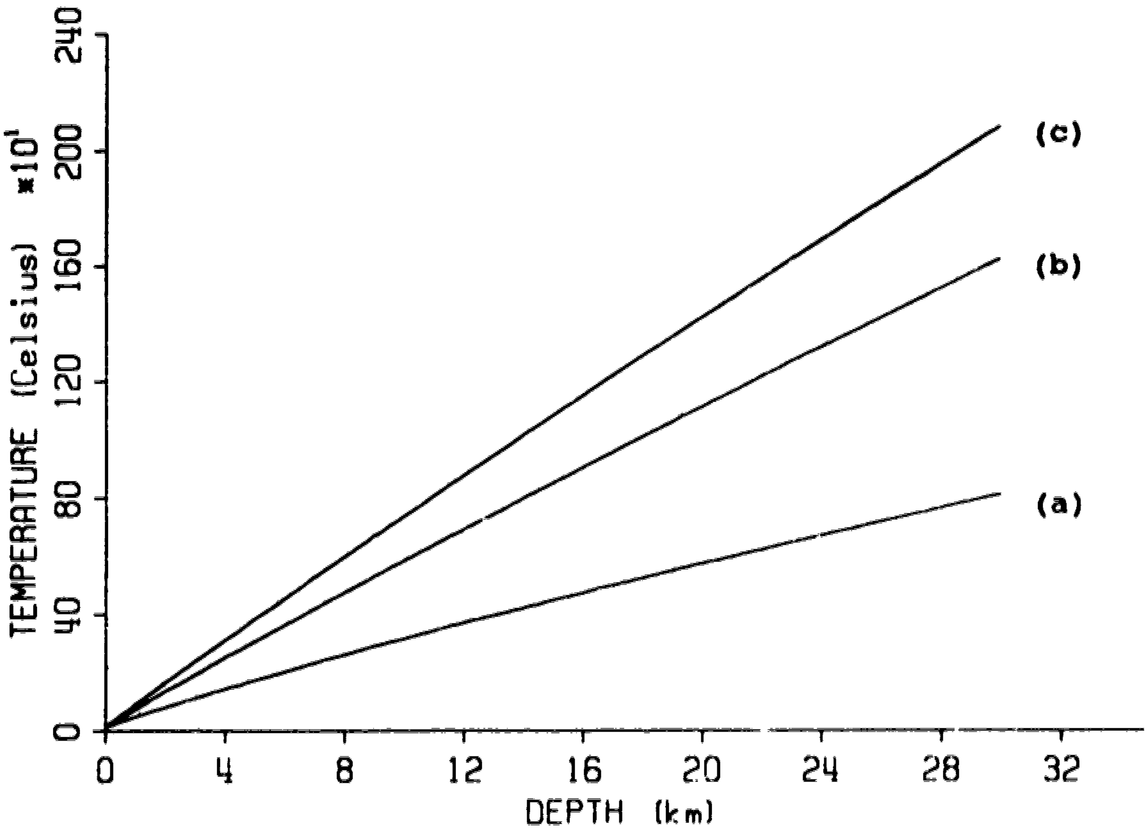

Fig. 6.3: Calculated geotherms for surface HFD values of 90 (a), 160 (b) and 200 (c) mW/m². The values of the parameters used to performed the calculation are described in the text.

the geotherm corresponding to a surface HFD value of 160 mW/m^2, 2086 °C, for the geotherm corresponding to a surface HFD value of 200 mW/m^2 and 817 °C, for the geotherm corresponding to 90 mW/m^2.

In the presence of free water, at depths near the bottom of the crust, intermediate to mafic rocks melt near 700 °C to give a water-saturated melt of electrical resistivity of about 0.1 ohm-m (Wannamaker, 1986; Schwarz, 1990). On the other hand, in high-grade lower crustal rocks, where water is bound in hydrous minerals like amphibole and biotite, melting occurs at temperatures of about 850-900 °C in the absence of carbon dioxide and the melt has an electrical resistivity of about 1 ohm-m (Wannamaker, 1986). However, experimental work by Peterson and Newton (1989) indicates that carbon dioxide bearing lower crustal rocks with pyroxene or hydrous equivalents also melt at about 700 °C. These results, together with the results from the MT survey which show that at depths of about 30 km the electrical resistivity below the area where the HFD values are the highest is about 1000 ohm-m (see the maps in Appendix III), and the results of the seismic refraction surveys which show that the P wave velocity near the base of the crust is near the range expected for mafic non melted rocks, lead to the conclusion that HFD values in excess of 90 to 100 mW/m^2 are probably too high. Higher value than this would lead to partial melt, and the evidence clearly indicates that partial melt is not present in the lower crust below the region of the MT survey.

Furthermore, the existence of a positive Bouguer anomaly in the region of the AGA also suggests that very hot (and, therefore less dense) material is not present in the crust (Palmason, 1976; Werner and Kable, 1980).

Heat flow density studies and geotherms constructed for other Hercynian regions in Europe show that surface HFD values range from 56 to 80 mW/m^2 and the temperatures at Moho depths range from 540 to 740 °C (Cermak, 1982). Stegena and Meissner (1985) calculated that the temperatures at the Moho depth in the Hercynian structures along the European geotraverse are about 390 °C.

6.4. Interpretation and synthesis of the results

One of the main conclusions from the previous section is that the HFD values reported to be 160 mW/m^2 (Haenel and Staroste, 1988) and 230 mW/m^2 (Duque, 1991; Duque and Mendes-Victor, 1993) in the central region of the AGA, should not be used to extrapolate the temperature distribution to middle and lower crustal levels. This does not mean that those HFD anomalously high values are not real; what it means is that they probably result from water flow through faults or fractures in the shallow part of the crust. The MT survey indicates (as was shown in Chapter III) that water may circulate in faults to create zones of low electrical resistivity in an otherwise high electrical resistivity environment. This appears tc be true for the Messejana fault. The existence of water in the Ferreira-Ficalho overthrust does not seem so obvious because it separates two different tectonic regions (the Ossa-Morena and the South-Portuguese zones) that exhibit different geological characteristics (see Figure 1.2). However, water has been reported in thrust zones and faults (e.g., Fyfe et al., 1978; Fyfe, 1986; Fyfe and Kerrich, 1985; McCaig, 1988, 1989; Forster and Evans, 1991), and it is possible that water flowing through the Ferreira-Ficalho overthrust also contributes to the high HFD values of the AGA. On the other hand, calculations of the electrical resistivities of crustal fluids as a function of temperature, pressure and dissolved solids indicate values that range from 0.1 to 1 ohm-m (Nesbitt, 1993), which would explain the low electrical resistivity zones which coincide with the Messejana fault and the Ferreira-Ficalho overthrust.

Figure 6.4 shows the tectonic map of the study area superimposed on a general sketch of the high and low electrical resistivity regions at a depth of 500 m. The 500 and 5 ohm-m isolines are shown and the shaded areas represent low electrical resistivity regions at shallow depths. The low electrical resistivity area to the north includes MT sites 26, 27, 28 and 31. It is located in a region where Precambrian to Silurian undifferentiated rocks outcrop (see Figure 1.2) and is crossed by the Messejana fault and the Vidigueira fault. It may be an extensively

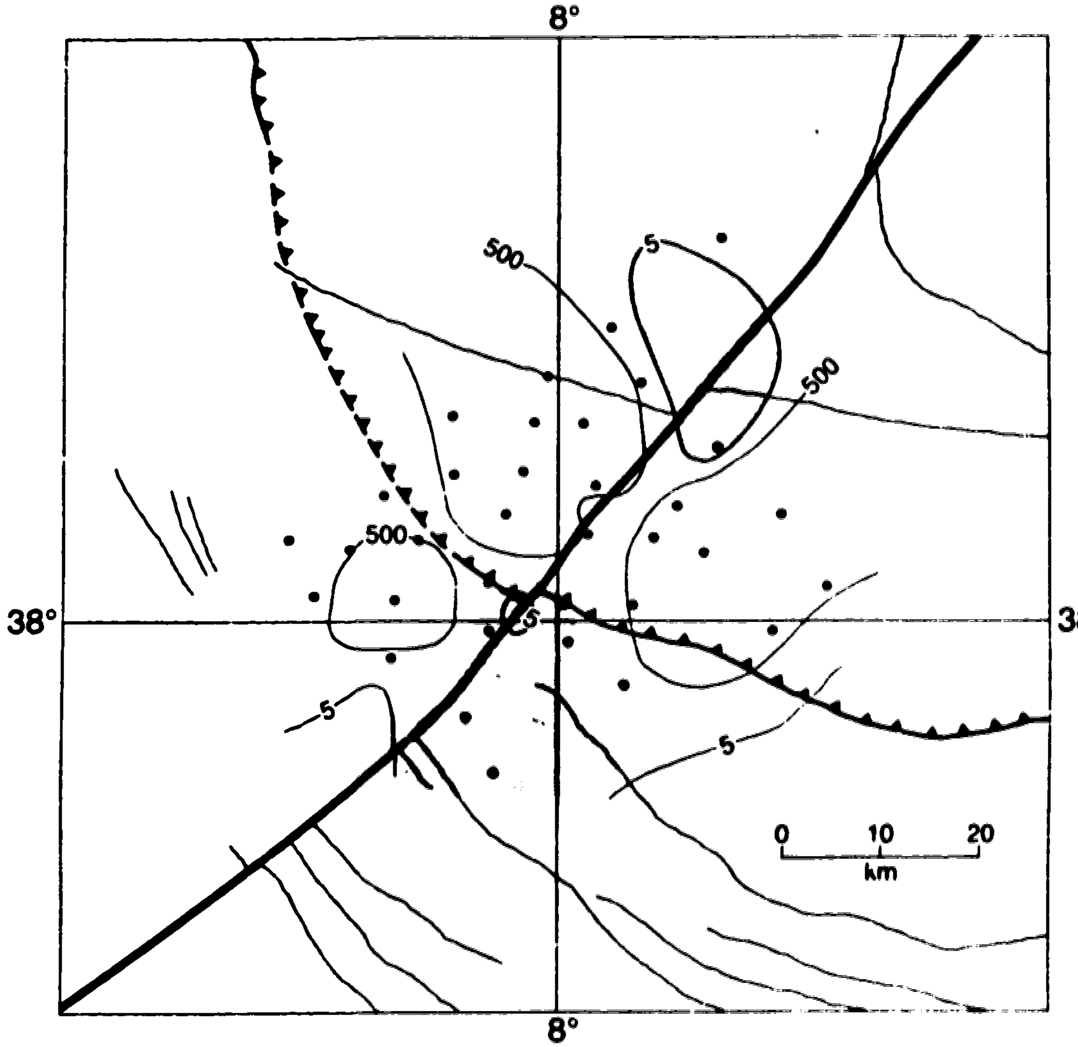

Fig. 6.4: Distribution of low electrical resistivity areas (shaded) in the region of the MT study superimposed on a tectonic map. The MT sites are also shown (dots).

fractured zone that is a result of the Hercynian orogeny and contacts among different rock formations. The most probable interpretation appears to be that water again plays an important role in lowering the electrical resistivity here to values less than 10 ohm-m at shallow depths. In Figure 1.1 the HFD isolines do not close in the northern region, possibly because of the lack of data. This low electrical resistivity area may correspond to the central area of the AGA and as such coincides with a discharge area at relatively shallow depths. The only difficulty with this interpretation is that in the study area and in the surrounding regions there are no hydrothermal manifestations (Hydrogeological Map of Southern Portugal, 1989, Geological Survey of Portugal), which should be expected with such high HFD values.

Water does not seem to explain all the features that can be observed in Figure 6.4. The low electrical resistivities in the southern region, which includes MT sites 2, 4, 33, and 34 correspond to undifferentiated Devonian and Carboniferous rocks (see Figure 1.2), mainly slates and schists. This is a region where economic ore deposits have been found and where formation porosities and permeabilities are low (Ribeiro et al., 1979; Hydrogeological Map of Southern Portugal, 1989, Geological Survey of Portugal) and the weathered zone is shallow (ten to a few hundred metres thick). Therefore, it is possible that the low electrical resistivities measured in there are due to the presence of sulphides or other metallic ores (Olhoeft, 1981; Schwarz, 1990; Jones, 1992). The acceptance of this interpretation depends, however, on the way they are distributed in the crust. In southern Portugal they frequently occur as veins and this means that large aereal low electrical resistivity regions are difficult to explain in terms of conducting mineralized zones.

A preferred explanation is, however, related to the kind of rock formations and lithologies found south of the Ferreira-Ficalho overthrust, i.e., shales, slates and schists (Oliveira et al., 1983; Geologic Map of Portugal, scales 1:1,000,000 and 1:200,000, Geological Survey of Portugal). Crustal rocks contain small amounts of carbon as anthracitic or graphitic material (Schwarz, 1990; Jodicke, 1992), which may greatly decrease their electrical resistivities. Furthermore, carbonaceous matter of microscopic size, found particularly in black shales, seems to have great importance in producing electrical conductivity anomalies. The finely disseminated organic carbon in most pelitic rocks, when exposed to low grade metamorphism, reaches a high coalifi ation stage which may lower the electrical resistivity to values of a few omh-m or even lower than 0.1 ohm-m (Stanley et al., 1987; Stanley, 1989; Jodicke, 1992). Duba et al. (1988) performed laboratory studies on Carboniferous rock samples abundant in black shales from a 5425 m deep well in Germany, and concluded that the measured low electrical resistivities were the result of a thin carbon film on the grain boundaries. Because of chemical stability reasons, this conductive process by organic carbon appears to take place only in the upper crust. Recently, however, Frost et al. (1989) documented the existence of grain-boundary graphite in lower crustal rocks, which could explain low electrical resistivity layers detected in the lower crust.

6.5. Conclusions

Since the region where the MT survey was carried out appears to be a low electrical resistivity region with a number of deep rooted high electrical resistivity blocks, and MT methods do not penetrate very deep in low electrical resistivity formations (because of the skin-depth effect - Chapter II), it is not possible to give a full picture of the lower crustal structure in this work, but a number of important conclusions can be reached.

In geoelectric terms, the Ossa-Morena and South-Portuguese zones are clearly distinct, the former being more resistive than the latter. The Messejana fault separates two very different geoelectrical domains, at least southwest of the Ferreira-Ficalho overthrust, and appears to be a deep feature, which penetrates the whole crust. The evidence suggests that the Messejana fault and the Ferreira-Ficalho overthrust contain saline fluids which create zones of low electrical resistivity. The AGA appears to result from upward water flow along the Messejana fault, the Ferreira-

Ficalho overthrust and possibly the Vidigueira fault. These are conduits for the water to flow and if so, then it is possible that the central part of the AGA is actually located about 20 km NE of the position shown in Figure 1.1, i.e., in the central region of the northern low electrical resistivity area shown in Figure 6.4. However, the thermal data are insufficient to prove or disprove this suggestion.

The results of Chapter III also show that the MT method can be an important tool to delineate and distinguish between different kinds of faults and therefore it may be useful in structural geology studies.

One-dimensional thermal modelling, in conjunction with MT and seismic refraction data, indicates that the high HFD values estimated in the central region of the AGA should not be used to calculate the temperature distribution in the crust or to generate thermal models of it. The high HFD values may be overestimated because of the water flow suggested above and, in this case, the AGA would be a local geothermal anomaly and would not represent the thermal state of the crust in the region.

The quality of the long period MT survey (Chapter III) is poor, and therefore its results should be used carefully. For periods of 500 s the directions of the induction arrows are scattered. However, for 5000 s the upper mantle is probably being detected and the arrows show a common direction parallel or approximately parallel to the Messejana fault. Induction arrows point to regions of high electrical conductivity, and they appear to be pointing into the Gorringe bank (located in offshore Portugal, SW of the study area), where it has recently been suggested that the nucleation of a subduction zone propagating towards the north exists (Ribeiro et al., 1988).

Finally, the electrical resistivity pattern in the region southwest of the Ferreira-Ficalho overthrust appears to be controlled by the existence of organic carbon contained in the rock types that outcrop there.

One of the important uses of 3D electromagnetic modelling is to establish the validity of 1D and 2D models to interpret natural environments. For the Portuguese data the results of Chapter IV show that the use of 1D inversion models and the Berdichevsky invariant were good approximations from which to construct 2D and 3D electromagnetic models. It is also apparent from Chapter IV that MT profiling may be inappropriate to infer electrical resistivity in areas with 3D character. The 2D profiles considered here gave no indication of the high electrical resistivity blocks that are located in the central region of the study area, only a few kilometres away.

6.6. Suggestions for future work

Some of the questions that were asked in Section 6.1 have been answered; others have not. It appears, though, that southern Portugal is an interesting region to be studied in geoelectrical terms and, therefore, the continuation of the initial MT survey reported in this work should be pursued by: (1) carrying out more measurements of the magnetotelluric field in areas adjacent to that already surveyed; (2) measuring the vertical component of the magnetic field at the MT sites of the present study, so that induction arrows can be calculated; (3) measuring the regional magnetotelluric field at longer periods to provide better electrical information about the lower crust and upper mantle.

Improvement of the software packages for two-dimensional and three-dimensional modelling should also be carried out. In particular, higher resolution 3D models than that used here are needed if a quantitative analysis of the study area is to be achieved.

Field as well as numerical approaches to the static shift effect should also be continued, aiming at a better understanding of the problem and possible ways to compensate for it.

A better understanding of the geological structure of southern Portugal would be achieved if, in conjunction with more MT measurements, more HFD measurements and a few seismic reflection surveys were performed. This could provide more information about such questions as: are the low electrical resistivity zones in the South-Portuguese zone a result of saline fluids, graphite or mineralization, and are the low velocity zones a result of enhanced porosity or slightly higher temperature in the middle crust?

REFERENCES

Airy, G.B., 1868, Comparison of magnetic disturbances recorded by the self-registering magnetometers at the Royal Observatory, Greenwich with magnetic disturbances deduced from the corresponding terres trial galvanic currents recorded by the self-registering galvanometer in the Royal Observatory, Philosophical Transactions of the Royal Society, 158, 465.

Bahr, K., 1988, Interpretation of the magnetotelluric impedance tensor: regional induction and local telluric distortion, Journal of Geophysics, 62, 119-127.

Bailey, R.C., 1977, Electromagnetic induction over the edge of a perfectly conducting ocean: the H-polarization case, Geophysical Journal of the Royal Astronomical Society, 48, 385-392.

Banda, E., 1988, Crustal parameters in the Iberian Peninsula, Physics of the Earth and Planetary Interiors, 51, 222-225.

Beamish, D., 1986, Geoelectric structural dimensions from magnetotelluric data: methods of estimation, old and new, Geophysics, 51, 1,298-1,309.

Beamish, D., 1990, A deep geoelectric survey of the Carnmenellis granite, Geophysical Journal International, 102, 679-693.

Bentley, C.R., 1973, Error estimation in two-dimensional magnetotelluric analyses, Physics of the Earth and Planetary Interiors, 7, 423-430.

Berdichevsky, M.N. and Dmitriev, V.I., 1976a, Basic principles of interpretation of magneto-telluric sounding curves, in: Geoelectrical and Geothermal Studies, KAPG Geophysical Monograph, Adam, A.(ed.), Academia Kiado, Budapest, Hungary, 164-221.

Berdichevsky, M.N. and Dmitriev, V.I., 1976b, Distortions of magnetic and electric fields by near-surface lateral inhomogeneities, Acta Geodaetica Geophysica et Montanistica, 11, 447-483.

Berdichevsky, M.N., Vanyan, L.L., and Dmitriev, V.I., 1989, Methods used in the U.S.S.R. to reduce near-surface inhomogeneity effects on deep magnetotelluric sounding, Physics of the Earth and Planetary Interiors, 53, 194-206.

Berdichevsky, M.N., Vanyan, L.L., Kuznetsov, V.A., Levadny, V.T., Mandelbaum, M.M., Nechaeva, G.P., Okulessky,B.A, Shilosky, P.P., and Shpak, I.P., 1980, Geoelectrical model of the Baikal region, Physics of the Earth and Planetary Interiors, 22, 1-11.

Berktold, A., 1983, Electromagnetic studies in geothermal regions, Geophysical Surveys, 6, 173-200.

Bostick, F.X., 1986, Electromagnetic array profiling (EMAP), 56th Annual Meeting, Society of Exploration Geophysicists, Expanded Abstract, 60-61.

Brewitt-Taylor, C.R. and Weaver, J.T., 1976, On the finite difference solution of two-dimensional induction problems, Geophysical Journal of the Royal Astronomical Society, 47, 375-396.

Cadavid, S., 1977, Avance del mapa de isopacas de una "corteza normal" para la Peninsula Iberica y principales accidentes de posible alcance cortical, Boletim Geologico e Minero, 88, 93-98.

Caetano, H., 1983, Structure crustale de la zone Sud-Portugaise et de la zone Ossa-Morena d'après les études de sismologie experimentale, Thèse 3e. cycle, University of Paris VI, Paris.

Cagniard, L., 1953, Basic theory of the magnetotelluric method of geophysical prospecting, Geophysics, 18, 605-635.

Cantwell, W.H., 1960, Detection and analysis, of low frequency magnetotelluric signals, Unpublished Ph.D. thesis, MIT.

Cermak, V., 1982, Crustal temperature and mantle heat flow in Europe, Tectonophysics, 83, 123-142.

Cermak, V. and Lastovickova, M., 1987, Temperature profiles in the Earth of importance to deep electrical conductivity models, Pure and Applied Geophysics, 125, 255-284.

Chapman, D.S. and Furlong, K.P., 1992, Thermal state of the continental crust, in: Continental Lower Crust, Fountain, D.M, Arculus, R.J. and Kay, R.W. (eds.), Elsevier Scientific Publishing Company, 179-199.

Christensen, N.I., 1979, Compressional wave velocities in rocks at high temperatures and pressures, critical thermal gradients, and crustal low-velocity zones, Journal of Geophysical Research, 84, 6849-6857.

Clarke, J., Gamble, T.D., Goubau, W.M., Koch, R.H., and Miracky, R.F., 1983, Remote-reference magnetotellurics: equipment and procedures, Geophysical Prospecting, 31, 149-170.

Coggon, J.H., 1971, Electromagnetic and electrical modelling by the finite element method, Geophysics, 36, 132-155.

Collett, L.S. and Katsube, T.J., 1973, Electrical parameters of rocks in developing geophysical techniques, Geophysics, 38, 76-91.

Connerney, J.E.P., Nekut, A., and Kuckes, A.F., 1980, Deep crustal conductivity in the Adirondacks, Journal of Geophysical Research, 85, 2,603-2,614.

Correia, A., 1991, Concentrações em potássio, urânio e tório, e produção de calor em oito amostras rochosas colhidas em Portugal continental (submitted for publication in GEOCIÊNCIAS) (in Portuguese).

Correia, A. and Jones, F.W., 1993, A magnetotelluric survey in southern Portugal, (expanded abstract accepted for publication in: Anais do 3º Congresso Internacional da Sociedade Brasileira de Geofísica).

Correia, A., Jones, F.W., Dawes, G.K., and Hutton, V.R.S., 1991, Estudo magneto-telúrico de uma anomalia geotérmica em Portugal (expanded abstract accepted for publication in: Anais do 2º Congresso Internacional da Sociedade Brasileira de Geofísica)(in Portuguese).

Correia, A., Jones, F.W., Dawes, G., and Hutton, V.R.S., 1993, A magnetotelluric deep crustal study in south-central Portugal (accepted for publication in: Studia Geophysica et Geodaetica).

Correia, A., Duque, R., Maciel, C., Camelo, S., Almeida, C., and Victor, L., 1982, Primeiras determinações do fluxo de calor em Portugal, Boletim Informativo do INMG, 56, 3-13.

Das, U.C. and Verma, S.K., 1982, Electromagnetic response of an arbitrary shaped three-dimensional conductor in a layered Earth - numerical results, Geophysical Journal of the Royal Astronomical Society, 69, 55-66.

Dawes, G.J.K., 1980, Computer Program Library, Internal publication of the Department of Geophysics, University of Edinburgh.

Dawes, G.J.K., 1990, Short Period Automatic Magnetotelluric System (SPAM) Mk IIb, User's Manual, 38 pp.

Dawes, G.J.K. and Lagios, E., 1991, A magnetotelluric survey of the Nissyros geothermal field (Greece), Geothermics, 20, 225-235.

Dawson, T.W. and Weaver, J.T., 1979, Three-dimensional induction in a non-uniform thin sheet at the surface of a uniformly conducting Earth, Geophysical Journal of the Royal Astronomical Society, 59, 445-462.

d'Erceville, I. and Kunetz, G., 1962, The effect of a fault on the Earth's natural electromagnetic field, Geophysics, 27, 651-665.

Dobrin, M.B. and Savit, C.H, 1988, Introduction to Geophysical Prospecting, Fourth Edition, McGraw-Hill Book Company, 867 pp.

Dosso, H.W., 1966, Analogue model measurements for electromagnetic variations near vertical faults and dykes, Canadian Journal of Earth Sciences, 3, 287-303.

Dosso, H.W., 1973, A review of analogue model studies of the coast effect, Physics of the Earth and Planetary Interiors, 7, 294-302.

Dosso, H.W., Nienaber, W., and Hutton, V.R.S., 1980, An analogue model study of electromagnetic induction in the British Isles region, Physics of the Earth and Planetary Interiors, 22, 68-85.

Duba, A., 1976, Are laboratory electrical conductivity data relevant to the Earth?, Acta Geodaetica Geophysica et Montanistica, 11, 485-495.

Duba, A., Huenges, E., Nover, G., Will, G. and Jodicke, H., 1988, Impedance of black shale from Munsterland 1 borehole: an anomalous good conductor?, Geophysical Journal, 94, 413-419.

Duque, R., 1984, Modelos térmicos da crusta terrestre e do manto superior, Unpublished M.Sc. thesis, University of Evora (in Portuguese).

Duque, R., 1991, Contribuição do fluxo de calor para a caracterização da litosfera na região do Alentejo, Unpublished Ph.D. thesis, University of Évora (in Portuguese).

Duque, R. and Mendes-Victor, L., 1988, Novas determinações do fluxo de calor e temperatura em profundidade no sul de Portugal, National Physics Conference FISICA 88 (book of abstracts), Aveiro, Portugal (in Portuguese).

Duque, R. and Mendes-Victor, L., 1991, Heat flow and thermal field in south Portugal, International Workshop on Heat Flow and the Structure of the Lithosphere (book of abstracts), Bechyne, Czechoslovakia.

Duque, R. and Mendes-Victor, L., 1993, Heat flow and deep temperature in South Portugal, Studia Geophysica et Geodaetica, 37, 279-292.

Everett, J.E. and Hyndman, R.D., 1976, Geomagnetic variations and electrical conductivity structure in southwestern Australia, Physics of the Earth and Planetary Interiors, 1, 24-34.

Fischer, G., Schnegg, P.A., and Usadel, K.D., 1978, Electromagnetic response of an ocean-coast model to E-polarization induction, Geophysical Journal of the Royal Astronomical Society, 53, 599-616.

Forster, C.B. and Evans, J.P., 1991, Hydrogeology of thrust faults and crystalline thrust sheets: results of combined field and modeling studies, Geophysical Research Letters, 18, 979-982.

Frost, B.R., Fyfe, W.S., Tazaki, K. and Chan T., 1989, Grain-boundary graphite in rocks and implications for high electrical conductivity in the lower crust, Nature, 340, 134-136.

Fyfe, W.S., 1986, Fluids in deep continental crust, in: Reflection Seismology: The Continental Crust, Barazangi, M and Brown, L. (eds.), American Geophysical Union Geodynamics Series, 14, 33-39.

Fyfe, W.S. and Kerrich, R., 1985, Fluids and thrusting, Chemical Geology, 49, 353-362.

Fyfe, W.S., Price, N.J. and Thompson, A.B., 1978, Fluids in the Earth's Crust, Developments in Geochemistry, Elsevier Scientific Publishing Company, 383 pp.

Gamble, T.D., Goubau, W.M., and Clarke, J., 1979a, Magnetotellurics with a remote reference, Geophysics, 44, 53-68.

Gamble, T.D., Goubau, W.M., and Clarke, J., 1979b, Error analysis for remote reference magnetotellurics, Geophysics, 44, 959-968.

Goubau, W.M., Gamble, T.D., and Clarke, J., 1978, Magnetotelluric data analysis: removal of bias, Geophysics, 43, 1,157-1,166.

Gough, D.I., 1986, Seismic reflectors, conductivity, water and stress in the continental crust, Nature, 323, 143-144.

Gough, D.I., 1989, Magnetometer array studies, Earth structure and tectonic processes, Reviews of Geophysics, 27, 141-157.

Gregori, G.P. and Lanzerotti, L.J., 1980, Geomagnetic depth sounding by induction arrow representation, Reviews of Geophysics and Space Physics, 18, 203-210.

Groom, R.W. and Bailey, R.C., 1989, Decomposition of magnetotelluric impedance tensors in the presence of local three-dimensional galvanic distortion, Journal of Geophysical Research, 94, 1913-1925.

Haak, V. and Hutton, R., 1986, Electrical resistivity in the continental lower crust, in: The Nature of the Lower Continental Crust, Dawson, J.B., Carswell, D.A., Hall, J., and Wedepohl, K.H. (eds.), Geological Society Special Publication no. 24, 35-49.

Haenel, R. and Staroste, E., 1988, Atlas of the Geothermal Resources in the European Community, Austria and Switzerland, Commission of the European Communnities, Verlag Th. Schaefer, Hannover, 74 pp, 110 plates.

Hermance, J.F., 1973, Processing of magnetotelluric data, Physics of the Earth and Planetary Interiors, 7, 349-364.

Hildenbrand, T.G., Rosenbaum, J.G. and Kauahikaua, J.P., 1993, Aeromagnetic study of the Island of Hawaii, Journal of Geophysical Research, 98, 4099-4119.

Hirn, A., Senos, L., and Caetano, H., 1981, Variações da profundidade da Moho na regiâo da Grande Falha do Alentejo, Unpublished report of the National Institute of Meteorology and Geophysics of Portugal, 19 pp (in Portuguese).

Hjelt, S.E., 1988, Regional EM studies in the 80's, Surveys in Geophysics, 9, 349-387.

Hobbs, B.A., 1975, Analytical solutions to global and local problems of electromagnetic induction in the Earth, Physics of The Earth and Planetary Interiors, 10, 250-261.

Hohmann, G.W., 1971, Electromagnetic scattering by conductors in the Earth near a line source of current, Geophysics, 36, 101-131.

Hohmann, G.W., 1988, Numerical modelling for electromagnetic methods of Geophysics, in: Electromagnetic Methods in Applied Geophysics, Volume 1, Theory, Nabighian, M.N. (ed.), Investigations in Geophysics no. 3, SEG, Tulsa, Oklahoma.

Hyndman, R.D. and Shearer, P.M., 1989, Water in the lower continental crust: modelling magnetotelluric and seismic reflection results, Geophysical Journal International, 98, 343-365.

Ingham, M.R., 1988, The use of invariant impedances in magnetotelluric interpretation, Geophysical Journal, 92, 165-169.

Jacobs, J.A., 1970, Physics and Chemistry in Space, Vol. 1, Springer-Verlag, Berlin, 179 pp.

Jacobs, J.A., Kato, Y., Matsushita, S., and Troitskaya, V.A., 1964, Classification of geopmagnetic pulsations, Journal of Geophysical Research, 69, 180-181.

Jiracek, G.R., 1990, Near-surface and topographic distortions in electromagnetic induction, Surveys in Geophysics, 11, 163-203.

Jodicke, H., 1990, Interpretation of conductivity models, Review paper, 10th Workshop on Electromagnetic Induction in the Earth, Ensenada, Mexico.

Jodicke, H., 1992, Water and graphite in the Earth's crust - An approach to interpretation of conductivity models, Surveys in Geophysics, 381-407.

Jones, A.G., 1977, Geomagnetic induction studies in southern Scotland, Unpublished Ph.D thesis, University of Edinburgh.

Jones, A.G., 1981, On the type classification of lower crustal layers under Precambrian regions, Journal of Geophysics, 49, 226-233.

Jones, A.G., 1988, Static shift of magnetotelluric data and its removal in a sedimentary basin environment, Geophysics, 53, 967-978.

Jones, A.G., 1992, Electrical conductivity of the continental crust, in: Continental Lower Crust, Fountain, D.M, Arculus, R.J. and Kay, R.W. (eds.), Elsevier Scientific Publishing Company, 81-143.

Jones, A.G. and Hutton, R., 1979, A multi-station magnetotelluric study in southern Scotland - II. Monte-Carlo inversion of the data and its geophysical and tectonic implications, Geophysical Journal of the Royal Astronomical Society, 56, 351-368.

Jones, F.W., 1973, Induction in laterally non-uniform conductors: theory and numerical models, Physics of the Earth and Planetary Interiors, 7, 282-293.

Jones, F.W., 1974, The perturbation of slowly varying electromagnetic fields by three-dimensional conducting bodies, Canadian Journal of Physics, 52, 13, 1195-1202.

Jones, F.W. and Pascoe, L.J., 1971, A general computer programme to determine the perturbation of alternating electric currents in a two-dimensional model of a region of uniform conductivity with an embedded inhomogeneity, Geophysical Journal of the Royal Astronomical Society, 24, 3-30.

Jones, F.W. and Pascoe, L.J., 1972, The perturbation of alternating geomagnetic fields by three-dimensional conductivity inhomogeneities, Geophysical Journal of the Royal Astronomical Society, 27, 479-485.

Jones, F.W. and Price, A.T., 1970, The perturbation of alternating geomagnetic fields by conductivity anomalies, Geophysical Journal of the Royal Astronomical Society, 20, 317-334.

Jones, F.W. and Price, A.T., 1971, The Geomagnetic effects of two-dimensional conductivity inhomogeneities at different depths, Geophysical Journal of the Royal Astronomical Society, 22, 333-345.

Jones, F.W. and Thomson, D.J., 1974, A discussion of the finite difference method in computer modelling of electrical conductivity structures, Geophysical Journal of the Royal Astronomical Society, 37, 537-543.

Jones, F.W. and Vozoff, K., 1978, The calculation of magnetotelluric quantities for three-dimensional inhomogeneities, Geophysics, 43, 1,167-1,175.

Jones, F.W., Correia, A., Dawes, G.K., Hutton, V.R.S., Jones, P., and MacDonald, K., 1992, Preliminary results of a magneto-telluric survey over a geothermal anomaly in Portugal, Physics of the Earth and Planetary Interiors, 73, 274-281.

Julivert, M. and Martinez, F.J., 1987, The structure and evolution of the Hercynian fold belt in the Iberian Peninsula, in: The Anatomy of Mountain Belts, Schaer, J.P. and Rodgers, J. (eds.), Princeton University Press, 65-103.

Julivert, M., Martinez, F.J., and Ribeiro, A., 1980, The Iberian segment of the European Hercynian foldbelt, in: Géologie de l'Europe, Cogné, J. et Slansky, M. (eds.), Mémoire du B.R.G.M. no. 108, 132-158.

Kaufman, A.A. and Keller, G.V., 1981, The Magnetotelluric Sounding Method, Elsevier Scientific Publishing Company, 595 pp.

Keller, G.V., 1987, Rock and mineral properties, in: Electromagnetic Methods in Applied Geophysics - Theory, Volume 1, Nabighian, M.N. and [illegible] J.D. (eds.), Investigations in Geophysics [illegible] Society of Exploration Geophysicists, 13 [illegible].

Keller, G.V. and Frischknecht [illegible] Electrical Methods in Geophysical Pr[illegible] Pergamon Press Ltd., New York, 519 pp.

Ku, C.C., Hsieh, M.S., and Lim, [illegible], The topographic effect in electromagnetic fields, Canadian Journal of Earth Sciences, 10, 645-656.

Kurtz, R.D., 1982, Magnetotelluric interpretation of crustal and mantle structure in the Grenville Province, Geophysical Journal of the Royal Astronomical Society, 70, 373-397.

Kurtz, R.D., DeLaurier, J.M., and Gupta, J.C, 1986, A magnetotelluric sounding across Vancouver Island detects the subducting Juan de Fuca Plate, Nature, 321, 596-599.

Kurtz, R.D., DeLaurier, J.M., and Gupta, J.C, 1990, The electrical conductivity distribution beneath Vancouver Island: a region of active plate subduction, Journal of Geophysical Research, 95, 10,929-10,946.

Lachenbruch, A.H., 1968, Preliminary geothermal model of the Sierra Nevada, Journal of Geophysical Research, 73, 6977-6989.

Lachenbruch, A.H. and Bunker, C.M., 1971, Vertical gradients of heat production in the continental crust - 2. Some estimates from borehole data, Journal of Geophysical Research, 76, 3852-3860.

Lee, C.D., Vine, F.J., and Ross, R.G., 1983, Electrical conductivity models for continental crust based on laboratory measurements on high grade metamorphic rocks, Geophysical Journal of the Royal Astronomical Society, 72, 353-372.

Lee, K.H., Pridmore, D.F., and Morrison, H.F., 1981, A hybrid three-dimensional electromagnetic modelling scheme, Geophysics, 46, 796-805.

Lemos de Sousa, M.J. and Oliveira, J.T.(eds.), 1983, The Carboniferous In Portugal, Memórias dos Serviços Geológicos de Portugal no.29, Lisboa, Portugal.

Lines, L.R., 1972, A numerical study of the perturbation of alternating geomagnetic fields near island and coastline structures, Unpublished M.Sc. thesis, The University of Alberta.

Lines, L.R. and Jones, F.W., 1973a, The perturbation of alternating geomagnetic fields by three-dimensional island structures, Geophysical Journal of the Royal Astronomical Society, 32, 133-154.

Lines, L.R. and Jones, F.W., 1973b, The perturbation of alternating geomagnetic fields by an island near a coastline, Canadian Journal of Earth Sciences, 10, 510-518.

MacDonald, K.J., 1991, An LMT study in the Alentejo Region in Portugal, unpublished fourth year memoir, Department of Geology and Geophysics, University of Edinburgh, 51 pp.

Madden, T. and Nelson, P., 1964, A defence of Cagniard's magnetotelluric method, in: Magnetotelluric Methods, Vozoff K. (ed.), Geophysics Reprint Series no. 5, SEG, 89-102.

Madden, T.R. and Swift, C.M., 1969, Magnetotelluric studies of the electrical conductivity structure of the crust and upper mantle, in:: The Earth's Crust and Upper Mantle, Hart, P.J. (ed.), American Geophysical Union, Geophysical Monograph no. 13, 469-479.

Madden, T. and Thompson, W., 1965, Low frequency electromagnetic oscillations of the Earth-ionosphere cavity, Reviews of Geophysics, 3, 211-254.

Martinez-Garcia, M., 1990, Electromagnetic induction in geothermal fields and volcanic belts, Review paper, 10th Workshop on Electromagnetic Induction in the Earth, Ensenada, Mexico.

Matsushita, S. and Campbell, W.H. (eds.), 1967, Geophysics and Geomagnetic Phenomena, Academic Press, New York.

McCaig, A.M., 1988, Deep fluid circulation in fault zones, Geology, 16, 867-870.

McCaig, A.M., 1989, Fluid flow through fault zones, Nature, 340, 600.

Mendes-Victor, L.A., Camelo, S.M., and Duque, R.M., 1986, Fluxo de calor em Portugal - Alentejo, National Physics Conference (book of abstracts), Braga, Portugal.

Mendes-Victor, L.A., Simões, J.Z., and Matias, L.M., 1988, The program of deep seismic sounding in Portuguese mainland, in: Fifth EGT Workshop: the Iberian Peninsula, Banda, E. and Mendes-Victor, L.A. (eds.), European Science Foundation, 13-21.

Miranda, J.M., Galdeano, A., Rossignol, J.C., and Mendes-Victor, L.A., 1988, The aeromagnetic survey of Portugal (1980.0) and some tectonic implications, in: Proceedings of the Fifth EGT Workshop - The Iberian Peninsula, Banda, E. and Mendes-Victor, L.A. (eds.), 123-130.

Miranda, J.M., Galdeano, A., Rossignol, J.C., and Mendes-Victor, L.A., 1989, Aeromagnetic anomalies in mainland Portugal and their tectonic implications, Earth and Planetary Science Letters, 95, 161-172.

Miranda, J.M. and Mendes-Victor, L.A., 1991, Carta aeromagnética de Portugal, Escala 1/1,000,000, Nota Explicativa, Serviççs Geológicos de Portugal, Lisboa, 14 pp.

Morse, F.M. and Feshbach, H., 1964, Methods of Theoretical Physics, McGraw-Hill Book Company,Inc., New York, 1978 pp.

Mueller, St. and Ansorge, J., 1989, The crustal structure of western Europe, in: Annual Review of Earth and Planetary Sciences, Wetherwill, G.W., Albee, A.L., and Stehli, F.G. (eds.), Volume 17, 335-360.

Mueller, S., Prodehl, C., Mendes, A.S., and Sousa Moreira, V., 1973, Crustal structure in the southwestern part of the Iberian Peninsula, Tectonophysics, 20, 307-318.

Munhá, J., 1981, Igneous and metamorphic petrology of the Iberian Pyrite Belt volcanic rocks, Unpublished Ph.D. thesis, The University of Western Ontario.

Nabighian, M.N., 1987, Electromagnetic Methods in Applied Geophysics, Volume 1, Theory, Investigations in Geophysics no. 3, SEG, Tulsa, Oklahoma.

Nesbitt, B.E., 1993, Electrical resistivities of crustal fluids, Journal of Geophysical Research, 98, 4301-4310.

Neves, A., 1957, The generalized magneto-telluric method, Unpublished Ph.D. thesis, MIT.

Newman, G.A, Hohmann, G.W., and Anderson, W.L., 1986, Transient electromagnetic response of a three-dimensional body in layered earths, Geophysics, 51, 1608-1627.

Nienaber, W., Dosso, H.W., and Hutton, V.R.S., 1981, Electromagnetic induction in the British Isles region: analogue model and field station results, Physics of the Earth and Planetary Interiors, 27, 122-132.

Olhoeft, G.R., 1980, Electrical properties of rocks, in: Physical Properties of Rocks and Minerals, Thoulaikian, Y.S., Judd, W.R., and Roy, R.F. (eds), McGraw-Hill Book Co., 257-330.

Olhoeft, G.R., 1981, Electrical properties of granite with implications for the lower crust, Journal of Geophysical Research, 86, 931-936.

Oliveira, J.T., 1983, The marine Carboniferous of south Portugal: a stratigraphic and sedimentological approach, in: The Carboniferous of Portugal, Lemos de Sousa, M.J. and Oliveira, J.T., Memorias dos Servicos Geologicos de Portugal, 29, 3-37.

Oliveira, J.T. (coordinator), 1984, Carta Geológica de Portugal, Escala 1/200,000 Notícia Explicativa da Folha 7, Serviços Geológicos de Portugal, Lisboa, Portugal.

Orange, A.S., 1989, Magnetotelluric exploration for hydrocarbons. Proceedings of the IEEE, 77, 287-317.

Ormaasen, D.E. and Raade, G., 1978, Heat generation versus depth of crystallization for Norwegian monzonitic rocks, Earth and Planetary Science Letters, 39, 145-150.

Palmason, G., 1976, Geophysical methods in geothermal exploration, Proceedings of the 2nd U.N. Symposium on the Development and Use of Geothermal Resources, 1175-1184.

Park, S.K., 1985, Distortion of magnetotelluric sounding curves by three-dimensional structures, Geophysics, 50, 795-797.

Park, S.K. and Livelybrooks, D.W., 1989, Quantitative interpretation of rotationally invariant parameters in magnetotellurics, Geophysics, 54, 1,483-1,490.

Park, S.K., Orange, A.S., and Madden, T.R., 1983, Effects of three-dimensional structure on magnetotelluric sounding curves, Geophysics, 48, 1,402-1,405.

Parkinson, W.D., 1962, The influence of continents and oceans on geomagnetic variations, Geophysical Journal of the Royal Astronomical Society, 6, 441-449.

Parkinson, W.D., 1983, Introduction to Geomagnetism, Scottish Academic Press, Edinburgh, Scotland.

Parkhomenko, E.I., 1982, Electrical resistivity of minerals and rocks at high temperature and pressure, Review of Geophysics and Space Physics, 29, 193-218.

Pascoe, L.J. and Jones, F.W., 1972, Boundary conditions and calculations of surface values for the general two-dimensional electromagnetic induction problem, Geophysical Journal of the Royal Astronomical Society, 27, 179-193.

Patra, H.P. and Mallick, K., 1980, Geosounding Principles, 2; Time-Varying Geoelectric Soundings, Elsevier Scientific Publishing Company, 419 pp.

Patrick, F.W. and Bostick, F.X., 1969, Magnetotelluric modelling techniques, Elec. Geophys. Res. Lab., University of Texas, Technical Report no. 59.

Peterson, J.W. and Newton, R.C., 1989, Carbon dioxide-enhanced melting of biotite-bearing rocks at deep-crustal pressure-temperature conditions, Nature, 340, 378-380.

Price, A.T., 1962, The theory of magnetotelluric methods when the source field is considered, Journal of Geophysical Research, 67, 1,907-1,918.

Pridmore, D.F., Hohmann, G.W., Ward, S.H., and Sill, W.R., 1981, Investigation of finite element modelling for electrical and electromagnetic data in three dimensions, Geophysics, 46, 1,009-1,024.

Raiche, A.P., 1974, An integral equation approach to three-dimensional modelling, Geophysical Journal of the Royal Astronomical Society, 36, 363-376.

Ranganayaki, R.P., 1984, An interpretative analysis of magnetotelluric data, Geophysics, 49, 1,730-1,748.

Ranganayaki, R.P. and Madden, T.R., 1980, Generalized thin sheet analysis in magnetotellurics: an extension of Price's analysis, Geophysical Journal of the Royal Astronomical Society, 60, 445-457.

Rankin, D., 1962, The magnetotelluric effect of a dyke, Geophysics, 27, 666-676.

Rankin, D, Garland, G.D., and Vozoff, K., 1965, An analogue model for the magnetotelluric effect, Journal of Geophysical Research, 70, 1,939-1,945.

Reddy, I.K. and Rankin, D., 1973, Magnetotelluric response of a two-dimensional sloping contact by the finite element method, Pure and Applied Geophysics, 105, 847-857.

Reddy, I.K., Rankin, D., and Phillips, R.J., 1977, Three-dimensional modelling in magnetotelluric and magnetic variation sounding, Geophysical Journal of the Royal Astronomical Society, 51, 313-325.

Reynolds, R.L., Rosenbaum, J.R., Hudson, M.R. and Fishman, N.S., 1990, Rock magnetism, the distribution of magnetic minerals in the Earth's crust, and aeromagnetic anomalies, in: Geologic Applications of Modern Aeromagnetic Surveys, U.S. Geological Survey Bulletin, 1924, 24-45.

Ribeiro, A., Antunes, M.T., Ferreira, M.P., Rocha, R.B., Soares, A. F., Zbyszewski, G., Moitinho de Almeida, F., de Carvalho, D., and Monteiro, J.H., 1979, Introduction à la Géologie Générale du Portugal, Serviços Geológicos de Portugal, Lisboa, Portugal.

Ribeiro, A., Kullberg, M.C., Cabral, J., Madeira, J., Brum, A.P. and Moniz, C., 1988, Alpine geodynamics of the west - Iberia margin, in: Fifth EGT Workshop: the Iberian Peninsula, Banda, E. and Mendes-Victor, L.A. (eds.), European Science Foundation, 91-98.

Rokityansky, I.I., 1982, Geoelectromagnetic investigation of the Earth's crust and mantle, Springer-Verlag, Berlin, 381 pp.

Roy, R.F., Blackwell, D.D. and Birch, F., 1968, Heat generation of plutonic rocks and continental heat flow provinces, Earth and Planetary Science Letters, 5, 1-12.

Rybach, L., 1976, Radioactive heat production in rocks and its relation to other petrophysical parameters, Pure and Applied Geophysics, 114, 309-318.

Schermerhorn, L.J.G., Priem, H.N.A., Boelrijk, N.A.I.M., Hebeda, E.H., Verdumen, E.A.Th., and Verschure, R.H., 1978, Age and origin of the Messejana dolerite fault-dyke system (Portugal and Spain) in the light of the opening of the North Atlantic Ocean, Journal of Geology, 86, 299-309.

Schott, J., Montigny, R. and Thuizat, R., 1981, Paleomagnetism and potassium argon age of the Messejana dyke (Portugal and Spain): angular limitation to the rotation of the Iberian Peninsula since the middle Jurassic, Earth and Planetary Science Letters, 53, 457-467.

Schwarz, G., 1990, Electrical conductivity of the Earth's crust and upper mantle, Surveys in Geophysics, 11, 133-161.

Schwarz, G., Haak, V., and Rath, V., 1985, Electrical conductivity studies in the Travale geothermal field, Italy, Geothermics, 14, 653-661.

Shankland, T.J., 1975, Electrical conduction in rocks and minerals: parameters for interpretation, Physics of the Earth and Planetary Interiors, 10, 209-219.

Shankland, T.J. and Waff, H.S., 1974, Conductivity in fluid-bearing rocks, Journal of Geophysical Research, 79, 4863-4868.

Shankland, T.J. and Ander, M.C., 1983, Electrical conductivity, temperatures and fluids in the lower crust, Journal of Geophysical Research, 88, 9475-9484.

Silvester, P. and Haslam, C.R.S., 1972, Magnetotelluric modelling by the finite element method, Geophysical Prospecting, 20, 872-891.

Sims, W.E., Bostick, F.X., and Smith, H.J.W., 1971, The estimation of magnetotelluric impedance tensor elements from measured data, Geophysics, 36, 938-942.

Smith, G.D., 1969, Numerical Solution of Partial Differential Equations, Oxford University Press.

Sousa Moreira, V., Mueller, St., Mendes, A.S., and Prodehl, C., 1977, The deep structure of southern Portugal, Publication of the Institute of Geophysics of the Polish Academy of Sciences, A-4(115), 35-41.

Srivastava, S.P., 1965, Method of interpretation of magnetotelluric data when the source field is considered, Journal of Geophysical Research, 70, 945-954.

Stanley, W.D., 1989, Comparison of geoelectrical/tectonic models for suture zones in the western U.S.A. and eastern Europe: are black shales a possible source of high conductivities?, Physics of the Earth and Planetary Interiors, 53, 228-238.

Stanley, W.D., Finn, C. and Plesha, J.L., 1987, Tectonics and conductivity structures in the southern Washington Cascades, Journal of Geophysical Research, 92, 10179-10193.

Stanley, W.D., Mooney, W.D., and Fuis, G.S., 1990, Deep crustal structure of the Cascade Range and surrounding regions from seismic refraction and magnetotelluric data, Journal of Geophysical Research, 95, 19,419-19,438.

Stegena, L. and Meissner, R., 1985, Velocity structure and geothermics of the Earth's crust along the European geotraverse, Tectonophysics, 121, 87-96.

Sternberg, B.K., Washburne, J.C. and Pellerin, L., 1988, Correction for the static shift in magnetotellurics using transient electromagnetic soundings, Geophysics, 53, 1459-1468.

Sternberg, B.K., Buller, P.L., Kisabeth, J.L. and Mehreteab, E., 1984, Electrical methods for hydrocarbon exploration II. Magnetotelluric (MT) method, in: Proceedings from the SMU Symposium III "Unconventional Methods in Exploration for Petroleum and Natural Gas", 202-230.

Stratton, J.A., 1941, Electromagnetic Theory, McGraw-Hill Book Company, Inc., New York, 615 pp.

Sule, P.O. and Hutton, V.R.S., 1986, A broadband magnetotelluric study in southeastern Scotland - data acquisition, analysis and 1-D modelling, Annales Geophysicae, 4, 145-155.

Swanberg, C.A., 1972, Vertical distribution of heat generation in the Idaho batholith, Journal of Geophysical Research, 77, 2508-2513.

Swift, C.M., Jr., 1967, A magnetotelluric investigation of an electric conductivity anomaly in southwestern United States, Unpublished Ph.D. thesis, MIT.

Swift, C.M., Jr., 1971, Theoretical magnetotelluric and Turam responses from two-dimensional inhomogeneities, Geophysics, 36, 38-52.

Tikhonov, A.N., 1950, On determining electrical characteristics of the deep layers of the Earth's crust, in: Magnetotelluric Methods, Vozoff K. (ed.), Geophysics Reprint Series no. 5, SEG, 2-3.

Ting, S.C. and Hohmann, G.W., 1981, Integral equation modelling of three-dimensional magnetotelluric response, Geophysics, 46, 182-197.

Torres, L. and Lisboa, M., 1988, Standardization of gravity and magnetic data of part of Iberia including offshore area, in: Proceedings of the Fifth EGT Workshop - The Iberian Peninsula, Banda, E. and Mendes-Victor, L.A. (eds.), 111-121.

Vozoff, K., 1972, The magnetotelluric method in the exploration of sedimentary basins, Geophysics, 37, 98-141.

Vozoff, K. (ed.), 1986, Magnetotelluric methods, Geophysics Reprint Series no. 5, Society of Exploration Geophysicists, Tulsa, Oklahoma.

Vozoff, K., 1991, The magnetotelluric method, in: Electromagnetic Methods in Applied Geophysics, Volume 2, Applications, Part B, Nabighian, M.N. (ed.), Investigations in Geophysics no. 3, SEG, Tulsa, Oklahoma.

Wait, J.R., 1954, On the relationship between telluric currents and the Earth's magnetic field, Geophysics, 19, 281-289.

Wait, J.R., 1962, Theory of magneto-telluric fields, Journal of Research, National Bureau of Standards-D, Radio propagation, 66D, 509-541.

Wannamaker, P.E., 1986, Electrical conductivity of water-undersaturated crustal melting, Journal of Geophysical Research, 91, 6321-6327.

Wannamaker, P.E. and Hohmann, G.W., 1991, Electromagnetic induction studies, Reviews of Geophysics, Supplement, 405-415.

Wannamaker, P.E., Ward, S.H. and Hohmann, G.W., 1982, Magnetotelluric responses of three-dimensional bodies in layered earths, Rep. DOE/ID 12079-87, Res. Inst., Earth Sci. Lab., University of Utah, Salt Lake City.

Wannamaker, P.E., Hohmann, G.W., and San Filipo, W.A., 1984a, Electromagnetic modelling of three-dimensional bodies in layered earths using integral equations, Geophysics, 49, 60-74.

Wannamaker, P.E., Hohmann, G.W., and Ward, S.H., 1984b, Magnetotelluric responses of three-dimensional bodies in layered earths, Geophysics, 49, 1517-1533.

Wannamaker, P.E., Stodt, J.A. and Rijo, L., 1986, Two-dimensional topographic responses in magnetotellurics modeled using finite elements, Geophysics, 51, 2131-2144.

Ward, S.H. and Hohmann, G.W., 1987, Electromagnetic theory for geophysical applications 1987, in: Electromagnetic Methods in Applied Geophysics, Volume 1, Theory, Nabighian, M.N. (ed.), Investigation in Geophysics no. 3, SEG, Tulsa, Oklahoma.

Weaver, J.T., 1963, The electromagnetic field within a discontinuous conductor with reference to geomagnetic micropulsations near a coastline, Canadian Journal of Physics, 41, 484-495.

Weaver, J.T. and Brewitt-Taylor, C.R., 1978, Improved boundary conditions for the numerical solution of E-polarization problems in geomagnetic induction, Geophysical Journal of the Royal Astronomical Society, 54, 309-317.

Weidelt, P., 1975, Electromagnetic induction in three-dimensional structures, Journal of Geophysics, 41, 85-109.

Werner, D. and Kahle, H.-G., 1980, A geophysical study of the Rhinegraben - I, Geophysical Journal of the Royal Astronomical Society, 62, 617-630.

Whittall, K.P. and Oldenburg, D.W., 1992, Inversion of Magnetotelluric Data for a One-Dimensional Conductivity, Geophysical Monograph Series no. 5, Society of Exploration Geophysicists, Tulsa, 114 pp.

Williamson, K., Hewllet, C., and Tammemagi, H.Y., 1974, Computer modelling of electrical conductivity structures, Geophysical Journal of the Royal Astronomical Society, 37, 533-536.

Word, D.R., Smith, H.W., and Bostick, F.X., 1971, Crustal investigations by the magnetotelluric tensor impedance method, in: The Structure of Physical Properties of the Earth's Crust, Heacock, J.G. (ed.), American Geophysical Union, Geophysical Monograph no. 14, 397-416.

APPENDIX I

FIELD DATA RESULTS FOR THE 34 MT SITES

For each site the f llowing quantities are shown:

First page: apparent electrical in the north-south direction (RHO XY), phase in the north-south direction (PHASE XY), apparent electrical resistivity in the east-west direction (RHO YX), phase in the east-west direction (PHASE YX), COHERENCY, NUMBER OF ESTIMATES and SKEW.

Second page: apparent electrical resistivity and phase along the strike direction (MAJOR), and perpendicular to the strike direction (MINOR), COHERENCY, NUMBER OF ESTIMATES, SKEW, AZIMUTH and apparent electrical resistivity and phase invariant (INVARIANT).

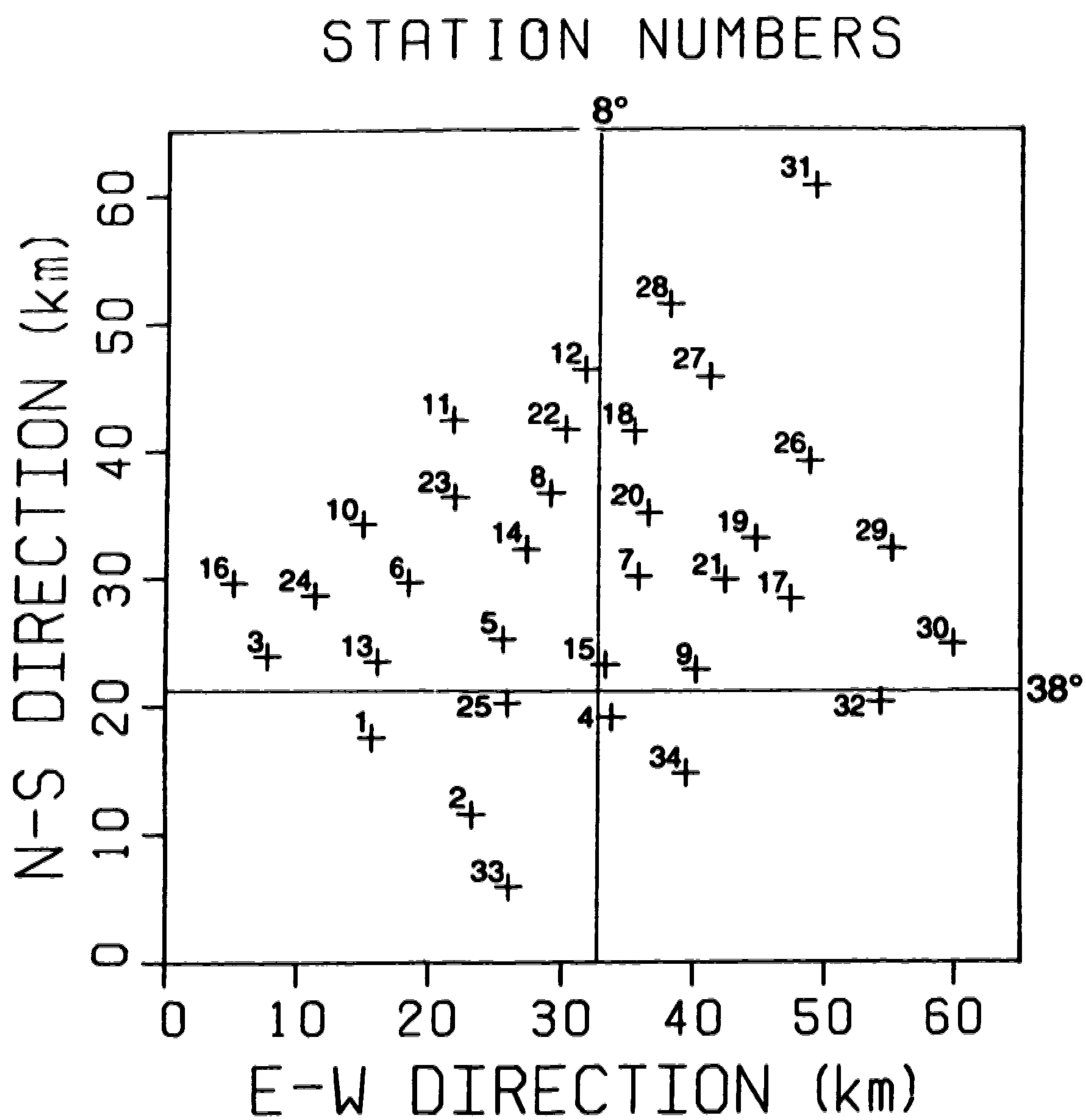
STATION NUMBERS
8°
38°
N-S DIRECTION (km)
E-W DIRECTION (km)
0
10
20
30
40
50
60
1
2
3
4
5
6
7
8
9
10
11
12
13
14
15
16
17
18
19
20
21
22
23
24
25
26
27
28
29
30
31
32
33
34

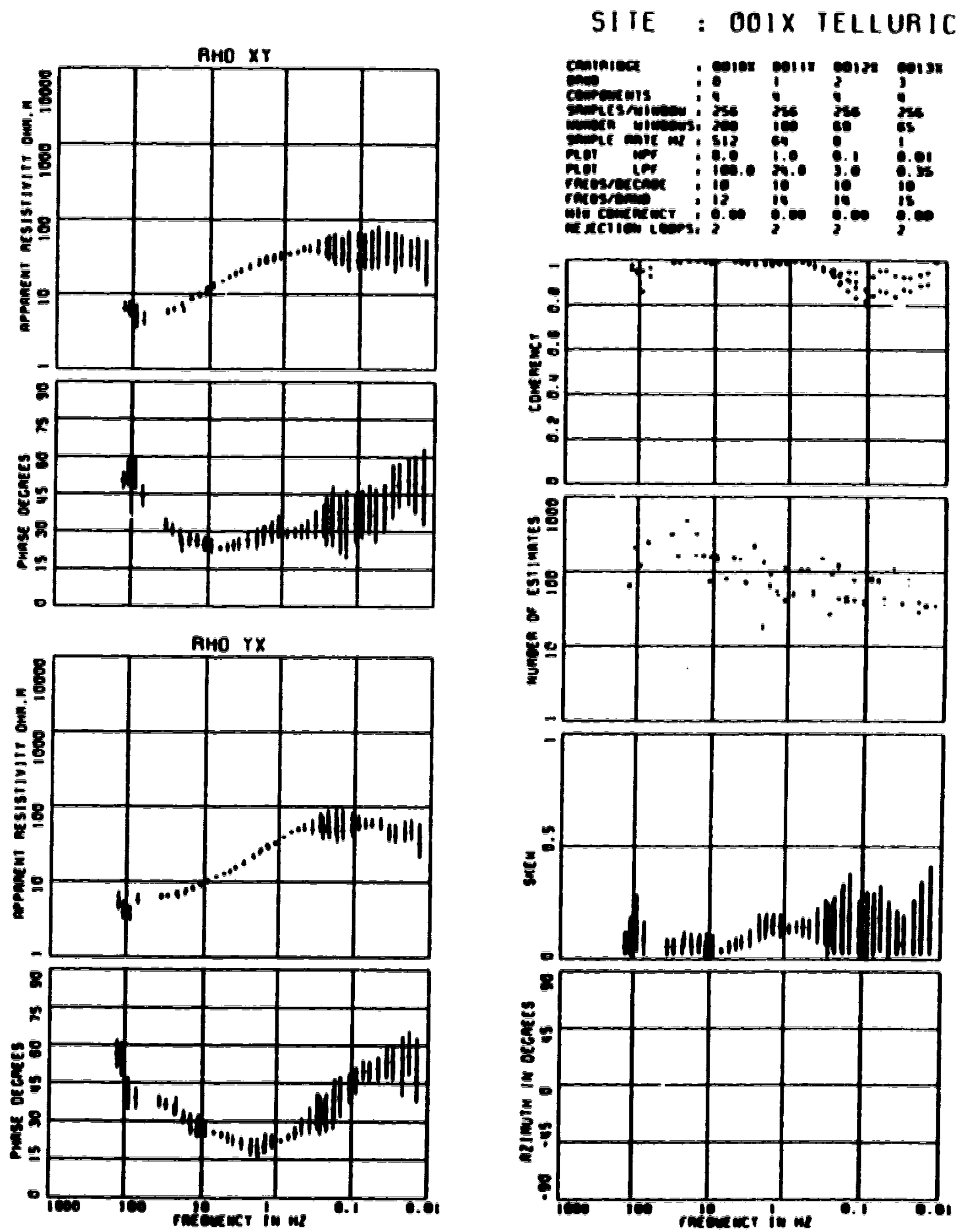
SITE : 001X TELLURIC
RHO XY
APPARENT RESISTIVITY OHM.M
PHASE DEGREES
RHO YX
APPARENT RESISTIVITY OHM.M
PHASE DEGREES
FREQUENCY IN HZ
COHERENCY
NUMBER OF ESTIMATES
SKEW
AZIMUTH IN DEGREES
FREQUENCY IN HZ

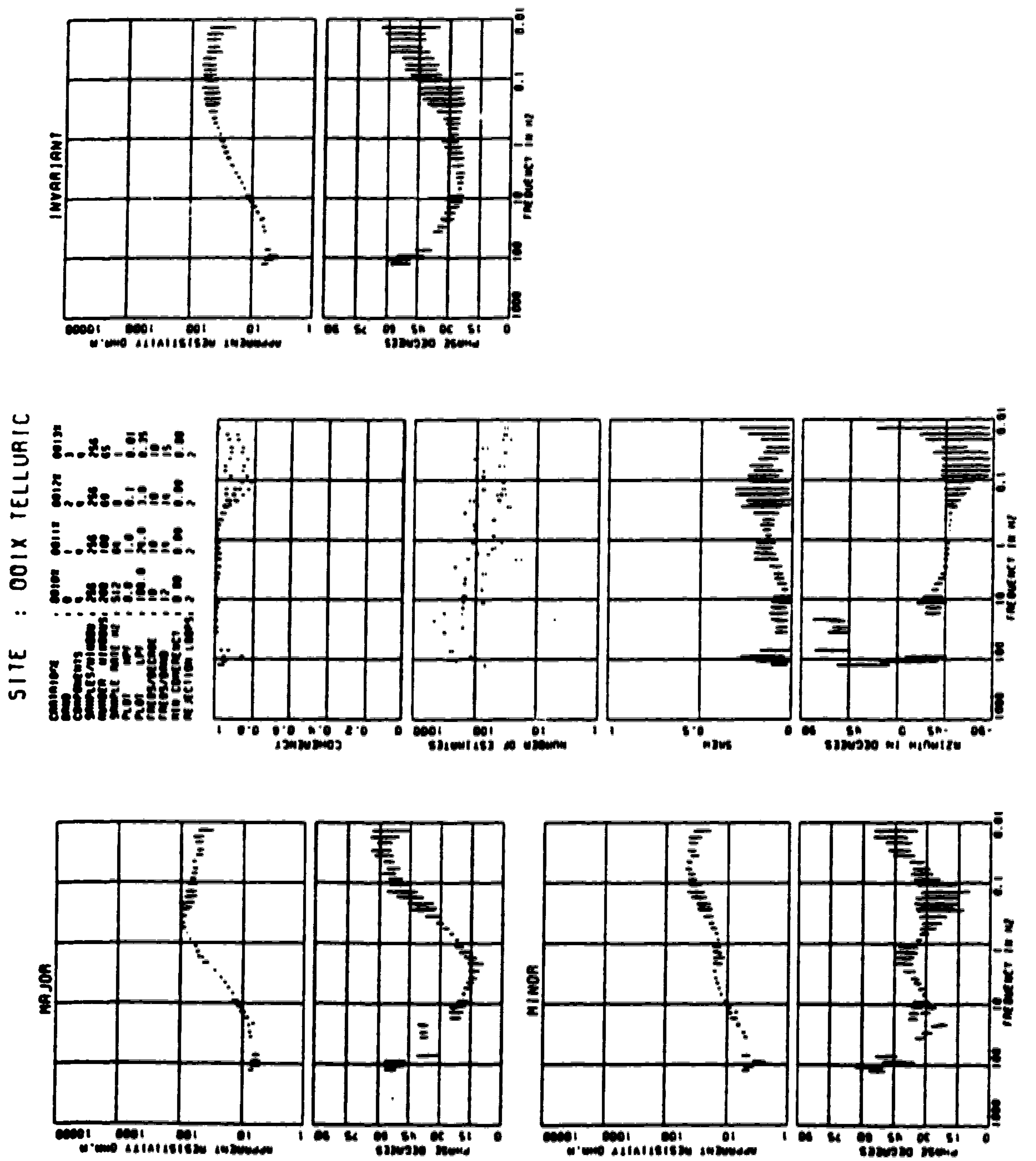
INVARIANT
SITE : OOIX TELLURIC
MAJOR
MINOR

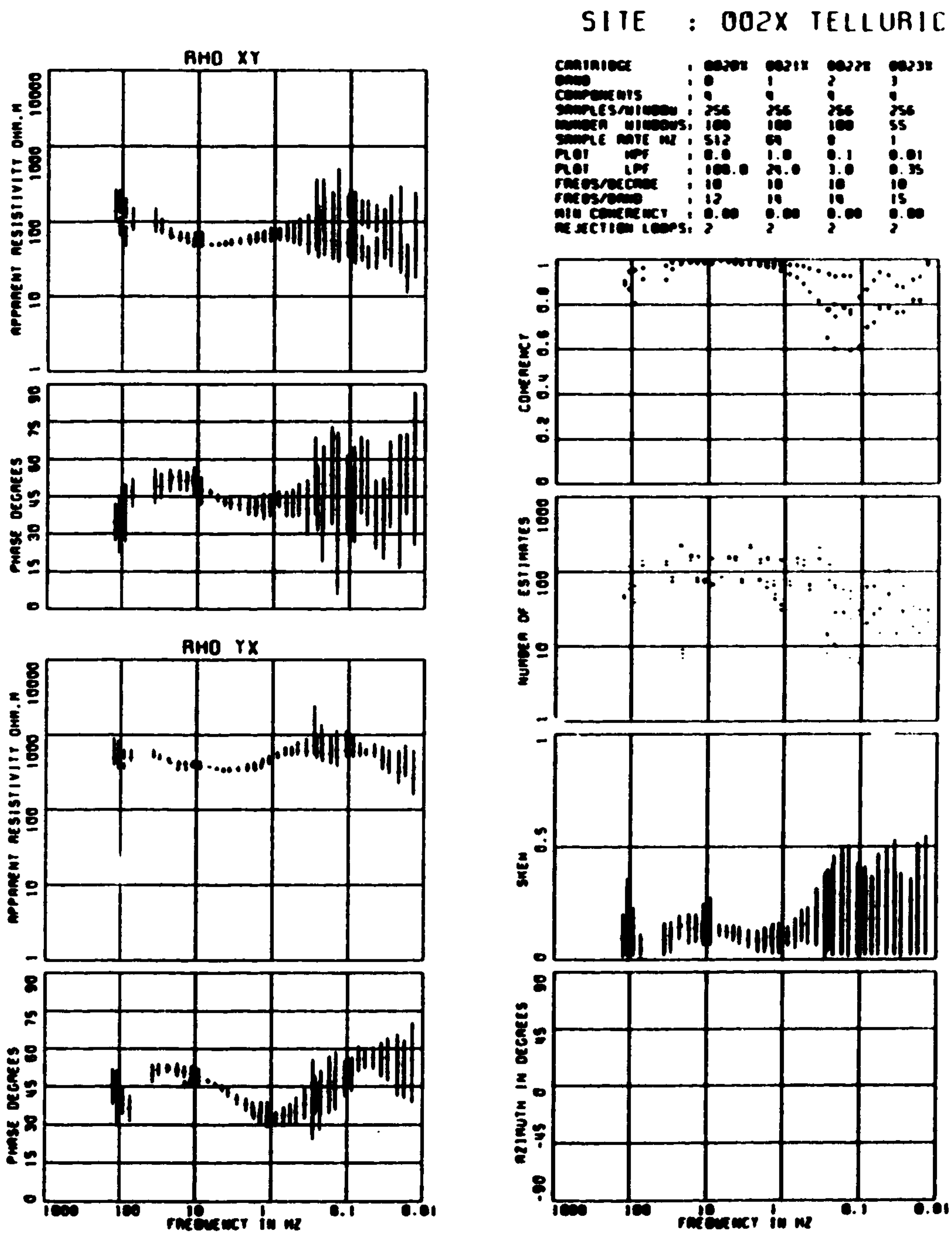

SITE : 002X TELLURIC
CARTRIDGE : 0020X 0021X 0022X 0023X
BAND : 0 1 2 3
COMPONENTS : 4 4 4 4
SAMPLES/WINDOW : 256 256 256 256
NUMBER WINDOWS: 100 100 100 55
SAMPLE RATE HZ : 512 64 8 1
PLOT HPF : 8.0 1.0 0.1 0.01
PLOT LPF : 100.0 24.0 3.0 0.35
FREQS/DECADE : 10 10 10 10
FREQS/BAND : 12 14 14 15
MIN COHERENCY : 0.00 0.00 0.00 0.00
REJECTION LOOPS: 2 2 2 2
RHO XY
APPARENT RESISTIVITY OHM.M
PHASE DEGREES
RHO YX
APPARENT RESISTIVITY OHM.M
PHASE DEGREES
FREQUENCY IN HZ
COHERENCY
NUMBER OF ESTIMATES
SKEW
AZIMUTH IN DEGREES
FREQUENCY IN HZ

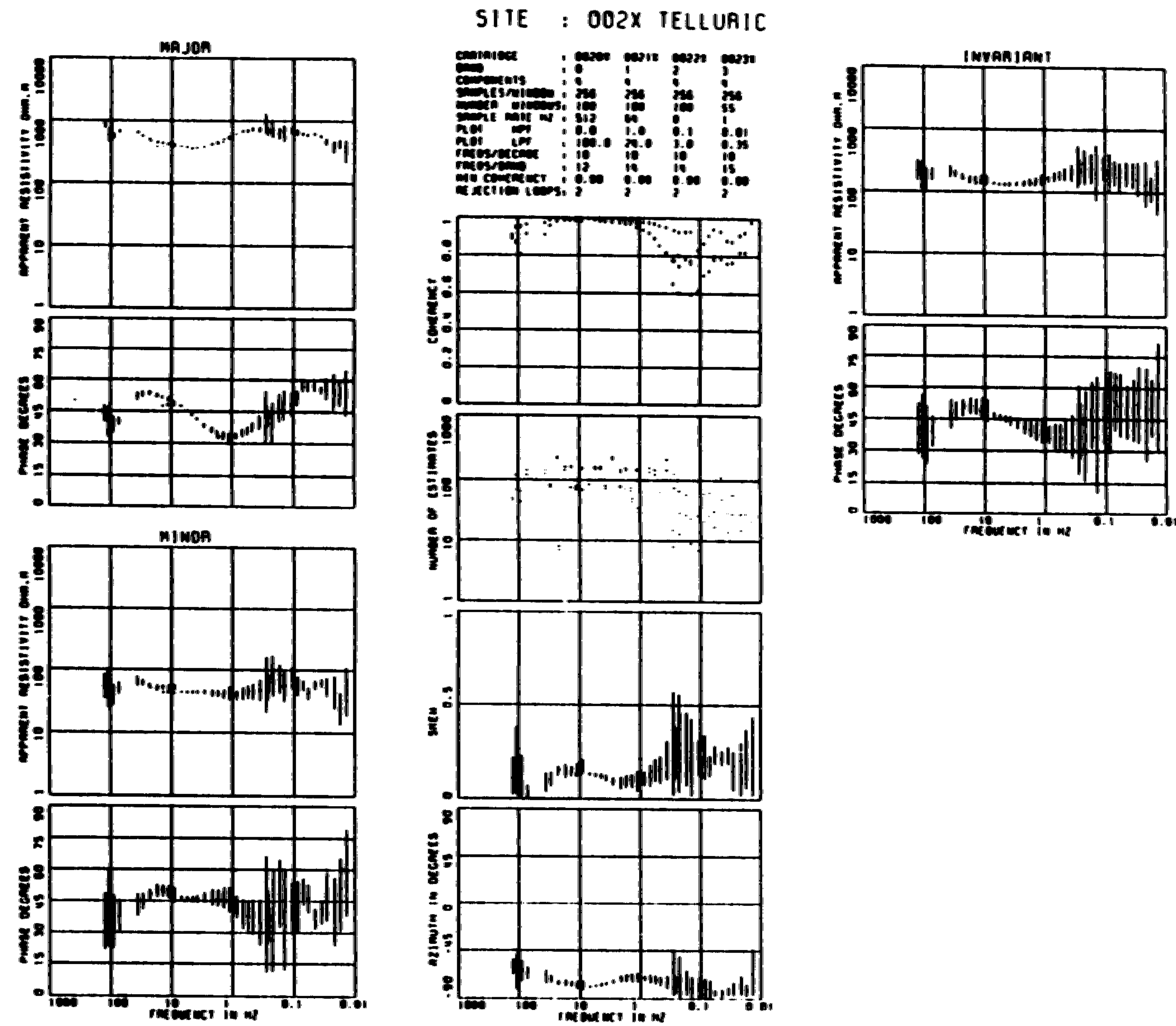
SITE : 002X TELLURIC
MAJOR
MINOR
INVARIANT
APPARENT RESISTIVITY OHM.M
PHASE DEGREES
COHERENCY
NUMBER OF ESTIMATES
SKEW
AZIMUTH IN DEGREES
FREQUENCY IN HZ

SITE : OC3X TELLURIC

CARTRIDGE	: 0030X	0031X	0032X	0033X
BAND	: 0	1	2	3
COMPONENTS	: 4	4	4	4
SAMPLES/WINDOW	: 256	256	256	256
NUMBER WINDOWS	: 100	100	100	61
SAMPLE RATE HZ	: 512	64	8	1
PLOT HPF	: 0.0	1.0	0.1	0.01
PLOT LPF	: 100.0	24.0	3.0	0.35
FREQS/DECADE	: 10	10	10	10
FREQS/BAND	: 12	14	14	15
MIN COHERENCY	: 0.00	0.00	0.00	0.00
REJECTION LOOPS	: 2	2	2	2

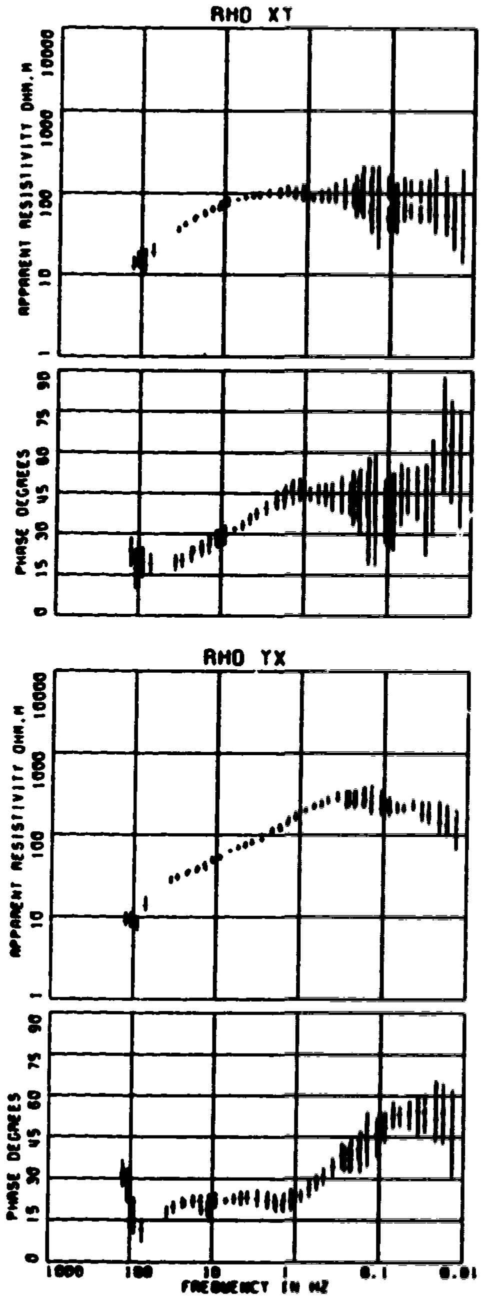

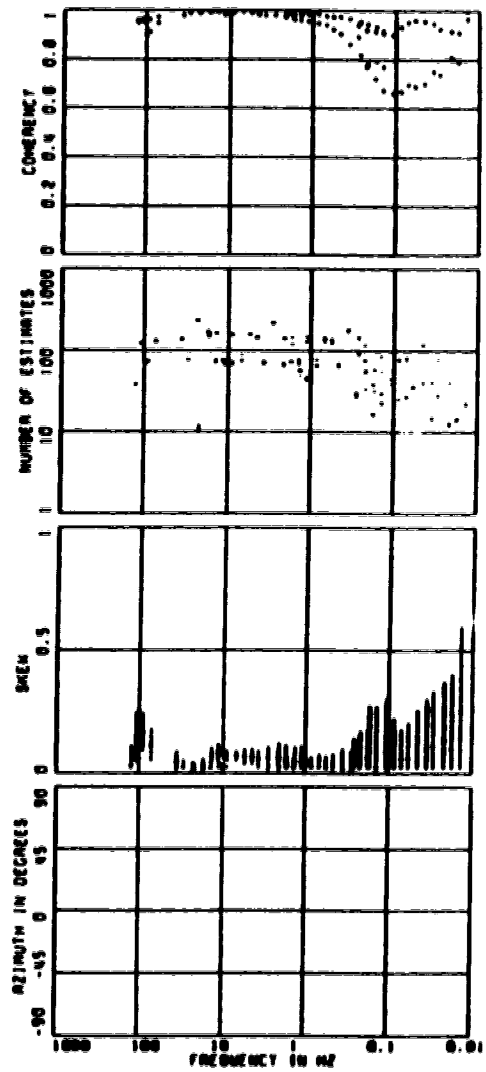

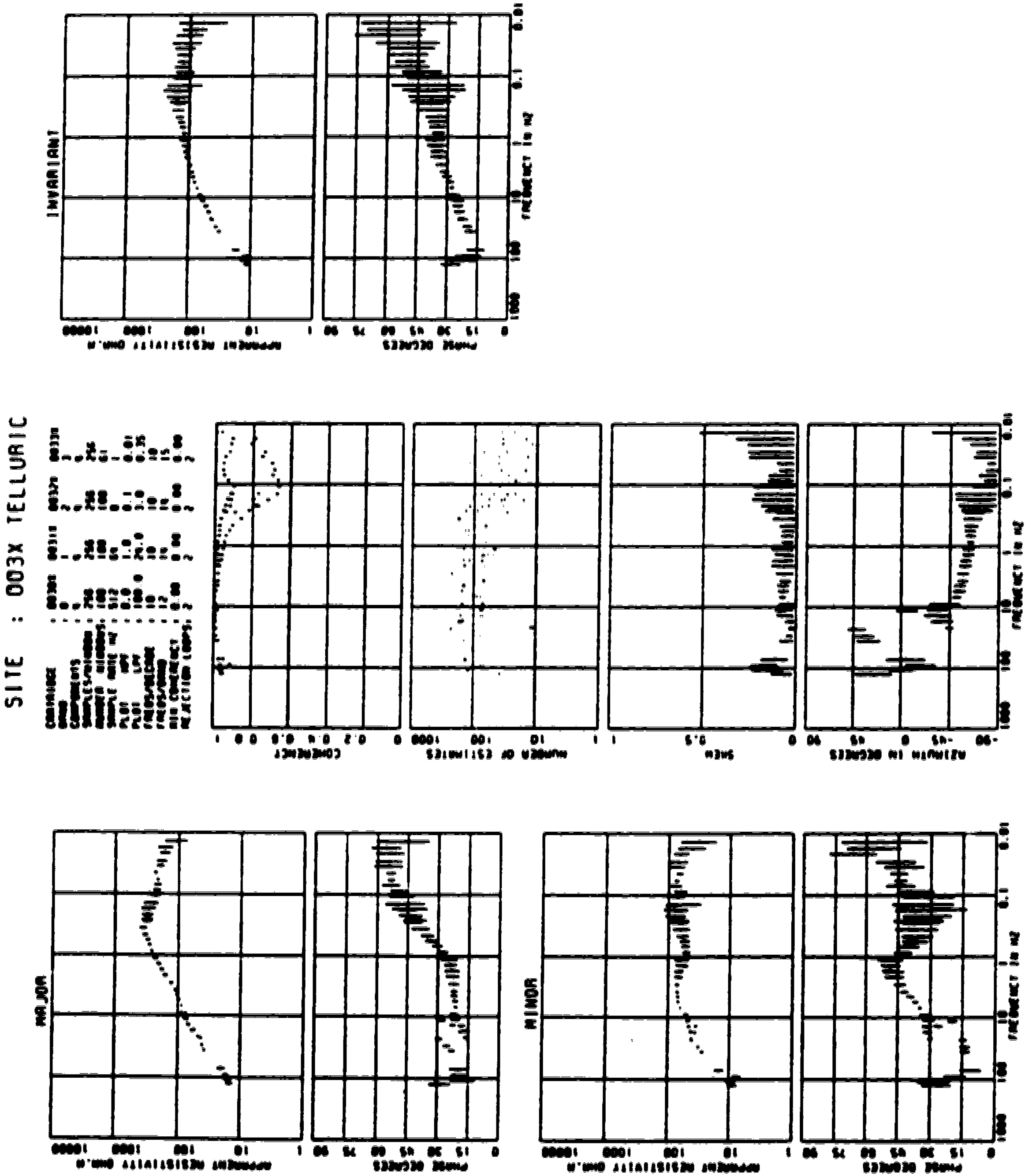
SITE : 003X TELLURIC
INVARIANT
MAJOR
MINOR

SITE : 004X TELLURIC

CARTRIDGE	:	004OX	0041X	0042X	0043X
BAND	:	0	1	2	3
COMPONENTS	:	4	4	4	4
SAMPLES/WINDOW	:	256	256	256	256
NUMBER WINDOWS	:	54	80	100	52
SAMPLE RATE HZ	:	512	64	8	1
PLOT HPF	:	8.0	1.0	0.1	0.01
PLOT LPF	:	100.0	24.0	3.0	0.35
FREQS/DECADE	:	10	10	10	10
FREQS/BAND	:	12	14	14	15
MIN COHERENCY	:	0.00	0.00	0.00	0.00
REJECTION LOOPS	:	2	2	2	2

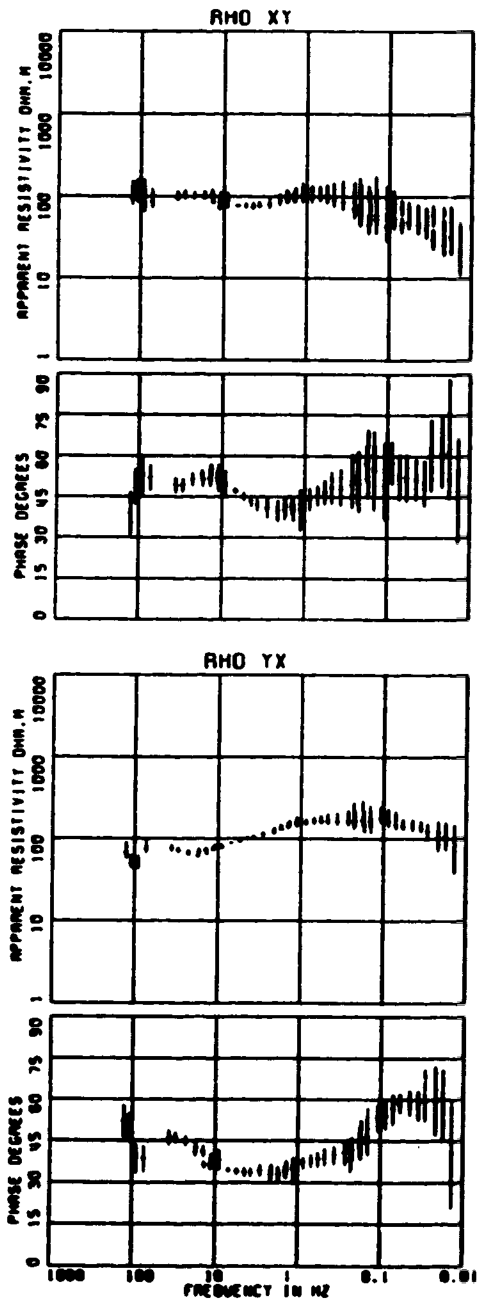

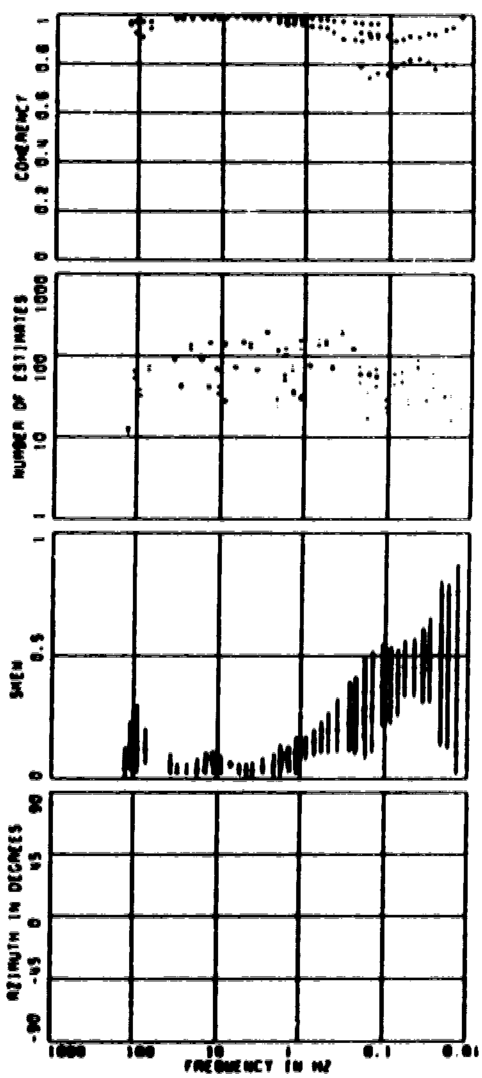

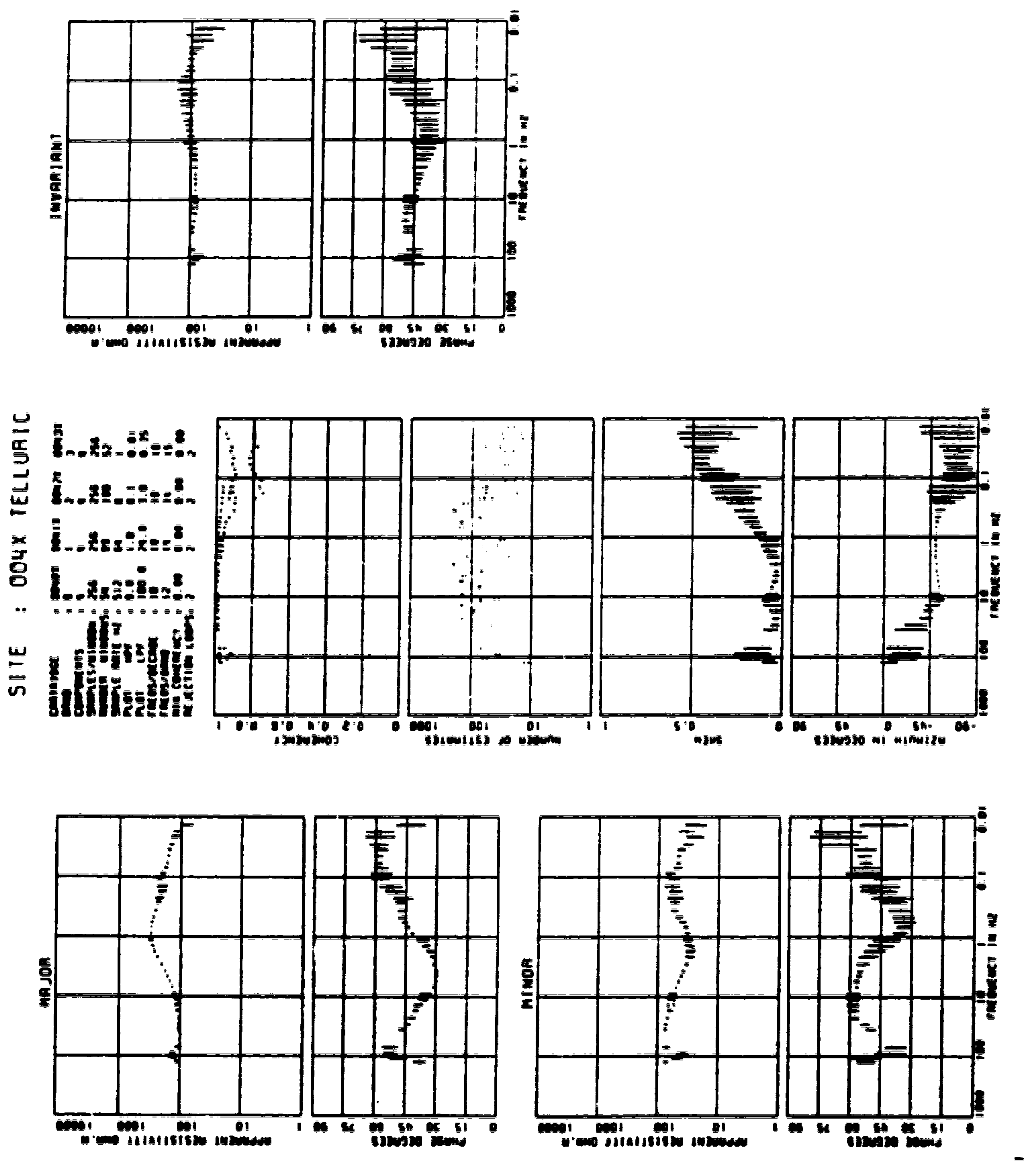
SITE : 004X TELLURIC
INVARIANT
MAJOR
MINOR
FREQUENCY IN HZ
APPARENT RESISTIVITY OHM.M
PHASE DEGREES
COHERENCY
NUMBER OF ESTIMATES
SKEW
AZIMUTH IN DEGREES

SITE : 005X TELLURIC

CARTRIDGE :	0050X	0051X	0052X	0053X
BAND :	0	1	2	3
COMPONENTS :	4	4	4	4
SAMPLES/WINDOW :	256	256	256	256
NUMBER WINDOWS:	100	100	100	50
SAMPLE RATE HZ :	512	64	8	1
PLOT HPF :	8.0	1.0	0.1	0.01
PLOT LPF :	100.0	25.0	3.0	0.35
FREQS/DECADE :	10	10	10	10
FREQS/BAND :	12	14	14	15
MIN COHERENCY :	0.00	0.00	0.00	0.00
REJECTION LOOPS:	2	2	2	2

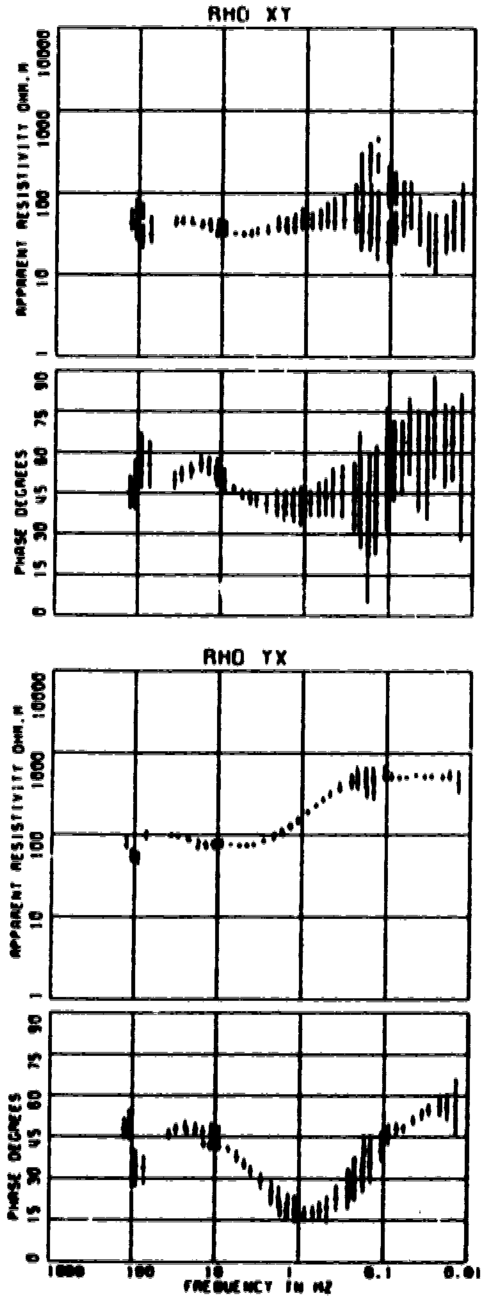

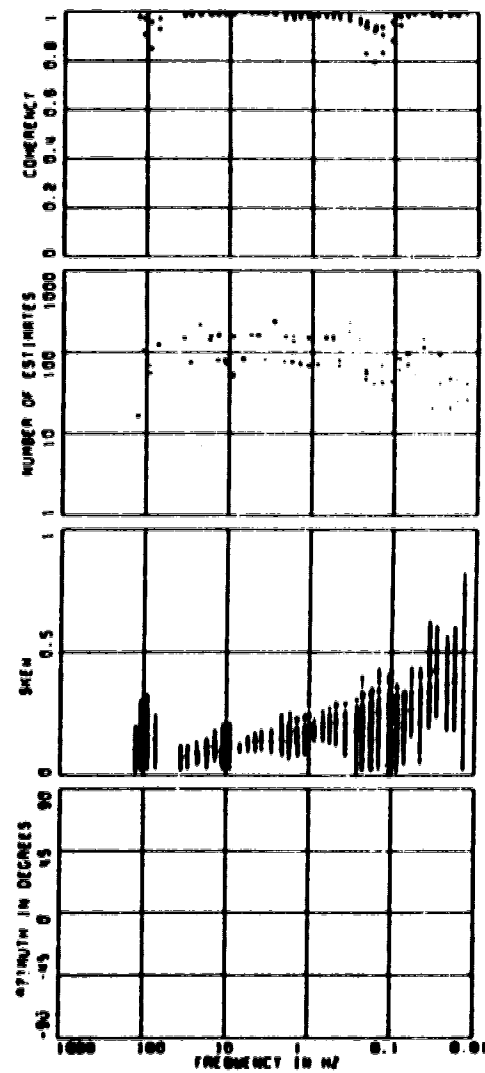

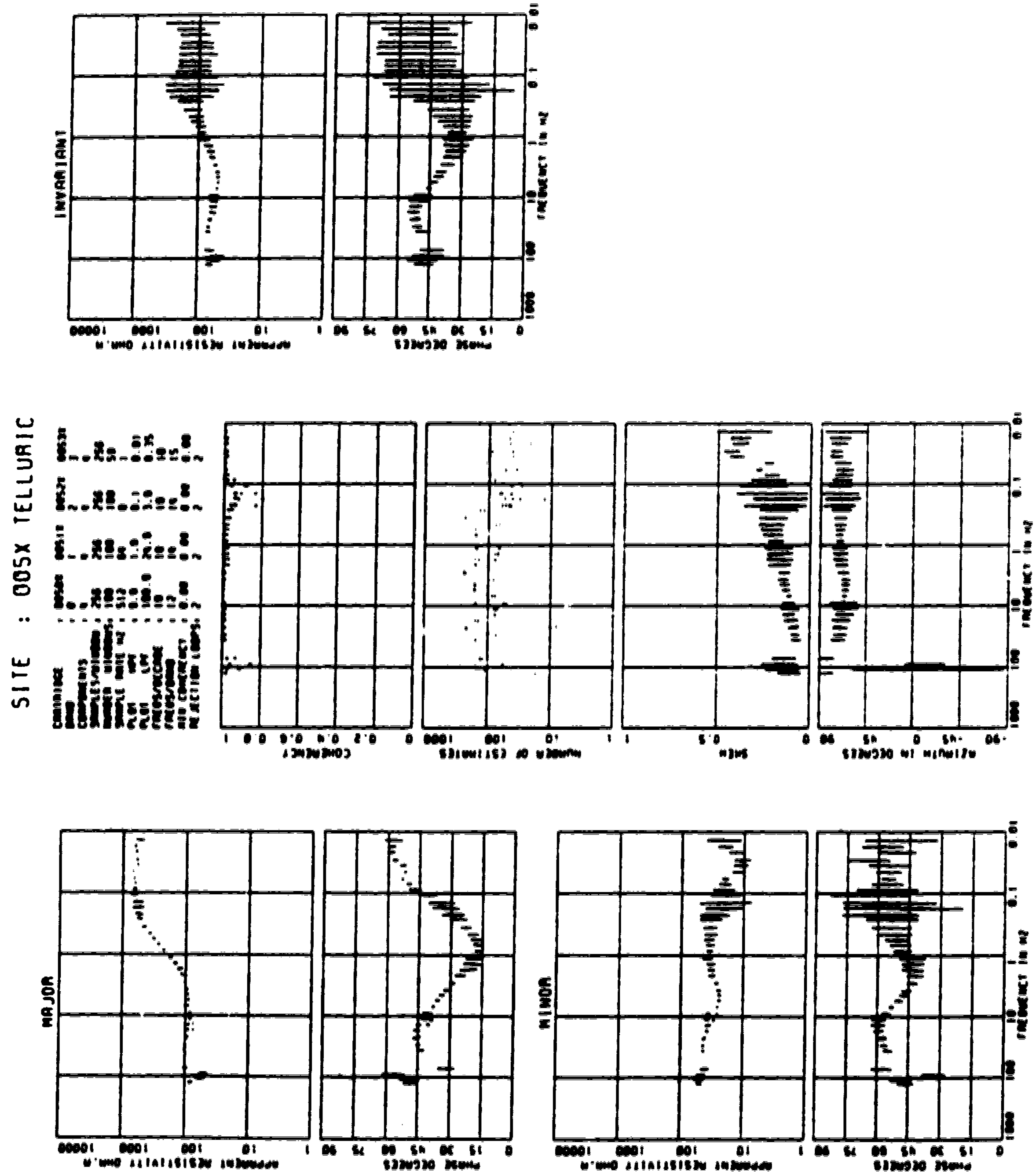
SITE : 005X TELLURIC
INVARIANT
MAJOR
MINOR
APPARENT RESISTIVITY OHM.M
PHASE DEGREES
FREQUENCY IN HZ
COHERENCY
NUMBER OF ESTIMATES
SKEW
AZIMUTH IN DEGREES

SITE : 006X TELLURIC

CARTRIDGE	:	0060X	0061X	0062X	0063X
BAND	:	0	1	2	3
COMPONENTS	:	4	4	4	4
SAMPLES/WINDOW	:	256	256	256	256
NUMBER WINDOWS	:	100	100	100	52
SAMPLE RATE HZ	:	512	64	8	1
PLOT HPF	:	0.0	1.0	0.1	0.01
PLOT LPF	:	100.0	24.0	3.0	0.35
FREQS/DECADE	:	10	10	10	10
FREQS/BAND	:	12	14	14	15
MIN COHERENCY	:	0.00	0.00	0.00	0.00
REJECTION LOOPS	:	2	2	2	2

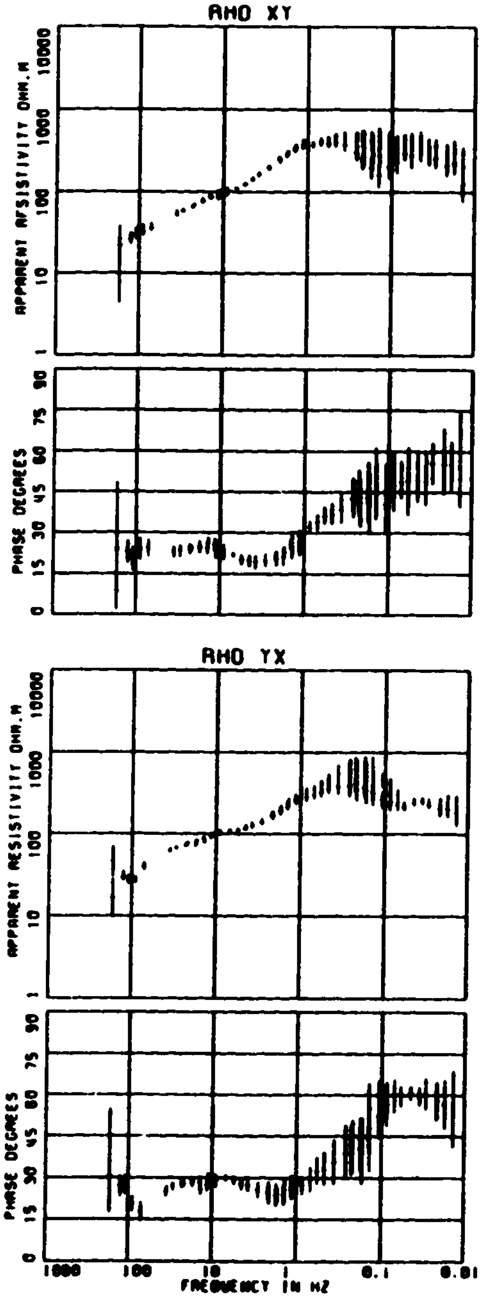

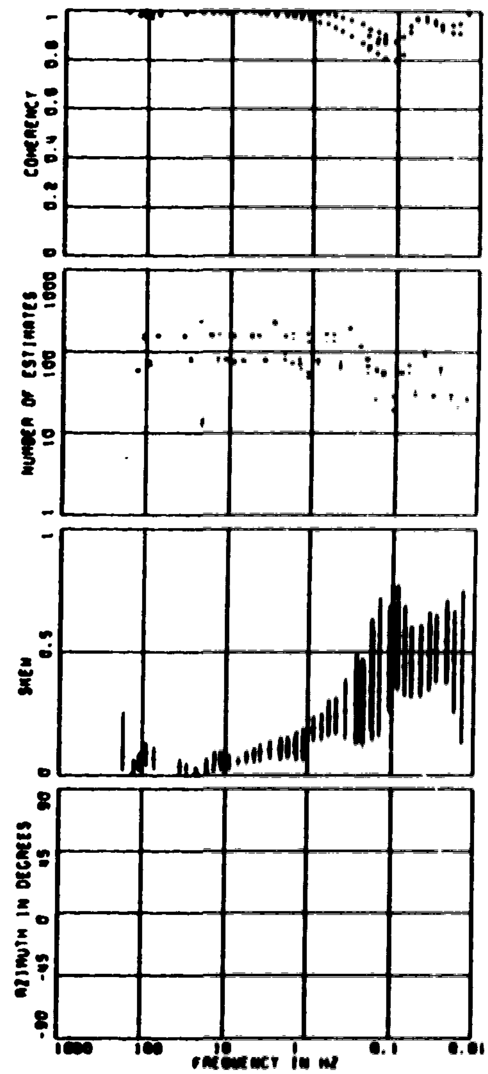

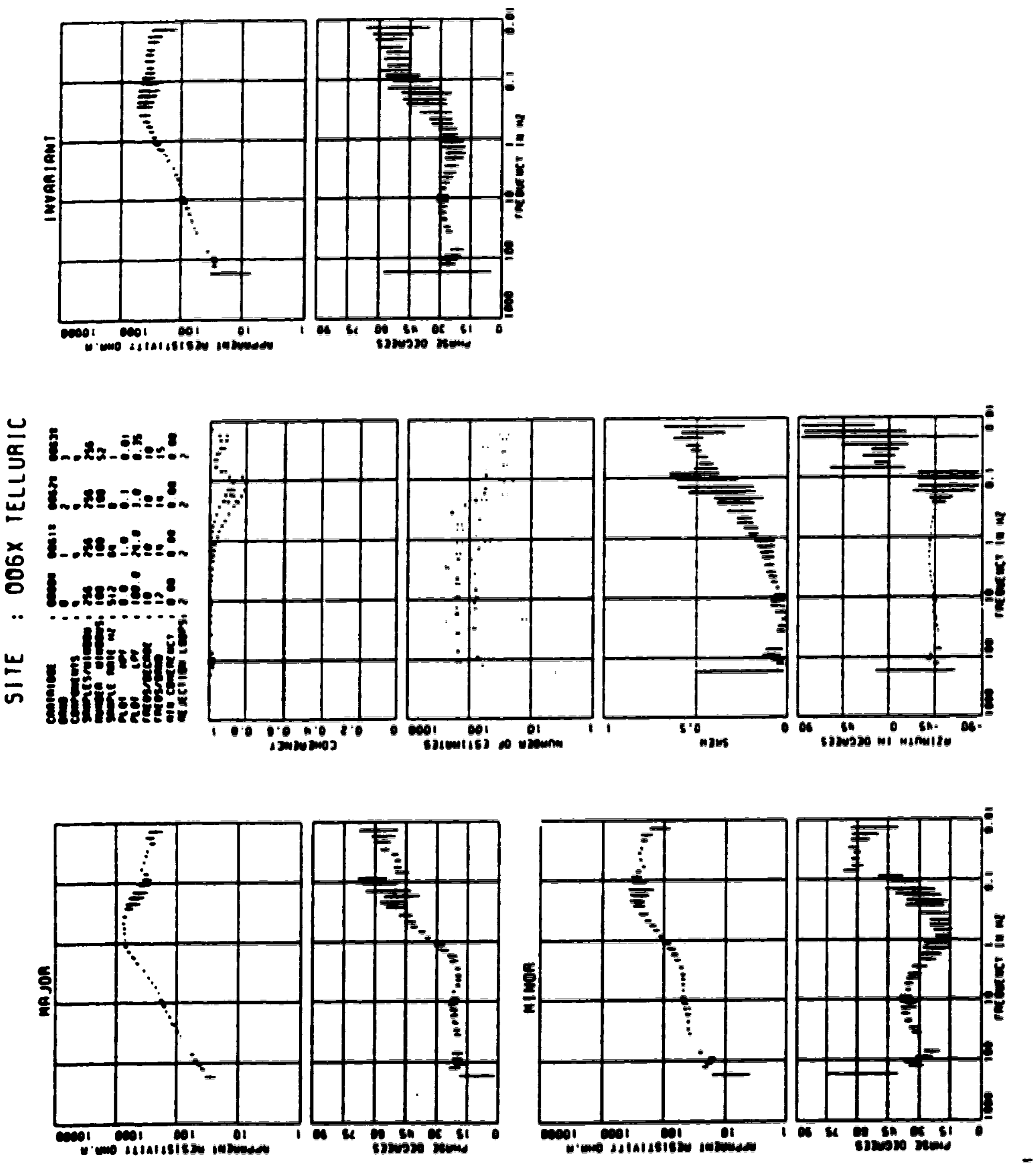
SITE : 006X TELLURIC
INVARIANT
MAJOR
MINOR

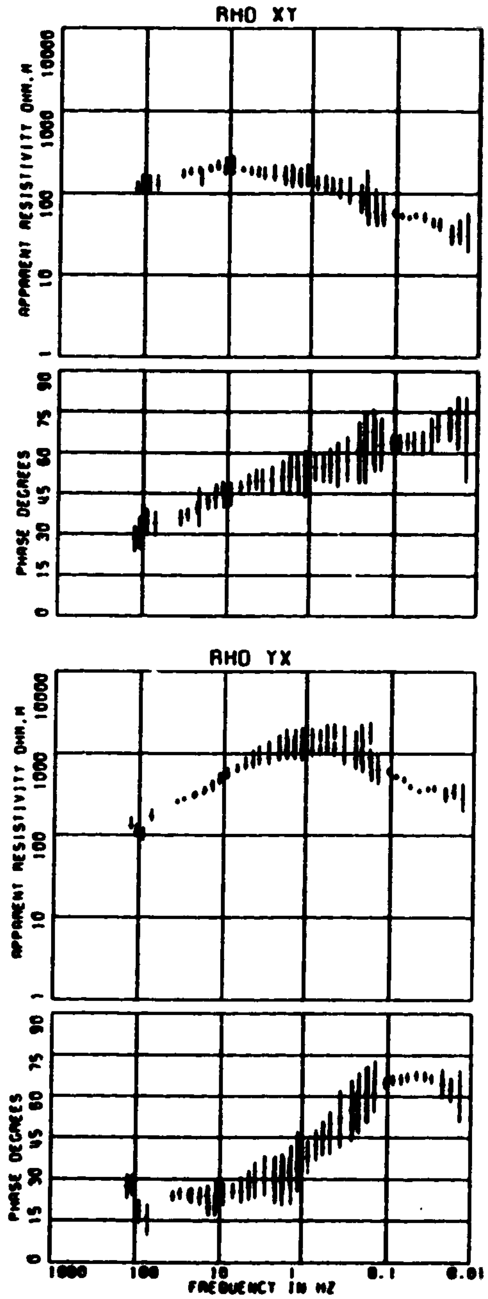

SITE : 007X TELLURIC

CARTRIDGE	:	0070X	0071X	0072X	0073X
BAND	:	0	1	2	3
COMPONENTS	:	4	4	4	4
SAMPLES/WINDOW	:	256	256	256	256
NUMBER WINDOWS	:	100	100	100	41
SAMPLE RATE HZ	:	512	64	8	1
PLOT HPF	:	8.0	1.0	0.1	0.01
PLOT LPF	:	100.0	20.0	3.0	0.35
FREQS/DECADE	:	10	10	10	10
FREQS/BAND	:	12	14	14	15
MIN COHERENCY	:	0.00	0.00	0.00	0.00
REJECTION LOOPS	:	2	2	2	2

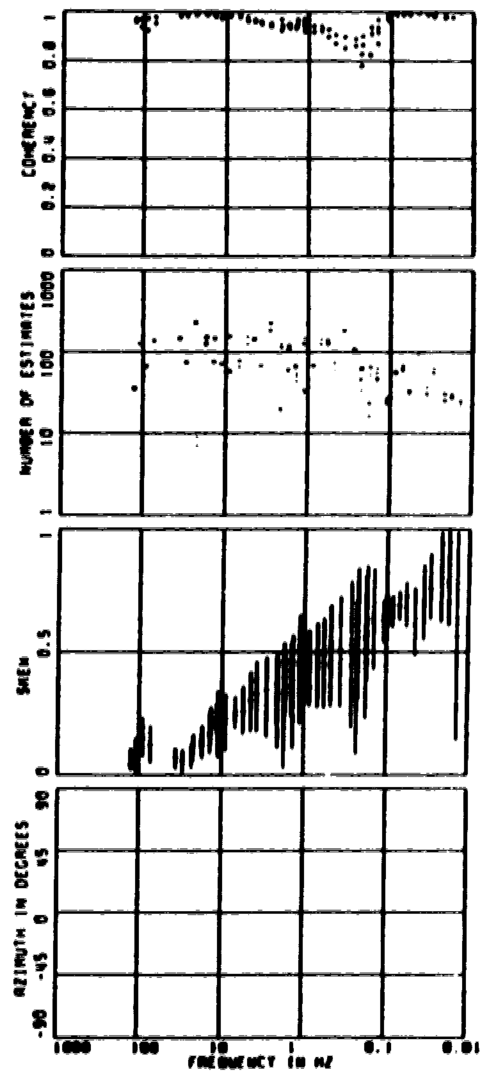

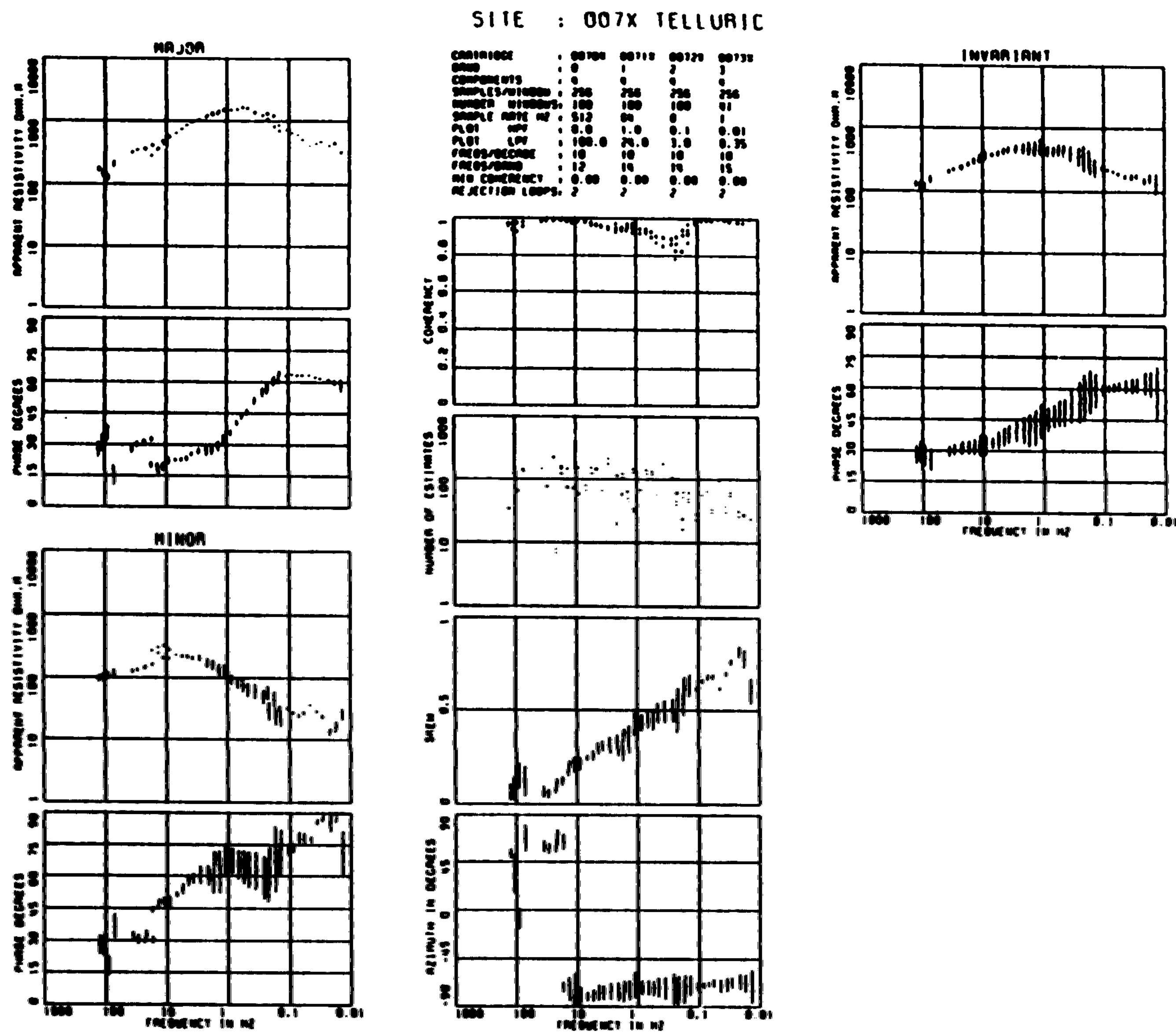
SITE : 007X TELLURIC
MAJOR
MINOR
INVARIANT
APPARENT RESISTIVITY OHM.M
PHASE DEGREES
COHERENCY
NUMBER OF ESTIMATES
SKEW
AZIMUTH IN DEGREES
FREQUENCY IN HZ

SITE : 008X TELLURIC

CARTRIDGE	:	0080X	0081X	0082X	0083X
BAND	:	0	1	2	3
COMPONENTS	:	4	4	4	4
SAMPLES/WINDOW	:	256	256	256	256
NUMBER WINDOWS	:	252	100	100	42
SAMPLE RATE HZ	:	512	64	8	1
PLOT HPF	:	0.0	1.0	0.1	0.01
PLOT LPF	:	100.0	24.0	3.0	0.35
FREQS/DECADE	:	10	10	10	10
FREQS/BAND	:	12	14	14	15
MIN COHERENCY	:	0.00	0.00	0.00	0.00
REJECTION LOOPS	:	2	2	2	2

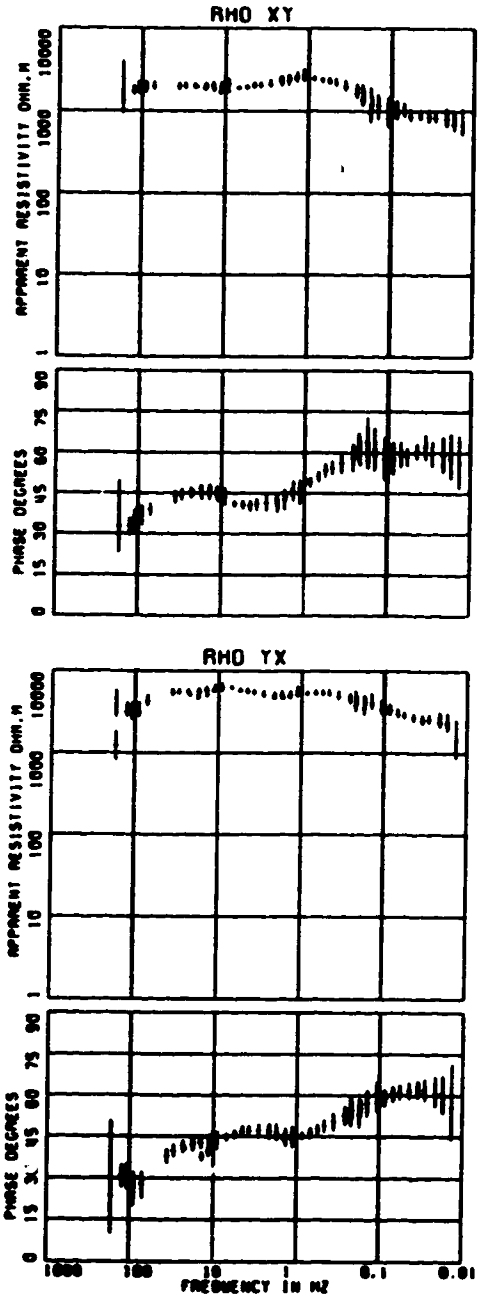

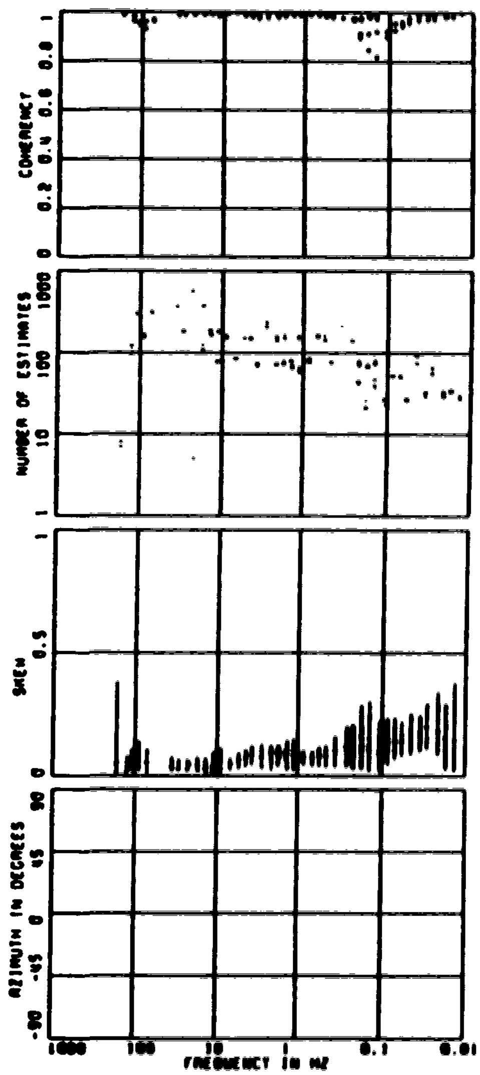

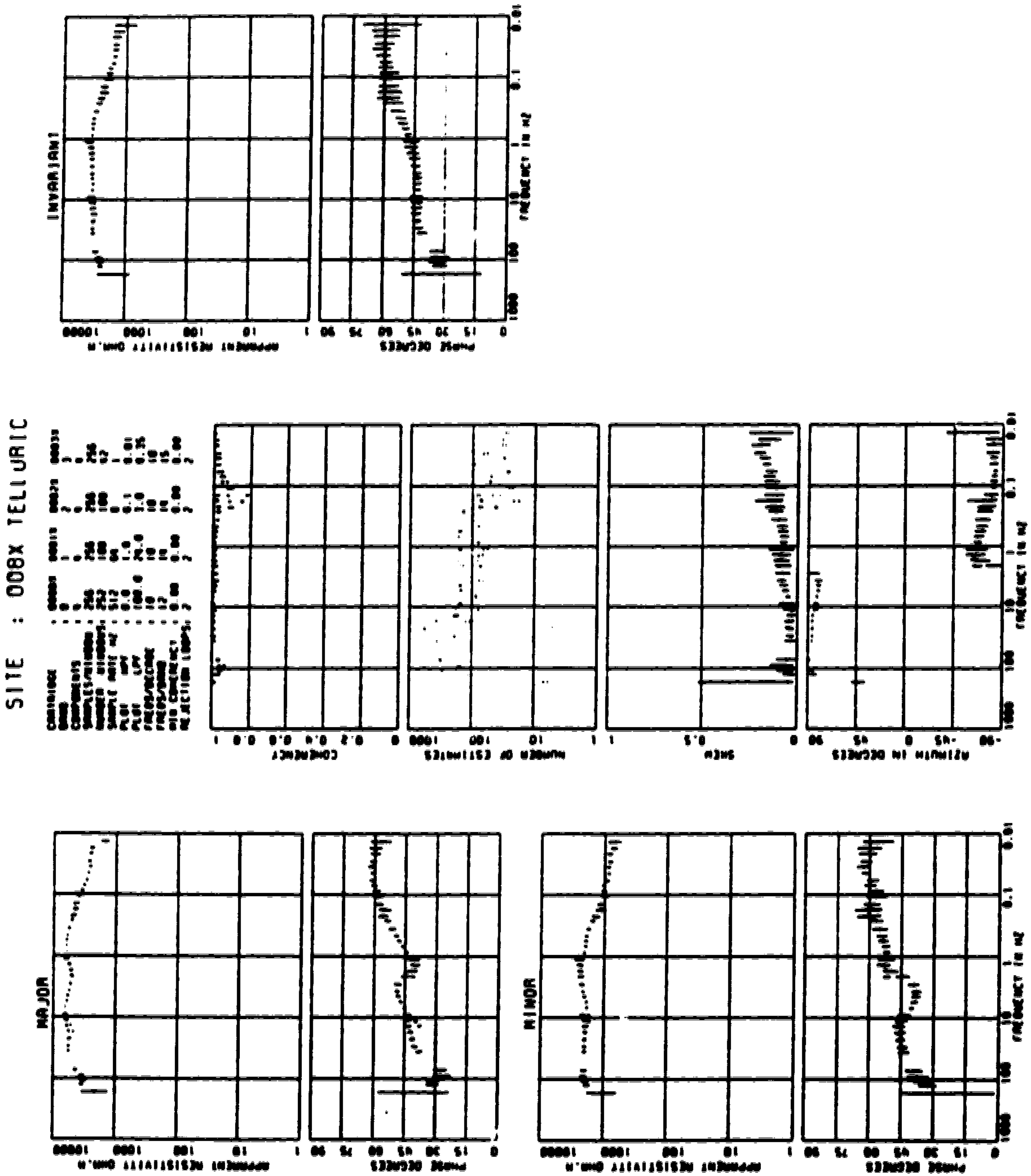
SITE : 008X TELLURIC
INVARIANT
MAJOR
MINOR
FREQUENCY IN HZ
APPARENT RESISTIVITY OHM.M
PHASE DEGREES
COHERENCY
NUMBER OF ESTIMATES
SKEW
AZIMUTH IN DEGREES

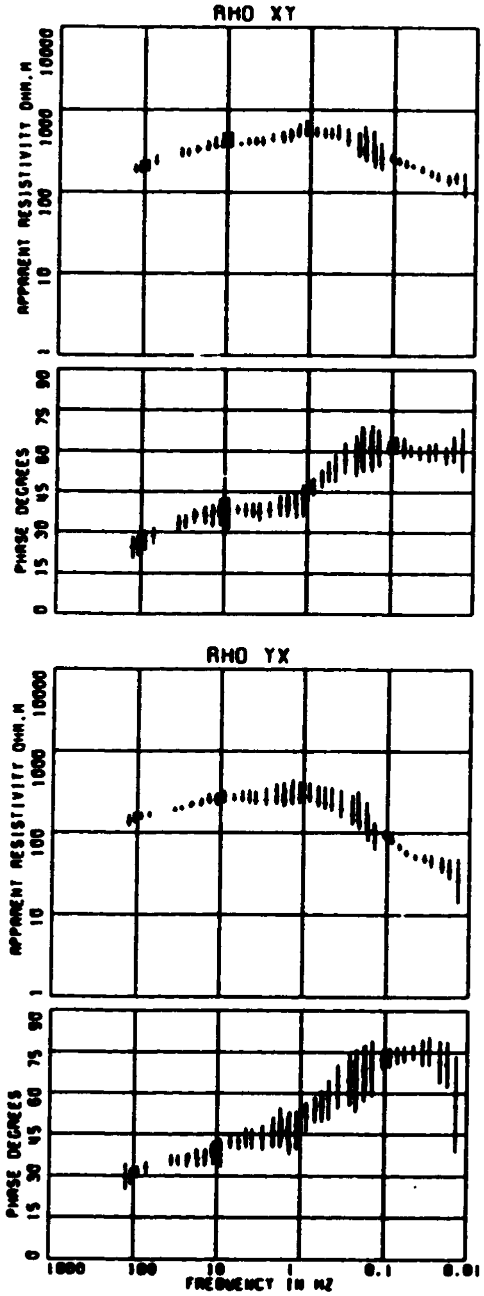

SITE : 009X TELLURIC

CARTRIDGE :	0090X	0091X	0092X	0093X
BAND :	0	1	2	3
COMPONENTS :	4	4	4	4
SAMPLES/WINDOW :	256	256	256	256
NUMBER WINDOWS:	100	100	100	50
SAMPLE RATE HZ :	512	64	8	1
PLOT HPF :	8.0	1.0	0.1	0.01
PLOT LPF :	100.0	20.0	3.0	0.35
FREQS/DECADE :	10	10	10	10
FREQS/BAND :	12	14	14	15
MIN COHERENCY :	0.00	0.00	0.00	0.00
REJECTION LOOPS:	2	2	2	2

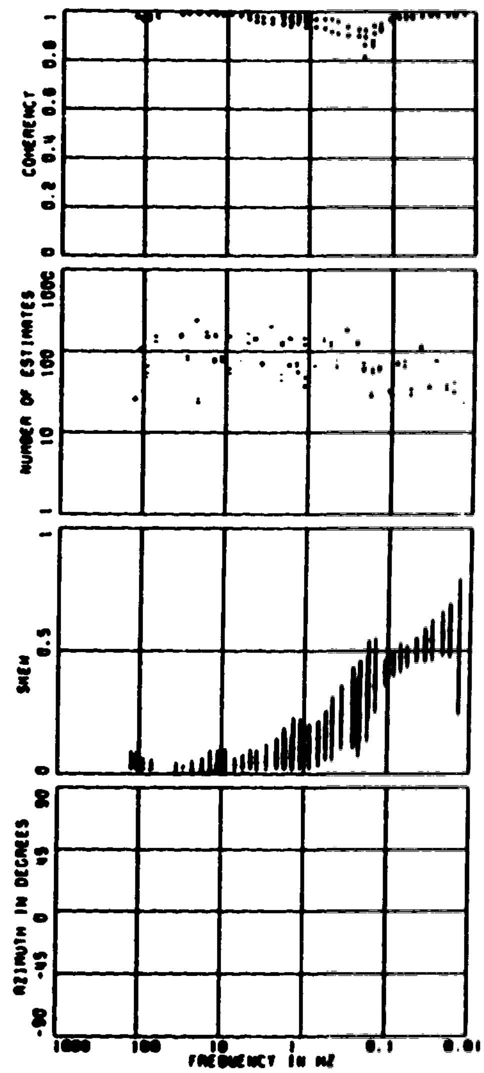

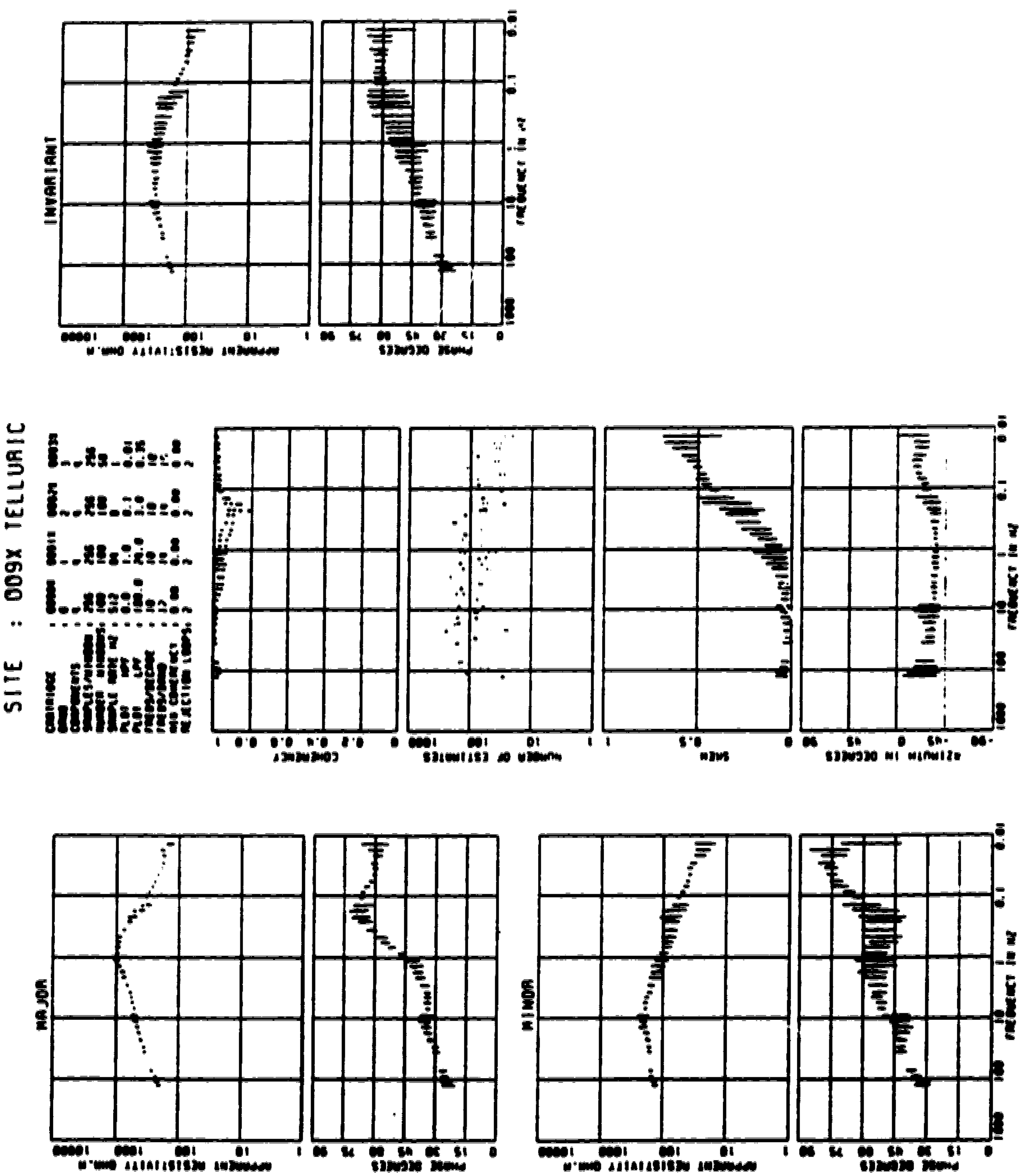
SITE : 009X TELLURIC
INVARIANT
MAJOR
MINOR

SITE : 010X TELLURIC

CARTRIDGE :	0100X	0101X	0102X	0103X
BAND :	0	1	2	3
COMPONENTS :	4	4	4	4
SAMPLES/WINDOW :	256	256	256	256
NUMBER WINDOWS:	100	100	127	60
SAMPLE RATE HZ :	512	64	8	1
PLOT HPF :	0.0	1.0	0.1	0.01
PLOT LPF :	100.0	24.0	3.0	0.35
FREQS/DECADE :	10	10	10	10
FREQS/BAND :	12	14	14	15
MIN COHERENCY :	0.00	0.00	0.00	0.00
REJECTION LOOPS:	2	2	2	2

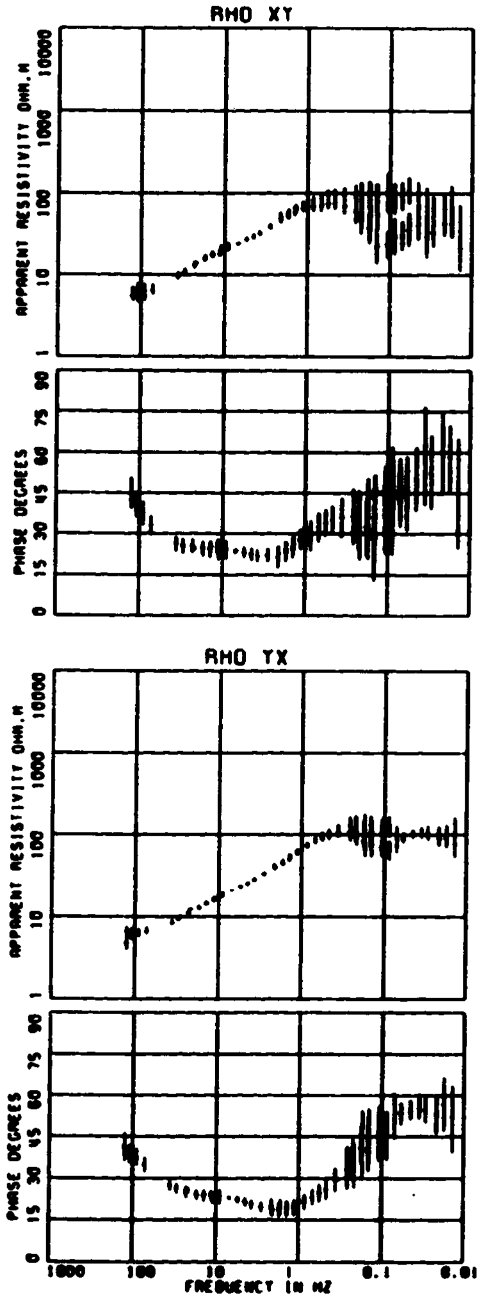

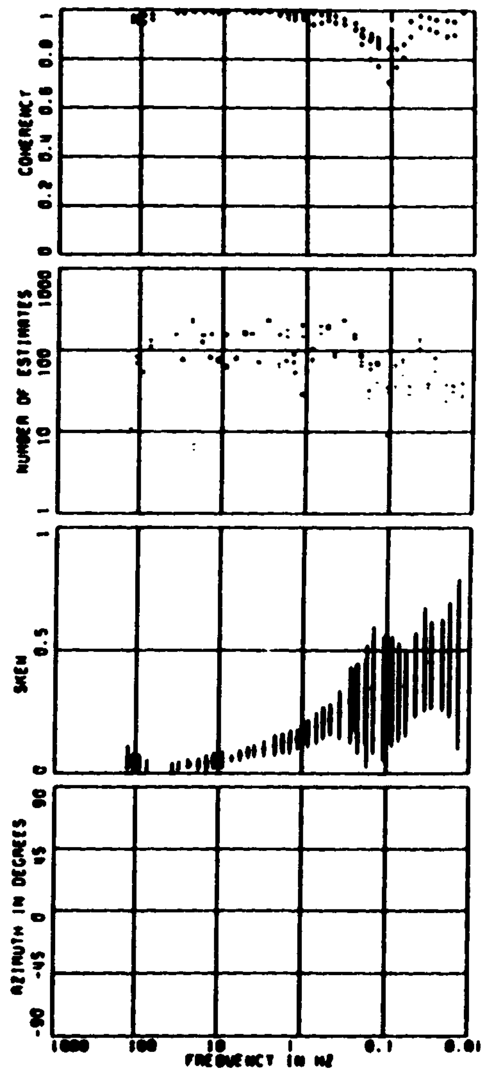

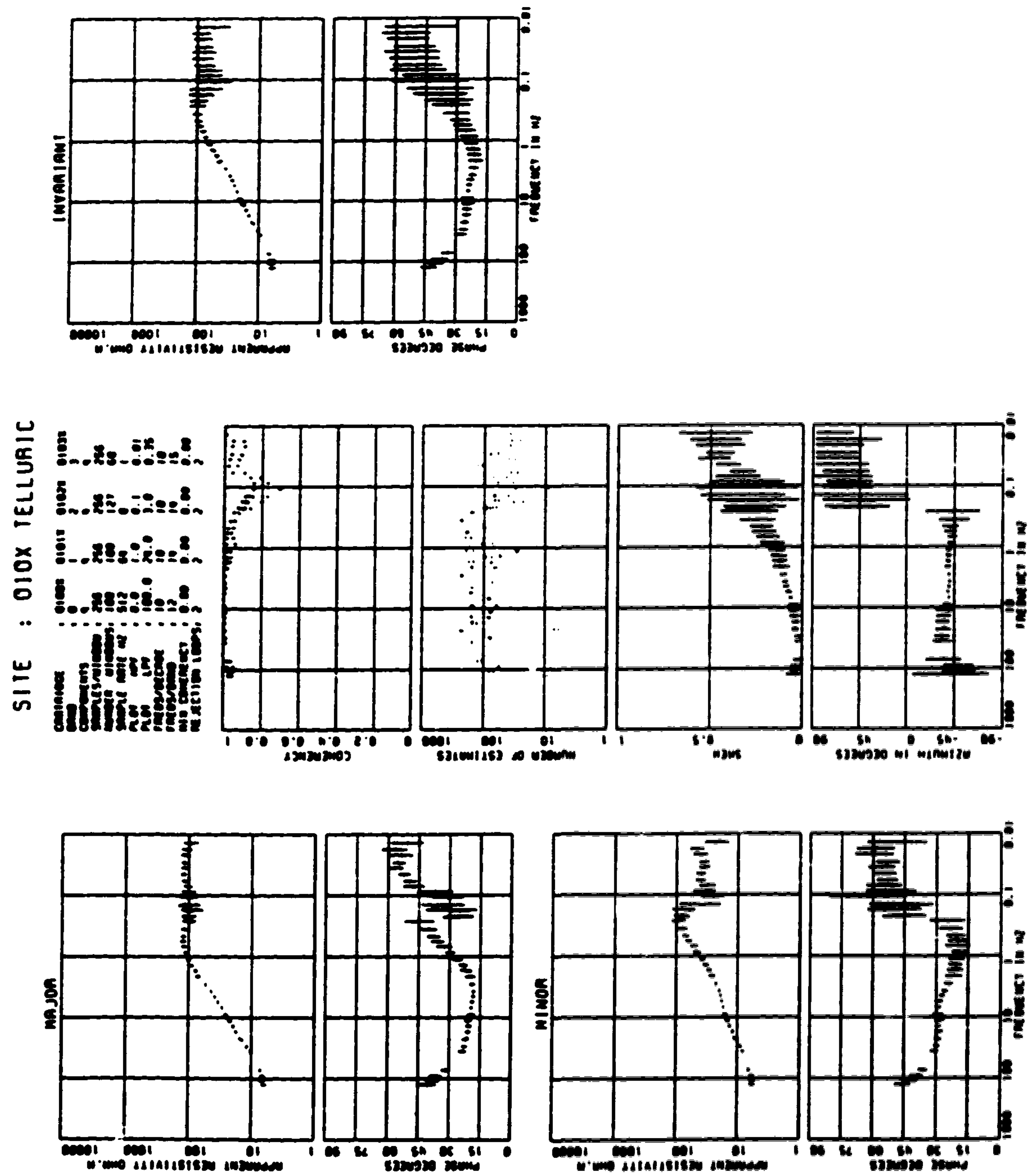
INVARIANT
SITE : 010X TELLURIC
MAJOR
MINOR
FREQUENCY IN HZ
APPARENT RESISTIVITY OHM.M
PHASE DEGREES
COHERENCY
NUMBER OF ESTIMATES
SKEW
AZIMUTH IN DEGREES

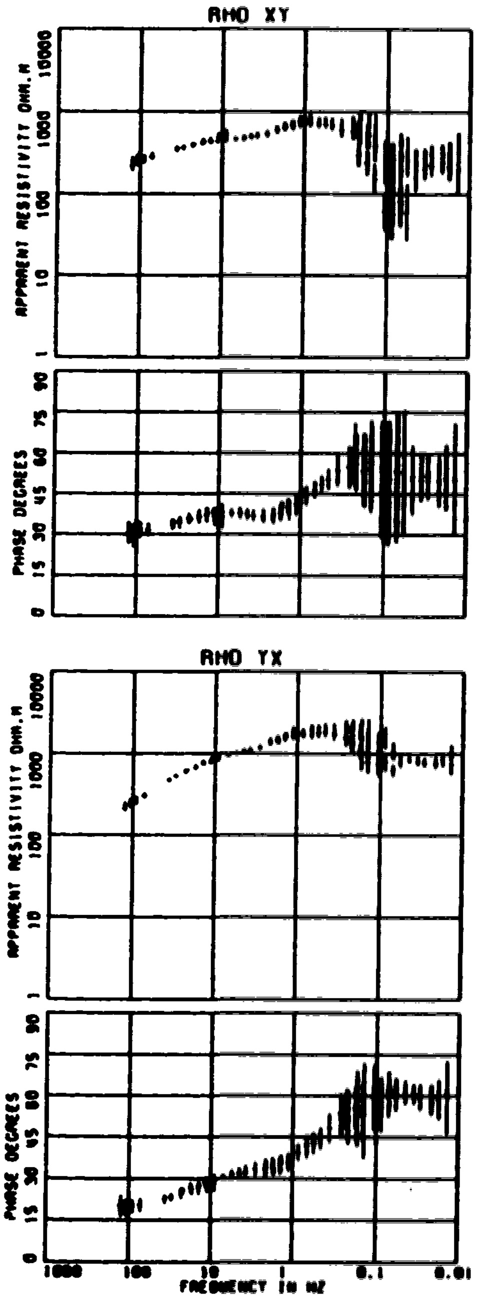

SITE : 011X TELLURIC

CARTRIDGE	:	0110X	0111X	0112X	0113X
BAND	:	0	1	2	3
COMPONENTS	:	4	4	4	4
SAMPLES/WINDOW	:	256	256	256	256
NUMBER WINDOWS	:	100	83	100	60
SAMPLE RATE HZ	:	512	64	8	1
PLOT HPF	:	8.0	1.0	0.1	0.01
PLOT LPF	:	100.0	24.0	3.0	0.35
FREQS/DECADE	:	10	10	10	10
FREQS/BAND	:	12	14	14	15
MIN COHERENCY	:	0.80	0.80	0.80	0.80
REJECTION LOOPS	:	2	2	2	2

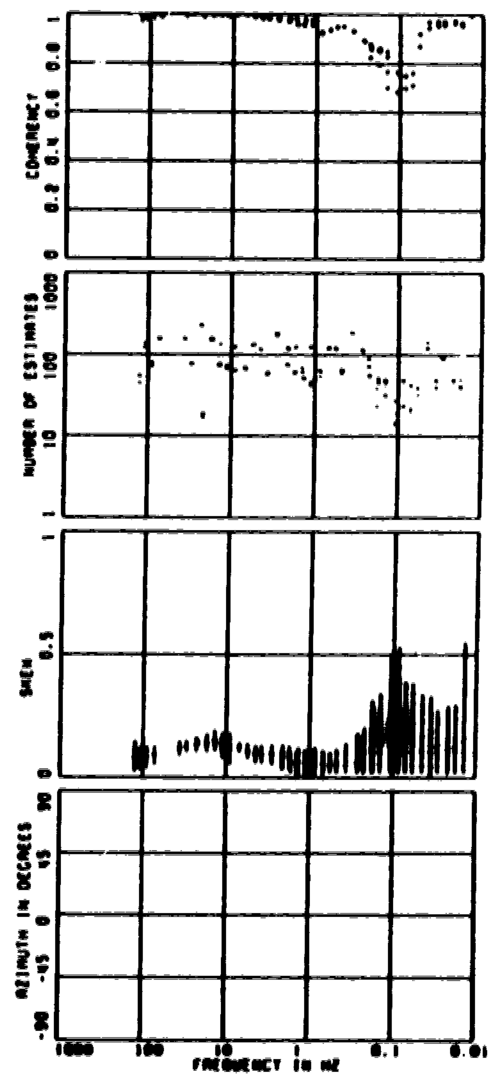

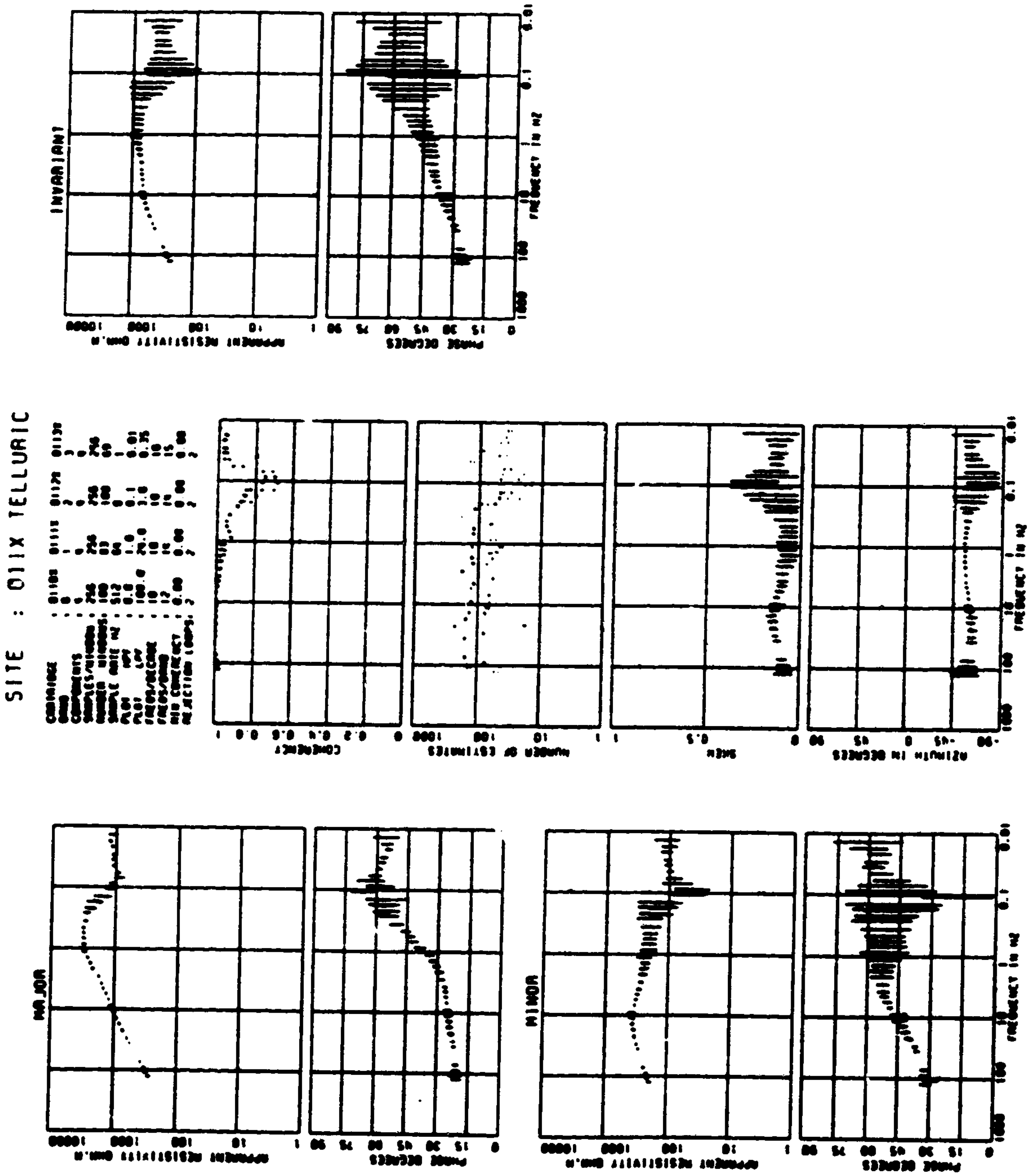
SITE : 011X TELLURIC
INVARIANT
MAJOR
MINOR
FREQUENCY IN HZ
APPARENT RESISTIVITY OHM.M
PHASE DEGREES
COHERENCY
NUMBER OF ESTIMATES
SKEW
AZIMUTH IN DEGREES

SITE : 012X TELLURIC

CARTRIDGE :	0120X	0121X	0122X	0123X
BAND :	0	1	2	3
COMPONENTS :	4	4	4	4
SAMPLES/WINDOW :	256	256	256	256
NUMBER WINDOWS:	100	100	100	57
SAMPLE RATE HZ :	512	64	8	1
PLOT HPF :	8.0	1.0	0.1	0.01
PLOT LPF :	100.0	24.0	3.0	0.35
FREQS/DECADE :	10	10	10	10
FREQS/BAND :	12	14	14	15
MIN COHERENCY :	0.00	0.00	0.00	0.00
REJECTION LOOPS:	2	2	2	2

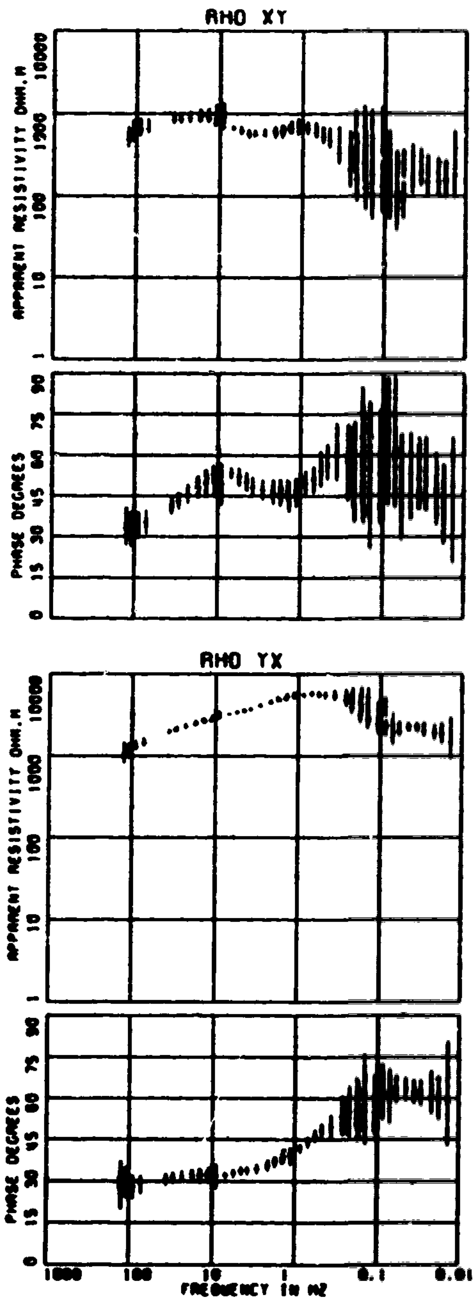

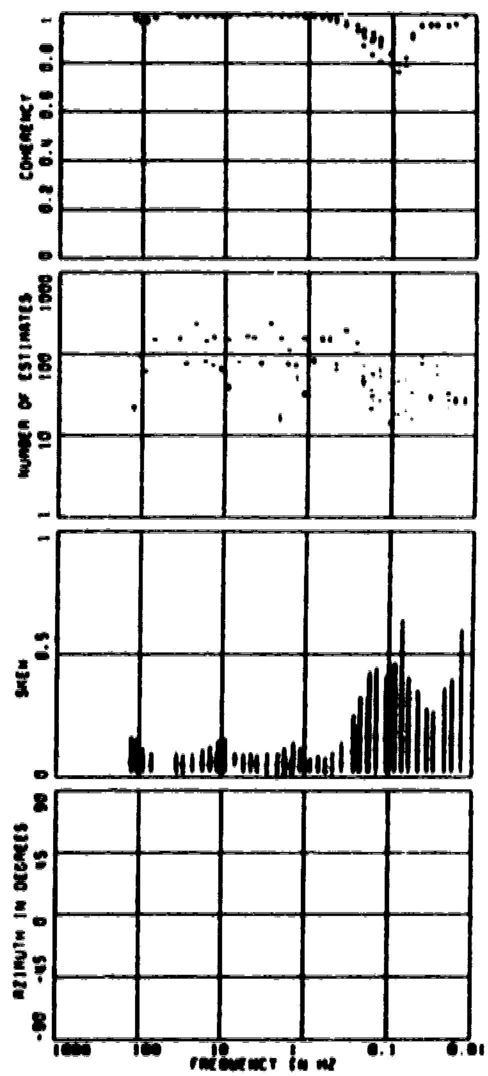

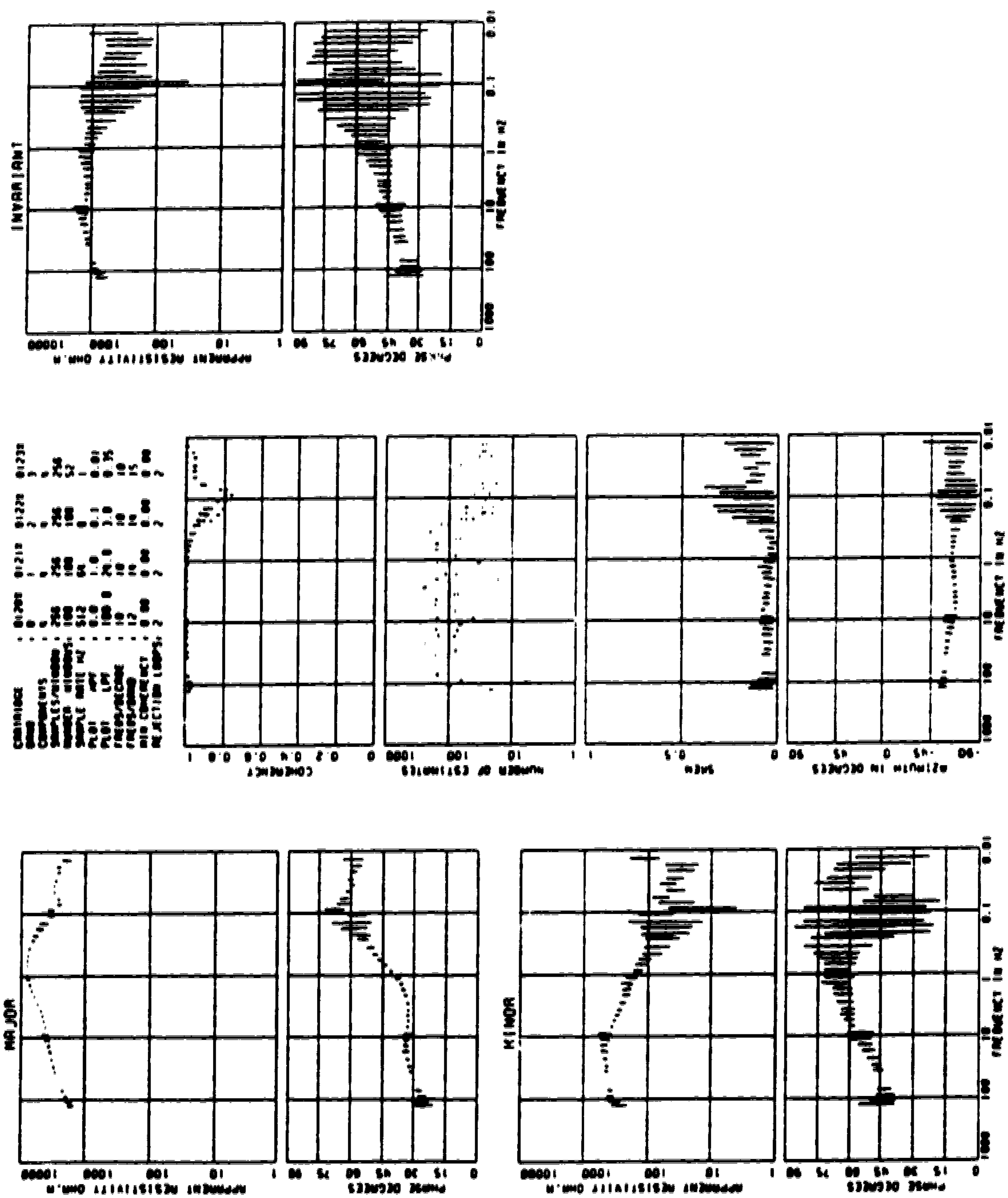
SITE : 012X TELLURIC
INVARIANT
MAJOR
MINOR

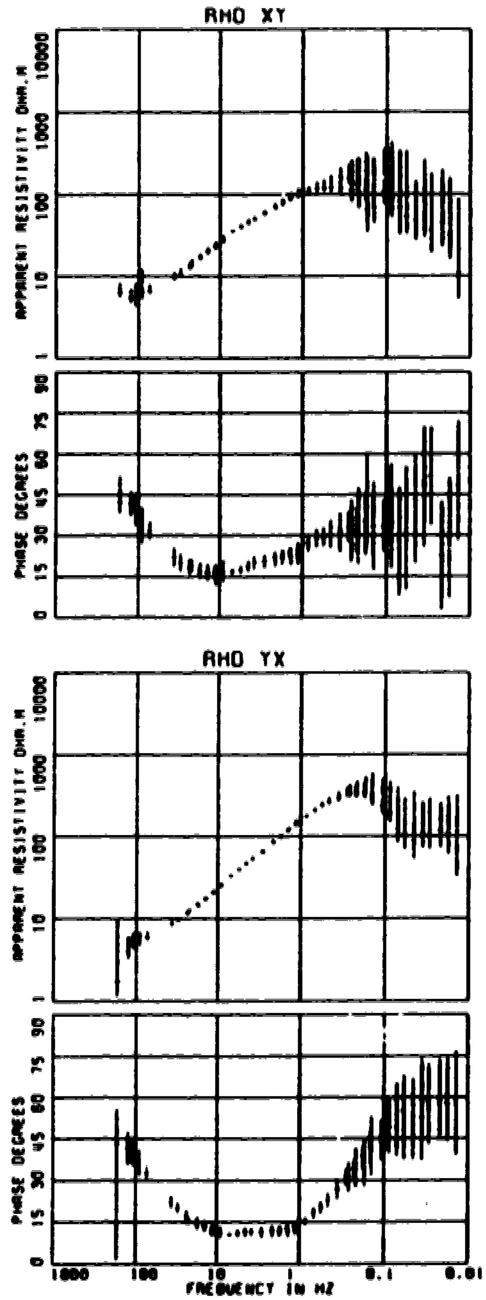

SITE : 013X TELLURIC

CARTRIDGE	:	0130X	0131X	0132X	0133X
BAND	:	0	1	2	3
COMPONENTS	:	4	4	4	4
SAMPLES/WINDOW	:	256	256	256	256
NUMBER WINDOWS	:	100	100	100	91
SAMPLE RATE HZ	:	512	64	8	1
PLOT HPF	:	8.0	1.0	0.1	0.01
PLOT LPF	:	100.0	20.0	3.0	0.35
FREQS/DECADE	:	10	10	10	10
FREQS/BAND	:	12	14	14	15
MIN COHERENCY	:	0.00	0.00	0.00	0.00
REJECTION LOOPS	:	2	2	2	2

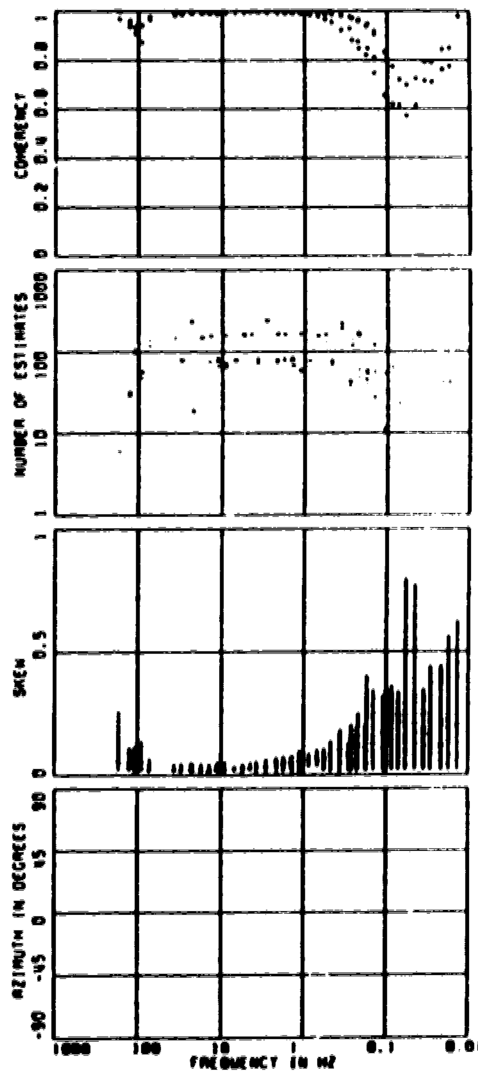

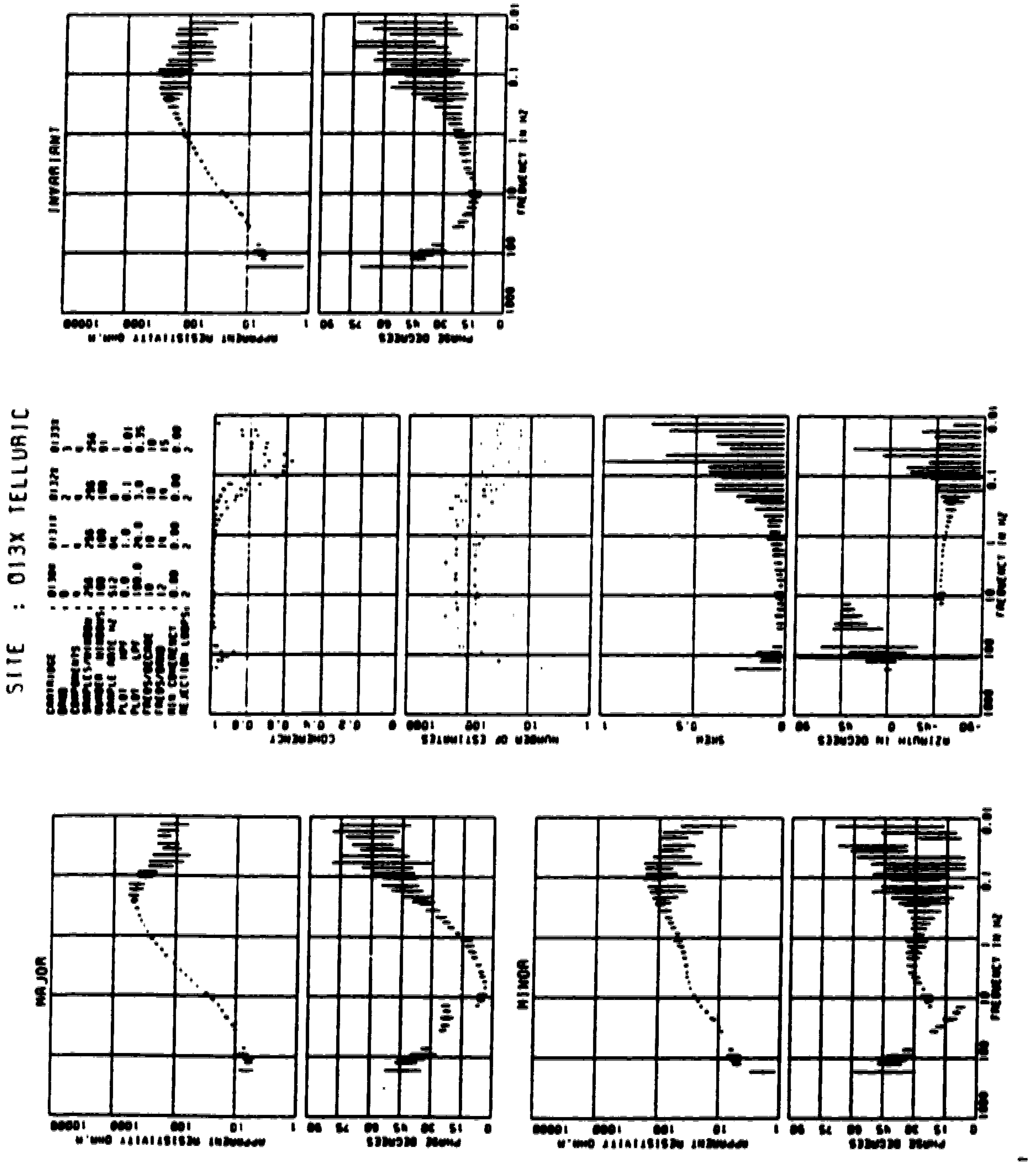
SITE : 013X TELLURIC
INVARIANT
MAJOR
MINOR
FREQUENCY IN HZ
APPARENT RESISTIVITY OHM.M
PHASE DEGREES
COHERENCY
NUMBER OF ESTIMATES
SKEW
AZIMUTH IN DEGREES

SITE : 014X TELLURIC

CARTRIDGE	:	0140X	0141X	0142X	0143X
BAND	:	0	1	2	3
COMPONENTS	:	4	4	4	4
SAMPLES/WINDOW	:	256	256	256	256
NUMBER WINDOWS	:	100	100	100	67
SAMPLE RATE HZ	:	512	64	8	1
PLOT HPF	:	0.0	1.0	0.1	0.01
PLOT LPF	:	100.0	24.0	3.0	0.35
FREQS/DECADE	:	10	10	10	10
FREQS/BAND	:	12	14	14	15
MIN COHERENCY	:	0.00	0.00	0.00	0.00
REJECTION LOOPS	:	2	2	2	2

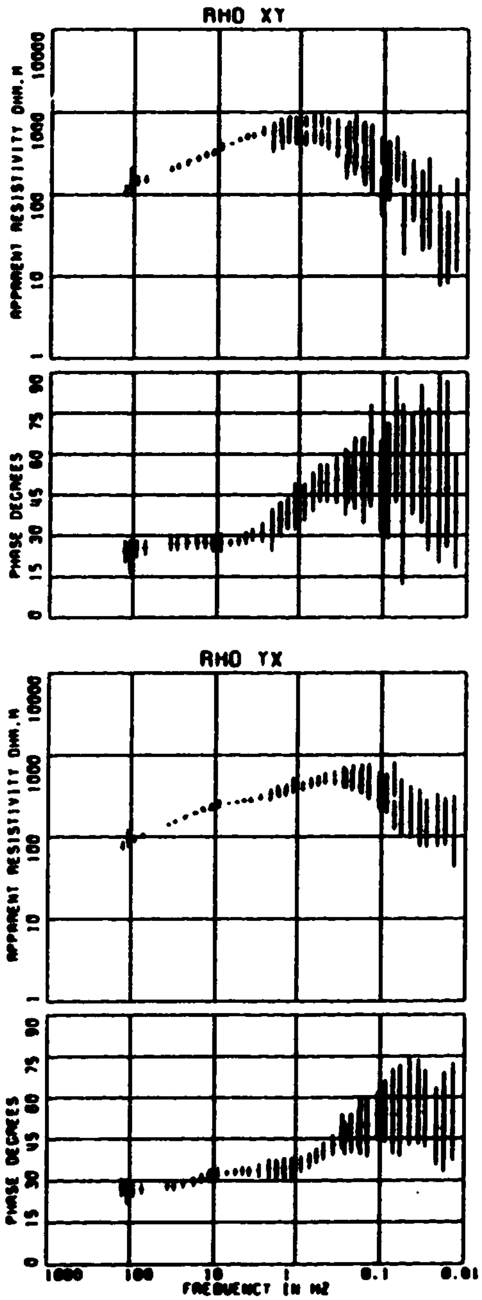

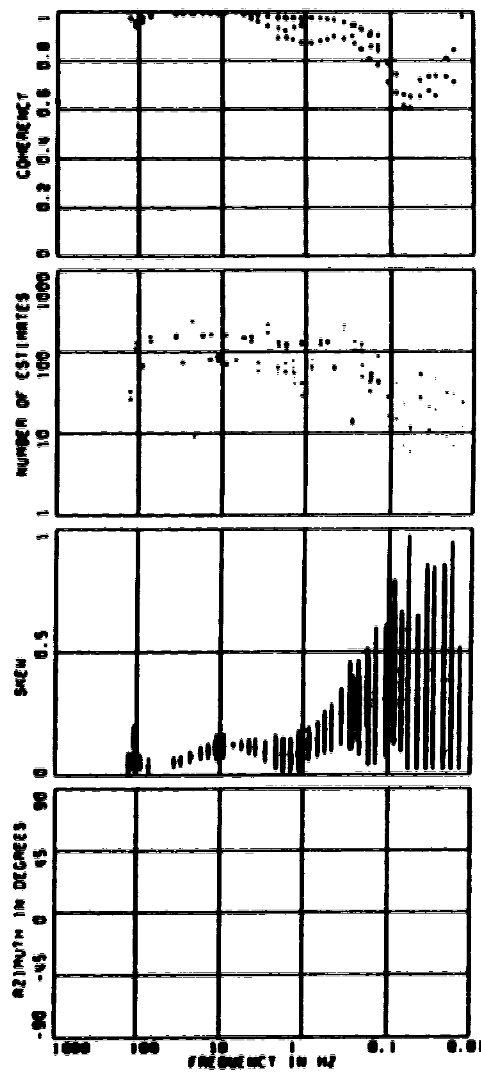

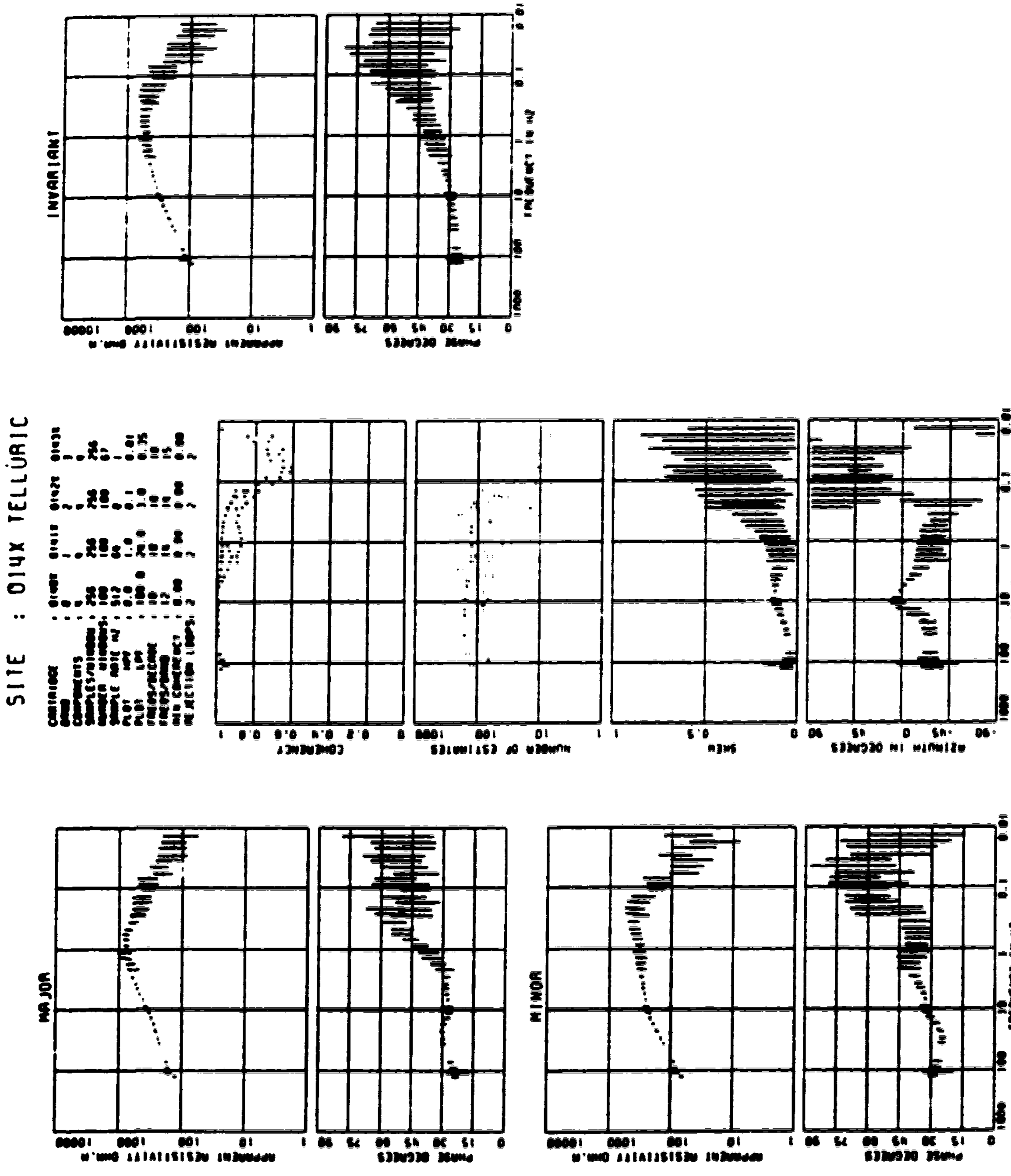
INVARIANT
SITE : 014X TELLURIC
MAJOR
MINOR

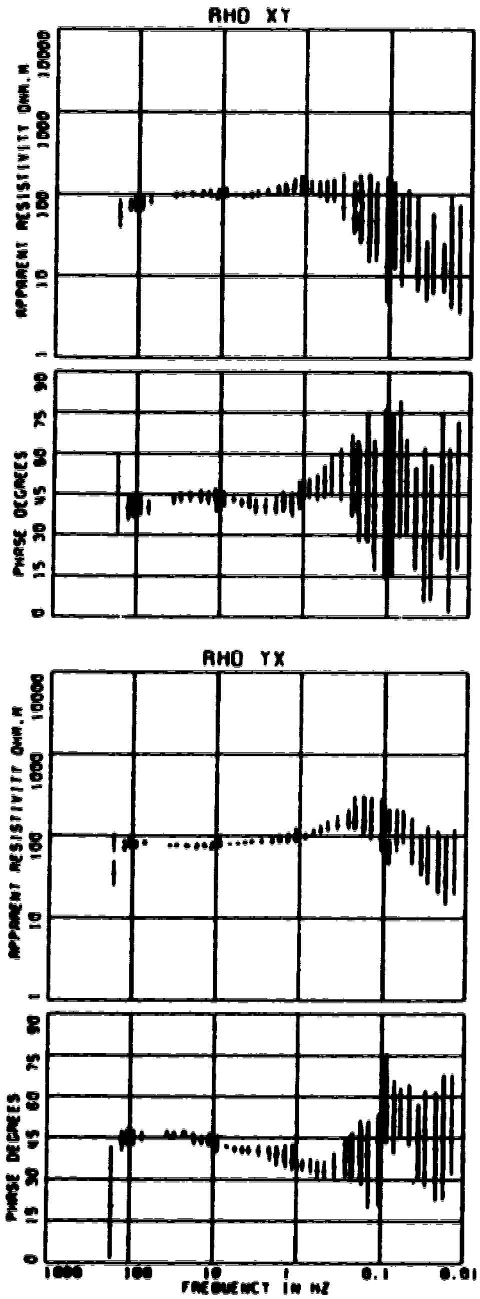

SITE : 015X TELLURIC

CARTRIDGE	:	0150X	0151X	0152X	0153X
BAND	:	0	1	2	3
COMPONENTS	:	4	4	4	4
SAMPLES/WINDOW	:	256	256	256	256
NUMBER WINDOWS	:	100	100	90	50
SAMPLE RATE HZ	:	512	64	8	1
PLOT HPF	:	8.0	1.0	0.1	0.01
PLOT LPF	:	100.0	25.0	3.0	0.35
FREQS/DECADE	:	10	10	10	10
FREQS/BAND	:	12	14	14	15
MIN COHERENCY	:	0.00	0.00	0.00	0.00
REJECTION LOOPS	:	2	2	2	2

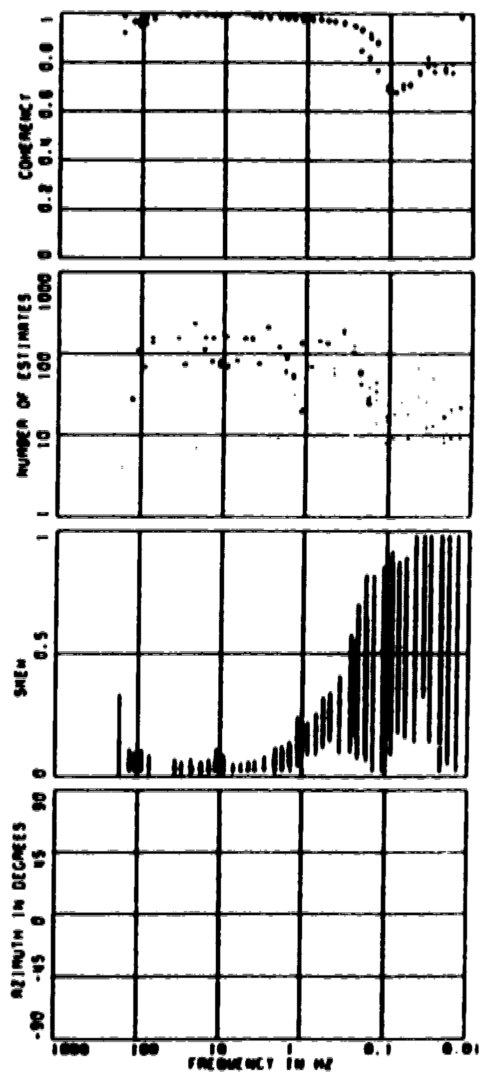

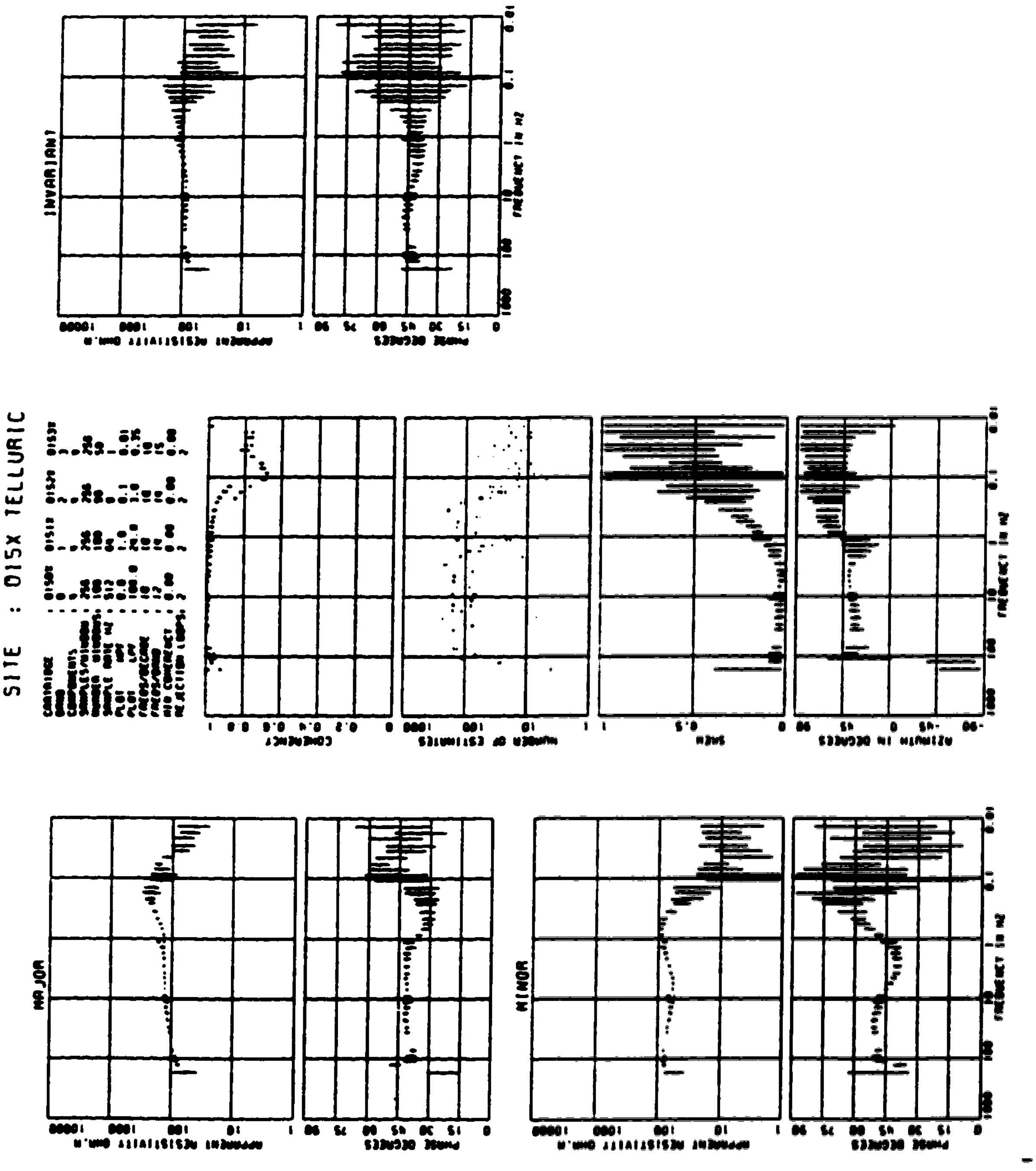
INVARIANT
SITE : D15X TELLURIC
MAJOR
MINOR

SITE : 016X TELLURIC

CARTRIDGE	:	0160X	0161X	0162X	0163X
BAND	:	0	1	2	3
COMPONENTS	:	4	4	4	4
SAMPLES/WINDOW	:	256	256	256	256
NUMBER WINDOWS	:	150	100	100	64
SAMPLE RATE HZ	:	512	64	8	1
PLOT HPF	:	8.0	1.0	0.1	0.01
PLOT LPF	:	100.0	24.0	3.0	0.35
FREQS/DECADE	:	10	10	10	10
FREQS/BAND	:	12	14	14	15
MIN COHERENCY	:	0.00	0.00	0.00	0.00
REJECTION LOOPS	:	2	2	2	2

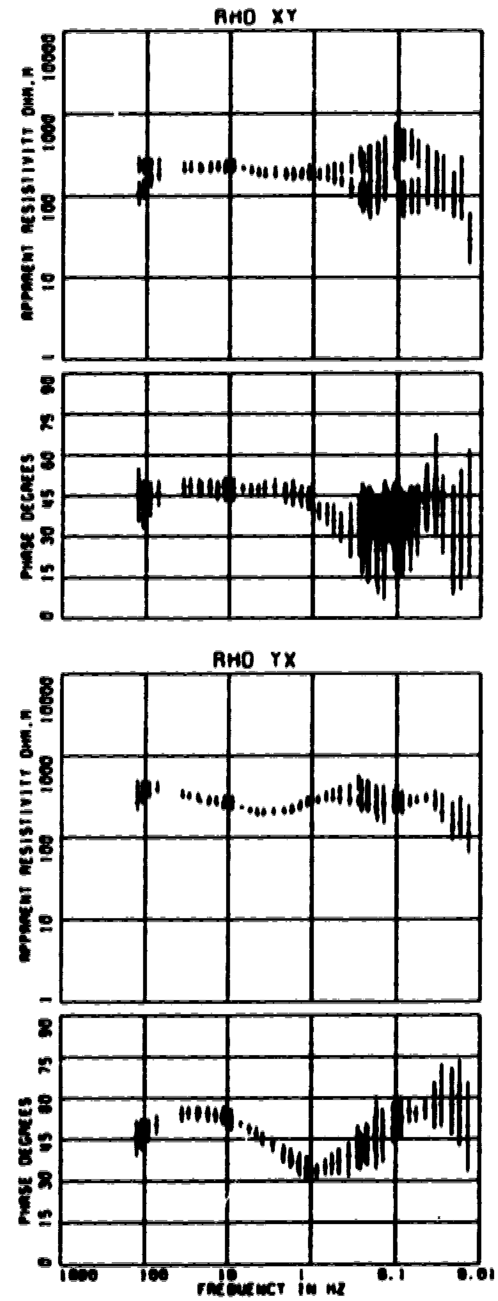

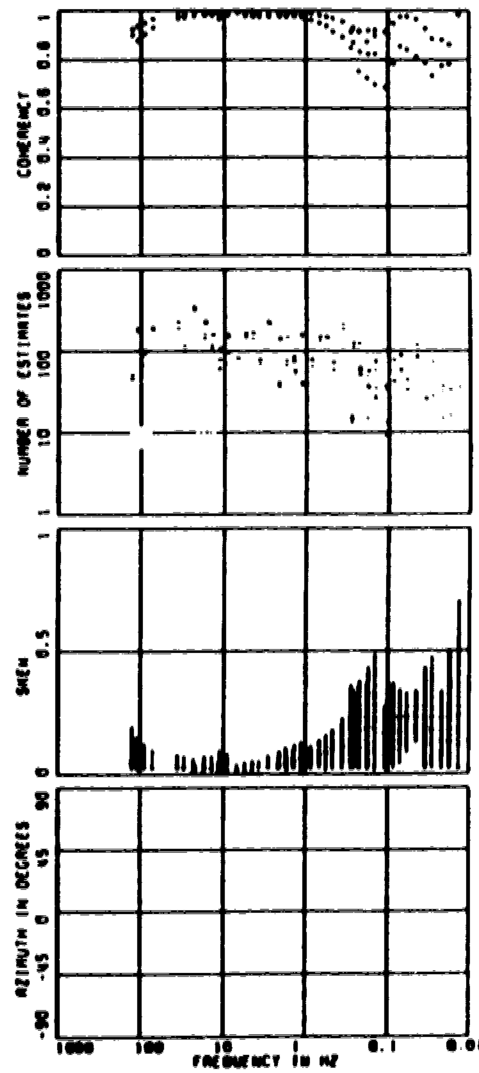

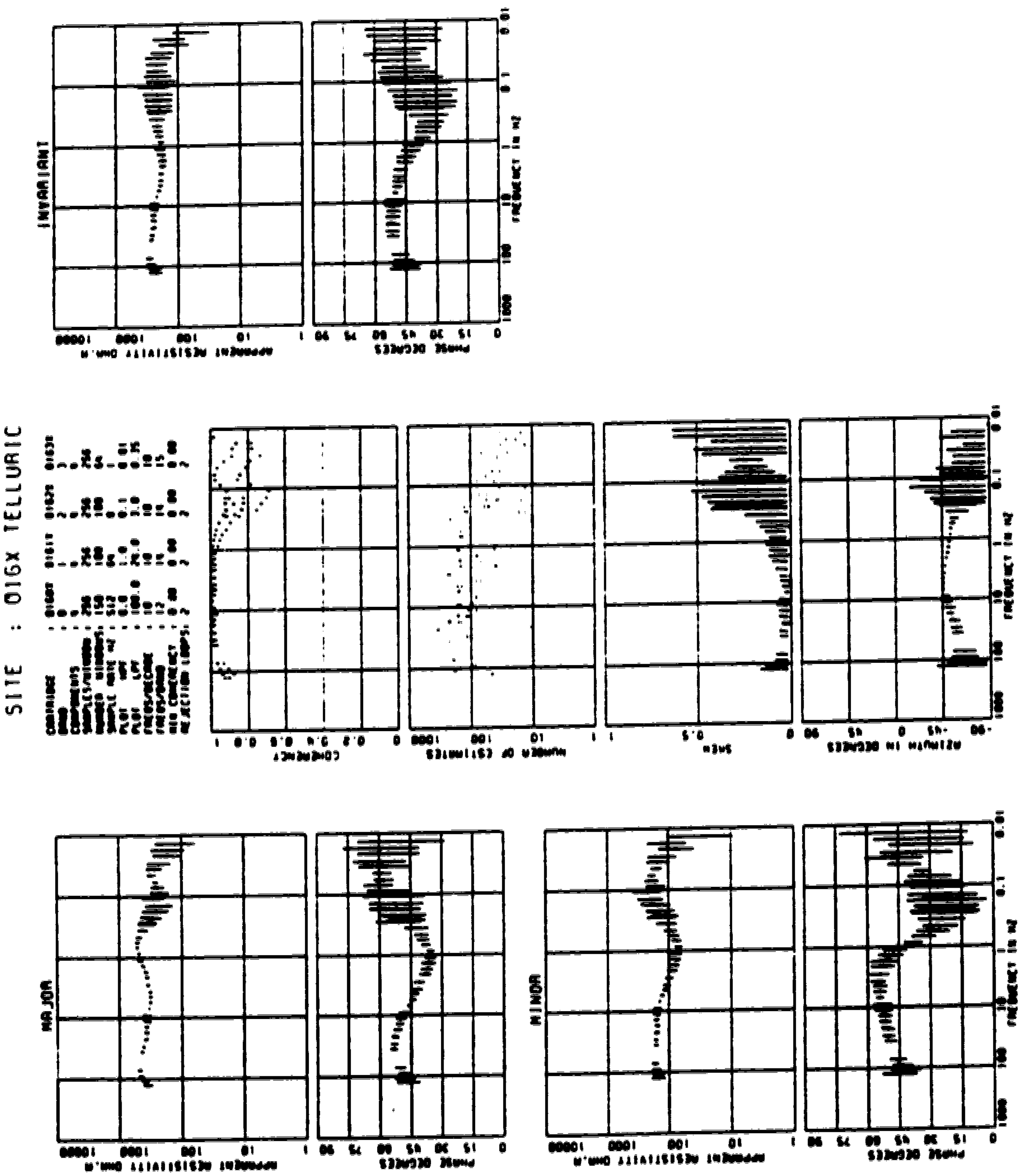
SITE : 0IGX TELLURIC
INVARIANT
MAJOR
MINOR

SITE : 017X TELLURIC

CARTRIDGE	: 0170X	0171X	0172X	0173X
BAND	: 0	1	2	3
COMPONENTS	: 4	4	4	4
SAMPLES/WINDOW	: 256	256	256	256
NUMBER WINDOWS	: 100	100	100	31
SAMPLE RATE HZ	: 512	64	8	1
PLOT HPF	: 8.0	1.0	0.1	0.01
PLOT LPF	: 100.0	24.0	3.0	0.35
FREQS/DECADE	: 10	10	10	10
FREQS/BAND	: 12	14	14	15
MIN COHERENCY	: 0.00	0.00	0.00	0.00
REJECTION LOOPS	: 2	2	2	2

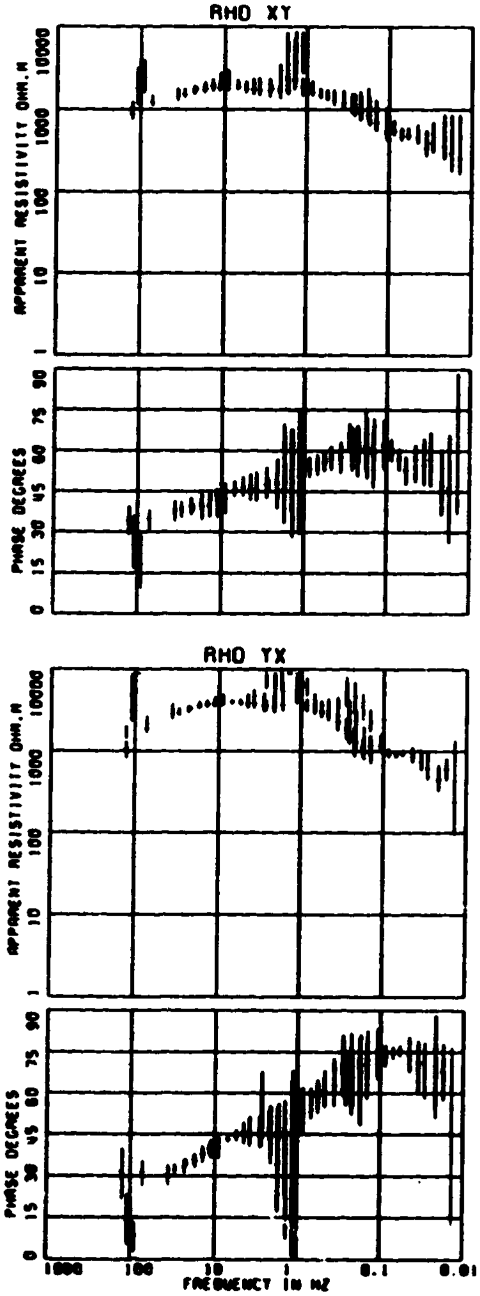

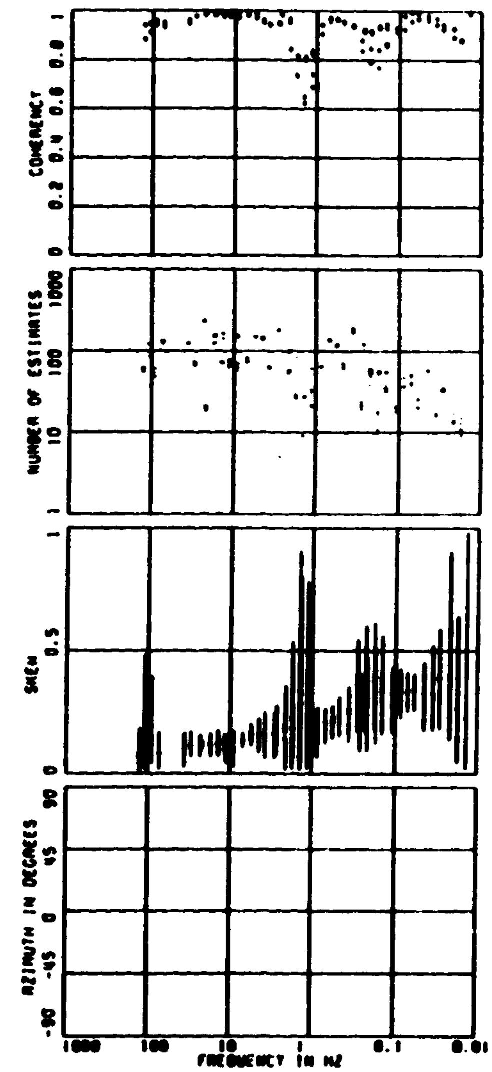

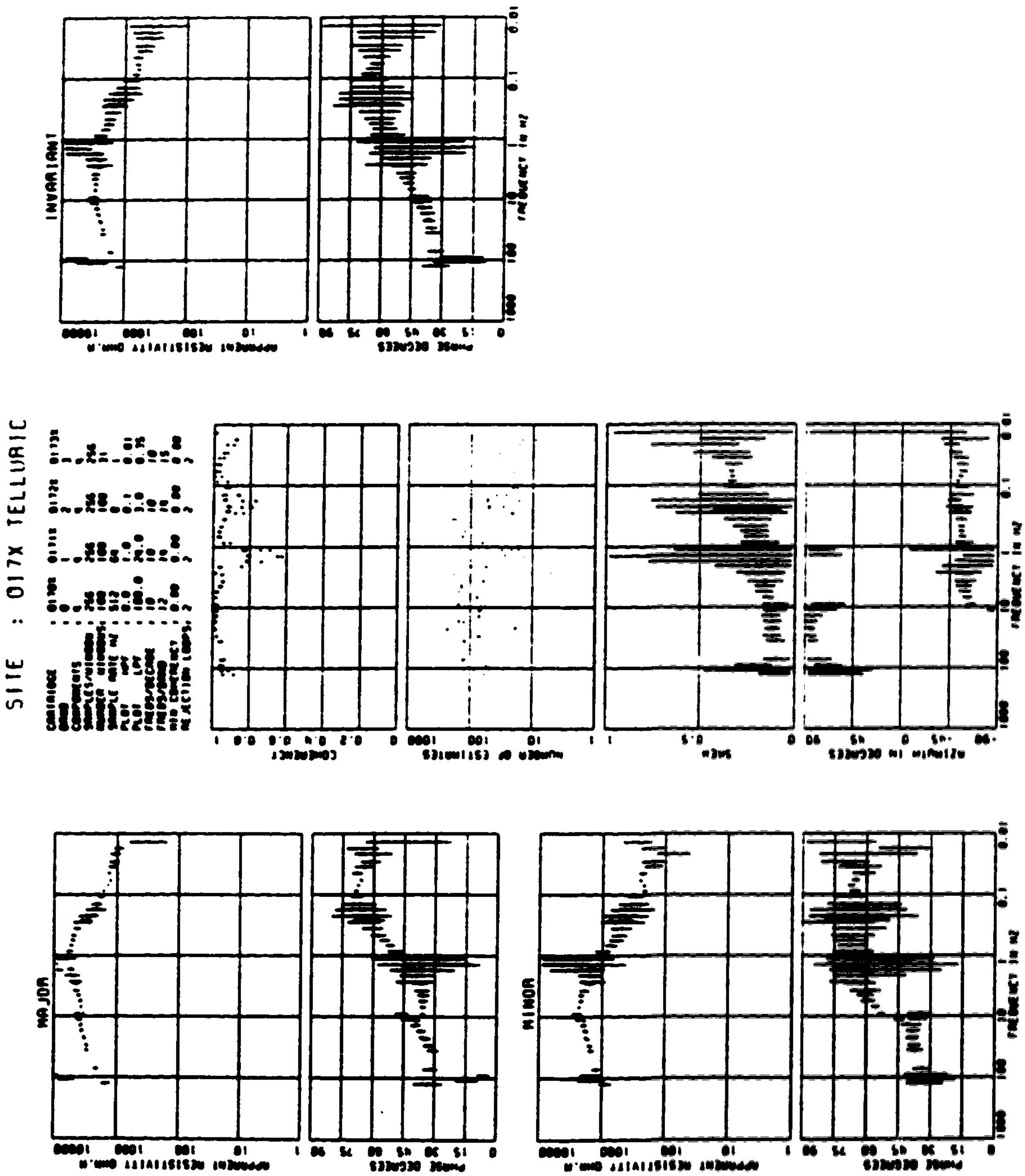
SITE : 017X TELLURIC
INVARIANT
MAJOR
MINOR
APPARENT RESISTIVITY OHM.M
PHASE DEGREES
FREQUENCY IN HZ
COHERENCE
NUMBER OF ESTIMATES
SKEW
AZIMUTH IN DEGREES

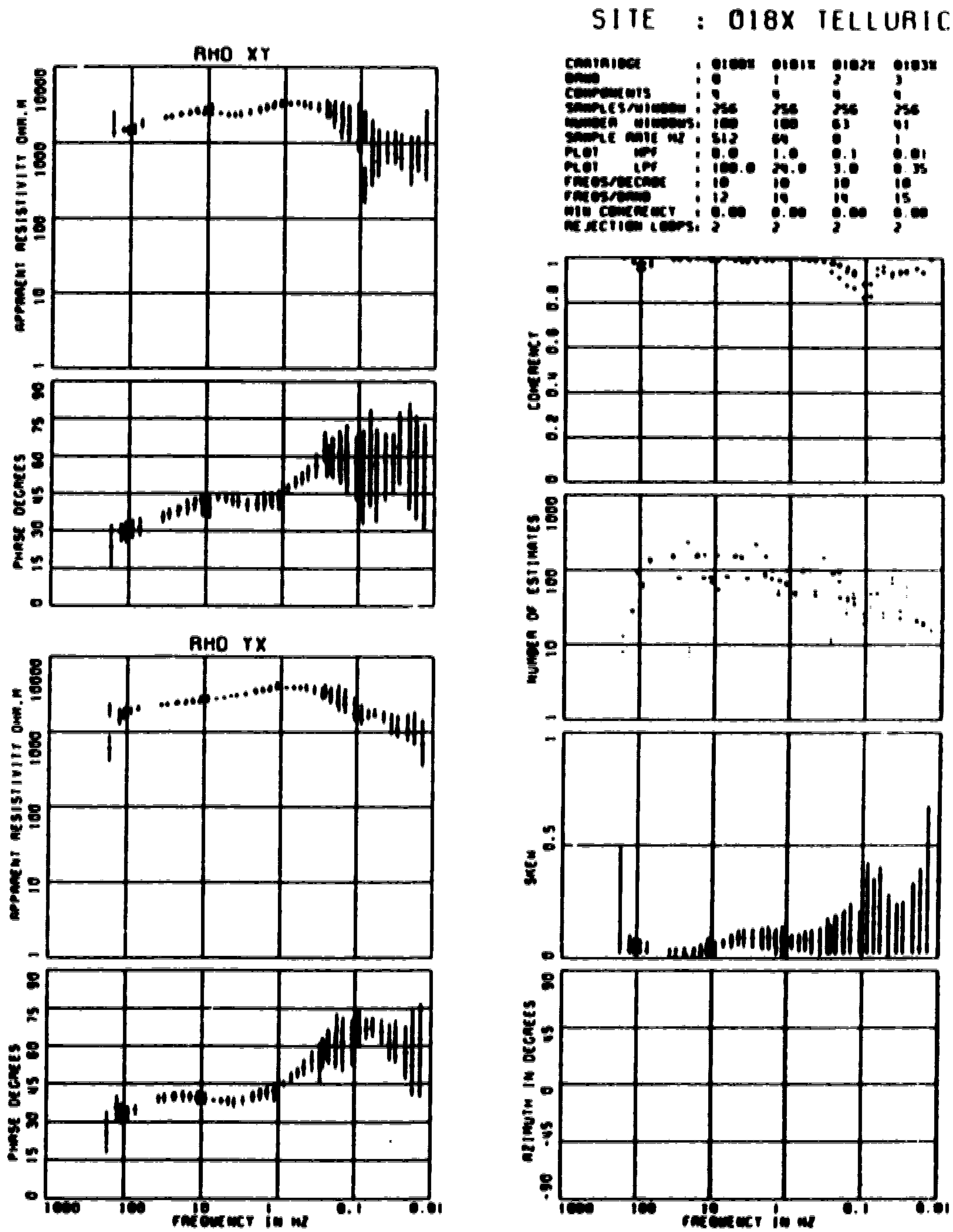
SITE : 018X TELLURIC
CARTRIDGE : 0100X 0101X 0102X 0103X
BAND : 0 1 2 3
COMPONENTS : 4 4 4 4
SAMPLES/WINDOW : 256 256 256 256
NUMBER WINDOWS: 100 100 63 41
SAMPLE RATE HZ : 512 64 8 1
PLOT HPF : 0.0 1.0 0.1 0.01
PLOT LPF : 100.0 24.0 3.0 0.35
FREQS/DECADE : 10 10 10 10
FREQS/BAND : 12 14 14 15
MIN COHERENCY : 0.00 0.00 0.00 0.00
REJECTION LOOPS: 2 2 2 2
RHO XY
APPARENT RESISTIVITY OHM.M
PHASE DEGREES
RHO YX
COHERENCY
NUMBER OF ESTIMATES
SKEW
AZIMUTH IN DEGREES
FREQUENCY IN HZ

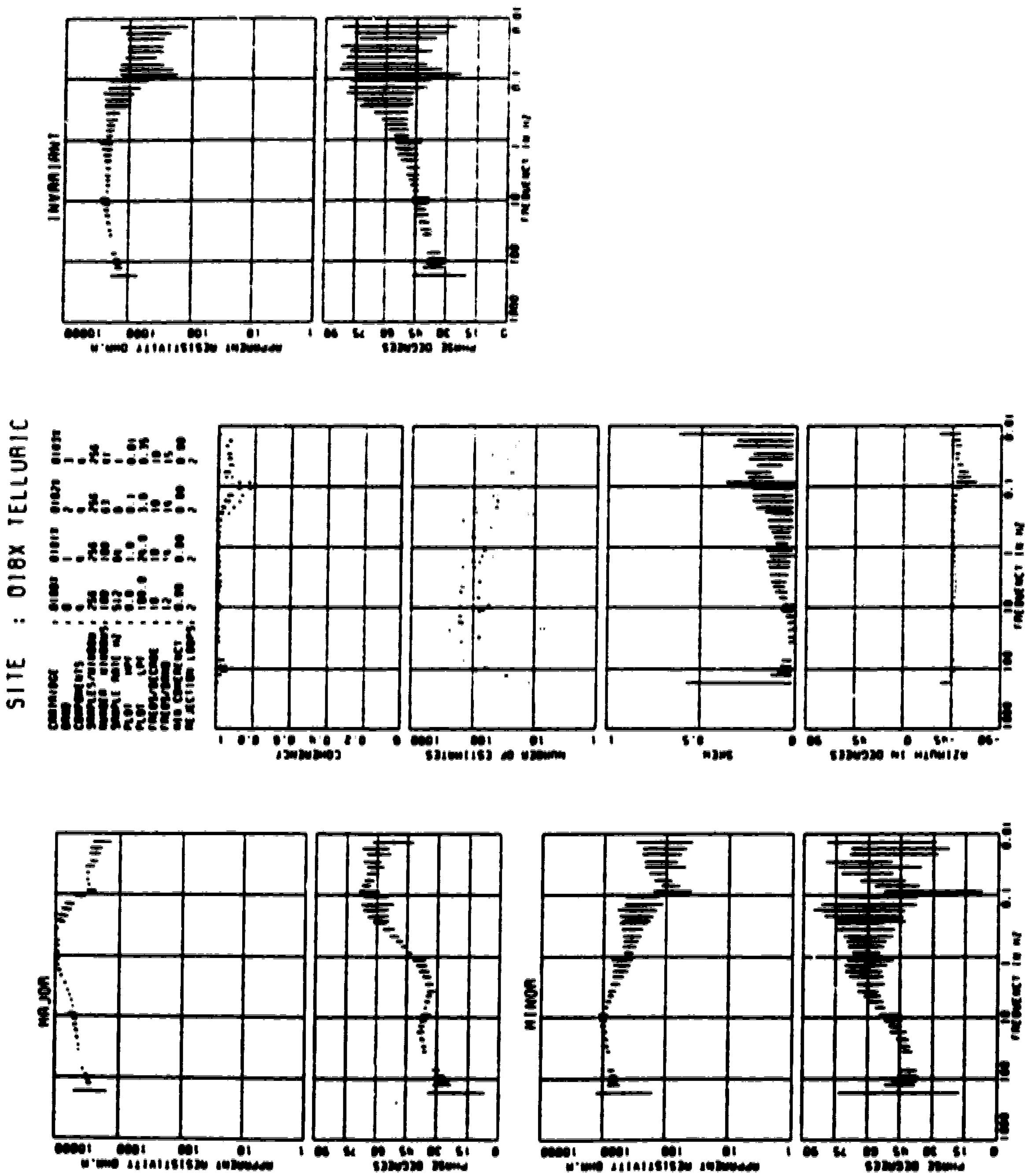
INVARIANT
SITE : 018X TELLURIC
MAJOR
MINOR

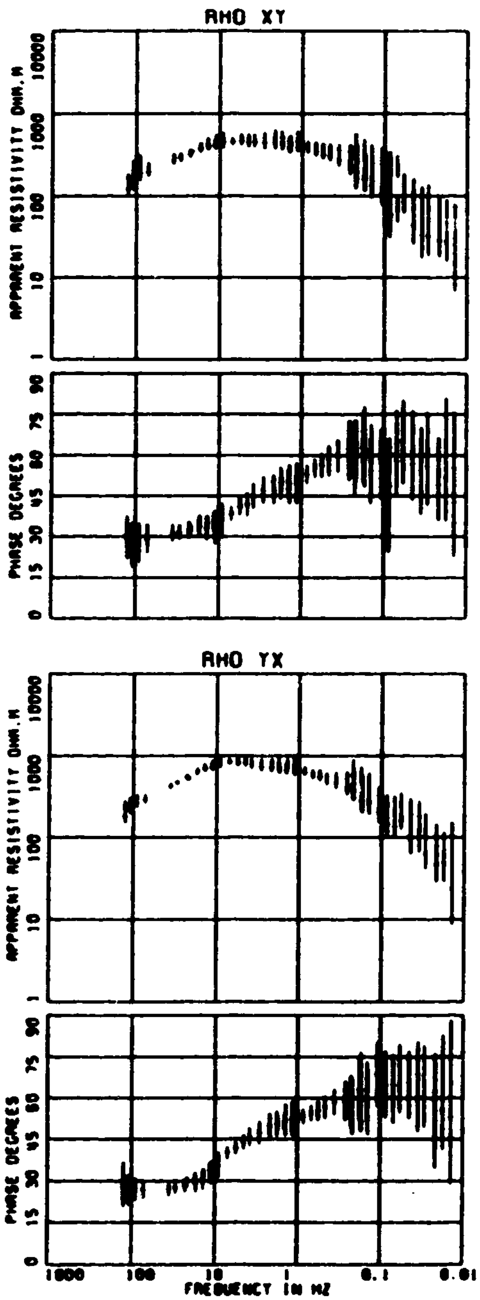

SITE : 019X TELLURIC

CARTRIDGE	:	0190X	0191X	0192X	0193X
BAND	:	0	1	2	3
COMPONENTS	:	4	4	4	4
SAMPLES/WINDOW	:	256	256	256	256
NUMBER WINDOWS	:	100	100	100	60
SAMPLE RATE HZ	:	512	64	8	1
PLOT HPF	:	8.0	1.0	0.1	0.01
PLOT LPF	:	100.0	24.0	3.0	0.35
FREQS/DECADE	:	10	10	10	10
FREQS/BAND	:	12	14	14	15
MIN COHERENCY	:	0.00	0.00	0.00	0.00
REJECTION LOOPS	:	2	2	2	2

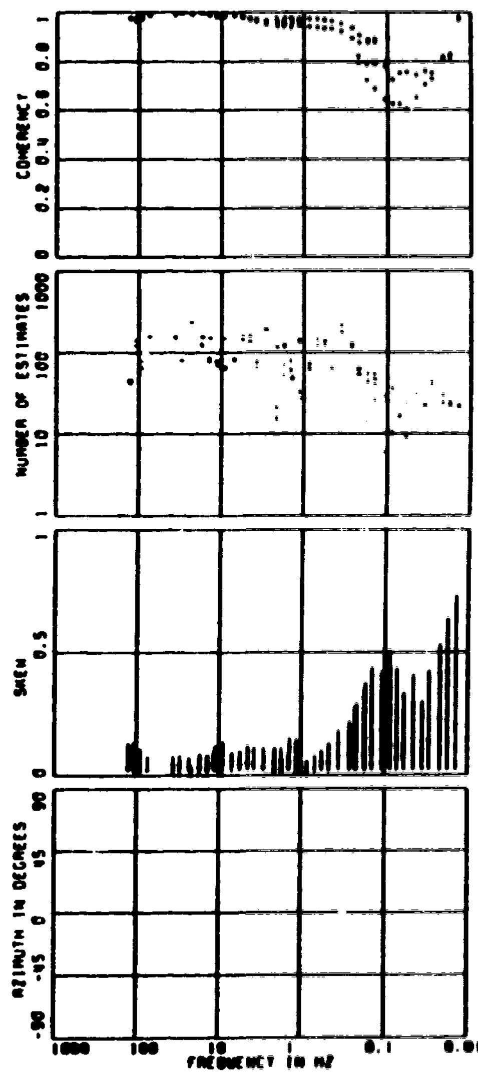

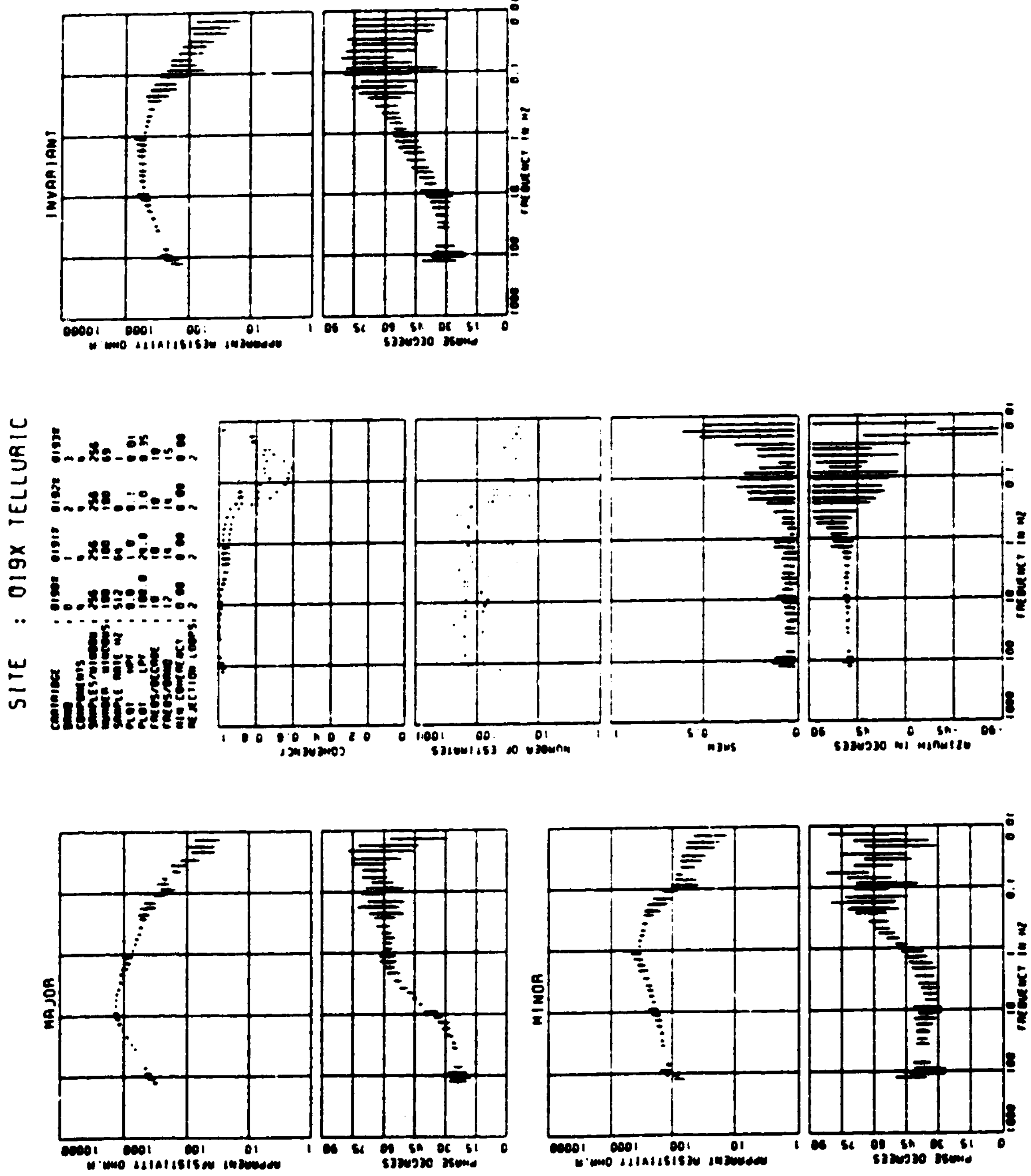
SITE : 019X TELLURIC
INVARIANT
MAJOR
MINOR
APPARENT RESISTIVITY OHM.M
PHASE DEGREES
FREQUENCY IN HZ
COHERENCE
NUMBER OF ESTIMATES
SKEW
AZIMUTH IN DEGREES

SITE : 020X TELLURIC

CARTRIDGE :	0200X	0201X	0202X	0203X
BAND :	0	1	2	3
COMPONENTS :	4	4	4	4
SAMPLES/WINDOW :	256	256	256	256
NUMBER WINDOWS:	85	100	100	41
SAMPLE RATE HZ :	512	64	8	1
PLOT HPF :	8.0	1.0	0.1	0.01
PLOT LPF :	100.0	24.0	3.0	0.35
FREQS/DECADE :	10	10	10	10
FREQS/BAND :	12	14	14	15
MIN COHERENCY :	0.00	0.00	0.00	0.00
REJECTION LOOPS:	2	2	2	2

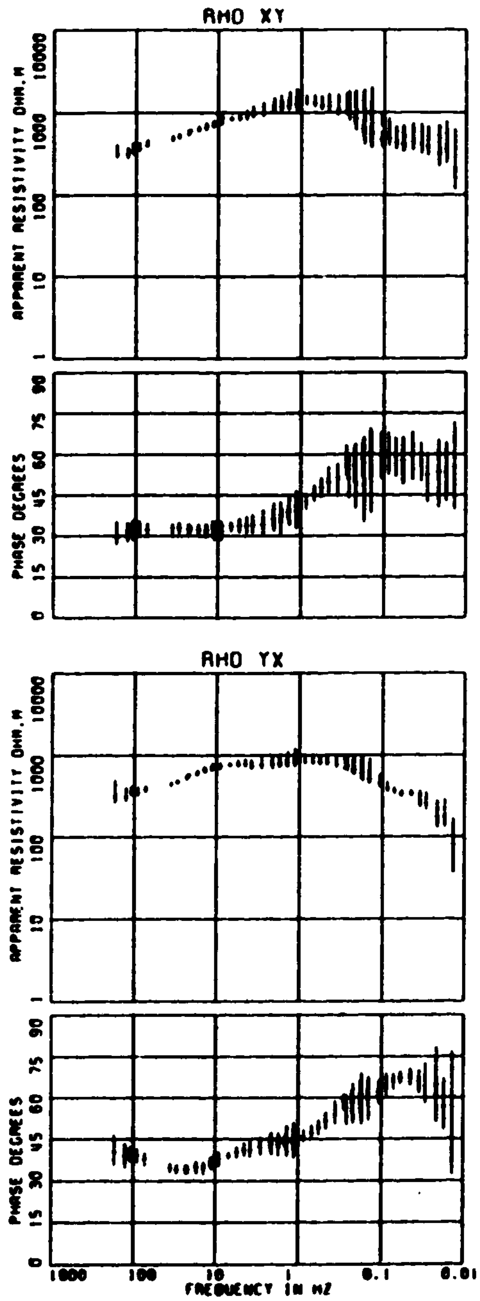

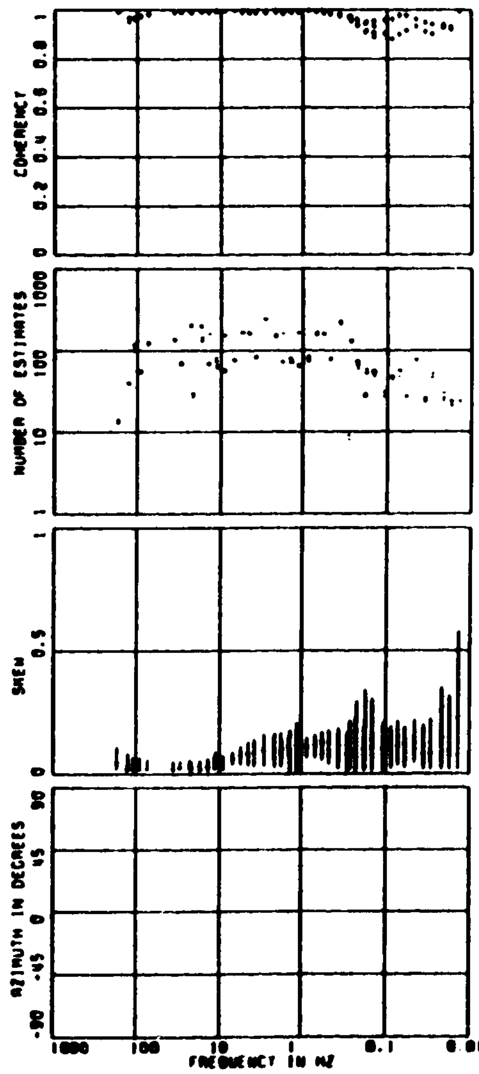

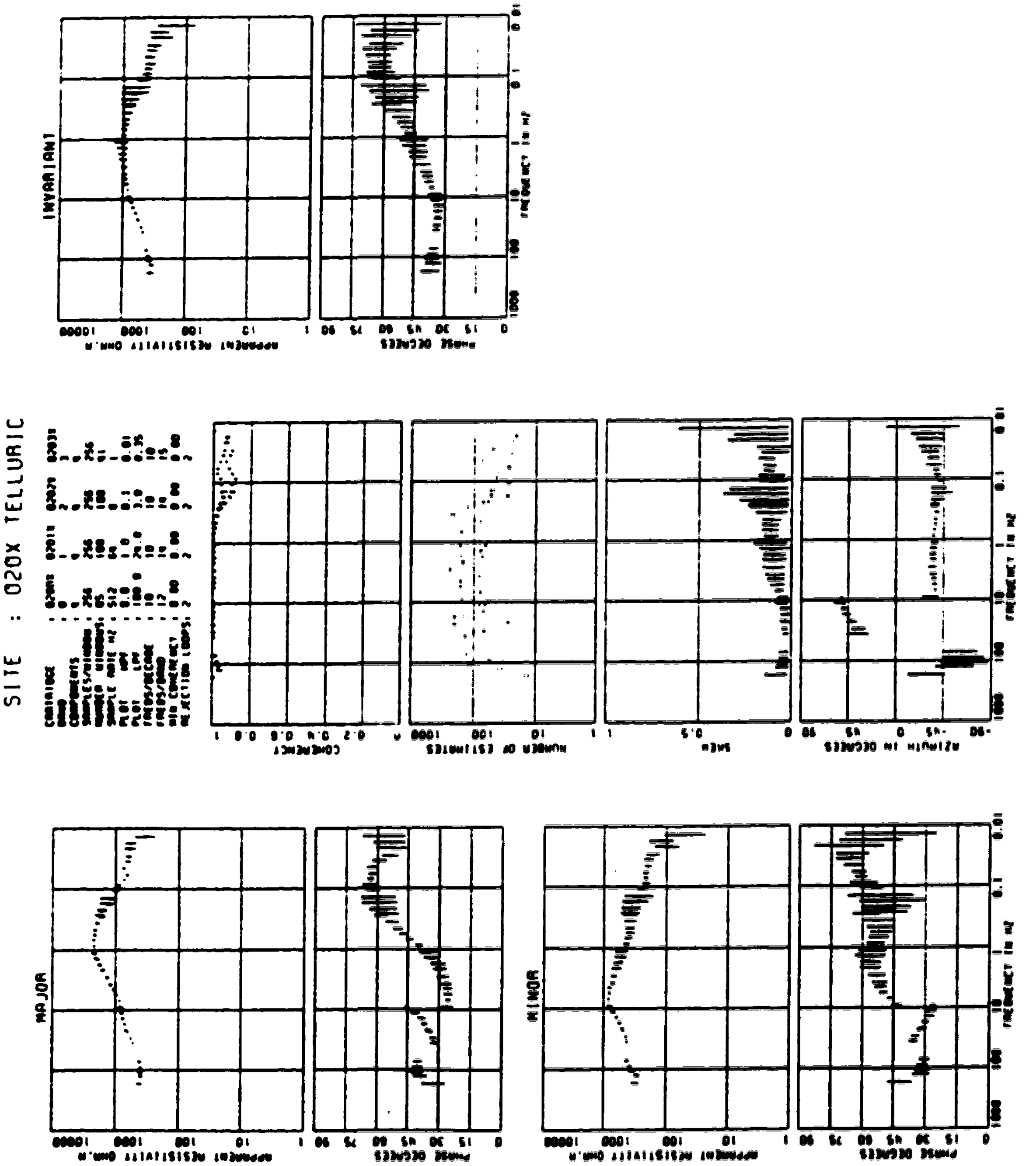
SITE : 020X TELLURIC
INVARIANT
MAJOR
MINOR
APPARENT RESISTIVITY OHM.M
PHASE DEGREES
FREQUENCY IN HZ
COHERENCY
NUMBER OF ESTIMATES
SKEW
AZIMUTH IN DEGREES

SITE : 021X TELLURIC

CARTRIDGE	: 0210X	0211X	0212X	0213X
BAND	: 0	1	2	3
COMPONENTS	: 4	4	4	4
SAMPLES/WINDOW	: 256	256	256	256
NUMBER WINDOWS	: 100	100	100	62
SAMPLE RATE HZ	: 512	64	8	1
PLOT HPF	: 8.0	1.0	0.1	0.01
PLOT LPF	: 100.0	24.0	3.0	0.35
FREQS/DECADE	: 10	10	10	10
FREQS/BAND	: 12	14	14	15
MIN COHERENCY	: 0.00	0.00	0.00	0.00
REJECTION LOOPS	: 2	2	2	2

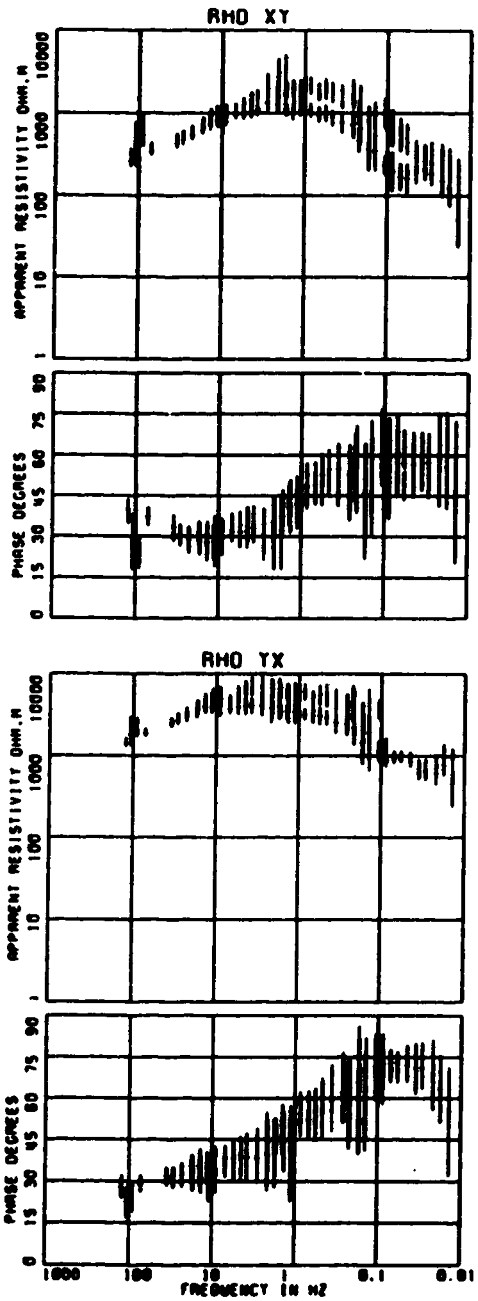

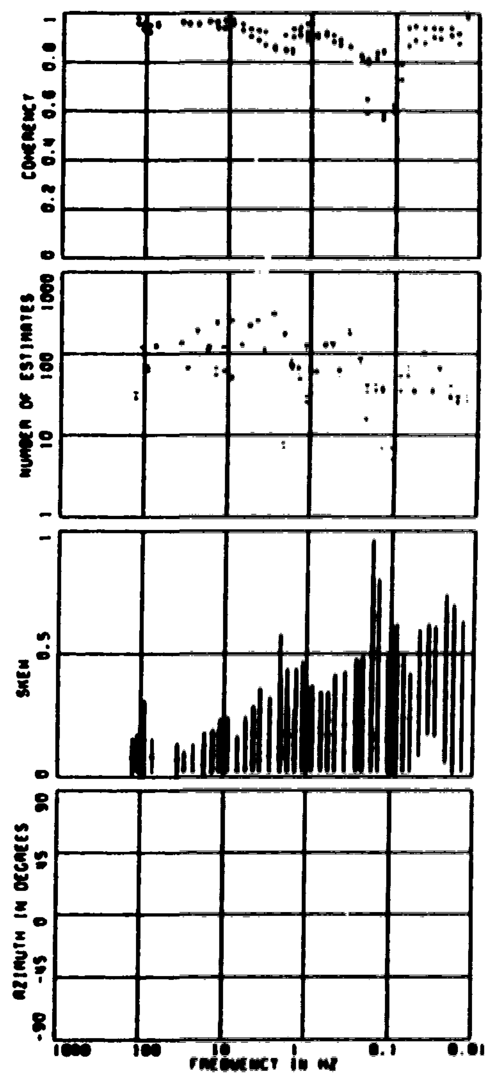

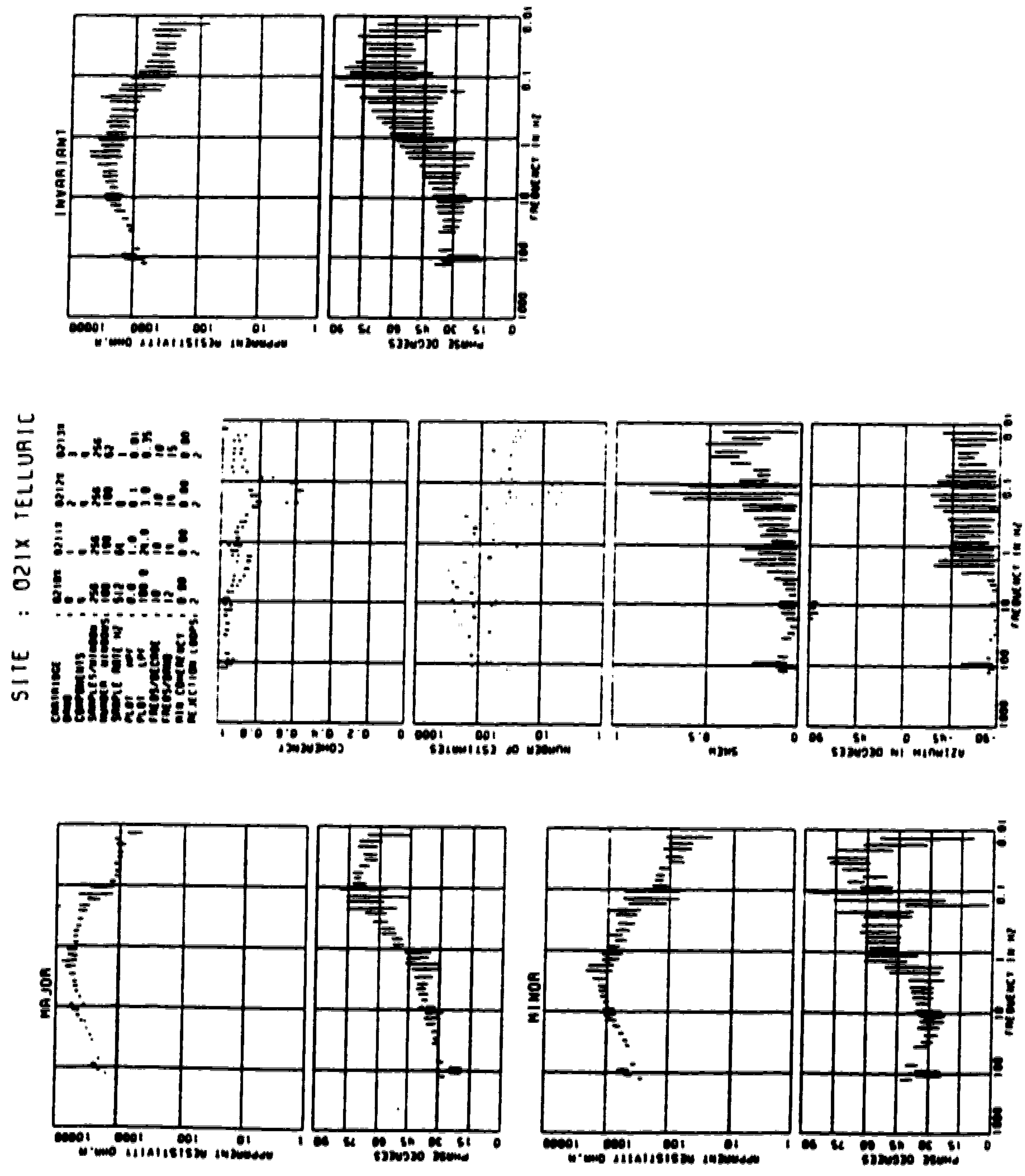
INVARIANT
SITE : O21X TELLURIC
MAJOR
MINOR
APPARENT RESISTIVITY OHM.M
PHASE DEGREES
COHERENCY
NUMBER OF ESTIMATES
SKEW
AZIMUTH IN DEGREES
FREQUENCY IN HZ

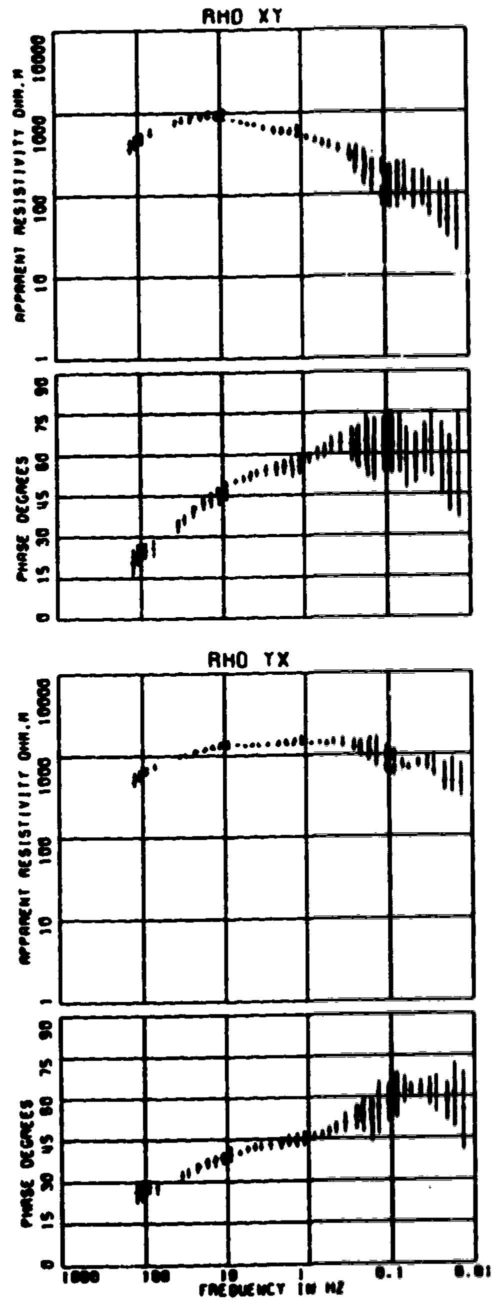

SITE : 022X TELLURIC

CARTRIDGE	:	0220X	0221X	0222X	0223X
BAND	:	0	1	2	3
COMPONENTS	:	4	4	4	4
SAMPLES/WINDOW	:	256	256	256	256
NUMBER WINDOWS	:	100	100	99	53
SAMPLE RATE HZ	:	512	64	8	1
PLOT HPF	:	8.0	1.0	0.1	0.01
PLOT LPF	:	100.0	24.0	3.0	0.35
FREQS/DECADE	:	10	10	10	10
FREQS/BAND	:	12	14	14	15
MIN COHERENCY	:	0.00	0.00	0.00	0.00
REJECTION LOOPS	:	2	2	2	2

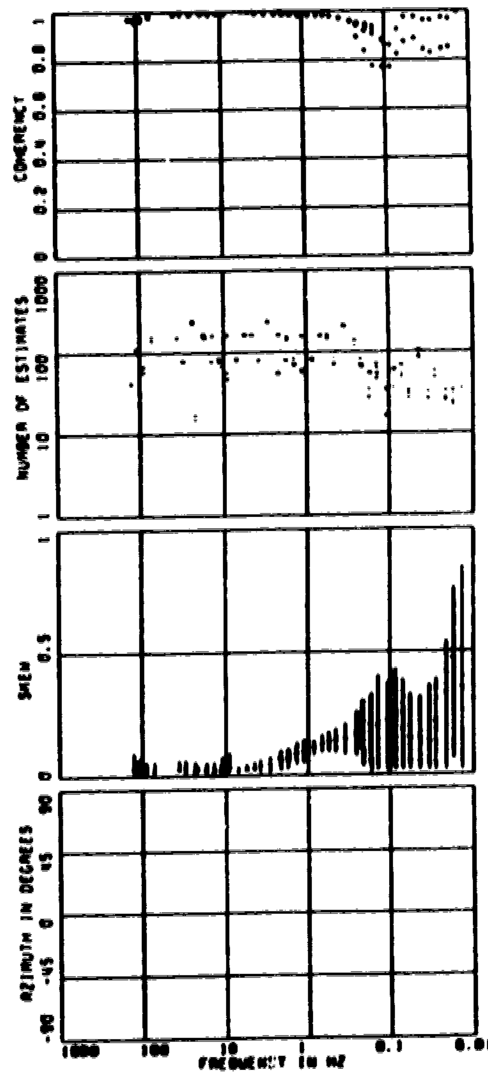

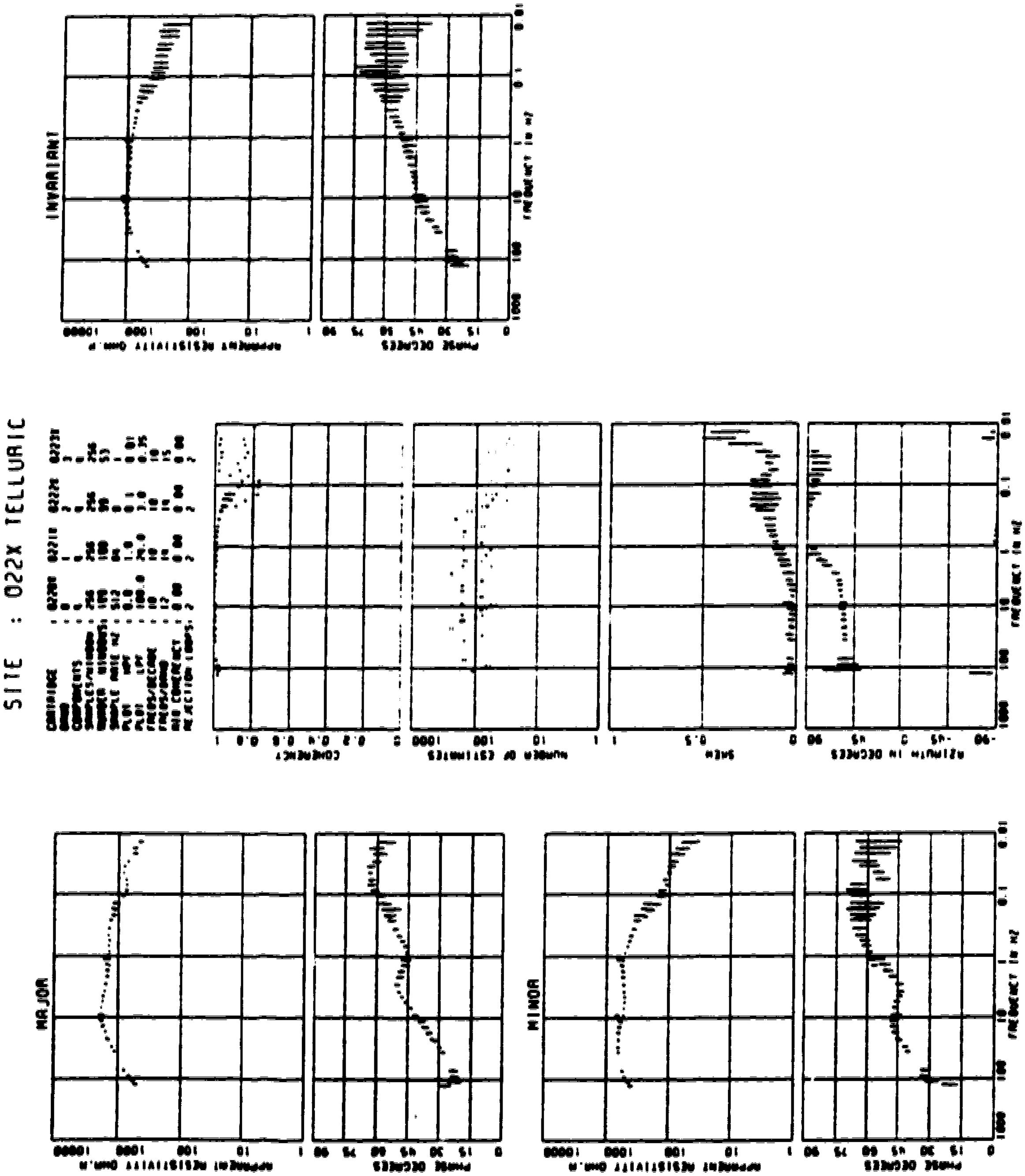
INVARIANT
SITE : 022X TELLURIC
MAJOR
MINOR

SITE : 023X TELLURIC

CARTRIDGE	: 0230X	0231X	0232X	0233X
BAND	: 0	1	2	3
COMPONENTS	: 4	4	4	4
SAMPLES/WINDOW	: 256	256	256	256
NUMBER WINDOWS	: 100	100	66	82
SAMPLE RATE HZ	: 512	64	8	1
PLOT HPF	: 8.0	1.0	0.1	0.01
PLOT LPF	: 100.0	24.0	3.0	0.35
FREQS/DECADE	: 10	10	10	10
FREQS/BAND	: 12	14	14	15
MIN COHERENCY	: 0.80	0.80	0.80	0.80
REJECTION LOOPS	: 2	2	2	2

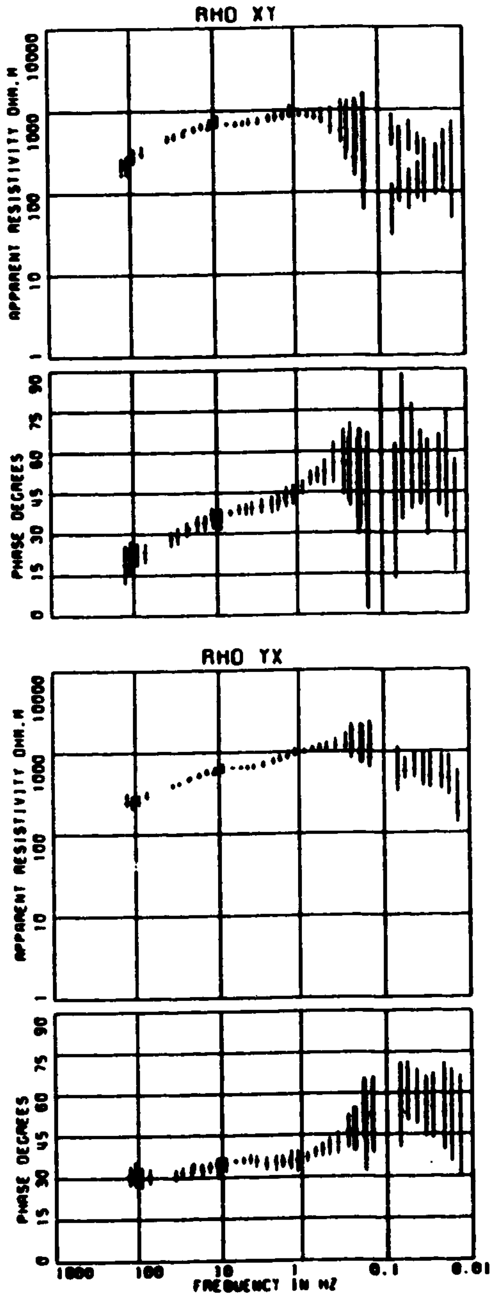

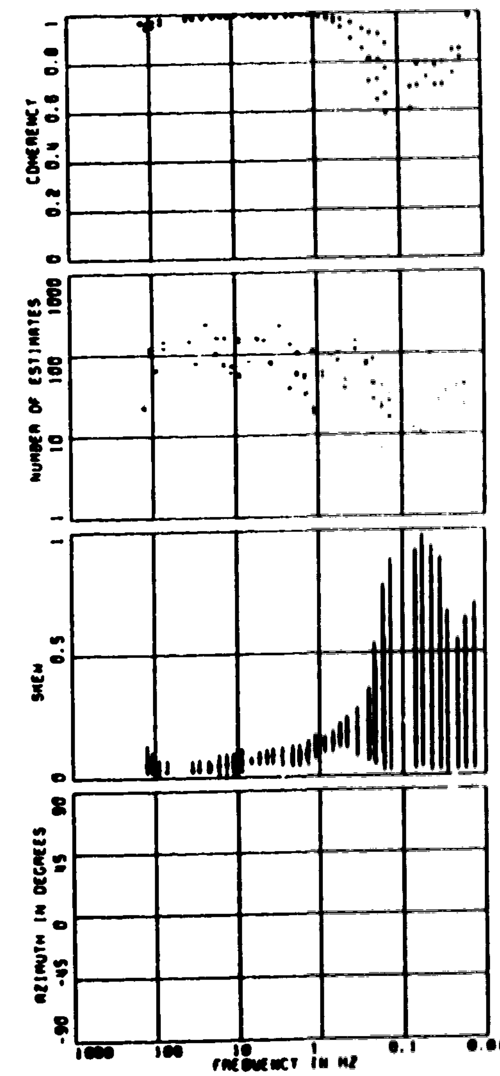

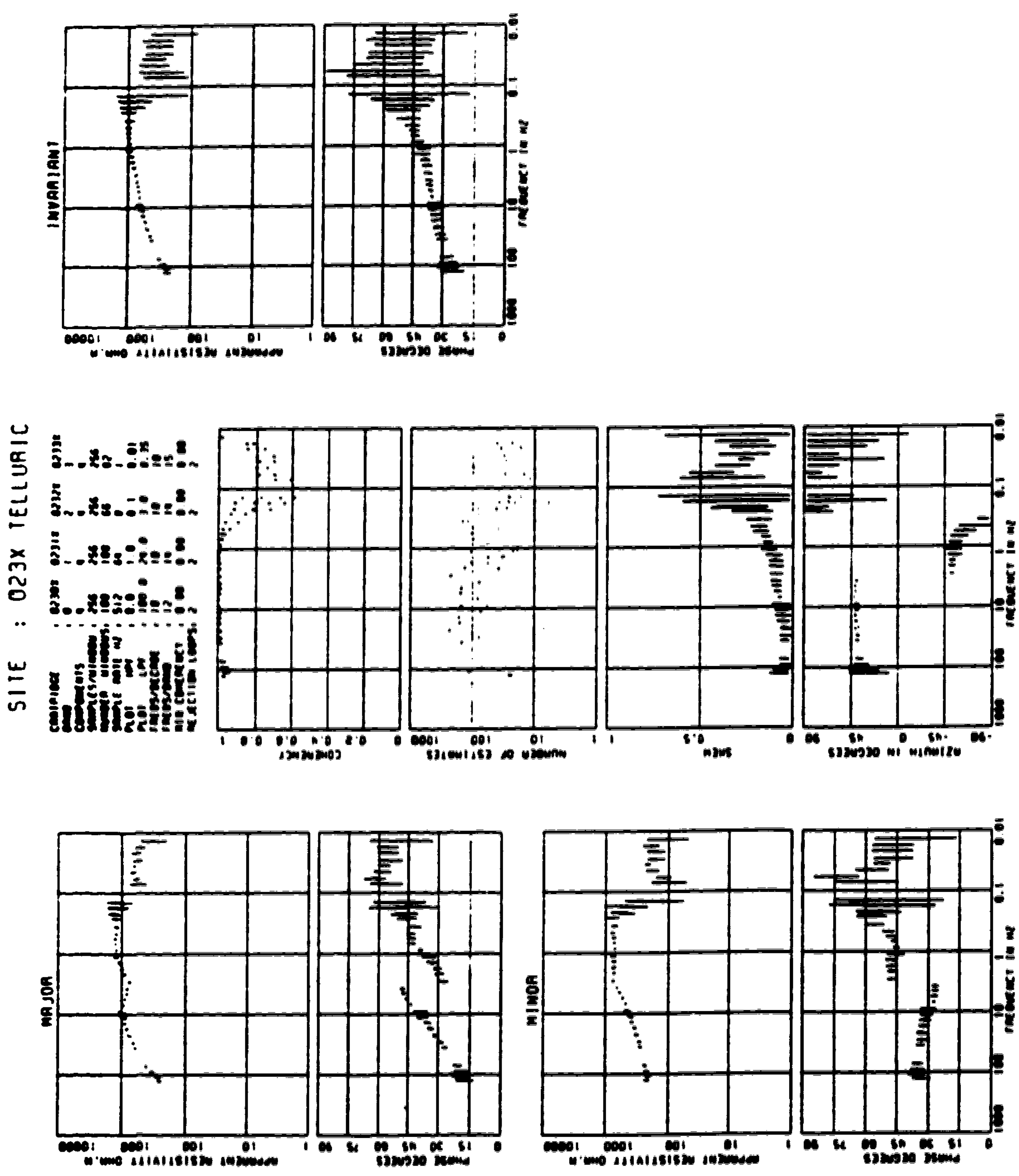
SITE : O23X TELLURIC
INVARIANT
MAJOR
MINOR
APPARENT RESISTIVITY OHM.M
PHASE DEGREES
FREQUENCY IN HZ
COHERENCY
NUMBER OF ESTIMATES
SKEW
AZIMUTH IN DEGREES

SITE : 024X TELLURIC

CARTRIDGE	:	0240X	0241X	0242X	0243X
BAND	:	0	1	2	3
COMPONENTS	:	4	4	4	4
SAMPLES/WINDOW	:	256	256	256	256
NUMBER WINDOWS	:	100	100	100	70
SAMPLE RATE HZ	:	512	64	8	1
PLOT HPF	:	8.0	1.0	0.1	0.01
PLOT LPF	:	100.0	24.0	3.0	0.35
FREQS/DECADE	:	10	10	10	10
FREQS/BAND	:	12	14	14	15
MIN COHERENCY	:	0.00	0.00	0.00	0.00
REJECTION LOOPS	:	2	2	2	2

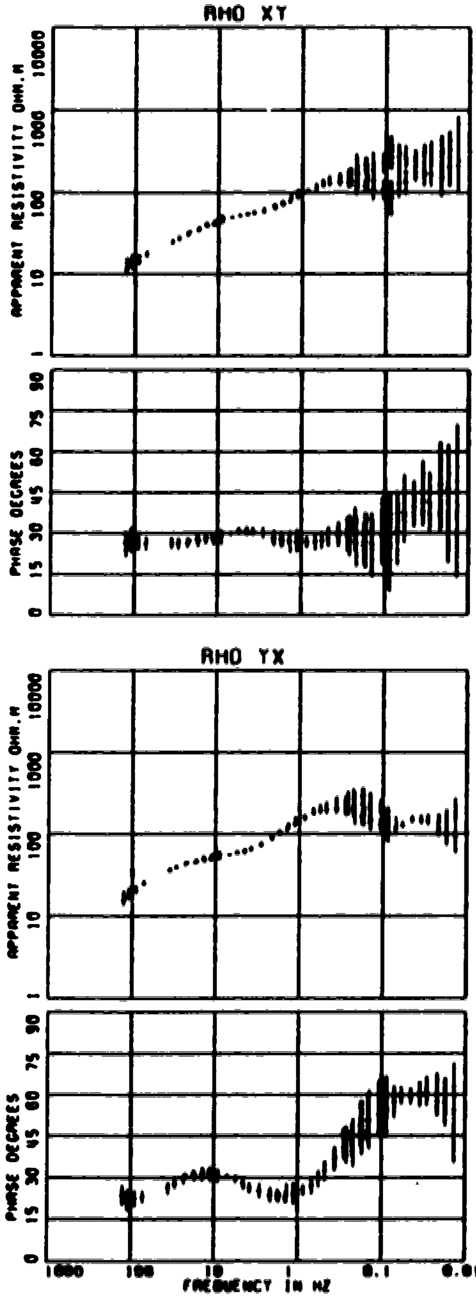

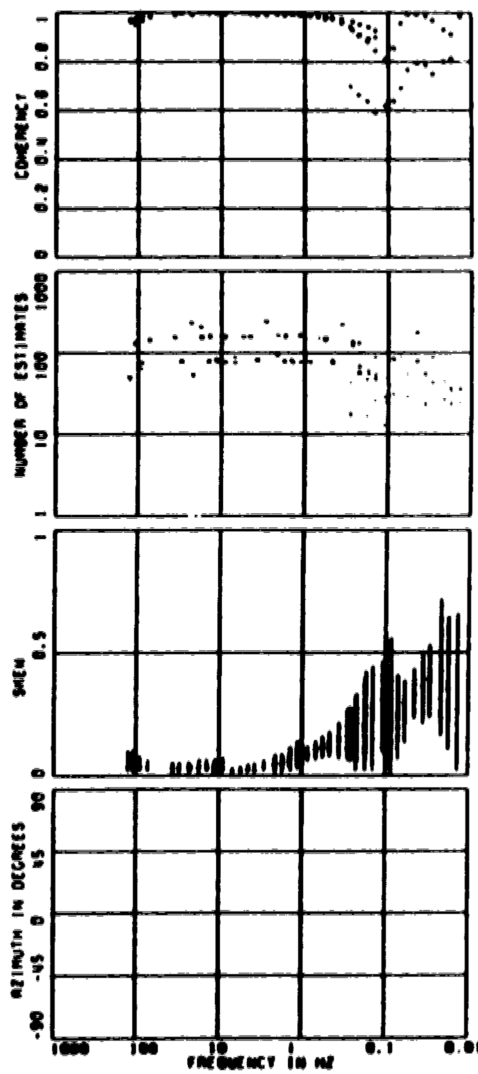

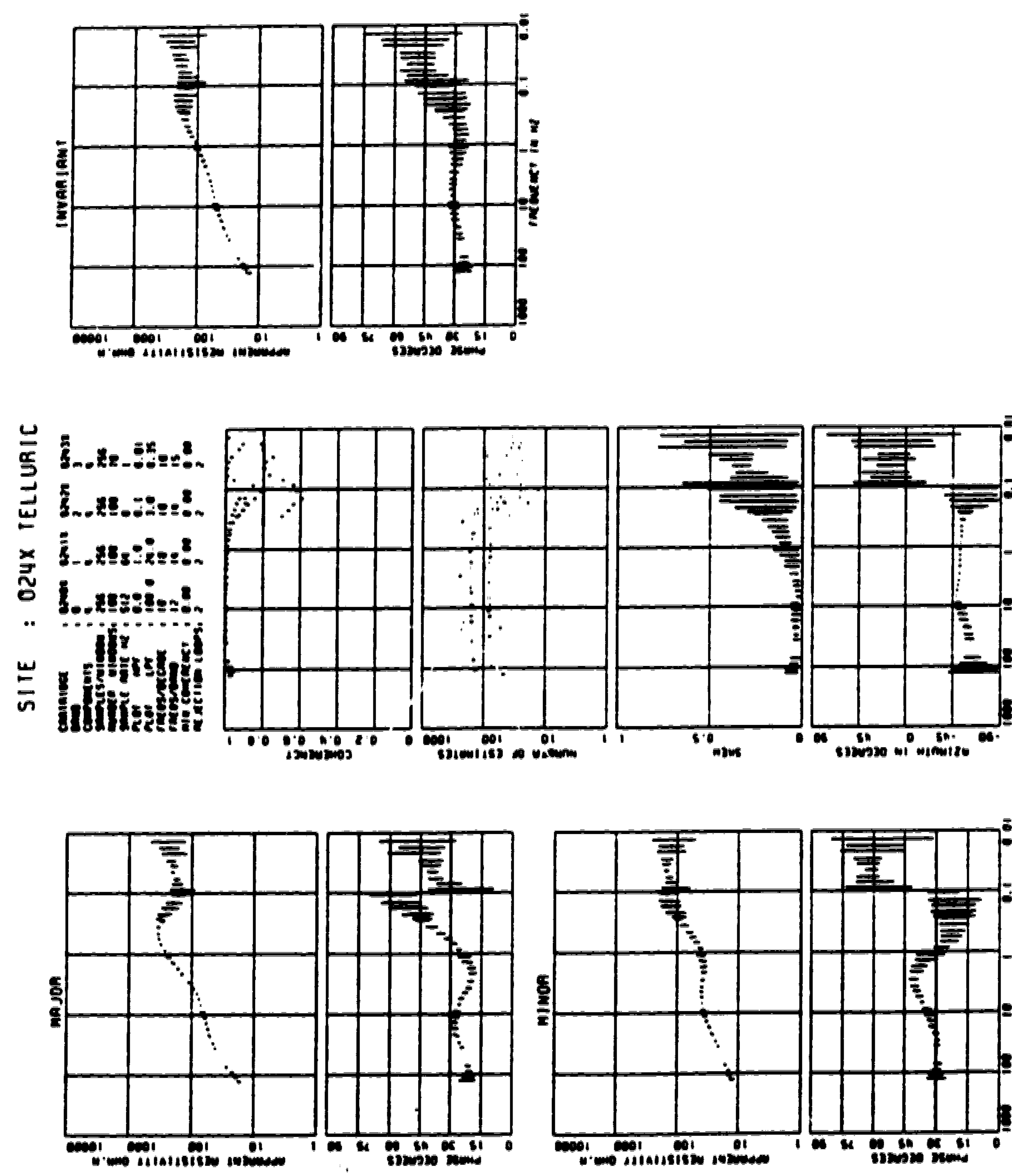

INVARIANT
SITE : 024X TELLURIC
MAJOR
MINOR

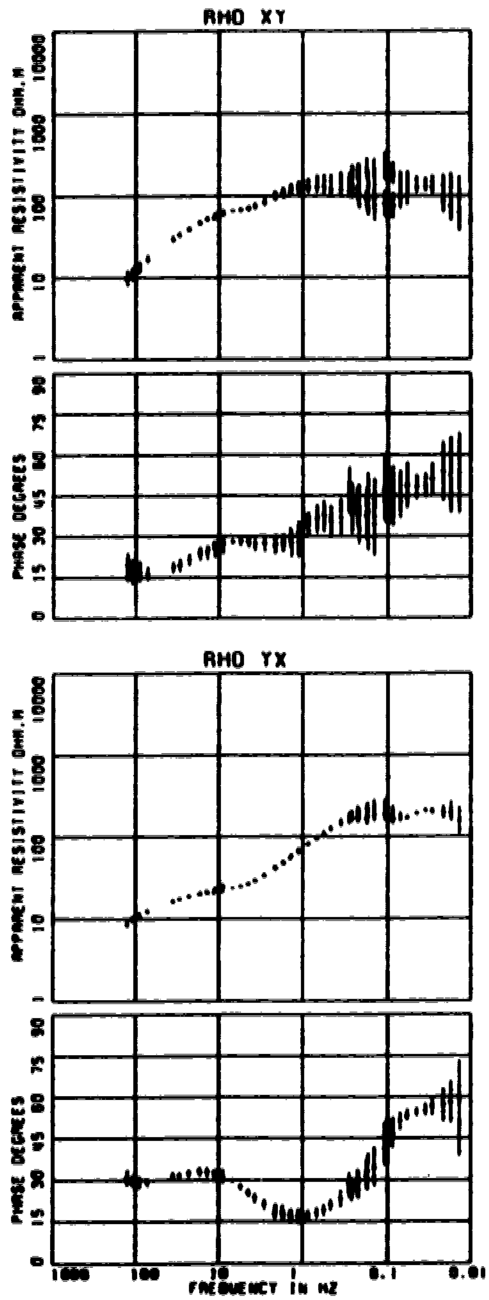

SITE : 025X TELLURIC

CARTRIDGE	:	0250X	0251X	0252X	0253X
BAND	:	0	1	2	3
COMPONENTS	:	4	4	4	4
SAMPLES/WINDOW	:	256	256	256	256
NUMBER WINDOWS	:	100	100	100	61
SAMPLE RATE HZ	:	512	64	8	1
PLOT HPF	:	0.0	1.0	0.1	0.01
PLOT LPF	:	100.0	24.0	3.0	0.35
FREQS/DECADE	:	10	10	10	10
FREQS/BAND	:	12	14	14	15
MIN COHERENCY	:	0.00	0.00	0.00	0.00
REJECTION LOOPS	:	2	2	2	2

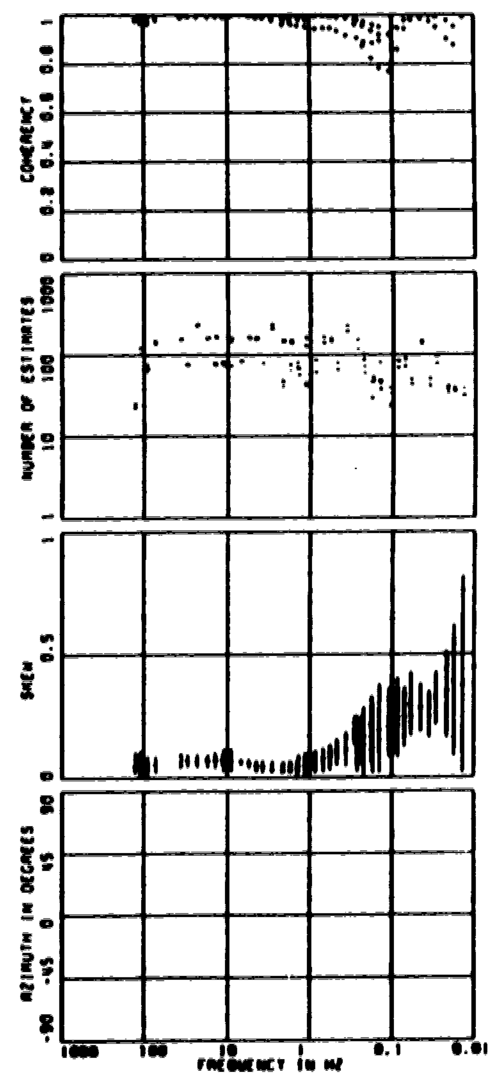

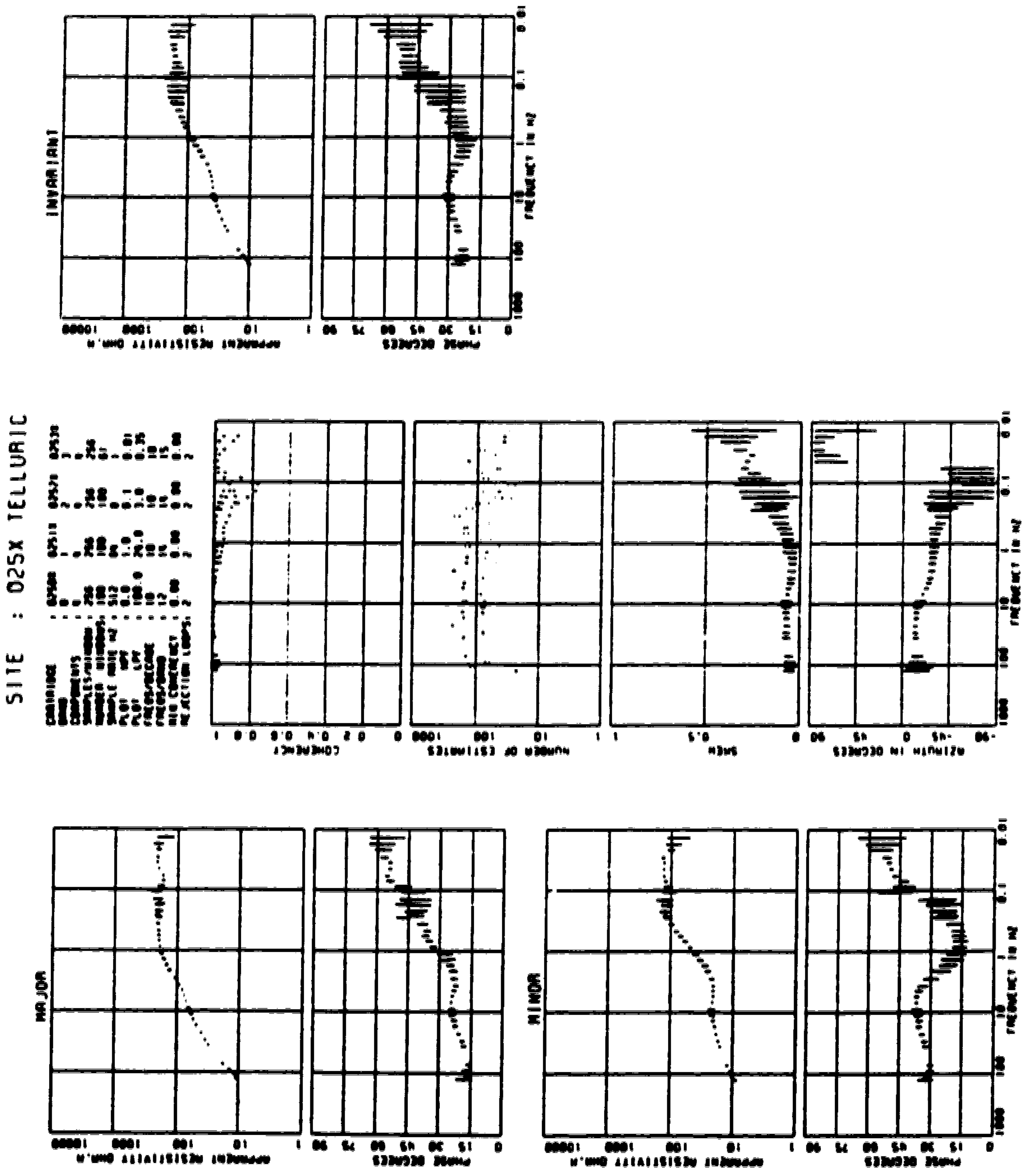
INVARIANT
SITE : 025X TELLURIC
MAJOR
MINOR

SITE : 026X TELLURIC

CARTRIDGE	: 0260X	0261X	0262X	0263X
BAND	: 0	1	[illegible]	3
COMPONENTS	: 4	4	4	4
SAMPLES/WINDOW	: 256	256	256	256
NUMBER WINDOWS	: 100	91	100	97
SAMPLE RATE HZ	: 512	64	8	1
PLOT HPF	: 8.0	1.0	0.1	0.01
PLOT LPF	: 100.0	24.0	3.0	0.35
FREQS/DECADE	: 10	10	10	10
FREQS/BAND	: 12	14	14	15
MIN COHERENCY	: 0.00	0.00	0.00	0.00
REJECTION LOOPS	: 2	2	2	2

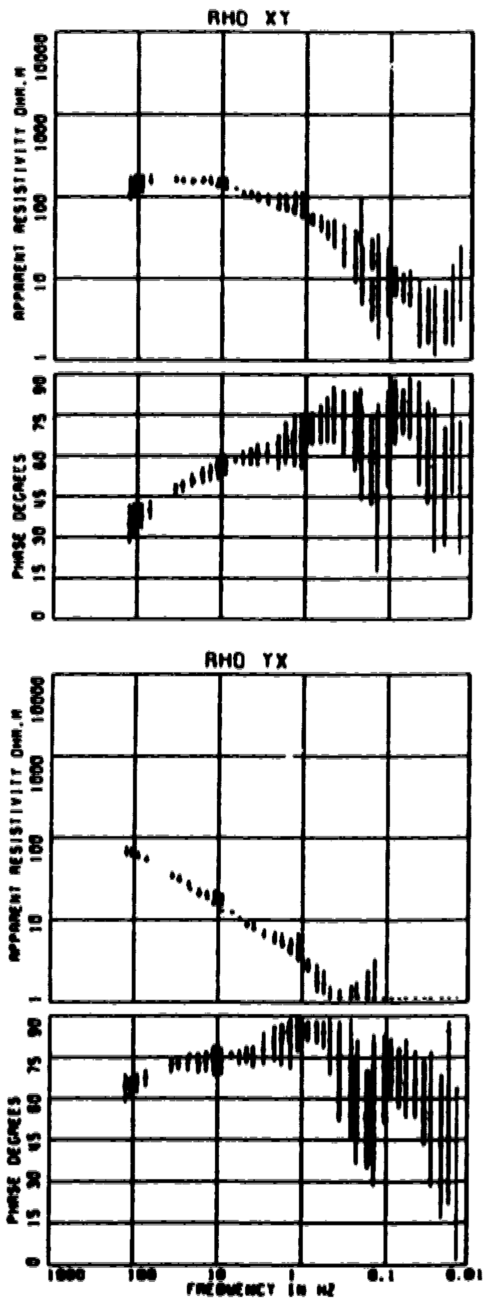

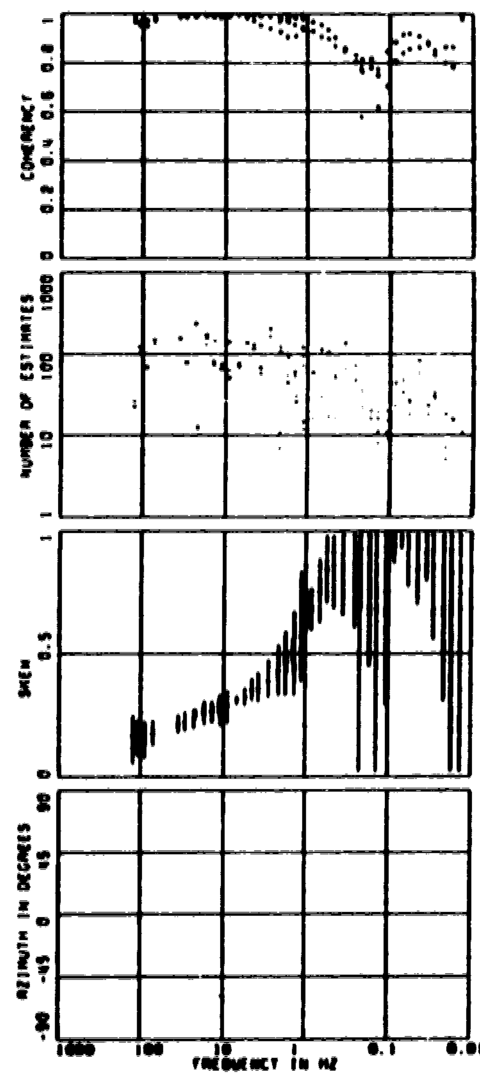

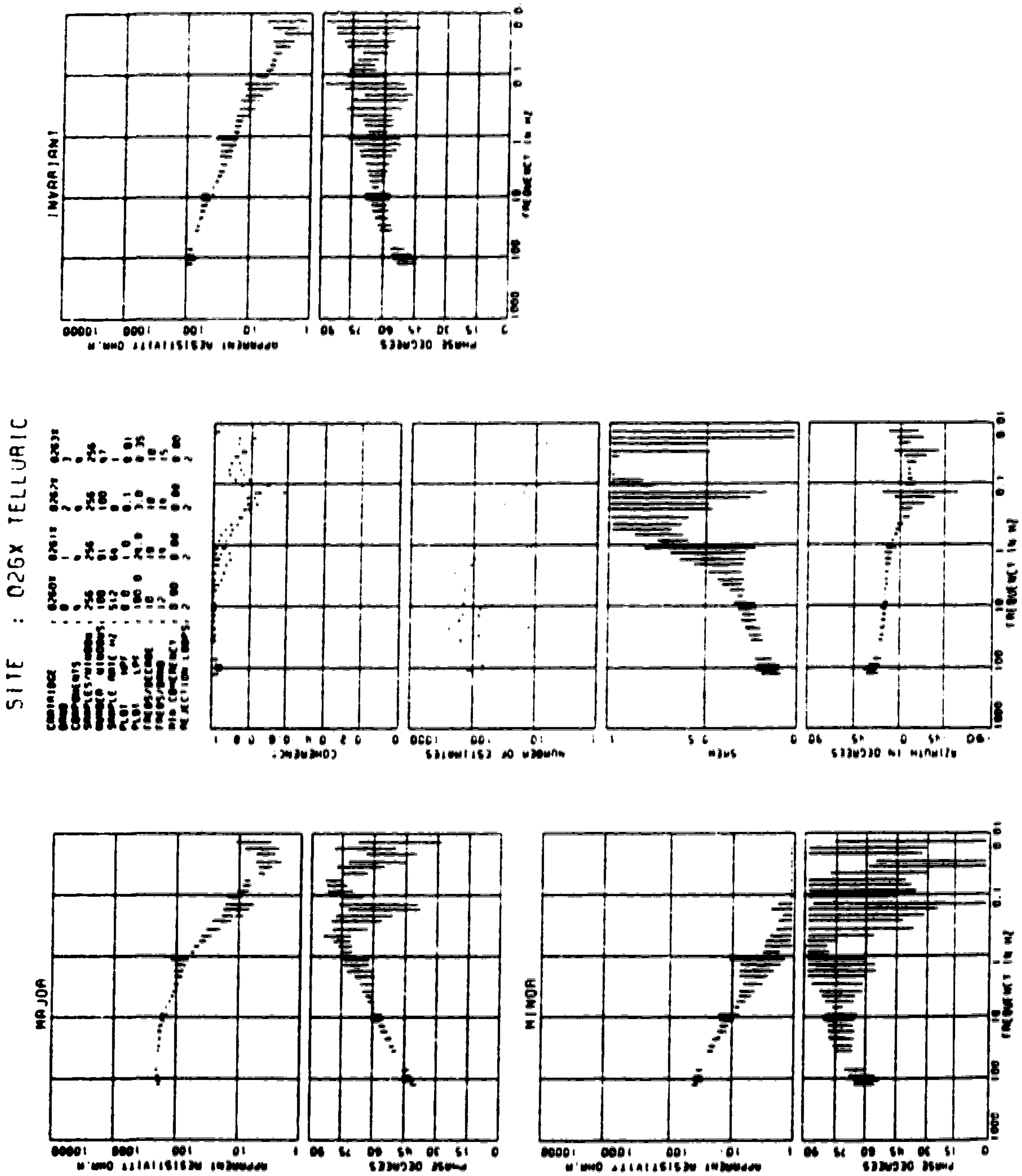

SITE : 02GX TELLURIC
INVARIANT
MAJOR
MINOR

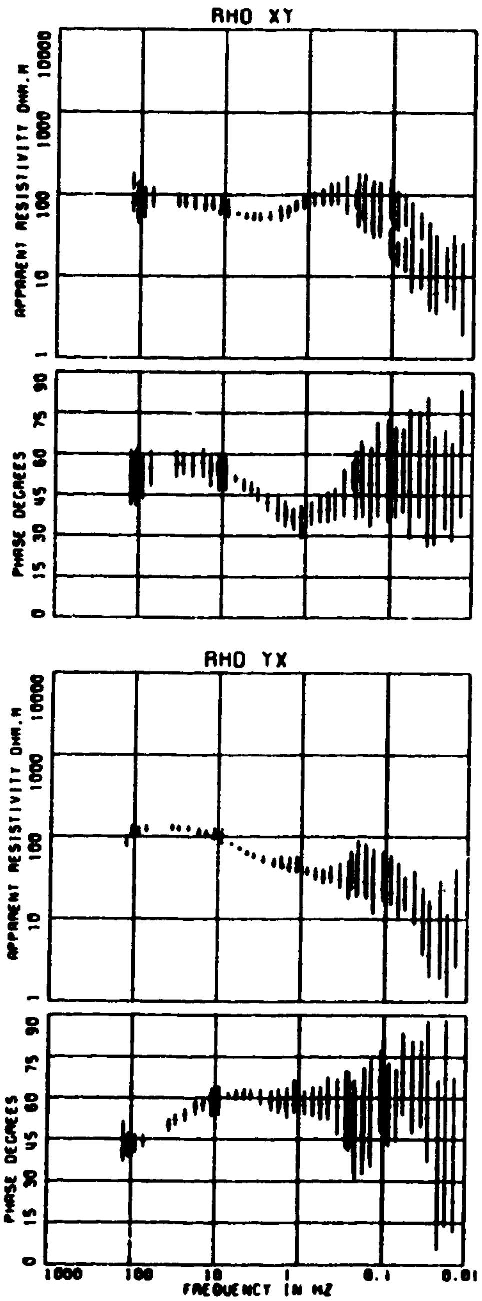

SITE : 027X TELLURIC

CARTRIDGE	:	0270X	0271X	0272X	0273X
BAND	:	0	1	2	3
COMPONENTS	:	4	4	4	4
SAMPLES/WINDOW	:	256	256	256	256
NUMBER WINDOWS	:	100	100	100	67
SAMPLE RATE HZ	:	512	64	8	1
PLOT HPF	:	8.0	1.0	0.1	0.01
PLOT LPF	:	100.0	24.0	3.0	0.35
FREQS/DECADE	:	10	10	10	10
FREQS/BAND	:	12	14	14	15
MIN COHERENCY	:	0.00	0.00	0.00	0.00
REJECTION LOOPS	:	2	2	2	2

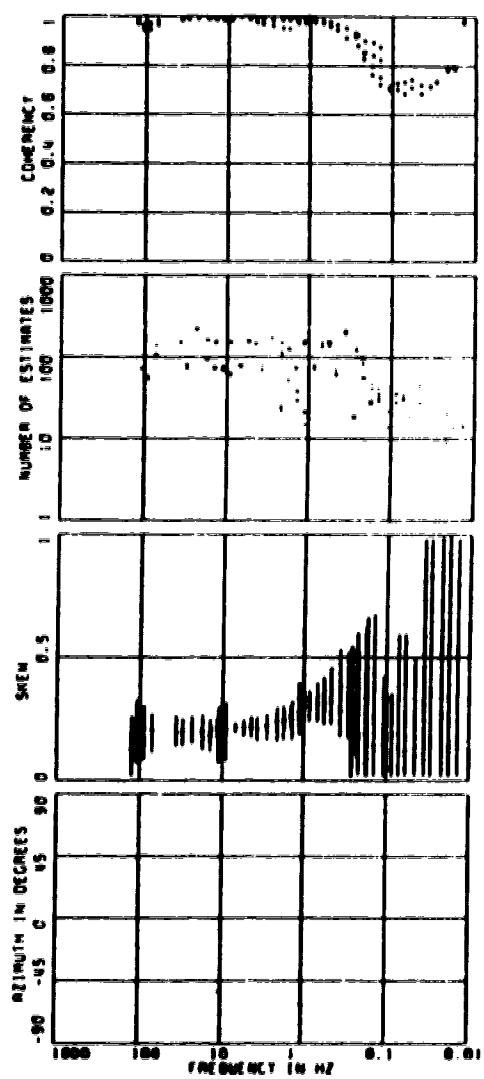

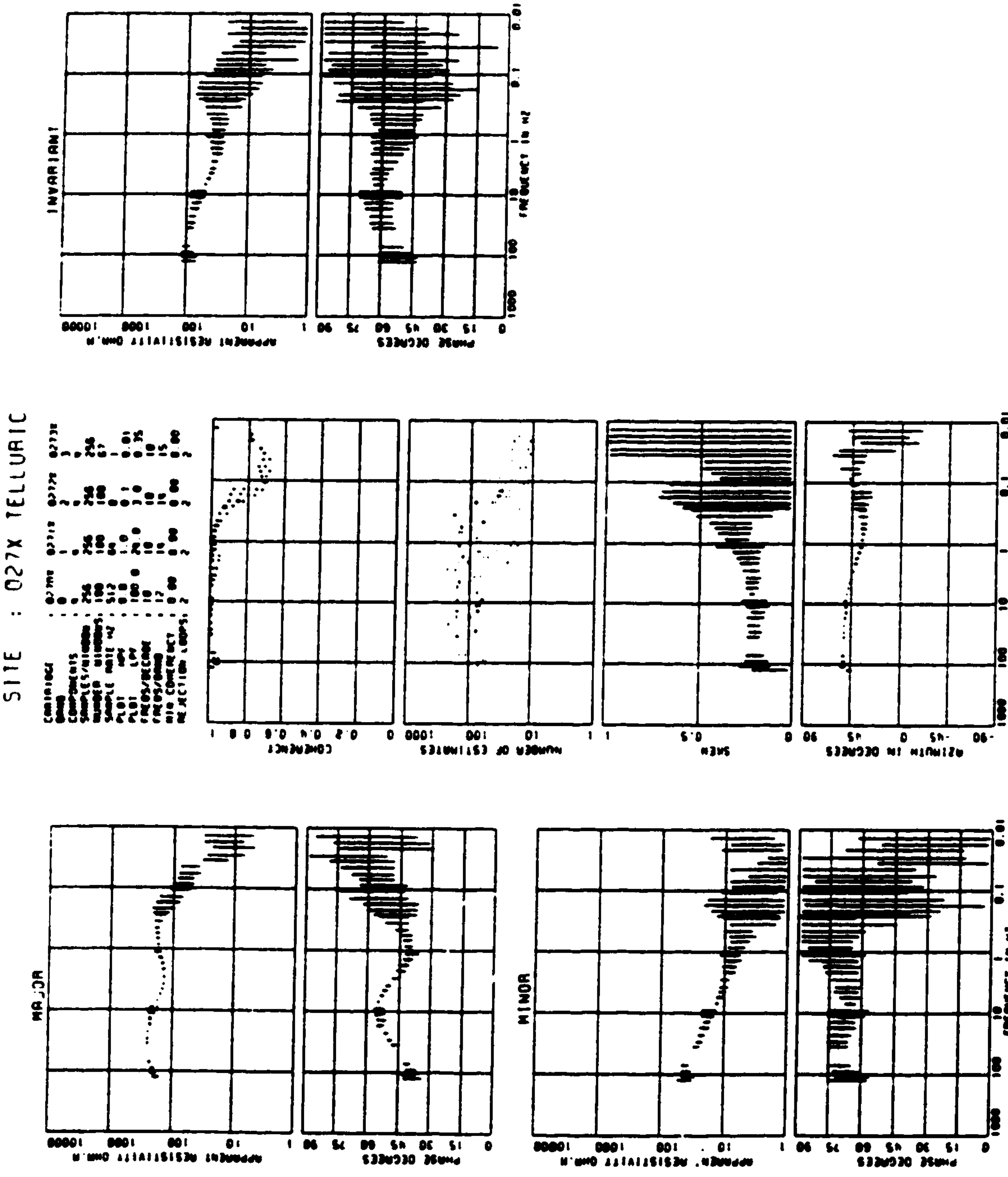

SITE : Q27X TELLURIC
INVARIANT
MAJOR
MINOR
FREQUENCY IN HZ
APPARENT RESISTIVITY OHM.M
PHASE DEGREES
COHERENCE
NUMBER OF ESTIMATES
SKEW
AZIMUTH IN DEGREES

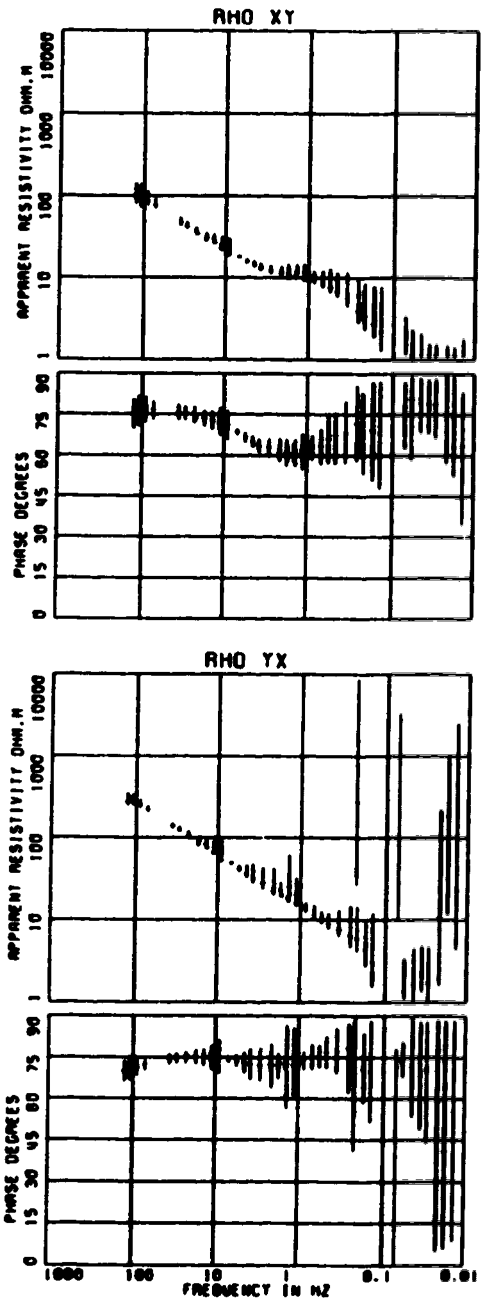

SITE : 028X TELLURIC

CARTRIDGE	:	0280X	0281X	0282X	0283X
BAND	:	0	1	2	3
COMPONENTS	:	4	4	4	4
SAMPLES/WINDOW	:	256	256	256	256
NUMBER WINDOWS	:	175	260	200	100
SAMPLE RATE HZ	:	512	64	8	1
PLOT HPF	:	8.0	1.0	0.1	0.01
PLOT LPF	:	100.0	24.0	3.0	0.35
FREQS/DECADE	:	10	10	10	10
FREQS/BAND	:	12	14	14	15
MIN COHERENCY	:	0.00	0.00	0.00	0.00
REJECTION LOOPS	:	2	2	2	2

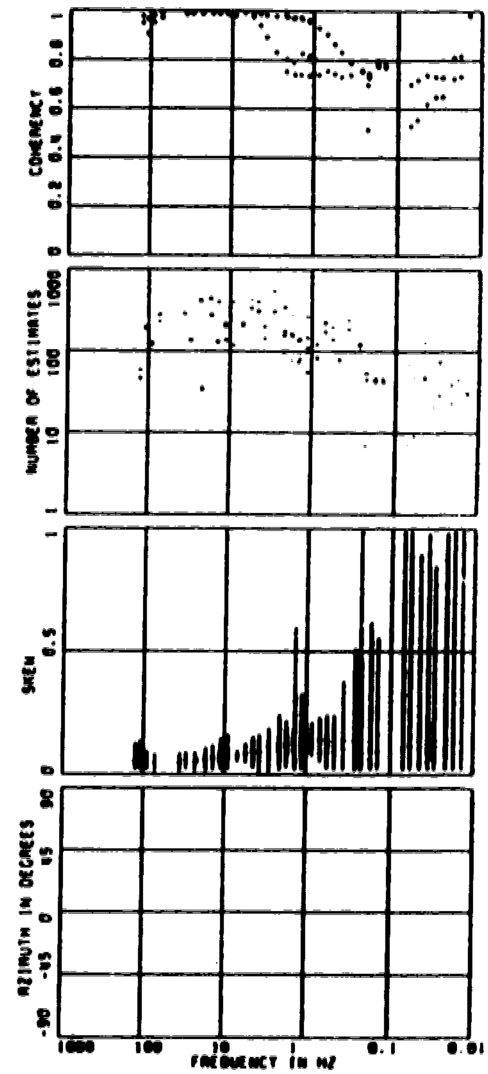

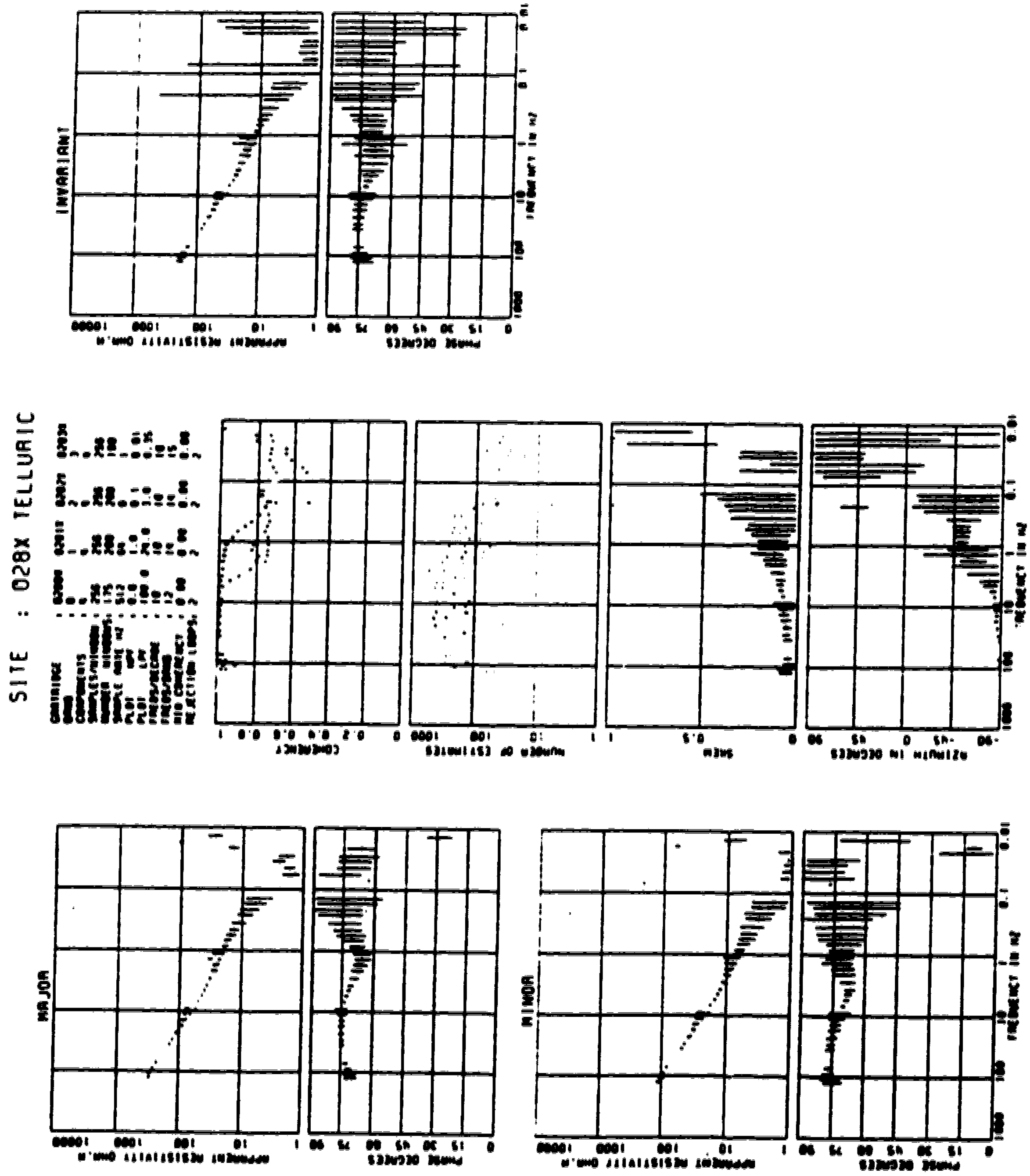
SITE : 028X TELLURIC
INVARIANT
MAJOR
MINOR

SITE : 029X TELLURIC

CARTRIDGE	:	0280X	0281X	0282X	0283X
BAND	:	0	1	2	3
COMPONENTS	:	4	4	4	4
SAMPLES/WINDOW	:	256	256	256	256
NUMBER WINDOWS	:	100	100	100	60
SAMPLE RATE HZ	:	512	64	8	1
PLOT HPF	:	8.0	1.0	0.1	0.01
PLOT LPF	:	100.0	24.0	3.0	0.35
FREQS/DECADE	:	10	10	10	10
FREQS/BAND	:	12	14	14	15
MIN COHERENCY	:	0.00	0.00	0.00	0.00
REJECTION LOOPS	:	2	2	2	2

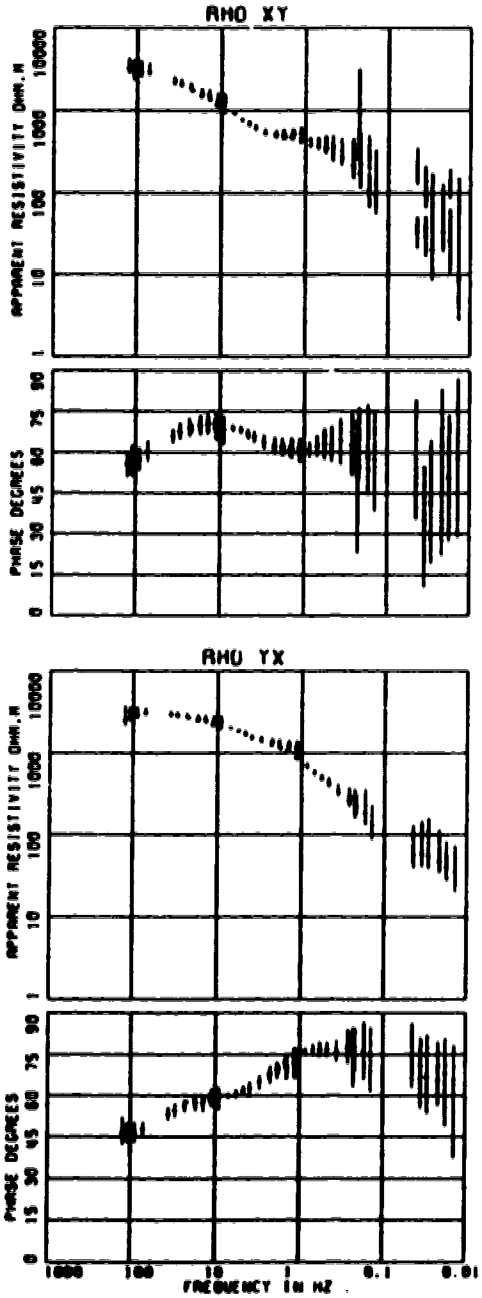

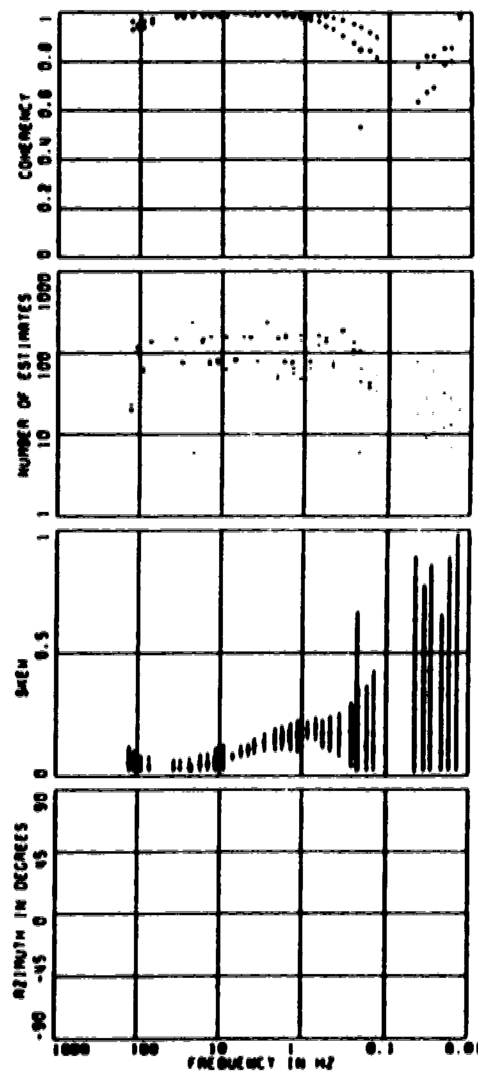

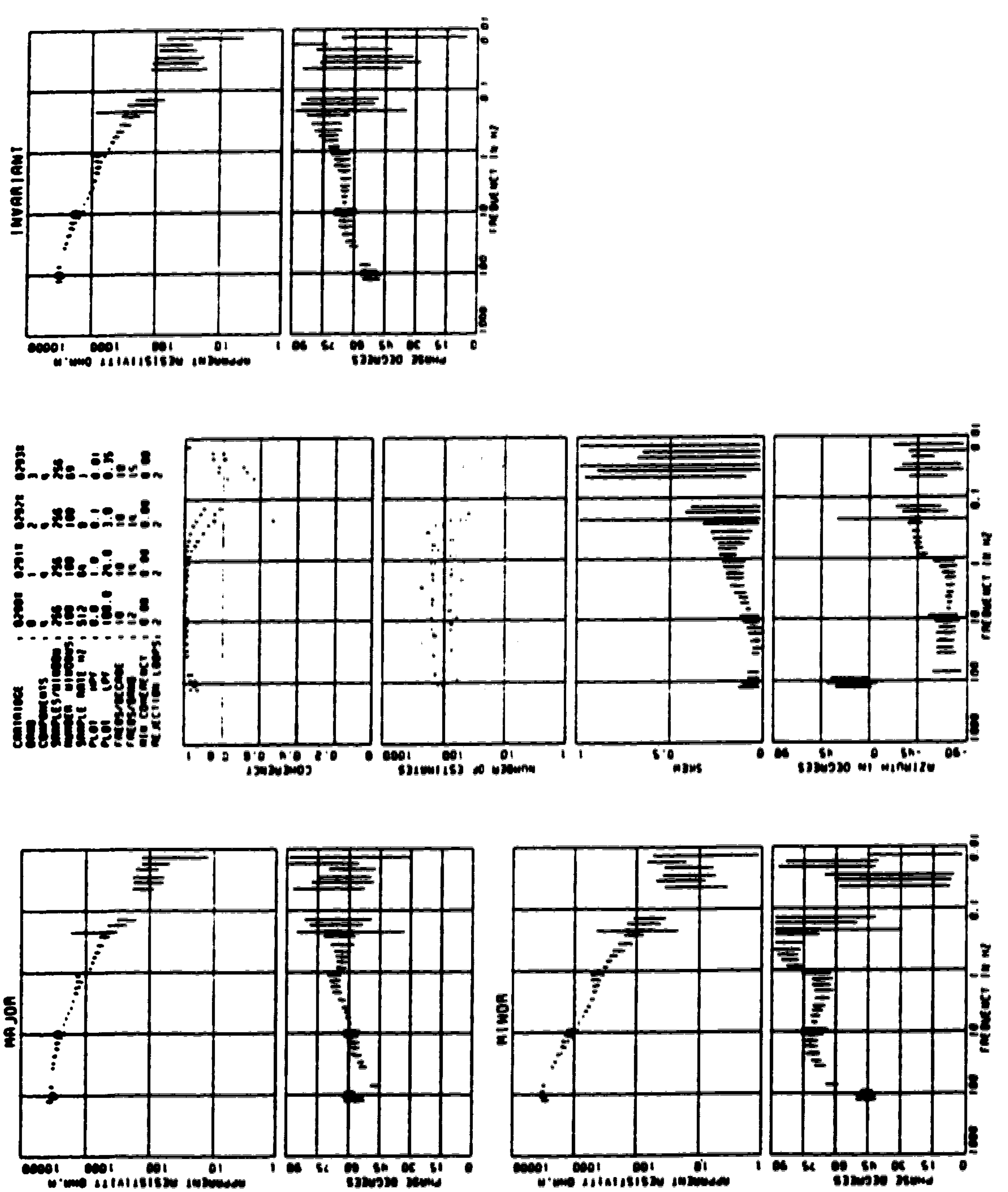
INVARIANT
SITE : 029X TELLURIC
MAJOR
MINOR

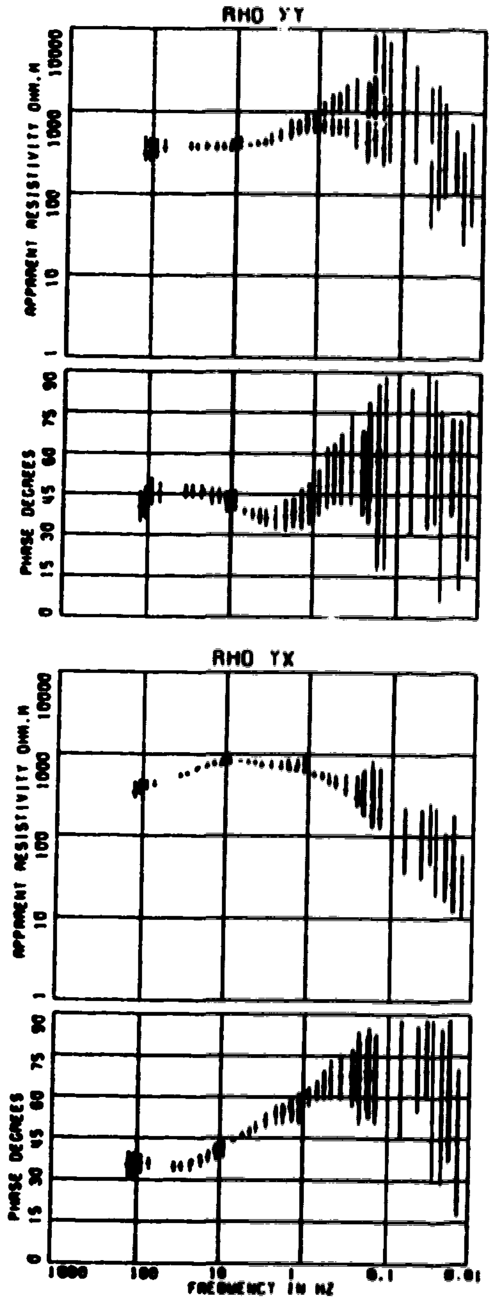

SITE : 030X TELLURIC

CARTRIDGE	:	0300X	0301X	0302X	0303X
BAND	:	0	1	2	3
COMPONENTS	:	4	4	4	4
SAMPLES/WINDOW	:	256	256	256	256
NUMBER WINDOWS	:	100	100	100	94
SAMPLE RATE HZ	:	512	64	8	1
PLOT HPF	:	8.0	1.0	0.1	0.01
PLOT LPF	:	100.0	24.0	3.0	0.35
FREQS/DECADE	:	10	10	10	10
FREQS/BAND	:	12	14	14	15
MIN COHERENCY	:	0.00	0.00	0.00	0.00
REJECTION LOOPS	:	2	2	2	2

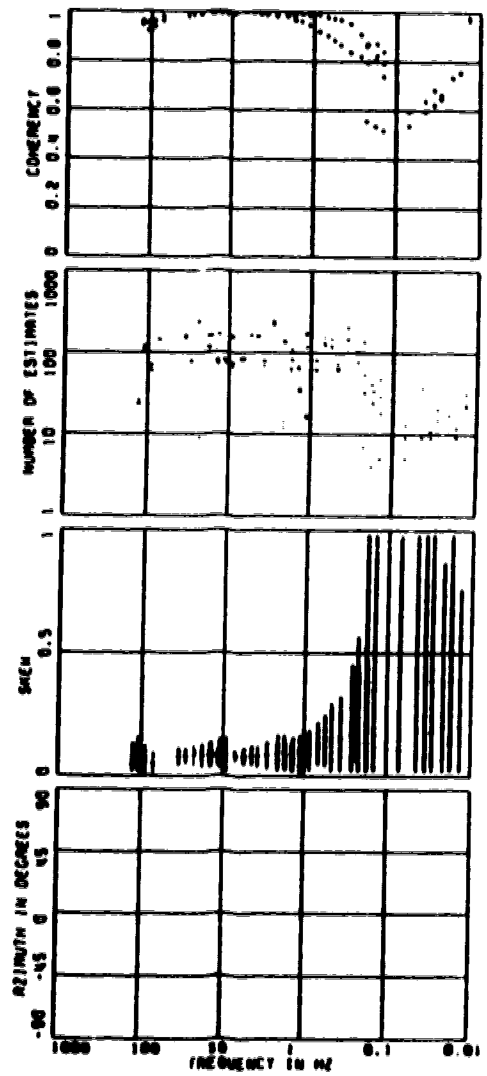

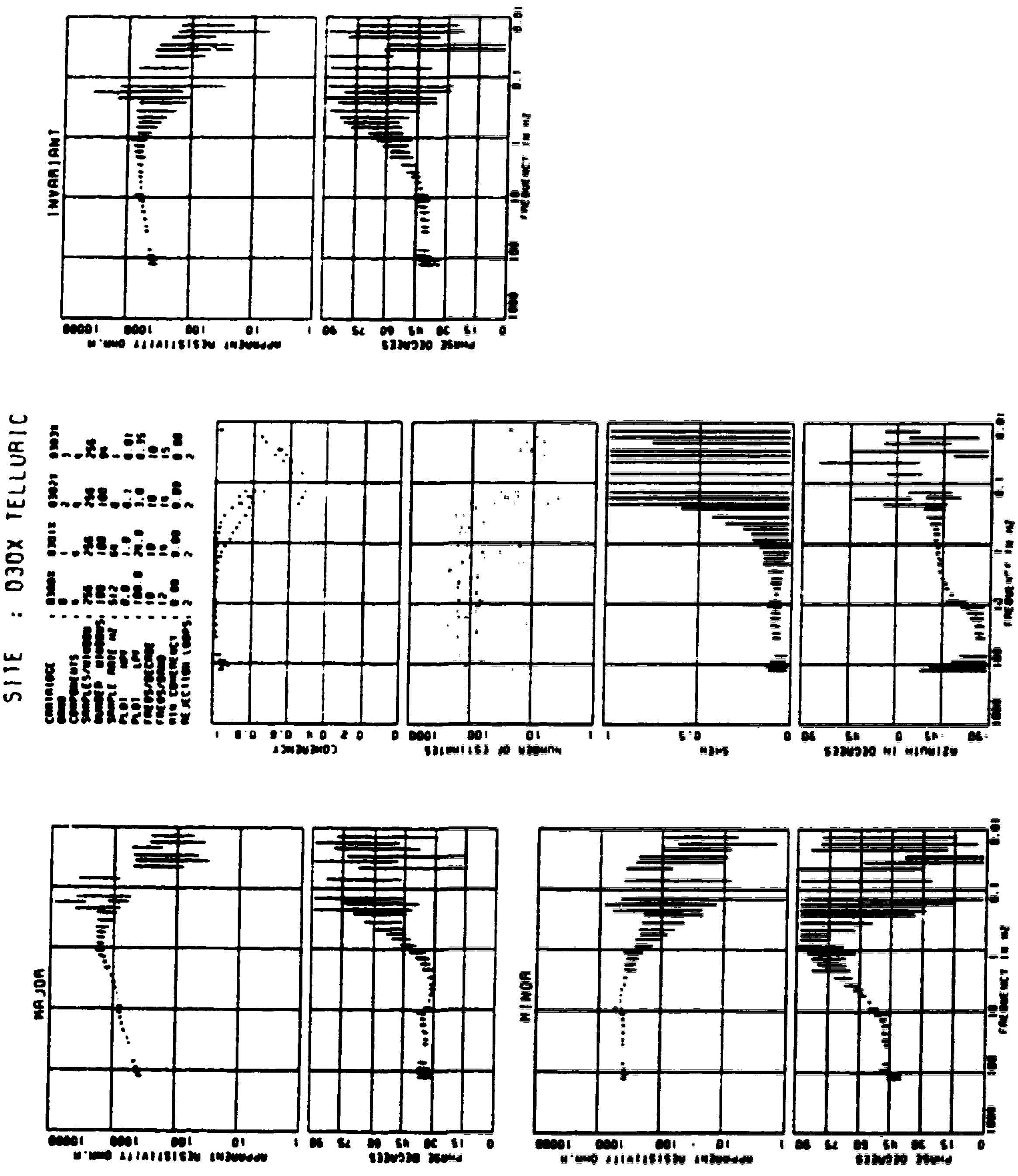
SITE : 030X TELLURIC
INVARIANT
MAJOR
MINOR
APPARENT RESISTIVITY OHM.M
PHASE DEGREES
FREQUENCY IN HZ
COHERENCY
NUMBER OF ESTIMATES
SKEW
AZIMUTH IN DEGREES

SITE : 031X TELLURIC

CARTRIDGE	:	0310X	0311X	0312X	0313X
BAND	:	0	1	2	3
COMPONENTS	:	4	4	4	4
SAMPLES/WINDOW	:	256	256	256	256
NUMBER WINDOWS	:	100	100	100	47
SAMPLE RATE HZ	:	512	64	8	1
PLOT HPF	:	8.0	1.0	0.1	0.01
PLOT LPF	:	100.0	24.0	3.0	0.35
FREQS/DECADE	:	10	10	10	10
FREQS/BAND	:	12	14	14	15
MIN COHERENCY	:	0.00	0.00	0.00	0.00
REJECTION LOOPS	:	2	2	2	2

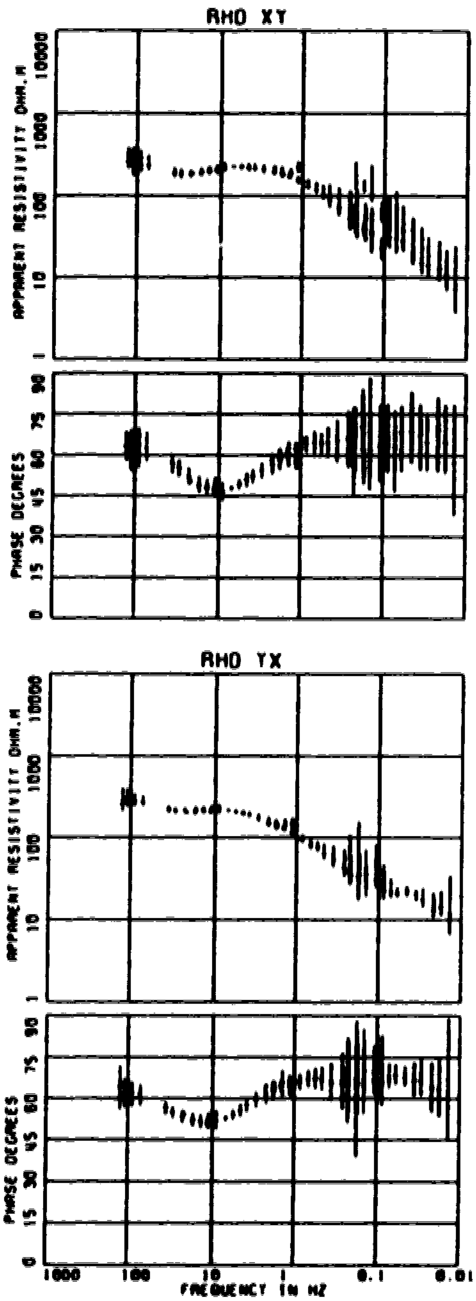

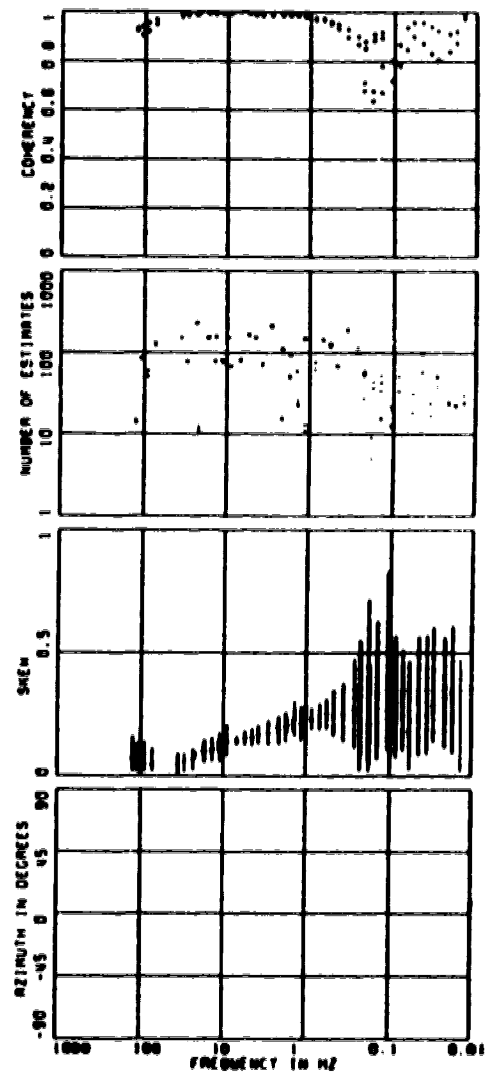

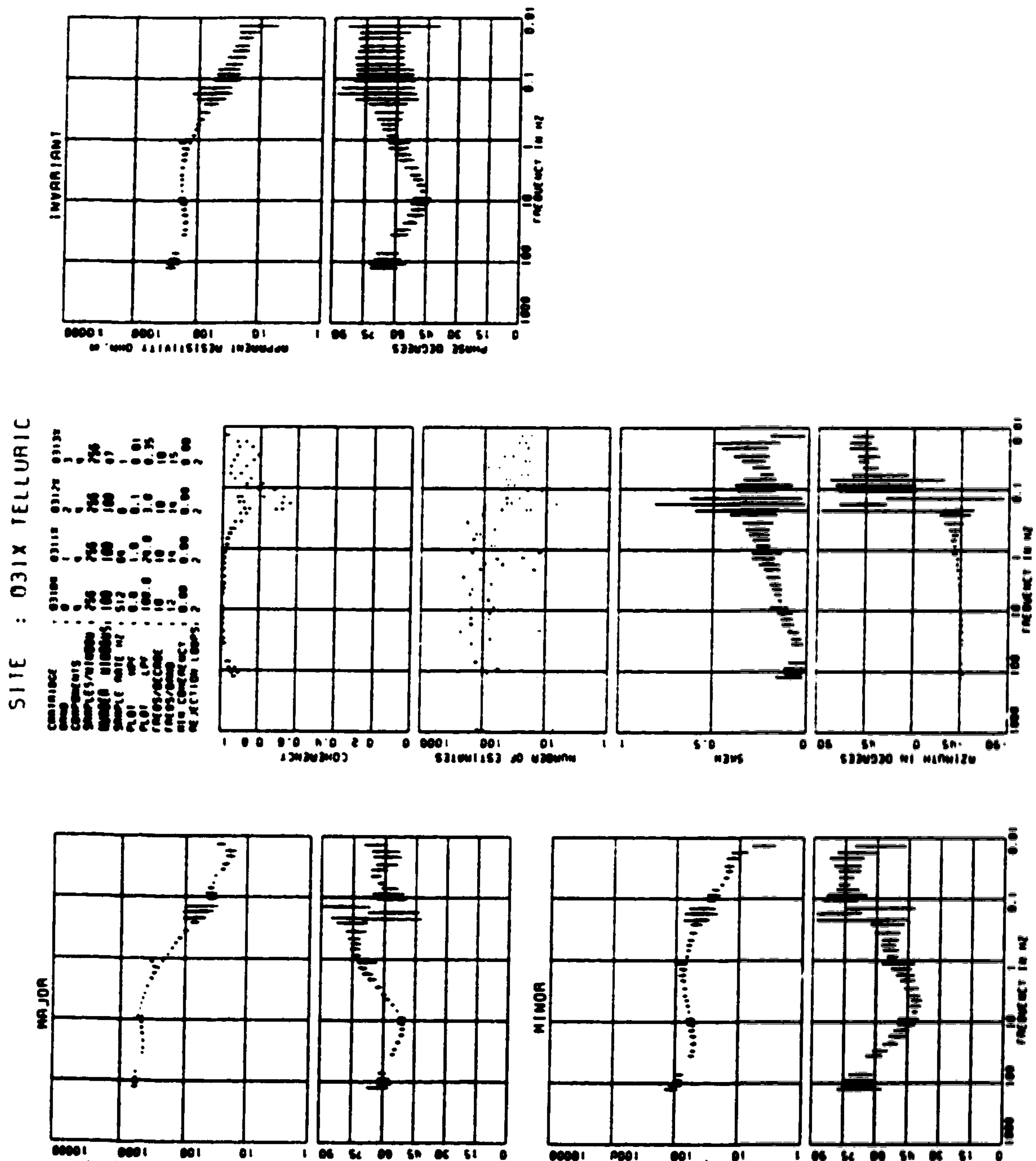
INVARIANT
SITE : 031X TELLURIC
MAJOR
MINOR

SITE : 032X TELLURIC

CARTRIDGE :	0320X	0321X	0322X	0323X
BAND :	0	1	2	3
COMPONENTS :	4	4	4	4
SAMPLES/WINDOW :	256	256	256	256
NUMBER WINDOWS:	100	100	97	55
SAMPLE RATE HZ :	512	64	8	1
PLOT HPF :	8.0	1.0	0.1	0.01
PLOT LPF :	100.0	24.0	3.0	0.35
FREQS/DECADE :	10	10	10	10
FREQS/BAND :	12	14	14	15
MIN COHERENCY :	0.00	0.00	0.00	0.00
REJECTION LOOPS:	2	2	2	2

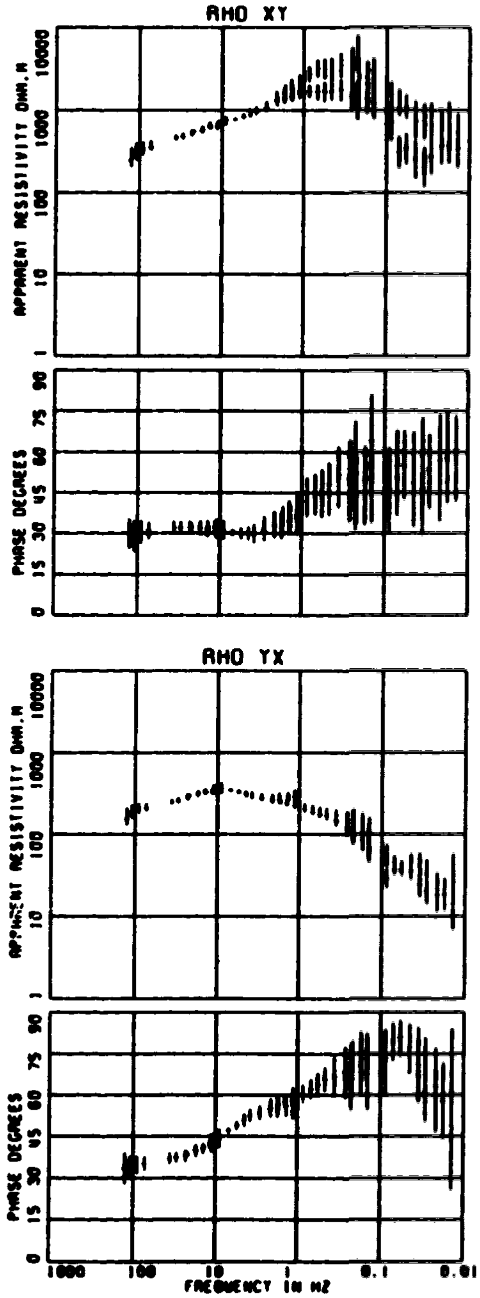

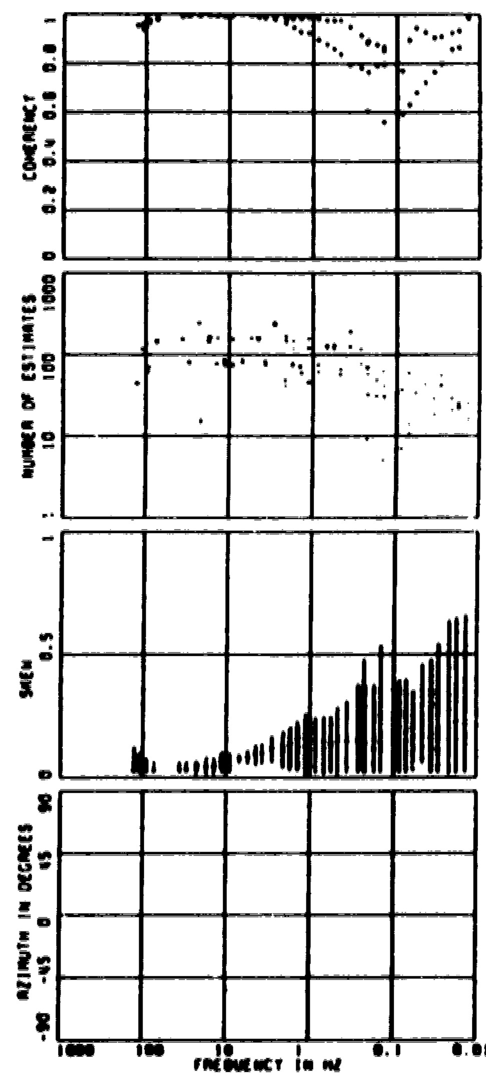

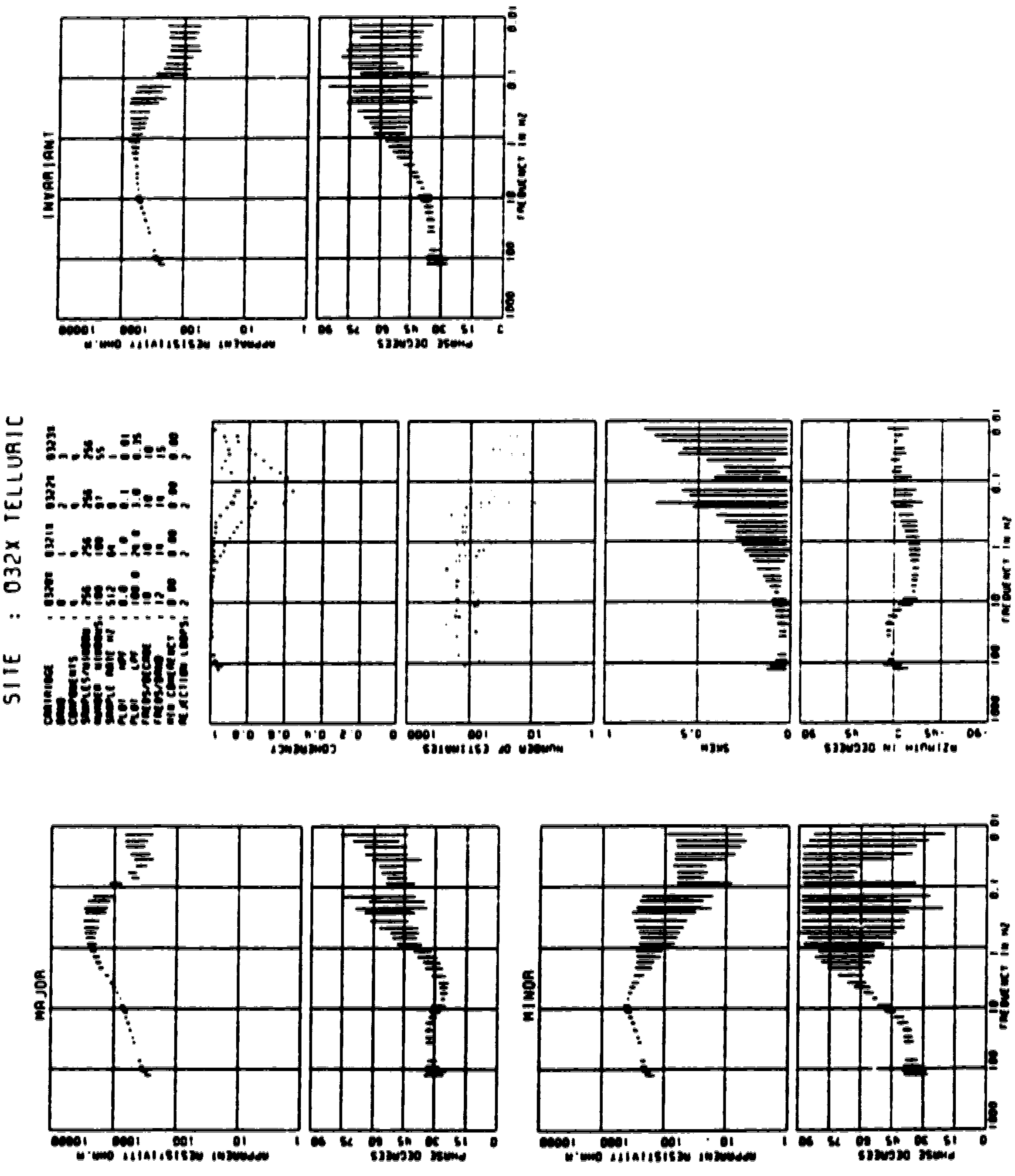
INVARIANT
SITE : 032X TELLURIC
MAJOR
MINOR
APPARENT RESISTIVITY OHM.M
PHASE DEGREES
FREQUENCY IN HZ
COHERENCY
NUMBER OF ESTIMATES
SKEW
AZIMUTH IN DEGREES

SITE : 033X TELLURIC

CARTRIDGE	:	0330X	0331X	0332X	0333X
BAND	:	0	1	2	3
COMPONENTS	:	4	4	4	4
SAMPLES/WINDOW	:	256	256	256	256
NUMBER WINDOWS	:	100	100	95	57
SAMPLE RATE HZ	:	512	64	8	1
PLOT HPF	:	0.0	1.0	0.1	0.01
PLOT LPF	:	100.0	25.0	3.0	0.35
FREQS/DECADE	:	10	10	10	10
FREQS/BAND	:	12	14	14	15
MIN COHERENCY	:	0.00	0.00	0.00	0.00
REJECTION LOOPS	:	2	2	2	2

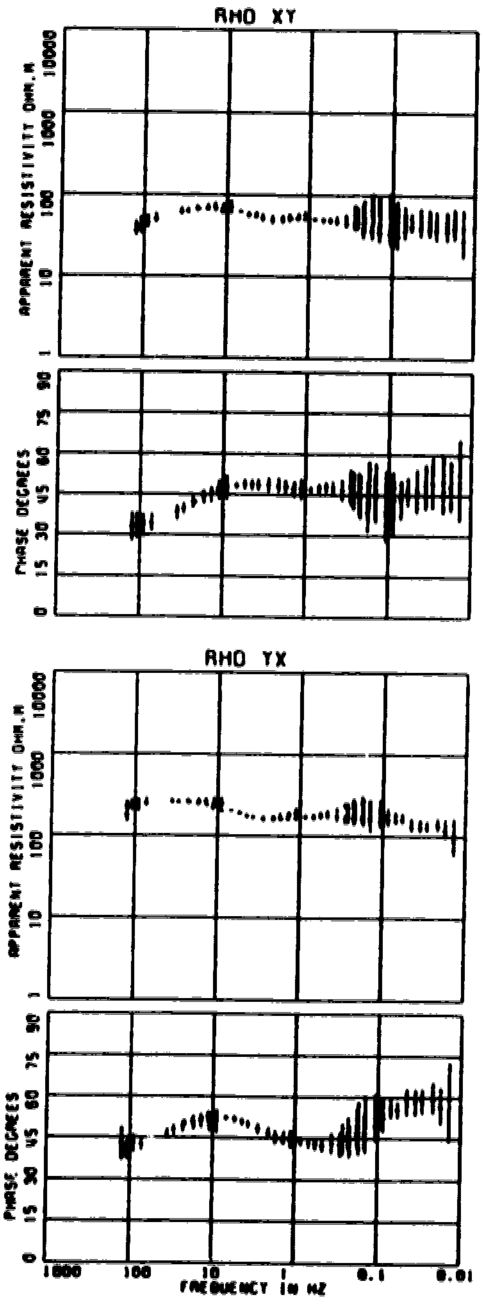

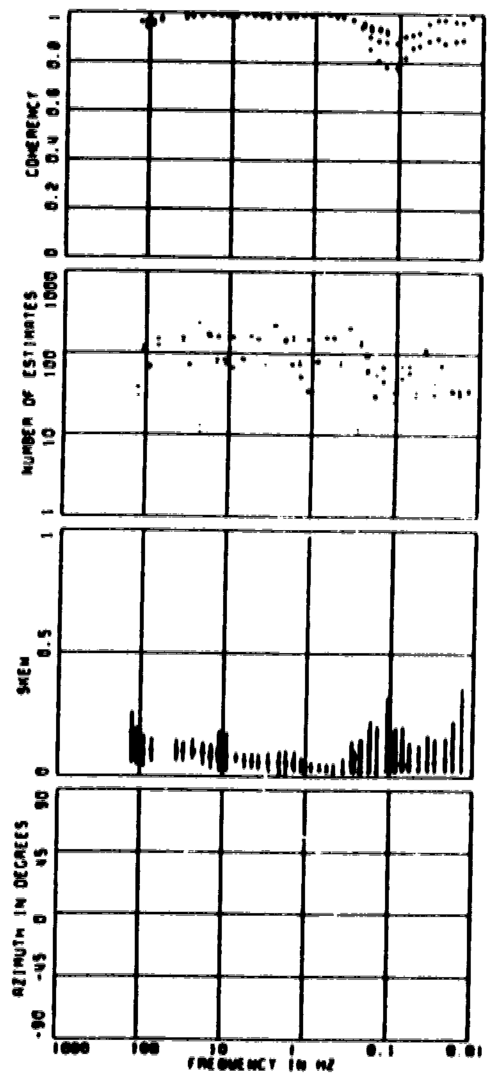

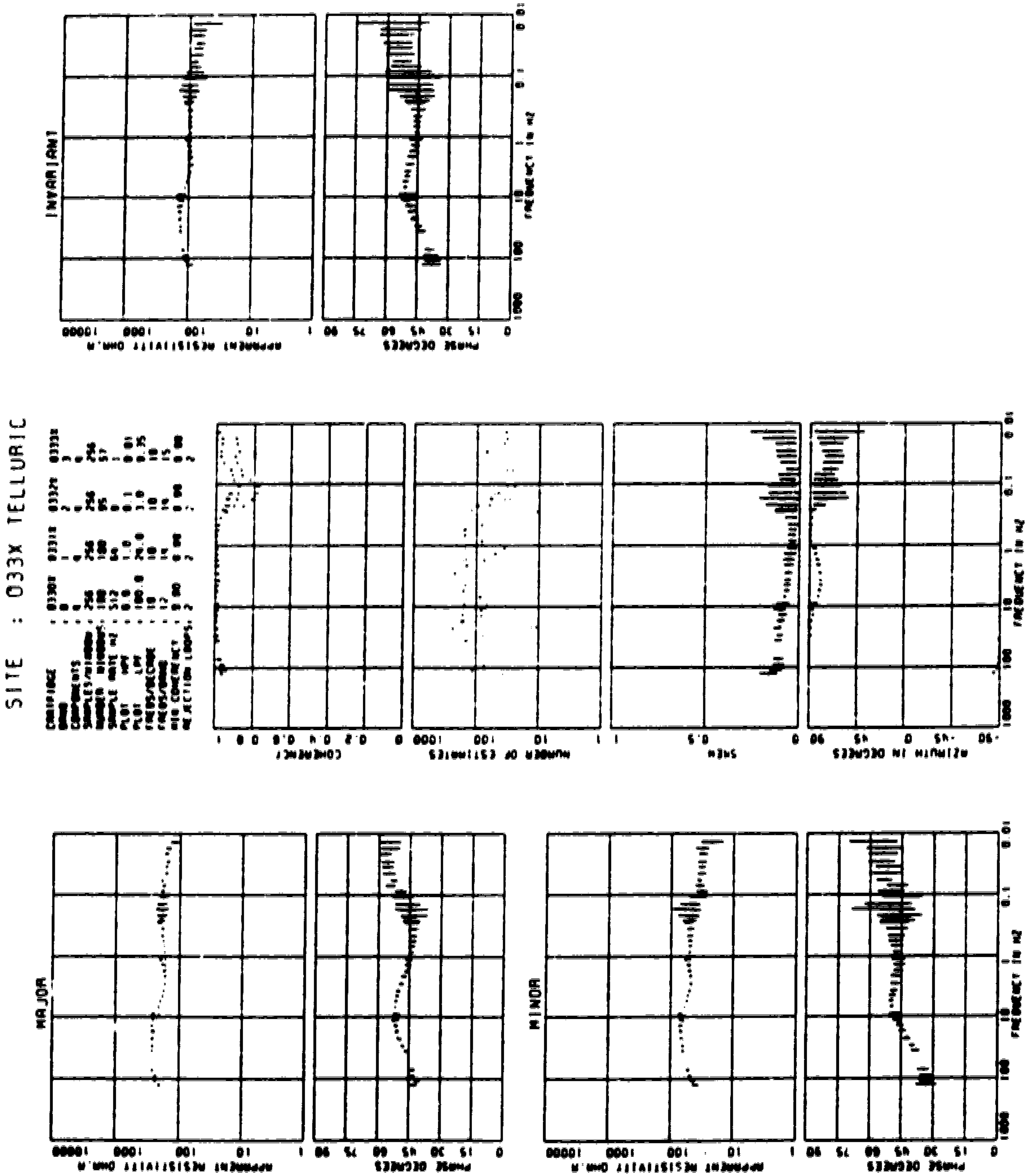
SITE : 033X TELLURIC
INVARIANT
MAJOR
MINOR
FREQUENCY IN HZ
APPARENT RESISTIVITY OHM.M
PHASE DEGREES
COHERENCY
NUMBER OF ESTIMATES
SKEW
AZIMUTH IN DEGREES

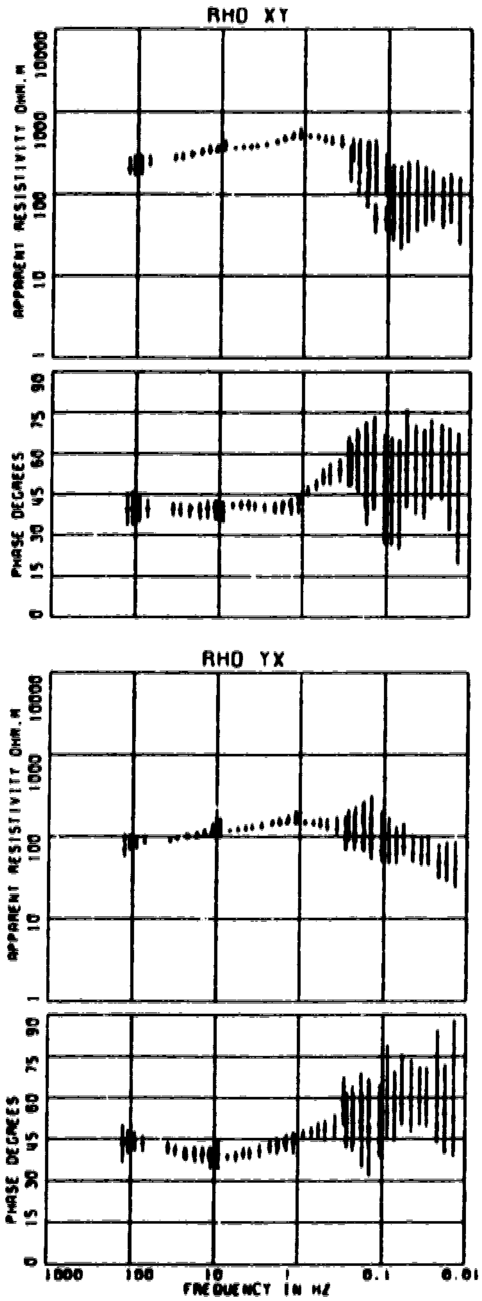

SITE : 034X TELLURIC

CARTRIDGE	:	0340X	0341X	0342X	0343X
BAND	:	0	1	2	3
COMPONENTS	:	4	4	4	4
SAMPLES/WINDOW	:	256	256	256	256
NUMBER WINDOWS	:	100	100	87	55
SAMPLE RATE HZ	:	512	64	8	1
PLOT HPF	:	8.0	1.0	0.1	0.01
PLOT LPF	:	100.0	24.0	3.0	0.35
FREQS/DECADE	:	10	10	10	10
FREQS/BAND	:	12	14	14	15
MIN COHERENCY	:	0.00	0.00	0.00	0.00
REJECTION LOOPS	:	2	2	2	2

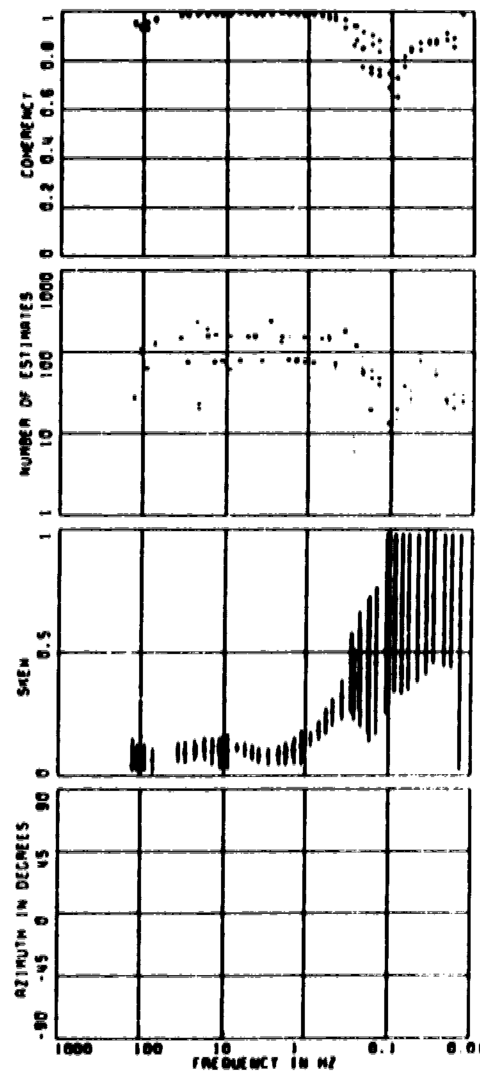

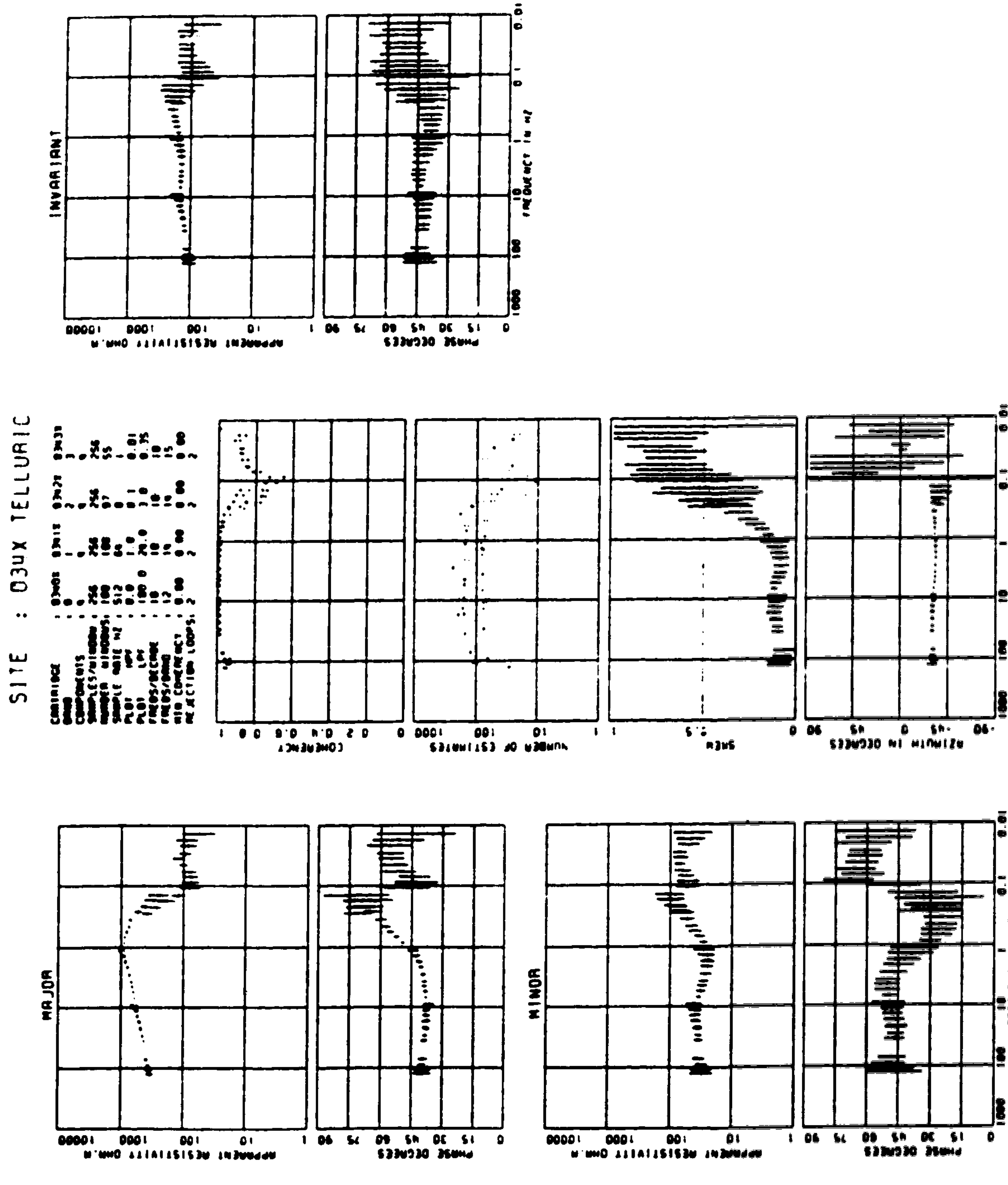
SITE : 03UX TELLURIC
INVARIANT
MAJOR
MINOR
APPARENT RESISTIVITY OHM.M
PHASE DEGREES
FREQUENCY IN HZ
COHERENCY
NUMBER OF ESTIMATES
SKEW
AZIMUTH IN DEGREES

APPENDIX II

ONE-DIMENSIONAL MODELS OF THE 34 MT SITES

For each site the following plots are shown:

Right part of the plot: electrical resistivity model of the site. The Rs refer to the range of electrical resistivities for the layer and the Ds refer to depth range of the boundary between two different layers.

Left part of the plot: field data invariant apparent electrical resistivity (top) and field data invariant phase (bottom). The field data are represented by crosses with error bars. The solid line represents the calculated apparent electrical resistivity and phase curves for the one-dimensional model shown in the right part of the plot.

1D Model for site 001X INVARIANT OF UP-DOWN MEAN

5 LAYERS WEIGHTED TENSOR

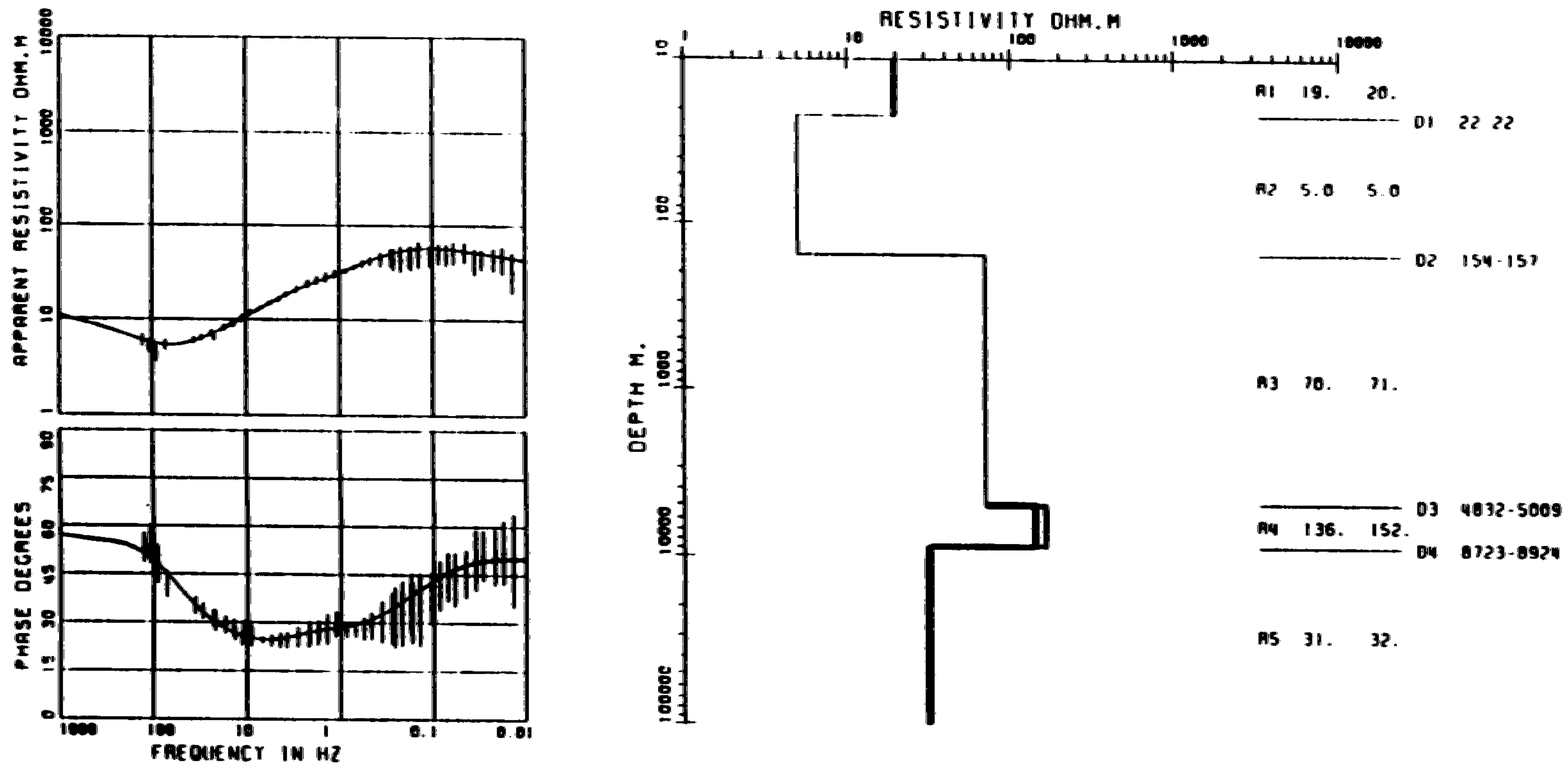

1D Model for site 002X INVARIANT OF UP-DOWN MEAN

5 LAYERS WEIGHTED TENSOR

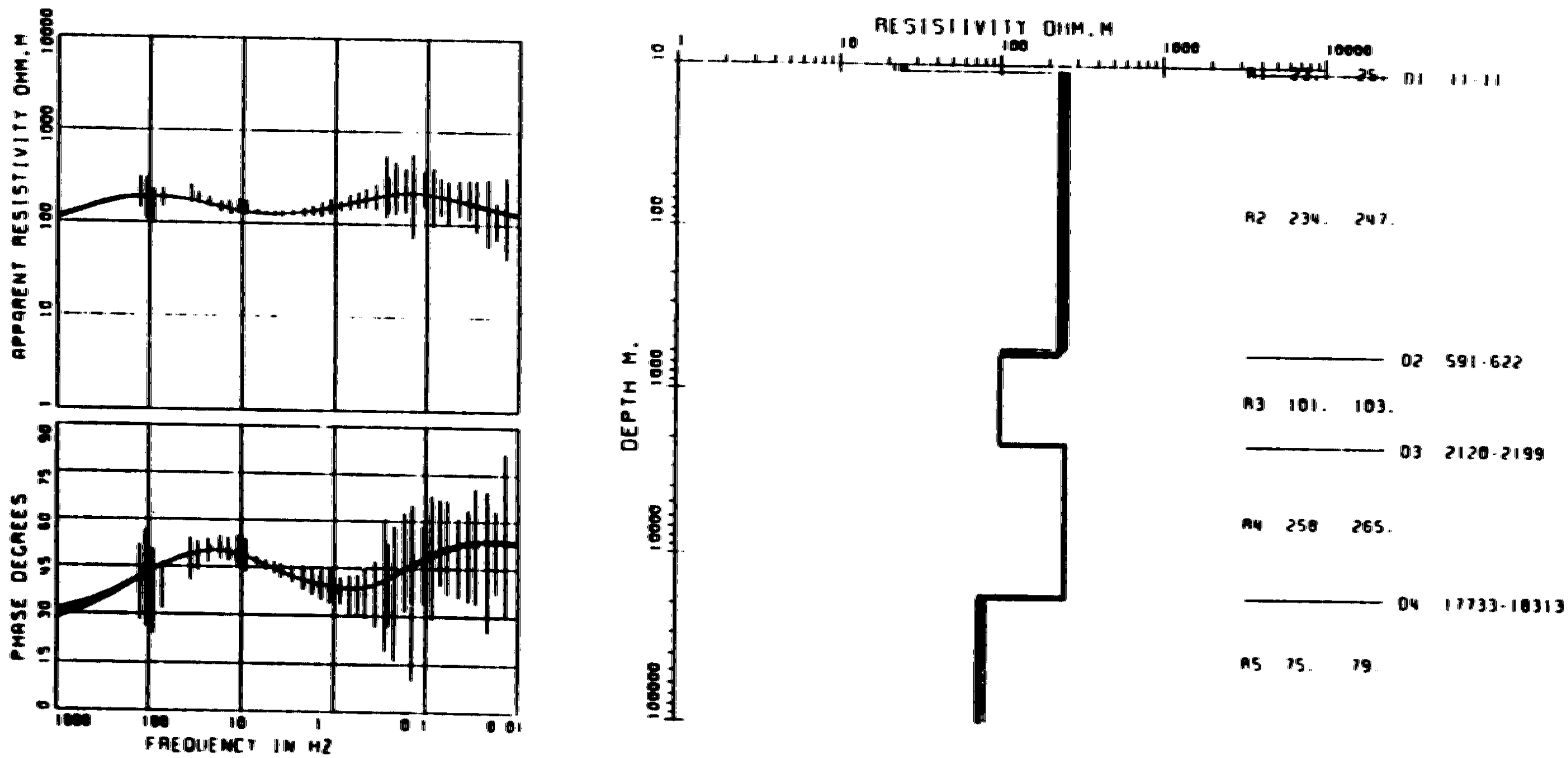

1D Model for site 003X INVARIANT OF UP-DOWN MEAN

3 LAYERS WEIGHTED TENSOR

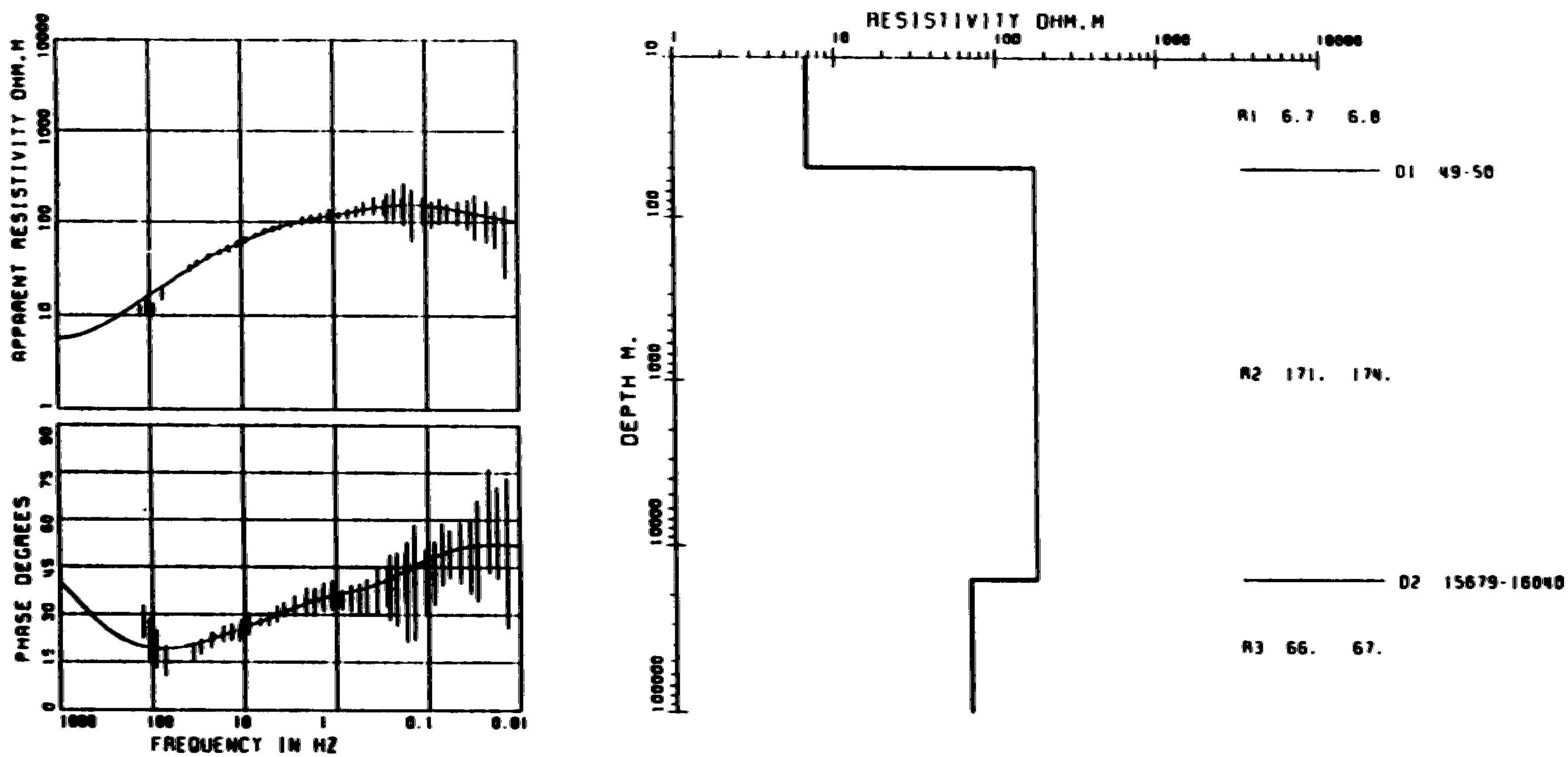

1D Model for site 004X INVARIANT OF UP-DOWN MEAN

3 LAYERS WEIGHTED TENSOR

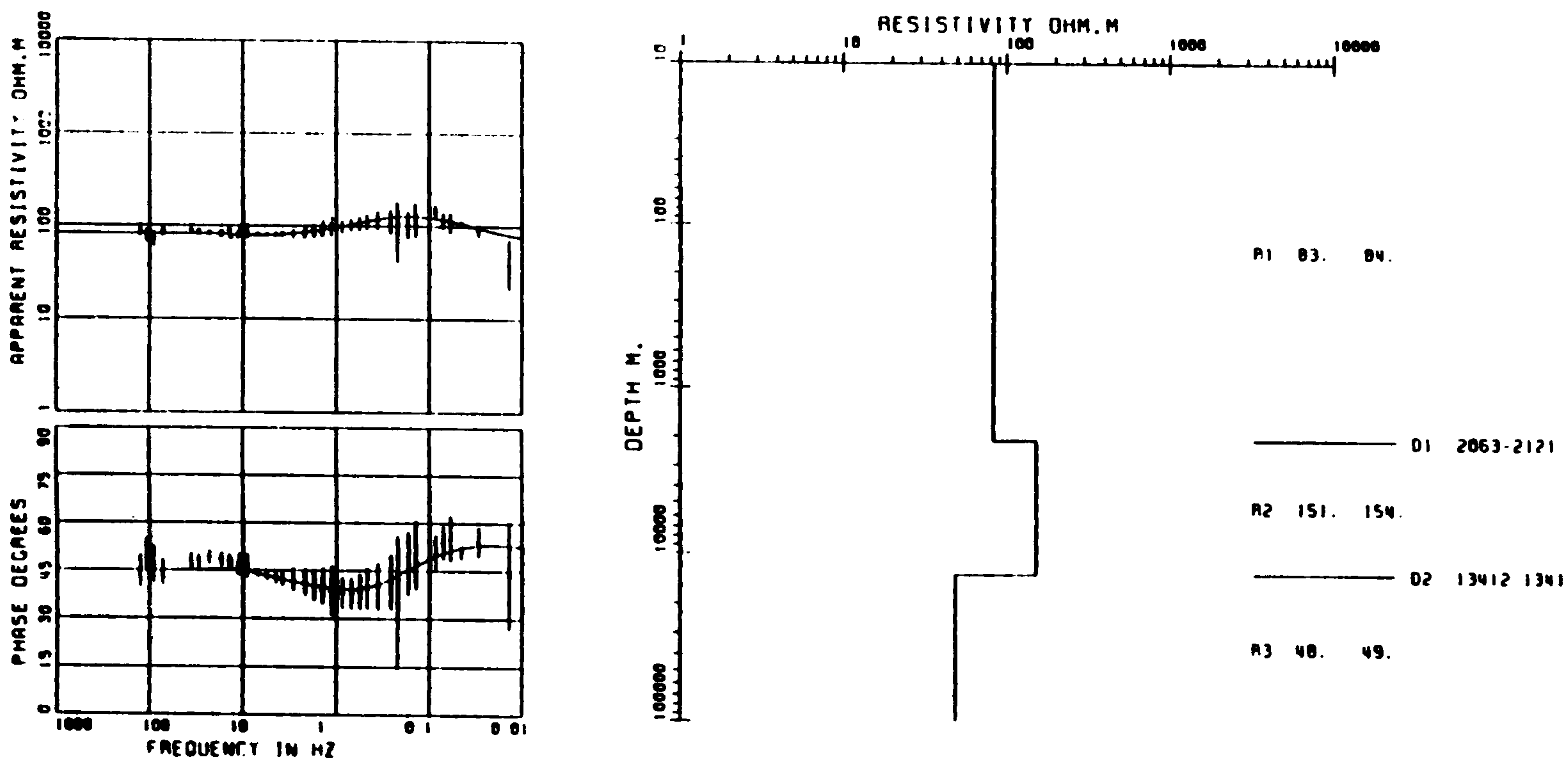

1D Model for site 005X INVARIANT OF UP-DOWN MEAN

4 LAYERS WEIGHTED TENSOR

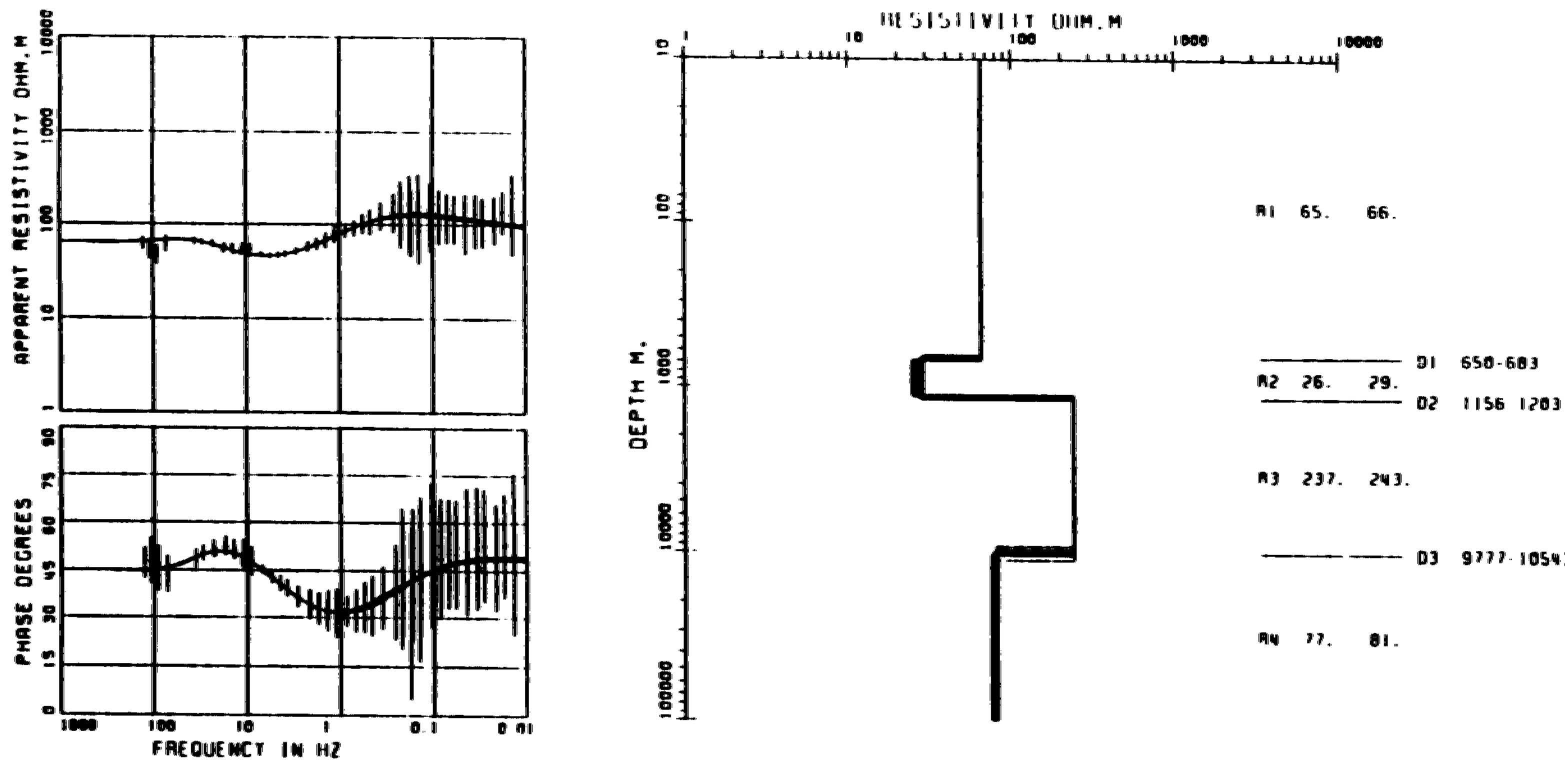

1D Model for site 006X INVARIANT OF UP-DOWN MEAN

4 LAYERS WEIGHTED TENSOR

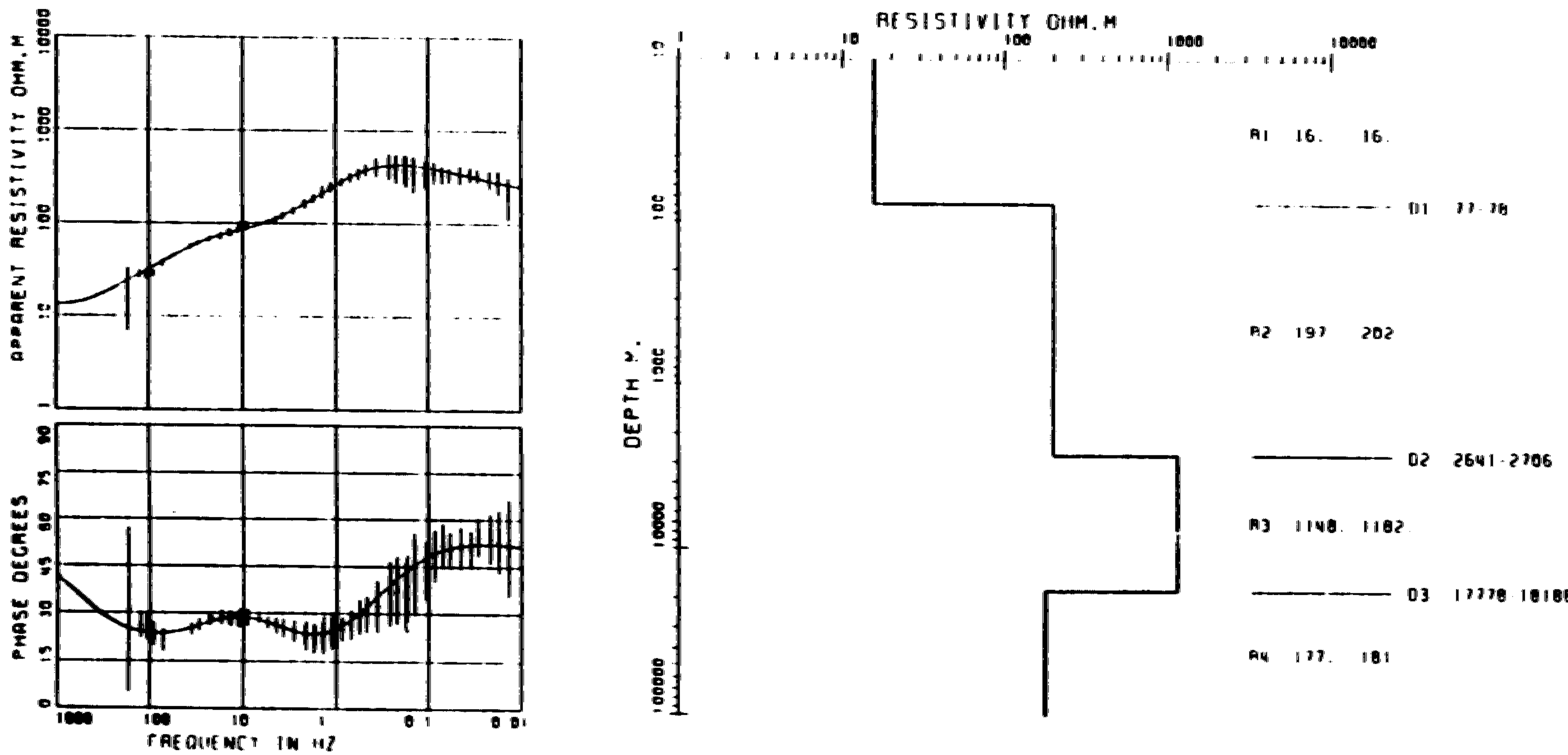

1D Model for site 007X INVARIANT OF UP-DOWN MEAN

3 LAYERS WEIGHTED TENSOR

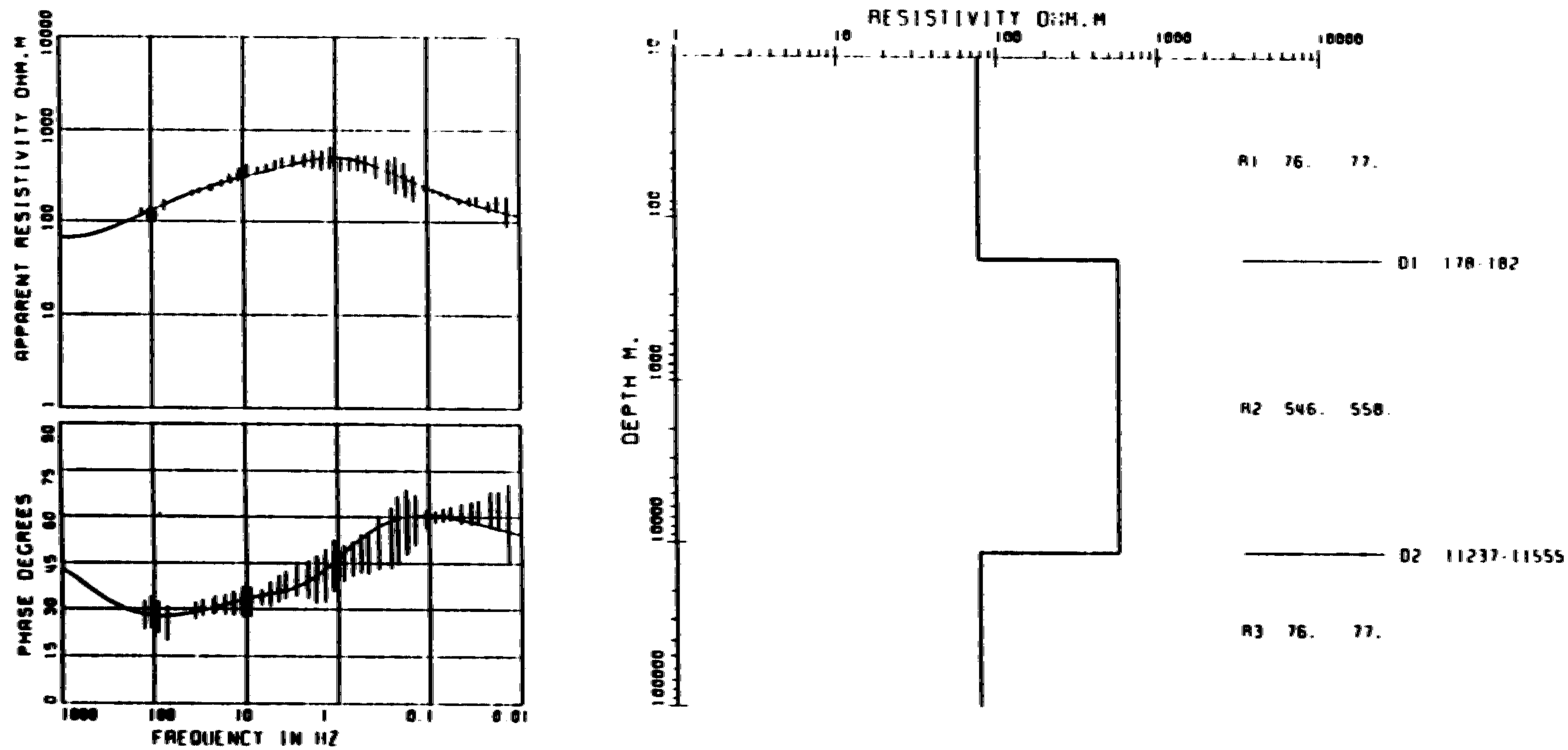

1D Model for site 008X INVARIANT OF UP-DOWN MEAN

4 LAYERS WEIGHTED TENSOR

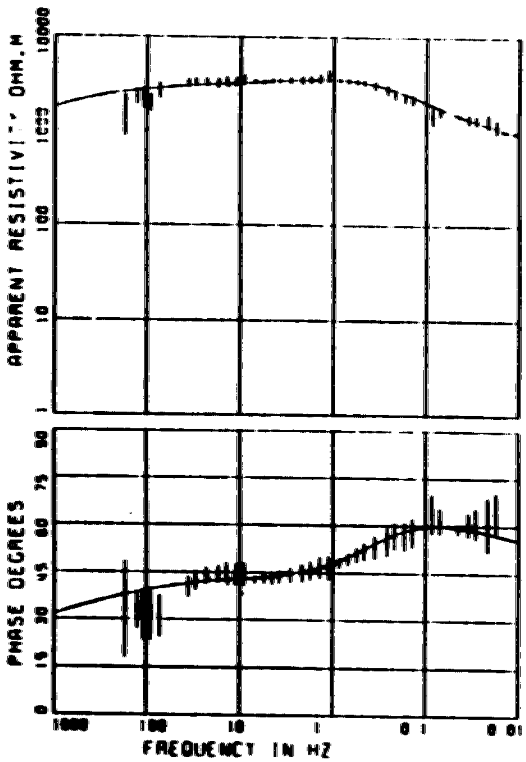

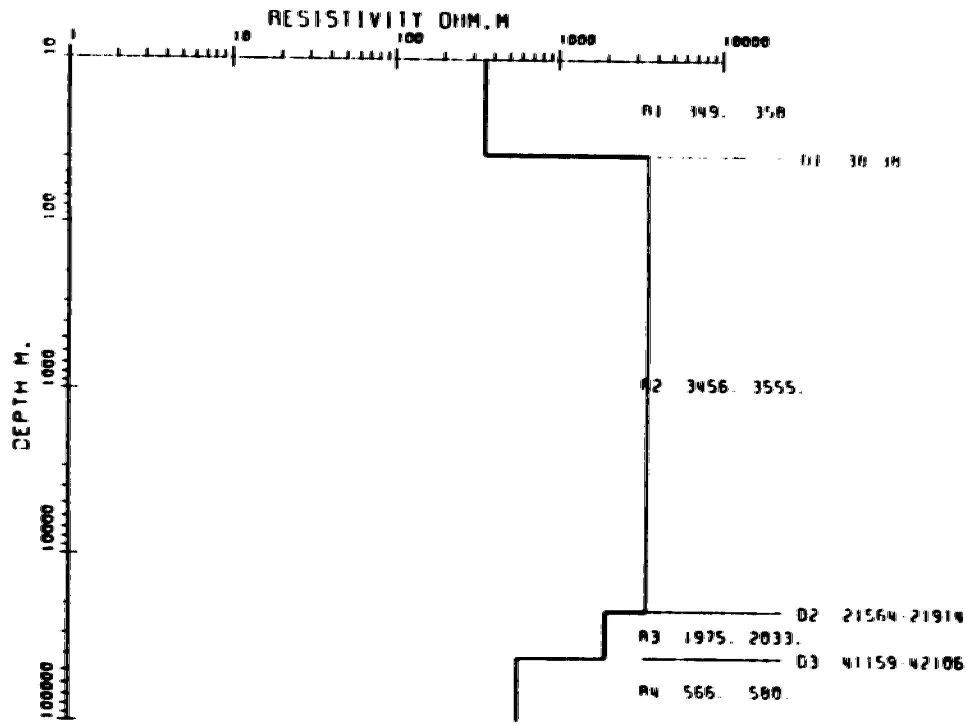

1D Model for site 009X INVARIANT OF UP-DOWN MEAN

3 LAYERS WEIGHTED TENSOR

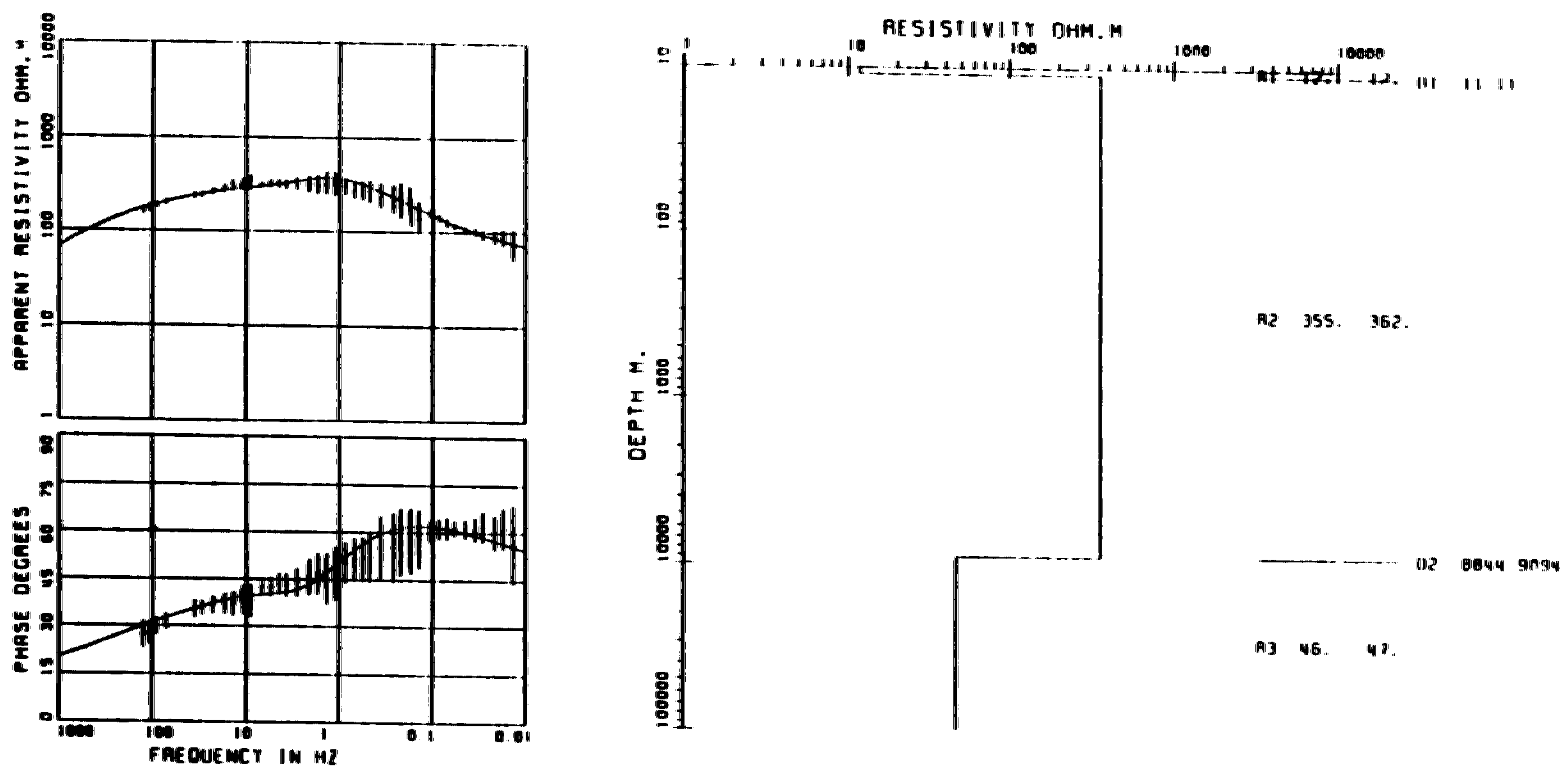

1D Model for site 010X INVARIANT OF UP-DOWN MEAN

5 LAYERS WEIGHTED TENSOR

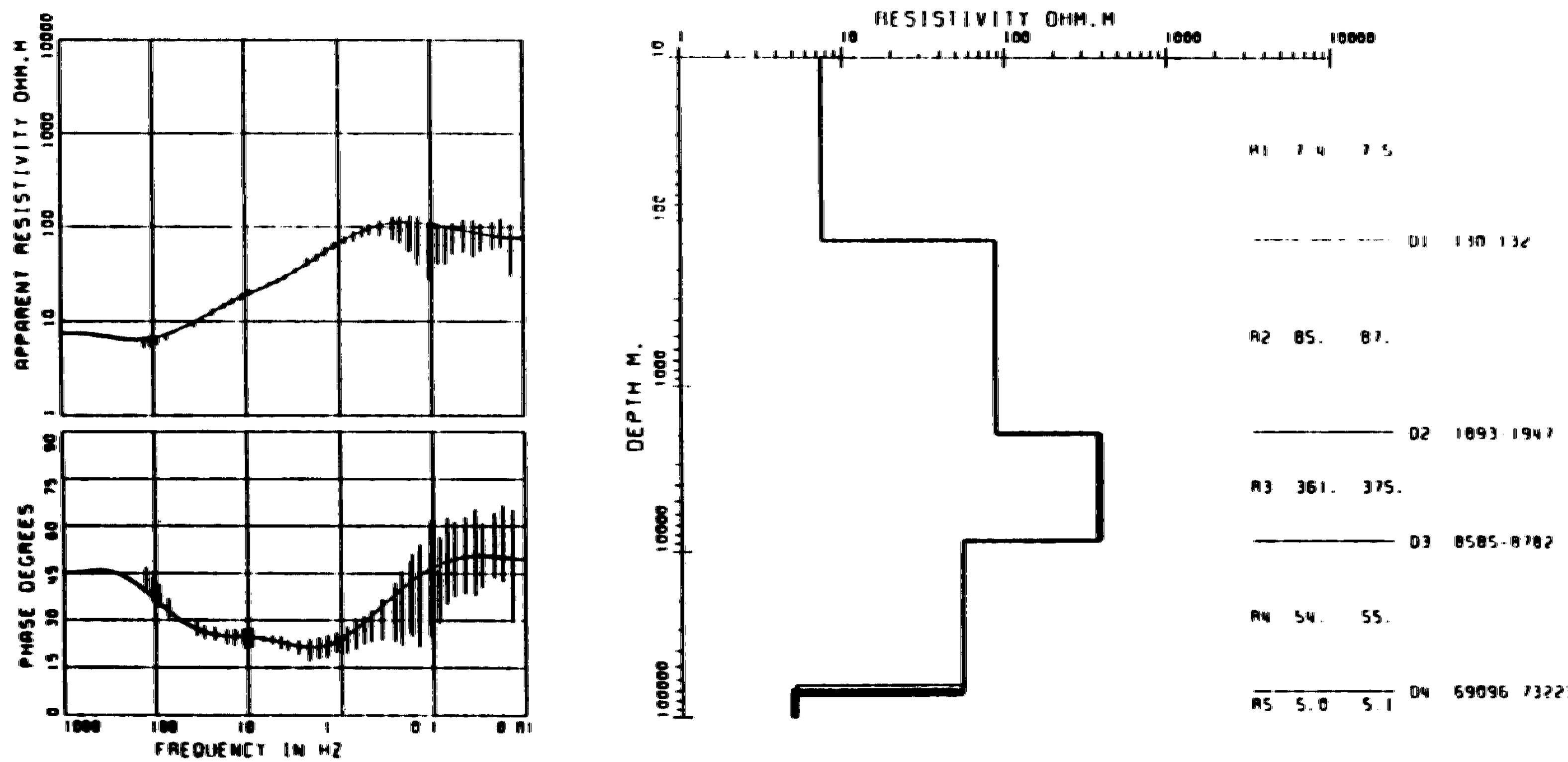

4 of/de 4

PM-1 3½"x4" PHOTOGRAPHIC MICROCOPY TARGET
NBS 1010a ANSI/ISO #2 EQUIVALENT

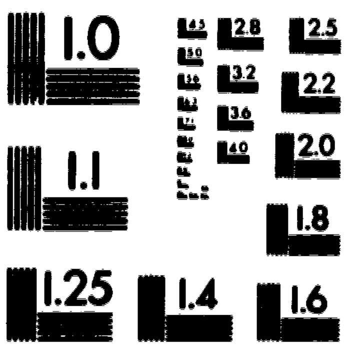

PRECISION℠ RESOLUTION TARGETS

1D Model for site 011X INVARIANT OF UP-DOWN MEAN

4 LAYERS WEIGHTED TENSOR

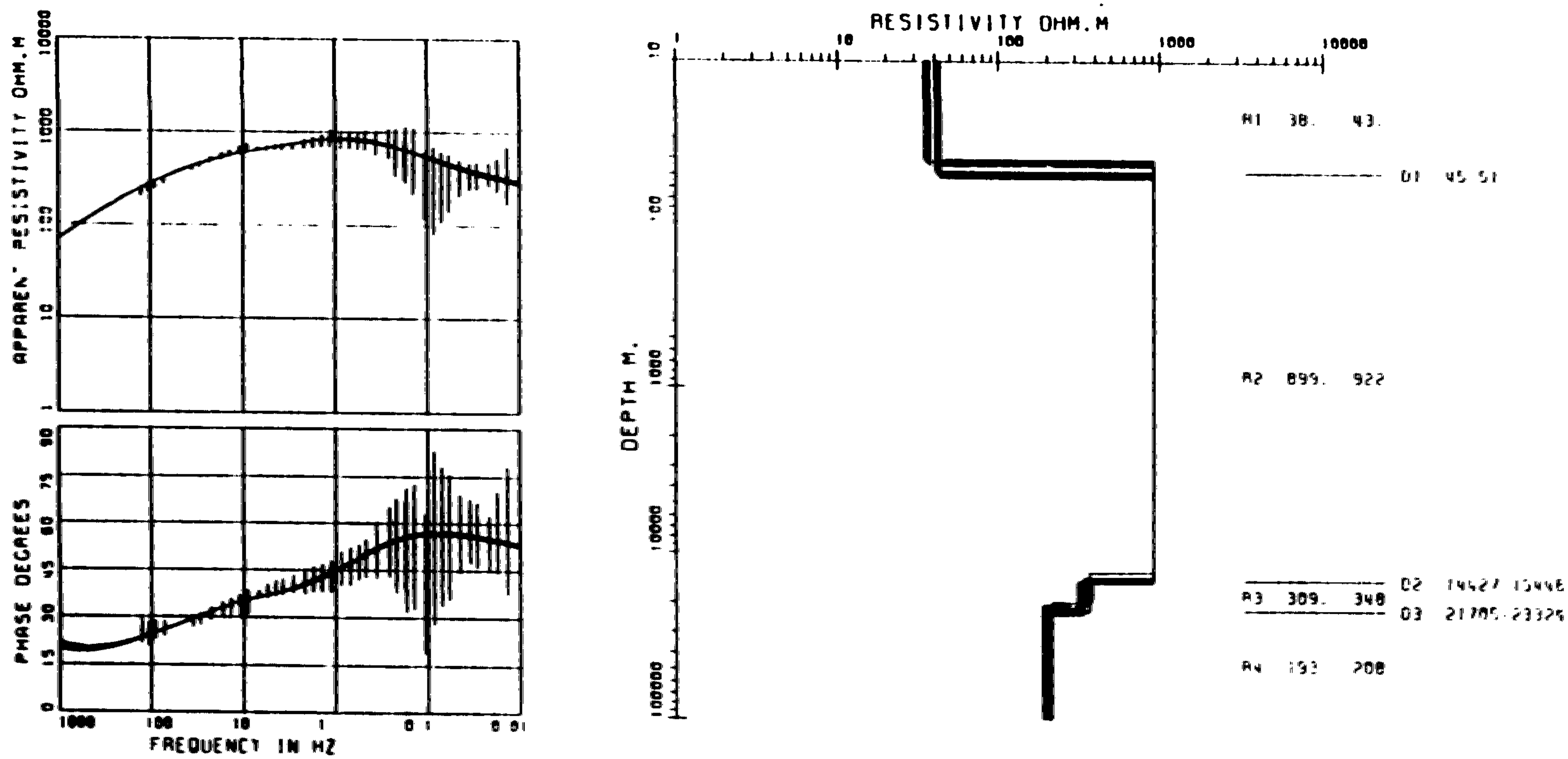

1D Model for site 012X INVARIANT OF UP DOWN MEAN

4 LAYERS WEIGHTED TENSOR

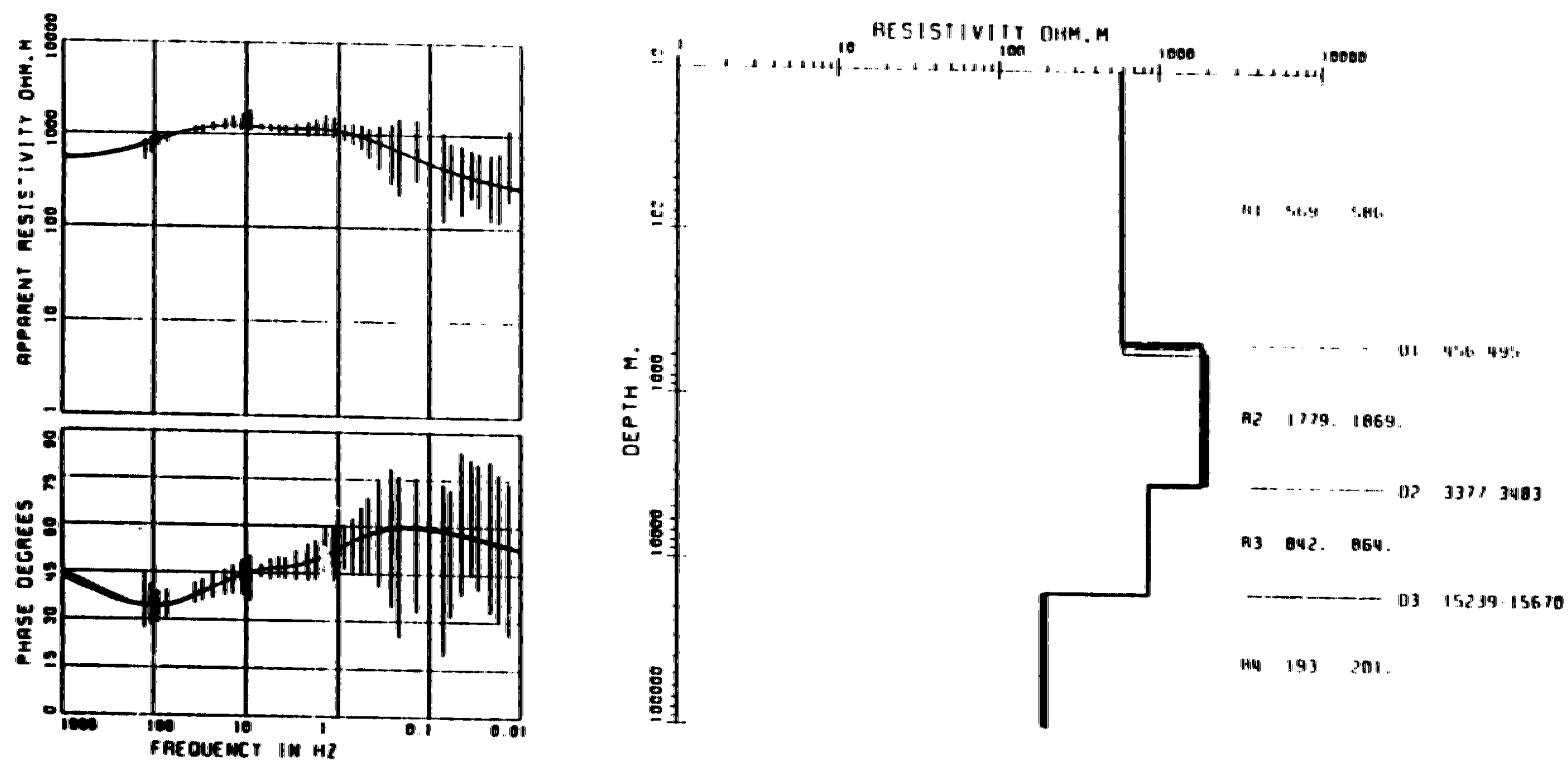

1D Model for site 013X INVARIANT OF UP-DOWN MEAN

4 LAYERS WEIGHTED TENSOR

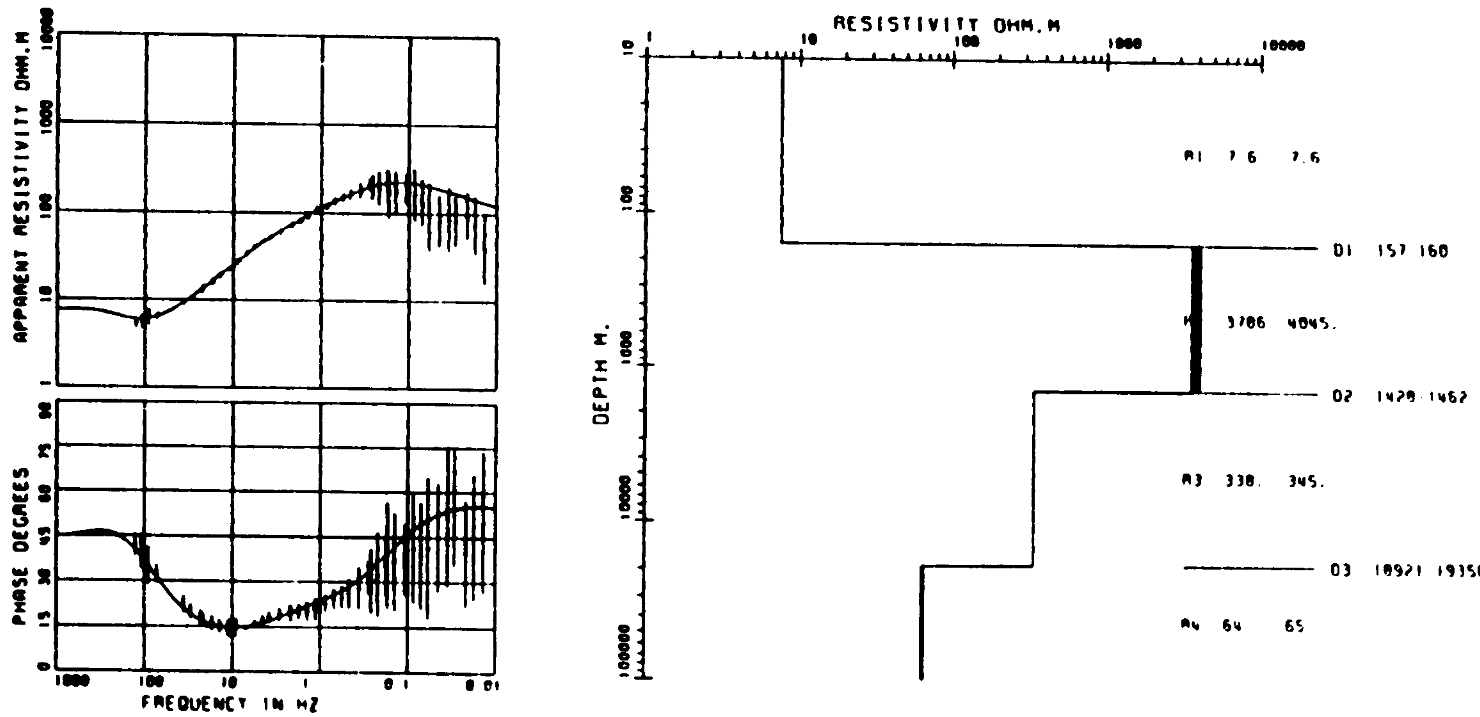

1D Model for site 014X INVARIANT OF UP-DOWN MEAN

4 LAYERS WEIGHTED TENSOR

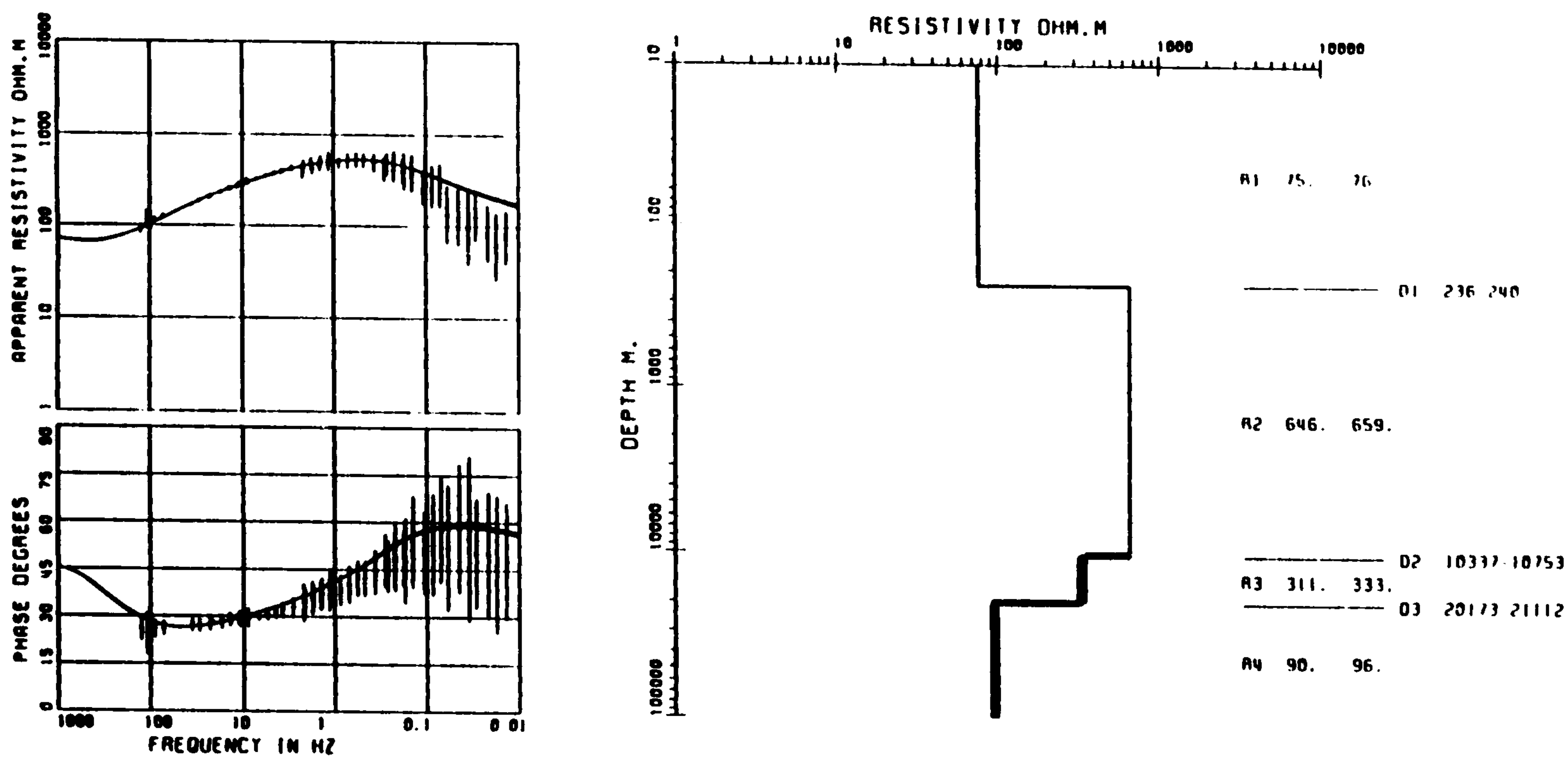

1D Model for site 015X INVARIANT OF UP-DOWN MEAN

4 LAYERS WEIGHTED TENSOR

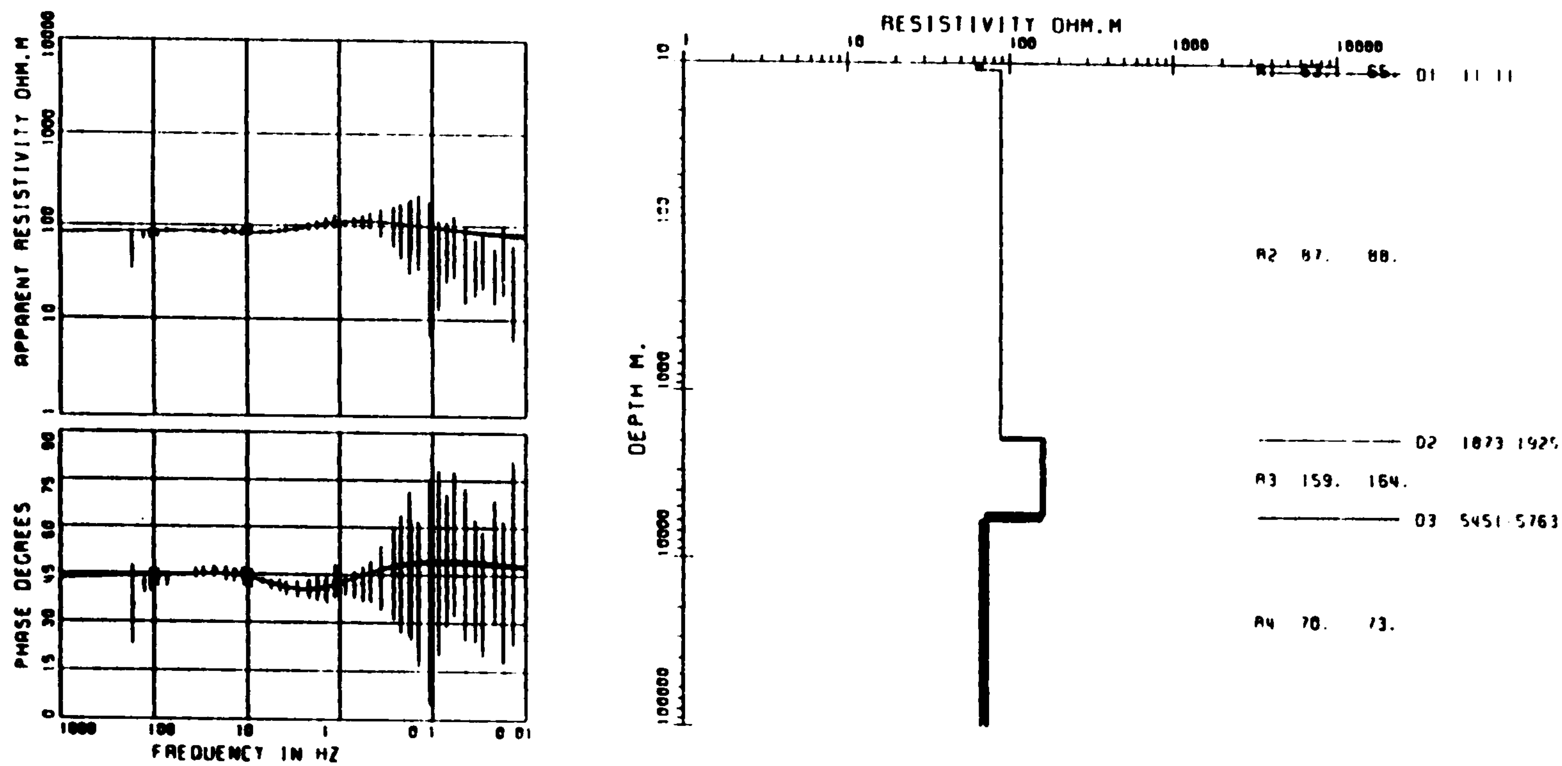

1D Model For site 016X INVARIANT OF UP-DOWN MEAN

4 LAYERS WEIGHTED TENSOR

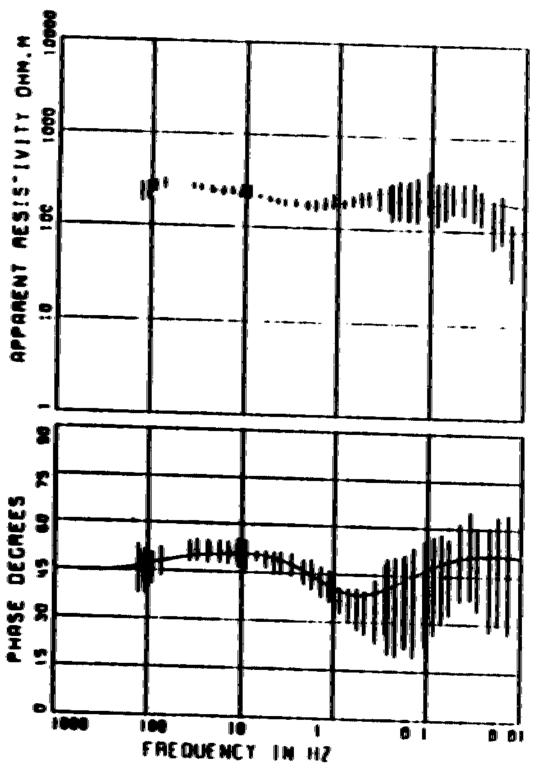

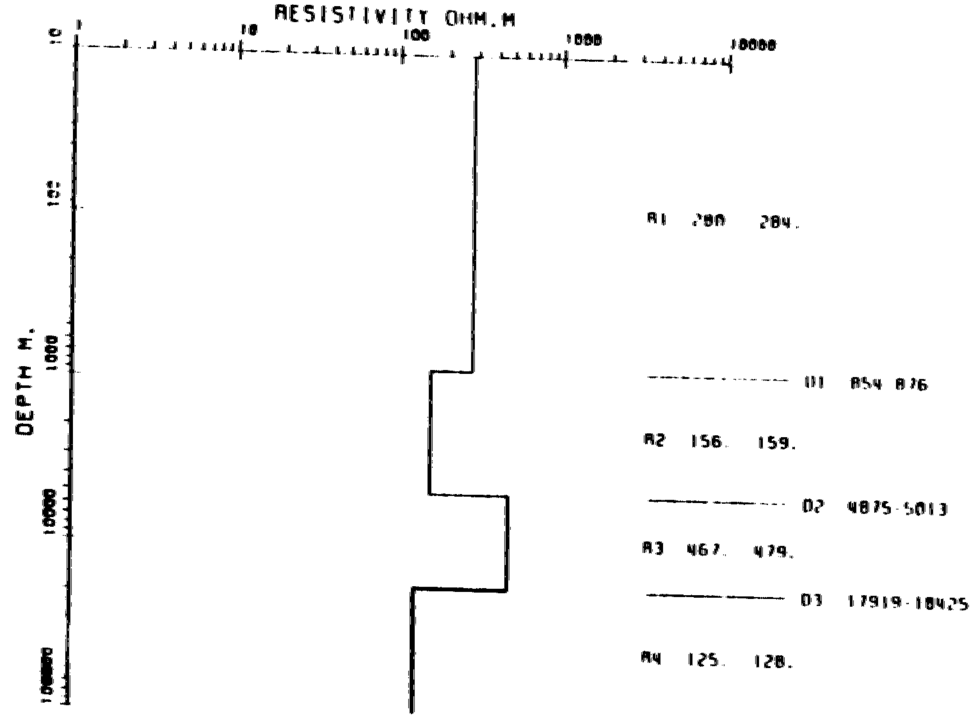

1D Model for site 017X INVARIANT OF UP-DOWN MEAN

4 LAYERS WEIGHTED TENSOR

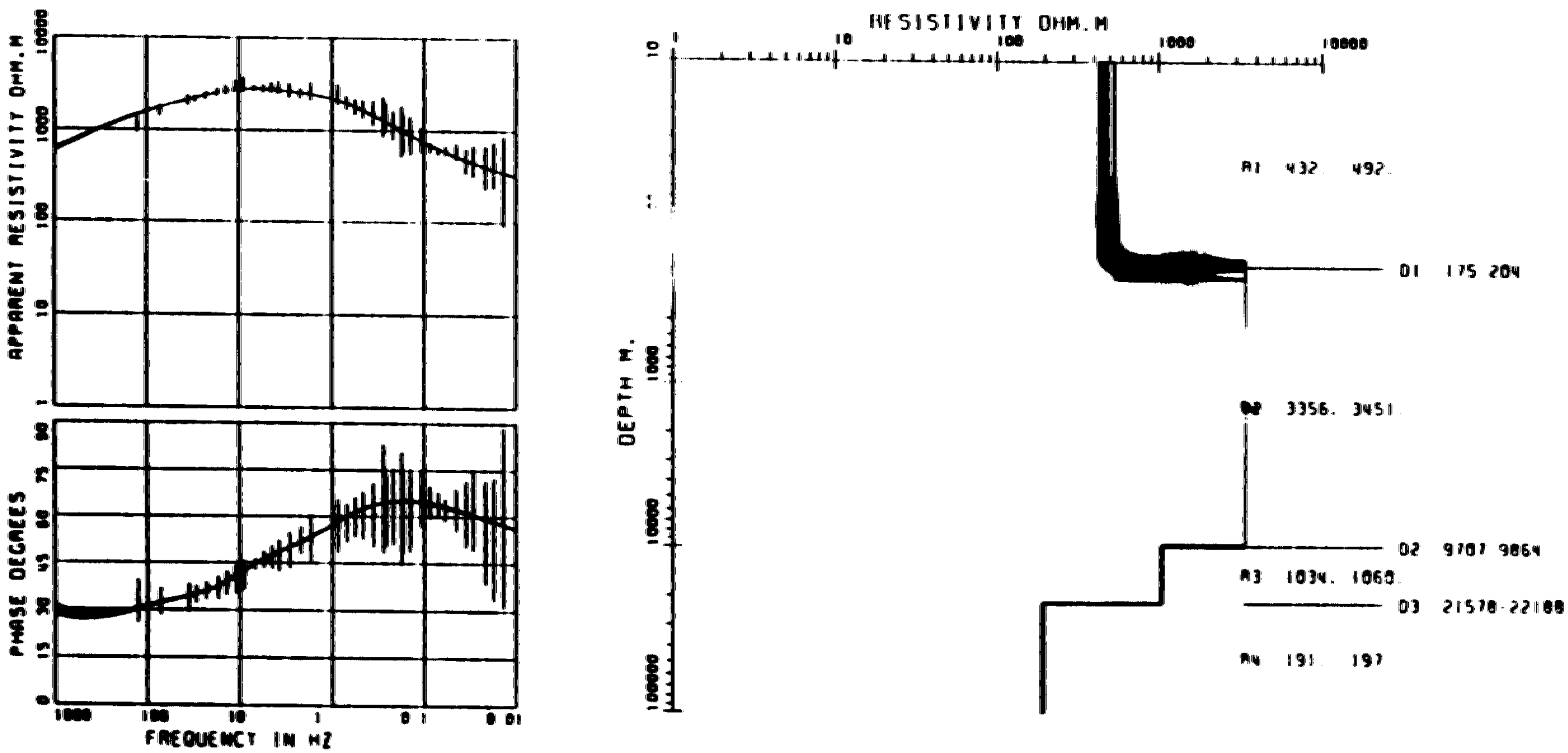

1D Model for site 018X INVARIANT OF UP-DOWN MEAN

4 LAYERS WEIGHTED TENSOR

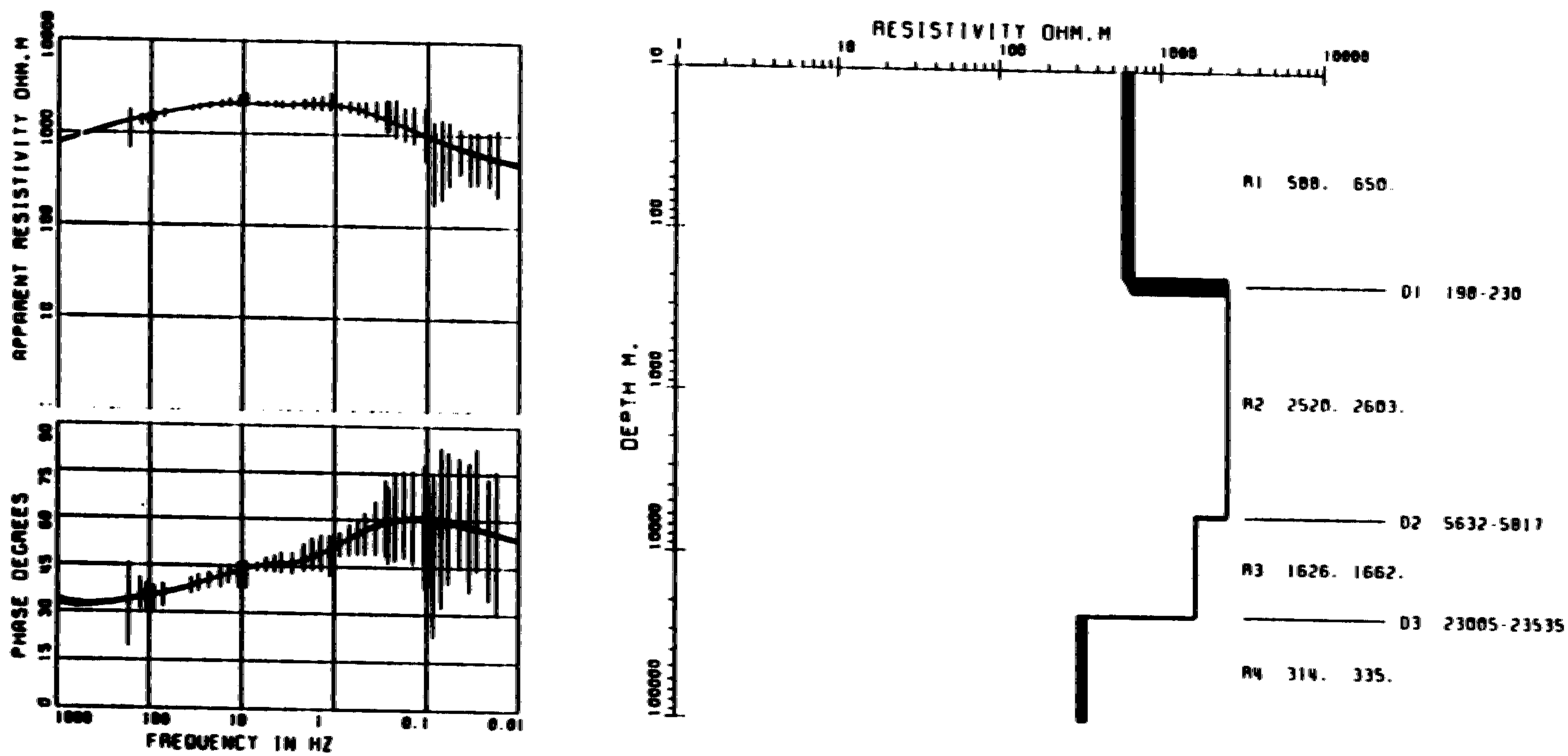

1D Model for site 019X INVARIANT OF UP-DOWN MEAN

4 LAYERS WEIGHTED TENSOR

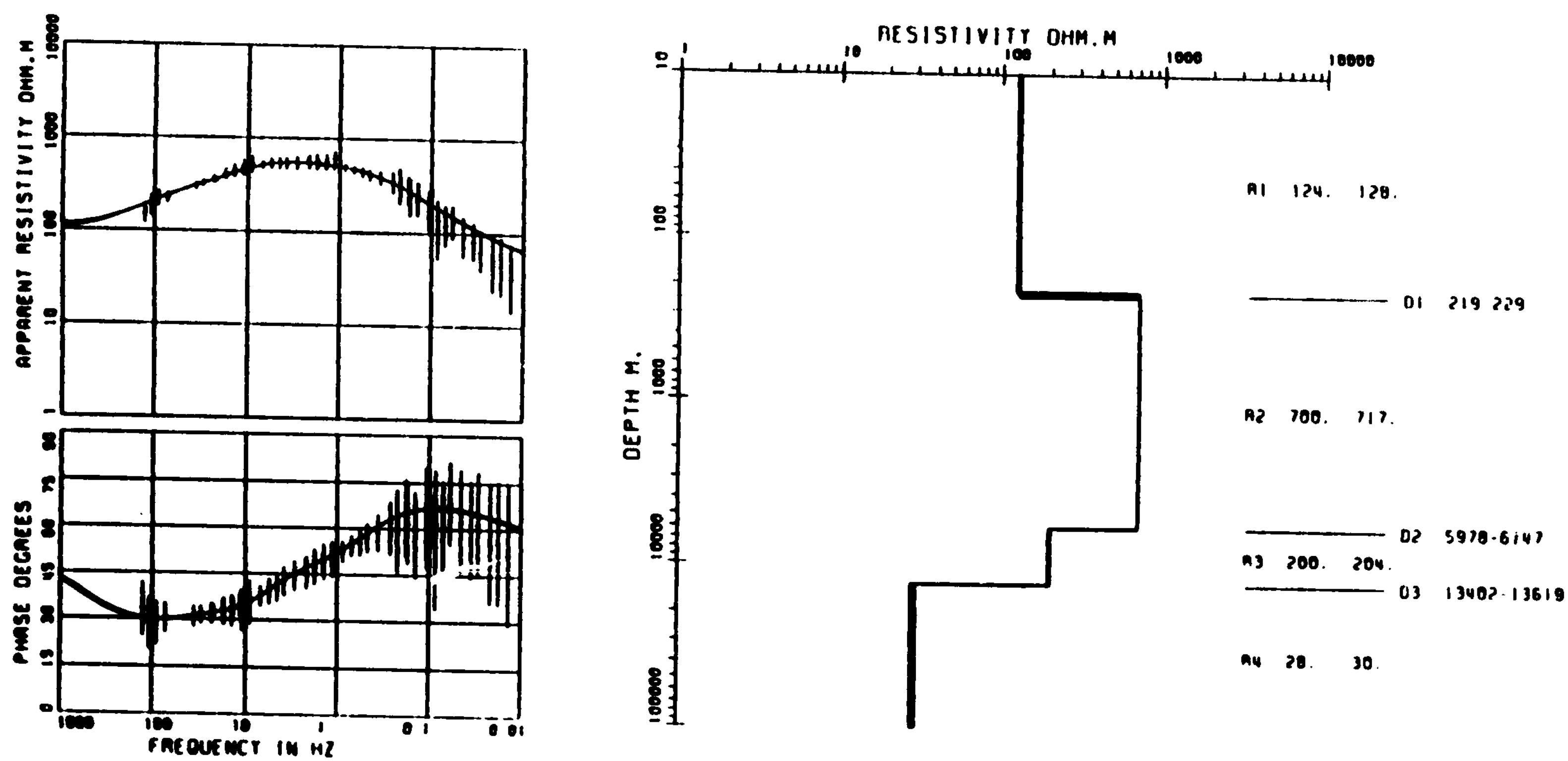

1D Model for site 020X INVARIANT OF UP-DOWN MEAN

4 LAYERS WEIGHTED TENSOR

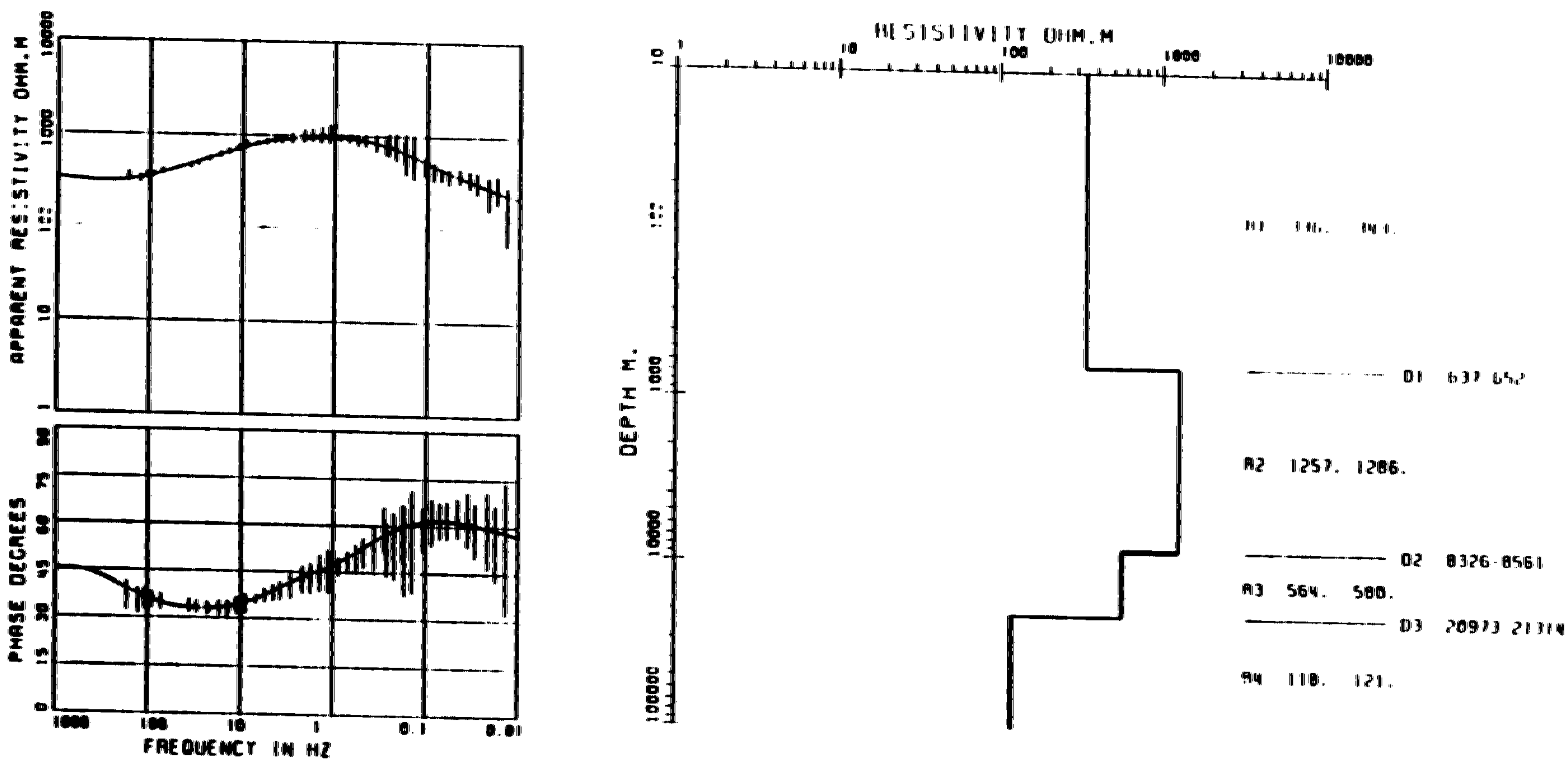

1D Model for site 021X INVARIANT OF UP-DOWN MEAN

4 LAYERS WEIGHTED TENSOR

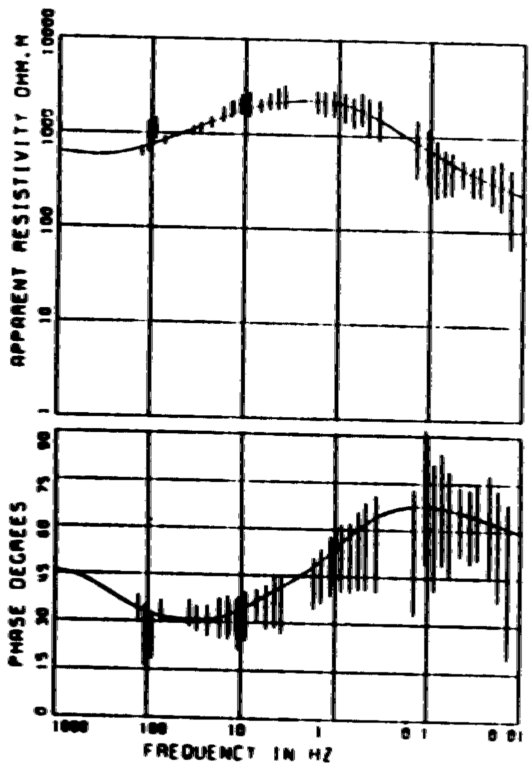

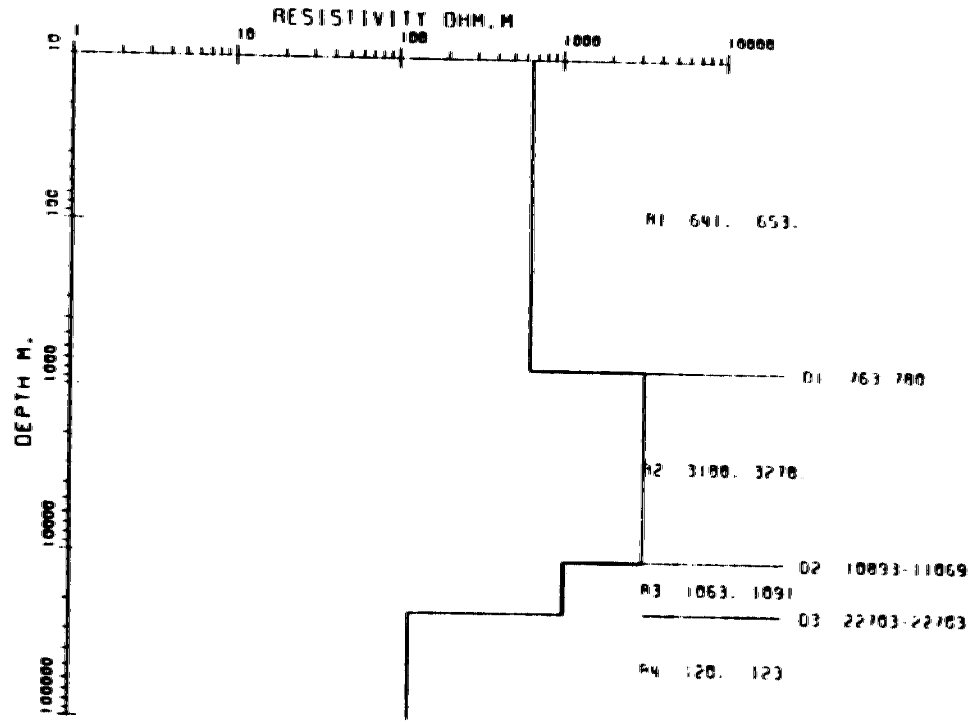

1D Model for site 022X INVARIANT OF UP-DOWN MEAN

4 LAYERS WEIGHTED TENSOR

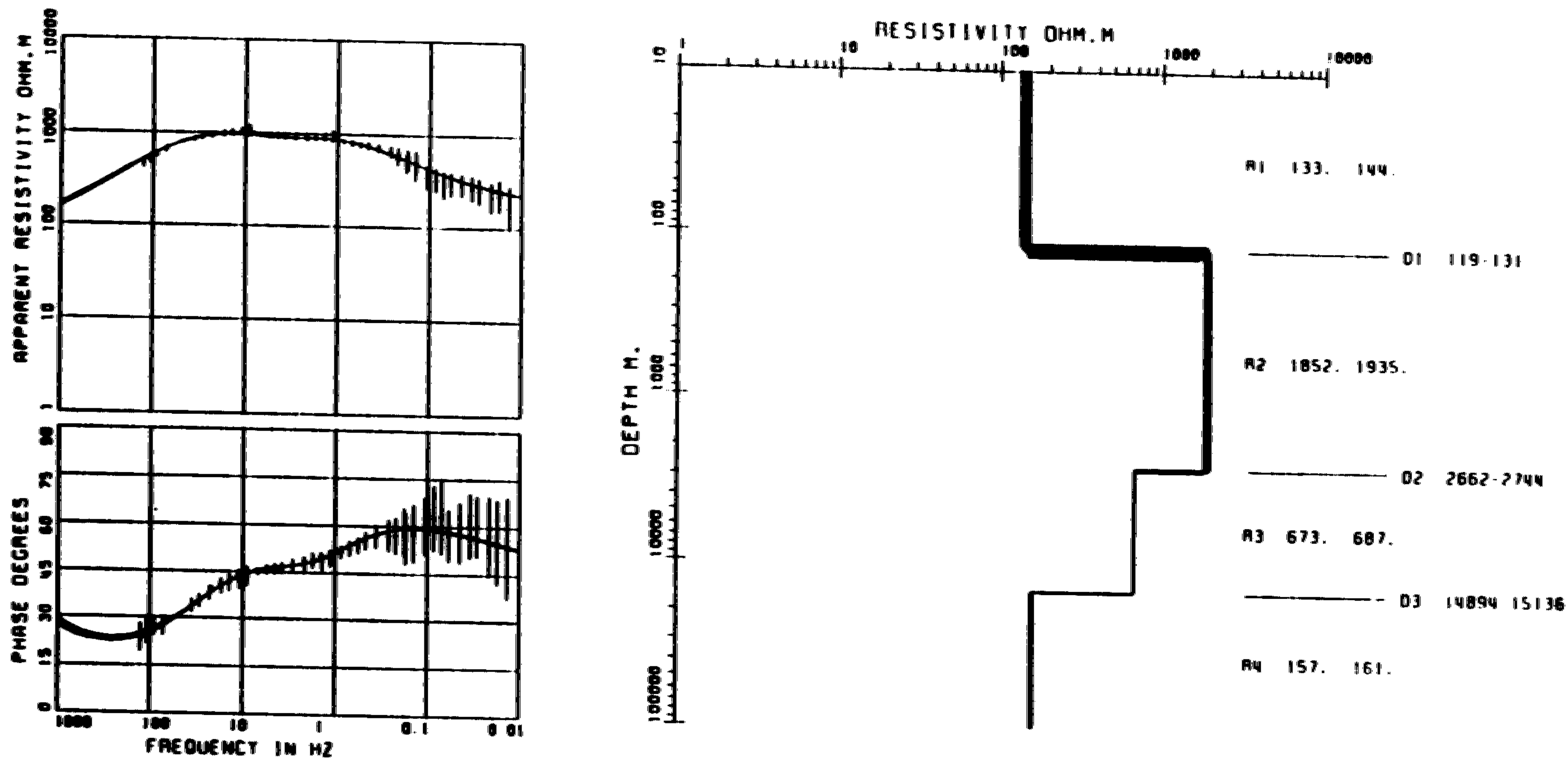

1D Model for site 023X INVARIANT OF UP-DOWN MEAN

3 LAYERS WEIGHTED TENSOR

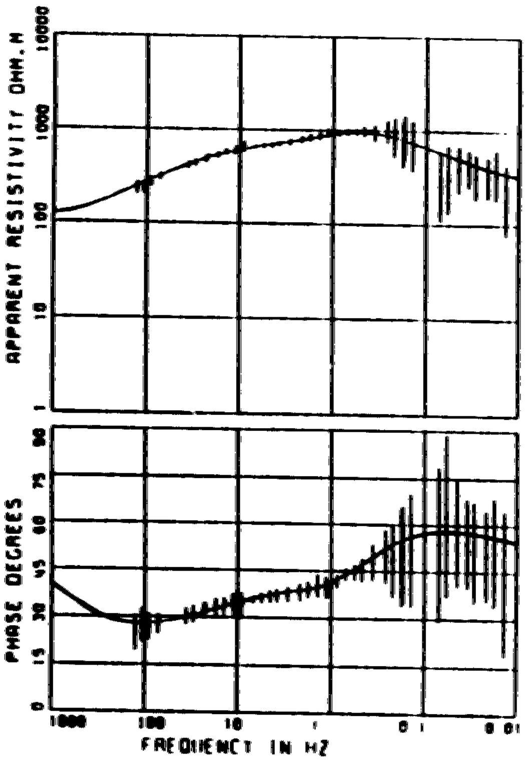

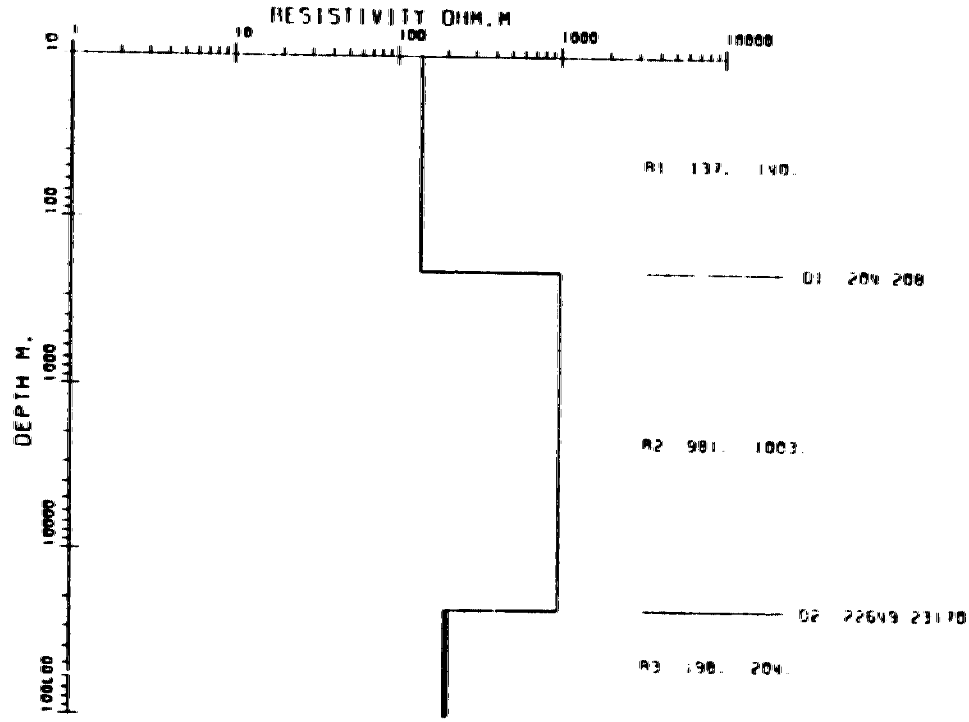

1D Model for site 024X INVARIANT OF UP-DOWN MEAN

4 LAYERS WEIGHTED TENSOR

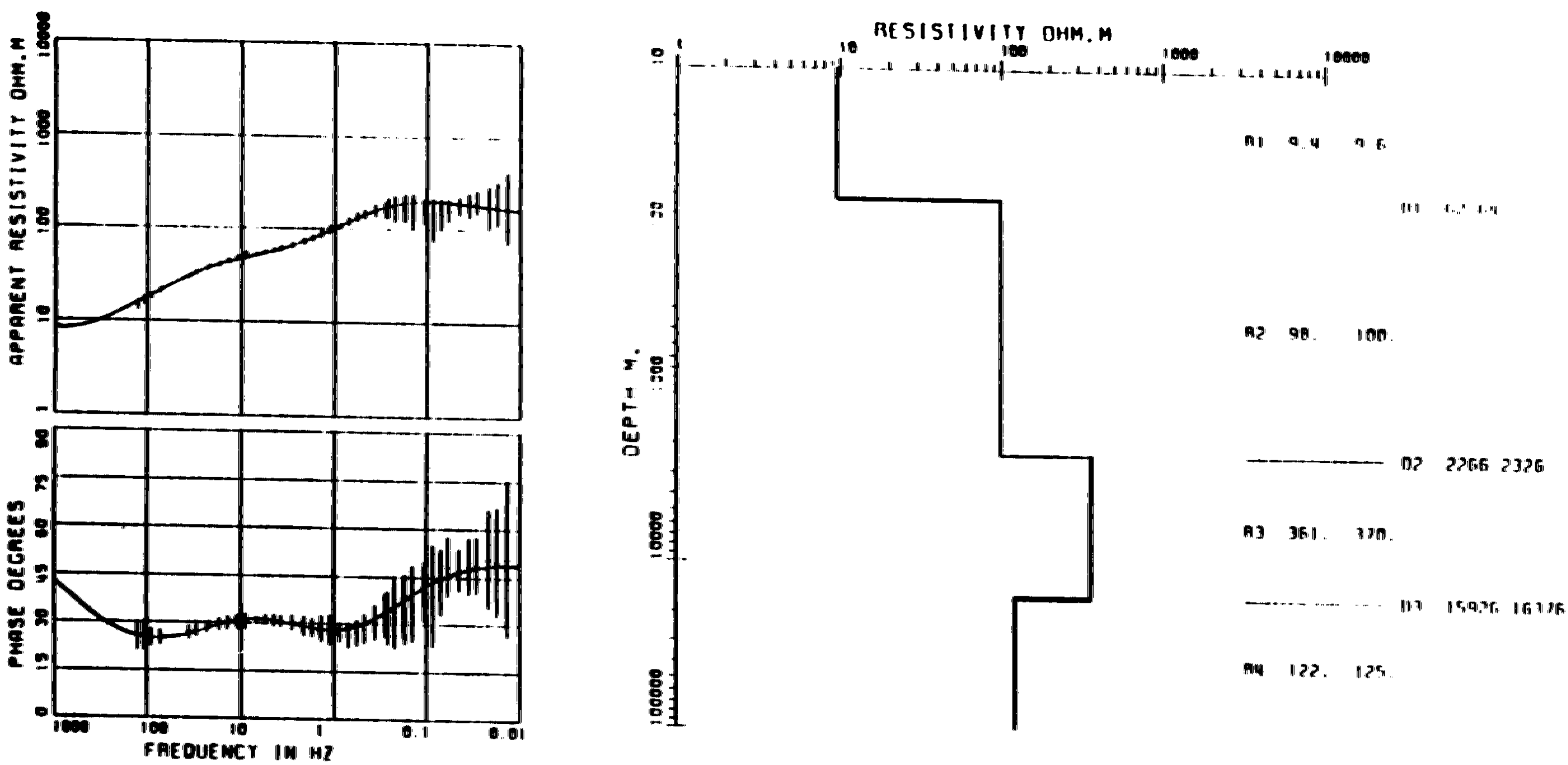

1D Model for site 025X INVARIANT OF UP-DOWN MEAN

4 LAYERS WEIGHTED TENSOR

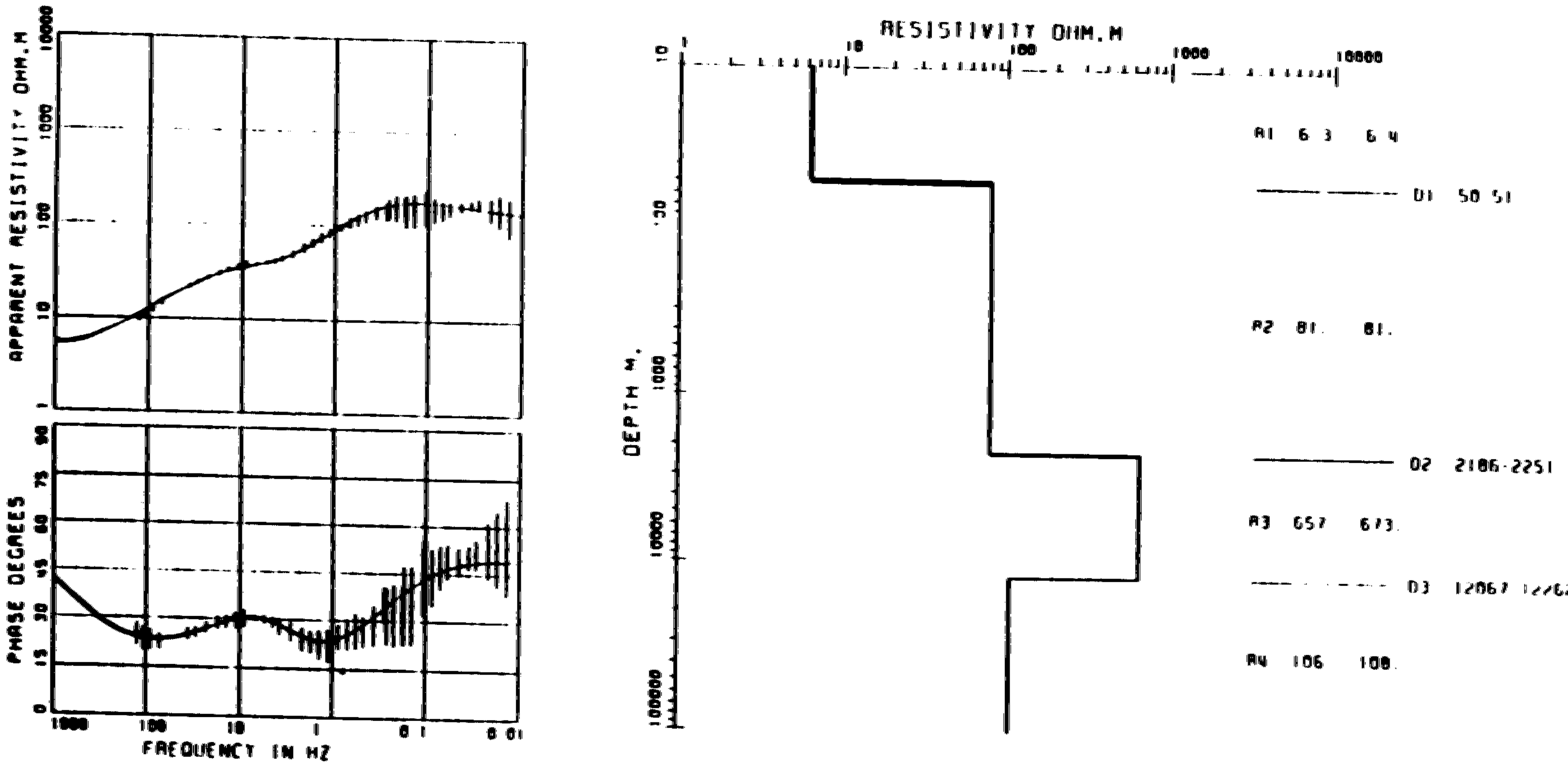

1D Model for site 026X INVARIANT OF UP-DOWN MEAN

3 LAYERS WEIGHTED TENSOR

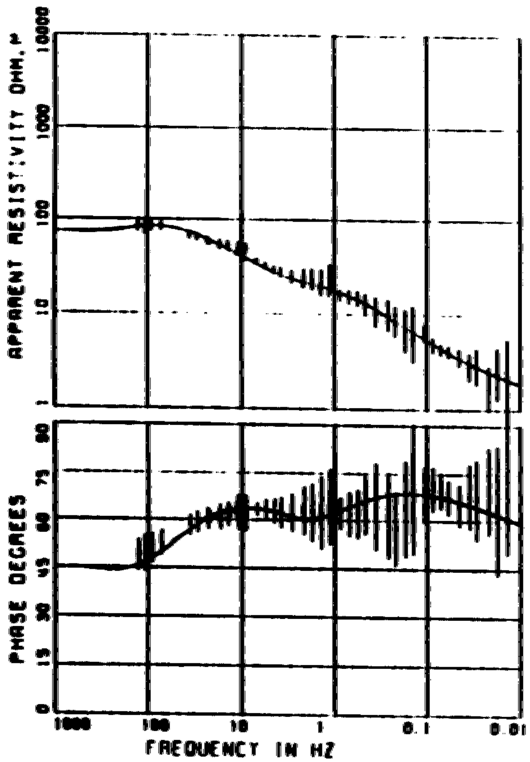

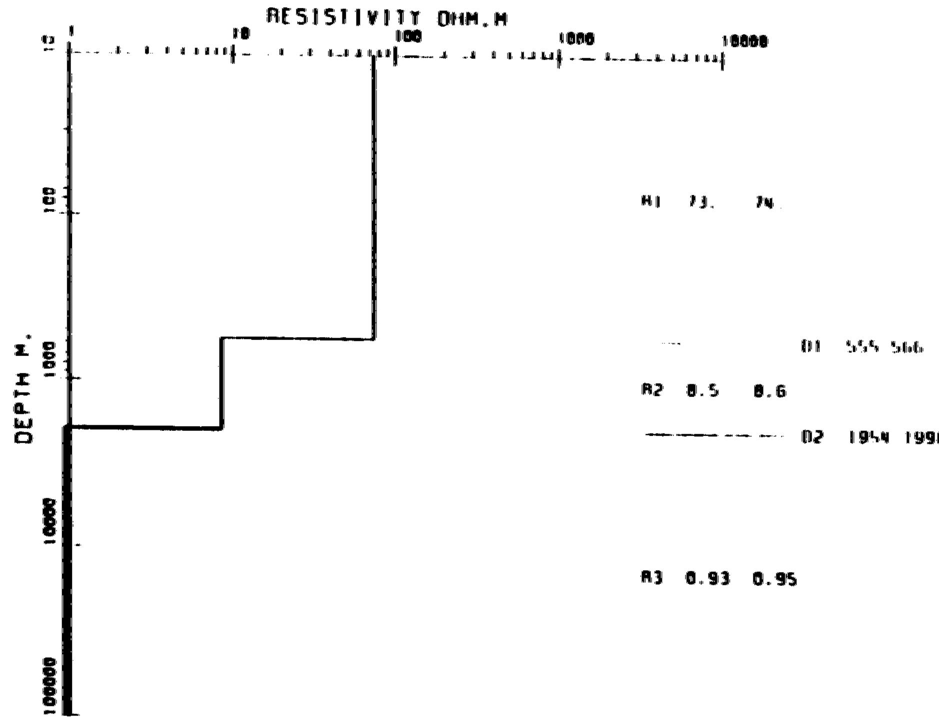

1D Model for site 027X INVARIANT OF UP-DOWN MEAN

3 LAYERS WEIGHTED TENSOR

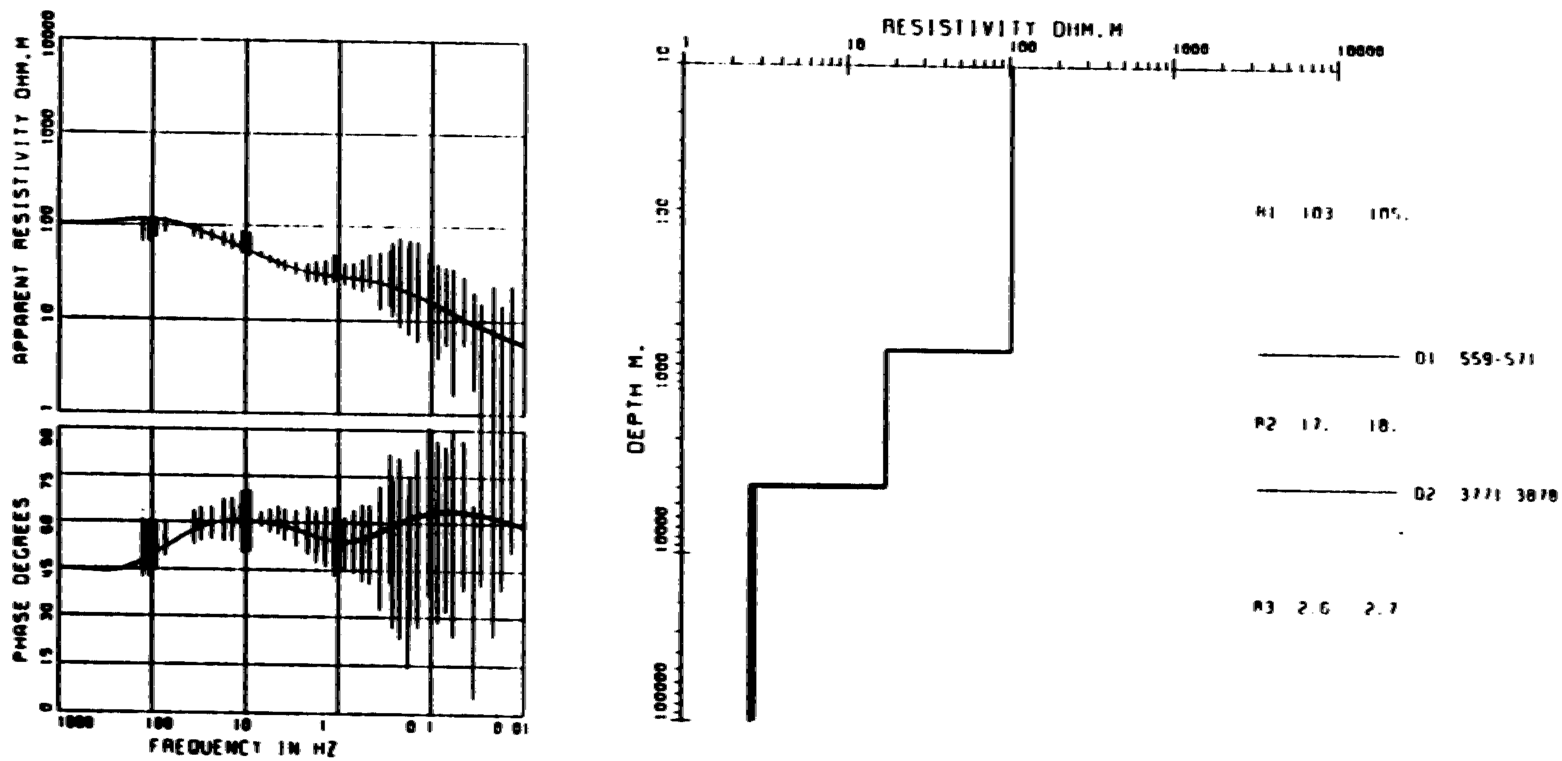

1D Model for site 028X INVARIANT OF UP-DOWN MEAN

3 LAYERS WEIGHTED TENSOR

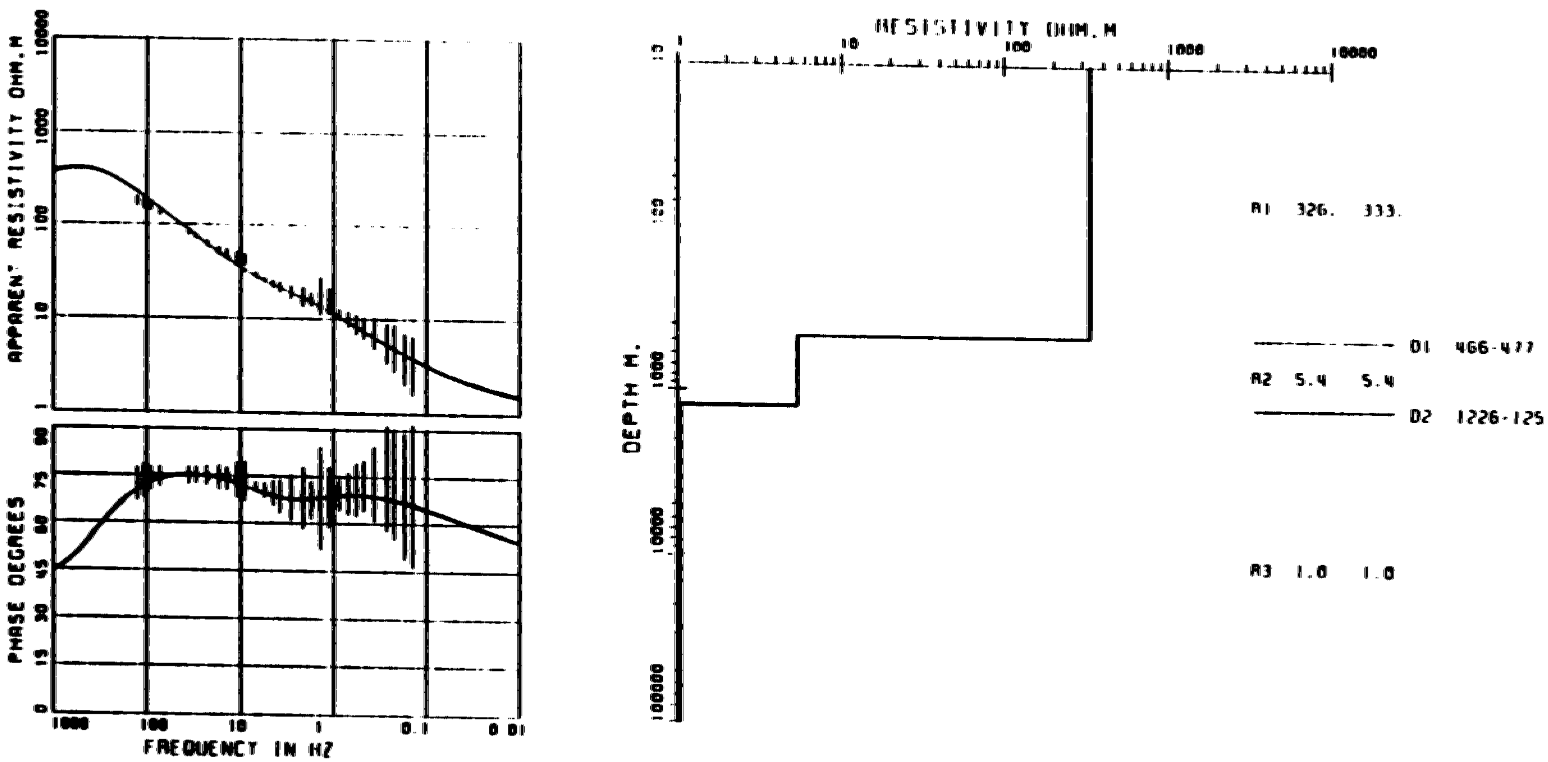

1D Model for site 029X INVARIANT OF UP-DOWN MEAN

3 LAYERS WEIGHTED TENSOR

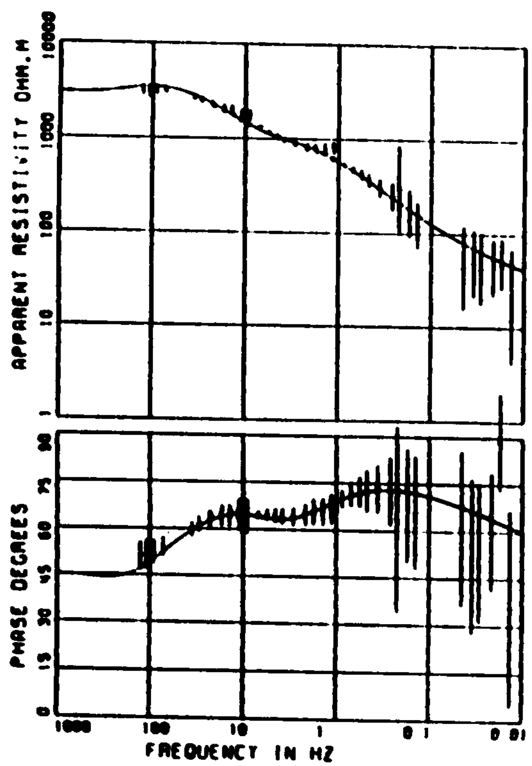

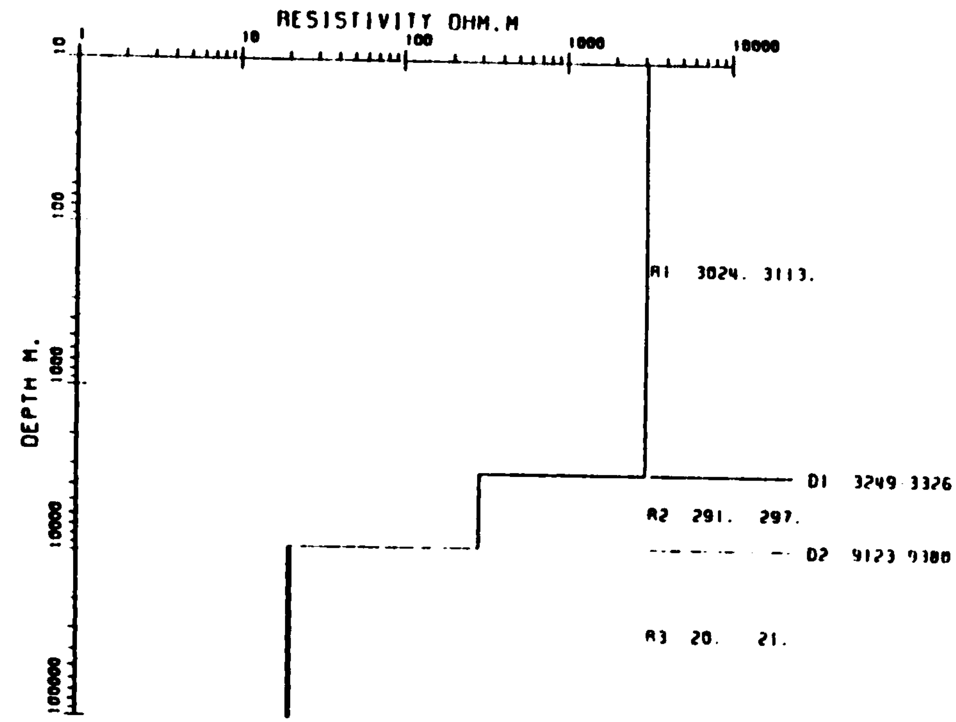

1D Model for site 030X INVARIANT OF UP-DOWN MEAN

3 LAYERS WEIGHTED TENSOR

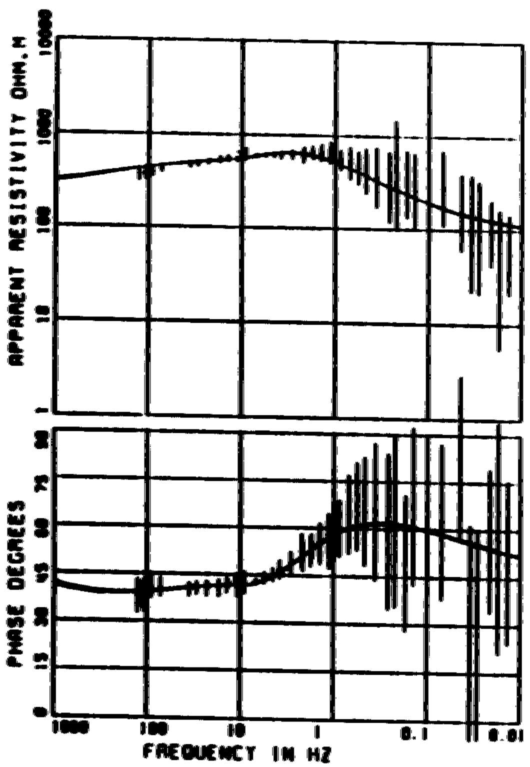

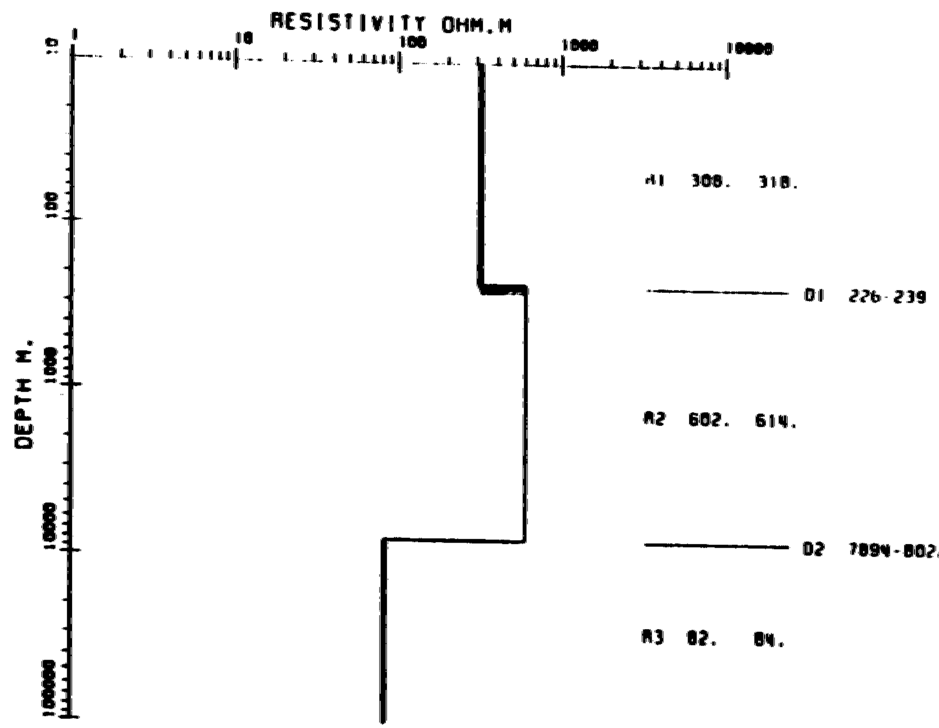

1D Model for site 031X INVARIANT OF UP-DOWN MEAN

4 LAYERS WEIGHTED TENSOR

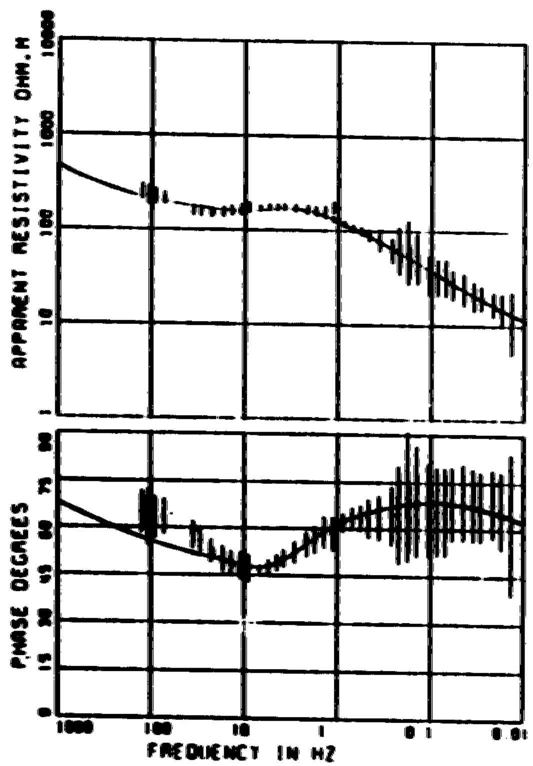

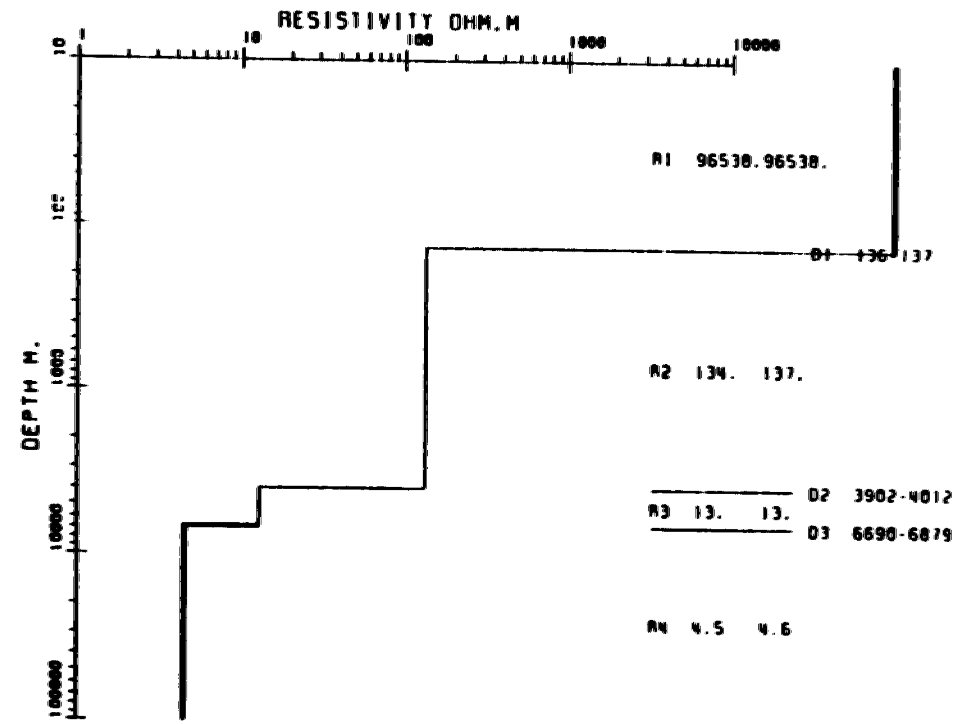

1D Model for site 032X INVARIANT OF UP-DOWN MEAN

3 LAYERS WEIGHTED TENSOR

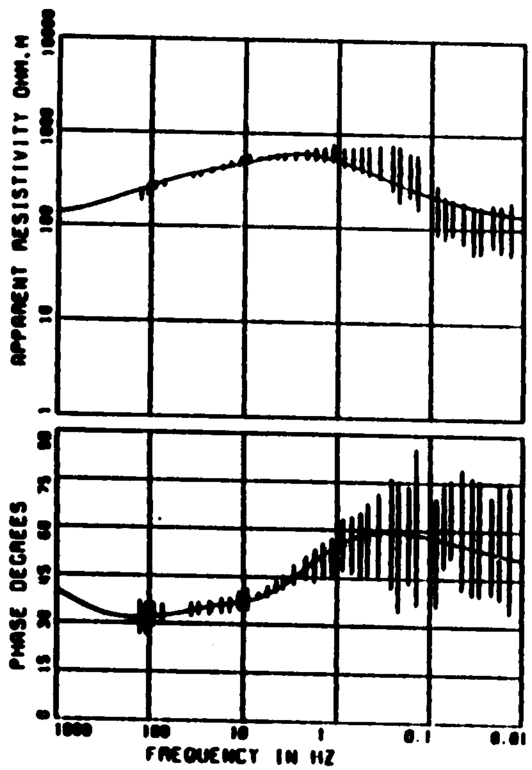

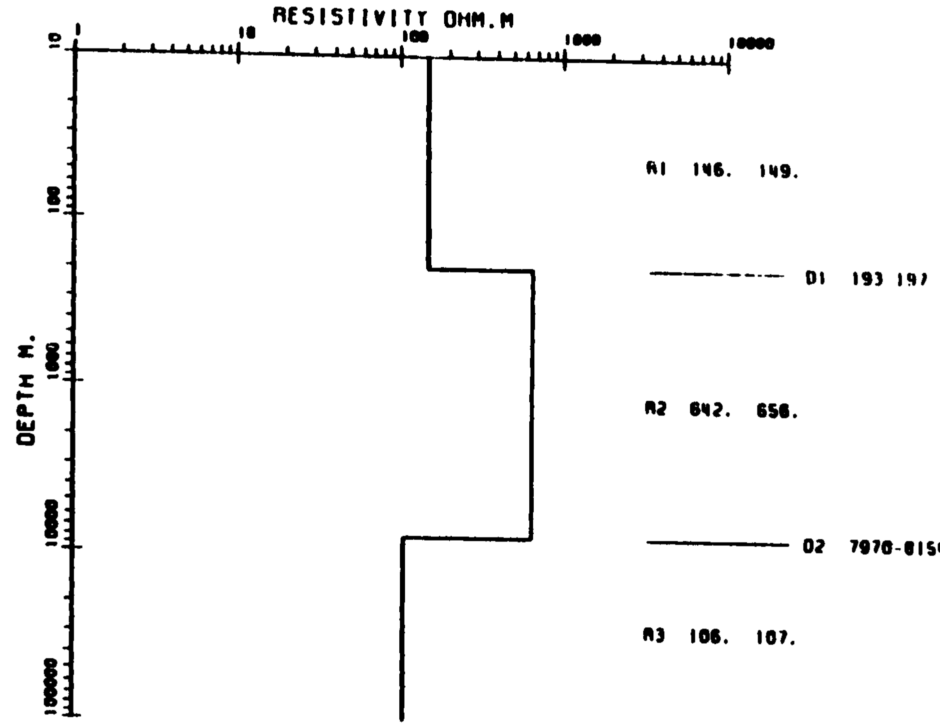

1D Model for site 033X INVARIANT OF UP-DOWN MEAN

6 LAYERS WEIGHTED TENSOR

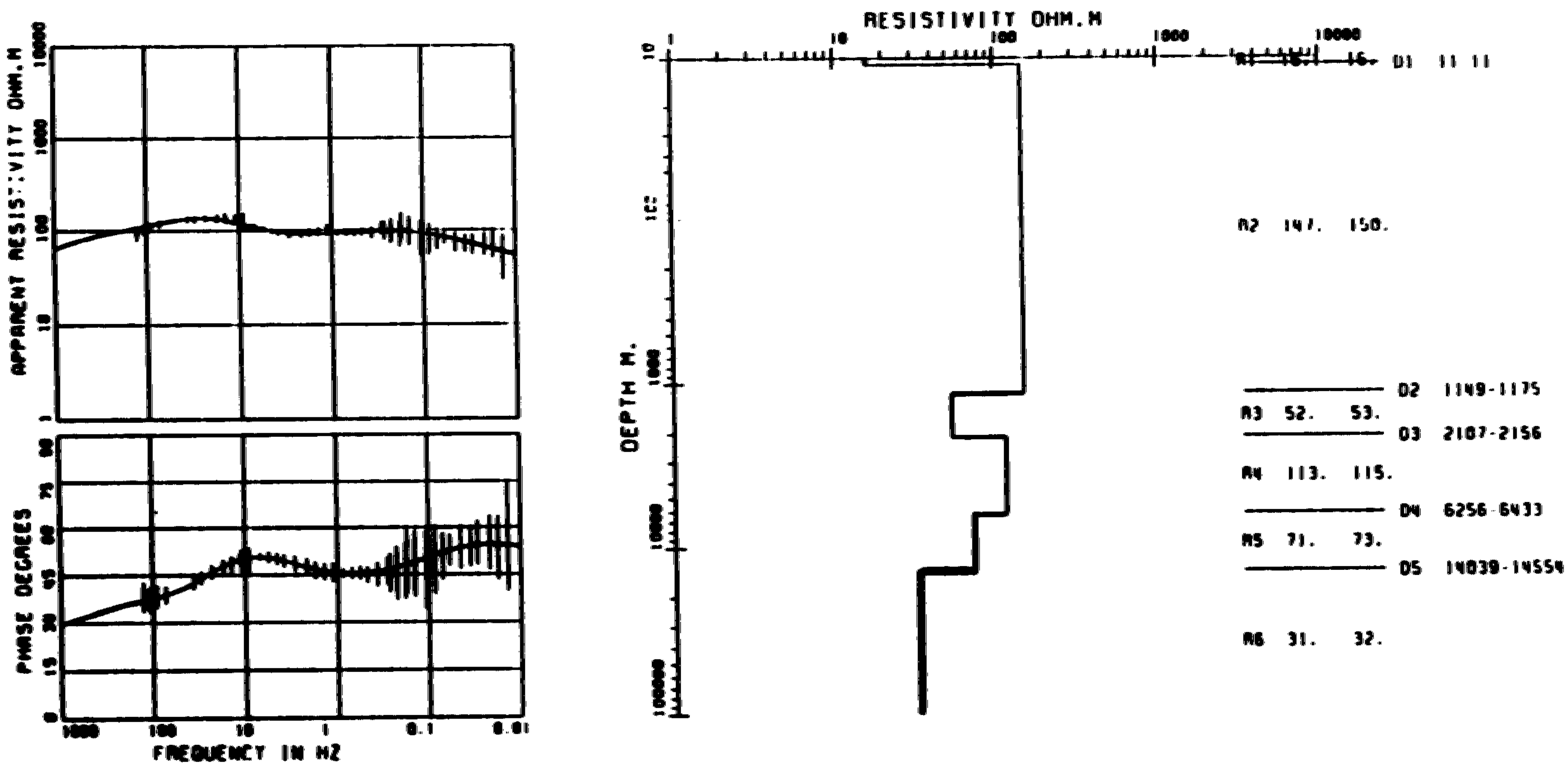

1D Model for site 034X INVARIANT OF UP-DOWN MEAN

4 LAYERS WEIGHTED TENSOR

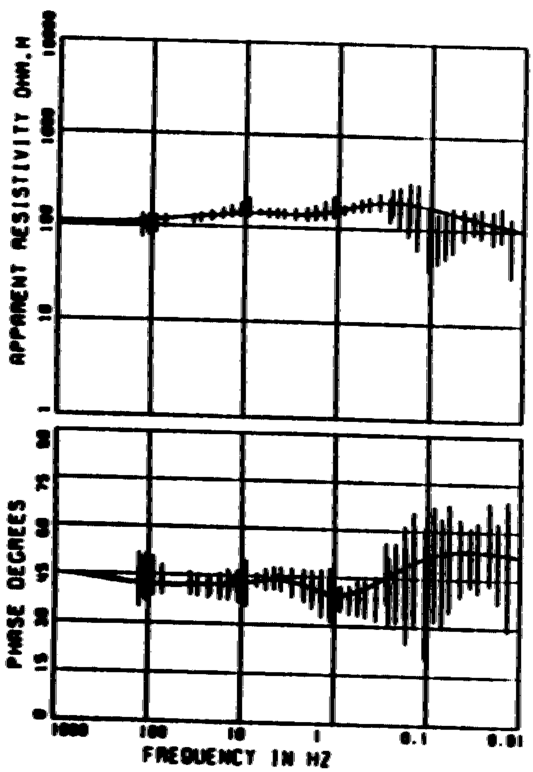

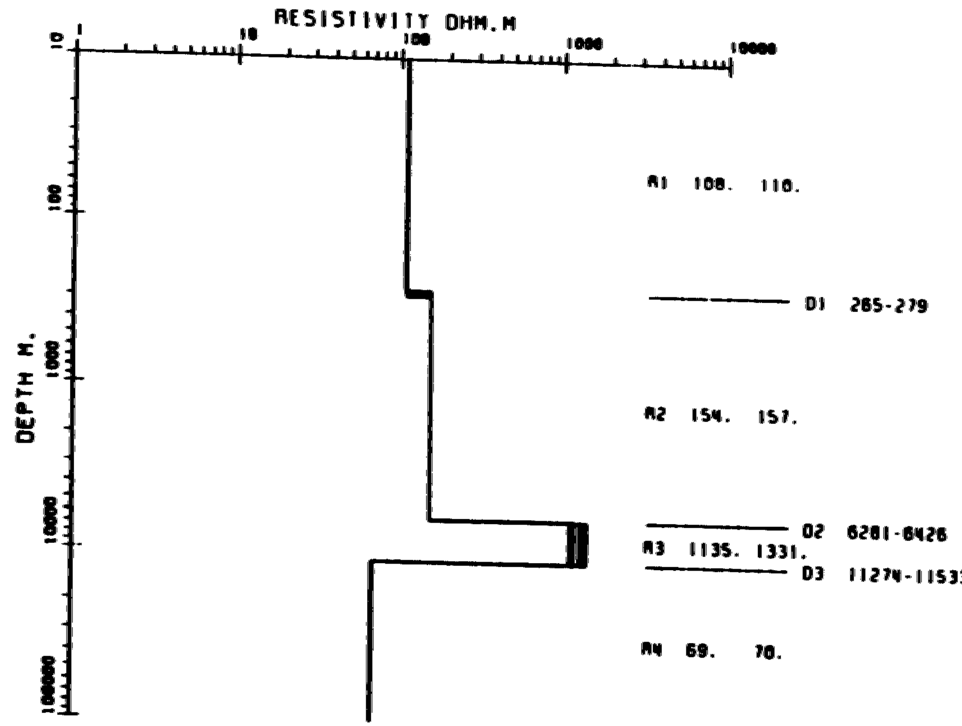

APPENDIX III

ELECTRICAL RESISTIVITY MAPS AT SEVERAL DEPTHS

The isolines are electrical resistivities in ohm-m.

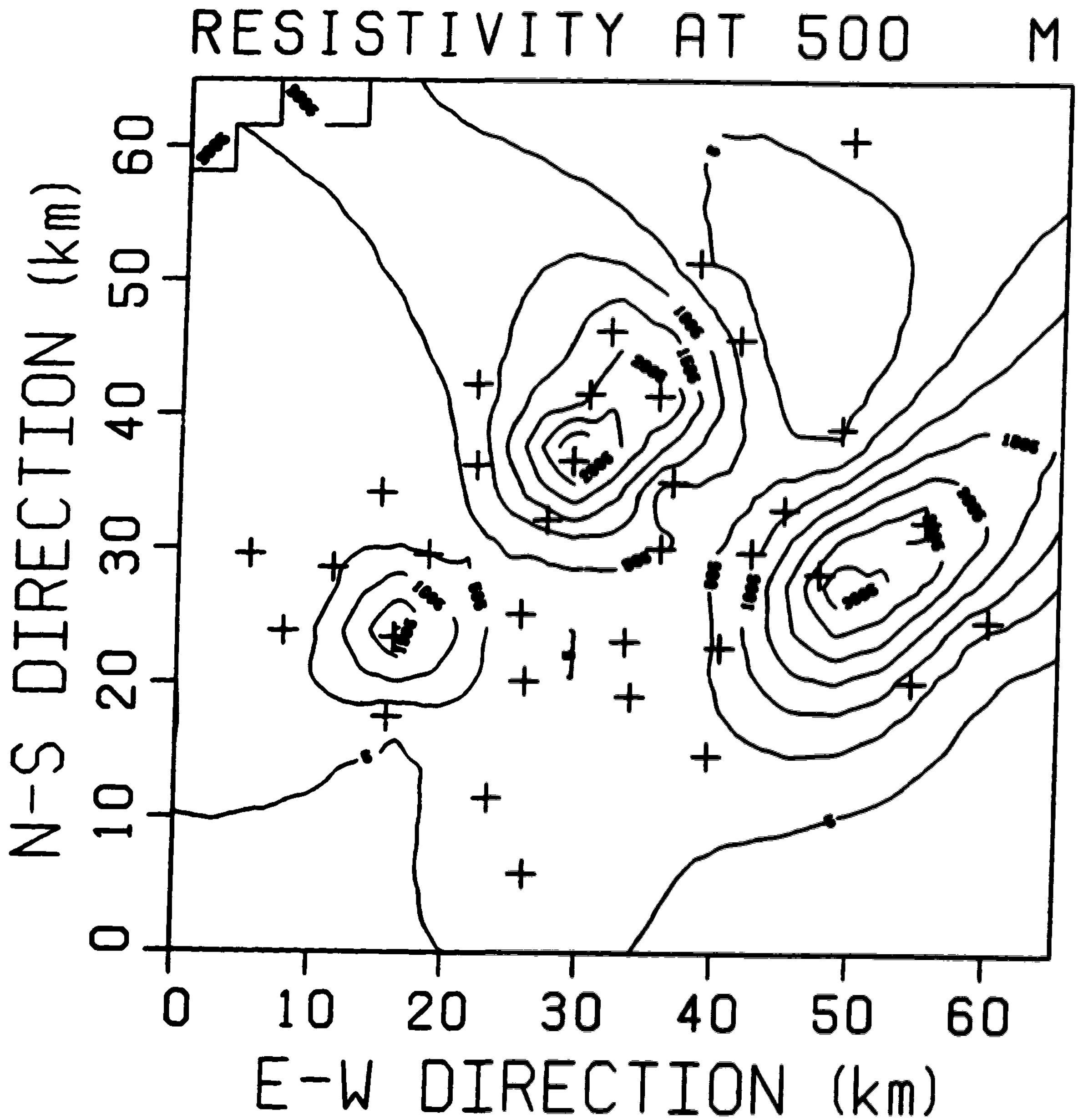
RESISTIVITY AT 500 M
N-S DIRECTION (km)
E-W DIRECTION (km)
0
10
20
30
40
50
60

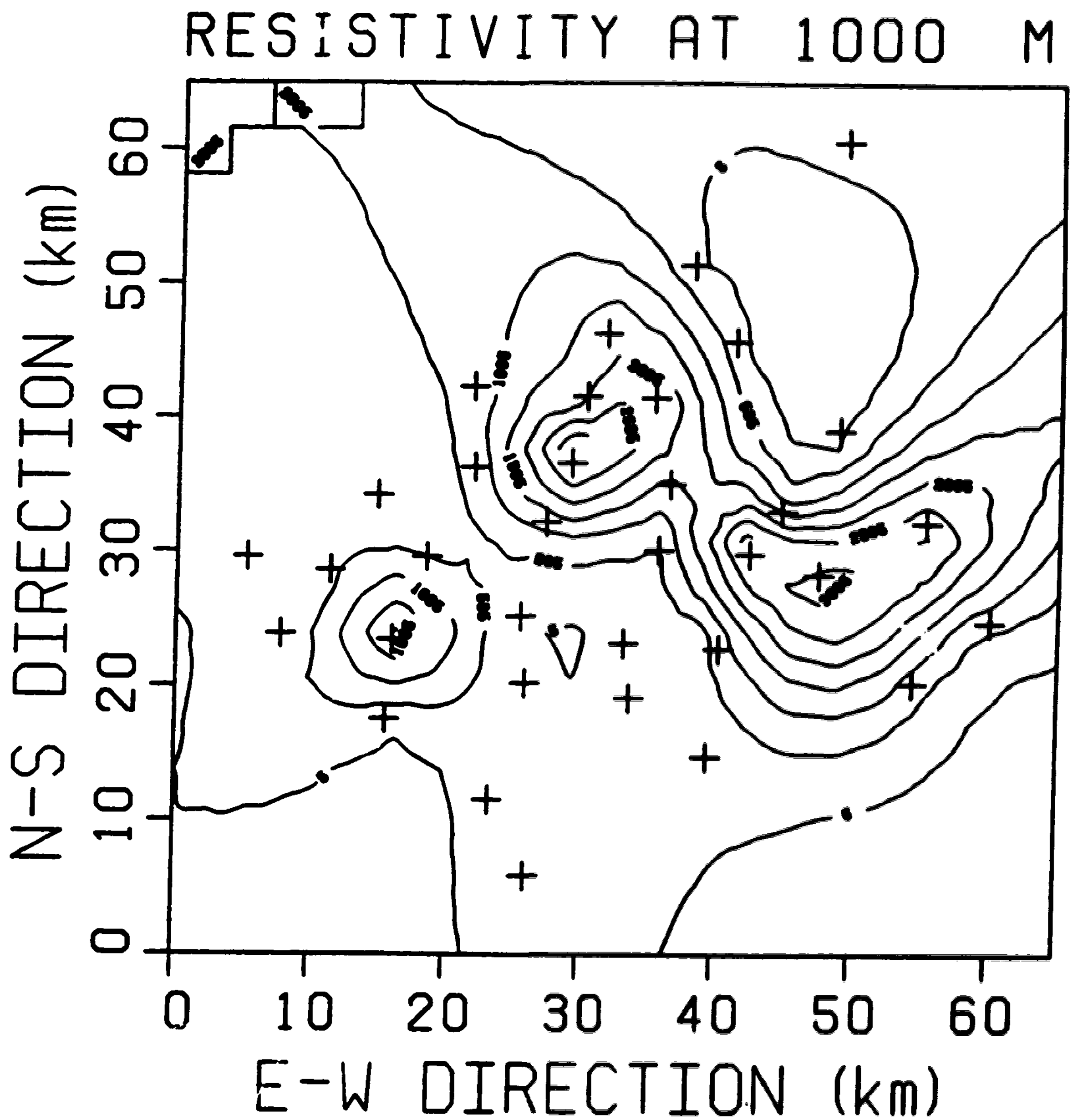
RESISTIVITY AT 1000 M
N-S DIRECTION (km)
E-W DIRECTION (km)
0
10
20
30
40
50
60

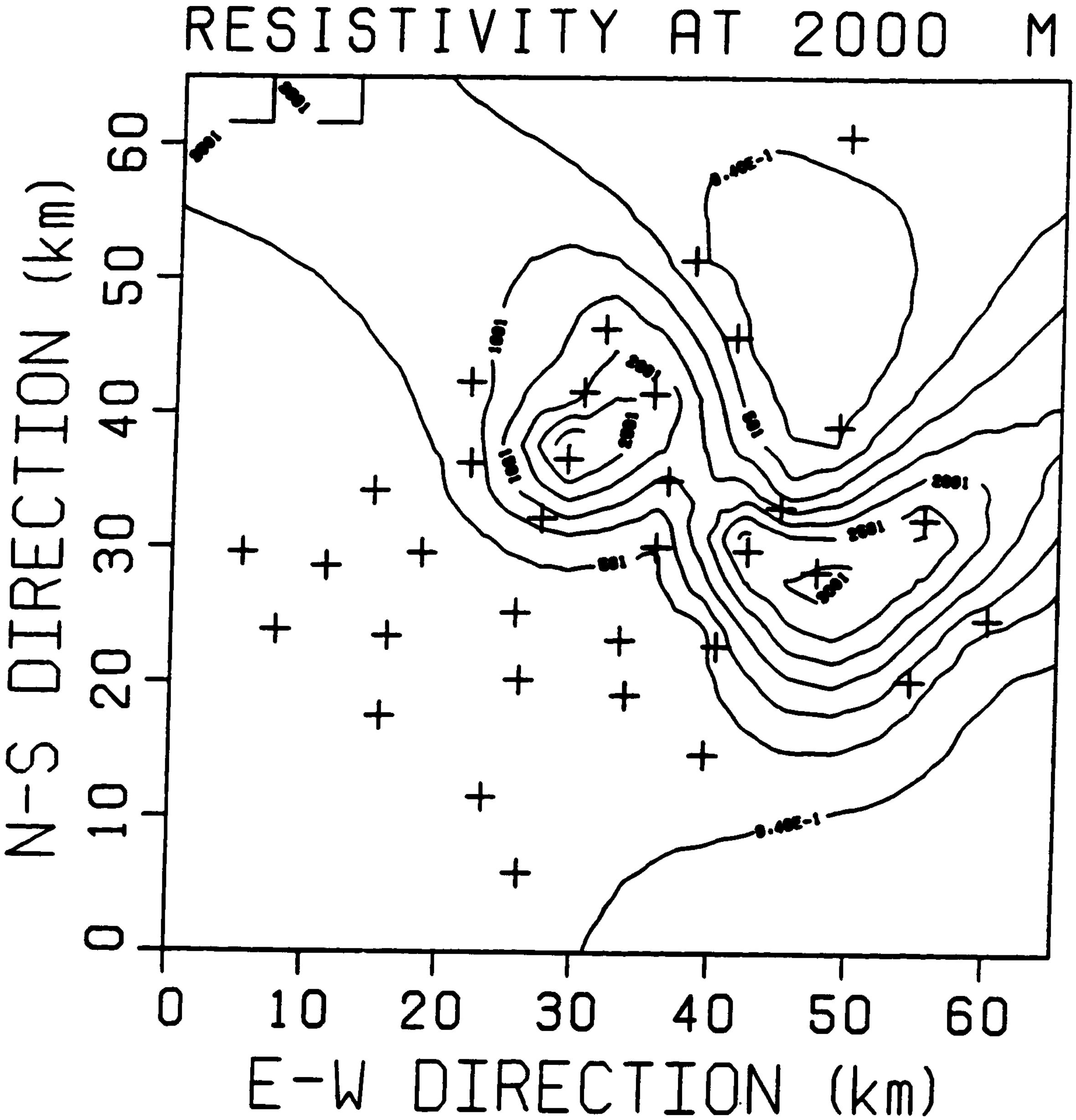
RESISTIVITY AT 2000 M
N-S DIRECTION (km)
E-W DIRECTION (km)
0
10
20
30
40
50
60

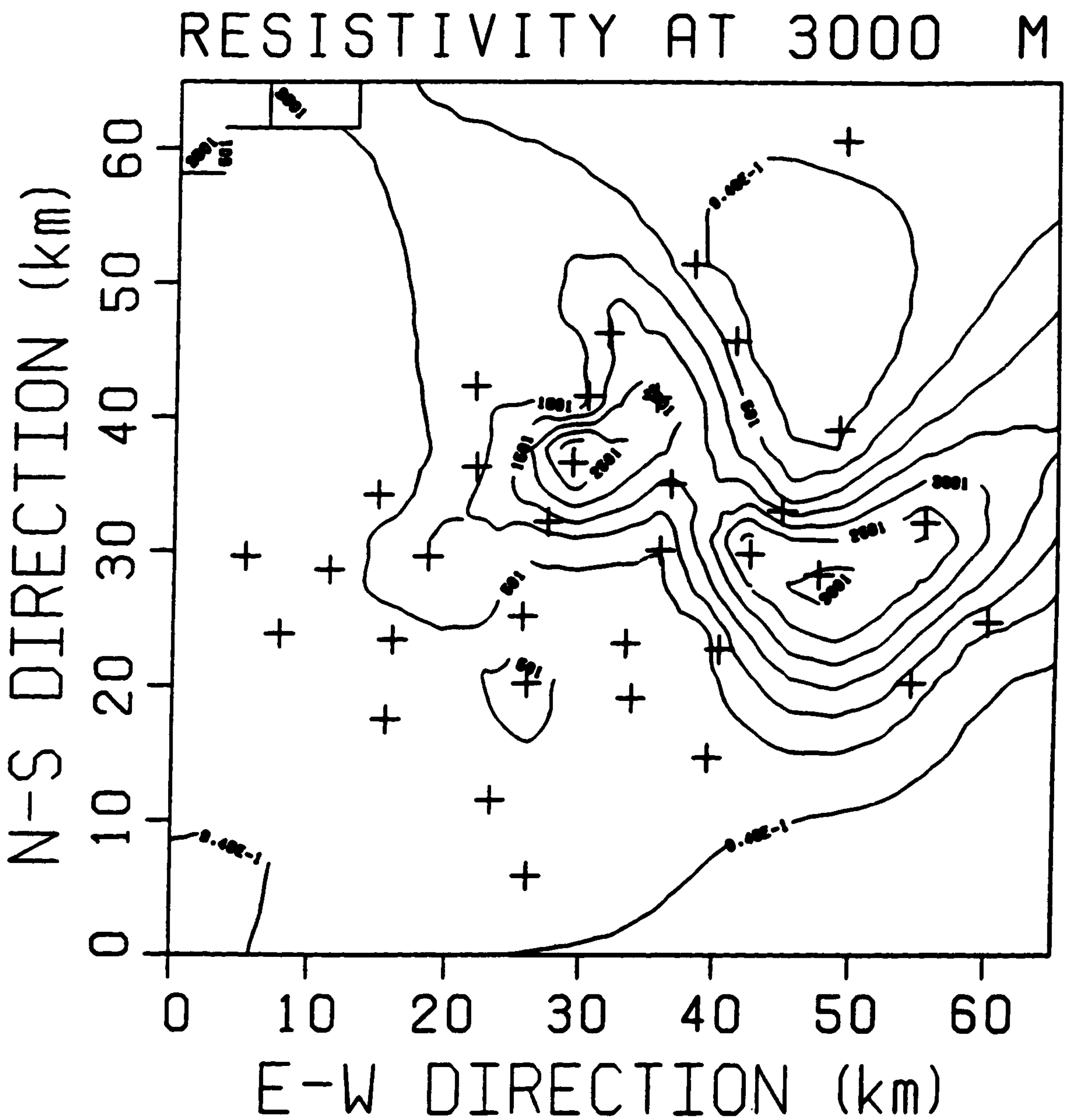

RESISTIVITY AT 3000 M
N-S DIRECTION (km)
E-W DIRECTION (km)
0
10
20
30
40
50
60

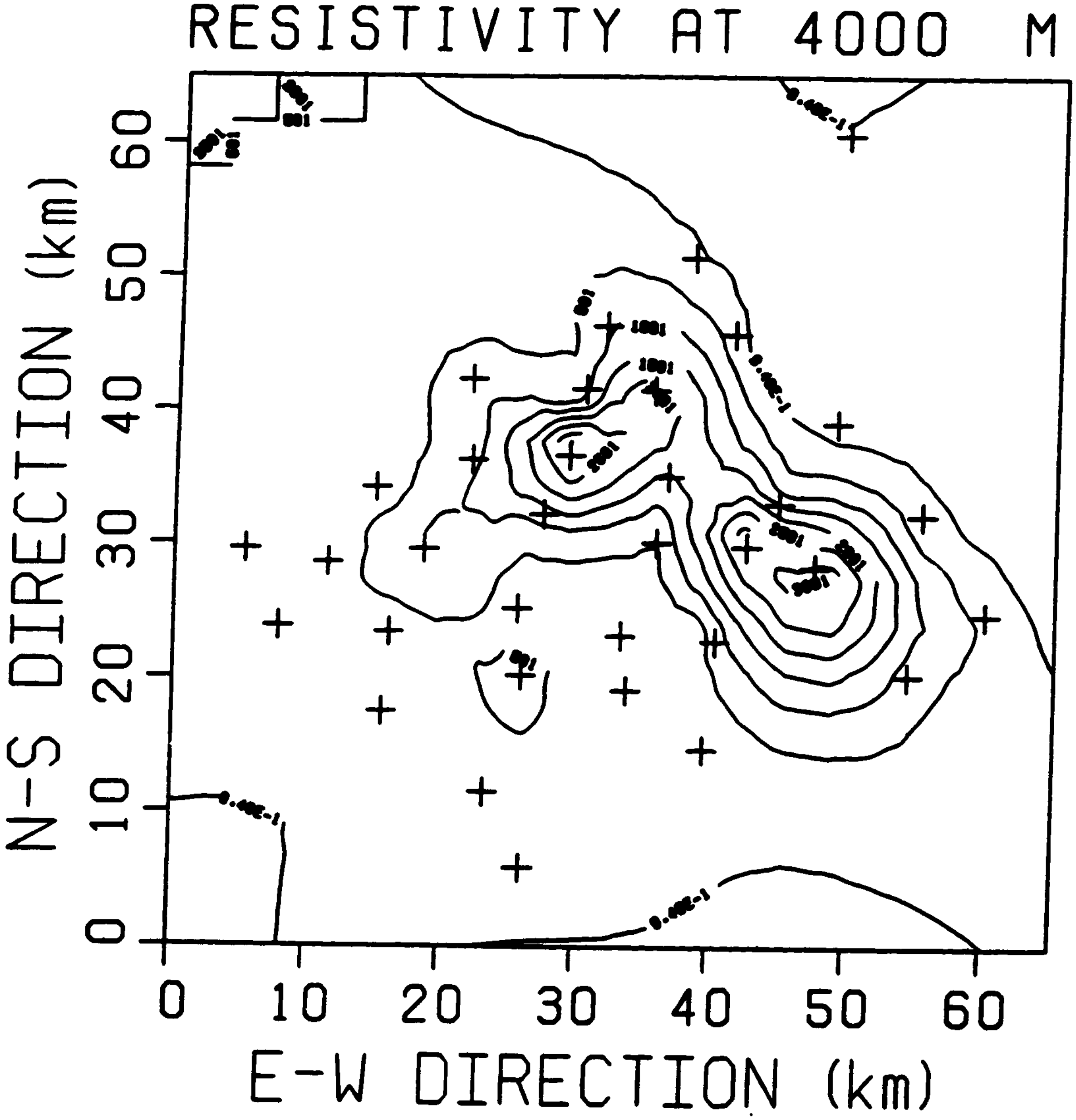
RESISTIVITY AT 4000 M
N-S DIRECTION (km)
0
10
20
30
40
50
60
E-W DIRECTION (km)
0
10
20
30
40
50
60

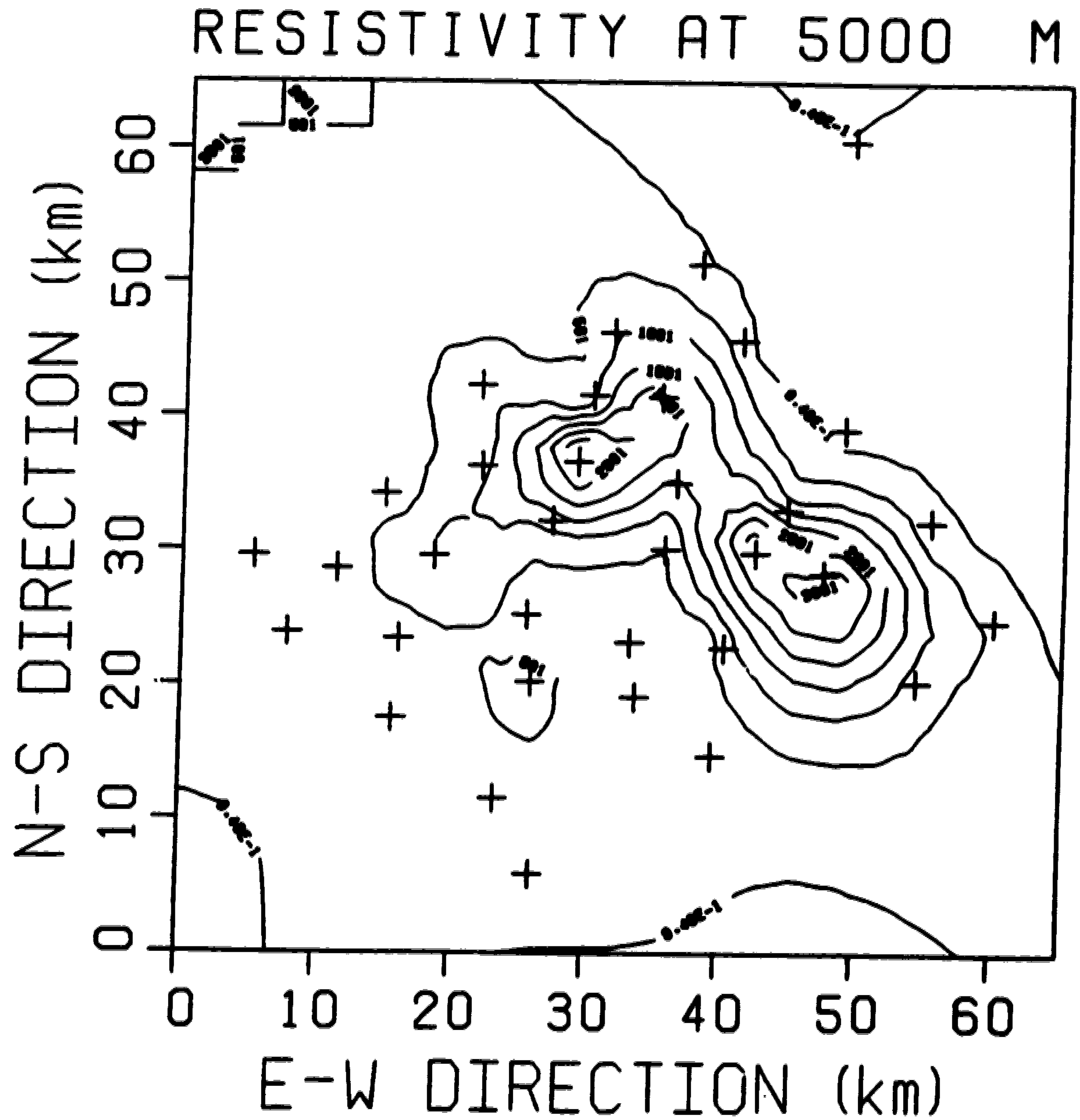
RESISTIVITY AT 5000 M
N-S DIRECTION (km)
E-W DIRECTION (km)
0
10
20
30
40
50
60

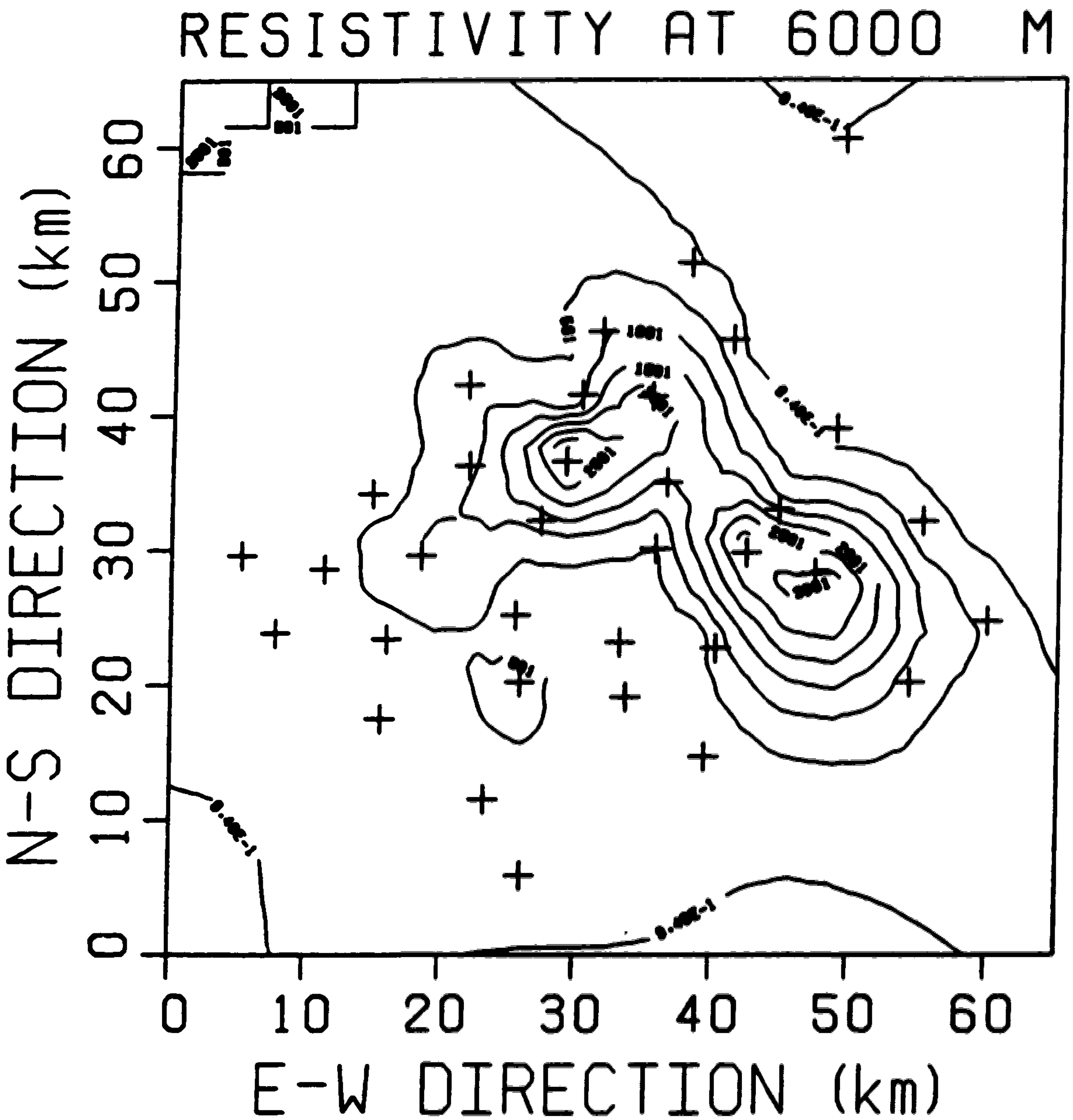
RESISTIVITY AT 6000 M
N-S DIRECTION (km)
E-W DIRECTION (km)
0
10
20
30
40
50
60

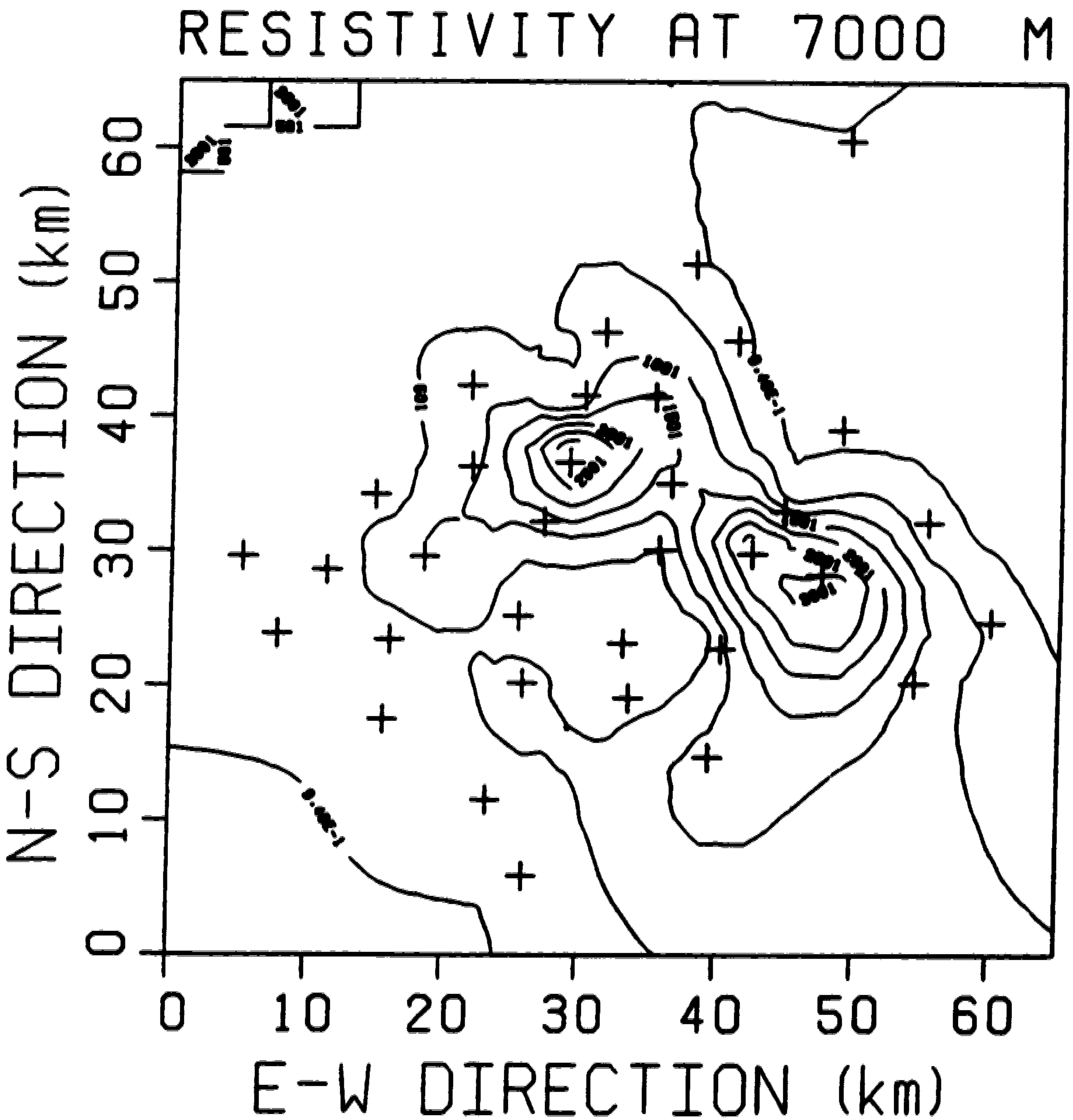

RESISTIVITY AT 7000 M
N-S DIRECTION (km)
E-W DIRECTION (km)
0
10
20
30
40
50
60

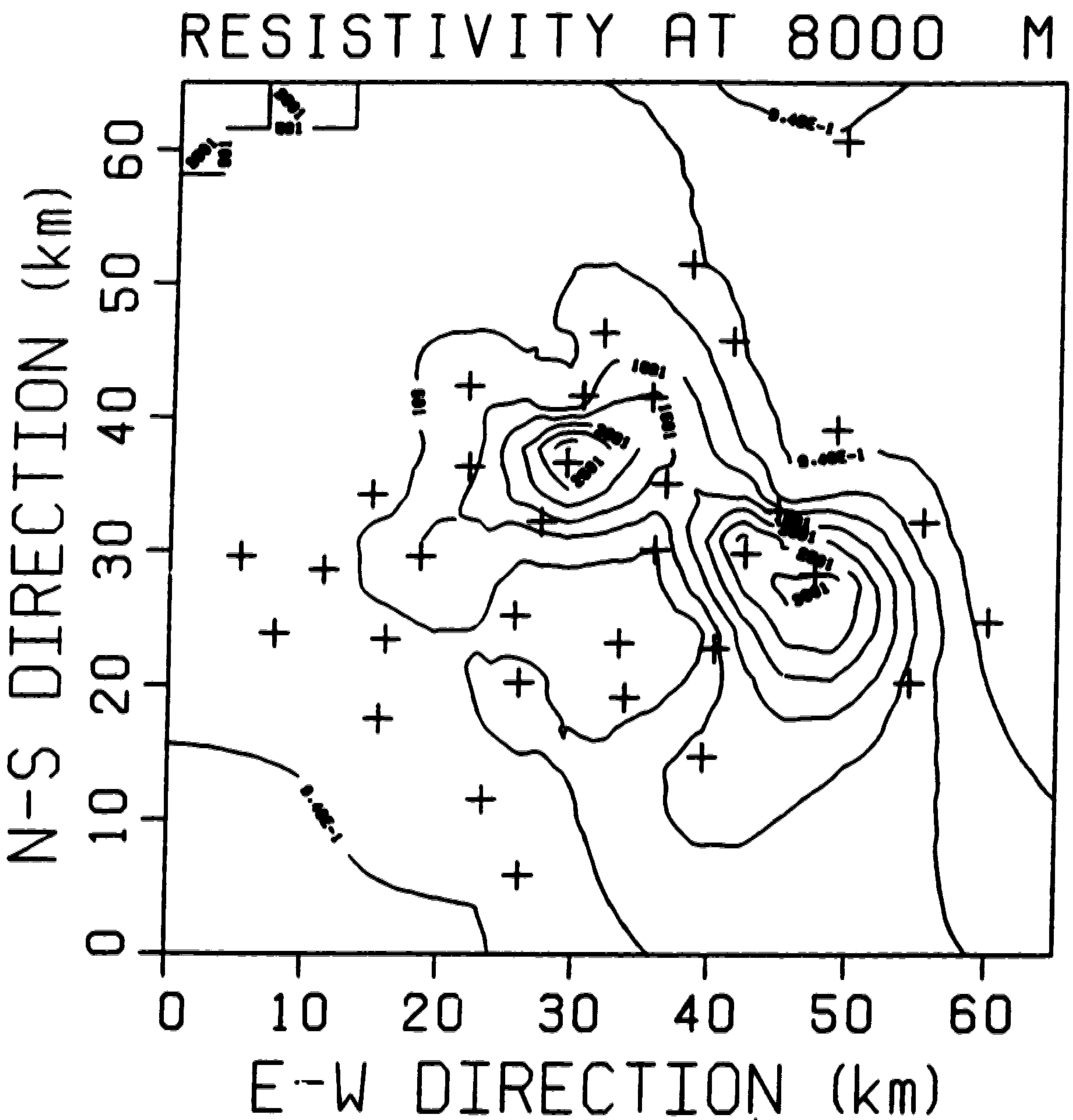

RESISTIVITY AT 8000 M
N-S DIRECTION (km)
E-W DIRECTION (km)
0
10
20
30
40
50
60

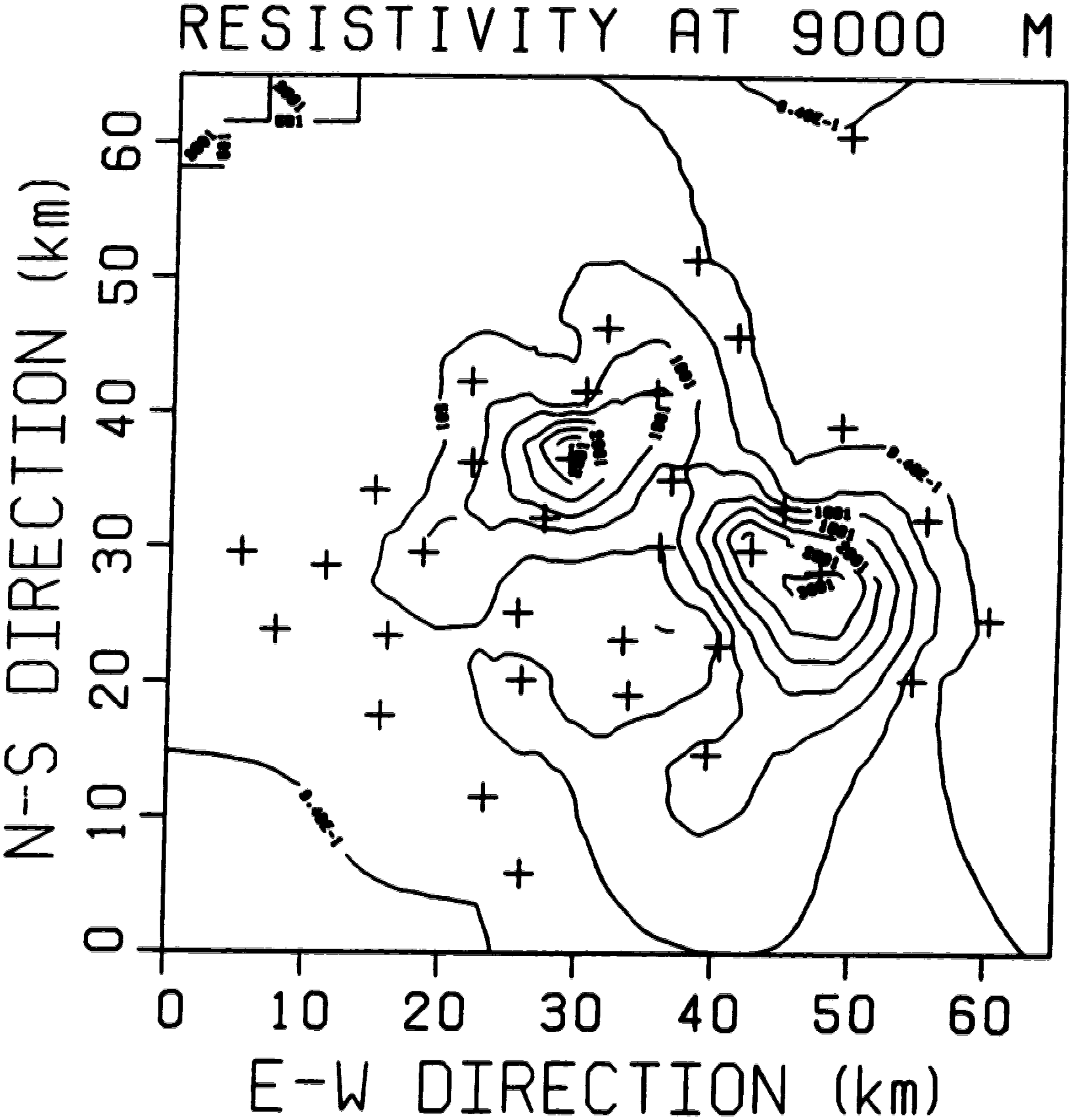
RESISTIVITY AT 9000 M
N-S DIRECTION (km)
E-W DIRECTION (km)
0
10
20
30
40
50
60

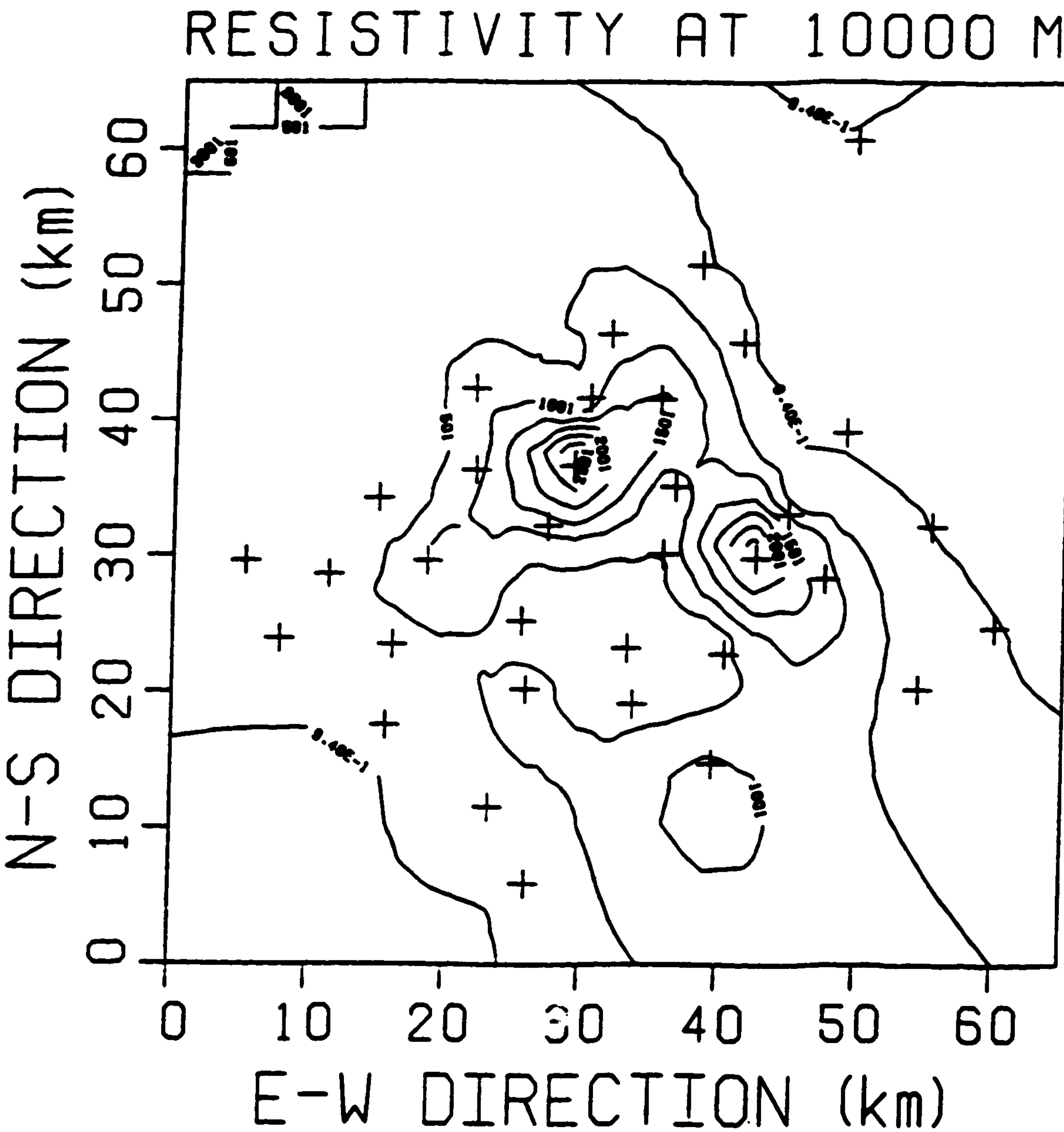
RESISTIVITY AT 10000 M
N-S DIRECTION (km)
E-W DIRECTION (km)
0
10
20
30
40
50
60

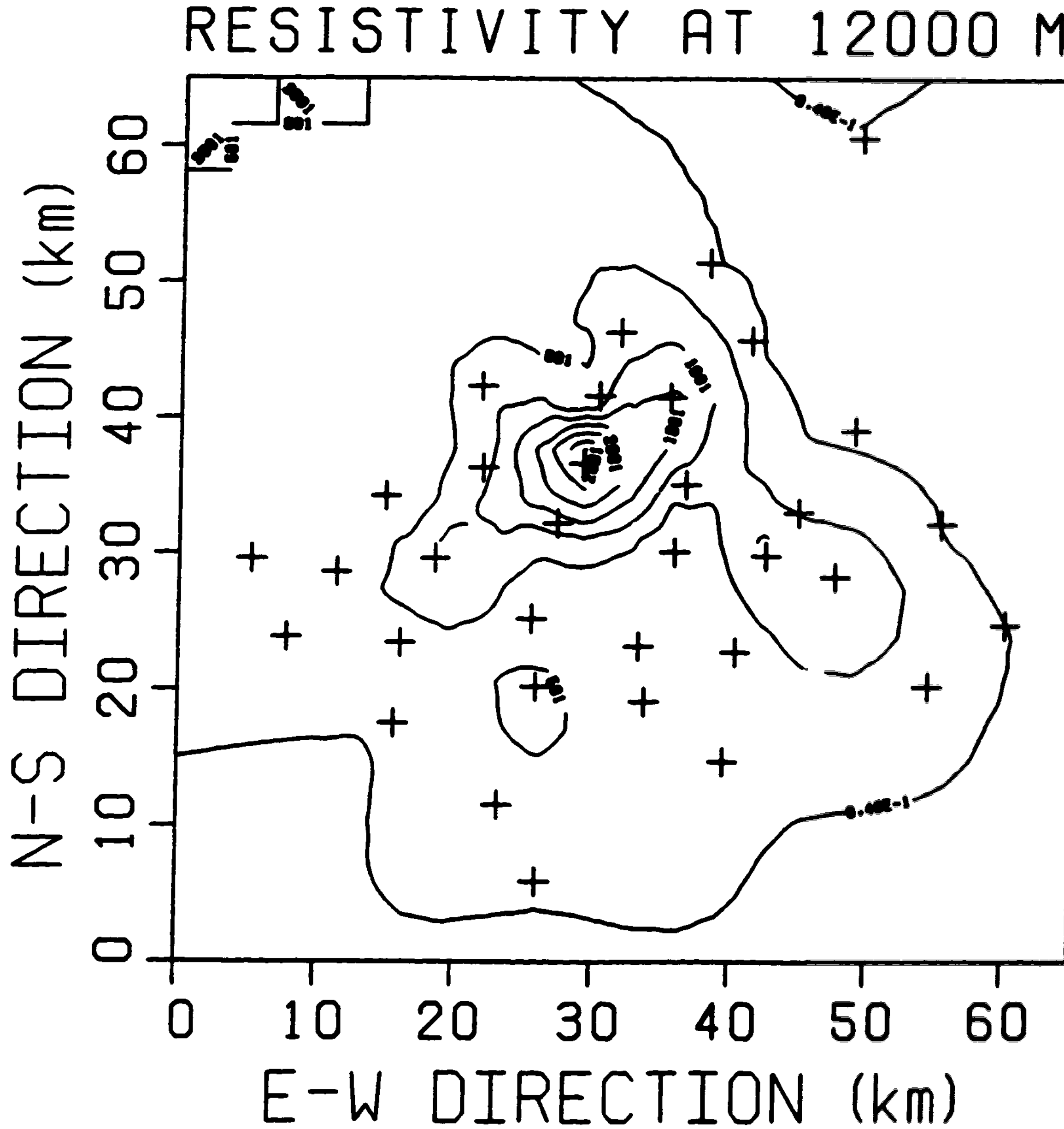
RESISTIVITY AT 12000 M
N-S DIRECTION (km)
E-W DIRECTION (km)
0
10
20
30
40
50
60

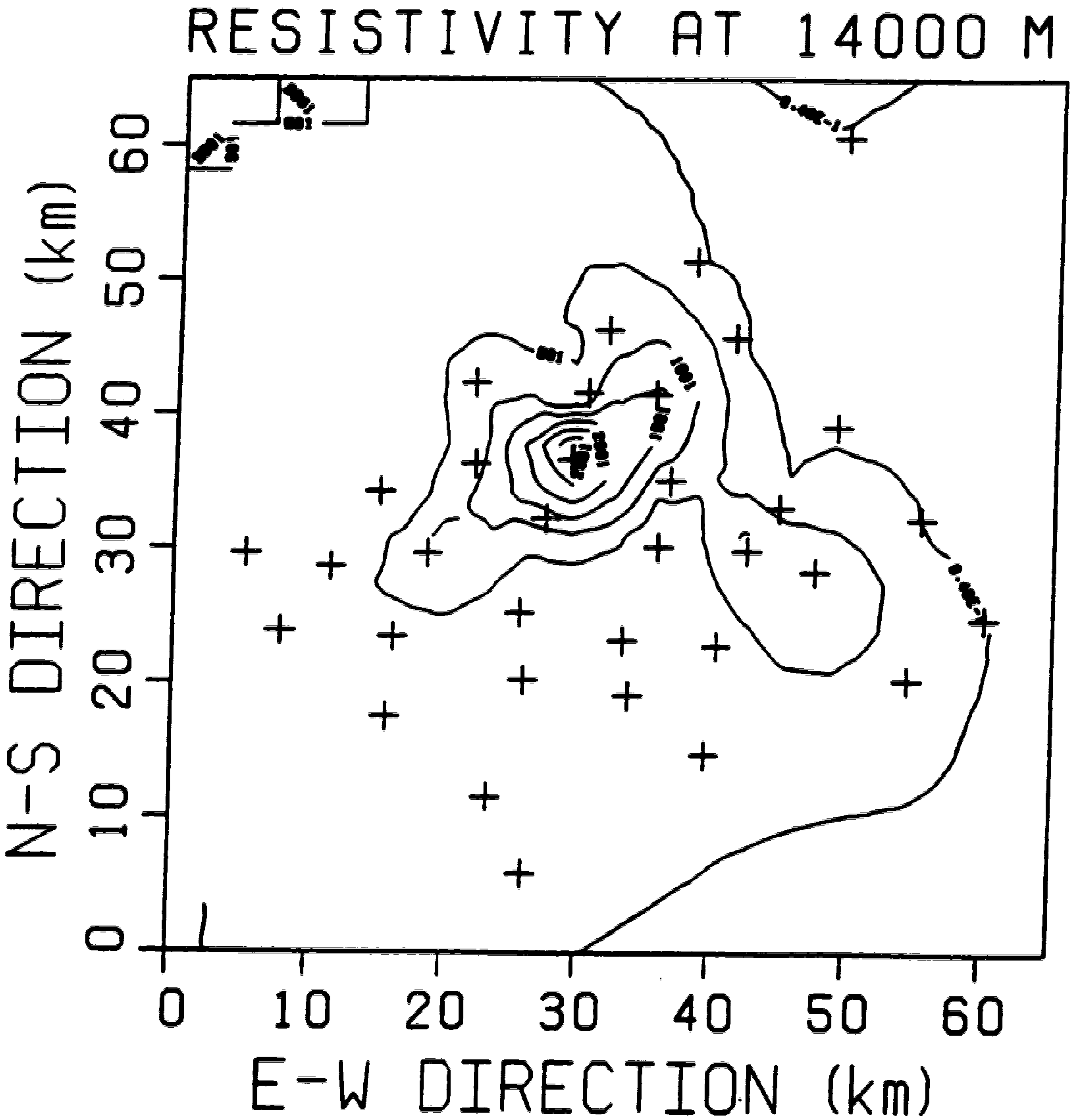
RESISTIVITY AT 14000 M
N-S DIRECTION (km)
E-W DIRECTION (km)
0
10
20
30
40
50
60

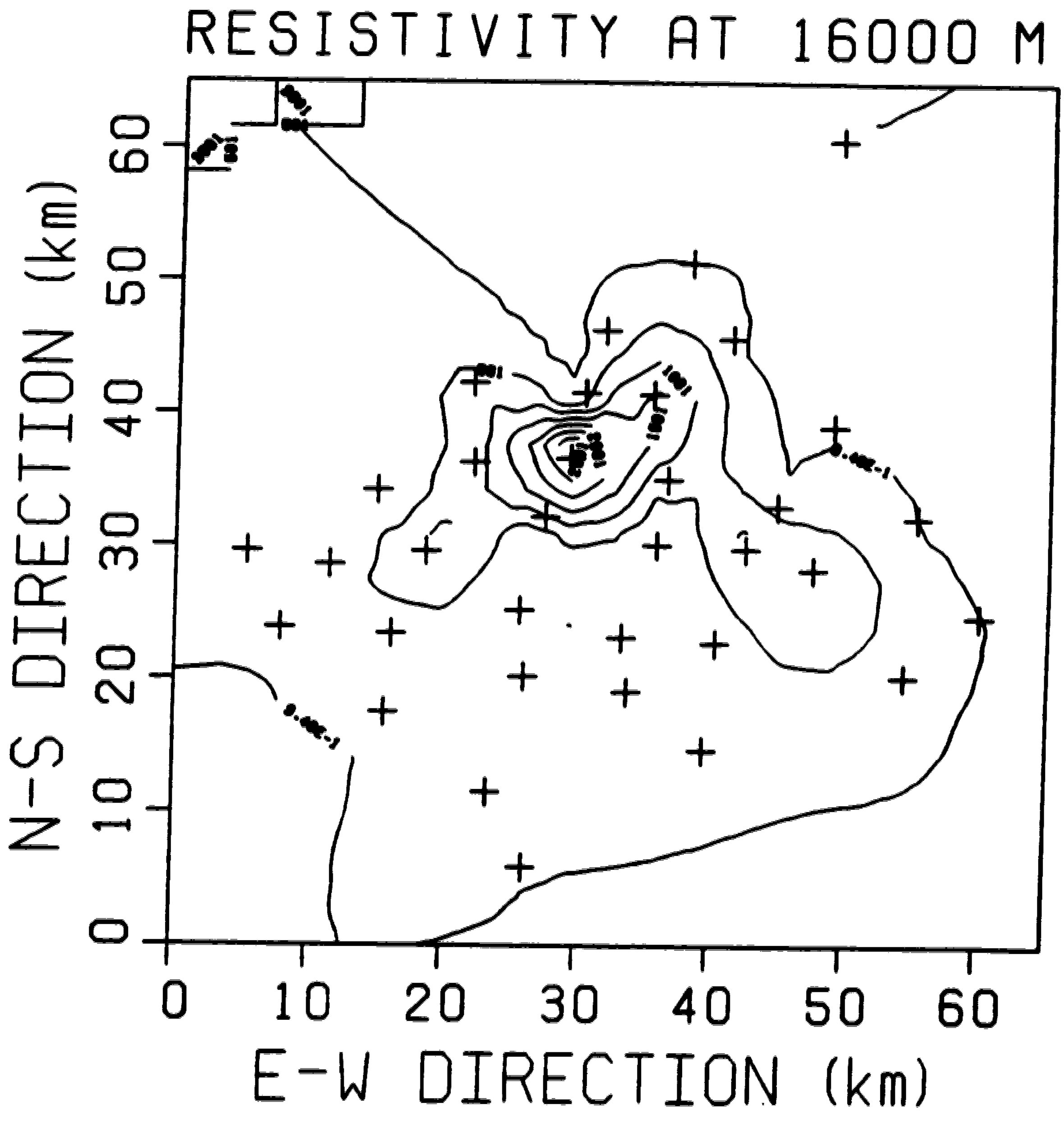
RESISTIVITY AT 16000 M
N-S DIRECTION (km)
E-W DIRECTION (km)
0
10
20
30
40
50
60

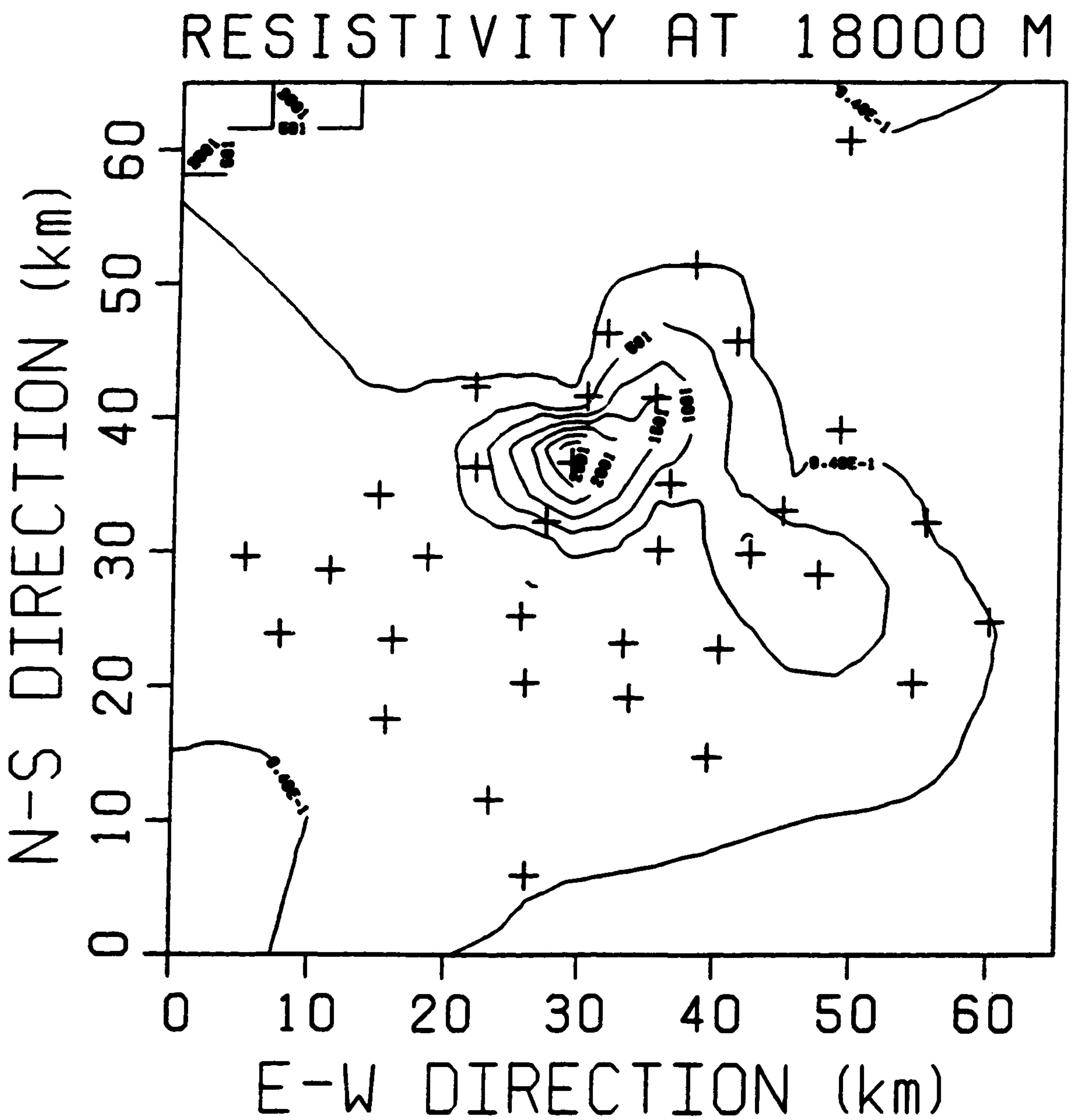

RESISTIVITY AT 18000 M
N-S DIRECTION (km)
E-W DIRECTION (km)
0
10
20
30
40
50
60

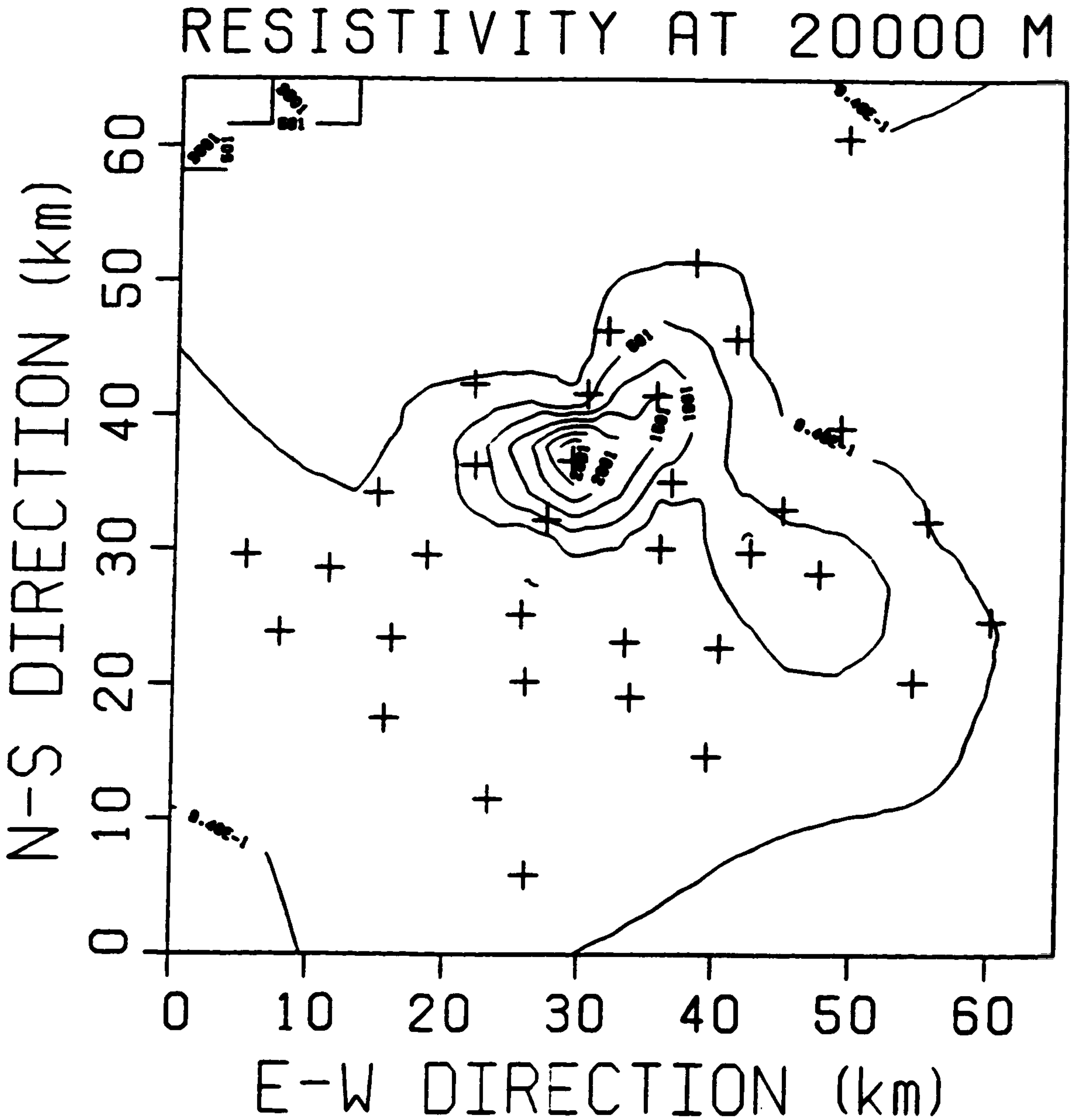
RESISTIVITY AT 20000 M
N-S DIRECTION (km)
E-W DIRECTION (km)
0
10
20
30
40
50
60

RESISTIVITY AT 22000 M

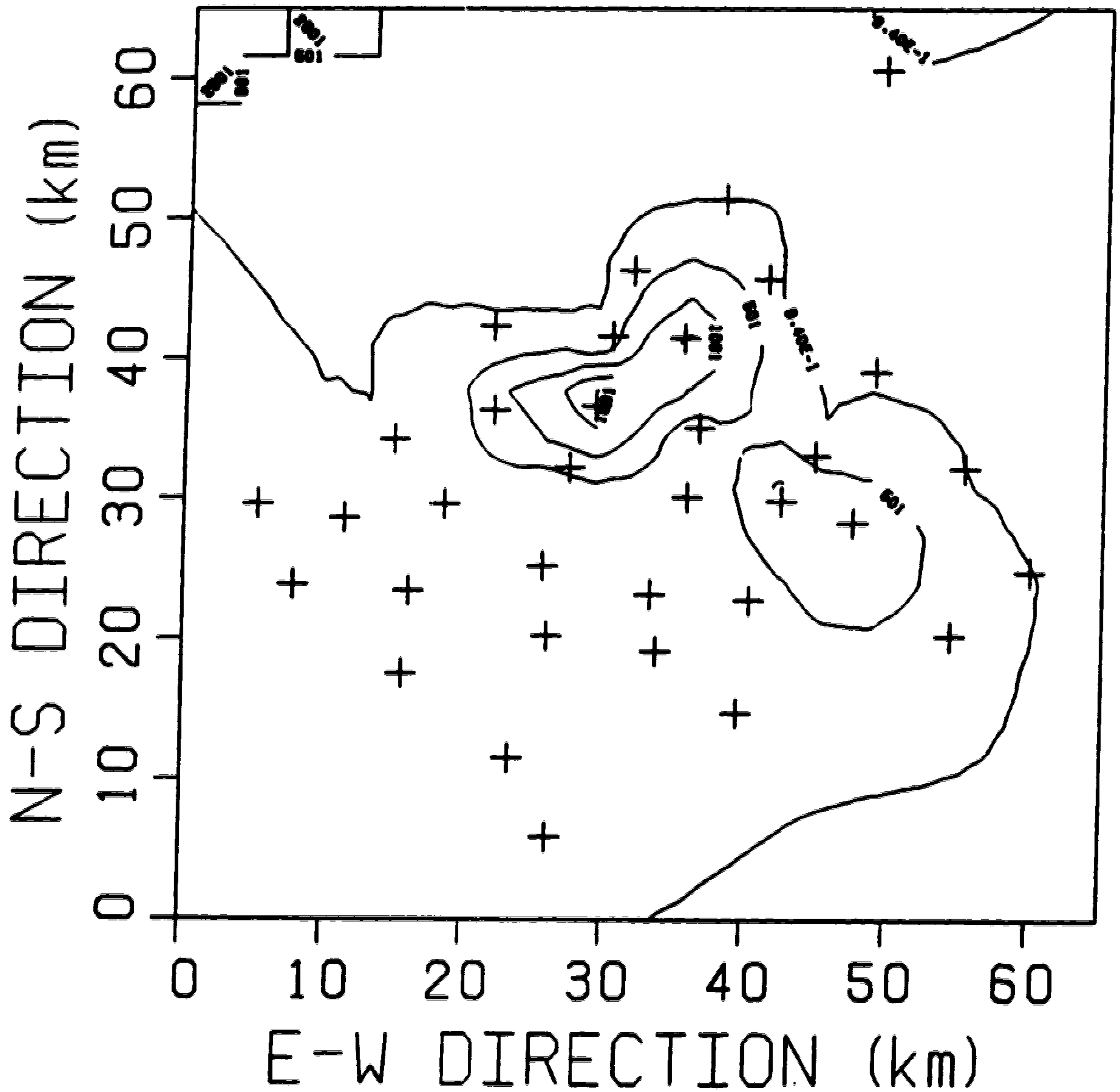

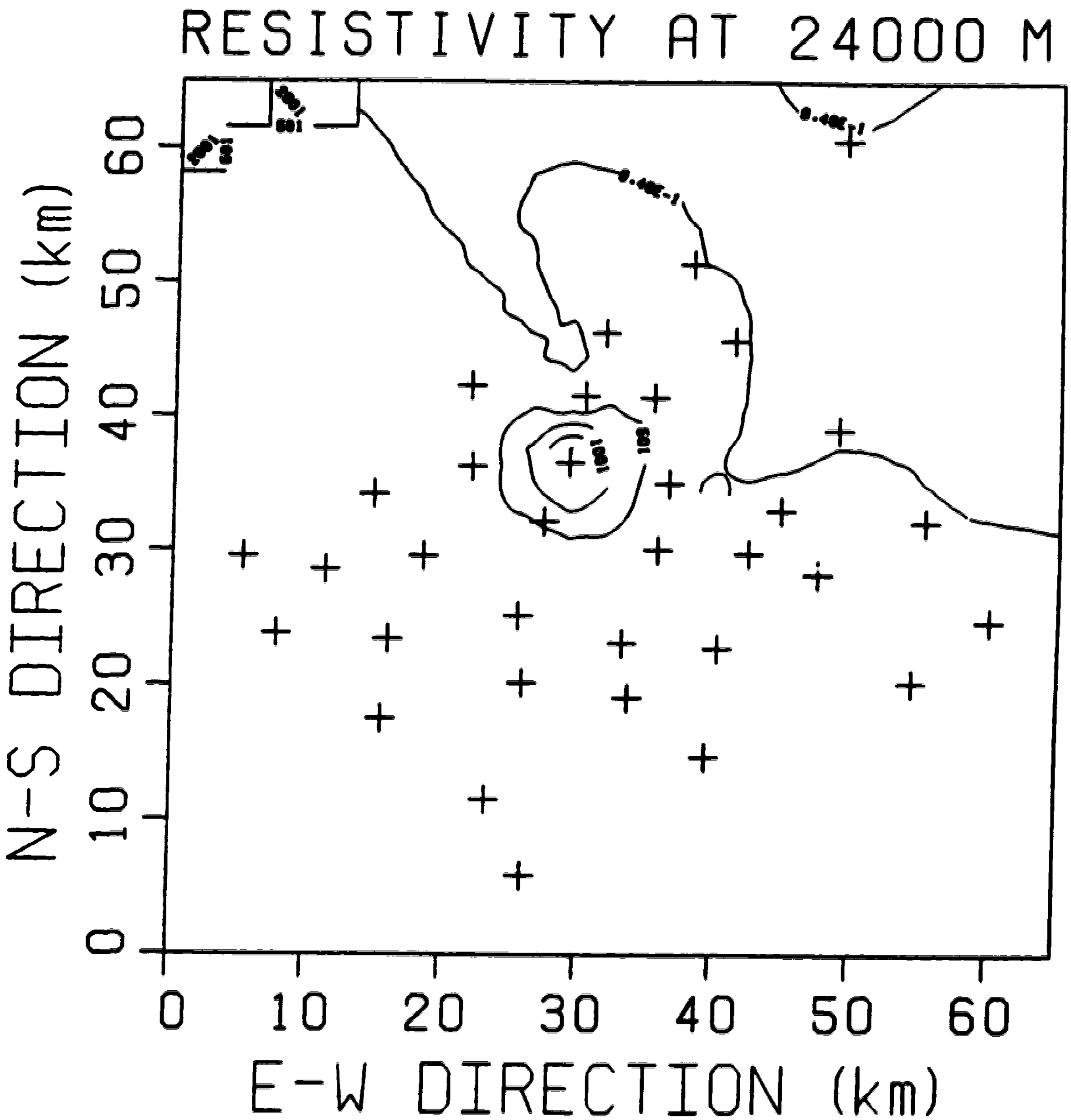

RESISTIVITY AT 24000 M
N-S DIRECTION (km)
E-W DIRECTION (km)
0
10
20
30
40
50
60

RESISTIVITY AT 26000 M

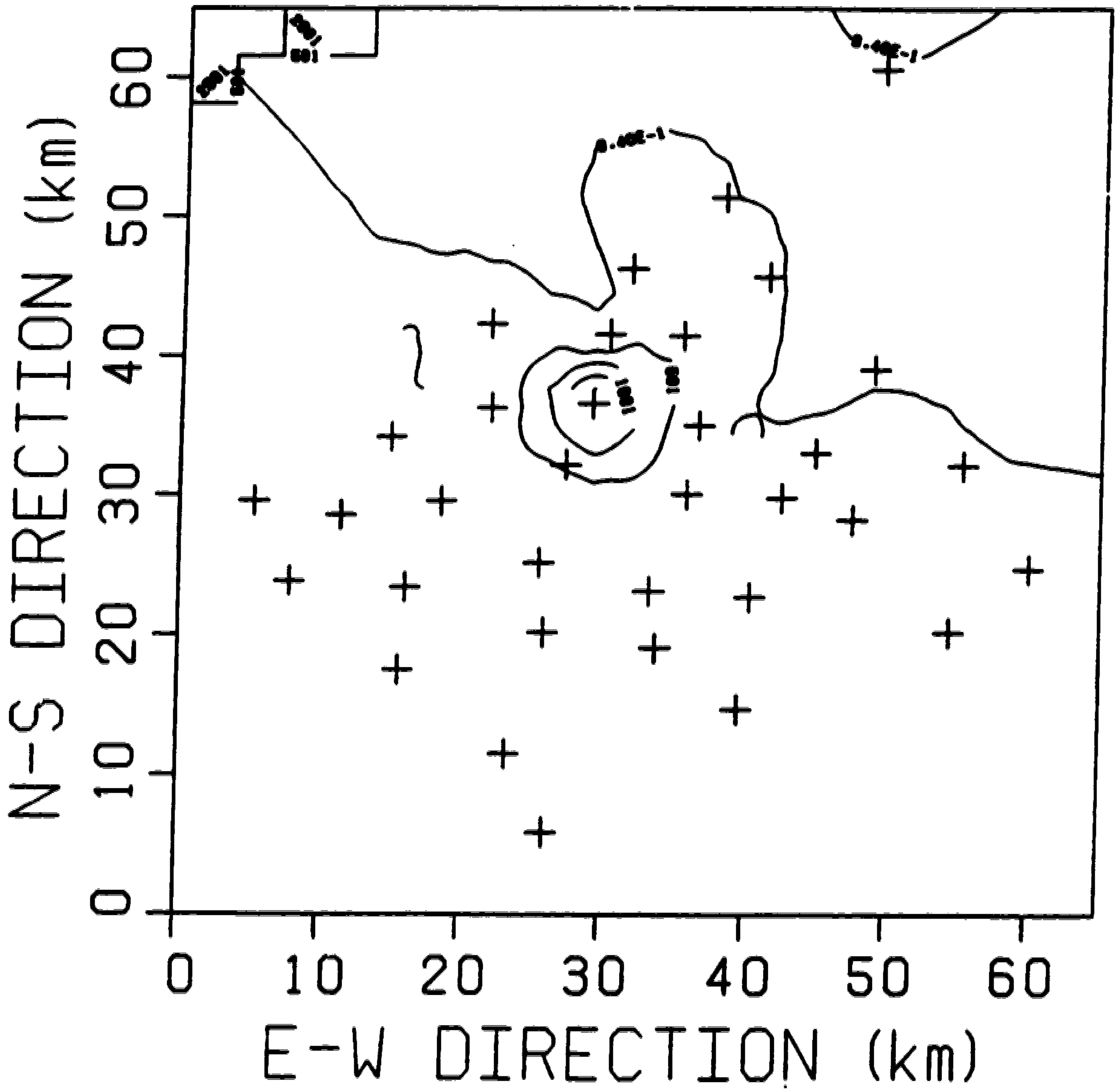

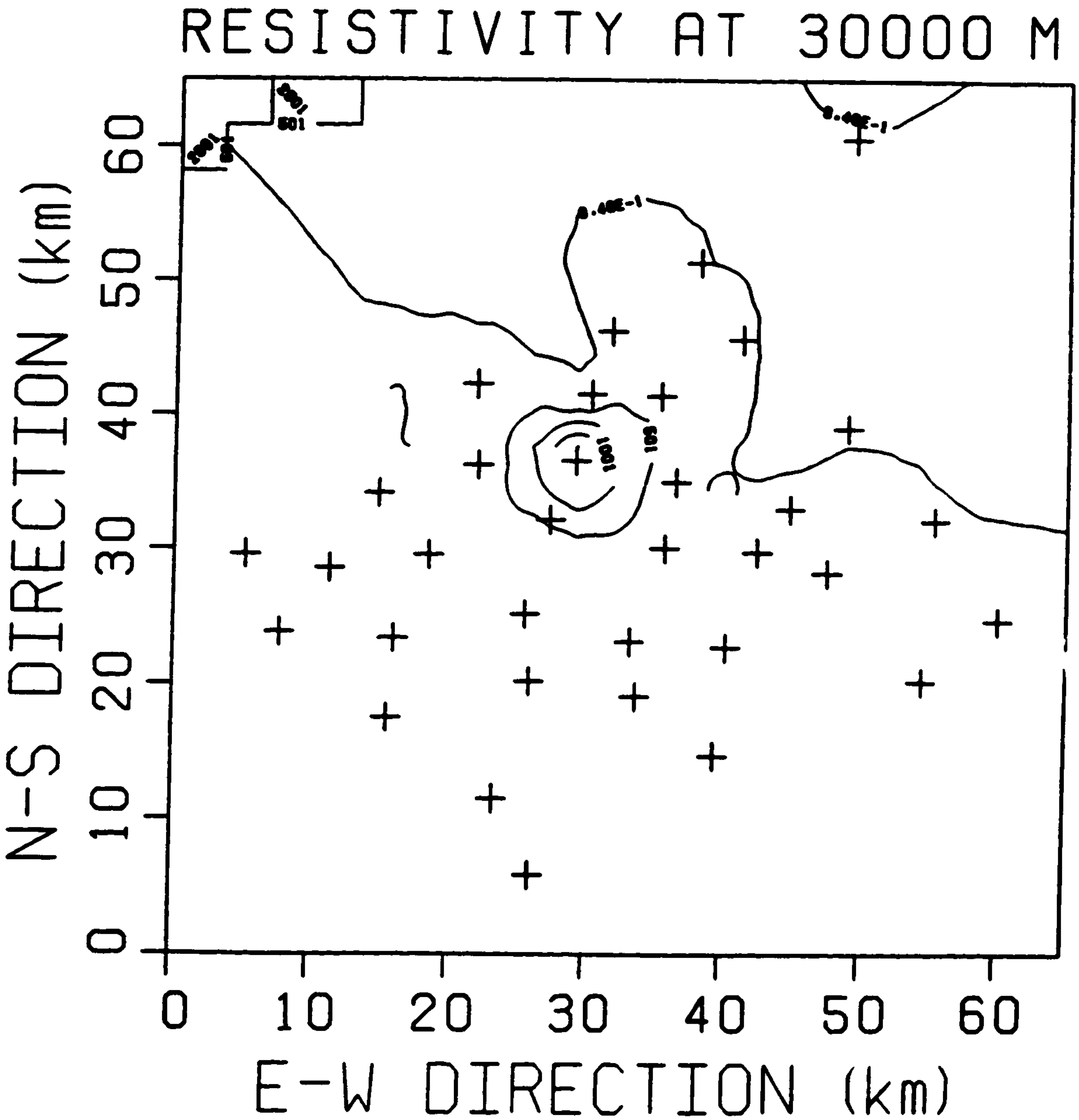

RESISTIVITY AT 30000 M
N-S DIRECTION (km)
E-W DIRECTION (km)
0
10
20
30
40
50
60

APPENDIX IV

COMPARISON BETWEEN 3D MODEL RESULTS AND FIELD DATA RESULTS

Refer to Figure 1.2 and Figure 3.8 for locations of the MT sites. Crosses indicate field data and stars indicate 3D model results.

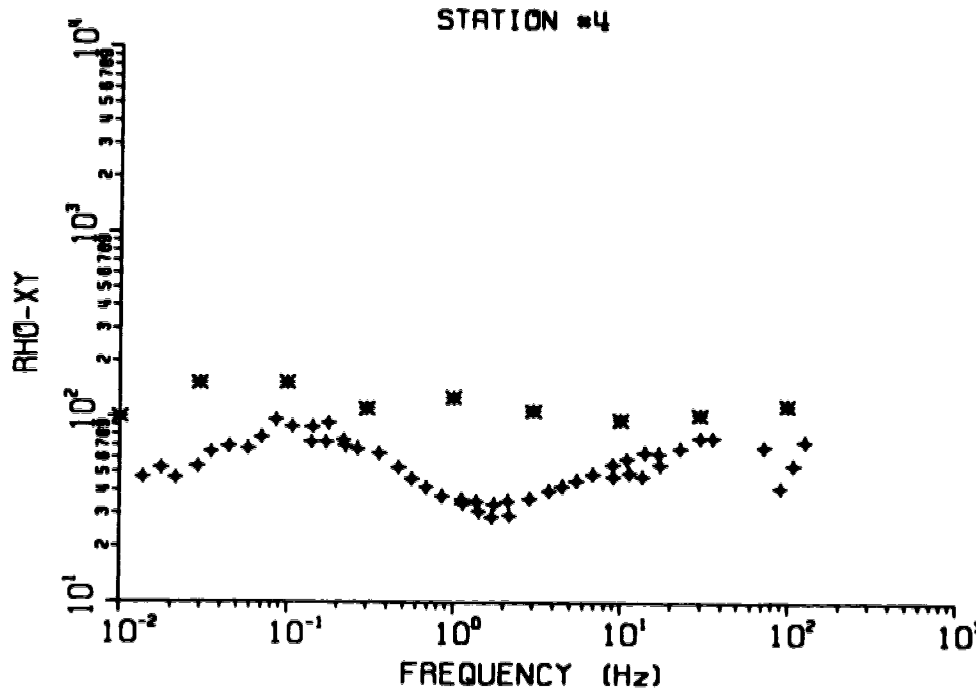
STATION #4
RHO-XY
FREQUENCY (Hz)

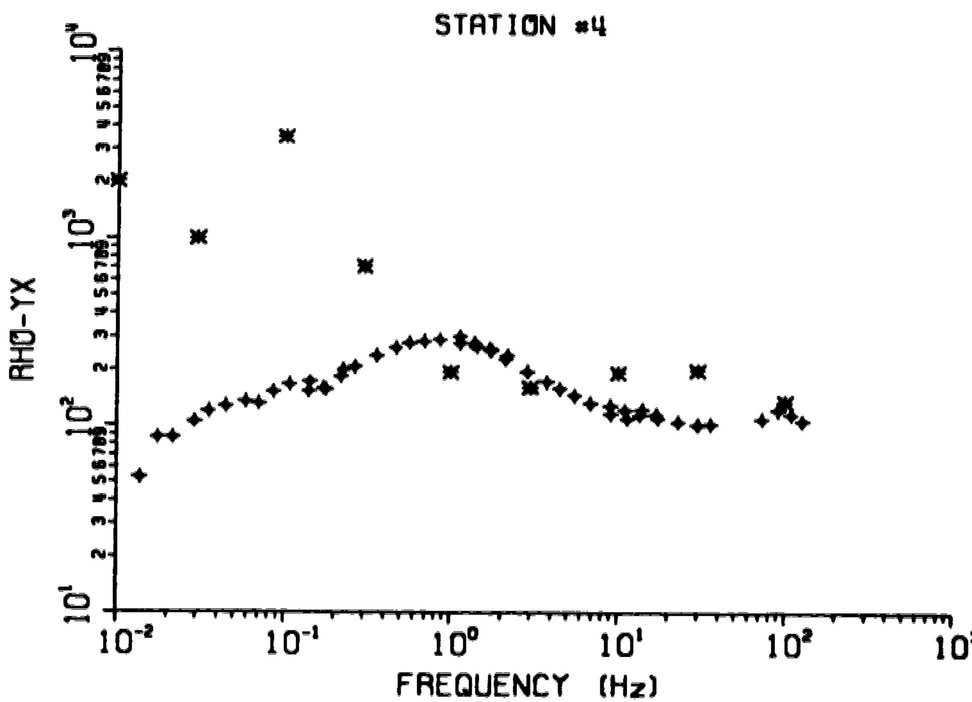
STATION #4
RHO-YX
FREQUENCY (Hz)

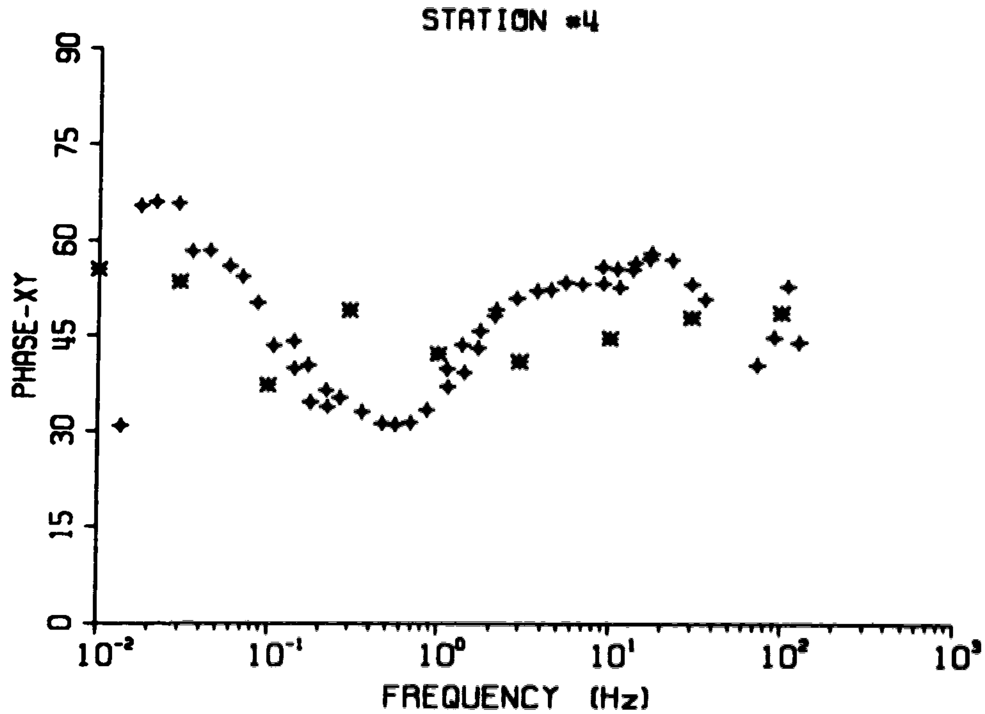
STATION #4
PHASE-XY
0
15
30
45
60
75
90
10^{-2}
10^{-1}
10^{0}
10^{1}
10^{2}
10^{3}
FREQUENCY (Hz)

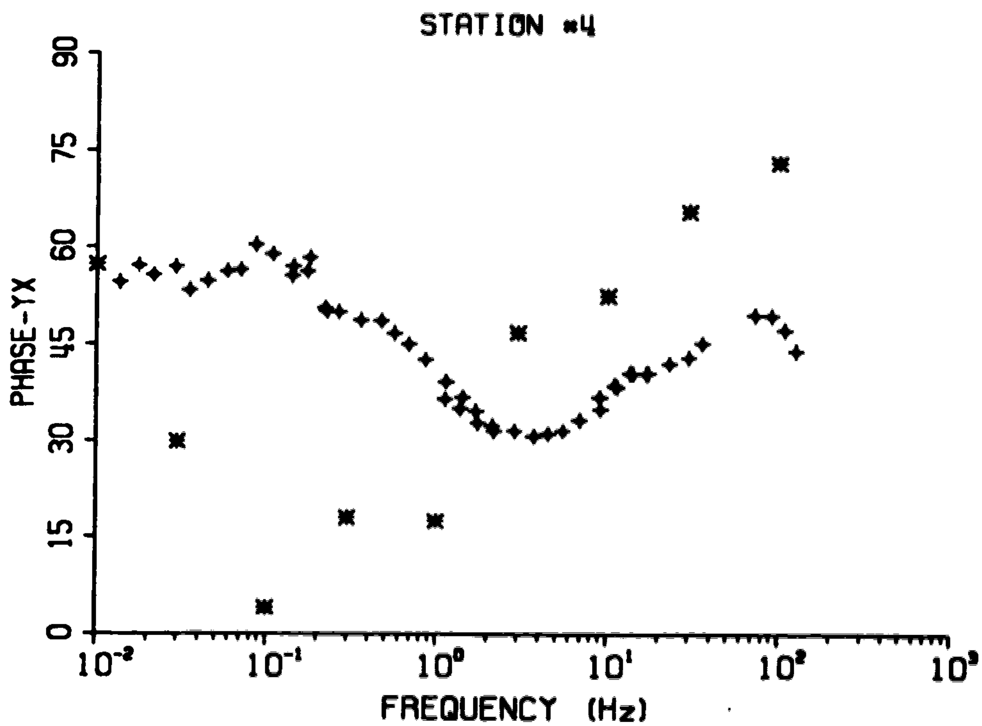
STATION #4
PHASE-YX
0
15
30
45
60
75
90
10^{-2}
10^{-1}
10^{0}
10^{1}
10^{2}
10^{3}
FREQUENCY (Hz)

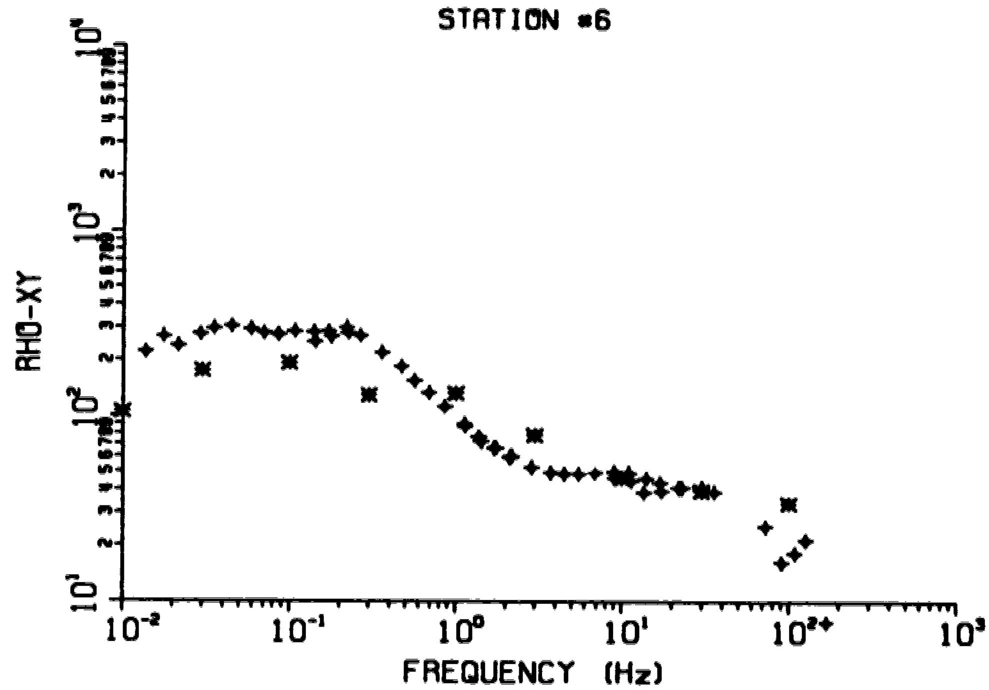
STATION *6
RHO-XY
FREQUENCY (Hz)

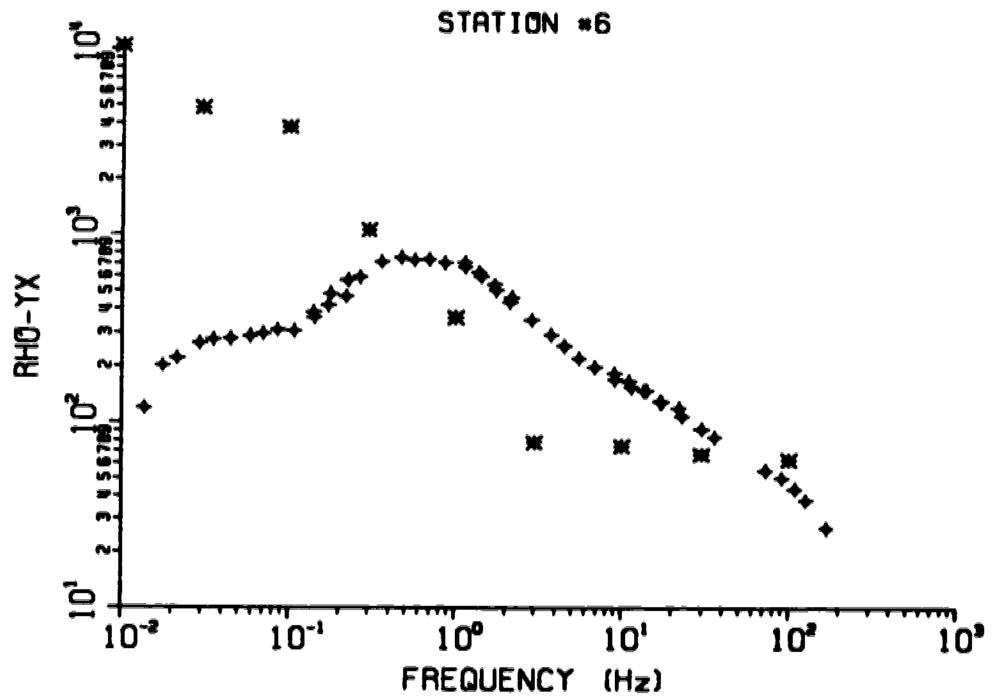
STATION *6
RHO-YX
FREQUENCY (Hz)

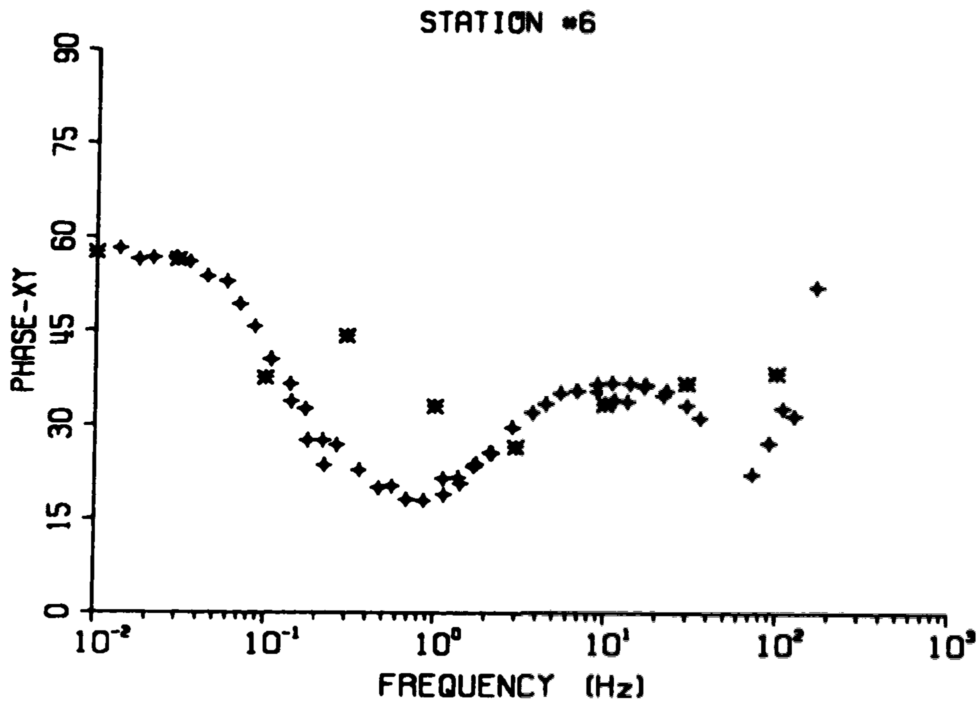
STATION #6
PHASE-XY
0
15
30
45
60
75
90
10^{-2}
10^{-1}
10^{0}
10^{1}
10^{2}
10^{3}
FREQUENCY (Hz)

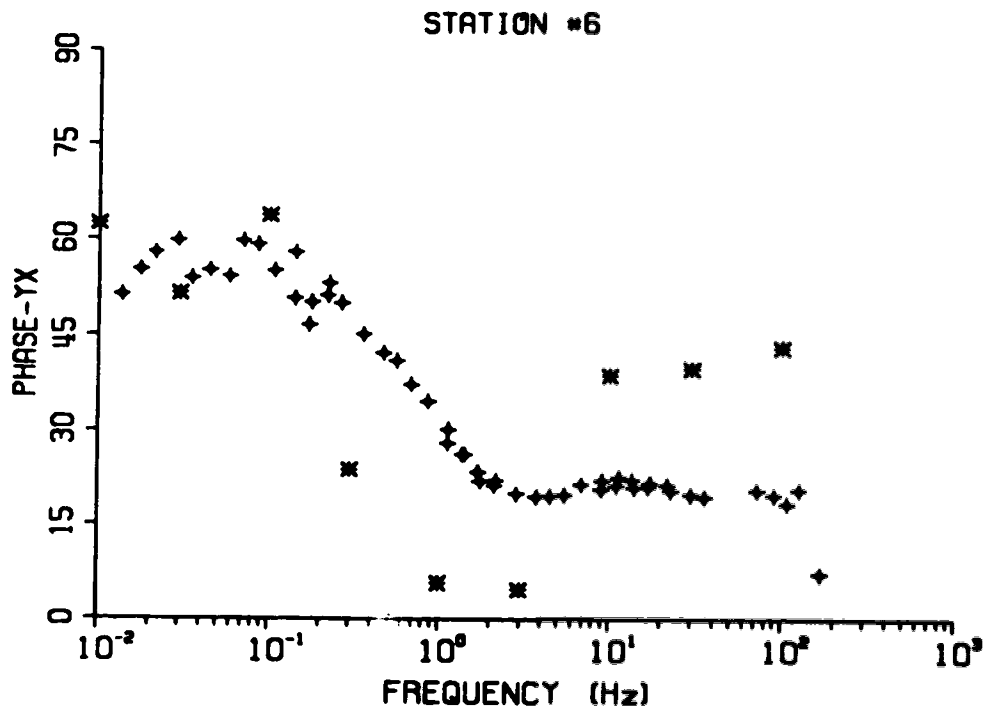
STATION #6
PHASE-YX
0
15
30
45
60
75
90
10^{-2}
10^{-1}
10^{0}
10^{1}
10^{2}
10^{3}
FREQUENCY (Hz)

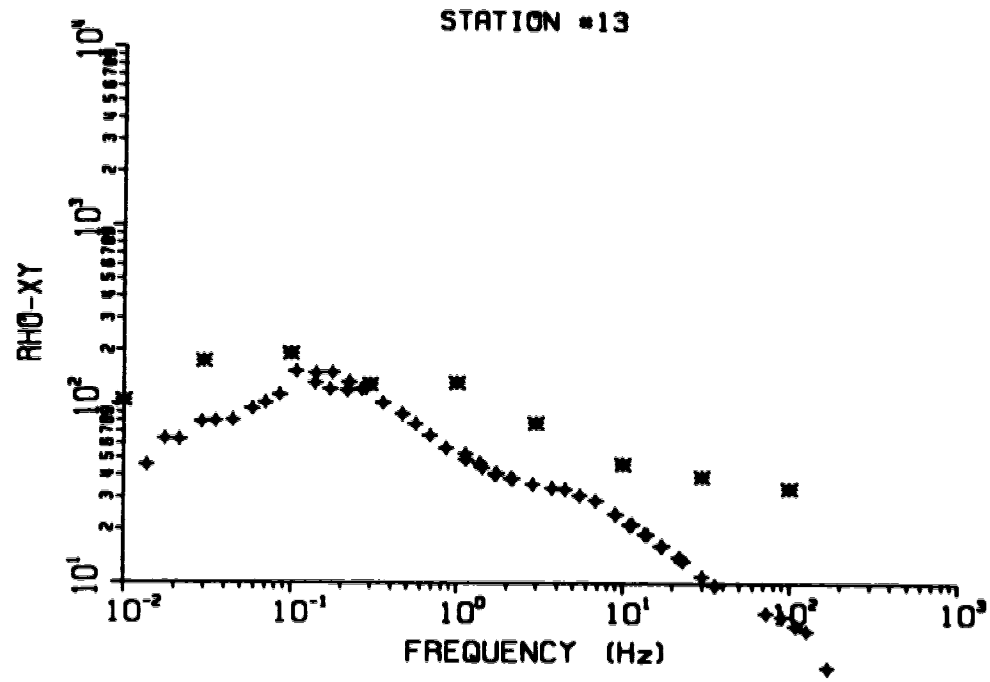
STATION *13
RHO-XY
FREQUENCY (Hz)

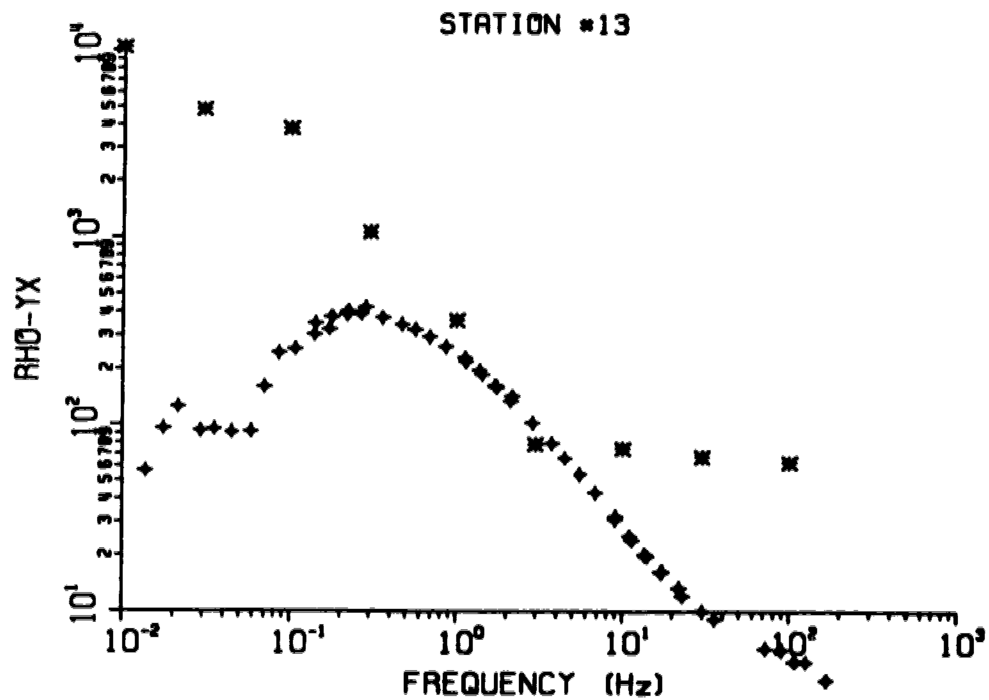
STATION *13
RHO-YX
FREQUENCY (Hz)

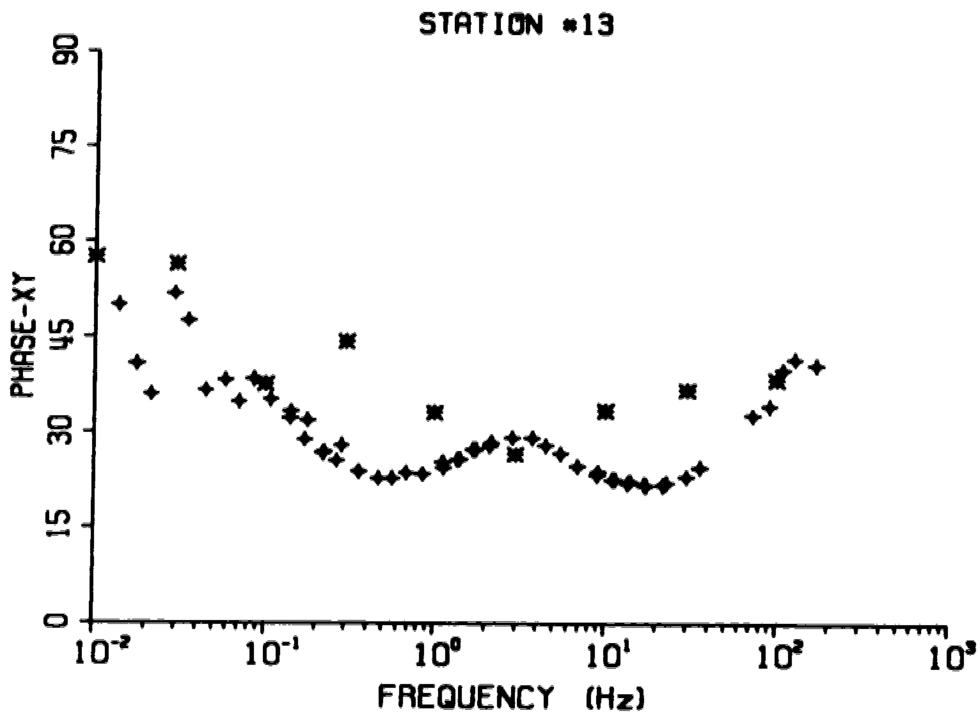
STATION *13
PHASE-XY
0
15
30
45
60
75
90
10^{-2}
10^{-1}
10^{0}
10^{1}
10^{2}
10^{3}
FREQUENCY (Hz)

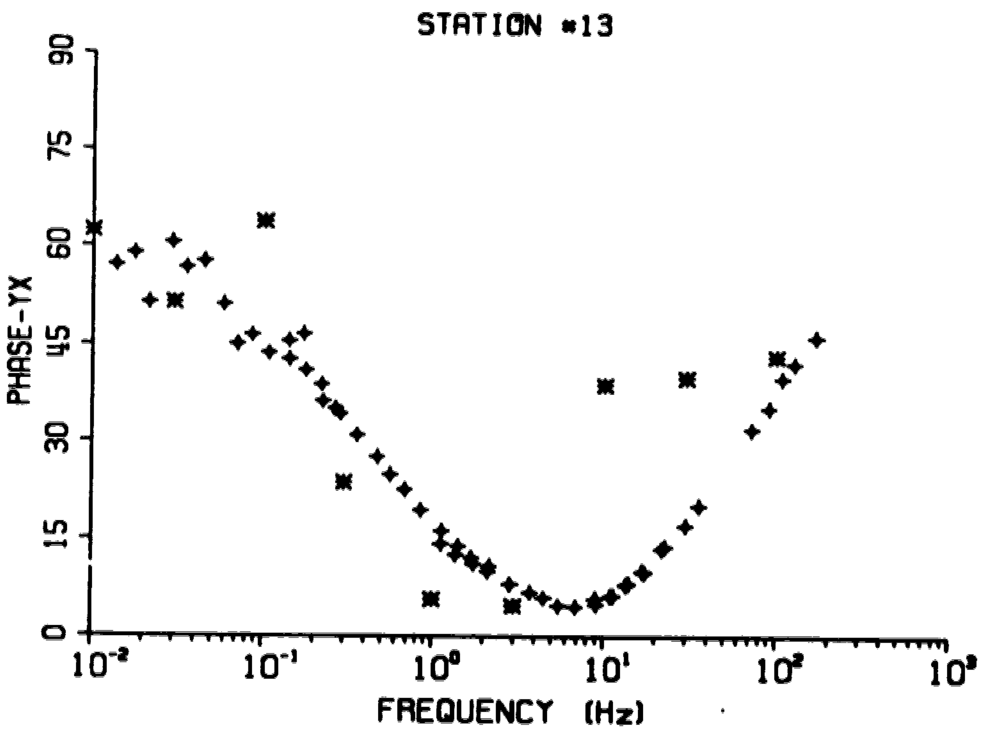
STATION *13
PHASE-YX
0
15
30
45
60
75
90
10^{-2}
10^{-1}
10^{0}
10^{1}
10^{2}
10^{3}
FREQUENCY (Hz)

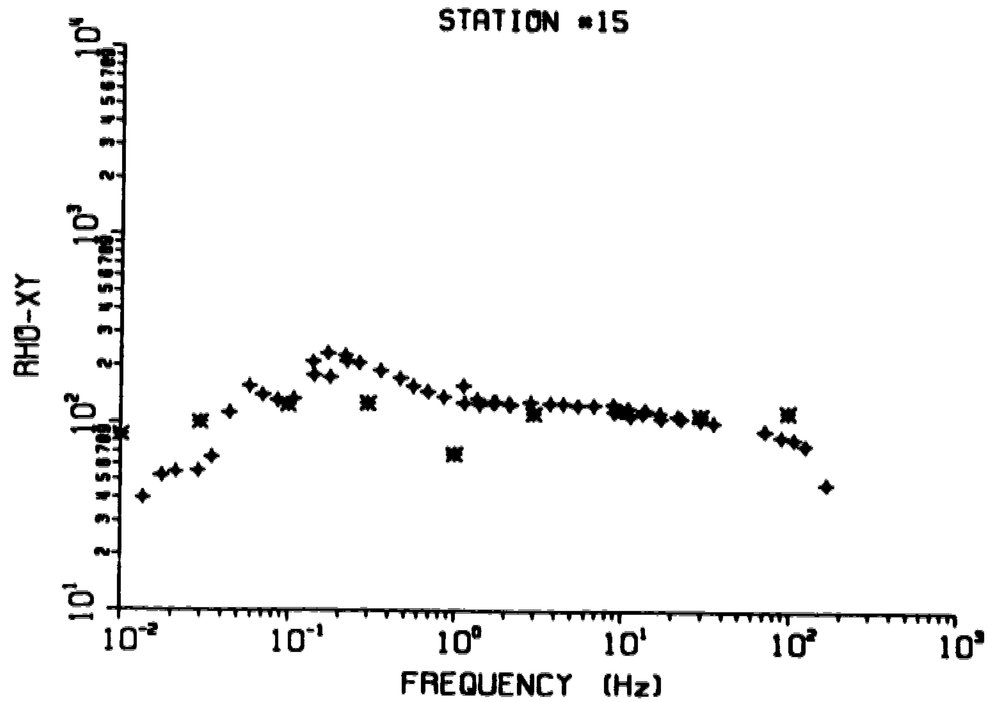
STATION *15
RHO-XY
FREQUENCY (Hz)

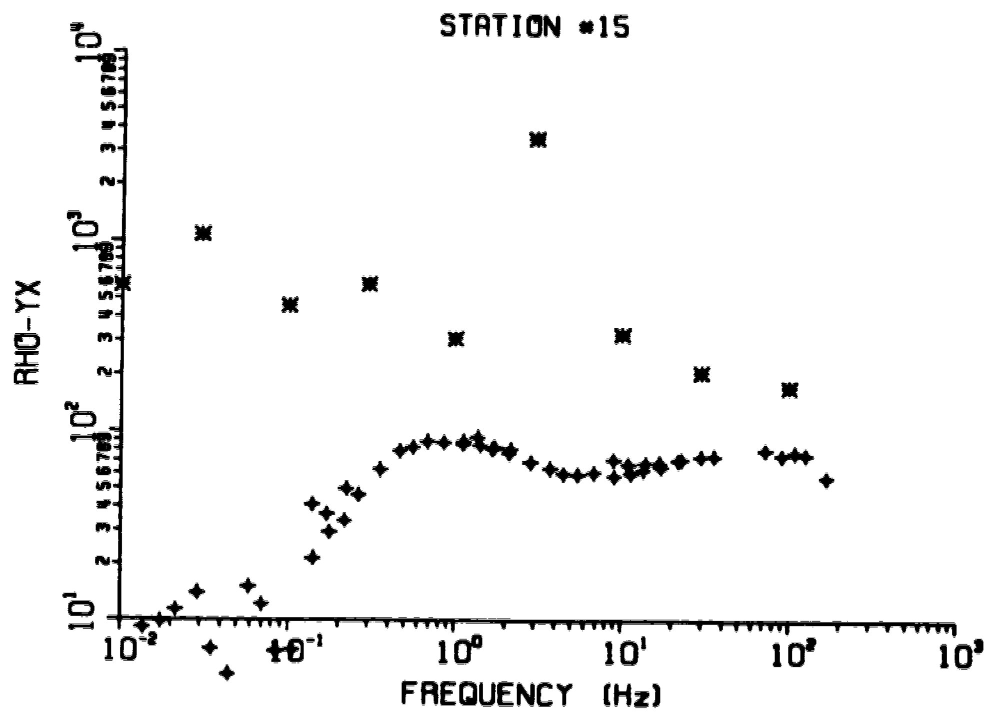
STATION *15
RHO-YX
FREQUENCY (Hz)

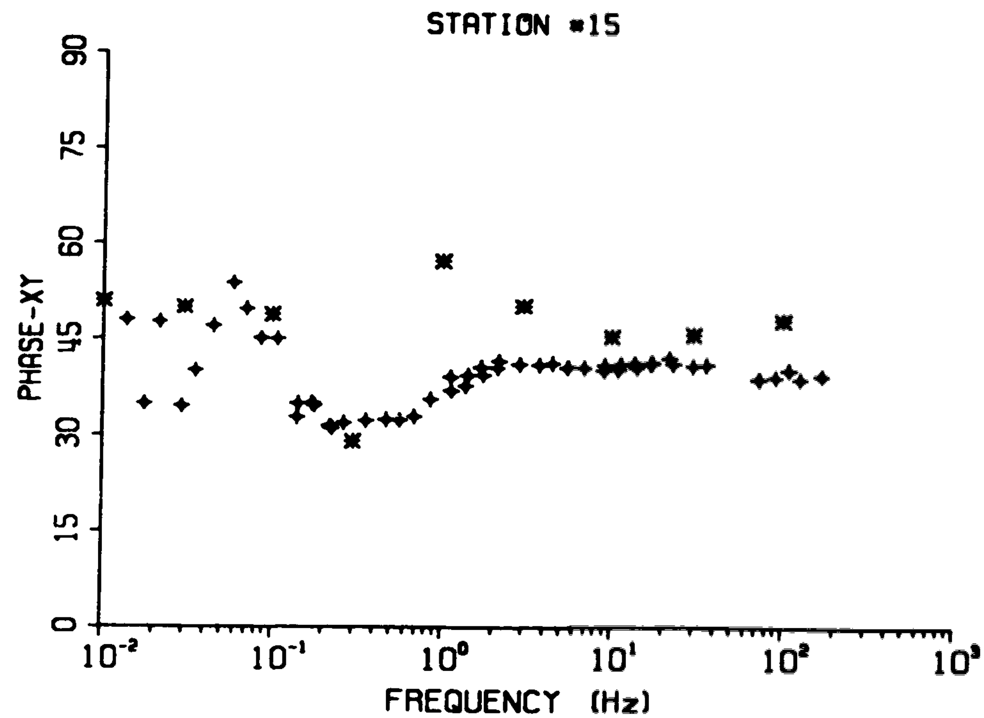
STATION *15
PHASE-XY
0
15
30
45
60
75
90
FREQUENCY (Hz)

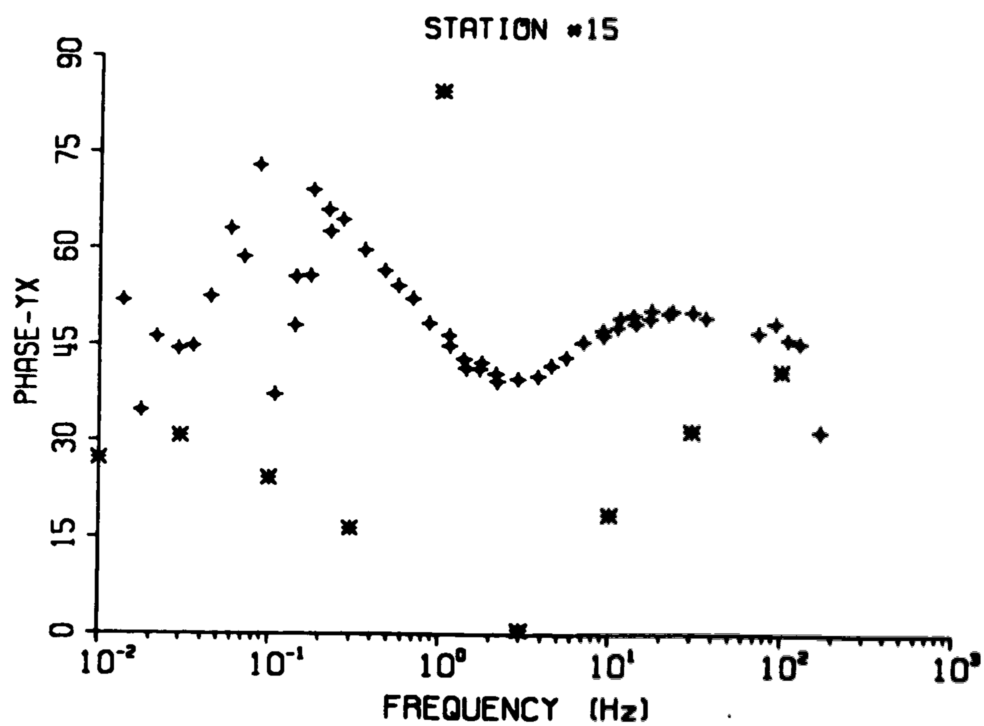
STATION *15
PHASE-YX
0
15
30
45
60
75
90
FREQUENCY (Hz)

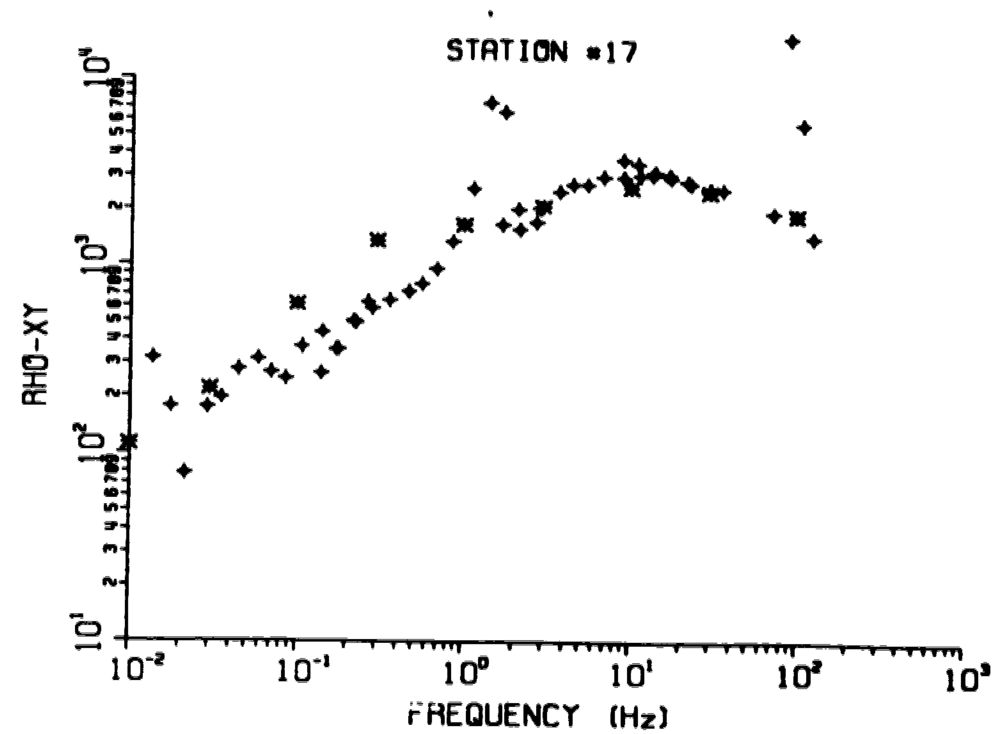
STATION #17
RHO-XY
FREQUENCY (Hz)

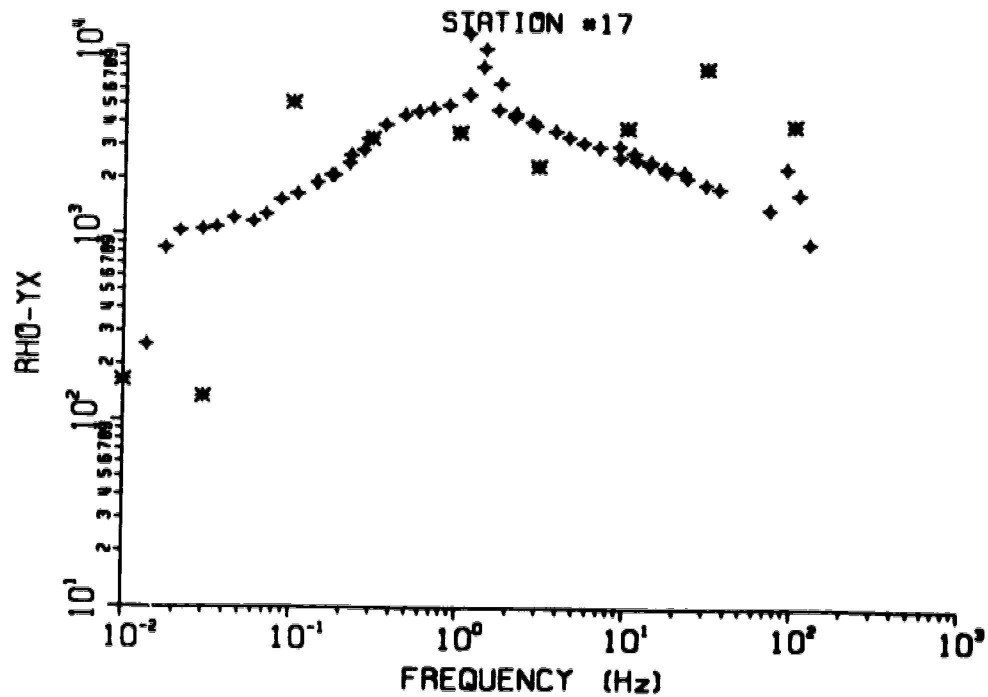
STATION #17
RHO-YX
FREQUENCY (Hz)

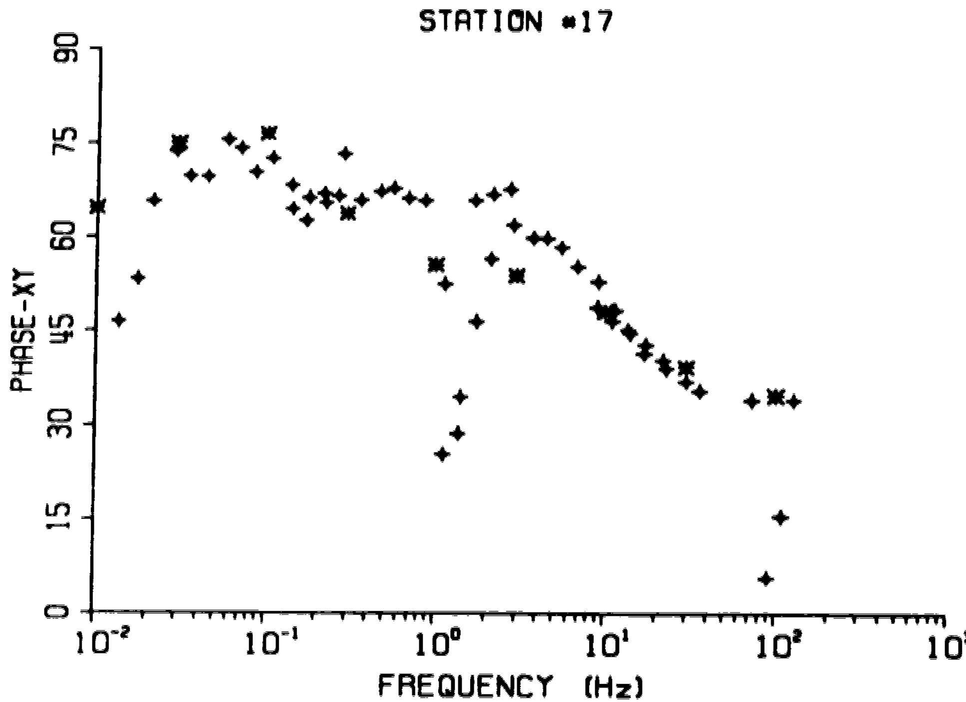
STATION *17
PHASE-XY
0
15
30
45
60
75
90
10^{-2}
10^{-1}
10^{0}
10^{1}
10^{2}
10^{3}
FREQUENCY (Hz)

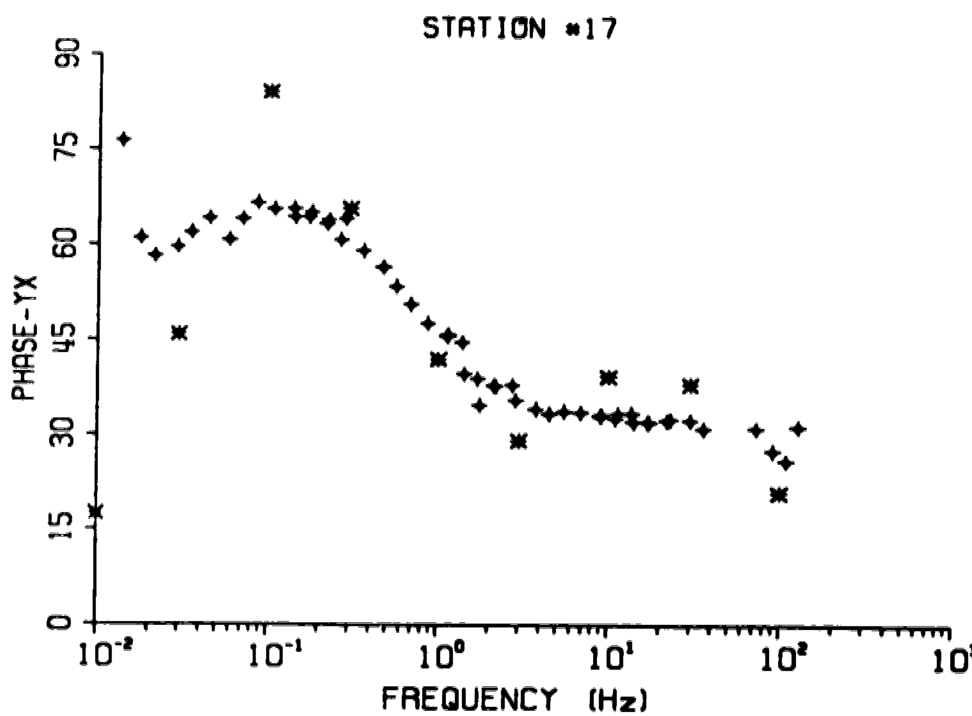
STATION *17
PHASE-YX
0
15
30
45
60
75
90
10^{-2}
10^{-1}
10^{0}
10^{1}
10^{2}
10^{3}
FREQUENCY (Hz)

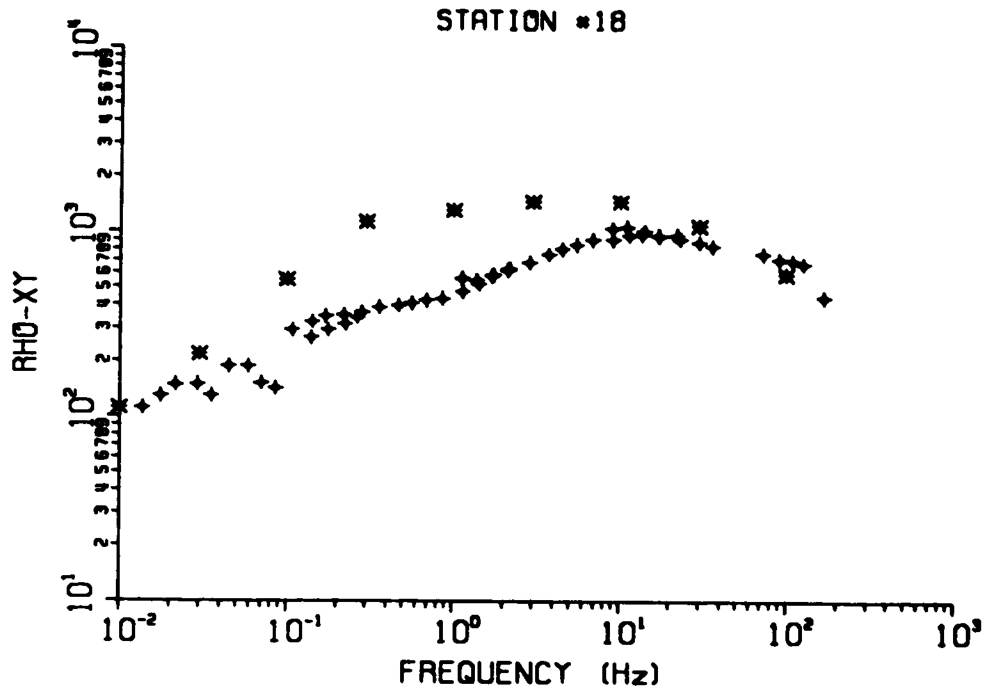
STATION *18
RHO-XY
FREQUENCY (Hz)

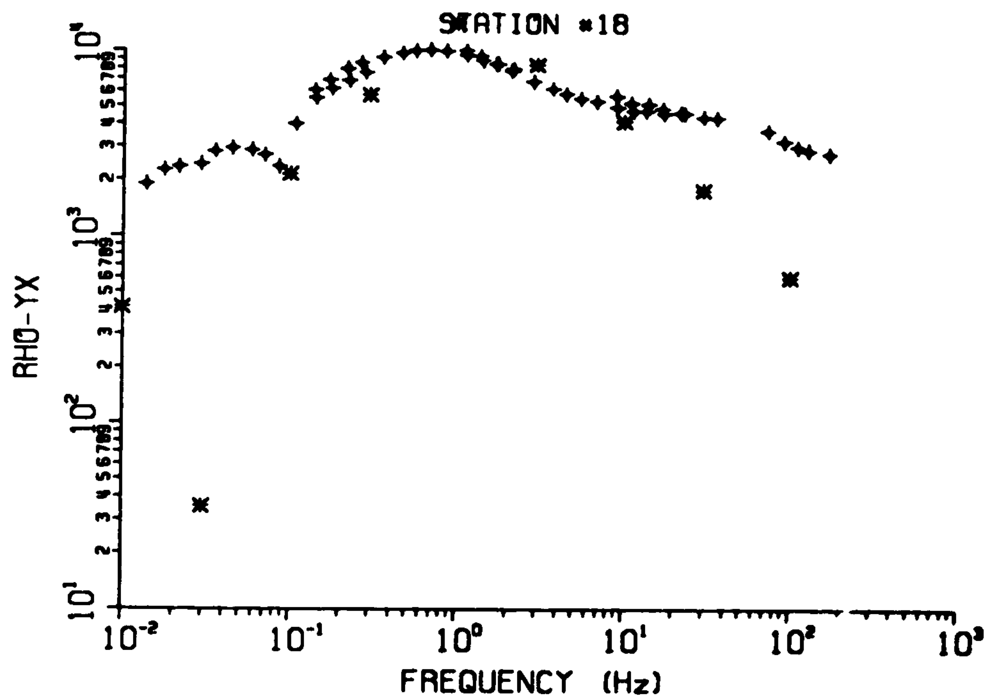
STATION *18
RHO-YX
FREQUENCY (Hz)

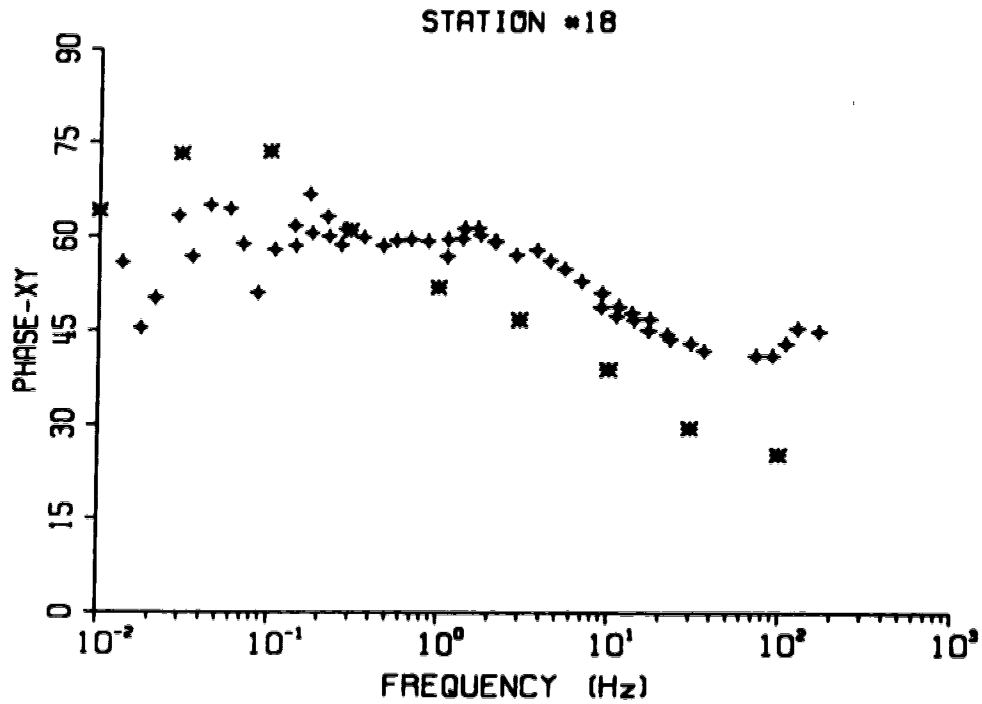
STATION #18
PHASE-XY
90
75
60
45
30
15
0
10^{-2}
10^{-1}
10^{0}
10^{1}
10^{2}
10^{3}
FREQUENCY (Hz)

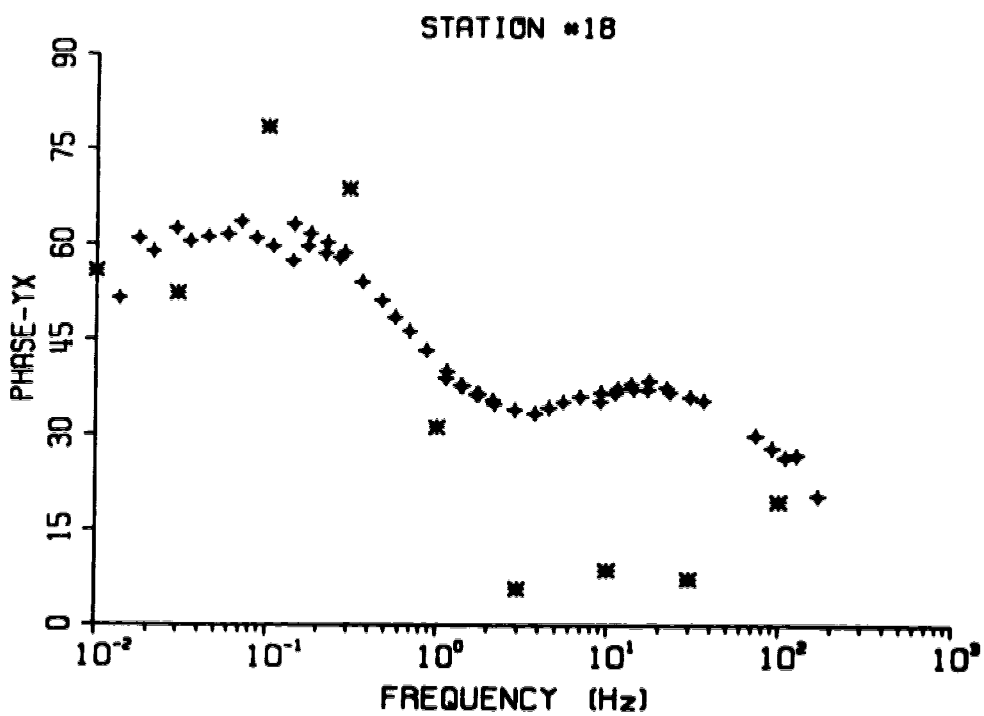
STATION #18
PHASE-YX
90
75
60
45
30
15
0
10^{-2}
10^{-1}
10^{0}
10^{1}
10^{2}
10^{3}
FREQUENCY (Hz)

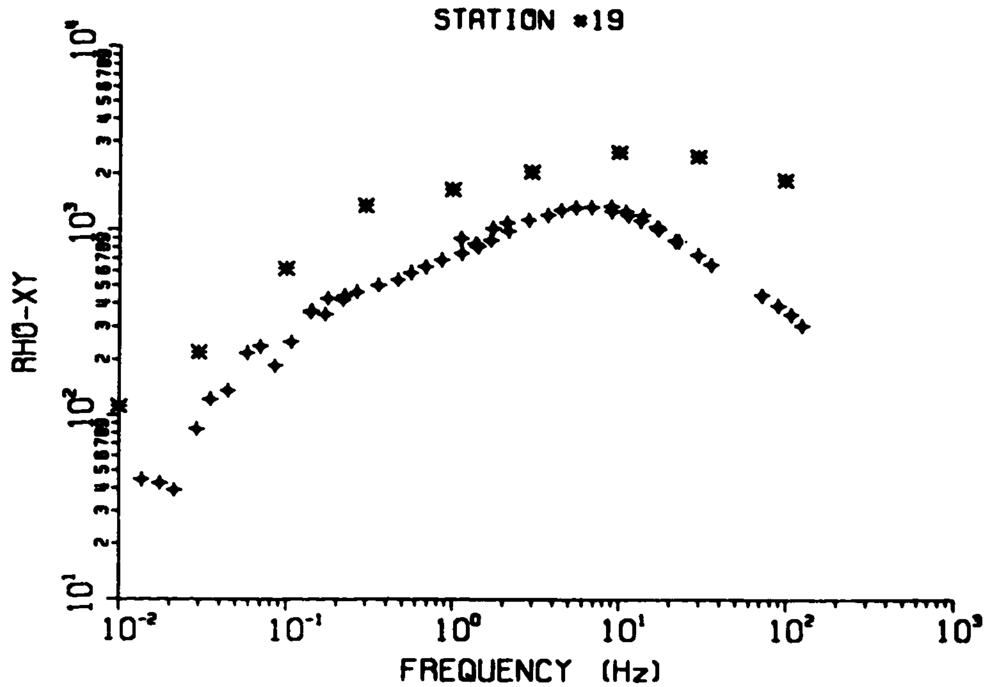
STATION *19
RHO-XY
FREQUENCY (Hz)

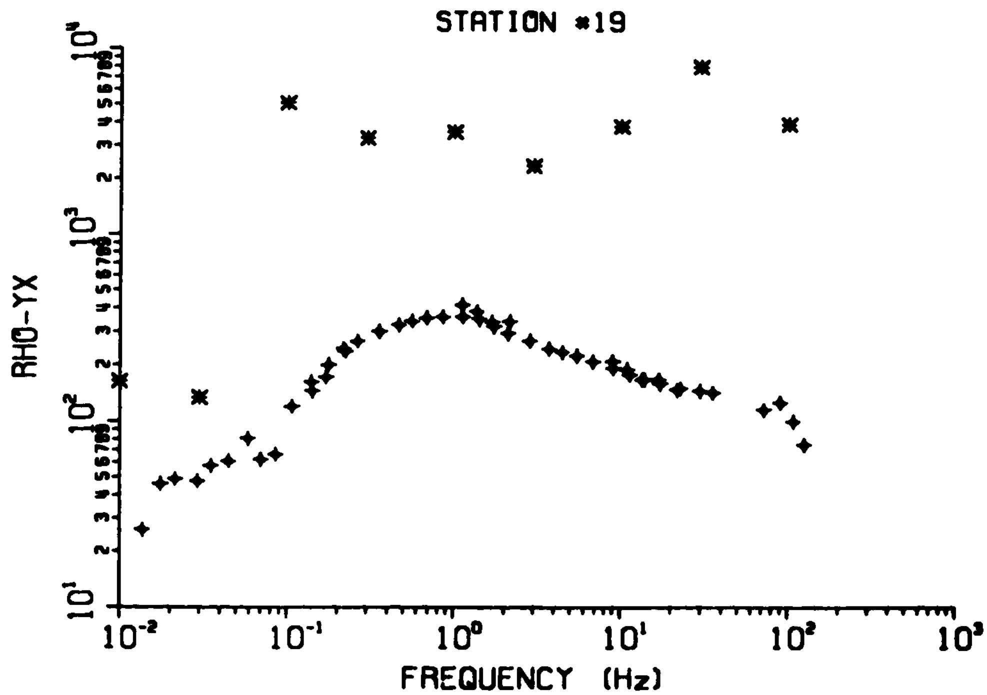
STATION *19
RHO-YX
FREQUENCY (Hz)

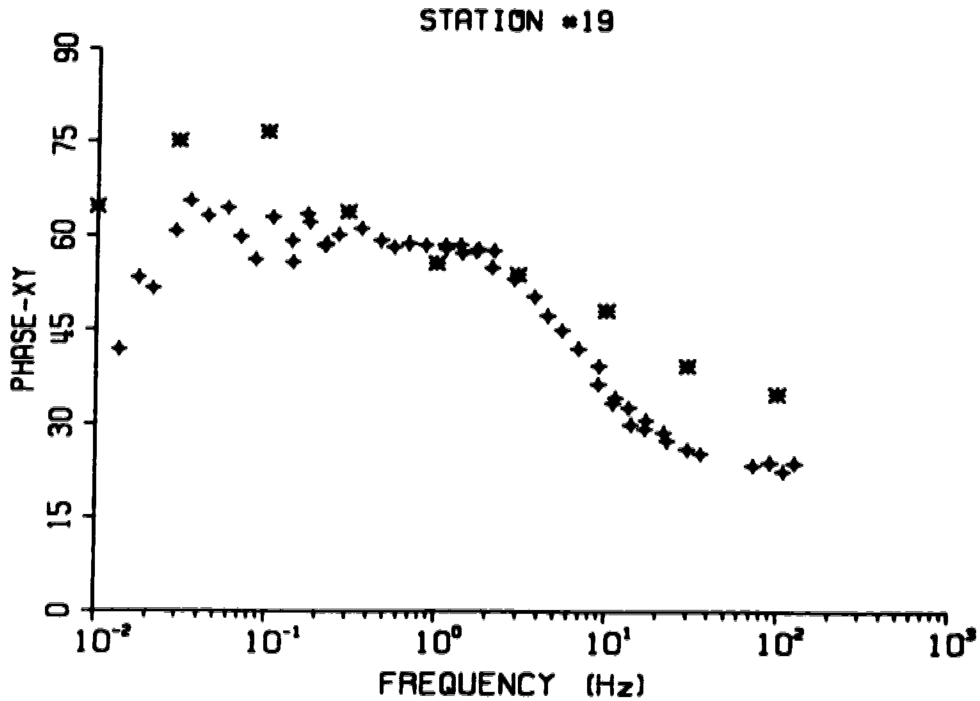
STATION #19
PHASE-XY
0
15
30
45
60
75
90
10^{-2}
10^{-1}
10^{0}
10^{1}
10^{2}
10^{3}
FREQUENCY (Hz)

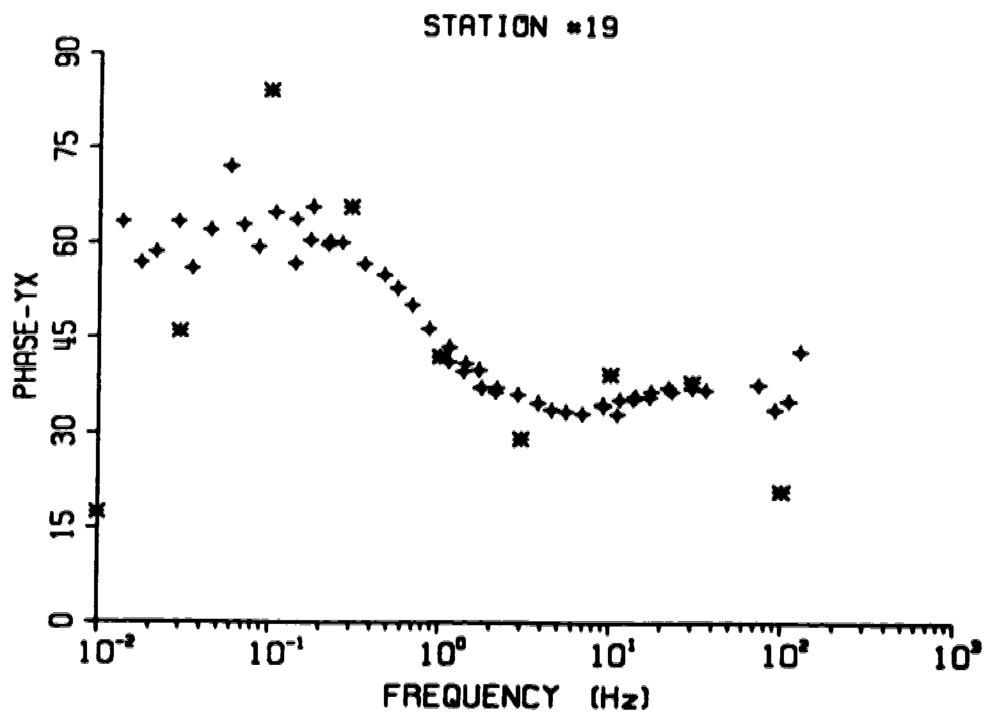
STATION #19
PHASE-YX
0
15
30
45
60
75
90
10^{-2}
10^{-1}
10^{0}
10^{1}
10^{2}
10^{3}
FREQUENCY (Hz)

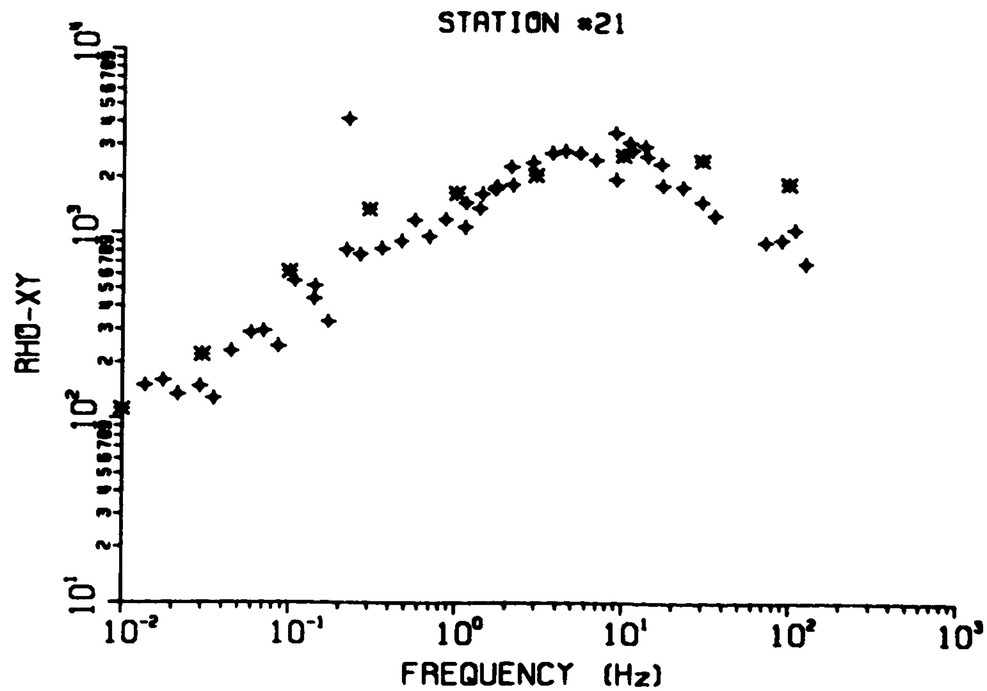
STATION *21
RHO-XY
FREQUENCY (Hz)

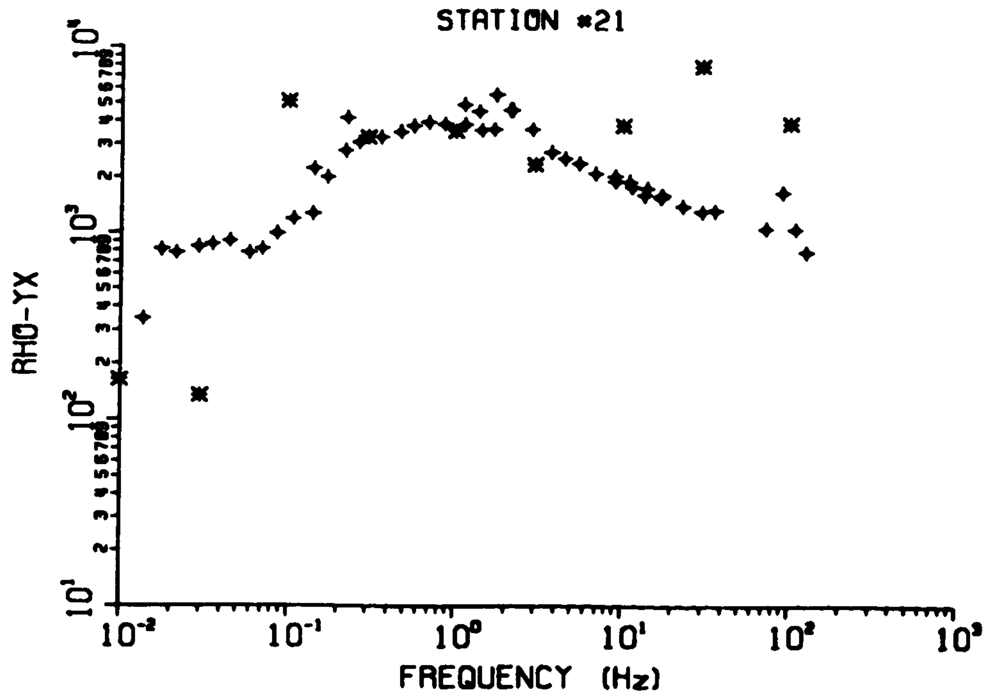
STATION *21
RHO-YX
FREQUENCY (Hz)

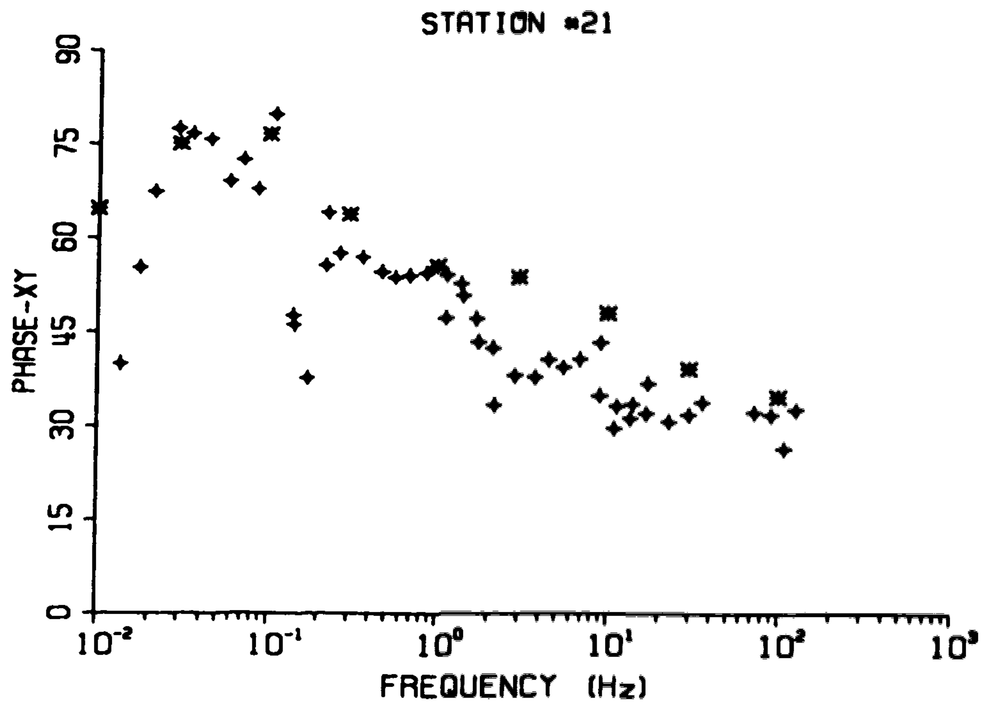
STATION *21
PHASE-XY
FREQUENCY (Hz)

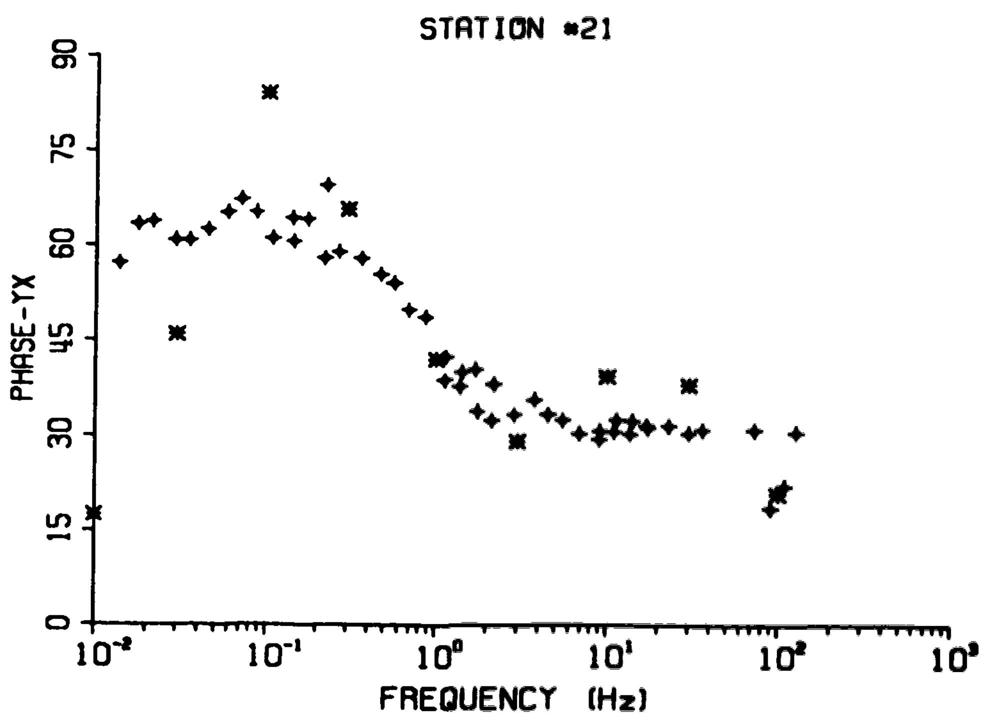
STATION *21
PHASE-YX
FREQUENCY (Hz)

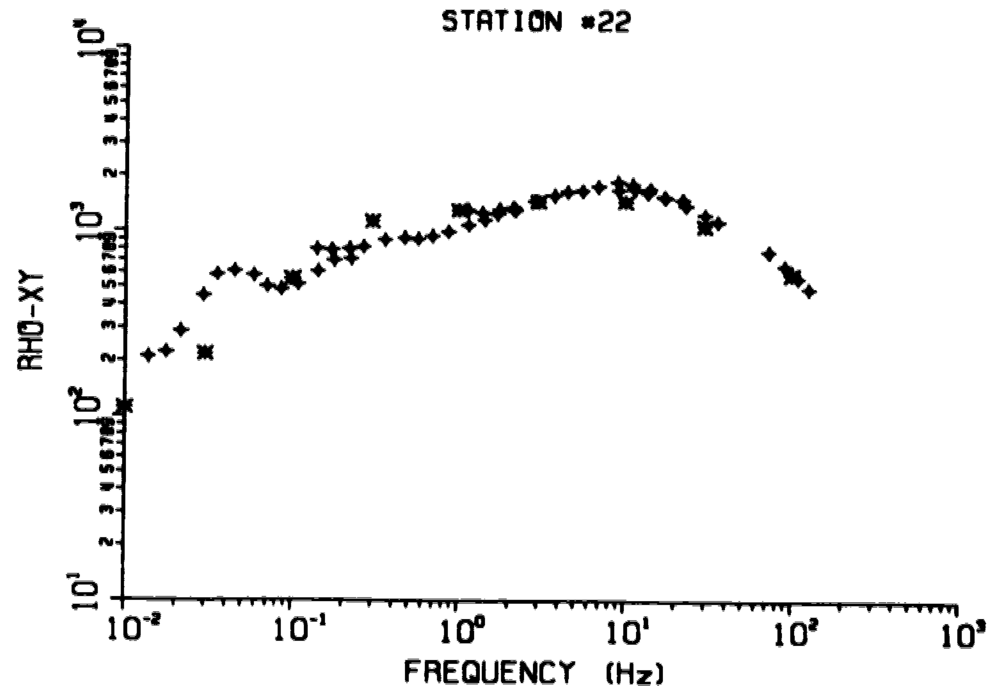
STATION *22
RHO-XY
FREQUENCY (Hz)

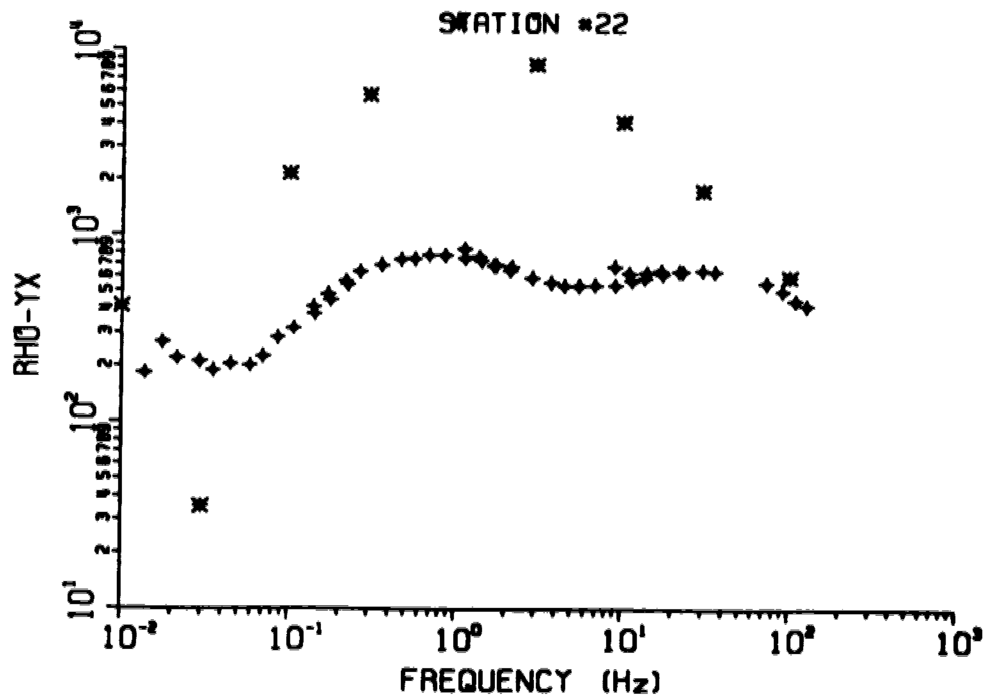
STATION *22
RHO-YX
FREQUENCY (Hz)

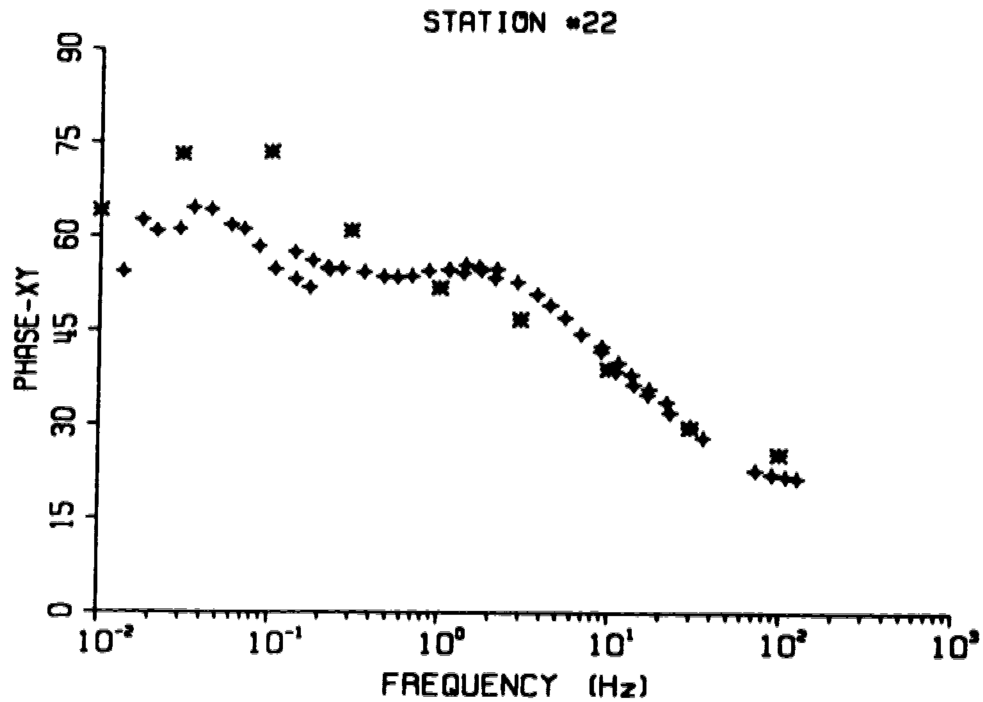
STATION #22
PHASE-XY
0
15
30
45
60
75
90
FREQUENCY (Hz)

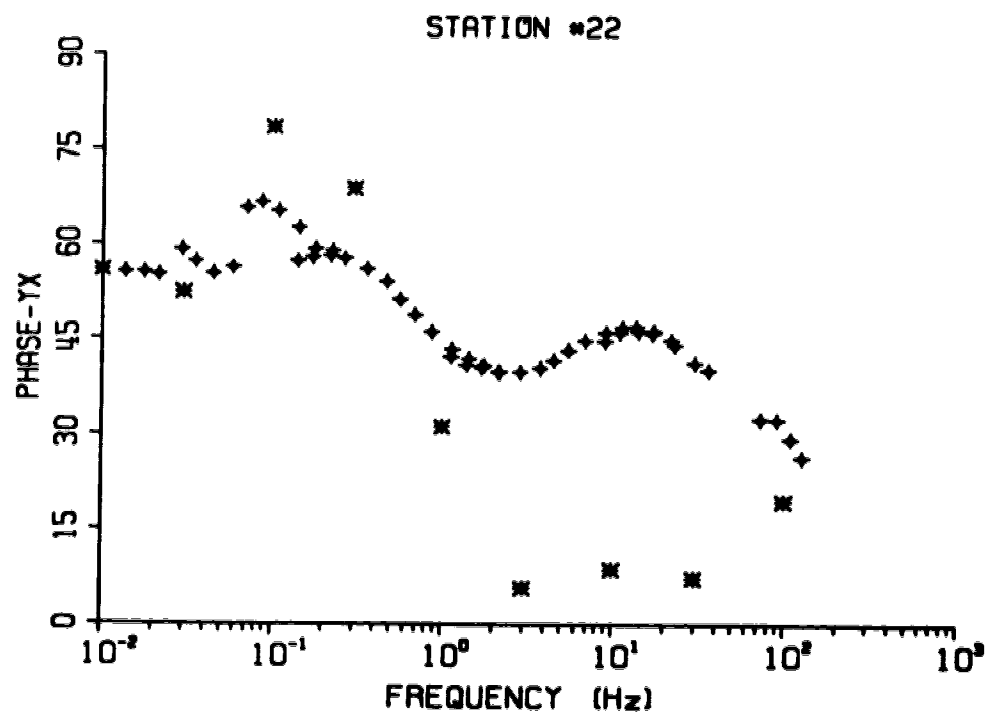
STATION #22
PHASE-YX
0
15
30
45
60
75
90
FREQUENCY (Hz)

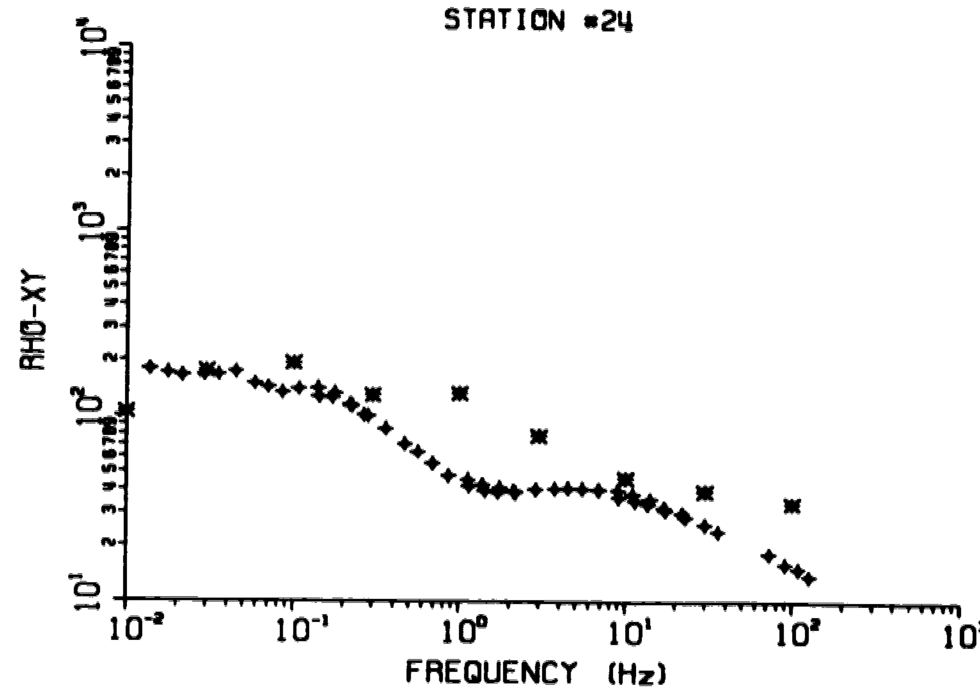
STATION #24
RHO-XY
FREQUENCY (Hz)

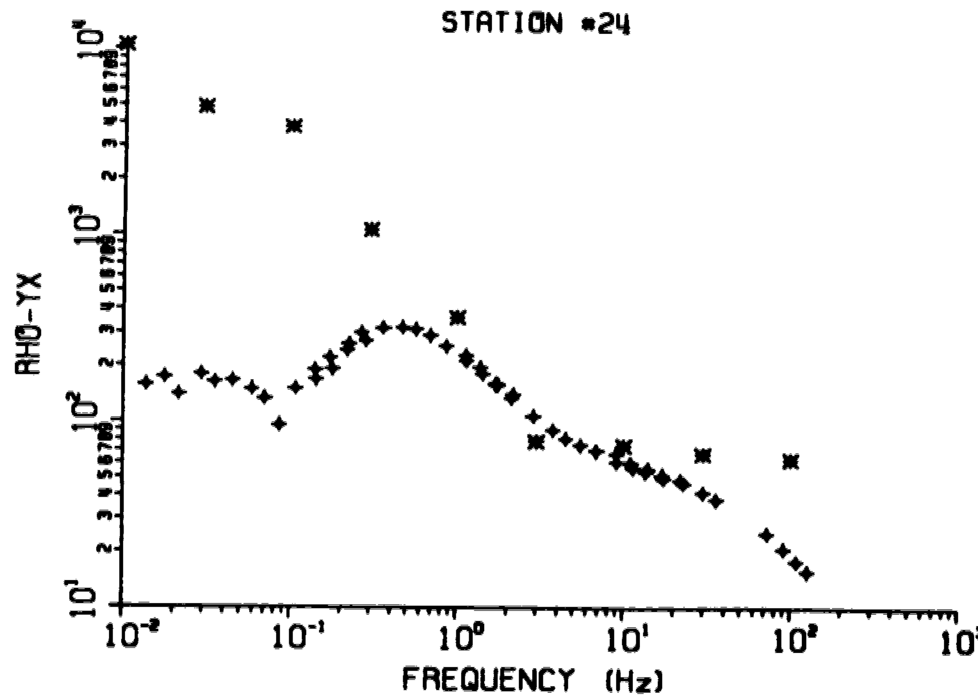
STATION #24
RHO-YX
FREQUENCY (Hz)

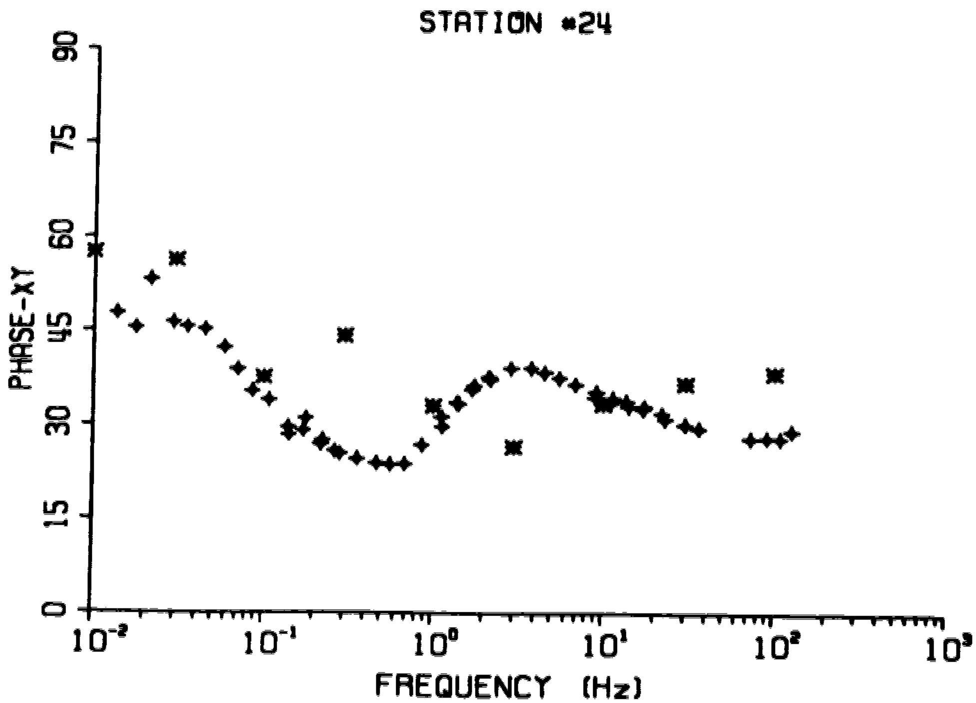
STATION *24
PHASE-XY
FREQUENCY (Hz)

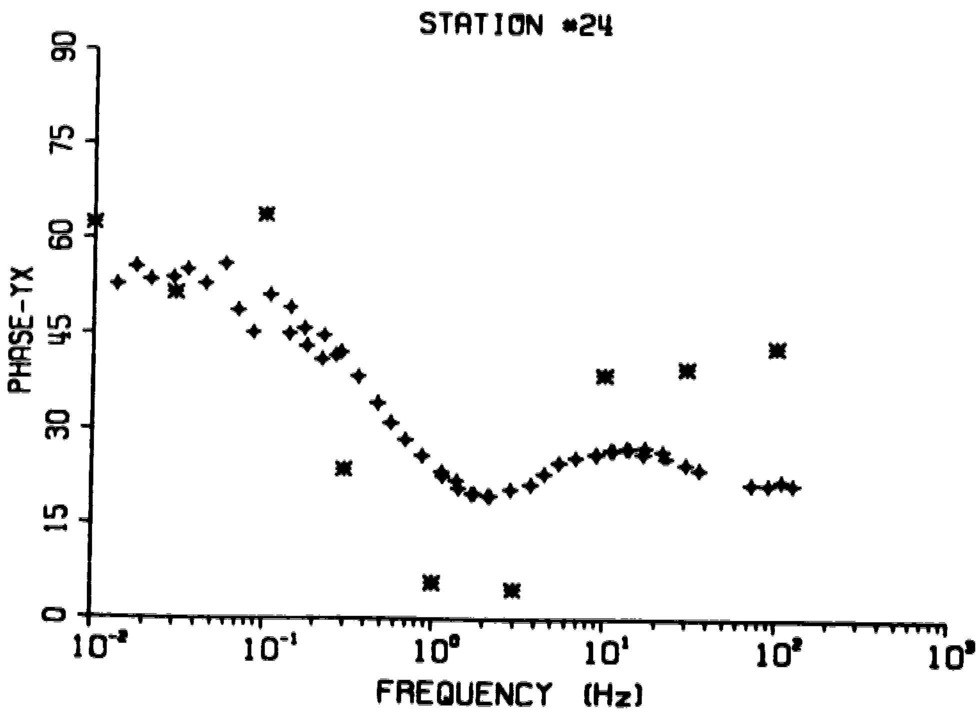
STATION *24
PHASE-YX
FREQUENCY (Hz)

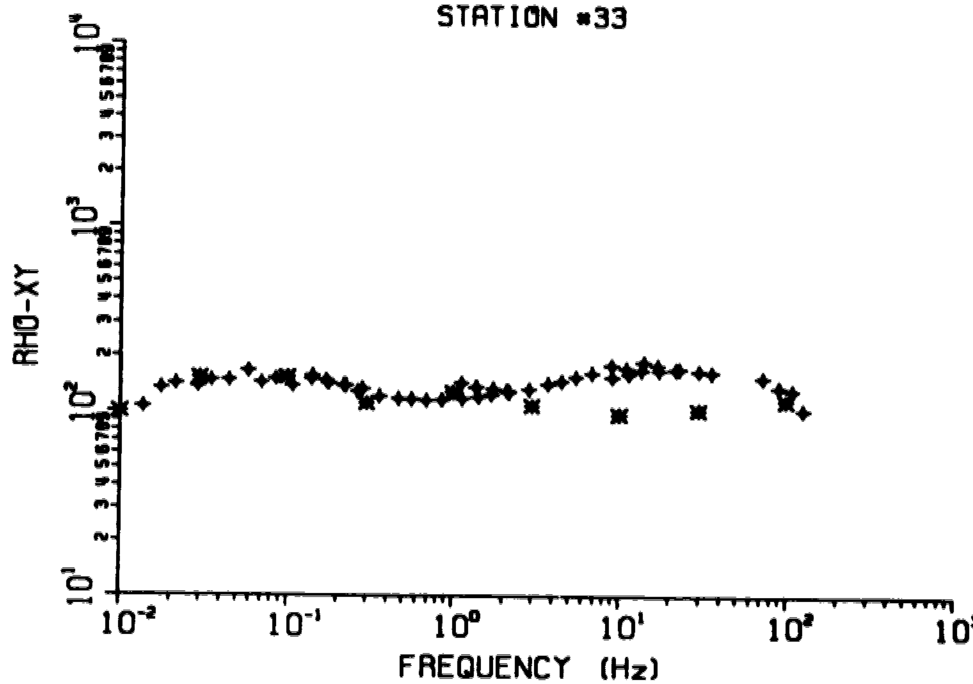
STATION #33
RHO-XY
FREQUENCY (Hz)
10^{1}
10^{2}
10^{3}
10^{4}
10^{-2}
10^{-1}
10^{0}
10^{1}
10^{2}
10^{3}

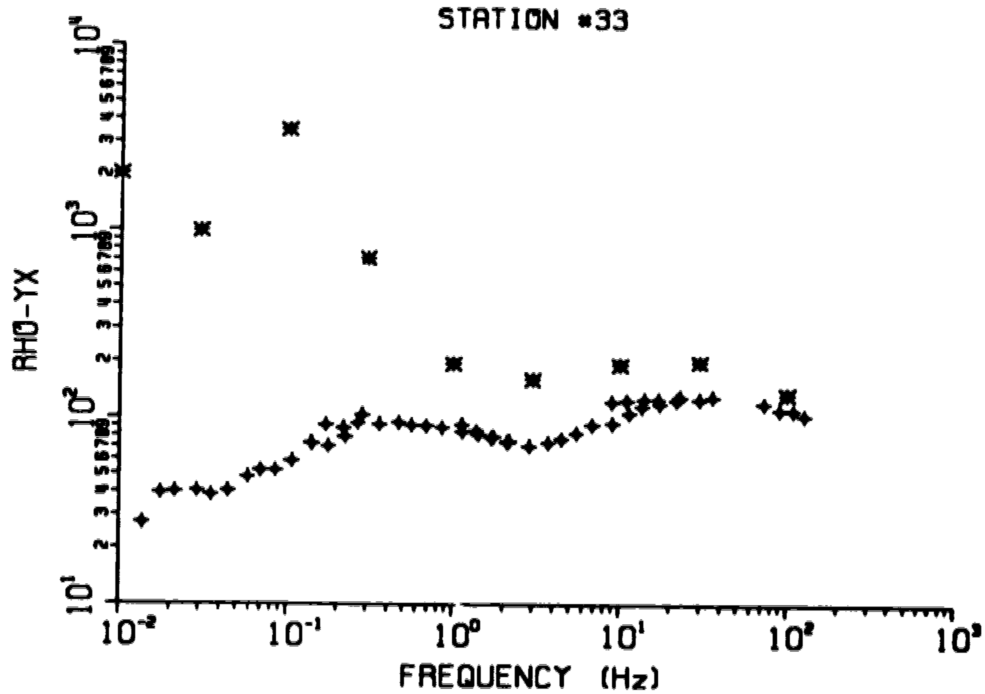
STATION #33
RHO-YX
FREQUENCY (Hz)
10^{1}
10^{2}
10^{3}
10^{4}
10^{-2}
10^{-1}
10^{0}
10^{1}
10^{2}
10^{3}

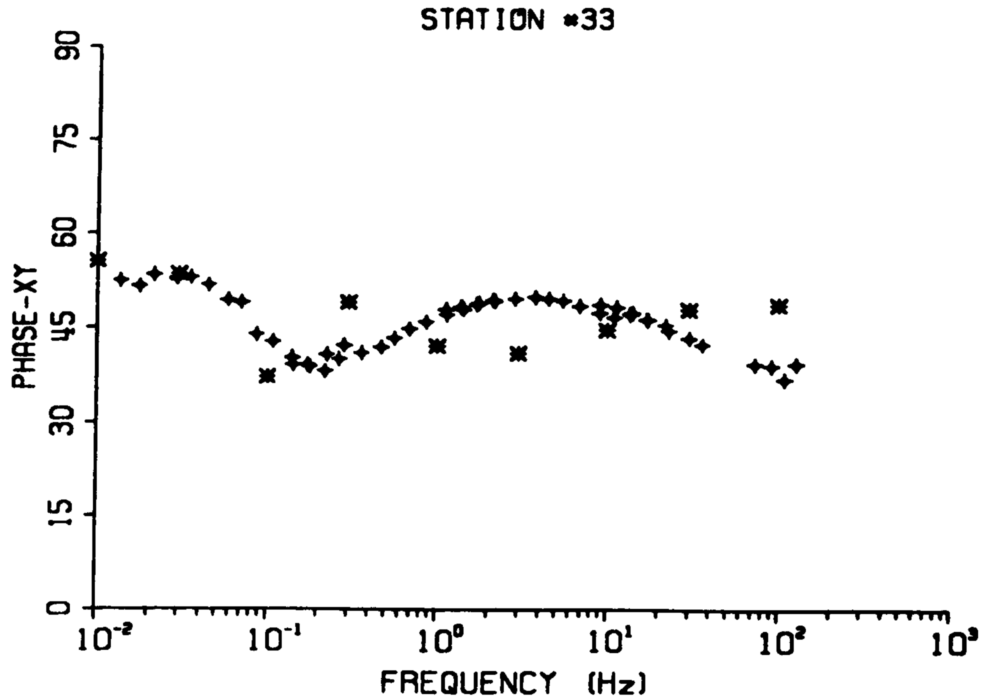
STATION *33
PHASE-XY
0
15
30
45
60
75
90
10^{-2}
10^{-1}
10^{0}
10^{1}
10^{2}
10^{3}
FREQUENCY (Hz)

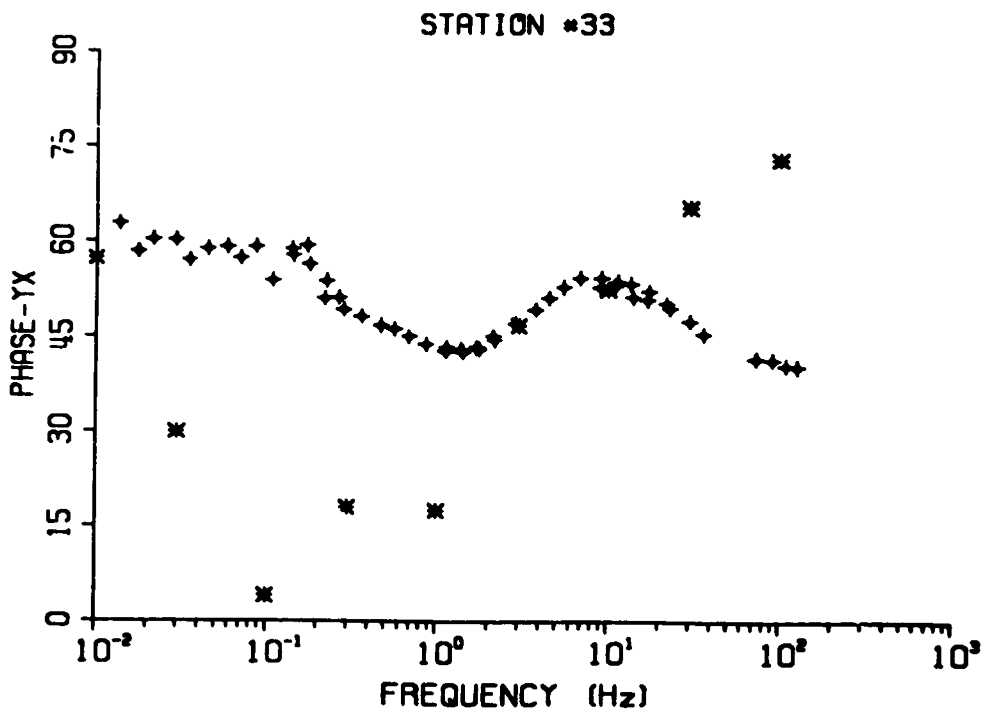
STATION *33
PHASE-YX
0
15
30
45
60
75
90
10^{-2}
10^{-1}
10^{0}
10^{1}
10^{2}
10^{3}
FREQUENCY (Hz)

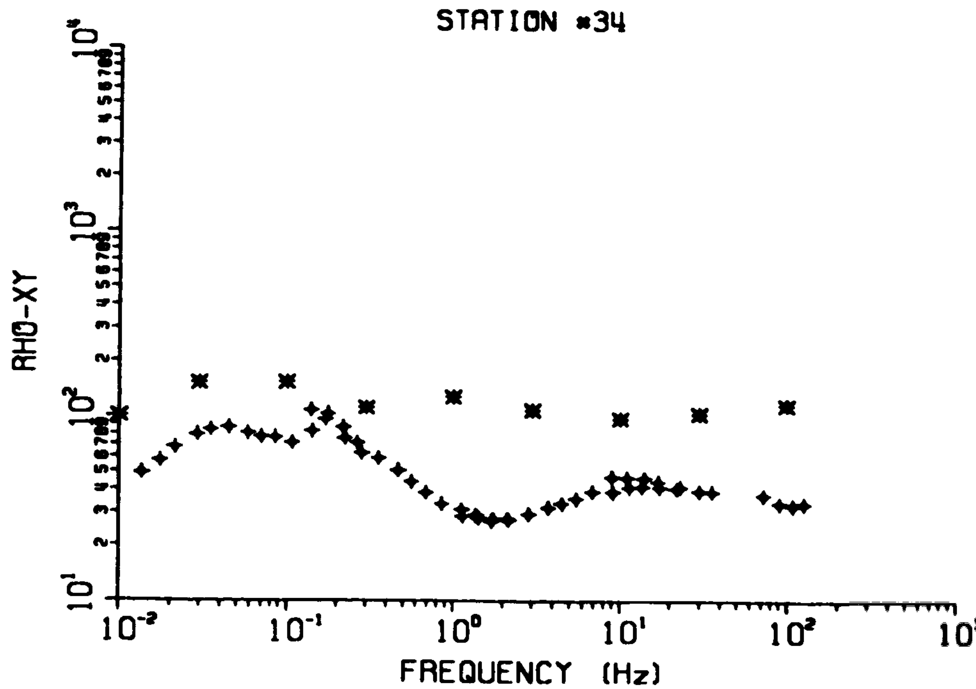
STATION *34
RHO-XY
FREQUENCY (Hz)

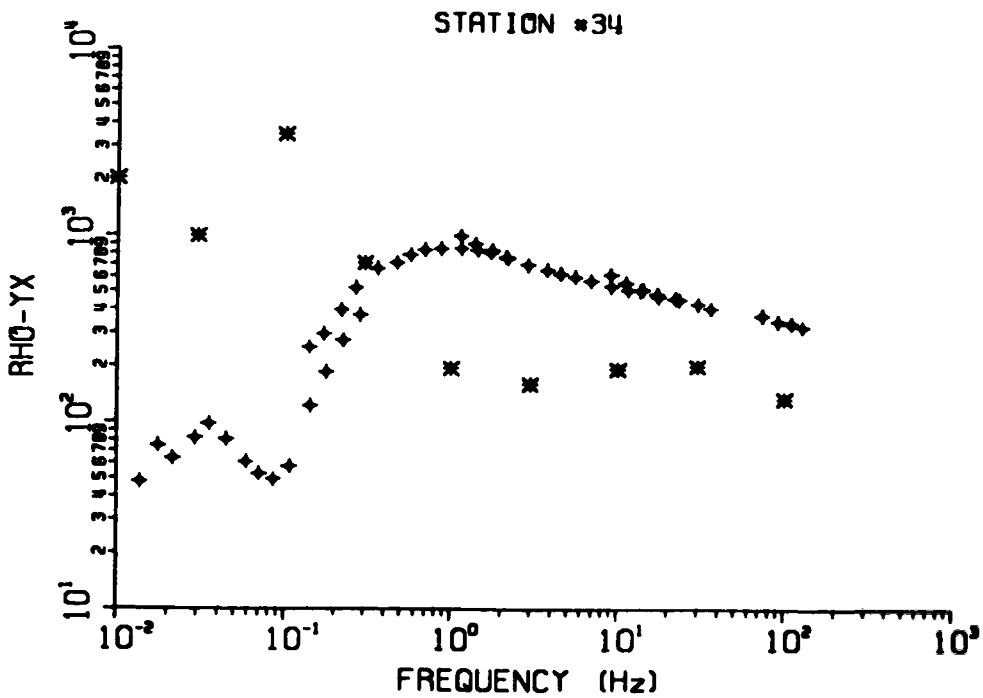
STATION *34
RHO-YX
FREQUENCY (Hz)

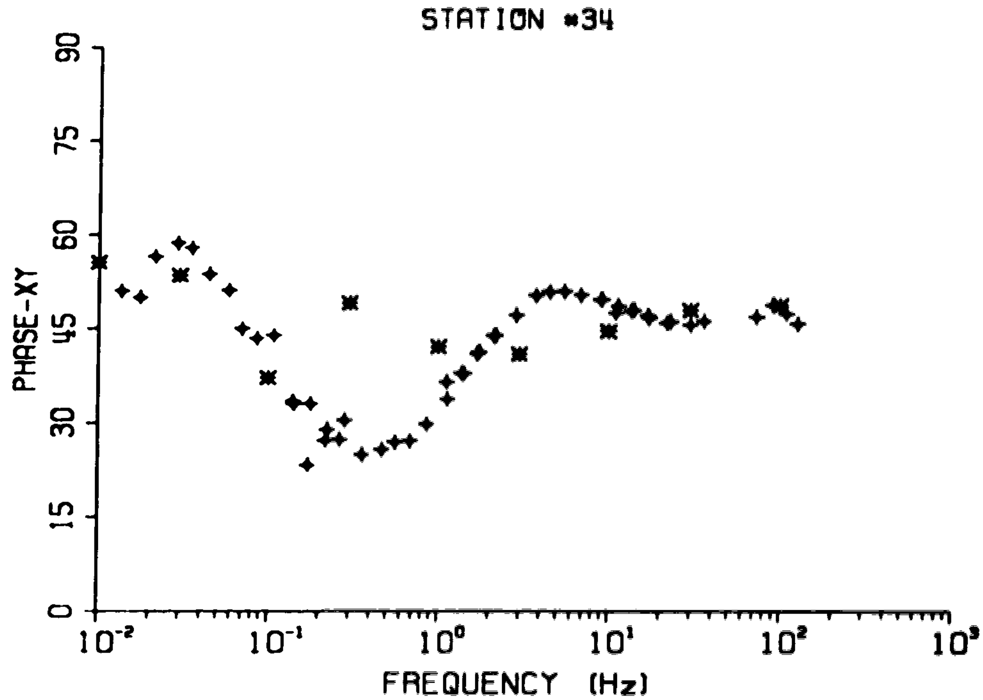

STATION #34
PHASE-XY
FREQUENCY (Hz)

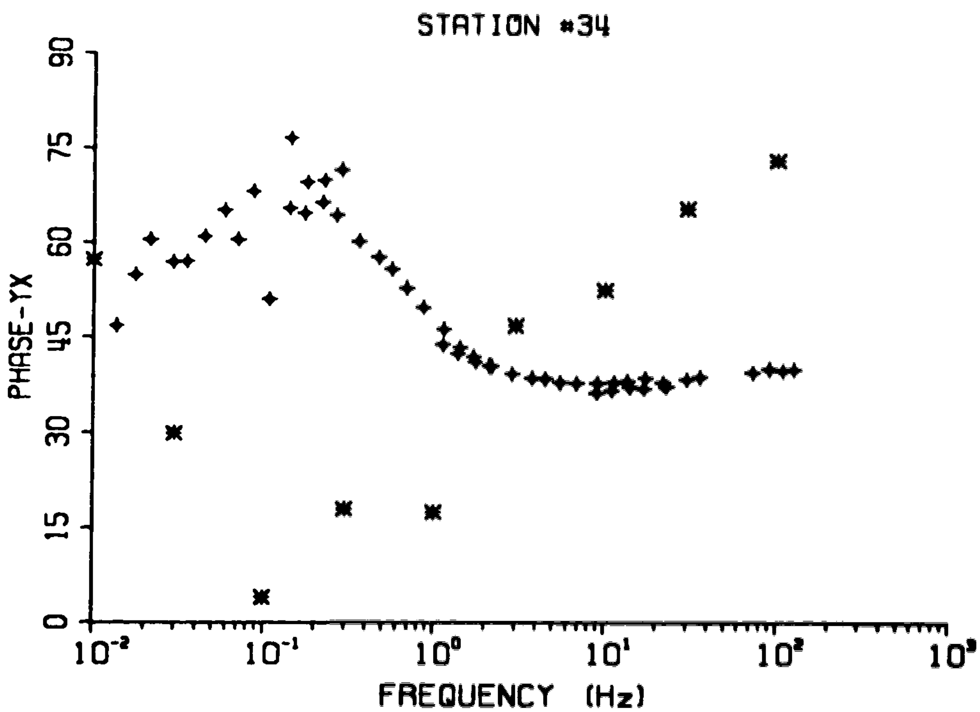

STATION #34
PHASE-YX
FREQUENCY (Hz)

END

26-08-96

FIN